

**Fundamental Understanding and
Modelling of Turbulent Premixed
Flame Wall Interaction:
A Direct Numerical Simulation
Based Analysis**



Jiawei Lai

Mechanical and Systems Engineering
Newcastle University

This dissertation is submitted for the degree of
Doctor of Philosophy

July 2017

To my grandfather. 献给阿公。

Declaration

I hereby declare that this thesis is my own work and that I have correctly acknowledge the work of others. This submission is in accordance with Newcastle University and School of Engineering guidance on good academic conduct. I certify that no part of the material offered has been previously submitted by me for a degree or other qualification in this or any other University. I confirm that the word length is within the prescribed range as advised by my school and faculty. I confirm that this thesis does not contain collaborative work. This thesis contains approximately 93,855 words, 107 figures and 4 tables.

Jiawei Lai

July 2017

Acknowledgements

Firstly, I would like to convey sincere gratitude to my supervisor, Prof Nilanjan Chakraborty for his unwavering support, guidance and inspiration. Nilan is the best supervisor I have ever seen. I am grateful to Dr David Swailes and Prof Markus Klein for their encouragement and help during the PhD period. I would like to express my sincere thanks to Prof R. S. Cant, Dr Daniel Wacks, and Dr Tamir Brosh for their help in my research. I would like to thank Dr Andrew Aspden for providing the insight discussion on the thesis. I would like to thank Mr Ian Pitcher and Mr David Wall for their help and support.

Thanks to Newcastle University for the Oversea Research Scholarship and the School of Engineering for the financial support throughout this PhD. Additionally, I am grateful to the Combustion Institute for the travel grants, which have allowed me to attend and present my works.

I would like to thank Dr Yuan Gao, Dr Dipal Patel, Sahin Yigit, Bruno Machado, Chris Stafford, Lizhong Yi, Sam Wood, Gulcan Ozel Erol, Bill Papas, and Ilias Konstantinou for their pleasant company in the office, numerous discussions and cups of coffee throughout this PhD. Outside the lab, I would like to thank Dr Boru Jia, Dr Pengfei Duan, and Xialin Xie for their company in the final stage of my PhD.

I am grateful to my family, my grandmother, parents, brothers and sisters for great encouragement and supports.

Finally, my sincere thanks go to my wife Xin Shi for her insights, patience and motivations.

Abstract

This thesis focuses on fundamental physical understanding and modelling of turbulent premixed flame-wall interaction by using Direct Numerical Simulation (DNS) data. Three-dimensional compressible simulations of turbulent premixed flame-wall interaction have been carried out for head-on quenching (HOQ) of statistically planar flames by an isothermal inert wall and also for oblique quenching of a V-flame by two isothermal inert sidewalls (top and bottom walls). Simulations have been conducted for different values of Damköhler, Karlovitz and global Lewis numbers (i.e. Da , Ka and Le), and the chemical mechanism is simplified by a single-step Arrhenius type irreversible chemistry for the sake of computational economy in the interest of a detailed parametric analysis. The flame-wall interaction has been characterised in terms of wall heat flux magnitude and wall Peclet number (i.e. normalised wall normal distance). It has been found that the maximum wall heat flux magnitude decreases, whereas the minimum wall Peclet number (which quantifies the flame quenching distance) increases with increasing Lewis number in the case of laminar head-on quenching of planar flames. However, the minimum wall Peclet number for $Le < 1.0$ turbulent premixed flames has been to be smaller than the corresponding laminar value, whereas the minimum Peclet number in the case of turbulent flames with $Le \geq 1.0$ remains comparable to the corresponding laminar values. It has been found that heat loss through the wall and flame quenching in the vicinity of the wall significantly affect dilatation rate distribution in the near-wall region, and has influences on the behaviours of the invariants of the velocity gradient tensor, which in turn influences statistical behaviours of flow topology and enstrophy distribution in the near-wall region. The statistical behaviours of vorticity and enstrophy transports in the near-wall region and the distribution of flow topologies within the flame, and their evolution with flame quenching have been analysed in detail using DNS data, and important fundamental physical insights have been gained regarding the flame-quenching processes associated with the flame-wall interaction.

The DNS data has been explicitly Reynolds averaged to analyse the statistical behaviours of turbulent kinetic energy, scalar variance, turbulent scalar flux, Flame

Surface Density (FSD) and scalar dissipation rate (SDR) and their transport in the near-wall regions. It has been found that existing closures of these quantities do not adequately capture their near-wall behaviours and in this thesis modifications to the existing closures have been proposed based on a-priori DNS analysis to account for the wall effects in such a manner that the modified closures perform well both near to and away from the wall. Furthermore, it has been found both FSD and SDR based conventional reaction rate closures do not adequately capture the mean reaction rate close to the wall, and the current analysis offers alternative reaction rate closure expressions both in the contexts of FSD and SDR based modelling approaches. Thus, the current thesis offers a unified modelling strategy for premixed flame-wall interaction in the context of Reynolds Averaged Navier-Stokes (RANS) simulations for the very first time.

Finally, in order to validate the findings based on simple chemistry DNS, a limited number of DNS calculations of head-on quenching has been conducted using a multi-step chemical mechanism for methane-air combustion. It has been found that the statistics of wall heat flux magnitude and wall Peclet number obtained from detailed chemistry simulations are in good qualitative and quantitative agreements with the corresponding results from simple chemistry DNS. However, detailed chemistry DNS reveals the presence of heat release at the wall during early stages of flame quenching, whereas heat release remains identically zero at the wall for simple chemistry DNS. In spite of this difference, an FSD based reaction rate closure which was proposed based on a-priori analysis of simple chemistry DNS has been found to work also for detailed chemistry DNS data without any modification. This provides the confidence in the models which have been proposed based on the analysis of simple chemistry DNS data.

Table of contents

List of figures	xvii
List of tables	xxvii
Nomenclature	xxix
1 Introduction	1
1.1 Motivation	2
1.1.1 A brief history of combustion	2
1.1.2 Modern combustion and its problems	4
1.1.3 Background of flame-wall interaction	5
1.2 Turbulence	8
1.3 Direct numerical simulation	11
1.3.1 Simulation tools	11
1.3.2 Direct numerical simulations of flame-wall interaction	12
1.4 Objectives of this analysis	13
1.5 Thesis outline	14
2 Mathematical Background	17
2.1 Problem description	17
2.2 Governing equations	19
2.3 Thermochemistry	21
2.4 Non-dimensional numbers	23
2.5 Non-dimensional number in the flame-wall interaction	25
2.6 Investigation of turbulence	26
2.6.1 Vorticity and entrophy transport	27
2.6.2 Flow topology	28
2.7 Favre-averaged approach to numerical simulations of turbulent combustion	30
2.7.1 Turbulent kinetic energy transport	31

2.7.2	RANS modelling of turbulent combustion	32
2.7.3	Flame surface density transport	33
2.7.4	Scalar dissipation rate transport	34
2.7.5	Turbulent scalar flux transport	35
2.7.6	Reaction progress variable variance transport	36
3	Literature Review	39
3.1	Premixed flames	39
3.1.1	Laminar premixed flames	39
3.1.2	Turbulent premixed flames	40
3.1.3	Combustion regimes	41
3.2	Modelling of turbulent combustion	43
3.2.1	Flamelet approaches	43
3.2.2	Progress variable variance	45
3.3	Flame surface density	45
3.4	Scalar dissipation rate	47
3.5	Turbulent scalar flux	48
3.6	Flame-wall interaction configurations	48
3.7	Combustion models for flame-wall interaction	51
3.8	Vorticity and enstrophy topology	52
3.9	Flow topology	53
4	Numerical Implementation	57
4.1	Spatial resolution and physical scales	57
4.2	Initialisation of turbulence	58
4.3	Navier Stokes Characteristic Boundary Conditions	60
4.3.1	Inlet boundary condition	64
4.3.2	Partial non-reflecting outlet boundary condition	64
4.3.3	Wall boundary condition	66
4.4	Implementation of HOQ with simplified chemistry	66
4.5	Implementation of sidewall quenching of turbulent V-flames	68
4.6	Implementation of HOQ with a detailed chemical mechanism	69
5	Results & Discussion 1: A Physical Insight	71
5.1	Results and discussion outlines	72
5.2	Global flame behaviour: wall heat flux and Peclet number and their Lewis number dependence	73

5.2.1	Laminar flame	73
5.2.2	Turbulent flame	74
5.3	Statistical behaviour of vorticity and enstrophy transport	81
5.3.1	Flame turbulence interaction and vorticity distribution	81
5.3.2	Statistical behaviour of the magnitude of vorticity components	82
5.3.3	Statistical behaviour of vorticity transport	84
5.3.4	Statistical behaviour of the enstrophy transport	89
5.3.5	Summary of the key results	96
5.4	Flow topology distribution	97
5.4.1	Distributions of P , Q and R	97
5.4.2	Flow topology distribution	108
5.4.3	Influence of flow topology on the wall heat flux	120
5.4.4	Summary of the key results	122
5.5	Statistical analysis and modelling of the turbulent kinetic energy transport	125
5.5.1	Distributions of turbulent kinetic energy \tilde{k} and its dissipation rate $\tilde{\epsilon}$	125
5.5.2	Statistical behaviour of the turbulent kinetic energy transport	128
5.5.3	Modelling of the mean velocity gradient term T_{K1}	129
5.5.4	Modelling of the mean pressure gradient term T_{K2}	133
5.5.5	Modelling of the pressure dilatation term T_{K3}	135
5.5.6	Modelling of the molecular diffusion and dissipation contribution T_{K4}	139
5.5.7	Modelling of the pressure transport term T_{K5}	143
5.5.8	Modelling of the turbulent transport term T_{K6}	147
5.5.9	Summary of the key results	151
5.6	Statistical analysis and modelling of the scalar variance transport	154
5.6.1	Statistical Behaviour of the Variance $\widetilde{c''^2}$ Transport	154
5.6.2	Modelling of Turbulent Transport of Scalar Variances	155
5.6.3	Algebraic Closure of Turbulent Scalar Flux $\overline{\rho u_i'' c''}$	160
5.6.4	Modelling of Reaction Rate Term T_{3v}	162
5.6.5	Summary of the key results	164
5.6.6	Chapter closing remarks	164
6	Results & Discussion 2: The Combustion Modelling	167
6.1	Statistical analysis and modelling of the scalar dissipation rate transport	167
6.1.1	Modelling of mean reaction rate closure and its Lewis number dependence	168

6.1.2	Statistical behaviour of the SDR transport	170
6.1.3	Algebraic closure of SDR	183
6.1.4	Modelling of turbulent transport term T_1	187
6.1.5	Modelling of density variation term T_2	193
6.1.6	Modelling of the turbulent scalar interaction term T_3	195
6.1.7	Modelling of the Combined Reaction Rate, Dissipation and Diffusivity Gradient Terms ($T_4 - D_2 + f(D)$)	206
6.1.8	Summary of the key results	210
6.2	Statistical analysis and modelling of flame surface density transport . .	211
6.2.1	Closure for the mean reaction rate $\bar{\omega}$	211
6.2.2	Modelling of the turbulent transport term T_{F1}	213
6.2.3	Modelling of the tangential strain rate term T_{F2}	215
6.2.4	Modelling of propagation and curvature terms $T_{F3} + T_{F4}$	217
6.2.5	Summary of the key results	221
6.3	Statistical analysis and modelling of turbulent scalar flux transport . .	222
6.3.1	Statistical behaviours of the terms in turbulent scalar flux transport equation	222
6.3.2	Modelling of the turbulent transport term T_{1c}	225
6.3.3	Modelling of the turbulent transport term ($T_{4c} + T_{5c}$)	229
6.3.4	Modelling of the molecular dissipation terms ($T_{6c} + T_{7c}$)	233
6.3.5	Modelling of the reaction rate velocity correlation term T_{8c}	235
6.3.6	Summary of the key results	238
6.4	Chapter closing remark	239
7	Results & Discussion 3: Oblique Quenching and Detailed Chemistry Simulations	241
7.1	Oblique quenching by isothermal inert walls	242
7.1.1	Heat flux and quenching distance	242
7.1.2	Flow topology analysis	245
7.1.3	Summary of the key results for the oblique quenching	247
7.2	Turbulent premixed methane-air flames using a detailed chemistry mechanism	249
7.2.1	Quenching characteristics	249
7.2.2	Modelling of the mean reaction rate closure	256
7.2.3	Summary of the key results for the detailed chemistry simulation	257

8	Conclusions & Future work	259
8.1	Conclusions	259
8.2	Future follow up	264
	References	267
	Appendix A List of Publications	283

List of figures



















1.1	Illustration of fire used by early human	2
1.2	Fireworks	3
1.3	World energy consumption	5
1.4	Illustration of Davy lamp	6
1.5	Metal gauze experiment in a tube filled with methane gases. (a) Ignite gas in one end. (b, c) The flame is created and propagates along the tube. (d) Insert a piece of metal gauze in the centre of the tube and repeat the same process. (e) The flame is quenched at the gauze.	7
1.6	Illustration of turbulence flame wall interaction	8
1.7	Pillars of Creation	9
1.8	A schematic diagram of turbulent energy spectrum	12
1.9	A flow chart of the stucture of current thesis	15
2.1	Description of computational domain: HOQ (Top), Side-wall quenching (Bottom).	18
2.2	Classification of $S1-S8$ topologies (UF = unstable focus, UN = unstable node, SF = stable focus, SN = stable node, S = saddle, C = compressing, ST = stretching) in the $Q-R$ plane with the lines r_{1a} , r_{1b} and r_2 dividing the topologies, and black daksed lines indicates $Q = R = 0$	29
3.1	Schematic diagram for laminar premixed flame	40
3.2	A regime diagram for tuburlent premixed combustion	42
3.3	The Bray-Moss-Libby pdf of c	44
3.4	Configurations for flame-wall interactions	50
4.1	Schematic diagram of LODI	62
5.1	Flow chart for Results & Discussion chapter 5 and 6	72

5.2	Temporal evolutions of Peclet number Pe (based on $T = 0.9$ isosurface) and non-dimensional wall heat flux Φ for laminar flame with $Le = 1.0$.	74
5.3	Temporal evolutions of the maximum, mean and minimum values of Peclet number Pe (based on $T = 0.9$ isosurface) and non-dimensional wall heat flux Φ for turbulent cases A-E with $Le = 0.8, 1.0$ and 1.2 .	75
5.4	Variations of \tilde{c} and \tilde{T} with x_1/δ_Z at different time instants for turbulent cases A-E with $Le = 0.8, 1.0$ and 1.2 .	77
5.5	Distributions of reaction progress variable c , non-dimensional temperature T and non-dimensional reaction rate $\dot{\omega} \times \delta_Z/\rho_0 S_L$ contours for turbulent case D with $Le = 0.8, 1.0$ and 1.2 at $t = \delta_Z/S_L, 2\delta_Z/S_L, 4\delta_Z/S_L, 6\delta_Z/S_L$ on central $x_1 - x_2$ plane.	80
5.6	Distributions of $(\omega_i \omega_i)^{1/2} \times \delta_Z/S_L$ and c (white line from 0.1 to 0.9 with step of 0.2 from left to right) fields on $x_1 - x_2$ mid plane for turbulent case E with $Le = 0.8, 1.0$ and 1.2 at $t = 1, 2$ and $4\delta_Z/S_L$.	82
5.7	Variations of $\overline{(\omega_i \omega_i)^{1/2}} \times \delta_Z/S_L$ (—) and $15 \times \bar{\omega} \times \delta_Z/\rho_0 S_L$ (—) and \tilde{c} with x_1/δ_Z for cases A, C and E at $t = 2\delta_Z/S_L, 6\delta_Z/S_L$ and $10\delta_Z/S_L$ (1 st -3 rd row).	83
5.8	[Variations of $\overline{\rho(\omega_i - \tilde{\omega}_i)^{1/2}} \times \delta_Z/S_L$ (—), $\overline{\rho(\omega_1 - \tilde{\omega}_1)^{1/2}} \times \delta_Z/S_L$ (—), $\overline{\rho(\omega_2 - \tilde{\omega}_2)^{1/2}} \times \delta_Z/S_L$ (—) and $\overline{\rho(\omega_3 - \tilde{\omega}_3)^{1/2}} \times \delta_Z/S_L$ (—) with x_1/δ_Z (log scale) for cases A, C and E (1 st -3 rd column) at $t = 2\delta_Z/S_L, 6\delta_Z/S_L$ and $10\delta_Z/S_L$ (1 st -3 rd row).	84
5.9	Variations of $\overline{(t_{1t}t_{1t})^{1/2}} \times \delta_Z^2/S_L^2$ (—), $\overline{(t_{21t}t_{21t})^{1/2}} \times \delta_Z^2/S_L^2$ (—), $\overline{(t_{22t}t_{22t})^{1/2}} \times \delta_Z^2/S_L^2$ (—), $\overline{(t_{3t}t_{3t})^{1/2}} \times \delta_Z^2/S_L^2$ (—) and $\overline{(t_{4t}t_{4t})^{1/2}} \times \delta_Z^2/S_L^2$ (—) with x_1/δ_Z (log scale) for cases A, C and E (1 st -3 rd column) at $t = 2\delta_Z/S_L, 6\delta_Z/S_L$ and $10\delta_Z/S_L$ (1 st -3 rd row).	86
5.10	Variations of $\overline{(t_{1n}t_{1n})^{1/2}} \times \delta_Z^2/S_L^2$ (—), $\overline{(t_{21n}t_{21n})^{1/2}} \times \delta_Z^2/S_L^2$ (—), $\overline{(t_{22n}t_{22n})^{1/2}} \times \delta_Z^2/S_L^2$ (—), $\overline{(t_{3n}t_{3n})^{1/2}} \times \delta_Z^2/S_L^2$ (—) and $\overline{(t_{4n}t_{4n})^{1/2}} \times \delta_Z^2/S_L^2$ (—) with x_1/δ_Z (log scale) for cases A, C and E (1 st -3 rd column) at $t = 2\delta_Z/S_L, 6\delta_Z/S_L$ and $10\delta_Z/S_L$ (1 st -3 rd row).	87
5.11	Variations of $T_I \times \delta_Z^3/S_L^3$ (—), $T_{II} \times \delta_Z^3/S_L^3$ (—), $T_{III} \times \delta_Z^3/S_L^3$ (—), $T_{IV} \times \delta_Z^3/S_L^3$ (—), $T_V \times \delta_Z^3/S_L^3$ (—), $T_{VI} \times \delta_Z^3/S_L^3$ (—) and $\bar{D}\bar{\Omega}/\bar{D}t \times \delta_Z^3/S_L^3$ (—) with x_1/δ_Z (log scale) for case A at $t = 2\delta_Z/S_L, 6\delta_Z/S_L$ and $10\delta_Z/S_L$ (1 st -3 rd row).	89

- 5.12 Variations of $T_I \times \delta_Z^3/S_L^3$ (—), $T_{II} \times \delta_Z^3/S_L^3$ (—), $T_{III} \times \delta_Z^3/S_L^3$ (—), $T_{IV} \times \delta_Z^3/S_L^3$ (—), $T_V \times \delta_Z^3/S_L^3$ (—), $T_{VI} \times \delta_Z^3/S_L^3$ (—) and $\bar{D}\bar{\Omega}/\bar{D}t \times \delta_Z^3/S_L^3$ (—) with x_1/δ_Z (log scale) for case E at $t = 2\delta_Z/S_L, 6\delta_Z/S_L$ and $10\delta_Z/S_L$ (1st-3rd row). 90
- 5.13 Variations of $\bar{\Psi}_\alpha = |\cos\theta_\alpha|$ (—), $\bar{\Psi}_\beta = |\cos\theta_\beta|$ (—) and $\bar{\Psi}_\gamma = |\cos\theta_\gamma|$ (—) with x_1/δ_Z (log scale) for cases A, C and E (1st-3rd column) at $t = 2\delta_Z/S_L, 6\delta_Z/S_L$ and $10\delta_Z/S_L$ (1st-3rd row). 92
- 5.14 Variations of T_{III} (—), $(\mu/\rho)\Delta^2\bar{\Omega}$ (—), $(\mu/3\rho)\vec{\omega} \cdot [\nabla \times \nabla(\nabla \cdot \vec{u})]$ (—) and $(-D_\nu)$ (—) with x_1/δ_Z (log scale) for case A at $t = 2\delta_Z/S_L, 6\delta_Z/S_L$ and $10\delta_Z/S_L$ (1st-3rd row). 94
- 5.15 Variations of T_{III} (—), $(\mu/\rho)\Delta^2\bar{\Omega}$ (—), $(\mu/3\rho)\vec{\omega} \cdot [\nabla \times \nabla(\nabla \cdot \vec{u})]$ (—) and $(-D_\nu)$ (—) with x_1/δ_Z (log scale) for case E at $t = 2\delta_Z/S_L, 6\delta_Z/S_L$ and $10\delta_Z/S_L$ (1st-3rd row). 95
- 5.16 Instantaneous $P^* = P \times \delta_Z/S_L$ fields for cases A, C and E (1st-3rd column) at $t = 2\delta_Z/S_L, 4\delta_Z/S_L$ and $6\delta_Z/S_L$ (1st-3rd row), white line presents c field from 0.1 to 0.9 with interval of 0.2 from left to right. . . 99
- 5.17 Instantaneous $Q^* = Q \times (\delta_Z/S_L)^2$ fields for cases A, C and E (1st-3rd column) at $t = 2\delta_Z/S_L, 4\delta_Z/S_L$ and $6\delta_Z/S_L$ (1st-3rd row), blue line presents c field from 0.1 to 0.9 with interval of 0.2 from left to right. . . 100
- 5.18 Instantaneous $R^* = R \times (\delta_Z/S_L)^3$ fields for cases A, C and E (1st-3rd column) at $t = 2\delta_Z/S_L, 4\delta_Z/S_L$ and $6\delta_Z/S_L$ (1st-3rd row), blue line presents c field from 0.1 to 0.9 with interval of 0.2 from left to right. . . 101
- 5.19 Variations of $\langle P^* \rangle = \langle P \rangle \times \delta_Z/S_L$ with x_1/δ_Z for $t = 2\delta_Z/S_L, 6\delta_Z/S_L, 10\delta_Z/S_L$. See Fig. 5.7 for background colour, also apply to Fig. 5.20 - 5.22, 5.27 and 5.28. 103
- 5.20 Variations of normalised terms $\{\langle Q \rangle$ (—), $\langle Q_S \rangle$ (—), $\langle Q_W \rangle$ (—, \triangle —) $\} \times (\delta_Z/S_L)^2$ with x_1/δ_Z for $t = 2\delta_Z/S_L, 6\delta_Z/S_L, 10\delta_Z/S_L$ 104
- 5.21 Variations of normalised vorticity magnitude $\{\langle R \rangle$ (—), $\langle R_S \rangle$ (—), $\langle PQ_W \rangle$ (—, \square —), $\langle -\omega_i S_{ij} \omega_j / 4 \rangle$ (—, \triangle —) $\} \times (\delta_Z/S_L)^2$ with x_1/δ_Z for $t = 2\delta_Z/S_L, 6\delta_Z/S_L, 10\delta_Z/S_L$ 106
- 5.22 Variations of normalised vorticity magnitude $\{\langle R_S \rangle$ (—, \square —), $\langle -P^3/3 \rangle$ (—, \triangle —), $\langle PQ_S \rangle$ (—), $\langle -S_{ij} S_{jk} S_{ki} / 3 \rangle$ (—, \triangle —) $\} \times (\delta_Z/S_L)^3$ with x_1/δ_Z for $t = 2\delta_Z/S_L, 6\delta_Z/S_L, 10\delta_Z/S_L$ 107
- 5.23 Joint PDFs of $Q^* = Q \times (\delta_Z/S_L)^2$ and $R^* = R \times (\delta_Z/S_L)^3$ on c -isosurfaces $c = 0.1, 0.3, 0.5, 0.7, 0.9$ for $t = 2\delta_Z/S_L$ and $6\delta_Z/S_L$ with case E and $Le = 1.0$ 109

5.24	Variations of volume fractions VF for topologies: Focal topologies S1 (—), S4 (—), S5 (—), S7 (—), nodal topologies S2 (— —), S3 (— — —), S6 (— — —), S8 (— — —) with c for $t = 2\delta_Z/S_L, 6\delta_Z/S_L, 10\delta_Z/S_L$ for cases A, C and E with $Le = 0.8, 1.0$ and 1.2	110
5.25	Variations of volume fractions VF for focal (—) and nodal (— — —) topologies with c for $t = 2\delta_Z/S_L, 6\delta_Z/S_L, 10\delta_Z/S_L$ for cases A, C and E with $Le = 0.8, 1.0$ and 1.2	112
5.26	Joint PDF between mean and Gaussian curvatures (i.e. $\kappa_m \times \delta_Z$ and $\kappa_g \times \delta_Z^2$) for S1-8 at $t = 2\delta_Z/S_L$ and $6\delta_Z/S_L$ for cases E with $Le = 1.0$	114
5.27	Variations of $\langle \Lambda^* \rangle = \langle \Lambda \rangle \times \delta_Z^3/S_L$ (—) with x_1/δ_Z for $t = 2\delta_Z/S_L, 6\delta_Z/S_L, 10\delta_Z/S_L$ for cases A, C and E with $Le = 0.8, 1.0$ and 1.2 (Focal topologies S1 (—), S4 (—), S5 (—), S7 (—), nodal topologies S2 (— — —), S3 (— — —), S6 (— — —), S8 (— — —)).	117
5.28	Variations of $\langle V^* \rangle = \langle V \rangle \times (\delta_Z/S_L)^3$ (—) with x_1/δ_Z for $t = 2\delta_Z/S_L, 6\delta_Z/S_L, 10\delta_Z/S_L$ for cases A, C and E with $Le = 0.8, 1.0$ and 1.2 (Focal topologies S1 (—), S4 (—), S5 (—), S7 (—), nodal topologies S2 (— — —), S3 (— — —), S6 (— — —), S8 (— — —)).	119
5.29	(a) Temporal evolution of maximum (—), mean (—) and minimum (—) values of wall heat flux Φ for Case A, C and E with $Le = 0.8, 1.0$ and 1.2 . Vertical lines indicate time instants for $t = 2\delta_Z/S_L, 6\delta_Z/S_L$ and $10\delta_Z/S_L$ (left to right) (b) Wall heat flux contributions from topology S1 – S8 for $Le = 0.8, 1.0$ and 1.2 at different time instant $t = 2\delta_Z/S_L, 6\delta_Z/S_L$ and $10\delta_Z/S_L$ (top to bottom) with Case A, B and C.	121
5.30	Variations of \tilde{k}/S_L^2 and $\tilde{\varepsilon} \times \delta_Z/S_L^3$ for cases A, C and E (1 st -3 rd column) at $t = 2\delta_Z/S_L$ (—), $6\delta_Z/S_L$ (—) and $10\delta_Z/S_L$ (—).	126
5.31	Variations of \tilde{c} and \tilde{T} for cases A, C and E (1 st -3 rd column) at $t = 2\delta_Z/S_L$ (—), $6\delta_Z/S_L$ (—) and $10\delta_Z/S_L$ (—).	127
5.32	Variations of term T_{K1} (—), T_{K2} (—), T_{K3} (— — —), T_{K4} (—), T_{K5} (— — —) and T_{K6} (—) with x_1/δ_Z for cases A, C and E (1 st -3 rd column) at $t = 2\delta_Z/S_L, 6\delta_Z/S_L$ and $10\delta_Z/S_L$ (1 st -3 rd row). All terms are non-dimensionalised by $\rho_0 S_L^3/\delta_Z$	130
5.33	Variations of $\widetilde{u_1'' u_1''}/S_L^2$ from DNS data (—) and according to the predictions of Eq. 5.8 (—), Eq. 5.11 (— o —) and Eq. 5.12 (—) with x_1/δ_Z for cases A, C and E (1 st -3 rd column) at $t = 2\delta_Z/S_L, 6\delta_Z/S_L$ and $10\delta_Z/S_L$ (1 st -3 rd row).	134

- 5.34 Variations of $T_{K2} \times \delta_Z / \rho_0 S_L^3$ from DNS (— + —) and according to the predictions of Eq. 5.16 (———), Eq. 5.17 (— o —) and Eq. 5.18 (———) with x_1 / δ_Z for cases A, C and E (1st-3rd column) at $t = 2\delta_Z / S_L$, $6\delta_Z / S_L$ and $10\delta_Z / S_L$ (1st-3rd row). 136
- 5.35 Variations of $T_{K3} \times \delta_Z / \rho_0 S_L^3$ from DNS (———) and according to the predictions of PDZ (———), PDN (— — —), PDC (— — —) and Eq. 5.30 (———) with x_1 / δ_Z for cases A, C and E (1st-3rd column) at $t = 2\delta_Z / S_L$, $6\delta_Z / S_L$ and $10\delta_Z / S_L$ (1st-3rd row). 140
- 5.36 Variations of $T_{K4} \times \delta_Z / \rho_0 S_L^3$ (———), $\nabla \cdot (\mu \cdot \nabla \tilde{k}) \times \delta_Z / \rho_0 S_L^3$ (———), $(-\bar{\rho}\tilde{\epsilon}) \times \delta_Z / \rho_0 S_L^3$ (— — —) and $T_V \times \delta_Z / \rho_0 S_L^3$ (— — —) with x_1 / δ_Z for cases A, C and E (1st-3rd column) at $t = 2\delta_Z / S_L$, $6\delta_Z / S_L$ and $10\delta_Z / S_L$ (1st-3rd row). 141
- 5.37 Variations of $T_V \times \delta_Z / \rho_0 S_L^3$ from DNS data (———), Eq. 5.31b (———), Eq. 5.31e (— o —) and Eq. 5.32 (———) with x_1 / δ_Z for cases A, C and E (1st-3rd column) at $t = 2\delta_Z / S_L$, $6\delta_Z / S_L$ and $10\delta_Z / S_L$ (1st-3rd row). . . 144
- 5.38 Variations of $-\overline{u_i'' \partial p' / \partial x_i} \times \delta_Z / \rho_0 S_L^3$ from DNS data (———), PTL (———), PTS (— — —), PTZR (— — —), PTDB (— — —), PTNKC (———) and Eq. 5.39 (— o —) with x_1 / δ_Z with x_1 / δ_Z for cases A, C and E (1st-3rd column) at $t = 2\delta_Z / S_L$, $6\delta_Z / S_L$ and $10\delta_Z / S_L$ (1st-3rd row). 148
- 5.39 Variations of $\overline{\rho u_1'' k} / \rho_0 S_L^3$ from DNS data (———), $(-\mu_t \partial \tilde{k} / \partial x_1) / \rho_0 S_L^3$ (———), Eq. 5.41f (— △ —), Eq. 5.41g (— o —) and Eq. 5.42 (———) with x_1 / δ_Z for cases A, C and E (1st-3rd column) at $t = 2\delta_Z / S_L$, $6\delta_Z / S_L$ and $10\delta_Z / S_L$ (1st-3rd row). 152
- 5.40 Variations of T_{1v} (———), T_{2v} (———), T_{3v} (———), D_{1v} (———), $(-D_{2v})$ (———) with x_1 / δ_Z at $t = 4\delta_Z / S_L$, $6\delta_Z / S_L$, $8\delta_Z / S_L$, $10\delta_Z / S_L$ for turbulent cases A - E with $Le = 0.8, 1.0$ and 1.2 156
- 5.41 Variations of $\overline{\rho u_1'' c''^2}$ extracted from DNS data (solid line) along with the predictions of Eqs. 5.47 (dotted line) and 5.48 (broken line) with x_1 / δ_Z at $t = 4\delta_Z / S_L$, $6\delta_Z / S_L$, $8\delta_Z / S_L$, $10\delta_Z / S_L$ for turbulent cases A - E with $Le = 0.8, 1.0$ and 1.2 159
- 5.42 Variations of $\overline{\rho u_1'' c''}$ extracted from DNS data (solid line) along with the predictions of Eqs. 5.55 (dotted circle line) and 5.56 (broken triangle line) with x_1 / δ_Z at $t = 4\delta_Z / S_L$, $6\delta_Z / S_L$, $8\delta_Z / S_L$, $10\delta_Z / S_L$ for turbulent cases A - E with $Le = 0.8, 1.0$ and 1.2 163

5.43	Variations of T_{3v} extracted from DNS data (solid line) along with the predictions of Eqs. 5.58 (dotted circle line) and 6.2 (broken triangle line) with x_1/δ_Z at $t = 4\delta_Z/S_L, 6\delta_Z/S_L, 8\delta_Z/S_L, 10\delta_Z/S_L$ for turbulent cases A - E with $Le = 0.8, 1.0$ and 1.2	165
6.1	Variations of $\bar{\omega}^+ = \bar{\omega} \times \delta_Z/\rho_0 S_L, \rho_0 S_L \Sigma_{\text{gen}} \times \delta_Z/\rho_0 S_L, 2\bar{\rho}\tilde{\epsilon}_c/(c_m - 1) \times \delta_Z/\rho_0 S_L$ and the prediction of Eq. 6.2 with x_1/δ_Z at different time instants for turbulent cases (a-e) A-E with $Le = 0.8$. Please refer to the table in Fig. 5.4 for the colour scheme.	171
6.2	Variations of $\bar{\omega}^+ = \bar{\omega} \times \delta_Z/\rho_0 S_L, \rho_0 S_L \Sigma_{\text{gen}} \times \delta_Z/\rho_0 S_L, 2\bar{\rho}\tilde{\epsilon}_c/(c_m - 1) \times \delta_Z/\rho_0 S_L$ and the prediction of Eq. 6.2 with x_1/δ_Z at different time instants for turbulent cases (a-e) A-E with $Le = 1.0$. Please refer to the table in Fig. 5.4 for the colour scheme.	172
6.3	Variations of $\bar{\omega}^+ = \bar{\omega} \times \delta_Z/\rho_0 S_L, \rho_0 S_L \Sigma_{\text{gen}} \times \delta_Z/\rho_0 S_L, 2\bar{\rho}\tilde{\epsilon}_c/(c_m - 1) \times \delta_Z/\rho_0 S_L$ and the prediction of Eq. 6.2 with x_1/δ_Z at different time instants for turbulent cases (a-e) A-E with $Le = 1.2$. Please refer to the table in Fig. 5.4 for the colour scheme.	173
6.4	Pdfs of c for $0 \leq x_1/\delta_Z \leq (Pe_{\text{min}})_L$ at different time instants for turbulent cases A - E and $Le = 0.8, 1.0$ and 1.2 . Please refer to the table in Fig. 5.4 for the colour scheme.	174
6.5	Variations of $\tilde{c}(1 - \tilde{c})$ (solid line) and \tilde{c}'' (dash line) at different time instants for turbulent cases A - E and $Le = 0.8, 1.0$ and 1.2 . Please refer to the table in Fig. 5.4 for the colour scheme.	174
6.6	Variations of  , T_1 ;  , T_2 ;  , T_3 ;  , T_4 ;  , $(-D_2)$;  , $f(D)$ with x_1/δ_Z at $t = 4\delta_Z/S_L, 6\delta_Z/S_L, 8\delta_Z/S_L, 10\delta_Z/S_L$ for turbulent cases (a-e) A - E with $Le = 0.8$	176
6.7	Variations of  , T_1 ;  , T_2 ;  , T_3 ;  , T_4 ;  , $(-D_2)$;  , $f(D)$ with x_1/δ_Z at $t = 4\delta_Z/S_L, 6\delta_Z/S_L, 8\delta_Z/S_L, 10\delta_Z/S_L$ for turbulent cases (a-e) A - E with $Le = 1.0$	177
6.8	Variations of  , T_1 ;  , T_2 ;  , T_3 ;  , T_4 ;  , $(-D_2)$;  , $f(D)$ with x_1/δ_Z at $t = 4\delta_Z/S_L, 6\delta_Z/S_L, 8\delta_Z/S_L, 10\delta_Z/S_L$ for turbulent cases (a-e) A - E with $Le = 1.2$	178
6.9	Variations of scalar gradient alignment markers $\bar{\Psi}_\alpha, \bar{\Psi}_\beta$ and $\bar{\Psi}_\gamma$ with x_1/δ_Z at $t = 4\delta_Z/S_L, 6\delta_Z/S_L, 8\delta_Z/S_L, 10\delta_Z/S_L$ and $12\delta_Z/S_L$ for turbulent cases A-E for $Le = 1.0$. The x-axis is shown in log scale for the inset. Please refer to the table in Fig. 5.4 for the colour scheme.	182

6.10	Variations of $(T_2 + T_3 + T_4 + f(D))$ and $(-D_2)$ with x_1/δ_Z at $t = 4\delta_Z/S_L, 6\delta_Z/S_L, 8\delta_Z/S_L, 10\delta_Z/S_L$ for turbulent cases (a-e) A - E with $Le = 0.8$. Please refer to the table in Fig. 5.4 for the colour scheme. . .	184
6.11	Variations of $(T_2 + T_3 + T_4 + f(D))$ and $(-D_2)$ with x_1/δ_Z at $t = 4\delta_Z/S_L, 6\delta_Z/S_L, 8\delta_Z/S_L, 10\delta_Z/S_L$ for turbulent cases (a-e) A - E with $Le = 1.0$. Please refer to the table in Fig. 5.4 for the colour scheme. . .	185
6.12	Variations of $(T_2 + T_3 + T_4 + f(D))$ and $(-D_2)$ with x_1/δ_Z at $t = 4\delta_Z/S_L, 6\delta_Z/S_L, 8\delta_Z/S_L, 10\delta_Z/S_L$ for turbulent cases (a-e) A - E with $Le = 1.2$. Please refer to the table in Fig. 5.4 for the colour scheme. . .	186
6.13	Variations of $\tilde{\varepsilon}_c^+ = \tilde{\varepsilon}_c \times \delta_Z/S_L$ obtained from DNS and the prediction of Eq. 6.16 and 6.17 with x_1/δ_Z at $t = 4\delta_Z/S_L, 6\delta_Z/S_L, 8\delta_Z/S_L, 10\delta_Z/S_L$ for turbulent cases (a-e) A - E with $Le = 0.8$. Please refer to the table in Fig. 5.4 for the colour scheme.	188
6.14	Variations of $\tilde{\varepsilon}_c^+ = \tilde{\varepsilon}_c \times \delta_Z/S_L$ obtained from DNS and the prediction of Eq. 6.16 and 6.17 with x_1/δ_Z at $t = 4\delta_Z/S_L, 6\delta_Z/S_L, 8\delta_Z/S_L, 10\delta_Z/S_L$ for turbulent cases (a-e) A - E with $Le = 1.0$. Please refer to the table in Fig. 5.4 for the colour scheme.	189
6.15	Variations of $\tilde{\varepsilon}_c^+ = \tilde{\varepsilon}_c \times \delta_Z/S_L$ obtained from DNS and the prediction of Eq. 6.16 and 6.17 with x_1/δ_Z at $t = 4\delta_Z/S_L, 6\delta_Z/S_L, 8\delta_Z/S_L, 10\delta_Z/S_L$ for turbulent cases (a-e) A - E with $Le = 1.2$. Please refer to the table in Fig. 5.4 for the colour scheme.	190
6.16	Variations of $\overline{\rho u_1'' \varepsilon_c} \times \delta_Z/\rho_0 S_L^2$ (—) with x_1/δ_Z along with the predictions by the T1CS model (—) and Eq. 6.21 (—) at for cases A, C and E (1 st - 3 rd column) at $t = 2\delta_Z/S_L, 6\delta_Z/S_L$ and $10\delta_Z/S_L$ (1 st - 3 rd row).	192
6.17	Variations of $T_2 \times \delta_Z^2/\rho_0 S_L^2$ (—) with x_1/δ_Z along with the predictions by the T1CS model (—) and Eq. 6.30 (—) at for cases A, C and E (1 st - 3 rd column) at $t = 2\delta_Z/S_L, 6\delta_Z/S_L$ and $10\delta_Z/S_L$ (1 st - 3 rd row).	196
6.18	Variations of $T_3 \times \delta_Z^2/\rho_0 S_L^2$ (—) with x_1/δ_Z along with T_{31} (—), T_{32} (—) and T_{33} (—) at for cases A, C and E (1 st - 3 rd column) at $t = 2\delta_Z/S_L, 6\delta_Z/S_L$ and $10\delta_Z/S_L$ (1 st - 3 rd row).	198
6.19	Variations of $T_{31} \times \delta_Z^2/\rho_0 S_L^2$ (—) with x_1/δ_Z along with T31MB (—), T31CS (—), T31M1 (—), T31M2 (—) and Eq. 6.38 (—) at for cases A, C and E (1 st - 3 rd column) at $t = 2\delta_Z/S_L, 6\delta_Z/S_L$ and $10\delta_Z/S_L$ (1 st - 3 rd row).	201

- 6.20 Variations of $T_{32} \times \delta_Z^2 / \rho_0 S_L^2$ (—) with x_1 / δ_Z along with T32MB (—), T32M1 (—), T32M2 (—), T31CS (—), and Eq. 6.43 (—) at for cases A, C and E (1st - 3rd column) at $t = 2\delta_Z / S_L$, $6\delta_Z / S_L$ and $10\delta_Z / S_L$ (1st - 3rd row). 203
- 6.21 Variations of $T_{33} \times \delta_Z^2 / \rho_0 S_L^2$ (—) with x_1 / δ_Z along with T33MB (—), T33M1 (—), T33M2 (—), T33M3 (—), T33CS (—), and Eq. 6.49 (—) at for cases A, C and E (1st - 3rd column) at $t = 2\delta_Z / S_L$, $6\delta_Z / S_L$ and $10\delta_Z / S_L$ (1st - 3rd row). 205
- 6.22 Variations of $[T_4 - D_2 + f(D)] \times \delta_Z^2 / \rho_0 S_L^2$ (—) with x_1 / δ_Z along with T4D2CS (—), and Eq. 6.55 (—) at for cases A, C and E (1st - 3rd column) at $t = 2\delta_Z / S_L$, $6\delta_Z / S_L$ and $10\delta_Z / S_L$ (1st - 3rd row). 209
- 6.23 Variations of the normalised mean reaction rate $\bar{\omega} \times \delta_Z / S_L$ (solid line), along with the predictions of $\rho_0 S_L \Sigma_{\text{gen}} \times \delta_Z / \rho_0 S_L$ (—), $Q_m \rho_0 S_L \Sigma_{\text{gen}} \times \delta_Z / \rho_0 S_L$ (dashed line), Al-shaalan and Rutland [2] model (dotted line), and $A_1(\rho_0 S_L / Le) \Sigma_{\text{gen}} \times \delta_Z / \rho_0 S_L$ (dashed circle line) at different $t^+ = t S_L / \delta_Z = 2$ (—); 6 (—). The same colour key applies for Figs. 212
- 6.24 Variations of the normalised turbulent flux $[(u_i)_s - \tilde{u}_i] \Sigma_{\text{gen}} \times \delta_Z / S_L$ (solid line) and the prediction of Eq. 6.62 (dashed line), and Eq. 6.62 with near-wall modification (dashed circle line) at different $t^+ = t S_L / \delta_Z$ 214
- 6.25 Variations of the strain rate term $T_{F2} \times \delta_Z^2 / S_L$ (solid line) along with the predictions of the Bruneaux *et al.* [20] model (dashed line) and the combined outcome of the models of T_{D1} , T_{N1} , T_{N2} with wall modifications (dashed circle line) at different $t^+ = t S_L / \delta_Z$ 218
- 6.26 Variations of $(T_{D1}$ (—), T_{D2} (—), $-T_{N1}$ (—), $-T_{N2}$ (—)) $\times \delta_Z^2 / S_L$ obtained from DNS (solid line) and the model predictions according to $\bar{c} = (1 + \tau g^a Le^{-b}) \tilde{c} / (1 + \tau g^a Le^{-b} \tilde{c})$, $\overline{(N_i N_j)_s} = \overline{(N_i)_s (N_j)_s} + (\delta_{ij} / 3) [1 - \overline{(N_k)_s (N_k)_s}]$, Eqs. 6.64 and respectively, with (dashed circle line) and without (dashed line) wall modifications at different $t^+ = t S_L / \delta_Z$ 219
- 6.27 Variations of the normalised curvature and propagation term $(T_{F3} + T_{F4}) \times \delta_Z^2 / S_L$ obtained from DNS data (solid line) and the predictions of the Bruneaux *et al.* [20] model (dashed line) and Eq. 6.68 with near-wall modification (dashed circle line) at different $t^+ = t S_L / \delta_Z$ 220
- 6.28 Variation of terms T_{1c} (—), T_{2c} (—), T_{3c} (—), T_{4c} (—), T_{5c} (—), T_{6c} (—), T_{7c} (—) and T_{8c} (—) with x_1 / δ_Z at $t = 2\delta_Z / S_L$, $6\delta_Z / S_L$, and $10\delta_Z / S_L$ for turbulent cases A - E with $Le = 0.8$, 1.0 and 1.2. All terms are non-dimensionalised by $\rho_0 S_L^2 / \delta_Z$ 224

- 6.29 Variation of terms $\overline{\rho u_1'' u_1'' c''} / \rho_0 S_L^2$ from DNS data (—), TDH (—), CC (— — —) and New model (—) with x_1/δ_Z at $t = 2\delta_Z/S_L$, $6\delta_Z/S_L$, and $10\delta_Z/S_L$ (1st - 3rd row) for turbulent cases A, C, and E (1st - 3rd column) with $Le = 0.8, 1.0$ and 1.2 228
- 6.30 Variation of terms $(T_{4c} + T_{5c}) \times \delta_Z / \rho_0 S_L^2$ from DNS data (—), PN (—), PC (— + —), PD (— ◇ —), PJO (— □ —), PLV (— ○ —), PDB (— △ —), modified PN model (—) with x_1/δ_Z at $t = 2\delta_Z/S_L$, $6\delta_Z/S_L$, and $10\delta_Z/S_L$ (1st - 3rd row) for turbulent cases A, C, and E (1st - 3rd column) with $Le = 0.8, 1.0$ and 1.2 232
- 6.31 Variation of terms $(T_{6c} + T_{7c}) \times \delta_Z / \rho_0 S_L^2$ from DNS data (—), DBML (—), DN (— — —), CC (—) and New model (—) with x_1/δ_Z at $t = 2\delta_Z/S_L$, $6\delta_Z/S_L$, and $10\delta_Z/S_L$ (1st - 3rd row) for turbulent cases A, C, and E (1st - 3rd column) with $Le = 0.8, 1.0$ and 1.2 236
- 6.32 Variation of terms $T_{8c} \times \delta_Z / \rho_0 S_L^2$ from DNS data (—), RB (—), RBM (— — —) and New model (—) with x_1/δ_Z at $t = 2\delta_Z/S_L$, $6\delta_Z/S_L$, and $10\delta_Z/S_L$ (1st - 3rd row) for turbulent cases A, C, and E (1st - 3rd column) with $Le = 0.8, 1.0$ and 1.2 237
- 7.1 (a) The instantaneous distribution of vorticity magnitude (background: red-high and white-low) and non-dimensional temperature (isosurface and side view, red-high and blue-low) and fuel mass fraction (lower wall view, red-high and blue-low) for the V-flame case. (b) Distributions of T and c (shown by white lines from 0 to 1 with 0.2 interval) at $t = 2t_{ft}$ for $x_1 - x_2$ mid-plane. Distributions of c around locations A1, B1 and C1 are shown in the inset. The locations A1, B1 and C1 in Fig. 7.1b correspond to $x_1 = 60\delta_Z$, $100\delta_Z$ and $140\delta_Z$ respectively. 244
- 7.2 Variations of Φ and Pe (maximum (—); mean (—); minimum (—)) with flow-through time $t_{ft} = L_1/U_{mean}$ 245
- 7.3 Variations of volume fraction VF for topologies conditional on c . Top figures: locations A1, B1 and C1 in the V-flame case at $t = 2.39t_{ft}$; Bottom figures: for the HOQ case at three time instants. Focal topologies S1 (—), S4 (—), S5 (—), S7 (—), nodal topologies S2 (— — —), S3 (— — —), S6 (— — —), S8 (— — —). 246
- 7.4 Percentages of wall heat flux magnitude contributions arising from individual flow topologies S1-S8 in the V-flame case from $0.24t_{ft}$ to $2.39t_{ft}$ (1st - 2nd column) and HOQ case from $t = 2\delta_Z/S_L$ to $20\delta_Z/S_L$ (3rd column). 247

7.5	Distributions of c based on Y_{CH_4} and non-dimensional temperature T at different time instants for (a) detailed chemistry case A, (b) simple chemistry case B. The time instants are different between cases A and B because of the difference in δ_{th} values.	250
7.6	Variation of c and T with x_1/δ_{th} at different time instants for case A and case B (right).	251
7.7	Variation of c , T , Ω_T and $\Omega_c = \dot{\omega} \times \delta_{\text{th}}/\rho_0 S_L$ with x_1/δ_{th} at different time instants for laminar head-on quenching for both detailed (A) and simple (B) chemistry cases.	252
7.8	Variation of mass fractions of CH_4 , O_2 , CO_2 , H_2O , CO , OH , HO_2 and H_2O_2 in the wall normal distance for head-on quenching of a laminar stoichiometric planar premixed flame at $t = 1.50\delta_{\text{th}}/S_L$ (—); $2.04\delta_{\text{th}}/S_L$ (—); $2.65\delta_{\text{th}}/S_L$ (—); $3.16\delta_{\text{th}}/S_L$ (—); $3.95\delta_{\text{th}}/S_L$ (—). . .	252
7.9	Variation of mass fractions of CH_4 , O_2 , CO_2 , H_2O , CO , OH , HO_2 , H_2O_2 and $\bar{\Omega}_T$ and $\bar{\Omega}_c$ in the wall normal distance for head-on quenching of a turbulent stoichiometric planar premixed flame (case A) at $t = 0.31\delta_{\text{th}}/S_L$ (—); $1.05\delta_{\text{th}}/S_L$ (—); $1.61\delta_{\text{th}}/S_L$ (—); $1.98\delta_{\text{th}}/S_L$ (—); $2.16\delta_{\text{th}}/S_L$ (—).	253
7.10	(a) Temporal evolution of maximum, mean and minimum values of wall Peclet number Pe (based on $T = 0.9$ isosurface) and non-dimensional wall heat flux Φ along with the corresponding variation obtained for head on quenching of a laminar one-dimensional flame (maximum —; mean —; minimum —; laminar —). (b) Variations of T (broken line) and $\Omega_c \times 0.4$ (solid line) for laminar flame simulation at $t = 1.50\delta_{\text{th}}/S_L$ (—); $2.04\delta_{\text{th}}/S_L$ (—); $2.65\delta_{\text{th}}/S_L$ (—); $3.16\delta_{\text{th}}/S_L$ (—); $3.95\delta_{\text{th}}/S_L$ (—) for case A (left) and case B (right).	255
7.11	Variations of $\bar{\Omega}_c = \bar{\omega} \times \delta_{\text{th}}/\rho_0 S_L$ (solid lines), along with the predictions of $\rho_0 S_L \Sigma_{\text{gen}} \times \delta_{\text{th}}/\rho_0 S_L$ (\triangle) and $A_1 \rho_0 S_L \Sigma_{\text{gen}} \times \delta_{\text{th}}/\rho_0 S_L$ (\circ) with x_1/δ_{th} for (a - b) cases A and B at $t = 0.31\delta_{\text{th}}/S_L$ (—); $1.05\delta_{\text{th}}/S_L$ (—); $1.61\delta_{\text{th}}/S_L$ (—); $1.98\delta_{\text{th}}/S_L$ (—); $2.16\delta_{\text{th}}/S_L$ (—).	256

List of tables

4.1	List of initial simulation parameters and non-dimensional numbers for head-on quenching cases	67
4.2	List of inflow simulation parameters and non-dimensional numbers for V-flame cases	69
4.3	Initial turbulence parameters away from the wall and the value of heat release for detailed chemistry	70
5.1	List of normalised flame surface area A_T/A_L and turbulent flame speed S_T/S_L at different stages of flame quenching for all cases considered here.	79

Nomenclature

Roman Symbols

$\bar{\alpha}^{(l)}$	polynomial coefficients
A_L	laminar flame surface area
A_P	projected area
A_T	turbulent flame surface area
A_m	frequency factor of step m
A_{ij}	invariant of the velocity-gradient tensor
B	pre-exponential factor
C	heat capacity
c	reaction progress variable
C_P	specific heats at constant pressure
C_V	specific heats at constant volume
D	mass diffusion coefficient
D_{pipe}	pipe diameter
Da	Damköhler number
E	stagnation internal energy
$E(\kappa)$	turbulent energy spectrum
e_i	eigenvalues

E_m	activation energy of step m
H	heat of reaction
h	enthalpy
h_α^0	enthalpy of formation of species α
k	turbulent kinetic energy
Ka	Karlovitz number
l	integral length scale
l_0	reference length
L_{11}	longitudinal integral length scale
l_e	characteristic length scale
L_i	domain length
Le	Lewis number
Ma	Mach number
\vec{N}	local flame normal vector
\vec{n}	normal vector
N_c	instantaneous SDR
n_m	temperature exponent of step m
P	invariant
Pr	Prantle number
Pe	Peclet number
Q	invariant
q_k	heat flux vector
R	invariant
R^0	ideal gas constant

Re	Reynolds number
Re_{crit}	critical Reynolds number
S_d	displacement speed
S_L	laminar flame speed
S_T	turbulent flame speed
S_{ij}	symmetric strain-rate tensor
Sc	Schmidt number
\hat{T}	instantaneous temperature
T	non-dimensional temperature
t	time
t_0	reference time
T_0	fresh gas temperature
T_w	wall temperature
\vec{u}	velocity vector
U	fluid velocity
u'	velocity fluctuation
u_0	reference velocity
u_e	characteristic velocity scale
u_i	fluid velocity component in x_i -direction
$V_{\alpha k}$	diffusion velocity vector of species α
W_α	molecular weight of species α
W_{ij}	anti-symmetric strain-rate tensor
x_i	Cartesian coordinate
Y_α	mass fraction of species α

Greek Symbols

α	Species
β	Zel'dovich number
Δx	grid spacing
Δ	filter size
δ	reaction zone thickness
δ_{th}	thermal flame thickness
δ_Z	Zel'dovich flame thickness
ϵ	turbulent dissipation rate
ε	dissipation rate
γ	ratio of specific heat
κ	wave number
k	turbulent kinetic energy
λ	thermal conductivity
μ	dynamic viscosity
ν	kinematic viscosity
$\nu'_{\alpha,m}$	reactant stoichiometric coefficient for step m
$\nu''_{\alpha,m}$	product stoichiometric coefficient for step m
$\dot{\omega}$	reaction rate
Ω	enstrophy
ω_c	production creation rate
$\vec{\omega}$	vorticity vector
Φ	non-dimensional wall heat flux
ϕ	wall heat flux

ρ	density
ρ_0	reference density
Σ_{gen}	generalised flame surface density
τ	heat release parameter
τ_{ki}	viscous stress tensor
θ_i	principal strain rate
η	Kolmogorov length scale
v_η	Kolmogorov velocity scale

Other Symbols

$D(\cdot)/Dt$	material derivative
\tilde{Q}	Favre-averaged of a general quantity Q
$f(c)$	burning mode probability density
∞	fully burned products
\mathcal{M}_k	Symbol for species k

Acronyms / Abbreviations

BML	Bray-Moss-Libby
CFD	Computational Fluid Dynamics
CH ₄	Methane
DNS	Direct Numerical Simulation
HOQ	Head-on quenching
LES	Large Eddy Simulation
pdf	probability density function
RANS	Reynolds Averaged Navier Stokes
SDR	Scalar Dissipation Rate
SWQ	Side-wall quenching

Chapter 1

Introduction



"Nature uses only the longest threads to weave her patterns, so each small piece of her fabric reveals the organization of the entire tapestry."

— Richard Feynman (1918-1988) ¹

¹Image: The great red spot in Jupiter atmosphere. The atmospheric turbulence is formed by the interaction of different bands of the atmosphere travel by different speeds. Source: *Jupiter: Overview: King of the Planets*. Digital image. *Solar System Exploration*. NASA. Web. 31 May 2016.



Fig. 1.1 Illustration of fire used by *Homo erectus*.

Source: *Story of humans*. Digital image. *Q-files The Great Illustrated Encyclopedia*.

Q-files. Access date: Web. 1 June 2016.

1.1 Motivation

Combustion processes involve complex interactions of fluid dynamics, heat and mass transfer with chemical kinetics. This section seeks to provide a brief introduction of combustion and why it is important for engineering applications and also for mitigation of environment pollution. This section also provides background information on the flame-wall interaction.

1.1.1 A brief history of combustion

Combustion is an oxidation process which is accompanied by the emission of light and heat. The relationship between human and combustion can be dated back to one million years ago in Africa [9] when the *Homo erectus* had sporadic control of fire. Harnessing fire had an enormous impact on the life of our direct hominin ancestors; it triggered a cascade of changes in the evolution. Using fire for cooking greatly increased the digestibility of food and provided higher caloric returns. More importantly, it altered anatomies such as brain size and gut volume. Moreover, fire protected early humans from large predators and provided more adaptable to the environment and a new context for social interaction [209].

The recognition and understanding of combustion for human beings started from harnessing of fire which is a vital feature of the mythology of every culture. Greek mythology stated the Titan Prometheus, who was punished by Zeus, stole fire from Mount Olympus and brought it to the human race. Sui ren introduced the practice of drilling wood for the fire in Chinese mythology. In Vedic literature, Agni is the fire god of Hinduism, who reflects the primordial powers to consume, transform and convey [149]. Thousands of years ago, ancient Chinese alchemists sought for the medicine for eternal life [63]. However, the ingredients such as sulphur and saltpetre which were mixed inside alchemical furnace did not encourage immortality, but those violent reactions were capable of causing explosions and death. Later, gunpowder was invented for early thermal weapons which led to an eventual development of the cannon and firearms. Apart from being weapons, a sparkled firework brought fantastic scenes and joys in human history and different cultures.



Fig. 1.2 Fireworks in the night sky

Source: *Family Feud: Memories of an Explosive Spring Festival*. Digital image. *thebeijinger*. True Run Media. Web. 1 June 2016.

Civilisation and the technology of combustion are inseparable. The development of the steam engine was one of the most important elements of the industrial revolution, as a result of the accumulation of experiences on the understanding and applications of combustion [190]. In the 17th century, German chemist Georg Ernst Stahl attempted to explain combustion processes by the phlogiston theory, where it stated *Phlogisticated* substances burn and release phlogiston on experimental basis [62]. Later in the 18th century, French chemist Antoine Lavoisier opposed the phlogiston theory and discovered

the role of oxygen in combustion [81] (the discovery was also claimed by English chemist Joseph Priestley [116]). Although Stahl's theory of phlogiston was replaced, his work encouraged the chemists of his time to explore scientific problems and contributed the transition between alchemy and chemistry [81].

Thermodynamics developed in the 19th century which deal with heat and work and their interrelation, which gradually became one of the important methods in the understanding of combustion process [117]. In the 1930s, Russian Chemist Nikolay Semenov [171] explained the mechanism of chemical kinetics, which has a significant impact on the combustion process. From the 1950s onward, the analysis of combustion includes a variety types of disciplines including Thermodynamics, Chemical kinetics, fluid mechanics, heat and mass transfer, turbulence, etc. [117]. The research of combustion met its first rapid development in the post-war era due to the enormous expansion of commercial air travel, the introduction of supersonic military aircraft [86] and rocket engine design [182]. Early development of the F-1 rocket engine for the Apollo program encountered serious combustion instability problems which caused catastrophic failure [83]. The research by Von Karman and his student Xuesen Qian, who was known as 'the father of Chinese space program' [211], contributed to the understanding of compressible flows and also suggested the application of continuum mechanics to the study of combustion problems [194, 107] in the 1950s. In-depth quantitative analysis for laminar combustion, turbulent combustion, flame stability and fire have been carried out in the next decades. Computational Fluid Dynamics (CFD), which is based on mathematical models with numerical methods, play a significant role in the analysis of engineering applications involving flow, heat and mass transfer and combustion. The use of CFD in the analysis of combustion phenomena has become an invaluable tool in academic research and industrial applications [178–180].

1.1.2 Modern combustion and its problems

In order to recover heat and produce mechanical output, combustion has to take place in a vessel (such as furnace, combustion chamber in gas turbine and cylinder of piston engine) in which flames are produced and developed. Thus, flame-wall interaction is inevitable in these processes. The area of combustion applications includes: power generation, process industry for production of engineering materials, household and industrial heating, safety protections from fire and explosions etc [117]. Nowadays, over 80% of world's energy supply comes from combustion sources [199]. Figure 1.3 shows the history and projection of world energy consumption from 1990 to 2040. In 2012, 84% of energy consumption was supplied by fuels, coal and natural gas. Renewable and

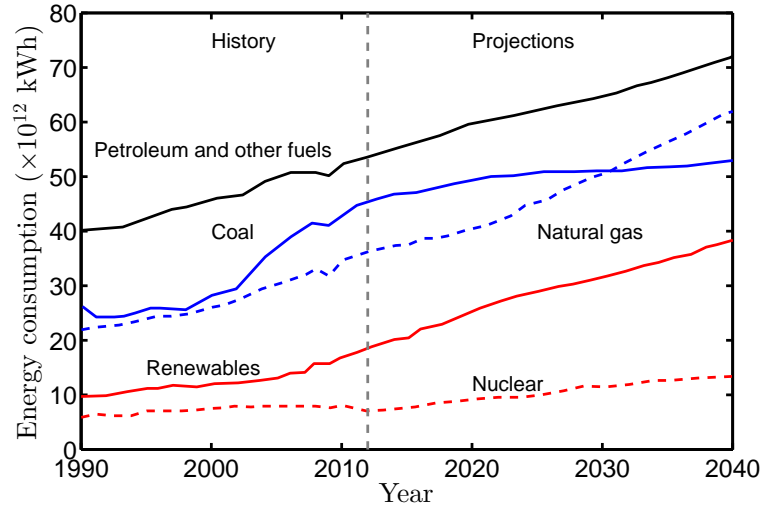


Fig. 1.3 World energy consumption 1990-2040 [82]

nuclear have a share which is expected to grow from 16% in 2012 to predicted 23% in 2040 [82]. The growing worldwide demand for energy is one of the greatest challenges faced by the mankind under the current situation. Developing countries such as China, India are undergoing exceptional economic growth which have dramatically increased their energy consumption and production since 2000 [148]. Based on today population and demand, it has only revealed a glimpse of the thirst for energy in following decades.

However, due to predominant dependence on the burning of fossil fuels, which have limited resource and emit greenhouse gas CO_2 , humanity is under an all-encompassing threat of energy sustainability and climate change which could imperil from world's food supply, peace and security, and more importantly human existence. As such, it is essential to study and understand combustion so that performance of combustors could be improved to reduce pollutant formation and energy efficiency through better design by optimising of combustion processes [61].

1.1.3 Background of flame-wall interaction

In early 19th century, Sir Humphry Davy [69] and George Stephenson [68] invented a mine lamp based on the principle of flame quenching by walls, which is one of the most initial studies of flame-wall interaction. The basic design of the mine lamp involves an ensemble of tubes, which have diameters smaller than the quenching distance of a flame, so that, the flame cannot propagate through the lamp to ignite the premixed gases in the mine field. However, radiated light from the flame and the air can propagate

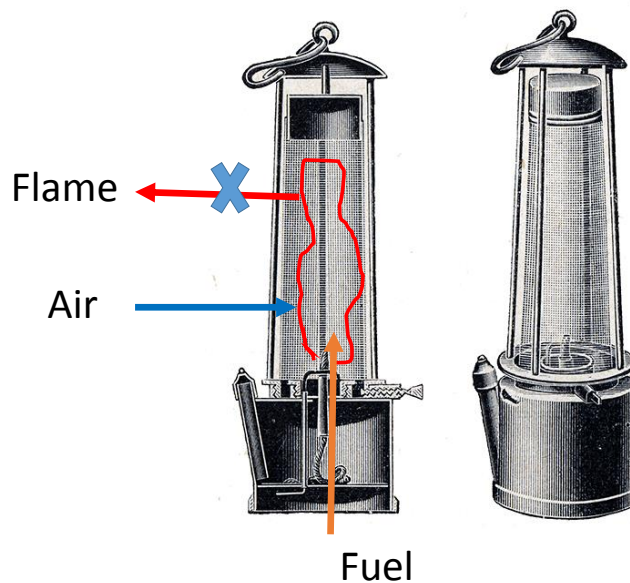


Fig. 1.4 Illustration of Davy lamp. Original figure from [142].

through the tubes (see fig. 1.4). Figure 1.5 illustrates the metal gauze experiment, where the metal gauze has been used in Davy's lamp. Davy conducted a series of test to find out the right size of diameters for using in the mine field. After he perfected his design, the invention of mine lamp significantly reduced the danger of explosion due to flammable gases, enabled miners to drill more safely and deeper and increased the production efficiency. Since then, flame-wall interaction remained an important subject not only for safety technology but also for combustion technology.

Fundamental physical understanding of premixed flame-wall interaction plays a pivotal role in optimising the thermal efficiency and pollutant emission in Spark Ignition (SI) engines [96], as well as, improving the design of combustion devices which are subject to high temperatures and thermal stresses. Since the adiabatic flame temperature of typical fuel-air mixtures is far greater than the melting point of the materials of combustor walls [157], and combustor lifespan is strongly affected by thermal stress which is induced by spatial and temporal fluctuations of wall temperature in combustion chambers in spark-ignition engines [96]. An accurate estimation of the wall heat fluxes plays a vital role in improving lifespan and design of the combustion devices. Flame quenching occurs in a few micrometres thick zone from the wall, where chemical reaction ceases to take place due to large heat fluxes and enthalpy loss from the flow to the wall. The near-wall quenching results in incomplete combustion and gives rise to thermal inefficiencies and pollutant emissions due to unburned hydrocarbon. As

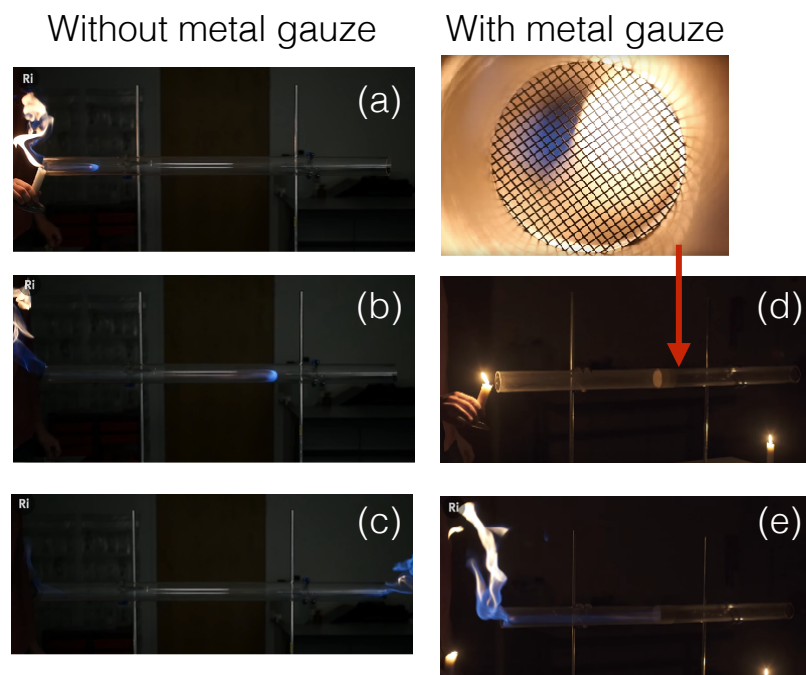


Fig. 1.5 Metal gauze experiment in a tube filled with methane gases. (a) Ignite gas in one end. (b, c) The flame is created and propagates along the tube. (d) Insert a piece of metal gauze in the centre of the tube and repeat the same process. (e) The flame is quenched at the gauze.

Source: *Fighting Firedamp - The Lamp that Saved 1,000 Lives*. Youtube
The Royal Institution. Mon. 27 Feb 2017.

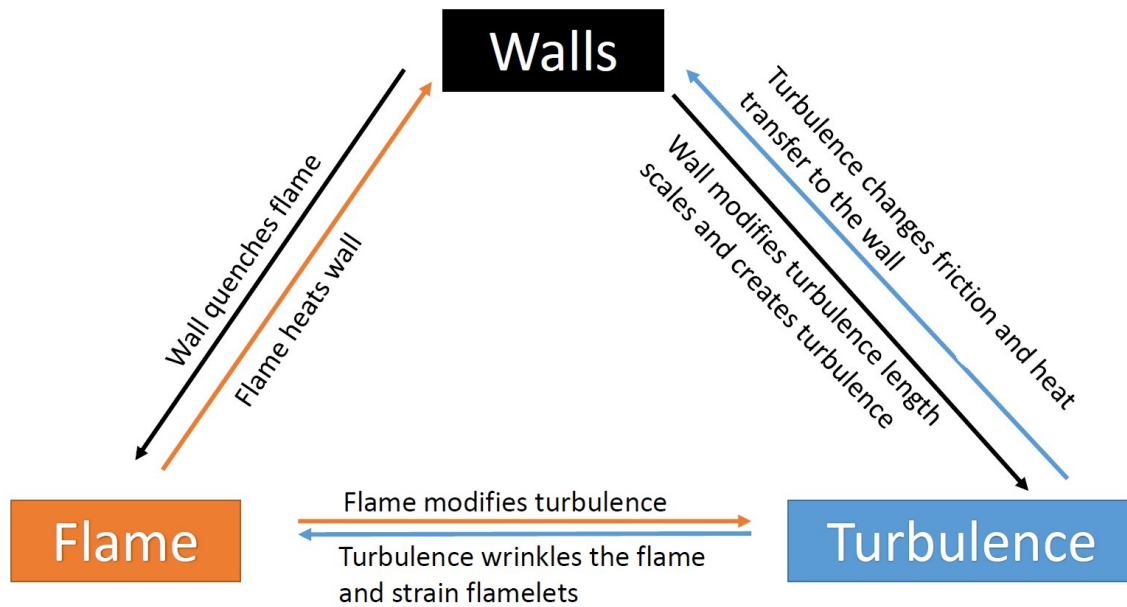


Fig. 1.6 Illustration of turbulence flame wall interaction. Reproduced from Poinso and Veynante [156].

a consequence of these small time and length scale, the analysis of flame-interaction remains a challenging task.

Figure 1.6 illustrates how flame, wall and turbulence interact. Understanding how flame interacts with the wall is not only sufficient, but the coupling between the wall and the turbulence along with flame-turbulence interaction are must also be considered [157]. Figure 1.6 demonstrates that the physics of flame-wall interaction in turbulent flows is multifaceted. Despite its importance and presence in modern combustors, the flame-wall interaction is not well understood, which motivates the investigation carried out in this thesis.

1.2 Turbulence

The ubiquity of turbulent flow in nature which ranges from the fragmentation of molecular clouds (see Fig. 1.7) in interstellar space to shimmering on the wrinkled surface of the river. Turbulence has a large influence on the transport characteristics of the flow in engineering applications (e.g. combustion systems). Thus it is necessary to predict turbulent flow characteristics accurately for the purpose of engine design of combustors. However, it is remarkably challenging to make such predictions [67]. This complex behaviour mainly originates due to the non-linear partial differential equations which govern the turbulent fluid motion. The conservation of mass and momentum



Fig. 1.7 Pillars of Creation

Source: *Hubble Goes High Def to Revisit the Iconic 'Pillars of Creation'*. Digital image. *Hubblesite*. NASA. Web. 1 June 2016.

are governed by the subsequent equations in incompressible flows:

$$\nabla \cdot \mathbf{u} = 0 \quad (1.1a)$$

$$\frac{D\mathbf{u}}{Dt} = -\nabla(p/\rho) + \nu\nabla^2\mathbf{u} \quad (1.1b)$$

where \mathbf{u} is the velocity vector, p is the fluid pressure, ρ is the fluid density and ν is the kinematic viscosity. The symbol $D(\cdot)/Dt$ is called the material derivative. The equation 1.1b can be rewritten as:

$$\frac{\partial\mathbf{u}}{\partial t} + (\mathbf{u} \cdot \nabla)\mathbf{u} = -\nabla(p/\rho) + \nu\nabla^2\mathbf{u} \quad (1.2)$$

The term $(\mathbf{u} \cdot \nabla)\mathbf{u}$ introduces non-linearity into the momentum conservation equation. The first term on the right-hand side of Eq. 1.1b arises from pressure force acting on the fluid, and the second term arises from viscous forces. Despite the fact that above equations describe the behaviour of a flow mathematically, a general analytic solution of the Navier-Stokes equations does not exist, and they need to be solved numerically.

The transition from laminar flow to turbulence flow was first examined by Osborne Reynolds [164]. The experiment was performed to study the behaviour of pipe flow by varying pipe diameter D_{pipe} , the velocity of the fluid U and the viscosity. Reynolds

number $Re \sim UD_{\text{pipe}}/\nu$ was established to provide a measure of relative importances of inertial and viscous forces. If inertial forces predominate the effects of viscous forces, the flow becomes turbulent. However, if viscous forces have predominance, any disturbance introduced into the flow will be damped, and the flow will remain laminar. In the experiment, it was found out that the flow becomes turbulent once a critical Reynolds number Re_{crit} is imposed.

Turbulent fluid motion exhibits a wide-ranging eddy sizes, Richardson introduced the concept of the energy cascade in which the turbulent kinetic energy from large eddies is distributed to smaller sized eddies and finally cascades through to the smallest eddies, where it is converted to heat by viscous dissipation [166]. Kolmogorov [115] extended the energy cascade concept from Richardson [166] into his pioneering theory. The parameters which have important influences on the turbulence are the dissipation rate of turbulent kinetic energy, ϵ and its viscosity, ν . The lifespan of a eddy is called eddy turnover time, l_e/u_e , where l_e and u_e are characteristic length and velocity scales associated with an eddy. For range values of Reynolds number, the dissipation of turbulent kinetic energy is governed by inertial effects and thus, ϵ can be further to scale by the kinetic energy decay rate for intergral eddies over their lifetime which leads to $\epsilon \sim u'^2/(l/u') \sim u'^3/l$. The rate of dissipation of energy at the smallest scales is $\epsilon \sim \overline{\nu S_{ij} S_{ij}}$, where $S_{ij} = 0.5(\partial u_i/\partial x_j + \partial u_j/\partial x_i)$ is the component of strain rate tensor, and, the strain rate tensor in the smallest scale can be scaled as: $S_{ij} \sim v_\eta/\eta$, here v_η is the smallest velocity scale and η is the smallest length scale of turbulence. The above descriptions lead to $\epsilon \sim u'^3/l \sim \nu v_\eta^2/\eta^2$. Furthermore, Reynolds number at the smallest scale, $Re_\eta = v_\eta \nu/\eta$, is expected to be the order to unity: $Re_\eta \sim 1$. For the above relations the smallest length scale in turbulent flow (i.e. the Kolmogorov length scale) can be estimated as:

$$\eta = \left(\frac{\nu^3}{\epsilon} \right)^{1/4} \quad (1.3)$$

Similarly the smallest velocity scale (i.e. Kolmogorov velocity scale) can be estimated as:

$$v_\eta = (\nu \epsilon)^{1/4} \quad (1.4)$$

A numerical simulation needs to resolve the Kolmogorov length scale to simulate turbulent flows without any physical approximation. The simulations where the

Kolmogorov length scale is resolved without any physical approximation are called Direct Numerical Simulations (DNS).

1.3 Direct numerical simulation

This section provides a brief introduction of flame-wall interaction and the role of numerical simulations.

1.3.1 Simulation tools

From the time of the advent of computers in the 50s of last century, Computational Fluid Dynamics (CFD) has arisen as an increasingly reliable and sophisticated tool to simulate and understand complex turbulent flow processes including turbulent combustion. Nowadays in the industry, CFD simulations are routinely carried out using Reynolds-Averaged Navier-Stokes (RANS) and Large Eddy Simulations (LES) where the physical processes correlated with length scales diminutive in comparison to the computational grid spacing need to be approximated using turbulence models. However, unavailability of reliable data for flame-wall interaction compromises the predictive aptitude of those models. Also, the boundary layers involving turbulent reacting flows are modelled (inaccurately) using the knowledge gained for isothermal flow conditions. In the last decade or so, the availability of increased computer power has offered an important research avenue to investigate the flame-wall interaction with the help of DNS where all the relevant turbulent length and time scales are satisfactorily resolved. An extensive review of CFD methods can be found in [104, 125]. Figure 1.8 presents the schematic diagram of the turbulent energy spectrum $E(\kappa)$ with the resolution offered by different simulation techniques, where Δ and Δx are the filter size and the grid spacing, respectively. The figure indicates that the computational grid of RANS and LES only partially resolve the energy spectrum. However, DNS resolves the most region of the turbulent energy spectrum $E(\kappa)$ and only a minor region related to the viscous dissipation which takes place at the sub-grid level.

Analysing turbulent reacting flows is complicated due to the presence of the reaction rate which is strongly non-linearly dependent on temperature. The existing methodologies for analysing of the non-reacting flows are not always applicable for reacting flows due to the complexity of combustion process. To simulate engineering combustion devices, the chemical aspects of the reacting flow must be addressed as well as the transport mechanisms associated with chemical heat release. Moreover, the

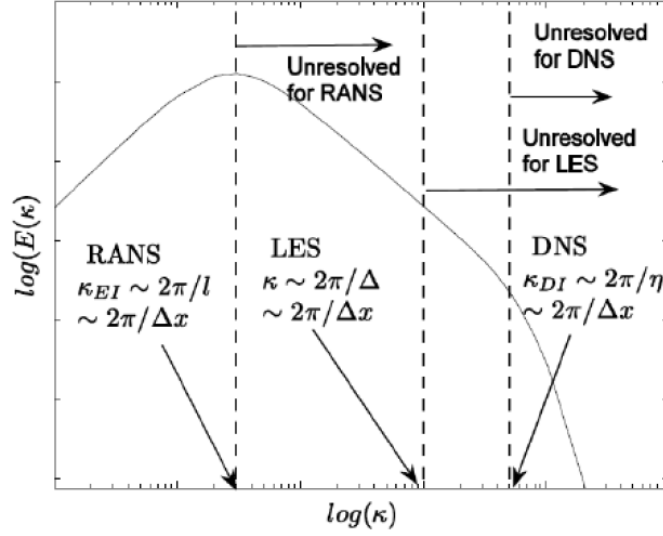


Fig. 1.8 A schematic diagram of turbulent energy spectrum $E(\kappa)$ with wave number κ showing the capabilities of different simulation techniques

transport properties of viscosity, mass diffusivity and thermal conductivity which are temperature dependent further increase the complexity of the behaviour of momentum, heat and mass transports.

1.3.2 Direct numerical simulations of flame-wall interaction

In last few decades Direct Numerical Simulations (DNS) contributed significantly to the fundamental understanding of non-reacting turbulent boundary layers, but thermal expansion due to chemical heat release leads to significant modifications to velocity and temperature distributions within turbulent reacting flow boundary layers. However, relatively limited effort has been directed to the analysis of wall-bound turbulent reacting flows using DNS simulations [156, 20, 21, 3, 2, 90, 65]. Poinso *et al.* [156] concentrated on head-on quenching of turbulent premixed flame-wall interaction based on two-dimensional DNS, which indicated that the vorticity field within the flame front is significantly affected by the presence of wall. Moreover, they investigated the statistical behaviours of wall heat flux and flame quenching distance. Bruneaux *et al.* [20] conducted three-dimensional incompressible DNS to premixed flame-wall interaction in a channel flow configuration, and this data was subsequently used to analyse the influences of the wall on the Flame Surface Density (FSD) transport [21]. Alshalaan and Rutland [3, 2] analysed the near wall statistics of FSD, turbulent scalar flux and wall heat flux based on DNS simulations of turbulent V-flame interaction

with an isothermal wall. DNS data [156, 20, 21, 3, 2, 90, 65] on turbulent premixed flame-wall interaction demonstrated that the maximum value of wall heat flux in turbulent flows can assume much greater values than the corresponding laminar flame value. This behaviour can be attributed to the convection of flame elements towards the wall [156]. Additionally, in turbulent channel flows, the flame elements are pushed towards the wall by the stream-wise vortices which lead to an increase in heat flux, whereas convection away from the wall tends to reduce the wall heat flux. Dabireau *et al.* [65] found out that the high wall flux values take place before the flame quenching occurs based on premixed flame-wall interaction for $\text{H}_2 + \text{O}_2$ mixtures. A detailed chemistry 3D DNS study carried out by Gruber [90] demonstrated that combustion instabilities in turbulent reacting flow boundary succeeding could create the flame flashback near the wall but their implications on the near wall modelling of turbulent premixed combustion, are yet to be analysed in detail. The modelling of turbulent premixed flame-wall interaction has received limited attention [21, 3, 2] and thus here aims to address this deficit in the existing literature by analysing the turbulent premixed combustion modelling in the near-wall region.

1.4 Objectives of this analysis

The purpose of this analysis to investigate turbulent premixed flame-wall interaction in a simple configuration using three-dimensional Direct Numerical Simulations (DNS). This DNS data will subsequently be explicitly Reynolds averaged to assess the performances of existing models on the corresponding unclosed quantities extracted from DNS data. Based on this *a-priori* DNS analysis modifications to the existing models will be suggested and new models will be proposed if necessary. The present project intends to address the following aspects in turbulent premixed flame-wall interaction:

- Simulations of different configurations for flame-wall interaction such as head-on quenching and side-wall quenching. The results obtained from DNS will be compared on existing findings and experiment results [156, 20, 21, 3, 2, 90, 65]. The fundamental physical insights obtained from DNS data will be used for assessments of the near-wall behaviour of turbulent combustion models used for RANS simulation. Based on the performance of the existing flame-wall interaction models, either modification to the existing models will be suggested, or new models will be proposed.

- Investigation and modelling of preferential diffusion on different aspects of flame-wall interaction arising from non-unity Lewis number, for different values of root-mean-square turbulent velocity fluctuation, the integral length scale of the turbulence, and effects of heat release parameters.
- To compare findings obtained from simple chemistry DNS with the corresponding results obtained from detailed chemistry DNS data.

1.5 Thesis outline

This PhD thesis contains seven chapters (see Fig 1.9), where this Chapter provides the necessary introduction. Chapter 2 provides the mathematical background of the current work and the relevant assumptions. A summary of existing research on computational analysis and modelling of turbulent premixed flame-wall interaction is provided in Chapter 3. Chapter 4 describes the numerical methods which are used in the present study along with the methodologies used for boundary condition specification and generation of initial conditions. Chapter 5 provides physical insights of head-on quenching of turbulent premixed flames using DNS simulations. The modelling various unclosed quantities for RANS are discussed in Chapter 6 based on an *a-priori* DNS analysis of head-on quenching DNS data. Chapter 7 presents the results for DNS of side-wall quenching of turbulent V-flame by isothermal inert walls and sample results for head-on quenching of statistically planar flames using detailed chemistry DNS. Finally, Chapter 8 summarises of this investigation and identifies further avenues of research.

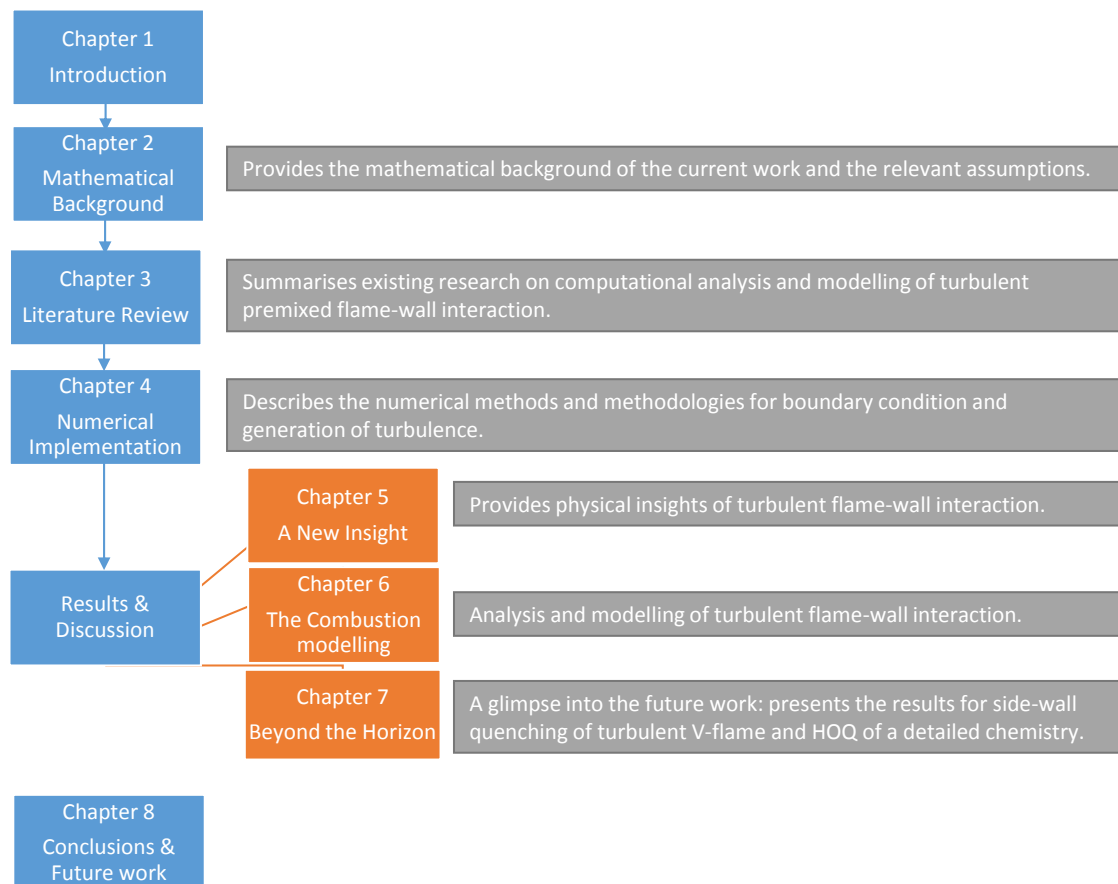


Fig. 1.9 A flow chart of the structure of current thesis

Chapter 2

Mathematical Background

This chapter presents the overview of the governing equations for DNS analysis of turbulent reacting flows along with the assumptions made for the purpose of the current analysis. Additionally, the derivation of the modelling aspects are also presented.

2.1 Problem description

The present DNS analysis of turbulent premixed flame-wall interaction is carried out in three types of configurations and their corresponding names used in the current thesis are listed as below. A DNS code SENGAs [102] was used to generate the one-step simplified chemistry DNS database and SENGAs2 [27] was used to produce the detailed methane-air chemistry database in the current work.

- Head-on quenching (HOQ) for one-step simplified chemistry simulation: A no-slip isothermal inert wall with temperature equal to the fresh gas temperature ($T_w = T_0$) is placed on the left hand side boundary in the x_1 -direction (i.e. $x_1 = 0$, see Fig. 2.1-left), where zero mass flux is enforced in the wall normal direction. A partially non-reflecting outlet boundary condition is specified for the domain boundary opposite to the isothermal wall. The transverse directions x_2 and x_3 are taken to be periodic.
- V-flame channel flow simulation with one-step simplified chemistry: A rectangular domain with the aforementioned wall boundary conditions are specified in x_2 -direction at $x_2 = 0$ (i.e. lower wall) and $x_2 = L_2$ (for upper wall where L_2 is the domain length in x_2 -direction). Turbulent inflow and partially non-reflecting boundary conditions are specified in x_1 -direction, whereas periodic boundaries are considered for x_3 -direction. A flame holder is placed in the vicinity of the

bottom wall at a certain distance from the inlet following the previous analysis by Alshalaan and Rutland [2].

- HOQ for 35 steps CH_4 -air detailed chemistry simulation: boundary conditions are taken to be the same as HOQ for simple chemistry simulation (see Fig. 2.1).

The spatial derivatives are evaluated by using 10th order central differencing scheme for the internal grid points [102]. The order of differentiation drops gradually to a one-sided 2th order scheme at the non-periodic boundaries. The flame is initialised using an unstrained steady planar laminar flame solution in both simple and detailed chemistry simulations of HOQ. For V-flame simulation, the flame holder is responsible for flame generation inside the domain.

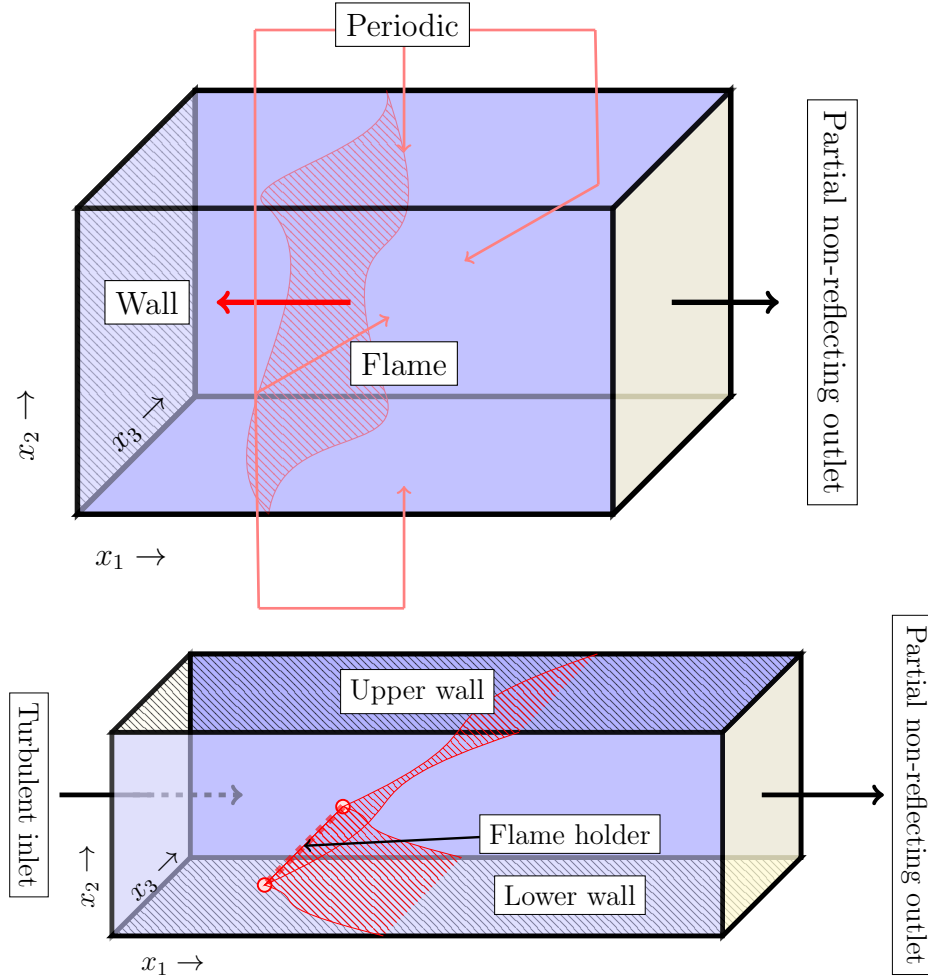


Fig. 2.1 Description of computational domain: HOQ (Top), Side-wall quenching (Bottom).

2.2 Governing equations

The three-dimensional motion of reactive gases is governed by mass, continuity, momentum, energy and species conservation equations. Those equations can be stated in Cartesian tensor notation in the following manner:

$$\frac{\partial}{\partial t}\rho + \frac{\partial}{\partial x_k}\rho u_k = 0 \quad (2.1a)$$

$$\frac{\partial}{\partial t}\rho u_i + \frac{\partial}{\partial x_k}\rho u_k u_i = -\frac{\partial}{\partial x_i}p + \frac{\partial}{\partial x_k}\tau_{ki} \quad (2.1b)$$

$$\frac{\partial}{\partial t}\rho E + \frac{\partial}{\partial x_k}\rho u_k E = -\frac{\partial}{\partial x_k}p u_k + \frac{\partial}{\partial x_k}\tau_{ki} u_i - \frac{\partial}{\partial x_k}q_k \quad (2.1c)$$

$$\frac{\partial}{\partial t}\rho Y_\alpha + \frac{\partial}{\partial x_k}\rho u_k Y_\alpha = \dot{\omega}_\alpha - \frac{\partial}{\partial x_k}\rho V_{\alpha,k} Y_\alpha, \quad \alpha = 1, \dots, N \quad (2.1d)$$

where ρ is the density, u_i is the i^{th} component of the velocity vector, p is the pressure, E is the stagnation internal energy, Y_α is the mass fraction of the species α in reacting mixture with total N species and its reaction rate $\dot{\omega}_\alpha$. τ_{ki} is the viscous stress tensor which is defined by:

$$\tau_{ki} = \mu \left(\frac{\partial u_k}{\partial x_i} + \frac{\partial u_i}{\partial x_k} \right) - \frac{1}{2} \mu \frac{\partial u_m}{\partial x_m} \delta_{ki} \quad (2.2)$$

where δ_{ki} is the Kronecker delta ($\delta_{ki} = 1$ for $k = i$, otherwise $\delta_{ki} = 0$) and μ is the dynamic viscosity. The compatibility condition of Y_α is specified as:

$$\sum_{\alpha=1}^N Y_\alpha = 1 \quad (2.3)$$

The thermal equation of state for the reacting mixture is:

$$p = \rho R^0 \hat{T} \sum_{\alpha=1}^N \frac{Y_\alpha}{W_\alpha} \quad (2.4)$$

where R^0 is the ideal gas constant, W_α is the molecular weight of species α and the caloric equation of state is defined as:

$$E = \sum_{\alpha=1}^N h_\alpha Y_\alpha - \frac{p}{\rho} + \frac{1}{2} u_k u_k \quad (2.5)$$

while the enthalpy h_α of species α is:

$$h_\alpha = \int_{T_0}^T C_{p,\alpha} d\hat{T} + h_\alpha^0 \quad (2.6)$$

in which $C_{p,\alpha}$ is the mass based specific heat capacity of species α , \hat{T} is the instantaneous temperature, T_0 is the fresh gas temperature (i.e. reference temperature) and h_α^0 is the enthalpy of formation of species α . The heat flux vector q_k is given by:

$$q_k = -\lambda \frac{\partial \hat{T}}{\partial x_k} + \rho \sum_{\alpha=1}^N h_\alpha V_{\alpha,k} Y_\alpha \quad (2.7)$$

where $V_{\alpha,k}$ is the diffusion velocity vector of the species α relative to the mixture, while it must satisfy the compatibility condition:

$$\sum_{\alpha=1}^N \rho V_{\alpha,k} Y_\alpha = 0 \quad (2.8)$$

The molar specific heat capacity $\bar{C}_{p,\alpha}$ at constant pressure depends on temperature for a semi-perfect gas. In SENG2 code, the temperature dependence is approximated by using a polynomial of the form:

$$\bar{C}_{p,\alpha} = R^0 \sum_{j=1}^J \bar{a}_{\alpha,j}^{(l)} T^{j-1} \quad (2.9)$$

where the degree $J - 1$ of the polynomial is taken to be 4 or 5, $\bar{a}^{(l)}$ is the polynomial coefficients with different intervals l of temperature. The selection of the coefficients can be seen in Ref. [110]. The final form for the molar enthalpy based on temperature dependent $\bar{C}_{p,\alpha}$ yields the following form:

$$\bar{h}_\alpha = R^0 \left[\sum_{j=1}^J \frac{\bar{a}_{\alpha,j}^{(L)}}{j} T^j + \bar{a}_{\alpha,J+1}^{(L)} \right] \quad (2.10)$$

L denotes as the lower end of the current temperature interval.

2.3 Thermochemistry

M steps of a reaction mechanism takes the following form:

$$\sum_{\alpha=1}^N \nu'_{\alpha,m} \mathcal{M}_{\alpha} \rightarrow \sum_{\alpha=1}^N \nu''_{\alpha,m} \mathcal{M}_{\alpha}, \quad m = 1, \dots, M \quad (2.11)$$

where \mathcal{M}_k is a symbol for species k , $\nu'_{\alpha,m}$ is the reactant stoichiometric coefficient for step m , $\nu''_{\alpha,m}$ is the product stoichiometric coefficients for step m . The chemical reaction rate $\dot{\omega}$ of species α for a mechanism involving N species and M steps can be stated as:

$$\dot{\omega}_{\alpha} = W_{\alpha} \sum_{m=1}^M \left[(\nu''_{\alpha,m} - \nu'_{\alpha,m}) A_m \hat{T}^{n_m} \exp \left(-\frac{E_m}{R^0 \hat{T}} \right) \prod_{\beta=1}^N \left(\frac{\rho Y_{\beta}}{W_{\beta}} \right)^{\nu'_{\beta,m}} \right] \quad (2.12)$$

while A_m is the frequency factor, n_m is the temperature exponent and E_m is the activation energy.

In the first part of the analysis, a one-step irreversible reaction is assumed due to the computational economy to allow for an extensive parametric analysis based on three-dimensional turbulent flame-wall interaction. In this context the generic chemical reaction for one-step chemistry takes the following form:



The objective of simplifying chemistry is to enable the replacement of the $N - 1$ conservation equations for the species mass fraction equations by a single conservation equation for the reaction progress variable c , which is defined based on the mass fraction of the reactant species Y_R in the following manner:

$$c = \frac{Y_{R0} - Y_R}{Y_{R0} - Y_{R\infty}} \quad (2.14)$$

According to Eq. 2.14, c increases monotonically from zero in the unburned gas (subscript 0) to unity in fully burned products (subscript ∞).

The reaction rate for the one-step reaction based on the simplified Arrhenius rate law is given as:

$$\dot{\omega} = B\rho(1 - c)\exp \left[\frac{-E}{R^0 \hat{T}} \right] \quad (2.15)$$

where B is the pre-exponential factor, E is the activation energy. The progress variable c balance equation is stated as:

$$\frac{\partial \rho c}{\partial t} + \frac{\partial \rho u_j c}{\partial x_j} = \dot{\omega} + \frac{\partial}{\partial x_j} \left[\rho D \frac{\partial c}{\partial x_j} \right] \quad (2.16)$$

The diffusion velocity appears in the equation is assumed to obey Fick's law of diffusion, D is the mass diffusion coefficient, which is a function of thermo-chemical variables:

$$\rho V_{cj} c = -\rho D \frac{\partial c}{\partial x_j} \quad (2.17)$$

The reaction progress variable transport equation could also be written in kinematic form for a $c = c^*$ isosurface in the following manner:

$$\left. \frac{\partial c}{\partial t} \right|_{c=c^*} + u_j \Big|_{c=c^*} \left. \frac{\partial c}{\partial x_j} \right|_{c=c^*} = S_d |\nabla c|_{c=c^*} \quad (2.18)$$

where S_d is the displacement speed of an isosurface $c = c^*$, and it is given by:

$$S_d = \frac{\dot{\omega}|_{c=c^*} + \frac{\partial}{\partial x_j} \left[\rho D \frac{\partial c}{\partial x_j} \right]_{c=c^*}}{\rho_{c=c^*} \sqrt{\left| \frac{\partial c}{\partial x_j} \frac{\partial c}{\partial x_j} \right|}} \quad (2.19)$$

The equations of state in simplified chemistry are:

$$p = \rho R \hat{T} \quad (2.20a)$$

$$E = C_v \hat{T} + \frac{1}{2} u_j u_j + H(1 - c) \quad (2.20b)$$

where H is the heat of reaction per unit mass of reactants consumed. The heat flux vector is give as:

$$q_k = -\lambda \frac{\partial \hat{T}}{\partial x_k} + \rho D H \frac{\partial c}{\partial x_k} \quad (2.21)$$

In detailed chemistry simulation (by SENG2), a more accurate approach or greater generality in the treatment of molecular transport phenomena is adopted, where the molecular transport coefficients for the mixture are assembled from molecular transport

data for each species. The Fick's law is rewritten as:

$$\rho V_{\alpha,k} Y_{\alpha} = -\hat{d}_{\alpha,k} - \rho D_{\alpha} Y_{\alpha} \hat{\theta}_{\alpha}^{(T)} \frac{1}{T} \frac{\partial T}{\partial x_k} \quad (2.22)$$

where $-\rho D_{\alpha} Y_{\alpha} \hat{\theta}_{\alpha}^{(T)} (1/T) \partial T / \partial x_k$ represents the thermal diffusion flux (or Soret effect), the quantity $\hat{\theta}_{\alpha}^{(T)}$ is the mixture-averaged thermal diffusion ratio for species α , and the quantity $\hat{d}_{\alpha,k}$ is given by:

$$\hat{d}_{\alpha,k} = \rho D_{\alpha} \frac{\partial Y_{\alpha}}{\partial x_k} + \rho D_{\alpha} Y_{\alpha} \frac{1}{W_m} \frac{\partial W_m}{\partial x_k} + \rho D_{\alpha} Y_{\alpha} \left(1 - \frac{W_{\alpha}}{W_m}\right) \frac{1}{p} \frac{\partial p}{\partial x_k} \quad (2.23)$$

where W_m is the effective molar mass for the mixture which is given by:

$$W_m = \sum_{\alpha=1}^N \frac{W_{\alpha}}{Y_{\alpha}} \quad (2.24)$$

In mixture averaged transport the heat flux vector is given as:

$$q_k = -\lambda \frac{\partial T}{\partial x_k} + \sum_{\alpha=1}^N \rho V_{\alpha,k} Y_{\alpha} h_{\alpha} - \sum_{\alpha=1}^N \frac{R^0 T}{W_{\alpha}} \hat{\theta}_{\alpha}^{(T)} \hat{d}_{\alpha,k} \quad (2.25)$$

where the second term on the right-hand side represents the diffusion thermal flux (or Dufour effect).

2.4 Non-dimensional numbers

The governing equations for a one-step chemistry DNS simulation are non-dimensionalised by using reference values of principal variables (i.e. $u_0, l_0, t_0, \rho_0, T_0$). Those variables are listed below:

- Reference velocity u_0 is taken to be the unstrained laminar flame speed S_L
- Reference length l_0 is taken to be the thermal flame thickness δ_{th} (see Eq. 2.28)
- Reference time t_0 can be represented by l_0/u_0
- Reference density ρ_0 is unburned gas density
- Reference temperature T_0 is unburned gas temperature

Additional reference values for the transport coefficients are $\mu_0, \lambda_0, \rho_0 D_0, C_{V0}$. The specific heats at constant pressure and volume C_P and C_V , thermal conductivity λ

and ρD are assumed to be constant in one-step simplified chemistry simulation with neglect of Soret and Dufour effects. The normalising pressure $P_0 = \rho_0 u_0^2$ is taken to be representative of dynamic instead of thermal-chemical effects. The temperature is non-dimensionalised by the adiabatic flame temperature T_{ad} and unburned gas temperature T_0 as:

$$T = \frac{\hat{T} - T_0}{T_{\text{ad}} - T_0} \quad (2.26)$$

Adiabatic flame temperature is the maximum flame temperature that could be achieved in the flame with the absence of differential diffusion:

$$T_{\text{ad}} = T_0 + \frac{H}{C_{P0}} \quad (2.27)$$

The thermal flame thickness is defined as:

$$\delta_{\text{th}} = \frac{T_{\text{ad}} - T_0}{\max|\nabla \hat{T}|_L} \quad (2.28)$$

where subscript ‘L’ refers to the values in steady unstrained planar flame. The non-dimensional parameters used in the study are as follows:

- $Re = (\rho_0 u_0 l_0)/\mu_0$ - Reynolds number provides the ratio of inertial force to viscous force
- $Pr = (\mu_0 C_{P0})/\lambda_0$ - Prandtl number provides the measure of momentum diffusion to thermal diffusion
- $Sc = \mu_0/(\rho_0 D_0)$ - Schmidt number provides the measure of momentum diffusion to mass diffusion
- $Ma = u_0/a_0$ - Mach number, where sonic speed $a_0 = \sqrt{\gamma R T_0}$ is the sonic speed according to ideal gas law
- $Le = \lambda_0/(\rho_0 C_{P0} D) = Sc/Pr$ - Lewis number represents the ratio of thermal diffusivity to mass diffusivity

The ratio of specific heat γ , the heat release parameter τ and α , the Zeldovich number β , and the pre-exponential factor B^* are given by:

$$\gamma = \frac{C_{P0}}{C_{V0}} \quad (2.29a)$$

$$\tau = \frac{\alpha}{1 - \alpha} = \frac{T_{ad} - T_0}{T_0} \quad (2.29b)$$

$$\beta = \frac{E(T_{ad} - T_0)}{RT_{ad}^2} \quad (2.29c)$$

$$B^* = \frac{Bl_0}{\rho_0 u_0} \exp\left(-\frac{\beta}{\alpha}\right) \quad (2.29d)$$

Based on the aforementioned non-dimensionalisation, the non-dimensional form of the governing equations take the following form:

$$\frac{\partial}{\partial t^+} \rho^+ + \frac{\partial}{\partial x_k^+} \rho^+ u_k^+ = 0 \quad (2.30a)$$

$$\frac{\partial}{\partial t^+} \rho^+ u_i^+ + \frac{\partial}{\partial x_k^+} \rho^+ u_k^+ u_i^+ = -\frac{\partial}{\partial x_i^+} P^+ + \frac{1}{Re} \frac{\partial}{\partial x_k^+} \tau_{ki}^+ \quad (2.30b)$$

$$\begin{aligned} \frac{\partial}{\partial t^+} \rho^+ E^+ + \frac{\partial}{\partial x_k^+} \rho^+ u_k^+ E^+ = & -(\gamma - 1) Ma^2 \frac{\partial}{\partial x_k^+} P^+ u_k^+ + \frac{1}{Re} (\gamma - 1) Ma^2 \frac{\partial}{\partial x_k^+} \tau_{ki}^+ u_i^+ \\ & + \frac{\tau}{RePr} \frac{\partial}{\partial x_k^+} \left[\lambda \frac{\partial T}{\partial x_k^+} \right] - \frac{\tau}{ReSc} \frac{\partial}{\partial x_k^+} \left[\rho^+ D^+ \frac{\partial c}{\partial x_k^+} \right] \end{aligned} \quad (2.30c)$$

$$\frac{\partial}{\partial t^+} \rho^+ c + \frac{\partial}{\partial x_k^+} \rho^+ u_k^+ c = \dot{\omega}^+ + \frac{1}{ReSc} \frac{\partial}{\partial x_k^+} \left[\rho^+ D^+ \frac{\partial c}{\partial x_k^+} \right] \quad (2.30d)$$

2.5 Non-dimensional number in the flame-wall interaction

The non-dimensional distance from the flame front and the wall is described by Peclet number Pe where it is used as an indicator of advective and diffusive strength from

the normal direction of the wall:

$$Pe = \frac{x_1}{\delta_Z} \quad (2.31)$$

The flame-wall distance x_1 is normalised by the Zel'dovich flame thickness $\delta_Z = \alpha_{T_0}/S_L$. Flame power is defined by the local consumption flame speed (or local flame speed) S_c , which changes when the flame moves towards the wall:

$$\text{Flame power} = \frac{\rho_0 S_c C_P (T_{ad} - T_0)}{\rho_0 S_L C_P T_0} = \frac{\tau S_c}{S_L} \quad (2.32)$$

Non-dimensional wall heat flux Φ is scaled by flame power, which is:

$$\Phi = \frac{|\phi|}{\rho_0 S_L C_P (T_{ad} - T_0)} \quad (2.33)$$

where ϕ is the wall heat flux which is measured as the heat flux at the wall. Both Pe and Φ changes with time during flame-wall interaction.

2.6 Investigation of turbulence

Laminar premixed flame propagates from the normal direction of the burned products towards the unburned reactants with a laminar flame speed of S_L . However, the flame front interacts with turbulent vortices may lead to increase in the propagation speed, mass consumption rate and reduction in the flame thickness. The statistical behaviour of vorticity $\vec{\omega}$ and enstrophy $\Omega = \vec{\omega} \cdot \vec{\omega}/2$ plays a significant role in the analysis of turbulent fluid motion [78, 162], and these statistics are significantly affected by heat release, density variation and flame normal acceleration in turbulent premixed flames [128]. Studying the flow topology (regionally organised motions) can capture this chaotic behaviour of turbulence. Though, analysing the vorticity transport, enstrophy transport, and flow topology provides a better understanding of the flame-wall interaction.

2.6.1 Vorticity and entrophy transport

The transport equation of the i^{th} component of vorticity $\omega_i = \varepsilon_{ijk}(\partial u_k / \partial x_j)$ is given by [44, 129, 191]:

$$\frac{\partial \omega_i}{\partial t} + u_k \frac{\partial \omega_i}{\partial x_k} = \underbrace{\omega_k \frac{\partial u_i}{\partial x_k}}_{t_{1i}} - \underbrace{\epsilon_{ijk} \frac{1}{\rho^2} \frac{\partial \rho}{\partial x_j} \frac{\partial \tau_{kl}}{\partial x_L}}_{t_{21i}} + \underbrace{\frac{\epsilon_{ijk}}{\rho} \frac{\partial^2 \tau_{kl}}{\partial x_j \partial x_L}}_{t_{22i}} - \underbrace{\omega_i \frac{\partial u_k}{\partial x_k}}_{t_{3i}} + \underbrace{\frac{\epsilon_{ijk}}{\rho^2} \frac{\partial \rho}{\partial x_j} \frac{\partial p}{\partial x_k}}_{t_{4i}} \quad (2.34)$$

In Eq. 2.34, \vec{t}_1 is the vortex-stretching term, whereas \vec{t}_{21} and \vec{t}_{22} arise from the misalignment between the gradients of viscous stress and density and from the diffusion of vorticity, respectively. For constant dynamic viscosity (i.e. $\mu = \text{constant}$) incompressible flows, \vec{t}_{22} becomes equal to $(\mu/\rho)\nabla^2 \vec{\omega}$. However, for constant dynamic viscosity compressible flows, \vec{t}_{22} takes the form $\vec{t}_{22} = (\mu/\rho)\nabla^2 \vec{\omega} + (\mu/3\rho)\nabla \times \nabla(\nabla \cdot \vec{u})$. The term \vec{t}_3 accounts for the dilatation contribution, and \vec{t}_4 is responsible for the baroclinic effects arising from the misalignment of the density and pressure gradients. Multiplying Eq. 2.34 by ω_i yields the transport equation for the enstrophy (i.e. $\Omega = \omega_i \omega_i / 2$) [44, 129]:

$$\begin{aligned} \frac{\partial \Omega}{\partial t} + u_k \frac{\partial \Omega}{\partial x_k} = & \underbrace{\omega_i \omega_k \frac{\partial u_i}{\partial x_k}}_{T_1} - \underbrace{\epsilon_{ijk} \omega_i \frac{1}{\rho^2} \frac{\partial \rho}{\partial x_j} \frac{\partial \tau_{kl}}{\partial x_L}}_{T_2} + \underbrace{\frac{\epsilon_{ijk} \omega_i}{\rho} \frac{\partial^2 \tau_{kl}}{\partial x_j \partial x_L}}_{T_3} \\ & - \underbrace{2\Omega \frac{\partial u_k}{\partial x_k}}_{T_4} + \underbrace{\frac{\epsilon_{ijk} \omega_i}{\rho^2} \frac{\partial \rho}{\partial x_j} \frac{\partial p}{\partial x_k}}_{T_5} \end{aligned} \quad (2.35)$$

The Reynolds-averaged enstrophy (i.e. $\bar{\Omega} = \overline{\omega_i \omega_i} / 2$, and the over-bar is defined as the Reynolds-averaged quantity) transport equation can be obtained using Eq. 2.35 as [44, 129]:

$$\begin{aligned} \frac{\partial \bar{\Omega}}{\partial t} + u_k \frac{\partial \bar{\Omega}}{\partial x_k} = & \underbrace{\overline{\omega_i \omega_k \frac{\partial u_i}{\partial x_k}}}_{T_I} - \underbrace{\overline{\epsilon_{ijk} \omega_i \frac{1}{\rho^2} \frac{\partial \rho}{\partial x_j} \frac{\partial \tau_{kl}}{\partial x_L}}}_{T_{II}} + \underbrace{\overline{\frac{\epsilon_{ijk} \omega_i}{\rho} \frac{\partial^2 \tau_{kl}}{\partial x_j \partial x_L}}}_{T_{III}} \\ & - \underbrace{\overline{2\Omega \frac{\partial u_k}{\partial x_k}}}_{T_{IV}} + \underbrace{\overline{\frac{\epsilon_{ijk} \omega_i}{\rho^2} \frac{\partial \rho}{\partial x_j} \frac{\partial p}{\partial x_k}}}_{T_V} \end{aligned} \quad (2.36)$$

The term T_I indicates the vortex-stretching contribution, whereas T_{II} arises due to misalignment between gradients of density and viscous stresses. The term T_{III} is responsible for molecular diffusion and dissipation of $\bar{\Omega}$, whereas T_{IV} and T_V represent the dilatation and baroclinic torque contributions respectively.

Under the assumption of constant dynamic viscosity, the dissipation rate $\tilde{\epsilon}$ of turbulent kinetic energy $\tilde{k} = \overline{\rho u_i'' u_i''}/2\bar{\rho}$ is closely related to enstrophy as: $\bar{\rho}\tilde{\epsilon} \approx 2\bar{\mu}\bar{\Omega}$ in the isotropic Kolmogorov turbulence [189]. It has been demonstrated in the present literature [130, 155, 191] that the influences of a flame on the major statistical characteristics of turbulent flow, such as $\tilde{k}, \tilde{\epsilon}, \bar{\Omega}$, remain qualitatively similar in the cases of temperature-dependent and constant dynamic viscosity. This similarity stems from the fact that, due to a decrease in the density ρ with increasing temperature, the kinematic viscosity $\nu = \mu/\rho$ increases in flames under both conditions. Here the constant viscosity assumption is adopted for the purpose of simplicity. Under such conditions, the mean dissipation rate $\tilde{\epsilon}$ is directly proportional to the mean enstrophy $\bar{\Omega}$. Therefore, the understanding of $\bar{\Omega}$ transport is crucial for addressing the modelling of the dissipation rate of turbulent kinetic energy.

2.6.2 Flow topology

The local flow topologies are characterised by the invariants of the velocity-gradient tensor [152, 57]:

$$A_{ij} = \frac{\partial u_i}{\partial x_j} = S_{ij} + W_{ij} \quad (2.37)$$

where the symmetric strain-rate tensor is $S_{ij} = 0.5(A_{ij} + A_{ji})$ and the anti-symmetric rotation rate tensor is $W_{ij} = 0.5(A_{ij} - A_{ji})$. The eigenvalues of A_{ij} are λ_1, λ_2 and λ_3 which are the solutions of the characteristics equation $\lambda^3 + P\lambda^2 + Q\lambda + R = 0$ with its invariants P, Q and R as specified below [152, 57]:

$$P = -\text{tr}(A_{ij}) = -(\lambda_1 + \lambda_2 + \lambda_3) = -S_{ii} \quad (2.38)$$

$$Q = \frac{1}{2} \left([\text{tr}(A_{ij})]^2 - \text{tr}(A_{ij}^2) \right) = \frac{1}{2} (P^2 - S_{ij}S_{ij} + W_{ij}W_{ij}) = Q_S + \underbrace{W_{ij}W_{ij}/2}_{Q_W} \quad (2.39)$$

$$R = -\det(A_{ij}) = \frac{1}{3} (-P^3 + 3PQ - S_{ij}S_{jk}S_{ki} - 3W_{ij}W_{jk}S_{ki}) \quad (2.40)$$

The discriminant D , is shown in the equation below, divides the $P - Q - R$ phase space into two regions: A_{ij} shows a focal topology for $D > 0$ region and it displays a

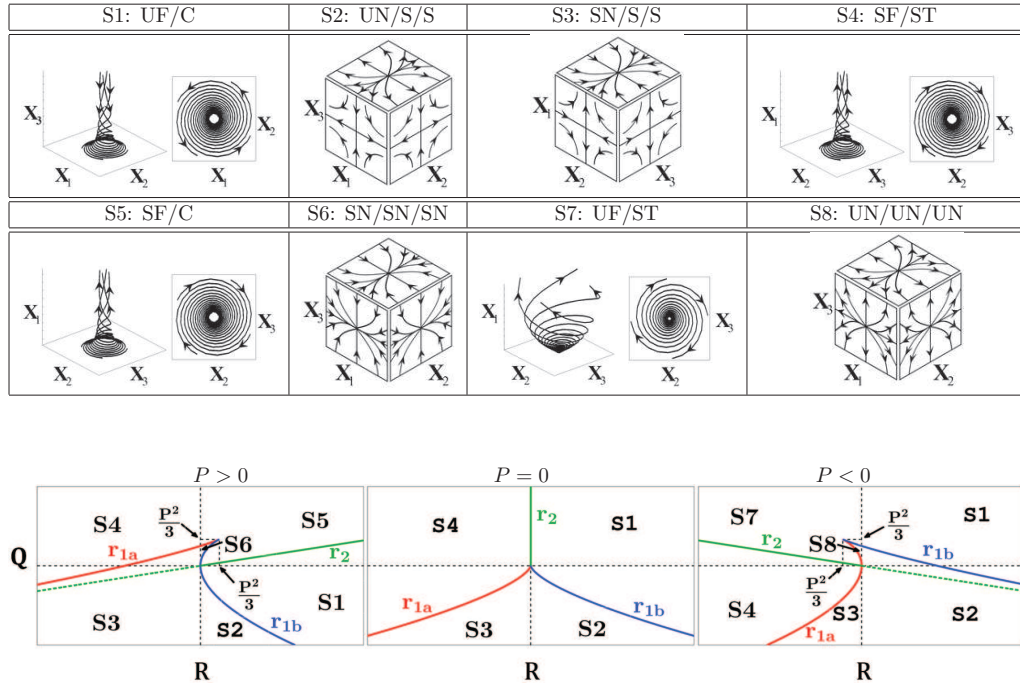


Fig. 2.2 Classification of $S1 - S8$ topologies (UF = unstable focus, UN = unstable node, SF = stable focus, SN = stable node, S = saddle, C = compressing, ST = stretching) in the $Q - R$ plane with the lines r_{1a} , r_{1b} and r_2 dividing the topologies, and black dashed lines indicates $Q = R = 0$.

nodal topology for $D < 0$ region [152, 57]:

$$D = \frac{1}{108} \left[27R^2 + (4P^3 - 18PQ)R + 4Q^3 - P^2Q^2 \right] \quad (2.41)$$

The surface $D = 0$ leads to two surfaces r_{1a} and r_{1b} in the $P - Q - R$ phase space:

$$r_{1a} = \frac{1}{3}P \left(Q - \frac{2}{9}P^2 \right) - \frac{2}{27}(-3Q + P^2)^{3/2} \quad (2.42)$$

$$r_{1b} = \frac{1}{3}P \left(Q - \frac{2}{9}P^2 \right) + \frac{2}{27}(-3Q + P^2)^{3/2} \quad (2.43)$$

Additionally, A_{ij} has purely imaginary eigenvalues on the surface r_2 which is given by $R = PR$. The surface r_{1a} , r_{1b} and r_2 , where r_2 is described by $PQ - R = 0$, divide the $P - Q - R$ phase space into the 8 distinct flow topologies as shown in Fig. 2.2.

2.7 Favre-averaged approach to numerical simulations of turbulent combustion

Turbulence has characteristic of random fluctuations of various physical variables. In low Mach number non-reactive turbulent flow, density variation is expected to be small, and density is considered to be constant. Thus, the popular engineering approach to simulate the turbulent non-reacting flow consists of numerically solving averaged quantities of the Navier-Stokes equation. However, density variation is significant due to the high heat release from the chemical reaction in turbulent reacting flows. Therefore, the transport equations in Eq. 2.1 need to take into account of density variations by using the Favre-averaged quantities, whereas for a general quantity q is $\tilde{q} = \overline{\rho q} / \bar{\rho}$ and $q'' = q - \tilde{q}$. Favre averaging on mass conservation and momentum transports from Eqs. 2.1a and 2.1b obtain:

$$\frac{\partial}{\partial t} \bar{\rho} + \frac{\partial}{\partial x_k} \bar{\rho} \tilde{u}_k = 0 \quad (2.44a)$$

$$\frac{\partial}{\partial t} \bar{\rho} \tilde{u}_i + \frac{\partial}{\partial x_k} \bar{\rho} \tilde{u}_k \tilde{u}_i = - \frac{\partial}{\partial x_i} \bar{p} + \frac{\partial}{\partial x_k} \bar{\tau}_{ki} - \underbrace{\frac{\partial}{\partial x_k} \overline{\rho u_k'' u_i''}}_{\text{Unclosed term}} \quad (2.44b)$$

Eq. 2.44b is similar to Eq. 2.1b, however Eq. 2.44b contains an unclosed term (Reynolds stress $\overline{\rho u_k'' u_i''}$) which cannot be determined by solving Eqs. 2.44a and 2.44b, and it presents the first closure problem for turbulence modelling [153, 106]. Turbulent flow

modelling for both reactive and non-reacting flows requires the knowledge of turbulent kinetic energy as the unclosed Favre-averaged Reynolds stresses $\overline{\rho u_i'' u_j''}$ are usually modelled using a gradient hypothesis as:

$$-\overline{\rho u_i'' u_j''} = \mu_t \left(\frac{\partial \tilde{u}_i}{\partial x_j} + \frac{\partial \tilde{u}_j}{\partial x_i} \right) - \frac{2}{3} \delta_{ij} \left[\mu_t \left(\frac{\partial \tilde{u}_k}{\partial x_k} \right) + \bar{\rho} \tilde{k} \right] \quad (2.45)$$

where μ_t is a turbulent eddy viscosity. The turbulent eddy viscosity μ_t can be expressed in terms of turbulent kinetic energy $\tilde{k} = \overline{\rho u_i'' u_i''} / 2\bar{\rho}$ and its dissipation rate $\tilde{\varepsilon} = \overline{\mu(\partial u_i'' / \partial x_j \partial u_i'' / \partial x_j)} / \bar{\rho}$ in the context of the $k - \varepsilon$ model [105, 210] with μ being the dynamic viscosity. In order to close the model, the transport equation for the turbulent kinetic energy k needs to be solved.

2.7.1 Turbulent kinetic energy transport

The transport equation for the turbulent kinetic energy $\tilde{k} = \overline{\rho u_i'' u_i''} / 2\bar{\rho}$ is in the following form:

$$\begin{aligned} \frac{\partial \bar{\rho} \tilde{k}}{\partial t} + \frac{\partial \bar{\rho} \tilde{u}_j \tilde{k}}{\partial x_j} = & \underbrace{-\overline{\rho u_i'' u_j''} \frac{\partial \tilde{u}_i}{\partial x_j}}_{T_{K1}} \underbrace{- \tilde{u}_i'' \frac{\partial \tilde{p}}{\partial x_i}}_{T_{K2}} + \underbrace{\overline{p' \frac{\partial u_k''}{\partial x_k}}}_{T_{K3}} \\ & + \underbrace{\overline{u_i'' \frac{\partial \tau_{ij}}{\partial x_j}}}_{T_{K4}} \underbrace{- \frac{\partial (\overline{p' u_i''})}{\partial x_i}}_{T_{K5}} \underbrace{- \frac{\partial (\frac{1}{2} \overline{\rho u_i'' u_k'' u_k''})}{\partial x_i}}_{T_{K6}} \end{aligned} \quad (2.46)$$

where the viscous stress tensor is defined as:

$$\tau_{ij} = \mu \left(\frac{\partial u_i}{\partial x_j} + \frac{\partial u_j}{\partial x_i} \right) - \frac{2}{3} \mu \delta_{ij} \frac{\partial u_k}{\partial x_k} \quad (2.47)$$

The term T_{K1} represents the production/destruction of turbulent kinetic energy by the mean velocity gradient term [215, 145, 41, 40]. The term T_{K2} is known as the mean pressure gradient term [215, 145, 41, 40]. The term T_{K3} arises due to the correlation between pressure and dilatation rate fluctuations and is referred to as the pressure dilatation term. The combined effects of molecular diffusion and viscous dissipation of turbulent kinetic energy are described by T_{K4} [215, 145, 41, 40]. The terms T_{K5} and T_{K6} represent transport of turbulent kinetic energy by pressure fluctuations and turbulent velocity fluctuations respectively. The term T_{K4} can alternatively be written

as [145, 41, 40]:

$$T_{K4} = \overline{u_i'' \frac{\partial \tau_{ij}}{\partial x_j}} = -\bar{\rho} \tilde{\varepsilon} + \underbrace{\left[\overline{u_i''} \frac{\partial}{\partial x_k} \left(\mu \frac{\partial u_k''}{\partial x_i} \right) - \frac{2}{3} \overline{u_i''} \frac{\partial}{\partial x_i} \left(\mu \frac{\partial u_k''}{\partial x_k} \right) \right]}_{T_V} + \frac{\partial}{\partial x_j} \left(\mu \frac{\partial \tilde{k}}{\partial x_j} \right) \quad (2.48)$$

2.7.2 RANS modelling of turbulent combustion

In RANS, the Favre-averaged progress variable transport takes the following form:

$$\frac{\partial \bar{\rho} \tilde{c}}{\partial t} + \frac{\partial \bar{\rho} \tilde{u}_j \tilde{c}}{\partial x_j} = \underbrace{\bar{\tilde{\omega}}}_{\text{Unclosed term}} + \underbrace{\frac{\partial}{\partial x_j} \left(\rho D \frac{\partial c}{\partial x_j} \right)}_{\text{Unclosed term}} - \underbrace{\frac{\partial \bar{\rho} u_j'' c''}{\partial x_j}}_{\text{Unclosed term}} \quad (2.49)$$

The RHS of Eq. 2.49 contains three unclosed terms. Modeling of the mean reaction rate $\bar{\tilde{\omega}}$ is the main goals of most studies [157]. It can be closed by either Scalar Dissipation Rate (SDR) or Flame Surface Density (FSD) approach. Further details will be shown in the Literature Review chapter.

Bray [17] derived the following closure for the mean reaction rate of reaction progress variable $\bar{\tilde{\omega}}$ in terms of SDR $\tilde{\varepsilon}_c$ for high Damköhler number (i.e. $Da \gg 1$) flames (see Eq.2.50). The Damköhler number Da can be written as: $Da = l S_L / u' \delta_{th}$, where u' is the root mean square (rms) value of turbulent velocity fluctuation.

$$\bar{\tilde{\omega}} = \frac{2 \bar{\rho} \tilde{\varepsilon}_c}{2c_m - 1} \quad (2.50)$$

where,

$$c_m = \frac{\int_0^1 [\dot{\omega} c f(c)]_L dc}{\int_0^1 [\dot{\omega} f(c)]_L dc} \quad (2.51)$$

In Eq.2.51 $f(c)$ is the burning mode probability density (pdf) and the subscript ‘L’ refers to the unstrained laminar flame quantities. For typical hydrogen/hydrocarbon-air flames c_m varies between 0.7 and 0.9.

The combined reaction rate and molecular diffusion term can be modelled as: $\bar{\tilde{\omega}} + \nabla \cdot (\rho D \nabla c) = (\rho S_d)_s \Sigma_{gen}$ where $(\psi)_s = \psi |\nabla c| / |\nabla c|$ denotes surface averaging [12], $S_d = (Dc/Dt) / |\nabla c|$ is the local displacement speed, and $\Sigma_{gen} = |\nabla c|$ is the generalised FSD [12]. For unity Lewis number flames the model $(\rho S_d)_s \approx \rho_0 S_L$ is often applied [94].

The modelling of the last term on the RHS of Eq. 2.49 represents turbulent transport of reaction progress variable and its modelling depends on the closure of turbulent scalar flux components $\overline{\rho u_j'' c''}$. The quantity $\overline{\rho u_j'' c''}$ is often closed in terms of an algebraic expression [122, 19, 202, 198, 97, 165, 35] or a modelled transport equation for $\overline{\rho u_j'' c''}$ [146, 34, 79].

In RANS, the Favre-averaged enthalpy transport can be written as the following form:

$$\frac{\partial \bar{\rho} \tilde{h}}{\partial t} + \frac{\partial \bar{\rho} \tilde{u}_j \tilde{h}}{\partial x_j} = \underbrace{\bar{\dot{\omega}}_T}_{\text{Unclosed term}} + \underbrace{\frac{\partial}{\partial x_j} \left(\lambda \frac{\partial h}{\partial x_j} \right)}_{\text{Unclosed term}} - \underbrace{\frac{\partial \overline{\rho u_j'' h''}}{\partial x_j}}_{\text{Unclosed term}} \quad (2.52)$$

In Eq. 2.52 $\bar{\dot{\omega}}_T$ is the heat release due to combustion, it can be written as:

$$\bar{\dot{\omega}}_T = H \bar{\dot{\omega}} \quad (2.53)$$

where H is the enthalpy of formation. The turbulent scalar flux of enthalpy $\overline{\rho u_j'' h''}$ can be approximated as:

$$\frac{\overline{\rho u_j'' h''}}{\rho_0 c_p (T_{\text{ad}} - T_0)} \approx \overline{\rho u_j'' T''} \quad (2.54)$$

Thus, in order to close the transport equation (Eq. 2.52), $\overline{\rho u_j'' T''}$ is needed to solve separately.

2.7.3 Flame surface density transport

The transport equation for Σ_{gen} takes the following form [94, 31, 23, 25, 108]:

$$\begin{aligned} \frac{\partial \Sigma_{\text{gen}}}{\partial t} + \frac{\partial \tilde{u}_j \Sigma_{\text{gen}}}{\partial x_j} = & \underbrace{\frac{\partial \left[(\overline{u_i})_s - \tilde{u}_i \right] \Sigma_{\text{gen}}}{\partial x_i}}_{T_{F1}} + \underbrace{\left((\delta_{ij} - N_i N_j) \frac{\partial u_i}{\partial x_j} \right)_s \Sigma_{\text{gen}}}_{T_{F2}} \\ & + \underbrace{\frac{\partial}{\partial x_i} \left[(\overline{S_d N_i})_s \Sigma_{\text{gen}} \right]}_{T_{F3}} + \underbrace{\left(S_d \frac{\partial N_i}{\partial x_i} \right)_s \Sigma_{\text{gen}}}_{T_{F4}} \end{aligned} \quad (2.55)$$

here, $\vec{N} = -\nabla c / |\nabla c|$ is the local flame normal vector. T_{F1} is turbulent transport term, T_{F2} arises from strain rate, T_{F3} is the propagation term and T_{F4} is the curvature term.

The terms $T_{F1} - T_{F4}$ are unclosed and thus need modelling. The near-wall modelling of $T_{F1} - T_{F4}$ will be addressed in Chapter 5 of this report.

2.7.4 Scalar dissipation rate transport

Chakraborty and Cant [40] demonstrated that Eq.2.50 remains valid even for low Damköhler number combustion (i.e. $Da < 1$) as long as the flamelet assumption remains valid. The transport equation of SDR $\tilde{\varepsilon}_c = \overline{\rho D \nabla c'' \cdot \nabla c''} / \bar{\rho}$ can be derived from the transport equation of reaction progress variable $\rho Dc/Dt = \dot{\omega} + \nabla \cdot (\rho D \nabla c)$ [137, 185], which takes the following form [186]:

$$\bar{\rho} \frac{\partial \tilde{\varepsilon}_c}{\partial t} + \bar{\rho} \tilde{u}_j \frac{\partial \tilde{\varepsilon}_c}{\partial x_j} = \underbrace{\frac{\partial}{\partial x_j} \left[\overline{\rho D \frac{\partial \varepsilon_c}{\partial x_j}} \right]}_{D_1} + T_1 + T_2 + T_3 + T_4 - D_2 + f(D) \quad (2.56a)$$

$$T_1 = \underbrace{-\frac{\partial(\overline{\rho u_j'' \varepsilon_c})}{\partial x_j}}_{T_{11}} - \underbrace{2\rho D u_j'' \left(\frac{\partial c''}{\partial x_j} \right) \left(\frac{\partial^2 \tilde{c}}{\partial x_j \partial x_k} \right)}_{T_{12}} \quad (2.56b)$$

$$T_2 = -2D \frac{\overline{[\dot{\omega} + \nabla \cdot (\rho D \nabla c)]}}{\rho} \frac{\partial c}{\partial x_k} \frac{\partial \rho}{\partial x_k} + 2 \frac{\tilde{D}}{\bar{\rho}} \frac{\partial \tilde{c}}{\partial x_k} \frac{\bar{\rho}}{x_k} \left[\overline{\dot{\omega} + \nabla \cdot (\rho D \nabla c)} - \frac{\overline{\rho u_l'' c''}}{\partial x_l} \right] \quad (2.56c)$$

$$T_3 = \underbrace{-2\rho D \frac{\partial \tilde{c}}{\partial x_j} \frac{\partial \tilde{u}_j''}{\partial x_k} \frac{\partial c''}{\partial x_k}}_{T_{31}} - \underbrace{-2\rho D \frac{\partial c''}{\partial x_j} \frac{\partial \tilde{u}_j''}{\partial x_k} \frac{\partial c''}{\partial x_k}}_{T_{32}} - \underbrace{-2\rho D \frac{\partial c''}{\partial x_j} \frac{\partial \tilde{c}''}{\partial x_k} \frac{\partial u_j}{\partial x_k}}_{T_{33}} \quad (2.56d)$$

$$T_4 = 2D \frac{\partial \tilde{\omega}}{\partial x_k} \frac{\partial c}{\partial x_k} - 2\tilde{D} \frac{\partial \tilde{\omega}}{\partial x_k} \quad (2.56e)$$

$$D_2 = 2\rho D^2 \frac{\partial^2 c''}{\partial x_k \partial x_i} \frac{\partial^2 c''}{\partial x_k \partial x_i} \quad (2.56f)$$

$$f(D) = 2D \frac{\partial c}{\partial x_k} \frac{\partial(\rho D)}{\partial x_k} \frac{\partial^2 c}{\partial x_j \partial x_j} + 2D \frac{\partial c}{\partial x_k} \frac{\partial^2(\rho D)}{\partial x_j \partial x_k} \frac{\partial c}{\partial x_j} - \frac{\partial}{\partial x_j} \left(\overline{\rho N_c \frac{\partial D}{\partial x_j}} \right) - 2\rho D \frac{\partial D}{\partial x_j} \frac{\partial}{\partial x_j} \left(\frac{\partial c}{\partial x_k} \frac{\partial c}{\partial x_k} \right) + \rho \frac{\partial c}{\partial x_k} \frac{\partial c}{\partial x_k} \left[\frac{\partial D}{\partial t} + u_j \frac{\partial D}{\partial x_j} \right]$$

$$\begin{aligned}
& -2\widetilde{D} \frac{\partial \tilde{c}}{\partial x_k} \frac{\partial(\bar{\rho}\widetilde{D})}{\partial x_k} \frac{\partial^2 \tilde{c}}{\partial x_j \partial x_k} - 2\widetilde{D} \frac{\partial \tilde{c}}{\partial x_k} \frac{\partial^2(\bar{\rho}\widetilde{D})}{\partial x_j \partial x_k} \frac{\partial \tilde{c}}{\partial x_j} \\
& + \frac{\partial}{\partial x_j} \left(\bar{\rho}\widetilde{D} \frac{\partial \tilde{c}}{\partial x_k} \frac{\partial \tilde{c}}{\partial x_k} \frac{\partial \widetilde{D}}{\partial x_j} \right) + 2\bar{\rho}\widetilde{D} \frac{\partial \widetilde{D}}{\partial x_j} \frac{\partial}{\partial x_j} \left(\frac{\partial \tilde{c}}{\partial x_k} \frac{\partial \tilde{c}}{\partial x_k} \right) \\
& - \bar{\rho} \frac{\partial \tilde{c}}{\partial x_k} \frac{\partial \tilde{c}}{\partial x_k} \left[\frac{\partial \widetilde{D}}{\partial t} + u_j \frac{\partial \widetilde{D}}{\partial x_j} \right] \tag{2.56g}
\end{aligned}$$

The first term on the left hand side of Eq.2.56a is the transient term and the second term on left hand side represents the effects of mean advection. The first and second term on the right hand side of Eq.2.56a (i.e. D_1 and T_1) denote the molecular diffusion and turbulent transport of $\tilde{\varepsilon}_c$ respectively. The term T_2 is referred to the density variation term due to heat release, whereas the turbulent scalar interaction term T_3 arises from the alignment of ∇c with local principal strain rates. The terms T_4 and $(-D_2)$ denote the contributions of chemical reaction and the molecular dissipation of $\tilde{\varepsilon}_c$ respectively. The term $f(D)$ arises due to diffusivity gradients. The terms $T_1, T_2, T_3, T_4, (-D_2)$ and $f(D)$ are unclosed and thus need modelling in RANS calculations in order to solve the $\tilde{\varepsilon}_c$ transport equations. Based on the scaling analysis by Swaminathan and Bray [185], T_2, T_{32}, T_4 and D_2 remain leading order contributors for all values of Damköhler number Da and turbulent Reynolds number $Re_t = \rho_0 u' l / \mu_0$, where ρ_0 is the unburned gas density, μ_0 is the unburned gas dynamics viscosity. A similar conclusion is drawn by Mantel and Borghi [137], where the effect of T_2 term has not been taken into account. DNS simulations [47, 48] suggest that the contributions of T_{31} and T_{32} remain negligible in $Da \gg 1$ combustion. However, both two terms have significant impact on $\tilde{\varepsilon}_c$ transport for $Da < 1$. According to Swaminathan and Bray [185] the terms T_{11} and T_{12} scale as $T_{11} \sim \rho_0 S_L^2 / \delta_{th}^2 \times (1/Re_t^{1/2} Da^{1/2})$ and $T_{12} \sim \rho_0 S_L^2 / \delta_{th}^2 \times (1/Re_t Da)$. According to Mantel and Borghi [137], T_{11} and T_{12} are scaled as: $T_{11} \sim \rho_0 u'^2 / l^2$ and $T_{12} \sim \rho_0 u'^2 / l^2 \times Re_t^{-1/2}$. For high Turbulent Reynolds number flow, it can be seen that T_{12} is likely to be negligible in comparison to T_{11} . Moreover, T_1 term can be approximated to $T_1 \approx -\partial(\overline{\rho u_j'' \varepsilon_c}) / \partial x_j$ and its modelling depends of the turbulent flux of scalar dissipation rate, $\overline{\rho u_j'' \varepsilon_c}$. The modelling of the quantities T_1, T_2, T_3, T_4, D_2 and $f(D)$ are discussed later by *a priori* analysis of DNS data.

2.7.5 Turbulent scalar flux transport

The exact transport equation of $\overline{\rho u_i'' c''}$ ($\overline{\rho u_i'' T''}$) can be derived based on momentum and reaction progress variable (non-dimensional temperature) transport equations

as [146, 34]:

$$\begin{aligned} \frac{\partial \overline{\rho u_i'' c''}}{\partial t} + \frac{\partial \overline{\rho \tilde{u}_j u_i'' c''}}{\partial x_j} = & \underbrace{-\frac{\partial \overline{\rho u_i'' u_j'' c''}}{\partial x_j}}_{T_{1c}} - \underbrace{\overline{\rho u_i'' u_j''} \frac{\partial \tilde{c}}{\partial x_j}}_{T_{2c}} - \underbrace{\overline{\rho u_j'' c''} \frac{\partial \tilde{u}_i}{\partial x_j}}_{T_{3c}} - \underbrace{\overline{c''} \frac{\partial \tilde{P}}{\partial x_i}}_{T_{4c}} \\ & \underbrace{-\overline{c''} \frac{\partial \tilde{P}'}{\partial x_i}}_{T_{5c}} + \underbrace{\left[u_i'' \frac{\partial}{\partial x_k} \left(\rho D \frac{\partial c}{\partial x_k} \right) \right]}_{T_{6c}} + \underbrace{\left[c_i'' \frac{\partial \tau_{ik}}{\partial x_k} \right]}_{T_{7c}} + \underbrace{\overline{u_i'' \dot{\omega}}}_{T_{8c}} \end{aligned} \quad (2.57a)$$

$$\begin{aligned} \frac{\partial \overline{\rho u_i'' T''}}{\partial t} + \frac{\partial \overline{\rho \tilde{u}_j u_i'' T''}}{\partial x_j} = & \underbrace{-\frac{\partial \overline{\rho u_i'' u_j'' T''}}{\partial x_j}}_{T_{1T}} - \underbrace{\overline{\rho u_i'' u_j''} \frac{\partial \tilde{T}}{\partial x_j}}_{T_{2T}} - \underbrace{\overline{\rho u_j'' T''} \frac{\partial \tilde{u}_i}{\partial x_j}}_{T_{3T}} - \underbrace{\overline{T''} \frac{\partial \tilde{P}}{\partial x_i}}_{T_{4T}} \\ & \underbrace{-\overline{T''} \frac{\partial \tilde{P}'}{\partial x_i}}_{T_{5T}} + \underbrace{\left[u_i'' \frac{\partial}{\partial x_k} \left(\rho D \frac{\partial T}{\partial x_k} \right) \right]}_{T_{6T}} + \underbrace{\left[T_i'' \frac{\partial \tau_{ik}}{\partial x_k} \right]}_{T_{7T}} + \underbrace{\overline{u_i'' \dot{\omega}}}_{T_{8T}} \end{aligned} \quad (2.57b)$$

The term T_{1c} (T_{1T}) represents turbulent transport of $\widetilde{u_i'' c''}$ ($\widetilde{u_i'' T''}$), where T_{2c} (T_{2T}) and T_{3c} (T_{3T}) represent turbulent scalar flux transport due to mean scalar and velocity gradients respectively. The terms T_{4c} (T_{4T}) and T_{5c} (T_{5T}) are responsible for turbulent scalar flux transport by mean and fluctuating pressure gradients respectively. The terms T_{6c} (T_{6T}) and T_{7c} (T_{7T}) originate due to mass diffusion and viscous stress respectively, and these terms act to reduce the magnitude of $\widetilde{u_i'' c''}$ ($\widetilde{u_i'' T''}$) irrespective of the nature of scalar flux transport. Thus, these terms are often referred to dissipation terms. The last term on the right-hand side T_{8c} (T_{8T}) originates from the correlation between reaction rate and reaction progress variable fluctuations. The terms T_{1c} (T_{1T}), T_{4c} (T_{4T}), T_{5c} (T_{5T}), T_{6c} (T_{6T}), T_{7c} (T_{7T}) and T_{8c} (T_{8T}) are the unclosed terms and need modelling, whereas the terms T_{2c} (T_{2T}) and T_{3c} (T_{3T}) are closed because modelled transport equations for $\overline{\rho u_i'' u_j''}$ and $\overline{\rho u_j'' c''}$ ($\overline{\rho u_j'' T''}$) are solved in the context of second-moment closure. The statistical behaviour and modelling of T_{1c} (T_{1T}), T_{4c} (T_{4T}), T_{5c} (T_{5T}), T_{6c} (T_{6T}), T_{7c} (T_{7T}) and T_{8c} (T_{8T}) will be discussed in result chapter.

2.7.6 Reaction progress variable variance transport

The scalar variance $\widetilde{c''^2}$ is one of the important quantities for the flamelet [19, 127, 186] and conditional moment [113] based closures. Besides, the variance $\widetilde{c''^2}$ is often required for the well-known Eddy Break Up (EBU) models [127]. Furthermore, $\widetilde{c''^2}$ is an

essential gradient of the tabulated chemistry based modelling of turbulent premixed combustion [?]. The transport equation of the reaction progress variable variance $\widetilde{c''^2}$ can be obtained using relation $\overline{\rho c''^2} = \overline{\rho c^2} - \overline{\rho} \widetilde{c}^2$ and the instantaneous transport equation of reaction progress variable $\rho(Dc/Dt) = \nabla(\rho D \nabla c) + \dot{\omega}$:

$$\begin{aligned} \frac{\partial \overline{\rho c''^2}}{\partial t} + \frac{\partial \overline{\rho u_j c''^2}}{\partial x_j} = & \underbrace{\frac{\partial}{\partial x_j} \left[\rho D \frac{\partial \widetilde{c''^2}}{\partial x_j} \right]}_{D_{1v}} - \underbrace{\frac{\partial \overline{\rho u'' c''^2}}{\partial x_j}}_{T_{1v}} - \underbrace{2 \overline{u_j'' c''}}_{T_{2v}} \frac{\partial \widetilde{c}}{\partial x_j} \\ & + \underbrace{2(\overline{\dot{\omega} c} - \overline{\dot{\omega}} \widetilde{c})}_{T_{3v}} - \underbrace{2 \overline{\rho} \widetilde{\varepsilon}_c}_{D_{2v}} \end{aligned} \quad (2.58)$$

In Eq.2.58, D_{1c} is a closed term which denotes the molecular diffusion of $\widetilde{c''^2}$, T_{1c} is the turbulent transport term, T_{2c} represents generation/destruction of $\widetilde{c''^2}$ by the mean scalar gradient, T_{3c} is the reaction rate contribution and $(-D_{2c})$ is the molecular dissipation term. The term T_{2c} is closed in the context of second-moment closure, so the terms T_{1c} , T_{3c} and $(-D_{2c})$ are the unclosed term in the context of $\widetilde{c''^2}$ closure. Equation 2.58 indicates that $(-D_{2c})$ closure translates to the modelling of SDR $\widetilde{\varepsilon}_c$.

Chapter 3

Literature Review

This chapter introduces the flamelets approach with a review of the turbulent premixed combustion modelling. The existing modelling strategies are mostly presented without the presence of walls. Having outlined in chapter 1 why flame-wall interaction is of particular significance in the contemporary design of combustion devices, this section explores the existing literature on near wall combustion and its modelling.

3.1 Premixed flames

Premixed combustion occurs in the ordinary petrol-fuelled engines, where the fuel and oxidizer are mixed to the molecular level in before ignition (some degree of inhomogeneity is normal in practical systems). Other examples of combustion devices which utilise premixed combustion are modern industrial gas turbine for power generation and the reheat system fitted to jet engines for supersonic aircraft. The most important characteristic of premixed flame is self-induced propagation, in which the premixed flame moves in the direction normal to its flame surface and consumes reactants.

3.1.1 Laminar premixed flames

The propagation rate of a laminar premixed flame is quantified by the laminar burning velocity. Since the direction of propagation is fixed by the local flame geometry, laminar flame speed S_L is used to describe the magnitude of the burning velocity vector. The laminar, unstretched, adiabatic flame speed depends on the thermochemistry of reactant mixture (pressure, temperature, and the mass fraction of the chemical species):

$$S_L = S_L(p, T_0, Y_\alpha), \quad \alpha = 1, \dots, N \quad (3.1)$$

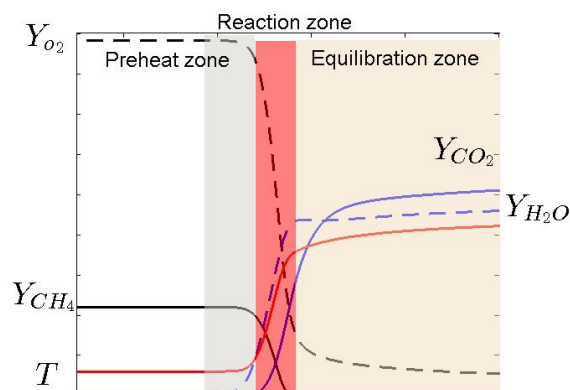


Fig. 3.1 Schematics diagram for laminar premixed flame.

For most hydrocarbon-air mixtures with reactants at ambient conditions, S_L is in a range from 0.3 to 0.6 m/s under atmospheric pressure. The quantity can be measured by experiment or computed using a suitably detailed reaction mechanism.

The structure of laminar premixed flame is illustrated in Fig. 3.1. The reaction zone is where most of the chemical reaction occurs. It is made up of many overlapping reactions and diffusion layers depending on the number of chemical reactants and species through a long and complex sequence of chemical proceedings. This zone is very thin which is much less than 1 mm, and the temperature is high enough for activating chemical reactions, breaking down chemical bonds and releasing reactive radical species. However, in the preheat zone temperature is not sufficient for maintaining reactions. The temperature of reactants is mainly raised by heat conduction as the reactants approach the reaction zone, and it is important that the reactants are supplied to the reaction zone from the preheat zone due to molecular diffusion. Most of the heat release occurs in the equilibration zone where the temperature is high enough to attain chemical equilibrium for the formation and dissociation of the major product species. Furthermore, in comparison to the reaction zone, chemistry in the equilibrium zone is much slower due to the prevalence of three-body recombination reactions [24]. Meanwhile, the heat release from the reaction zone and equilibrium zone conduct towards the preheat zone at a rate controlled by the molecular processes of transport and reaction.

3.1.2 Turbulent premixed flames

Inside combustion chamber of the spark-ignition engines and industrial gas turbines, the flow field is turbulent, and the chamber is designed to manage the production and

distribution of the turbulence for adjusting the burning rate. Turbulence modifies premixed flames in numerous ways. Eddies in turbulent flow contain a spectrum of length scales, and some eddies can wrinkle the flame surface and lead to increase surface area and increase consumption speed, whereas some eddies perturb the internal structure of the flame and the reactive-diffusive balance as mentioned in the previous section. The perturbation may lead to a reduction in the local flame propagation rate and also may cause local extinction in the case of intense turbulence.

The turbulent burning velocity is defined as the propagation velocity of the turbulent flame brush relative to the reactants in the direction normal to flame mean flame propagation direction [24]. Unlike laminar flame speed which mainly depends on the thermochemistry of reactant mixture, turbulent flame speed depends on the root-mean-square (rms) turbulence velocity fluctuation magnitude u and its integral length scale l of turbulence.

3.1.3 Combustion regimes

Chemical time scales in turbulent premixed flames are often much shorter than the large-scale turbulent time scales [17]. This implies that chemical reaction occurs in a premixed flame is limited to a thin propagating surface. Hence a thin reacting interface so-called flamelet separates unburned reactants and fully burned products in premixed combustion. This is the fundamental assumption of flamelet concept which implies that the modelling of the turbulent premixed combustion can be reduced to a two fluid problem. On the other hand, this analysis reduces to a description of flow variables in burnt and unburnt gases, burning rate and the flame surface. More simplifications can be carried out if it is assumed that the local structure of the reacting interface resembles a strained and curved laminar flame. Therefore, the consumption rate of the reactant can be calculated by that in laminar flame condition. The flamelet assumption is an effective way to decouple turbulence and chemistry. Cant and Bray [23] revealed that the chemical effects lead to the variations in local flame speed which can be calculated from the laminar flame calculation. The wrinkling and straining of laminar flamelet is mainly affected by turbulence. There is much controversy about the validity and the limitations of flamelet assumption. Thus, it is useful to consider a regime diagram with the intention of recognising the strength and limitations of the flamelet assumption. A regime diagram was proposed by Peters [153] is shown in fig 3.2:

Figure 3.2 is expressed in terms of non-dimensional parameters where L_{11} is the longitudinal integral length scale. They are the turbulent Reynolds number Re_t , turbulent Damköhler number Da and the Karlovitz number Ka and reaction zone

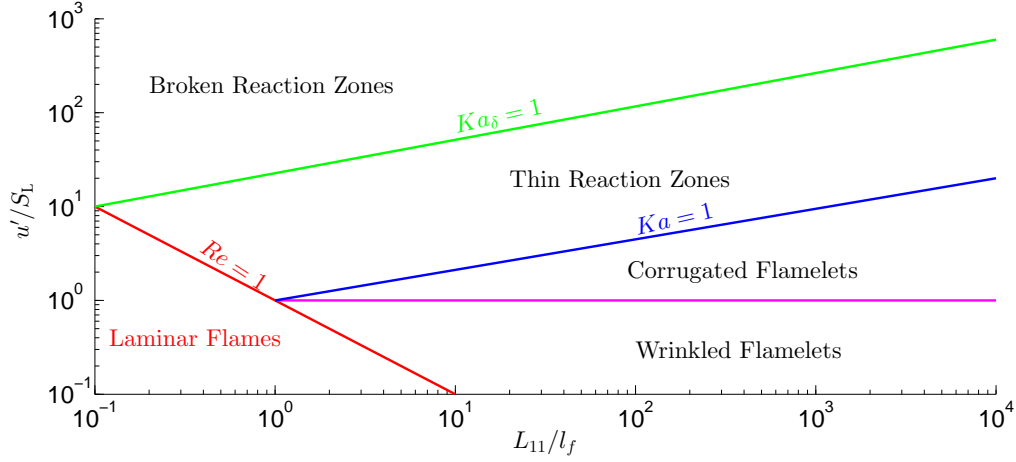


Fig. 3.2 A regime diagram for tuburlent premixed combustion.

Karlovitz number Ka_δ . The turbulent Damköhler number Da can be stated as $Da = \tau_t/\tau_f$, and τ_t is the turbulent time scale, which is given by $\tau_t = l/u'$, and τ_f is the chemical time scale, which is equal to D/S_L^2 . The Karlovitz number can be defined as $Ka = \tau_f/\tau_\eta$ with τ_η is Kolmogorov eddy turnover time, l_F is flame length scale, η is Kolmogorov length scale, ν_η is kolmogorov velocity scale. From the scaling relation which based on an assumption of equal diffusivity for all reactive scalars and Schmidt number $Sc = \nu/D$ is unity, Karlovitz number can be presented as:

$$Ka = \frac{\tau_f}{\tau_\eta} \sim \frac{\delta_{th}^2}{\eta^2} \sim \frac{\nu_\eta^2}{S_L^2} \quad (3.2)$$

and the reaction zone Karlovitz number Ka_δ is defined as:

$$Ka_\delta = \frac{\delta^2}{\eta^2} \quad (3.3)$$

where $\delta \sim \delta_{th}/10$ is the reaction zone thickness which leads to $Ka_\delta \sim Ka/100$. Thus, $Ka_\delta \approx 1.0$ indicates $Ka \sim 100$.

These non-dimensional parameters are related to each other in the following manner:

$$Re_t \sim Da^2 Ka^2 \quad (3.4)$$

The laminar flame exists in a turbulent flow when the flame stretch is less than a critical value [113]. Corrugated flamelets regime is given by the conditions of $Ka \leq 1$ and $Re_t > 1$. In this regime, the laminar flame thickness δ_{th} is smaller than the Kolmogorov length scale η . The turbulent velocity fluctuations have minor effect on the flame inner

structure. In the thin reaction zone regime $1 < Ka < Ka_\delta$ and $Re_t > 1$, unsteady fluctuation occurs in the preheat zone by the energetic turbulent eddies penetrating the flame structure. This leads to flame thickening, meanwhile, the reaction zone remains uninterrupted by turbulent motion. In the broken zones regime $Ka_\delta > 1$ and $Re_t > 1$, there are a significant amount of quenching and passive scalar mixing in a flame.

Flamelet modelling is valid for $Ka < 1$ and $Re_t > 1$, and the boundary given by $Ka = 1$ is known as the Klimov-Williams criterion [153]. However, Poinso *et al.* [158] found out that the Klimov-Williams criterion underestimates the flamelet regime. Penetration in the flame front by small-scale eddies exists, but yet these eddies are not energetic enough to indicate significant flame stretch. According to Poinso *et al.* [158], the suggestion is the flamelet assumption is able to extend to accommodate the flames where small-scale turbulence affects the internal structure but do not quench the flamelets.

3.2 Modelling of turbulent combustion

Favre averaged the Navier-Stokes equations in Eq. 2.1 gives rise to unknown quantities, in other word, unclosed terms, which is the main objective in RANS modelling. These unclosed terms are listed below:

- the Reynolds stress $\widetilde{u''_i u''_j}$
- the mean reaction rate $\bar{\omega}$
- the turbulent scalar fluxes $\widetilde{u''_i c}$ and $\widetilde{u''_i T}$

3.2.1 Flamelet approaches

The Bray-Moss-Libby (BML) approach [19] is a well-established flamelet model. The reaction progress variable c can be represented by using a presumed probability density function (pdf) with two delta functions at $c = 0$ and $c = 1$ (see Fig. 3.3). The pdf of c indicate the thin reacting surface that is entrenched in a turbulent flow. According to BML approach, the pdf of c can be expressed as:

$$p(c) = \alpha\delta(c) + \beta\delta(1-c) + \gamma f(c) \quad (3.5)$$

where $\alpha\delta(c)$ denotes the contribution of the reactants, $\beta\delta(1-c)$ denotes the contribution of the products, and $\gamma f(c)$ is the contribution arising from the reacting gas. The BML

assumes $\gamma \ll 1$ in the flamelet assumption for $Da \gg 1$ (e.g. $\alpha + \beta = 1$), whereas, the determination of α and β is given by:

$$\alpha = \frac{1 - \tilde{c}}{1 + \tau\tilde{c}} \quad \beta = \frac{(1 + \tau)\tilde{c}}{1 + \tau\tilde{c}} \quad (3.6)$$

Thus, a double delta pdf is used to provide closure for a range of mean quantities in terms of conditional moments at $c = 0$ and $c = 1$. The turbulent scalar flux of reaction progress variable can be expressed as:

$$\widetilde{u''c''} = \tilde{c}(1 - \tilde{c}) \left[\overline{(u_i)_P} - \overline{(u_i)_R} \right] \quad (3.7)$$

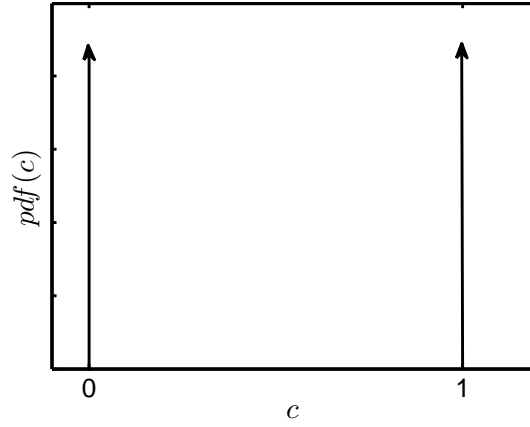


Fig. 3.3 The Bray-Moss-Libby pdf of c

where $\overline{(u_i)_P}$ and $\overline{(u_i)_R}$ are conditional Reynolds averaged velocity components in the products and reactants respectively. The Reynolds averaged reaction rate is modelled by using the local surface area to volume ratio which is given by the FSD Σ [19]:

$$\bar{\omega} = \rho_0 S_L I_0 \Sigma \quad (3.8)$$

where I_0 represents the effects of flame stretch [153]. A level set approaches G equation is another method for the thermo-chemical closure by solving a Reynolds averaged transport equation for the level set variables G field and its variance [153]. Otherwise, thermo-chemical closure in the flamelet regime can be solved by using a presumed pdf of c . The flamelet pdf is used along with a strained laminar flame calculation, where the laminar flame calculation can be used to tabulate the reaction rate as a function of c and I_0 . A flamelet assumption can simplify the pdf transport equation by allowing the reaction and diffusion terms to be lumped together and calculated as a

function of c based on laminar flame structure [161]. Vervisch *et al.* [200] discussed the interrelation between pdf and FSD approaches.

3.2.2 Progress variable variance

According to the BML model [19], one obtains:

$$\widetilde{c''^2} = \tilde{c}(1 - \tilde{c}) + O(\gamma_c) \quad (3.9)$$

where $O(\gamma_c)$ is the burning mode contribution. The contribution of $O(\gamma_c)$ can be neglected and $\widetilde{c''^2}$ assumes its maximum possible value $\tilde{c}(1 - \tilde{c})$ when $P(c)$ can be approximated by a bi-modal distribution with impulses at $c = 0$ and $c = 1.0$, and this condition is realised for high values of Damköhler number (i.e. $Da \gg 1$), where the flame front is thinner than the Kolmogorov length scale, and the turbulent eddies do not affect the flame structure. However, $O(\gamma_c)$ cannot be neglected for small values of Da (i.e. $Da < 1$) and subsequently $\widetilde{c''^2}$ remains smaller than $\tilde{c}(1 - \tilde{c})$, and thus it is necessary to solve variance transport equation along with other modelled conservation equations in the context of RANS simulations. It is true that many of models were based on BML analysis which is strictly valid for infinitely fast chemistry $Da \gg 1$. The scalar variance $\widetilde{c''^2}$ can be directly modelled as $\tilde{c}(1 - \tilde{c})$. The original BML based model expressions have already been modified by Chakraborty and Cant [35] for low Damköhler number (i.e. $Da < 1$) combustion in absence of the wall. Chakraborty and Swaminathan [50] and Malkeson and Chakraborty [135] analysed the statistical behaviours of scalar variance transport in turbulent premixed and stratified flames respectively. Furthermore, Chakraborty and Swaminathan [50] demonstrated that global Lewis number Le has significant influences on the various terms of the transport equation of $\widetilde{c''^2}$. However, all the aforementioned analyses have been carried out for flames which are away from the wall, and the analysis of reaction progress variable variance $\widetilde{c''^2}$ transport in the near-wall region during flame-wall interaction is yet to be addressed in existing literature.

3.3 Flame surface density

In order to obtain the closure of $\bar{\omega}$ (see 3.8), the FSD Σ is an important quantity to be modelled. FSD is often modelled in RANS and LES using an algebraic closure or by solving the transport equation. One of the algebraic closure approaches yield the

following expression for Σ [19]:

$$\Sigma = \frac{g\bar{c}(1 - \bar{c})}{\bar{\Sigma}_y \bar{L}_y} \quad (3.10)$$

where the constant g and the flamelet orientation factor $\bar{\Sigma}_y$ (i.e. mean value of cosine of the angle between the local flame normal and flame brush normal reactions) are evaluated from experimental data, \bar{L}_y is the integral length scale of the wrinkling and it can be related to the integral length scale of the turbulence as [23]:

$$\bar{L}_y = c_L l \left(\frac{u}{u_0} \right)^n \quad (3.11)$$

with constants $c_L \simeq 1.0$ and $n \simeq 1.0$. Gouldin *et al.* [88] proposed an alternative algebraic model for FSD which is based on fractal concepts:

$$\Sigma = \frac{1}{L_{\text{outer}}} \left(\frac{L_{\text{outer}}}{L_{\text{inner}}} \right)^{D_f - 2} \quad (3.12)$$

where L_{inner} and L_{outer} are the inner and outer cutoff scales of the flame front respectively, and D_f is the fractal dimension. Furthermore, the inner and outer cutoff scales of the flame front are based on the turbulent Kolmogorov scale η and the integral length scale l , respectively in the constant of RANS.

Marble and Broadwell [138] provided coherent flamelet model (CFM) to solve the modelled FSD transport equation for non-premixed turbulent combustion. The CFM is based on the physical processes that generate and destroy the flame surface area. In the studies of Candel and Poinso [22], Pope [160], Trouvé and Poinso [192], and Vervisch *et al.* [201] provided an exact FSD transport equation under theoretical considerations for a propagating flame surface, where the FSD is convected by the fluid flow, propagated by flame propagation, and produced/destroyed by the combined effects of propagation and curvature due to turbulence. The main modelling concerns on these strategies approaches are the effects of fluid strain rate and the effects of the curvature and propagation. The effects of fluid strain rate are employed a model which is scaled with the large scale turbulent strain rate in the flow, and the effects of propagation and curvature are generally modelled as a destruction term within the FSD transport equation.

The modelled FSD transport equation for premixed turbulent flame can be found in the existing literatures [25, 93, 108, 40, 37, 94, 46, 32, 132]. However, the RANS modelling of FSD based mean reaction rate closure in the near-wall region alongside

the modelling of the unclosed terms in the transport equation for the generalised FSD (i.e. $\Sigma_{\text{gen}} = |\overline{\nabla c}|$ [12]) has not yet been carried out.

3.4 Scalar dissipation rate

The SDR is a quantity of fundamental importance in the turbulent reacting flow [10]. Bray [17] demonstrated that the SDR in turbulent premixed flames is not only useful for the purpose of modelling micro-mixing but also for the closure of mean reaction rate. The instantaneous SDR is defined as:

$$\varepsilon_c = D \nabla c \cdot \nabla c \quad (3.13)$$

The mean reaction rate $\bar{\dot{\omega}}$ is proportional to the mean SDR in the context of Reynolds Averaged Navier Stokes (RANS) simulations [17, 186]:

$$\bar{\dot{\omega}} = \frac{2\bar{\rho}\tilde{\varepsilon}_c}{2c_m - 1} \quad (3.14)$$

A number of previous studies concentrated on various aspects of SDR closure in turbulent premixed combustion and a review of existing algebraic and transport equation based closures of SDR in the context of RANS simulations can be obtained in [15, 143, 49, 114]. It has been demonstrated based on DNS [40, 49, 50] studies that the global Lewis number (defined as the ratio of thermal diffusivity to mass diffusivity, i.e. $Le = \alpha_T/D$) plays an important role in the statistical behaviour of SDR in turbulent premixed flames in the absence of walls. It should be noted that it is not straightforward to assign a single characteristic Lewis number in actual flames because of the presence of various chemical species with different Lewis number. In turbulent premixed flames the Lewis number of the deficient reactant is often taken to characterise the combustion process and thus considered to be the global Lewis number [140]. Recently, Dinkelacker *et al.* [73] proposed a methodology of obtaining the effective Lewis number based on a linear function of mole fractions of the species inside the flame. A number of previous analytical [60, 151, 174], experimental [1, 126, 163] and numerical [49, 40, 50, 95, 170, 192, 30, 93, 33] concentrated on different aspects of Lewis number effects on turbulent premixed combustion in isolation and the same approach has been adopted in the current analysis. However, the effects of Le on the head-on quenching of premixed turbulent flame and its modelling using SDR closure have not been analysed in the existing literature. In this thesis, three-dimensional DNS simulations of head-on quenching of statistically planar turbulent premixed flames with

different values of turbulent Reynolds number Re_t (ranging from 50 to 100) and Lewis number Le (ranging from 0.8 to 1.2) have been carried out to analyse the near-wall SDR statistics.

3.5 Turbulent scalar flux

Turbulent scalar flux is a quantity of fundamental interest in heat and mass transfer in the analysis of turbulent flows [122]. To date, most analyses [19, 55, 169, 202] on statistical behaviour and modelling of turbulent scalar flux in turbulent reacting flows have been carried out for flows away from walls. The most commonly used turbulent scalar flux model assumes a gradient hypothesis [122] even though it is well-known [79, 111] that the gradient transport does not sufficiently approximate the statistical variation of turbulent scalar flux for both reacting and non-reacting flows. Furthermore, counter-gradient model has been reported based on theoretical [19], experimental [55] and computational [169] analyses. A counter-gradient transport is obtained when transport due to flame-normal acceleration dominates over the transport arising from turbulent velocity fluctuations [202]. By contrast, a gradient type transport is obtained when the transport due to turbulent velocity fluctuation overcomes that arising from flame normal acceleration [202]. Turbulent scalar flux can be closed by either an algebraic expression [19] or solving a modelled transport equation [111]. To date, most models for turbulent scalar flux and the unclosed terms of its transport equation for reacting flows have been proposed for flows sufficiently away from the wall.

3.6 Flame-wall interaction configurations

Poinsot *et al.* [156] have explored the fundamental aspects of flame-wall interaction using two-dimensional DNS with simple chemistry. They investigated the effects of wall distance on the local and global flame structure. Based on the simulation result, they derived the “law-of-the-wall” model which was used to describe the interaction between a turbulent premixed flame and a wall. Preliminary work on the interaction between turbulent premixed flames and channel wall was undertaken by Bruneaux *et al.* [20]. They identified that the turbulent convection of flame elements towards the wall acts to increase wall heat flux magnitude in turbulent flames in comparison to that in laminar flame-wall interaction. In another study from Bruneaux *et al.* [21], turbulent premixed flame propagation in the vicinity of a wall by using three-dimensional constant

density simulation has been carried out. The influence of the walls was investigated in terms of flamelet approach, where the wall influences on flamelet speed and the FSD transport have been addressed. They pointed out that during the turbulent flame-wall interaction, walls reduces the flame speed through enthalpy losses and leads to flame quenching and reduces the extent of flame wrinkling. The statistical behaviour of maximum wall heat fluxes in a diffusion flame burner has been carried out by Lataillade *et al.* [70]. Labuda [118] carried out an experimental study on wall induced flame quenching at high pressure. They measured wall heat flux and ionisation current for the cold wall for head-on quenching with a pressure range from 0.8 to 16 MPa. It was found that quenching distance is independent of the maximum wall heat flux. Laminar flame quenching in spark ignition engines was analysed experimentally by Ferguson and Keck [85]. In their study, they examined the characteristic length over a flame in a tube loses heat and proposed a Peclet number correlation. Truffin [193] proposed a new wall law which includes the effects of the turbulent flame during its interaction with the wall. This analysis mainly focuses on the heat transfer to the wall during quenching. It is based on the FSD concept using two-dimensional DNS results of a turbulent V-flame. Gruber *et al.* [90] carried out three-dimensional DNS of turbulent premixed H_2 –air V-flame interaction with isothermal walls, where the flame is anchored in a low-Reynolds number turbulent Poiseuille flow. Although the existing literature provided important of flame-wall interaction, detailed information on modelling of flame-wall interaction has not yet been conducted.

Three typical flame-wall interaction configurations (see fig 3.4) have been studied in existing literature [156]:

- Head-on quenching (HOQ)
- Side-wall quenching (SWQ)
- Tube quenching

Figure 3.4 illustrates that HOQ occurs when a flame front reaches a cold wall at a normal angle. A few studies [100, 98, 156] analysed HOQ by either numerical or experimental method. One-dimensional simulations of laminar flame-wall interaction were reported in Westbrook *et al.* [208]. The flame normal distance from the wall and the wall heat flux Φ change as flame propagating toward the wall. The effects of the wall, which are the reduction in the flame power combined with the increment of the wall heat flux Φ , become predominant as the flame is in a close distance toward the wall. Energy is extracted from the flame by the wall through heat diffusion. Studies

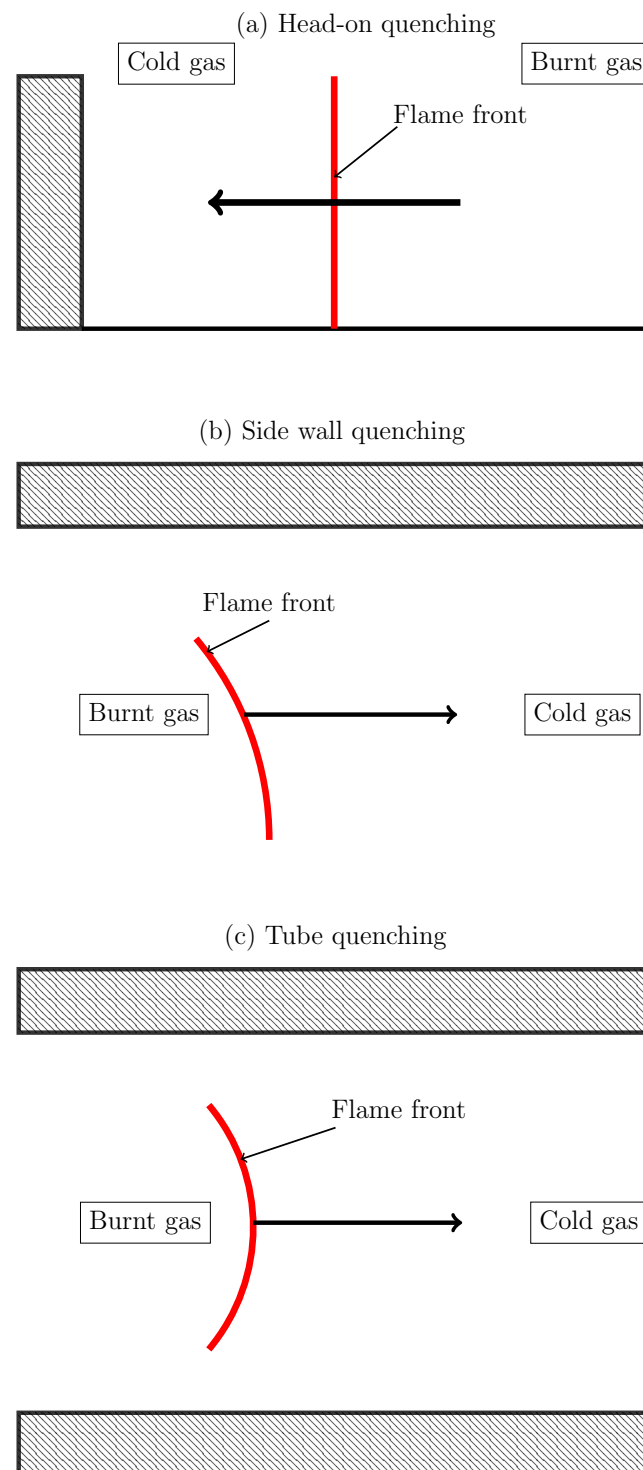


Fig. 3.4 Configurations for flame-wall interactions [156].

from Huang *et al.* [98], Vosen *et al.* [204] pointed out that at quenching, the wall heat flux Φ_Q is due to heat conduction in gas layer of thickness x_Q which can be written as:

$$\Phi_Q \approx - \left| \frac{\lambda(T_1 - T_W)}{x_Q} \right| \quad (3.15)$$

above equation the scaled wall heat flux Φ_Q at quenching can be expressed as:

$$\Phi_Q = \frac{T_1 - T_W}{T_1 - T_0} \frac{1}{Pe_Q} \quad (3.16)$$

Poinsot *et al.* [156] suggests that quenching started when the Peclet number Pe_Q of the flame front is in the order of three and the wall heat flux Φ_Q at quenching is on the order of 0.36. They also suggested that the flame stops propagating toward the wall which is about one-third of flame power. Kuo [117] notes that chemical effects such as equivalence ratio also have an impact on quenching distance. Conversely, Huang *et al.* [98] conducted a study on the effect of different fuels on Φ_Q , they found out that Φ_Q stays almost constant. Poinsot *et al.* [156] concluded that the HOQ problem is thermally controlled, a simplified chemistry assumption can be used to simulate such phenomenon.

Figure 3.4 illustrates SWQ case which is different from HOQ. A flame propagates parallel to a wall, and only localised quenching occurs. However, the entire flame front is affected in HOQ case. Relevant literature on the SWQ can be found in references [203, 156]. Poinsot *et al.* [156] suggested that the Peclet number Pe_Q is in the order of seven and the corresponding maximum heat flux is about 0.16.

The study of tube quenching can be dated back to Davy [69] and Stephenson in designing the mine lamp in the 19th century, which implies total flame quenching for a tube radius R less than the quenching distance. The study of Aly and Hermance [4] reveals that Peclet number for tube quenching based on the diameter can be closed to 50.

3.7 Combustion models for flame-wall interaction

In-cylinder turbulent flame propagation is a very complicated process. While it may be expected that the wall acts as a geometrical barrier in SI internal combustion engine, and so limits the expansion of flame front which leads to a greater reduction in the burning rate due to heat transfer from the flame front to the wall. The presence of the wall further reduces the extent of flame wrinkling. In essence, wall induced

quenching becomes unavoidable in SI engines. However, this quenching process can depend on the engine intake geometry, combustion chamber geometry and the operating conditions [72]. Existing evidence [71] indicates that suitable modelling of flame-wall interaction plays a vital stage to physical modelling of the combustion process.

DNS data shows that walls influence turbulent flames but incorporating coupling between turbulent flame and wall into a RANS code remain a challenge [157]. Existing combustion models often accounts for flame-wall interaction based on the influence from the wall on the turbulent time scales, where the modified time scales alter the mean reaction rate of the approaching flame. This approach often yields unphysical results due to incompatibilities between near-wall models and combustion models [157]. An early investigation by Poinso *et al.* [156] introduced “law-of-the-wall” model for reacting turbulent flows to incorporate wall effects in turbulent combustion models based on modifying models near walls using physical arguments from DNS results. A global sink term D_Q for flame surface density Σ is added to the transport equation in the first cell near the wall, where it can be represented the destruction of Σ by wall quenching. Bruneaux *et al.* [21] modified all terms of the Σ transport equation to take into account of the effects of the wall. The FSD transport equation for flame-wall interaction according to Bruneaux *et al.* [21] is written as:

$$\begin{aligned} \frac{\partial \Sigma}{\partial t} + \frac{\partial \tilde{u}_i \Sigma}{\partial x_i} = & \frac{\partial}{\partial x_i} \left(\frac{\nu_t}{\sigma_\Sigma} \frac{\partial \Sigma}{\partial x_i} \right) + \alpha_0 \frac{\varepsilon}{k} \Gamma_K \left(\frac{u'}{S_L}, \frac{l_t}{\delta_L} \right) \Sigma - \beta_0 \rho_0 S_L Q_m \frac{\Sigma^2}{\bar{\rho} \bar{Y}} \\ & + \frac{\partial}{\partial x_i} \left[S_L \left(1 - \frac{1 - Q_m}{0.3} \right) \right] \end{aligned} \quad (3.17)$$

where Y is the reduced mass fraction ($Y = 1$ for reactants and $Y = 0$ for products), Q_m is the quenching factor which is directly linked to the enthalpy loss to the wall:

$$Q_m = e^{-2\beta[1-(\tilde{T}+\tilde{Y})]} \quad (3.18)$$

Angelberger *et al.* [5] and Duclos *et al.* [76] have applied above transport equation into piston engine computations.

3.8 Vorticity and enstrophy topology

Several previous analyses focussed on the alignment of $\vec{\omega}$ with local principal strain rates in non-premixed [147, 14, 99] and premixed flames [91, 29]. These analyses have demonstrated that $\vec{\omega}$ aligns predominantly with the intermediate principal strain rate

similar to the non-reacting turbulent flows [197, 173, 6, 172, 134, 103, 196, 214, 131], but $\vec{\omega}$ also shows considerable alignment with the most extensive and compressive principal strain rates depending on the relative magnitudes of chemical and turbulent time scales. Chakraborty [29] has revealed that the global Lewis number Le has significant influences on the alignment of $\vec{\omega}$ with local principal strain rates. The analysis by Chakraborty [29] revealed that $\vec{\omega}$ predominantly aligns with the intermediate and the most compressive principal strain rates for low Lewis number flames (e.g. $Le = 0.34$) where the dilatation rate remains almost equal to the most extensive principal strain rate.

The analysis by Hamlington *et al.* [91] has indicated that enstrophy Ω drops from the unburned to burned gas side of flame-brush. On the contrary, Treurniet *et al.* [191] reported a localised increase of Ω within the flame-brush [191] for flames with high values of heat release parameter $\tau = (T_{ad} - T_0)/T_0$. Lipatnikov *et al.* [129] reported both generation and decay of enstrophy across the flame brush in the cases of high (e.g. $\tau = 6.53$) and low (e.g. $\tau = 1.5$) values of heat release parameter, respectively. These authors also analysed the terms of the enstrophy and vorticity transport equation for weakly turbulent premixed flames in the corrugated transport flamelets regime. Recently, Chakraborty *et al.* [44] have demonstrated that Le significantly affects the baroclinic torque contribution to the enstrophy transport and this may lead to an augmentation of Ω within a flame for small values of Le under a turbulent flow condition in the unburned gas, contrary to a decay of Ω across the flame with $Le = 1.0$.

3.9 Flow topology

Flow topologies are often characterised in terms of a three-dimensional space made up the three invariants (i.e. first P , second Q and third R) of the velocity gradient tensor $\partial u_i / \partial x_j$ [152, 57], where u_i is the i^{th} component of the velocity vector. The topologies are schematically shown in Fig. 1. To date, most analyses on flow topologies have been carried out for non-reacting incompressible flows. For incompressible flows, the first invariant P is identically zero, so the flow topology distribution is governed by Q and R . The analyses by Perry and Chong [152] and Soria *et al.* [177] indicated the topology $S4$ is predominantly obtained for positive values of second-invariant Q . Blackburn *et al.* [11] revealed that the topologies $S2$ and $S4$ remain dominant away from the wall for incompressible flows. It has been demonstrated by Chong *et al.* [56] and Chacin and Cantwell [28] that the joint probability density function (pdf) shows a “teardrop” structure, and subsequently Ooi *et al.* [150] provided the evidence

regarding the universality of this “teardrop” structure in $Q - R$ space. The physical explanations behind this “teardrop” structure of $Q - R$ joint pdf for incompressible flows have been provided by Elsinga and Marusic [84]. Both numerical and experimental investigations suggested that the “teardrop” structure of $Q - R$ joint pdf exists only in the fully turbulent region and not in the interface between turbulent and non-turbulent regions [56, 28]. The qualitative arguments for predominant physical mechanisms associated with individual topologies (e.g. enstrophy production is large in $S4$ topology whereas the strain rate production is associated with $S1$ topology) were postulated by Tsinober [195]. The interaction of flow topologies with passive scalar surface topology quantified in terms of Gauss and mean curvatures (i.e. κ_g and κ_m) was analysed in detail by Dopazo *et al.* [75]. It is worth noting that all the aforementioned analyses were conducted for incompressible fluids where the first invariant P is identically zero. However, in compressible flows the statistical behaviour of the first invariant of the strain rate tensor P plays an important role, and thus the location in three-dimensional $P - Q - R$ space determines the local flow topology. The structure of a compressible wake using the critical point theory in terms of P , Q and R was analysed by Chen *et al.* [53] for the very first time. Sondergaard *et al.* [176] characterised small-scale local flow geometries in a compressible turbulent shear flow in terms of P , Q and R . Maekawa *et al.* [133] and Suman and Girimaji [183] demonstrated that $S2$ and $S4$ topologies are predominant on the $Q - R$ plane for decaying isotropic compressible turbulence. The topology distributions in the inner and outer layers in turbulent compressible boundary layers were analysed using Direct Numerical Simulation (DNS) data by Wang and Lu [207]. It is worth noting that all these analyses were carried out for non-reacting flows.

Tanahashi *et al.* [188] was the first to analyse the flow topologies in turbulent premixed flames by to distinguish between strain dominated and vorticity dominated regions. Grout *et al.* [89] analysed flow topologies using DNS data of a reactive transverse fuel jet in cross-flow and revealed that $S8$ topology is associated with the regions of high heat release. Recently, Cifuentes and his co-workers [59, 58] analysed the distribution of flow topologies across the flame front using simple chemistry DNS database of premixed turbulent flames with unity Lewis number representing the flamelets regime of combustion and reported that the probability of finding the focal (nodal) flow topologies decrease (increase) across the flame front. Flow topology distributions in turbulent spray flames were analysed by Wacks and Chakraborty [205] using DNS data, which demonstrated that the flow topology distribution within the spray flames shows resemblance to the findings by Cifuentes *et al.* [59] and Grout

et al. [89]. Recently, Wacks *et al.* [206] analysed flow topology distributions for the different regimes of turbulent premixed combustion and it has found that the weakening of dilatation rate (in other words weakening of P) from the corrugated flamelets to the thin reaction zones to broken reaction zones regimes of premixed turbulent combustion plays a key role in the behaviours of the invariants of the strain rate tensor and their components, which in turn affects the distribution of flow topologies and their contributions to vorticity and scalar dissipation rate evolutions. In this respect, it is useful to note all the flow topology analyses for turbulent reacting flows were carried out for conditions which are not wall-bounded.

Chapter 4

Numerical Implementation

This chapter discusses the numerical methods for DNS and the implementation for HOQ and oblique wall quenching configurations. It starts with the spatial resolution and physical scales requirements for capturing the insights of turbulent combustion. The initialisation method for generating homogeneous and isotropic turbulent flow field is presented. Then, the DNS boundaries conditions for inlet, outlet and wall are discussed. Implementation of HOQ and oblique wall quenching configurations are discussed in details.

4.1 Spatial resolution and physical scales

The basic requirements of DNS of turbulent flame-wall interaction simulations are as follows:

- The domain length L should be large enough to accommodate the large scales of the flow ($L > 5l$)
- The grid size Δ_x should be fine enough to resolve the smallest scales of the flow ($\Delta_x \leq \eta$)
- The grid size Δ_x should be fine enough to resolve the flame structure ($\Delta_x \ll \delta_{th}$)
- The grid resolution near wall should be smaller than unity ($\rho_0 u_\tau \Delta_x / \mu_0 < 1$)

where u_τ and μ_0 are the friction velocity and unburned gas viscosity respectively.

DNS of non-reacting turbulent flows needs to resolve up to the Kolmogorov scale, which is the smallest eddy scale of the flow. If L is the length of a computational domain (or the shortest length in a rectangular domain) and N grid points are placed

in that length then, the grid size is given as $\Delta_x = L/(N - 1)$. Turbulent flow is characterised by velocity fluctuation u' and its integral length scale l . The size of L is taken to be the order of l ($L = (N - 1)\Delta_x \geq l$). The ratio of integral length scale to the Kolmogorov scale is given by: $\eta \sim Re_t^{3/4}$, and $l/\eta < N - 1$. Since grid size has to be greater or equal to the smallest scale of turbulence $\Delta_x \leq \eta$, the following criteria are adjusted:

$$N - 1 > Re_t^{3/4} \quad (4.1)$$

Above relation limits the number of grid required for DNS of a given turbulent Reynolds number Re_t .

Apart from resolving the turbulent scales, the resolution of chemical scales is also important for DNS of turbulent combustion. A single step irreversible chemistry requires at least ten grid points across the thermal flame thickness δ_{th} . However, for detailed chemistry, more grid points (~ 14 grid points) are needed across the δ_{th} . In another word, elementary cells $Q \approx 10$ for a single step irreversible chemistry, and $Q \approx 14$ for detailed chemistry to resolve the internal structure of the flame. Thus, the computational domain $L \approx [(N - 1)/Q]\delta_{th}$ which is led to:

$$\frac{l}{\delta_{th}} < \frac{L}{\delta_{th}} < \frac{N - 1}{Q} \quad (4.2)$$

The flame thickness can be replaced by diffusive flame thickness $\delta \approx \nu/S_L$. As a result, the product of Re_t and Da can lead to the following inequality:

$$Re_t Da = \frac{l^2 S_L}{\nu \delta} = \left(\frac{l}{\delta}\right)^2 < \left(\frac{N - 1}{Q}\right)^2 \quad (4.3)$$

4.2 Initialisation of turbulence

The initial conditions of DNS turbulent flow which are already good approximations of the solutions of the Navier-Stokes equations, which ensures truly turbulent solution in the simulation without unnecessary initial transients and reduces the time required to achieve a fully developed turbulence. However, without the closed form of a Navier-Stokes solution, or sufficiently detailed experimental data, it is essential to create the initial approximation numerically [26].

In the present analysis, the initial turbulent flow field away from the wall is a three-dimensional homogeneous isotropic turbulence with a specified energy spectrum.

In order to satisfy the continuity homogeneity and isotropy in the initial turbulent velocity field, the implementation in the Fourier space is the most convenient method from the theoretical perspective [26]. The velocity field \vec{u} is generated in Fourier space and inverse Fourier transformed to real space, and numerical approximation method is based on a pseudo-spectral method [167]. The continuity condition for incompressible flow satisfies the following condition:

$$\nabla \cdot \underline{u}(\underline{x}) = 0 \quad (4.4)$$

with an equivalent condition in Fourier space:

$$\bar{\kappa} \cdot \hat{\underline{u}}(\underline{\kappa}) = 0 \quad (4.5)$$

where $\bar{\kappa}$ is the linear wave number vector and $\hat{\underline{u}}(\underline{\kappa})$ is the Fourier transform of the real-space velocity vector $\underline{u}(\underline{x})$. Eqs 4.4 and 4.5 indicate $\hat{\underline{u}}$ and $\underline{\kappa}$ are orthogonal to each other. Hence, there is no component of $\hat{\underline{u}}$ in the direction of the wavenumber vector, and $\hat{\underline{u}}$ can be rewritten as:

$$\hat{\underline{u}}(\bar{\kappa}) = \alpha(\bar{\kappa})\underline{e}_1 + \beta(\bar{\kappa})\underline{e}_2 \quad (4.6)$$

Hence, \underline{e}_i indicates the unit basis vector (the direction of $i = 3$ is aligned with $\bar{\kappa}$). The complex functions $\alpha(\bar{\kappa})$ and $\beta(\bar{\kappa})$ are generated with random phase, but their magnitudes for each Fourier mode imitates the averaged energy of the energy spectrum $E(\kappa)$. The expressions for α and β take the following form:

$$\alpha = \sqrt{\frac{E(\bar{\kappa})}{2\pi\bar{\kappa}^2}} e^{i\theta_1 \cos\phi} \quad (4.7)$$

$$\beta = \sqrt{\frac{E(\bar{\kappa})}{2\pi\bar{\kappa}^2}} e^{i\theta_2 \sin\phi} \quad (4.8)$$

where θ_1 , θ_2 and ϕ are uniformly-distributed random phase angles. The $E(\kappa)$ is chosen the widely used spectrum in DNS given by Batchelor and Townsend [7], which represents the decaying isotropic turbulence:

$$E(\kappa) = c_0 \frac{\bar{\kappa}^4}{\bar{\kappa}_0^5} e^{-2(\bar{\kappa}/\bar{\kappa}_0)^2} \quad (4.9)$$

The Gaussian form provides a rapid roll-off of the energy at high wavenumber, and $\bar{\kappa}^4$ for low wavenumbers corresponds strictly to the incompressible limit [7]. c_0 is a multiplier, and the wavenumber $\bar{\kappa}_0$ corresponds to the peak energy. The following quantities of interest are:

(1) turbulent kinetic energy evaluated over the whole domain of initialisation:

$$k = \frac{3}{32} \sqrt{\frac{\pi}{2}} c_0 \quad (4.10)$$

(2) turbulence kinetic energy dissipation rate evaluated over the whole domain of initialisation:

$$\varepsilon = \frac{15}{16} \sqrt{\frac{\pi}{2}} \pi^2 \nu c_0 \bar{\kappa}_0^2 \quad (4.11)$$

This leads to the following expression of:

Longitudinal integral length scale

$$L_{11} = \frac{1}{\sqrt{2\pi k_0}} \quad (4.12)$$

Taylor length scale

$$\lambda^2 = \frac{1}{2\pi^2 \bar{\kappa}_0^2} \quad (4.13)$$

Kolmogorov length scale

$$\eta = \left[\frac{\nu^2}{\frac{15}{16} \sqrt{\frac{\pi}{2}} \pi^2 c_0 \bar{\kappa}_0^2} \right]^{1/4} \quad (4.14)$$

4.3 Navier Stokes Characteristic Boundary Conditions

DNS of unsteady compressible flow requires accurate control over wave reflection from the boundary of the domains. For this purpose, the Navier-Stokes Characteristic Boundary Conditions (NSCBC) method is proposed in boundaries setting of simulation domain [8]. Non-periodic simulations with flow inlet, outlet and walls conditions allow acoustic waves, and the simulation solutions are affected by the boundary conditions. NSCBC provides a guideline of specifying numerical and physical boundary conditions.

This method is based on a one-dimensional characteristic or local one-dimensional inviscid (LODI) analysis of the different waves crossing a given boundary of the computational domain. The governing equations can be stated as follows:

$$\frac{\partial \psi^*}{\partial t} + \nabla \cdot \mathbf{F} = \mathbf{D} + \mathbf{s} \quad (4.15)$$

where the vector of conservative variable is given as $\psi^* = \{\rho, \rho u, \rho v, \rho w, \rho E, \rho Y_k\}^T$, and where F is the vector of converctive fluxes which can be stated as $\nabla \cdot \mathbf{F} = \nabla_{(n)} \cdot \mathbf{F}^{(n)} + \nabla_{(t)} \cdot \mathbf{F}^{(t)}$, (n) denotes the normal and (t) denotes the tangential directions to the boundary, \mathbf{D} is the vector of diffusive fluxes and \mathbf{s} is the vector of source term.

The LODI scheme is specified by a characteristic analysis of a locally one-dimensional system of conservation equations:

$$\frac{\partial \psi^*}{\partial t} + \frac{\partial F_i}{\partial x} + C'_i = 0 \quad \text{where } i = 1 \text{ to } n \quad (4.16)$$

where ψ^* is a conservative variable vector, F_i is a representative flux vector and C'_i is a non-homogeneous term without derivatives. Rewriting the Eq. 4.16 based on the dependent variables ψ_i yields the following equation:

$$\frac{\partial \psi_i}{\partial t} + A_{ij} \frac{\partial \psi_j}{\partial x} + C_i = 0 \quad (4.17)$$

Eq. 4.16 and Eq. 4.17 are linked subsequently as:

$$\frac{\partial \psi^*}{\partial t} = P_{ij} \frac{\partial \psi_j}{\partial t} \quad \text{where } P_{ij} = \frac{\partial \psi_i^*}{\partial \psi_j} \quad (4.18)$$

$$\frac{\partial F_i}{\partial t} = Q_{ij} \frac{\partial \psi_j}{\partial t} \quad \text{where } Q_{ij} = \frac{\partial F_i}{\partial \psi_j} \quad (4.19)$$

In above equations, $A_{ij} = P_{ij}^{-1} Q_{kj}$ and $C_i = P_{ik}^{-1} C'_k$ where A_{ij} , P_{ij} and Q_{ij} are the components of the $n \times n$ matrices. The matrix A_{ij} has n linearly independent eigenvectors $S_{ik} A_{kp} S_{pj} = \Lambda_{ij}$ with the eigenvector matrix S_{ij} and diagonal matrix Λ_{ij} (where $\Lambda_{ij=i}$ is equal to the eigenvalues λ_i). By using the eigenvector matrix, Eq. 4.17 can be shown as:

$$S_{ij} \frac{\partial \psi_j}{\partial t} + \Lambda_{ik} S_{kj} \frac{\partial \psi_j}{\partial x} + S_{ij} C_j = 0 \quad (4.20)$$

Subsequently, the new vector $\vec{\xi}$ can be defined in the following manner:

$$d\xi_i = S_{ij}d\psi_j + S_{ij}C_j dt \quad (4.21)$$

and

$$\frac{\partial \xi_i}{\partial t} + \Lambda_{ik} \frac{\partial \xi_k}{\partial x} = 0 \quad (4.22)$$

or

$$\frac{\partial \xi_i}{\partial t} + \lambda_i \frac{\partial \xi_k}{\partial x} = 0 \quad (4.23)$$

Equation 4.23 has a characteristic velocity λ_i , and the second term of Eq. 4.20 is called the wave amplitude variation L_i . Figure 4.1 represents the schematic diagram of the wave amplitude variations L_i at the inlet and outlet boundaries.

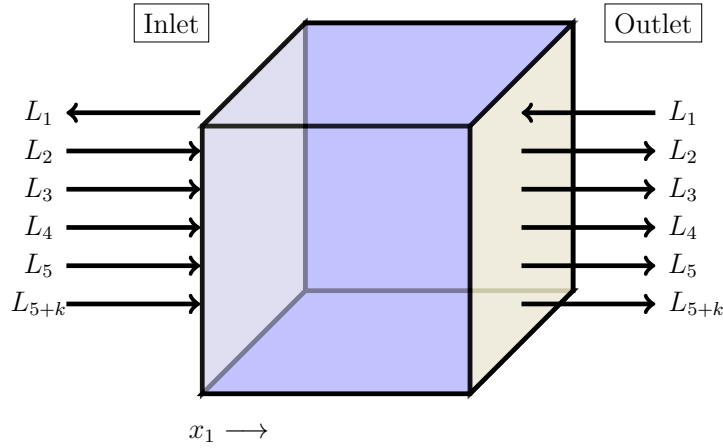


Fig. 4.1 Schematic diagram of the wave amplitude variations L_i at inlet and outlet boundaries

Following analysis is considered on x-boundary. The LODI system is described as [157]:

$$\frac{\partial}{\partial t} \begin{bmatrix} u_1 \\ u_2 \\ u_3 \\ \rho \\ p \\ Y_k \end{bmatrix} + \begin{bmatrix} (L_5 - L_1)/2\rho a \\ L_3 \\ L_4 \\ [L_2 + \frac{1}{2}(L_5 + L_1)]/a^2 \\ (L_5 + L_1)/2 \\ L_{5+k} \text{ for } k = 1, N \end{bmatrix} = \begin{bmatrix} 0 \\ 0 \\ 0 \\ 0 \\ 0 \\ 0 \end{bmatrix} \quad (4.24)$$

In above equation, L_i ($1 \leq i \leq 5 + N$) are the wave-based quantities, which is obtained from a characteristic analysis of the governing equations along x -direction. Furthermore, the wave-based quantities L_i provide the temporal rate of change of the amplitudes of the different acoustic, convective or entropy waves, which across the x -boundary [157]:

$$\mathbf{L} = \begin{bmatrix} L_1 \\ L_2 \\ L_3 \\ L_4 \\ L_5 \\ L_{5+i} \end{bmatrix} = \begin{bmatrix} \lambda_1 \left(\frac{\partial p}{\partial x_1} - \rho a \frac{\partial u_1}{\partial x_1} \right) \\ \lambda_2 \left(a^2 \frac{\partial \rho}{\partial x_1} - \frac{\partial p}{\partial x_1} \right) \\ \lambda_3 \frac{\partial u_2}{\partial x_1} \\ \lambda_4 \frac{\partial u_3}{\partial x_1} \\ \lambda_5 \left(\frac{\partial p}{\partial x_1} + \rho c \frac{\partial u_1}{\partial x_1} \right) \\ \lambda_{5+k} \frac{\partial Y_k}{\partial x_1} \text{ for } k = 1, N \end{bmatrix} \quad (4.25)$$

Here, the characteristic wave velocities λ_i is given by [157]:

$$\lambda_1 = u - a, \quad \lambda_2 = \lambda_3 = \lambda_4 = \lambda_{5+i} = u, \quad \lambda_5 = u + a \quad (4.26)$$

where a is the local speed of sound given by $a^2 = \gamma p / \rho$. The wave travelling towards the negative x_1 direction is indicated by the wave amplitude variation L_1 , and L_5 corresponds the wave travelling in the positive x_1 direction. L_2 is the entropy wave, and L_3 (L_4) corresponds the advection in transverse direction x_2 (x_3).

4.3.1 Inlet boundary condition

In current analysis, u_1 , u_2 , u_3 , ρ and c are specified. The wave amplitude variations are listed as below:

$$L_1 = (u_1 - a) \left(\frac{\partial p}{\partial x_1} - \rho a \frac{\partial u_1}{\partial x_1} \right) \quad (4.27)$$

$$L_3 = -\frac{\partial u_2}{\partial t} \quad (4.28)$$

$$L_4 = -\frac{\partial u_3}{\partial t} \quad (4.29)$$

$$L_5 = L_1 - 2\rho a \frac{\partial u_1}{\partial t} \quad (4.30)$$

$$L_2 = -\frac{1}{2}(L_1 + L_5) - a^2 \frac{\partial \rho}{\partial t} \quad (4.31)$$

The wave amplitude variation L_{5+k} which are associated with the progress variable are zero as it is considered homogeneous mixture from the inlet.

4.3.2 Partial non-reflecting outlet boundary condition

A perfectly non-reflecting condition might not lead to a well-posed problem [157]. For partial non-reflecting outlet, five characteristic waves L_2 , L_3 , L_4 , L_5 and L_{5+k} leaves the domain while L_1 is coming from outside the domain with a speed of $\lambda_1 = u_1 - a$, where the static pressure p_∞ is specified for well-posed solution (if the local pressure p at the boundary is less than p_∞ , a reflected wave is generated to bring p closer to p_∞). Therefore, the amplitude of incoming wave L_1 is defined as:

$$L_1 = K(p - p_\infty) \quad (4.32)$$

The form of constant K [168] is:

$$K = \sigma(1 - Ma_{\max}^2)a/L \quad (4.33)$$

where Ma_{\max} is the maximum Mach number in the flow and σ is a constant.

The LODI assumption has proved robust in most DNS studies of unidirectional mean flow. However, it becomes inadequate when multi-directionality of the flow has a dominate effect. In counterflow configuration, the transverse derivatives can not be neglected [213]. Therefore, the LODI is modified to take into account of the transverse derivatives as:

$$\frac{\partial}{\partial t} \begin{bmatrix} u_1 \\ u_2 \\ u_3 \\ \rho \\ p \\ Y_k \end{bmatrix} + \begin{bmatrix} (L_5 - L_1)/2\rho a \\ L_3 \\ L_4 \\ [L_2 + \frac{1}{2}(L_5 + L_1)]/a^2 \\ (L_5 + L_1)/2 \\ L_{5+k} \text{ for } k = 1, N \end{bmatrix} + \begin{bmatrix} \mathbf{v}_t \cdot \nabla_t u_1 \\ \mathbf{v}_t \cdot \nabla_t u_2 + (1/\rho)\partial p/\partial x_2 \\ \mathbf{v}_t \cdot \nabla_t u_3 + (1/\rho)\partial p/\partial x_3 \\ \nabla_t \cdot (\rho \mathbf{v}_t) \\ \mathbf{v}_t \cdot \nabla_t p + \gamma p \nabla_t \cdot \mathbf{v}_t \\ \mathbf{v}_t \cdot \nabla_t Y_i \text{ for } k = 1, N \end{bmatrix} = \begin{bmatrix} 0 \\ 0 \\ 0 \\ 0 \\ 0 \\ 0 \end{bmatrix} \quad (4.34)$$

where \mathbf{v}_t is the velocity vector in tangential directions. The above equation can be written in term of the incoming pressure waves' variations (leave and enter the domain) as [77]:

$$L_{1/5} = K_p(p - p_\infty) + K_{1/5}(u_1 - u_{1\infty}) + S_{1/5} + T_{1/5} + D_{1/5} \quad (4.35)$$

The constants K_p and $K_{1/5}$ enable the local pressure p and the velocity u_1 to return their target values within a chosen time scale to minimise unwanted reflection of the acoustic waves which leave the domain. The term $S_{1/5}$, $T_{1/5}$ and $D_{1/5}$ represent the pressure variations due to the source, transverse convection, and transverse diffusion

respectively, and they take the following forms [184]:

$$S = \frac{(1 - \gamma)K_S}{2} \left(\sum_{\alpha=1}^N h_{\alpha} \dot{\omega}_{\alpha} \right) \quad (4.36)$$

$$T_1 = K_T \left(u_t \frac{\partial p}{\partial x_t} + \gamma p \frac{\partial u_t}{\partial x_t} - \rho a u_t \frac{\partial u_1}{\partial x_t} \right) \quad (4.37)$$

$$T_5 = K_T \left(u_t \frac{\partial p}{\partial x_t} + \gamma p \frac{\partial u_t}{\partial x_t} + \rho a u_t \frac{\partial u_1}{\partial x_t} \right) \quad (4.38)$$

$$D = \frac{(\gamma - 1)K_D}{2} \left(\sum_{\alpha=1}^N h_{\alpha} \frac{\partial \rho Y_{\alpha} V_{\alpha t}}{\partial x_t} - \frac{\partial q_t}{\partial x_t} \right) \quad (4.39)$$

where the subscript t refers to the tangential directions to the boundary planes, K_S , K_T and K_D are constant for the configuration, and $K_T = (1 - Ma)$ suggest by Yoo and Im [213].

4.3.3 Wall boundary condition

All walls considered to be stationary and have characteristics of no-slip and impermeable. Therefore, they contain perfect reflections of acoustic waves, but there are no convective transports of any quantity through the wall. For an isothermal wall, all velocity components are equal to zero ($u_i = 0$), and the wall temperature is specified. The reactant species flux is equal to zero.

4.4 Implementation of HOQ with simplified chemistry

The simulations data have been carried out by a DNS code SENGAs [102] which solves standard conservation equations of mass, momentum, energy and species for compressible reacting flows in non-dimensional form. A rectangular box of dimensions $70.6\delta_Z \times 35.2\delta_Z \times 35.2\delta_Z$ has been taken for the simulation domain where $\delta_Z = \alpha_{T0}/S_L$ is the Zel'dovich flame thickness with α_{T0} and S_L being the thermal diffusivity of the unburned gas and the unstrained laminar burning velocity respectively. The simulation domain has been discretized using a uniform Cartesian grid of $512 \times 256 \times 256$, which ensures that there are ten grid points across the thermal flame thickness δ_{th} . The left-hand side of the domain boundary in the x_1 -direction (i.e. $x_1 = 0$) is taken to be a no-slip isothermal wall with temperature $T_W = T_0$, and zero mass flux is enforced in the wall normal direction. The boundary opposite to the isothermal wall is taken to be

Table 4.1 List of initial simulation parameters and non-dimensional numbers for head-on quenching cases

Case	A	B	C	D	E
u'/S_L	5.0	6.25	7.5	9.0	11.25
L_{11}/δ_{th}	1.67	1.44	2.5	4.31	3.75
Da	0.33	0.23	0.33	0.48	0.33
Ka	8.67	13.0	13.0	13.0	19.5

partially non-reflecting. The boundary conditions are specified using NSCBC technique [159]. The rest of domain boundaries in x_2 and x_3 directions are taken to be periodic. A 10th order central difference scheme is used for spatial differentiation of internal grid points but the order of differentiation decreases gradually to a one-sided 2nd order scheme at the non-periodic boundaries [102]. The time advancement is carried out by using an explicit third-order low storage Runge-Kutta scheme [212].

A steady unstrained planar laminar premixed flame solution is used to initialise the reactive field so that the $T = (\hat{T} - T_0)/(T_{ad} - T_0) = 0.9$ isosurface remains at a distance $20\delta_Z$ away from the wall. This allows for enough time for the flame to evolve before interacting with the wall. The turbulent fluctuating velocity field is initialised using a homogeneous isotropic field of turbulent velocity fluctuations, which is generated using a pseudo-spectral method [167] following the Batchelor-Townsend Spectrum [7], but the velocity components at the wall u_1 , u_2 and u_3 are specified to be zero to ensure no-slip condition. This field is allowed to evolve for an initial eddy turn-over time (i.e. $t_e = l/u'$ where l is the integral length scale and u' is the root-mean-square (rms) turbulent velocity magnitude) before interacting with the flame.

The initial values of normalised rms turbulent velocity fluctuation u'/S_L , the ratio of longitudinal integral length scale to thermal flame thickness L_{11}/δ_{th} for the turbulent velocity field away from the wall are listed in Table 4.1 along with the corresponding values of Damköhler number $Da = L_{11}S_L/\delta_{th}u'$ and Karlovitz number $Ka = (u'/S_L)^{3/2}(L_{11}/\delta_{th})^{-1/2}$. Table 4.1 indicates that the cases A, C and E have same values of Da , and cases B, C and D show the same values of Ka . Three different global Lewis numbers (i.e. $Le = 0.8, 1.0$ and 1.2) have been considered for each set of turbulence parameters considered here. Standard values are chosen for Prandtl number Pr and ratio of specific heats γ (i.e. $Pr = 0.7$ and $\gamma = 1.4$). For the present analysis, both the heat release parameter $\tau = (T_{ad} - T_0)/T_0$, and Zel'dovich number $\beta = E_{ac}(T_{ad} - T_0)/RT_{ad}^2$ are taken to be 6.0 (i.e. $\tau = 6.0$ and $\beta = 6.0$). These values are representative of iso-octane-air mixture with unburned gas temperature $T_0 \approx 325.0$ K

and equivalence ratio of 1.10 under atmospheric pressure. The simulations for turbulent cases have been carried out up to a time when the maximum, mean and minimum values of wall heat flux assume identical values following the flame quenching. The simulation time remains different from one case to another but the simulations for all cases were continued for $t \geq 12\delta_Z/S_L$ where $12\delta_Z/S_L$ corresponds to 21, 30, 21, 15 and 21 initial eddy turn over times for cases A-E respectively. The non-dimensional grid spacing next to the wall $y^+ = u_\tau \Delta x / \nu$ remains smaller than unity for all turbulent cases (the maximum value of y^+ has been found to be 0.93 during the course of the simulation), where $u_\tau = \sqrt{\tau_w / \rho}$, τ_w and ν are the friction velocity, mean wall shear stress, and kinematic viscosity respectively. For $y^+ = u_\tau \Delta x / \nu \approx 0.93$, the minimum normalised wall normal distance $u_\tau x_1 / \nu$ of $T = (\hat{T} - T_0) / (T_{ad} - T_0) = 0.9$ iso-surface has been found to be about 15.0 for the quenching flames considered here.

For the current analysis, all the Reynolds/Favre averaged quantities are evaluated by ensemble averaging the quantity in question in the transverse direction (i.e. over $x_2 - x_3$ plane) at a given x_1 location. The statistical convergence has been assessed by comparing the results using full and half of available sample sizes. In all cases, a satisfactory level of statistical convergence has been obtained, and the results based on full sample size will be presented in the next section for the sake of conciseness.

4.5 Implementation of sidewall quenching of turbulent V-flames

The same DNS code SENGAs [102] has been used to simulate the quenching of V-shaped flames by two sidewalls (See Fig. 2.1). Single step chemistry is used for the purpose of the computational economy. The simulation domain for V-flame is taken to be rectangular boxes of sizes $175.8\delta_Z \times 58.5\delta_Z \times 58.5\delta_Z$ (where the long-side of the domain is aligned with x_1 -direction). The computational domain is discretised by a uniform Cartesian mesh of size $900 \times 300 \times 300$ ensuring at least ten grid points across the thermal flame thickness δ_{th} . Furthermore, this resolution ensures that normalised grid size $\rho_0 u_\tau \Delta x / \mu_0$ remains smaller than unity, where u_τ and μ_0 are the friction velocity and unburned gas viscosity, respectively. No-slip wall boundary conditions are specified in x_2 -direction at $x_2 = 0$ (i.e. lower wall) and $x_2 = L_2$ (for upper wall where L_2 is the domain length in x_2 -direction), and flame normal mass fluxes are enforced to be zero for both top and bottom walls. Turbulent inflow and partially non-reflecting boundary conditions are specified in x_1 -direction, whereas periodic boundaries are considered for x_3 -direction. A flame holder with an approximate radius of $R_{fh} \approx 1.5\delta_{th}$ is placed

Table 4.2 List of inflow simulation parameters and non-dimensional numbers for V-flame cases

Case	V-flame	HOQ
u'/S_L	5.0	5.0
L_{11}/δ_{th}	1.67	1.67
Da	0.33	0.33
Ka	8.67	8.67
Le	1.0	1.0

at a distance $44\delta_Z$ from the inlet and $14.6\delta_Z$ from the lower wall to ensure the flame interacts more readily with the lower wall. The mean inlet velocity U_{mean} is taken to be $12.0S_L$ for the V-flame simulation. The simulations have been carried out for two complete flow-through times (i.e. $2t_{ft} = 2L_1/U_{mean}$, where L_1 is the domain length in x_1 -direction). The heat release parameter τ is taken to be 2.3, the Zel'dovich number β is taken to be 6.0 and the ratio of specific heats γ is equal to 1.4.

The turbulent flow conditions at the inlet for the V-flame configuration are listed in Table 4.2. For comparison purposes, HOQ simulations have been carried out for the same chemical mechanism and the initial values of u'/S_L and L_{11}/δ_{th} listed in Table 4.2 for cases V-flame and HOQ.

4.6 Implementation of HOQ with a detailed chemical mechanism

The detailed chemistry simulations have been conducted using a three-dimensional compressible code SENG2 [27]. The domain is taken to be a cube of each side equal to 7.65 mm which is discretized by a uniform grid of dimension $256 \times 256 \times 256$ ensuring 15 grid points across the thermal flame thickness δ_{th} . In SENG2, the spatial differentiation is carried out using a 10th order central difference scheme for the internal grid points, but the order of differentiation gradually decreases to a one-sided 4th order scheme at the non-periodic boundaries. The time advancement is carried out using an explicit low-storage 4th order Runge-Kutta scheme. The negative x_1 -direction is aligned with the mean direction of flame propagation. The left-hand boundary in the x_1 -direction is taken to be an inert isothermal wall which is kept at the unburned gas temperature T_0 , which is taken to be 300 K for this analysis. The boundary opposite to the wall is taken to be partially non-reflecting and is specified using the Navier-Stokes

Table 4.3 Initial turbulence parameters away from the wall and the value of heat release for detailed chemistry

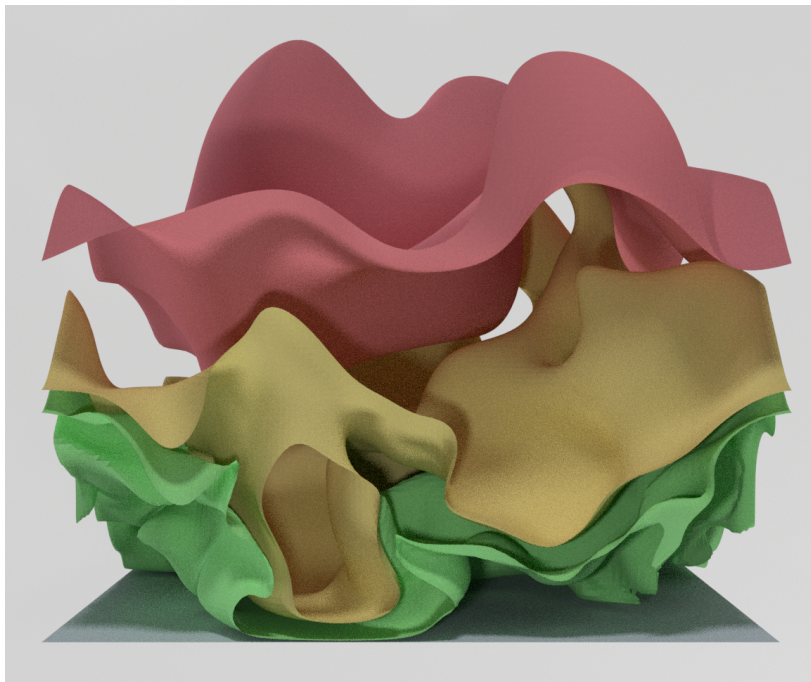
Case	Chemical Mechanism	u'/S_L	L_{11}/δ_{th}	Da	Ka	τ
A	16 species, 25 reactions	7.5	2.5	0.34	13.0	6.0
B	1-step irreversible	7.5	2.5	0.34	13.0	6.0

Characteristic Boundary Conditions (NSCBC) technique. The transverse directions are taken to be periodic. A detailed chemical mechanism (involving 16 species and 25 reactions and among these ten reactions are reversible) for atmospheric pressure combustion of methane-air mixture [175] has been considered for detailed chemistry simulations. The thermo-physical properties such as viscosity, thermal conductivity are taken to be functions of temperature and CHEMKIN [109] polynomials have been used to account for the temperature dependence of these physical properties. Mixture averaged transport is adopted for the current analysis. A steady state planar stoichiometric methane-air premixed flame under atmospheric pressure is used for initializing the reacting species and temperature fields. A homogeneous isotropic velocity field, generated using a standard pseudo-spectral method [167] following the Batchelor-Townsend spectrum [7], is used for the initialization of turbulent fluid motion away from the wall. The initial turbulent flow field parameters are shown in Table 4.3.

In order to compare the detailed chemistry simulation results with those obtained from simple chemistry simulation, three-dimensional DNS for a generic single step irreversible chemistry has been carried out. The thermo-physical properties such as dynamic viscosity, thermal conductivity, and density-weighted mass diffusivity are taken to be constant and independent of temperature, and the Lewis numbers of all the species are taken to be unity. For simple chemistry DNS the domain is taken to be $35.2\delta_Z \times 35.2\delta_Z \times 35.2\delta_Z$, which is discretized using a uniform grid of $256 \times 256 \times 256$ ensuring 10 grid points within δ_{th} . The simulations for head-on quenching have been conducted until the time when the volume-integrated heat release reduces by 20 % of its initial value.

Chapter 5

Results & Discussion 1: A Physical Insight



"From forth the fatal loins of these two foes, a pair of star-crossed lovers take their life." – Romeo and Juliet

— William Shakespeare (1564-1616) ¹

¹This picture shows the interaction between methane flame and the wall. Cooling of combustor walls is necessary because the burned gas temperature is often higher than the melting point of the combustor material. This cooling significantly affects the combustion processes in the near-wall region and the life span of the combustor itself. Grey surface indicates the cold wall; Green isosurface indicates flame temperature $400K$; Yellow isosurface indicates $650K$; Red isosurface indicates $1700K$.

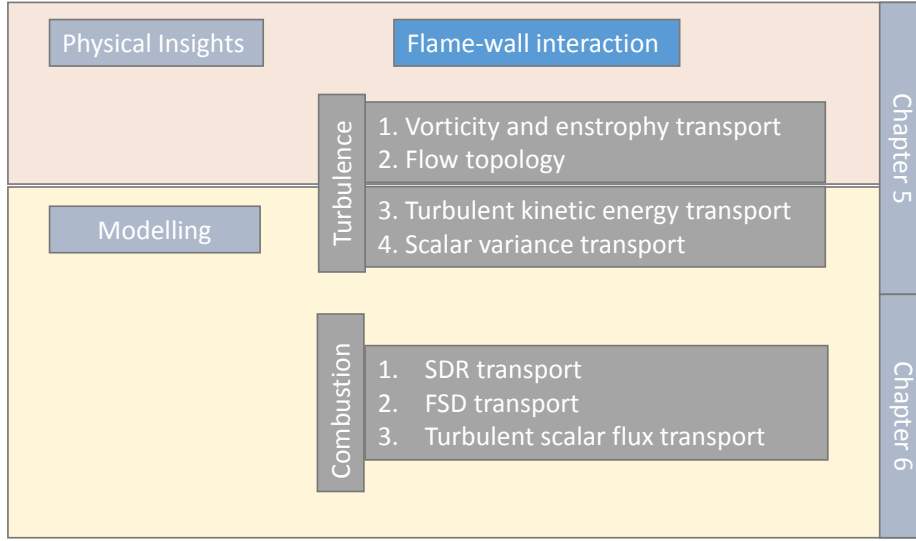


Fig. 5.1 Flow chart for Results & Discussion chapter 5 and 6

5.1 Results and discussion outlines

This chapter seeks to provide the physical insights of flame-wall interaction. Firstly, three-dimensional DNS of HOQ of turbulent premixed flame based on a single-step Arrhenius-type irreversible chemical reaction is chosen for the analysis by using the SENGGA, because three-dimensional DNS simulations with detailed chemistry are extremely expensive for a detailed parametric analysis [54]. Secondly, Chapter 5 and 6 are going to focus on the physical insights and modelling of turbulent flame-wall interaction (see Fig. 5.1). Finally, the extended results based on the detailed chemistry findings by using SENGGA2 code will be presented in Chapter 7 in the current thesis.

A global flame behaviour of head-on quenching of turbulent premixed flame is provided with the consideration of different turbulent cases and non-unity Lewis number effects. The primary focus of this chapter is on the interactions between the wall, turbulent motion and the flame. The statistical behaviours of vorticity and enstrophy in the near-wall region will be discussed in this chapters along with the influences of the flow topology on the wall heat fluxes. Finally, the behaviours and modelling of the turbulent kinetic energy and the scalar variance transports will be discussed in detail later in this chapter.

5.2 Global flame behaviour: wall heat flux and Peclet number and their Lewis number dependence

5.2.1 Laminar flame

The temporal evolution of non-dimensional temperature T , the reaction rate of progress variable $\dot{\omega}$, normalised wall heat flux magnitude Φ and wall Peclet number Pe for the head-on quenching of a premixed planar laminar flame with $Le = 1.0$ are shown in Fig. 5.2. It can be seen from Fig. 5.2 that the wall Peclet number Pe for the laminar flame decreases as the flame approaches the cold wall, which is accompanied by the increases of both the thermal gradient at the wall and the magnitude of the normalised wall heat flux Φ . This trend continues until the flame quenches completely when Pe attains its minimum value (i.e. the minimum distance of $T = 0.9$ isosurface from the wall) and Φ reaches its maximum value. The initiation of flame quenching can be seen from the significant drop in the chemical reaction rate $\dot{\omega}$, and the reaction rate completely disappears once the flame is completely quenched. The minimum Peclet number $(Pe_{\min})_L$ for laminar case indicates that the “quenching zone” stretches from the wall to the wall normal direction $x_1 = (Pe_{\min})_L$. After quenching, the isotherms gradually move away from the wall (i.e. Pe increases with time) due to thermal diffusion, which leads to a continuous reduction in Φ with time. This behaviour is consistent previous findings by Poinso *et al.* [156]. The same qualitative behaviour for the coupling of Φ and Pe has been observed for laminar $Le = 0.8$ and 1.2 flames. The minimum value of wall Peclet number for the laminar flame with $Le = 1.0$ is found to be $(Pe_{\min})_L = 2.83$, whereas the maximum magnitude of normalised heat flux assumes a value $(\Phi_{\max})_L = 0.34$. These values are consistent with previous experimental [98, 101, 204] and computational findings [156]. Fig. 5.2 also shows that the wall heat flux Φ starts to rise (i.e. $\Phi \neq 0.0$) at $Pe \approx 8$, the corresponding distance from the wall indicates that the flame is entering the “influence zone” before it gets finally quenched by the wall.

For non-unity Lewis number flames, the laminar results can be found in Fig. 5.3. The “influence zone” for both unity and non-unity cases are within the same order of magnitude. However, $(Pe_{\min})_L$ is found to increase with decreasing Le (e.g. $(Pe_{\min})_L = 3.09, 2.83$ and 2.75 for $Le = 0.8, 1.0$ and 1.2 respectively), whereas $(\Phi_{\max})_L$ increases with increasing Le (e.g. $(\Phi_{\max})_L = 0.30, 0.34$ and 0.35 for $Le = 0.8, 1.0$ and 1.2 respectively). The rate of thermal diffusion is slower than the rate of mass diffusion

in the $Le = 0.8$ case, and thus the reactants from the vicinity of the wall diffuse faster into the approaching flame than the thermal diffusion rate towards the wall. Therefore, the minimum Peclet number $(Pe_{\min})_L$ in the laminar $Le = 0.8$ case is found to be greater than in the unity Lewis number case. As $(\Phi_{\max})_L$ can be scaled as $(\Phi_{\max})_L \sim 1/(Pe_{\min})_L$, the value of $(\Phi_{\max})_L$ in the $Le = 0.8$ case is found to be smaller than in the unity Lewis number case. The rate of thermal diffusion is greater than the rate of diffusion of fresh reactants from the vicinity of the wall in the $Le = 1.2$ case, and thus the isotherms can reach closer to the wall before quenching than in the $Le = 1.0$ case. This in turn gives rise to smaller (greater) value of $(Pe_{\min})_L$ ($(\Phi_{\max})_L$) in the $Le = 1.2$ case than in the $Le = 1.0$ case.

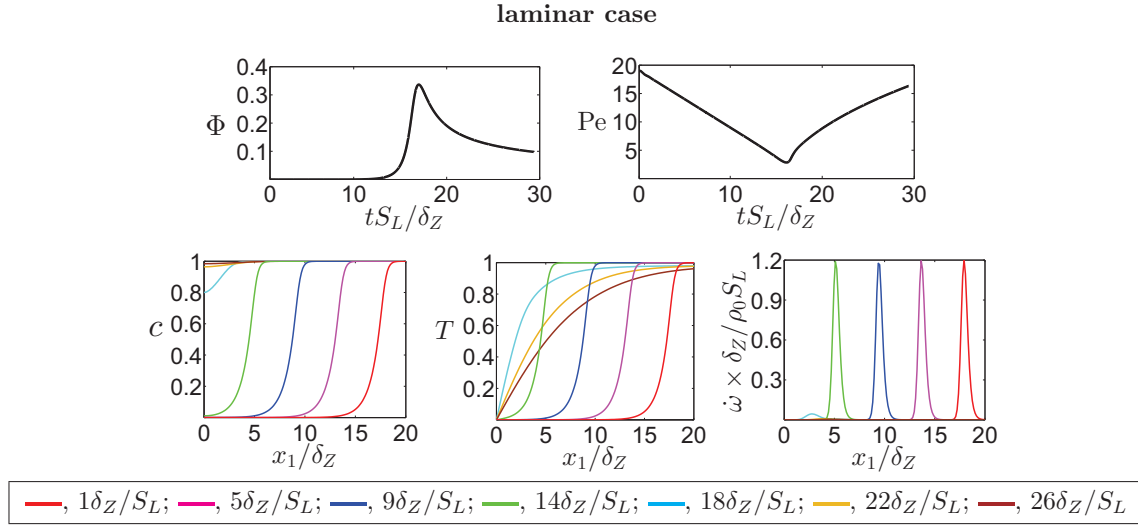


Fig. 5.2 Temporal evolutions of Peclet number Pe (based on $T = 0.9$ isosurface) and non-dimensional wall heat flux Φ for laminar flame with $Le = 1.0$.

5.2.2 Turbulent flame

It can be seen from Fig. 5.2 that a combination of the monotonic increase in Pe and decrease in Φ with time bears the signature of flame quenching in laminar flames. Drawing the same analogy, it can be expected that a combination of a monotonic increase of the minimum value of the wall Peclet number Pe_{\min} and a monotonic decrease of the maximum magnitude of wall heat flux Φ_{\max} with time is an indicator of flame quenching in turbulent flames. This can be verified from Fig. 5.3 which shows that the temporal evolutions of the maximum, mean and minimum values of Pe and Φ for the turbulent cases along with the corresponding variations obtained for head-on

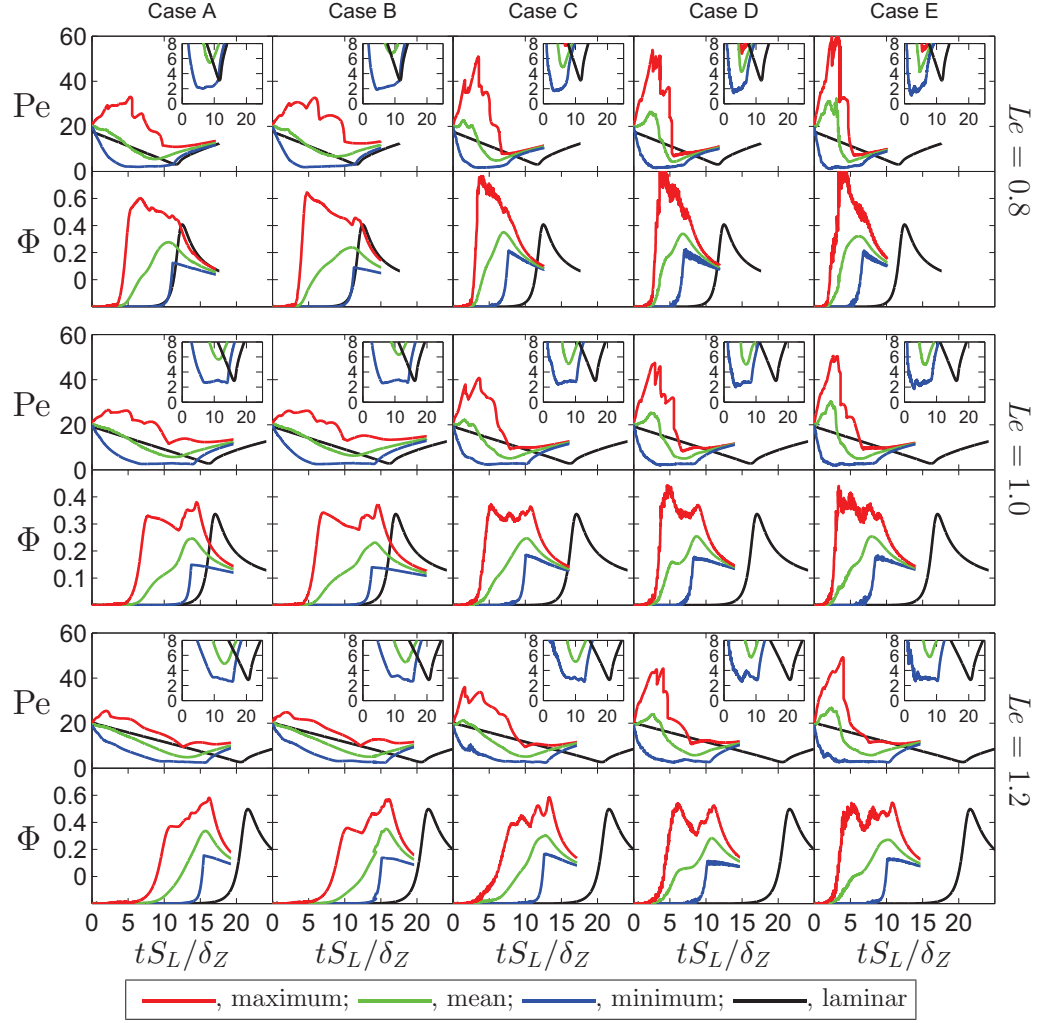


Fig. 5.3 Temporal evolutions of the maximum, mean and minimum values of Peclet number Pe (based on $T = 0.9$ isosurface) and non-dimensional wall heat flux Φ for turbulent cases A-E with $Le = 0.8, 1.0$ and 1.2 .

quenching of the laminar one-dimensional flames. The temporal evolutions of the variations of \tilde{c} and \tilde{T} in the wall normal direction are shown in Fig. 5.4 in order to explain the temporal variations of Pe and Φ . In the turbulent premixed flames, the isosurfaces of non-dimensional temperature T are no longer planar. The maximum (minimum) Peclet number Pe_{\max} (Pe_{\min}) represents the furthest (closest) normalised distance of the isotherm $T = 0.9$ from the wall (the maximum value for the reaction rate of a flame occurs in the region of the non-dimensional temperature of the flame reaches $T = 0.9$). The mean Peclet number Pe_{mean} represents the average distance of $T = 0.9$ from the wall. The minimum Peclet number Pe_{\min} provides a measurement

of the quenching distance for the premixed flames. A combination of the monotonic increases of Pe_{\min} and Pe_{\max} with time suggests that the isotherms are moving away from the wall as a result of the thermal diffusion following by flame quenching. Thus, both Pe_{\max} and Pe_{\min} are important quantities in the current analysis. Moreover, due to the flame wrinkling, different elements of the flame remain at different distances from the wall, and the flame front at the closest distance to the wall results to a high magnitude of wall heat flux Φ . The maximum magnitude of the wall heat flux Φ_{\max} is an important parameter in engineering applications because it determines the maximum cooling load. By contrast, the mean value of the wall heat flux Φ governs the mean cooling requirement. A combination of the monotonic decreases of Φ_{\min} , Φ_{mean} and Φ_{\max} with the time bears the signature of isotherms moving away from the wall following by flame quenching.

It can be seen from Fig 5.3 that Φ_{\max} assumes much greater values in the turbulent cases than the corresponding laminar values for all values of Le . Moreover, Fig 5.3 reveals that an increase in u' leads to an increase in Φ_{\max} . A rise of $u'/S_L \sim Re_t^{1/4} Ka^{1/2} \sim Re_t^{1/2} Da^{-1/2}$ leads to an increase in the flame wrinkling, which broadens the flame brush (see Fig. 5.4), and thus brings the flame elements close to the wall, where they eventually quench. This leads to the initiation of flame element quenching at an earlier time than in the corresponding laminar flame (see Fig 5.3). Last but not least, Fig 5.3 shows that the values of Pe_{\min} for the turbulent cases with $Le = 1.0$ and 1.2 are comparable the values in the corresponding laminar flame. However, the value of Pe_{\min} in turbulent $Le = 0.8$ flame is found to be smaller than its corresponding laminar flame value. A comparison between different Le cases reveals that the value of Φ_{\max} in the turbulent $Le = 0.8$ case is greater than the values of Φ_{\max} in the turbulent $Le \geq 1$ cases, which is in contrast to the Le dependence of $(\Phi_{\max})_L$ in laminar flames.

It is instructive to investigate the distributions of instantaneous reaction progress variable c , non-dimensional temperature T and chemical reaction rate $\dot{\omega}$ fields to explain the observed behaviours of Pe and Φ . The reaction progress variable and non-dimensional temperature fields for case D in the central $x_1 - x_2$ plane are shown in Fig. 5.5. For the unity Lewis number case, c and T are identical away from the wall, but these two quantities become significantly different from each other near the wall, where the quenching takes place. Since, in the case of head-on quenching the equality between c and T does not hold in the near-wall region due to the different boundary conditions for c (Neumann boundary condition) and T (Dirichlet boundary condition) at the wall. The same conclusion can be drawn from Fig. 5.4, where the variations

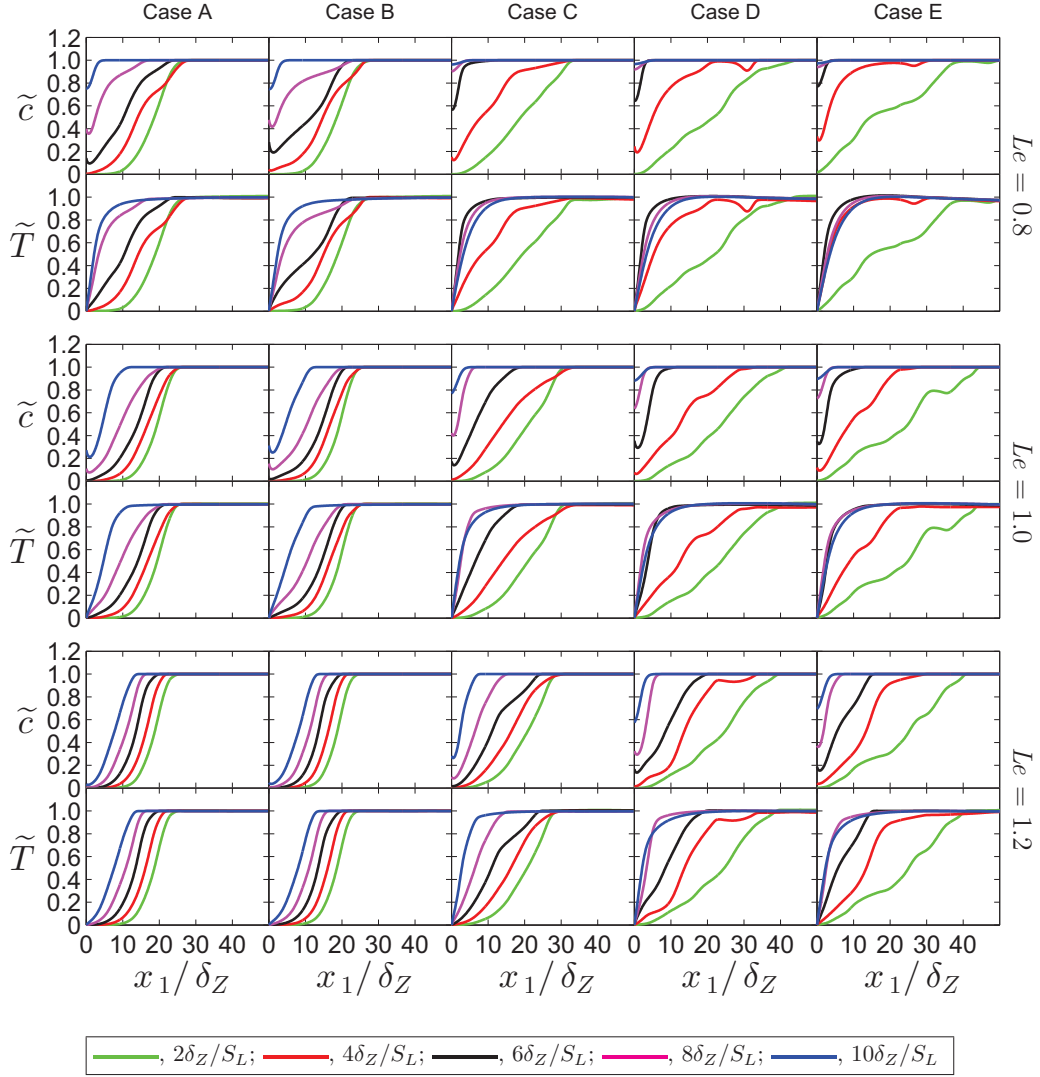


Fig. 5.4 Variations of \tilde{c} and \tilde{T} with x_1/δ_Z at different time instants for turbulent cases A-E with $Le = 0.8, 1.0$ and 1.2 .

of \tilde{c} and \tilde{T} in the wall normal direction are shown for different values of Le . Figure 5.5 shows that there are isolated pockets of the unburned/partially burned mixture in the vicinity of the wall even when Pe attains its minimum value and the flame starts to quench (indicated by the absence of $\dot{\omega}$ in the vicinity of the wall). Figure 5.5 indicates the existence of thermal inhomogeneity in the burned gas for the non-unity Lewis number flames even before the initiation of flame quenching. Super-adiabatic temperatures ($T > 1$) are observed for the non-unity Le cases when the flame is away from the wall. The high (low) values of temperature are associated with the region, where the flame surface is convex (concave) towards the reactants for the turbulent

$Le = 0.8$ cases. An opposite behaviour is observed for the turbulent $Le = 1.2$ cases. The focusing of reactants takes place at a higher rate than the rate of defocusing of heat for the flame wrinkles, which are convex towards the reactants in the turbulent $Le = 0.8$ cases. This gives rise to the simultaneous presence of high reactant concentration and temperature in the regions, which are convex towards the reactants for the turbulent $Le = 0.8$ cases, which in turn increases the rate of chemical reaction leading to high temperatures (e.g. super-adiabatic temperature). Just the opposite mechanism gives rise to high-temperature values in the regions where the flame front is concavely curved towards the reactants for the turbulent $Le = 1.2$ cases. Moreover, faster diffusion of reactants into the reaction zone than the rate of thermal diffusion out of this region in the turbulent $Le = 0.8$ cases gives rise to faster flame propagation than in the corresponding $Le = 1.0$ cases. Just the opposite mechanism leads to slower flame propagation in the turbulent $Le = 1.2$ cases than in the corresponding $Le = 1.0$ cases. Thus, the turbulent $Le = 0.8$ ($Le = 1.2$) cases exhibit flame quenching at an earlier (a later) time than in the corresponding turbulent $Le = 1.0$ cases.

The increases in the rate of flame propagation and the extent of flame wrinkling with decreasing Le can be substantiated from Table 5.1, where the normalised turbulent flame surface area A_T/A_L are listed at different time instants. The extent of flame wrinkling can be quantified by the normalised turbulent flame surface area A_T/A_L , where the flame surface area has been evaluated here using the volume integral $A = \int_V |\nabla c| dV$ for both turbulent and laminar flame cases (turbulent and laminar values are shown with subscripts ‘T’ and ‘L’ respectively). Table 5.1 also lists the normalised values of the turbulent flame speed S_T/S_L (where $S_T = (\rho_0 A_P)^{-1} \int_V \dot{\omega} dV$ where A_P is the projected area in the direction of mean flame propagation). It can be seen from Table 5.1 that both A_T/A_L and S_T/S_L increase initially with time (i.e. $t \leq 2\delta_Z/S_L$) due to an increase in flame wrinkling as a result of the flame-turbulent interaction, but both these quantities decay with time once the flame quenching is initiated (e.g. $t > 4\delta_Z/S_L$, see also Fig. 5.5). Table 5.1 further shows that both A_T/A_L and S_T/S_L assume high values for the cases with small Le and/or high values of u'/S_L when the flame is away from the wall (e.g. $t \leq 2\delta_Z/S_L$ in Fig. 5.5), and this behaviour is consistent with several previous analyses [1, 30, 33, 40, 42, 60, 93, 95, 126, 151, 163, 170, 174, 192]. However, the cases with small Le and/or high values of u'/S_L exhibit smaller values of A_T/A_L and S_T/S_L than the cases with high values of Le and/or small values of u'/S_L at later times (e.g. $t > 8\delta_Z/S_L$), because by then the flame is in more advanced stage of quenching in these cases than in the cases with high values of Le and/or small values of u'/S_L . The flame wrinkles come in the vicinity at the wall and starts to quench

at an earlier time instant for cases with higher rate of flame propagation and greater extent flame wrinkling and this trend strengthens with decreasing Le and increasing u'/S_L .

Table 5.1 List of normalised flame surface area A_T/A_L and turbulent flame speed S_T/S_L at different stages of flame quenching for all cases considered here.

		A		B		C		D		E	
	tS_L/δ_Z	A_T/A_L	S_T/S_L	A_T/A_L	S_T/S_L	A_T/A_L	S_T/S_L	A_T/A_L	S_T/S_L	A_T/A_L	S_T/S_L
$Le = 0.8$	1	1.62	1.61	1.69	1.68	3.50	3.47	3.26	3.23	5.33	5.29
	2	2.49	2.48	2.63	2.63	4.05	4.05	5.74	5.73	6.71	6.70
	4	2.64	2.62	2.36	2.35	2.69	2.67	2.32	2.30	1.50	1.48
	6	1.90	1.88	1.70	1.68	0.44	0.43	0.28	0.28	0.15	0.15
	8	0.94	0.93	1.07	1.06	0.04	0.04	0.03	0.03	0.02	0.02
	10	0.17	0.17	0.19	0.19	0.01	0.01	0.01	0.01	0.01	0.01
$Le = 1.0$	1	1.57	1.55	1.59	1.57	2.79	2.78	2.91	2.90	4.18	4.17
	2	1.67	1.66	1.60	1.59	2.99	2.99	3.95	3.93	4.77	4.76
	4	1.77	1.76	1.73	1.71	2.34	2.31	2.39	2.37	2.03	2.01
	6	1.64	1.62	1.68	1.66	1.43	1.41	0.74	0.74	0.68	0.67
	8	1.51	1.49	1.53	1.51	0.50	0.49	0.20	0.19	0.12	0.12
	10	0.86	0.85	0.85	0.84	0.09	0.09	0.03	0.03	0.03	0.03
$Le = 1.2$	1	1.29	1.28	1.22	1.21	1.92	1.91	2.04	2.02	2.68	2.66
	2	1.38	1.37	1.33	1.32	2.01	2.00	2.75	2.74	3.43	3.43
	4	1.31	1.03	1.28	1.27	1.82	1.81	1.98	1.96	1.57	1.55
	6	1.3	1.29	1.29	1.28	1.60	1.59	1.51	1.49	1.23	1.22
	8	1.23	1.22	1.24	1.23	1.12	1.11	0.60	0.60	0.47	0.46
	10	1.15	1.14	1.14	1.13	0.60	0.60	0.18	0.18	0.10	0.10

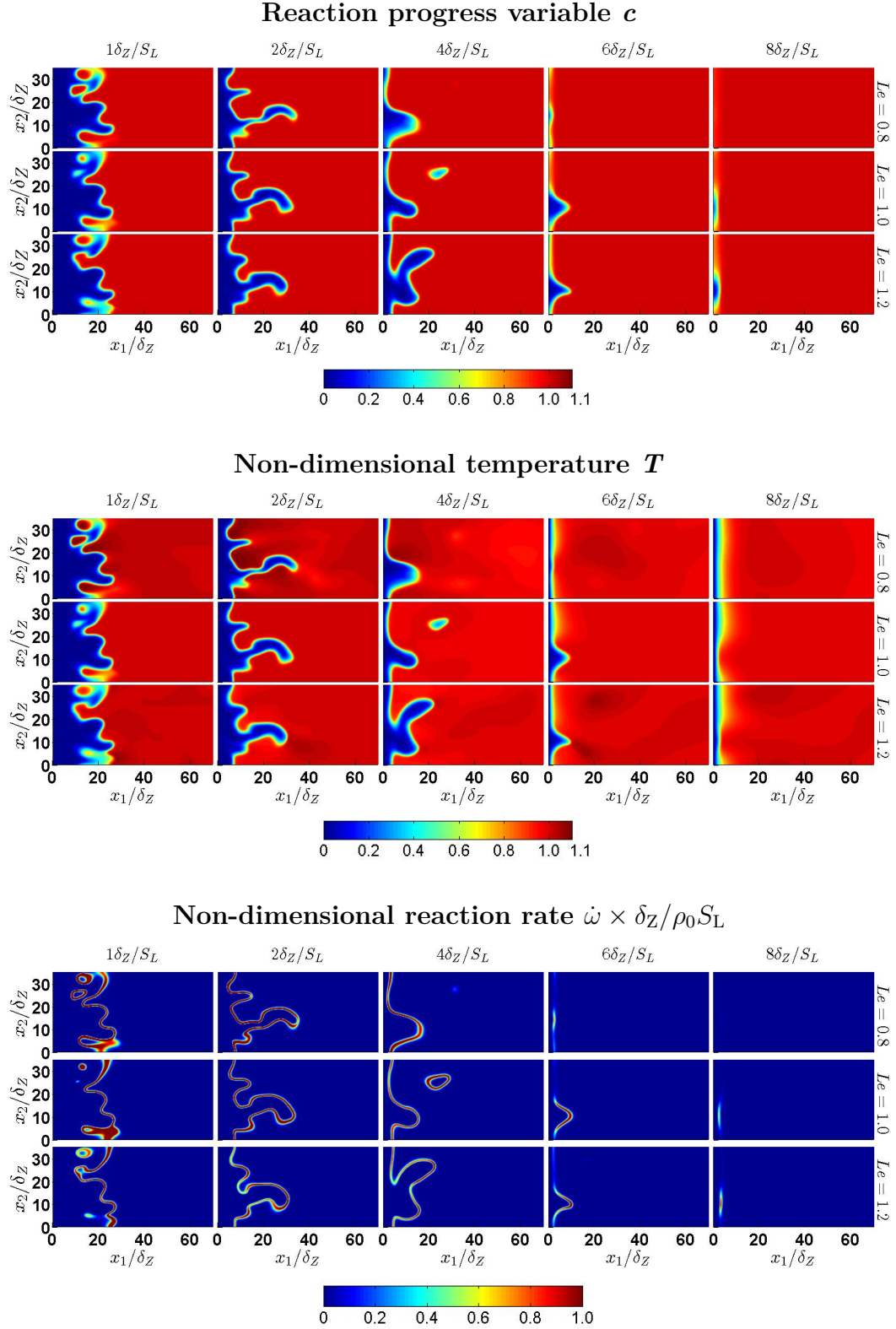


Fig. 5.5 Distributions of reaction progress variable c , non-dimensional temperature T and non-dimensional reaction rate $\dot{\omega} \times \delta_Z / \rho_0 S_L$ contours for turbulent case D with $Le = 0.8, 1.0$ and 1.2 at $t = \delta_Z / S_L, 2\delta_Z / S_L, 4\delta_Z / S_L, 6\delta_Z / S_L$ on central $x_1 - x_2$ plane.

5.3 Statistical behaviour of vorticity and enstrophy transport

The transport of vorticity $\vec{\omega}$ and enstrophy $\Omega = \vec{\omega} \cdot \vec{\omega} / 2$ in the near-wall region for head-on quenching of turbulent combustion by an isothermal inert wall is analysed in this section. The objectives of this section are:

- To demonstrate and explain the influences of the wall on the statistics of $\vec{\omega}$ and Ω , and the terms of their transport equations.
- To identify the influences of Le on $\vec{\omega}$ and Ω statistics, and their near-wall behaviour.

5.3.1 Flame turbulence interaction and vorticity distribution

The instantaneous distribution of $\sqrt{\omega_i \omega_i} \times \delta_Z / S_L$ in the central $x_1 - x_2$ plane for case E, along with c contours ranging from 0.1 to 0.9 (bottom to top), are presented in Fig 5.6. The large magnitudes of $\sqrt{\omega_i \omega_i} \times \delta_Z / S_L$ are concentrated on the unburned gas side of the flame and $\sqrt{\omega_i \omega_i} \times \delta_Z / S_L$ decreases significantly across the flame for all Le cases. This can be supported by Fig. 5.7 where the variations of $(\overline{\omega_i \omega_i})^{1/2}$ and scaled-up mean rate of production creation $\bar{\omega}_c$ with x_1 / δ_Z are shown for cases A, C and E. Case B and D are qualitatively similar to cases A and E respectively and thus are not shown in Fig. 5.7 and subsequent figures. Fig. 5.7 shows that $(\overline{\omega_i \omega_i})^{1/2}$ attains its highest value at the wall and gradually decays from unburned to burned gas side of the flame brush besides it is consistent with previous findings [129, 191], which also reported a decrease in the magnitude of vorticity within flame brush. The physical explanation for the decay of vorticity magnitude across the flame brush will be discussed later in this section by analysing the statistical behaviours of vorticity and enstrophy transport. The background colour in Figs. 5.7-5.15 indicates the Favre-averaged value of \tilde{c} , which illustrates the flame position at the corresponding time instants.

A comparison between $(\overline{\omega_i \omega_i})^{1/2}$ and $\bar{\omega}_c$ distributions reveals that before quenching $(\overline{\omega_i \omega_i})^{1/2}$ attains high magnitudes in the cases with high magnitude of u' / S_L (or small value of Le) cases (e.g. see the top right plot: case E, $Le = 0.8$, and $t = 2\delta_Z / S_L$). A comparison between spatial profiles of $\bar{\omega}_c$, obtained in the five cases at time instant $t = 2\delta_Z / S_L$, indicates that the mean flame brush thickness increase profoundly by an increase in u' / S_L from case A to case E. As a result, the leading edge of the flame brush is more close to the wall in case E when compared to case A. This difference in the $x_1 -$ coordinates of flame brush edges is of substantial importance of analysing the

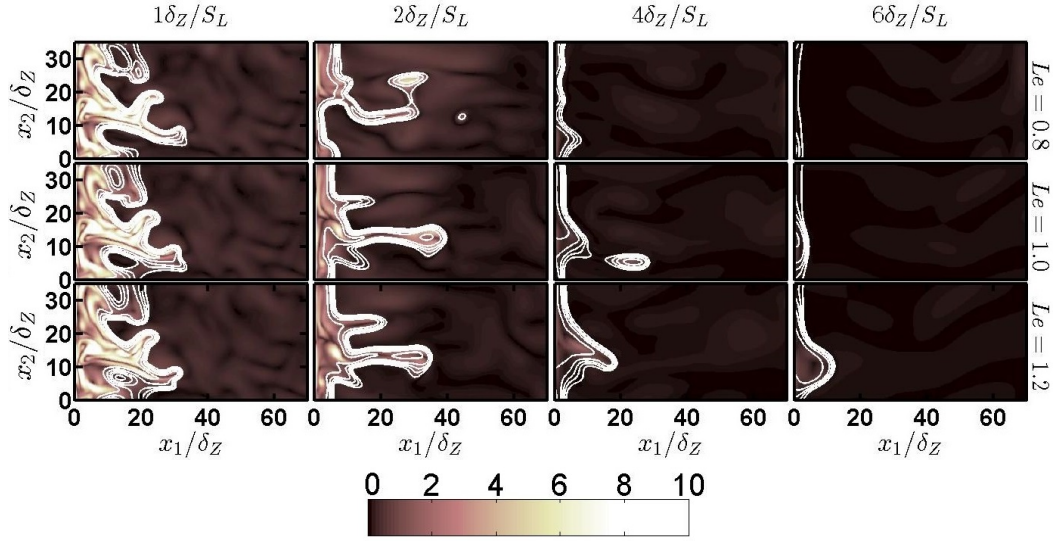


Fig. 5.6 Distributions of $(\omega_i \omega_i)^{1/2} \times \delta_Z/S_L$ and c (white line from 0.1 to 0.9 with step of 0.2 from left to right) fields on $x_1 - x_2$ mid plane for turbulent case E with $Le = 0.8, 1.0$ and 1.2 at $t = 1, 2$ and $4\delta_Z/S_L$.

results which are obtained at the time instant $t = 2\delta_Z/S_L$ because the flame in case E is closer to the wall (than in case A) before flame quenching taking place.

5.3.2 Statistical behaviour of the magnitude of vorticity components

The variations of the rms values of the normalised Favre-averaged vorticity magnitude $[\overline{\rho(\omega_i - \tilde{\omega}_i)^2/\bar{\rho}}]^{1/2} \times \delta_Z/S_L$ and its components $[\overline{\rho(\omega_1 - \tilde{\omega}_1)^2/\bar{\rho}}]^{1/2} \times \delta_Z/S_L$, $[\overline{\rho(\omega_2 - \tilde{\omega}_2)^2/\bar{\rho}}]^{1/2} \times \delta_Z/S_L$ and $[\overline{\rho(\omega_3 - \tilde{\omega}_3)^2/\bar{\rho}}]^{1/2} \times \delta_Z/S_L$ with x_1/δ_Z are shown for cases A, C and E in Fig. 5.8. A difference between the magnitude of $[\overline{\rho(\omega_1 - \tilde{\omega}_1)^2/\bar{\rho}}]^{1/2} \times \delta_Z/S_L$ and $[\overline{\rho(\omega_2 - \tilde{\omega}_2)^2/\bar{\rho}}]^{1/2} \times \delta_Z/S_L$ or $[\overline{\rho(\omega_3 - \tilde{\omega}_3)^2/\bar{\rho}}]^{1/2} \times \delta_Z/S_L$ has been found before the flame interacts with the wall (cf. violet, red and blue lines in the top right plot). The presence of the flame significantly modifies the initial isotropic vorticity field, and it is consistent with previous analyses [44, 91, 129, 191] which reported strong anisotropy between the vorticity components due to baroclinic torque contribution. The extent of this anisotropicity increases with decreasing (increasing) Le (u'/S_L) when the flame is away from the wall, and this anisotropic behaviour is particularly strong in the near-wall region. The component $[\overline{\rho(\omega_1 - \tilde{\omega}_1)^2/\bar{\rho}}]^{1/2} \times \delta_Z/S_L$ decays to close to the wall, whereas $[\overline{\rho(\omega_2 - \tilde{\omega}_2)^2/\bar{\rho}}]^{1/2} \times \delta_Z/S_L$ and $[\overline{\rho(\omega_3 - \tilde{\omega}_3)^2/\bar{\rho}}]^{1/2} \times \delta_Z/S_L$ increase significantly in the near-wall region. Fig. 5.8 indicates that $[\overline{\rho(\omega_2 - \tilde{\omega}_2)^2/\bar{\rho}}]^{1/2} \times \delta_Z/S_L$ and

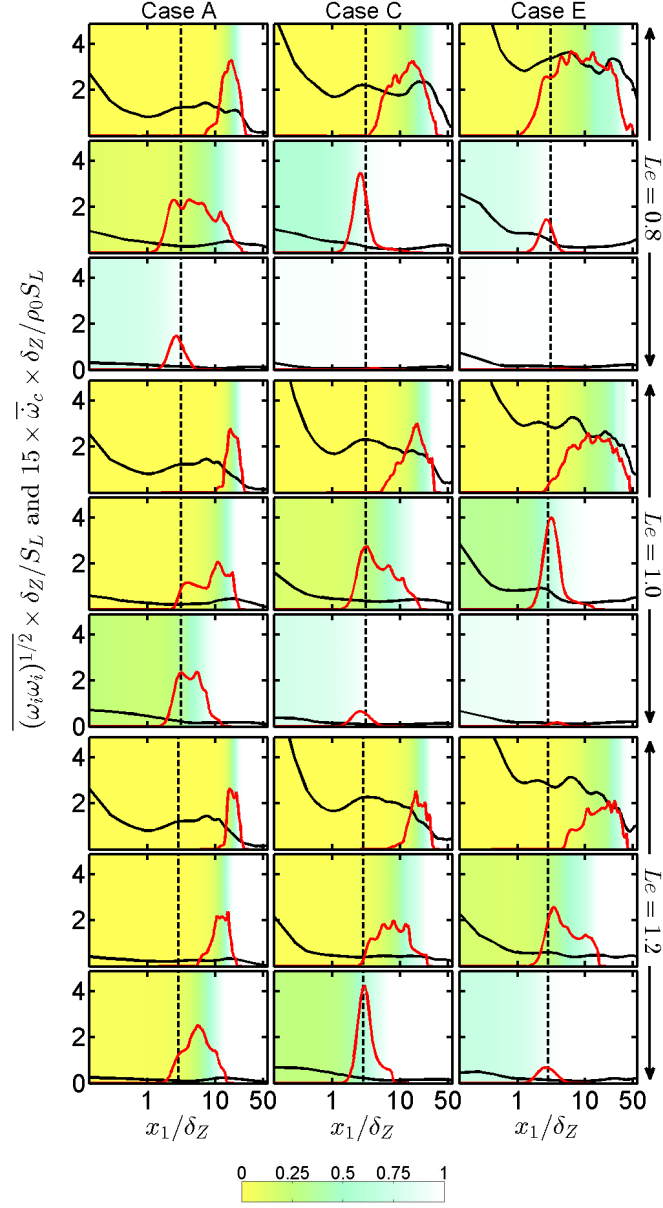


Fig. 5.7 Variations of $\overline{(\omega_i \omega_i)^{1/2}} \times \delta_Z / S_L$ (—) and $15 \times \overline{\tilde{\omega}} \times \delta_Z / \rho_0 S_L$ (—) and \tilde{c} with x_1 / δ_Z for cases A, C and E at $t = 2\delta_Z / S_L, 6\delta_Z / S_L$ and $10\delta_Z / S_L$ (1st -3rd row). For illustration purpose \tilde{c} is indicated by background colour and the vertical dotted-line shows $x_1 / \delta_Z = (Pe_{\min})_L$ for Figs. 5.7 - 5.14.

$[\rho(\omega_3 - \tilde{\omega}_3)^2 / \bar{\rho}]^{1/2} \times \delta_Z / S_L$ are principally responsible for the rise of $[\rho(\omega_i - \tilde{\omega}_i)^2 / \bar{\rho}]^{1/2} \times \delta_Z / S_L$ in the near-wall region.

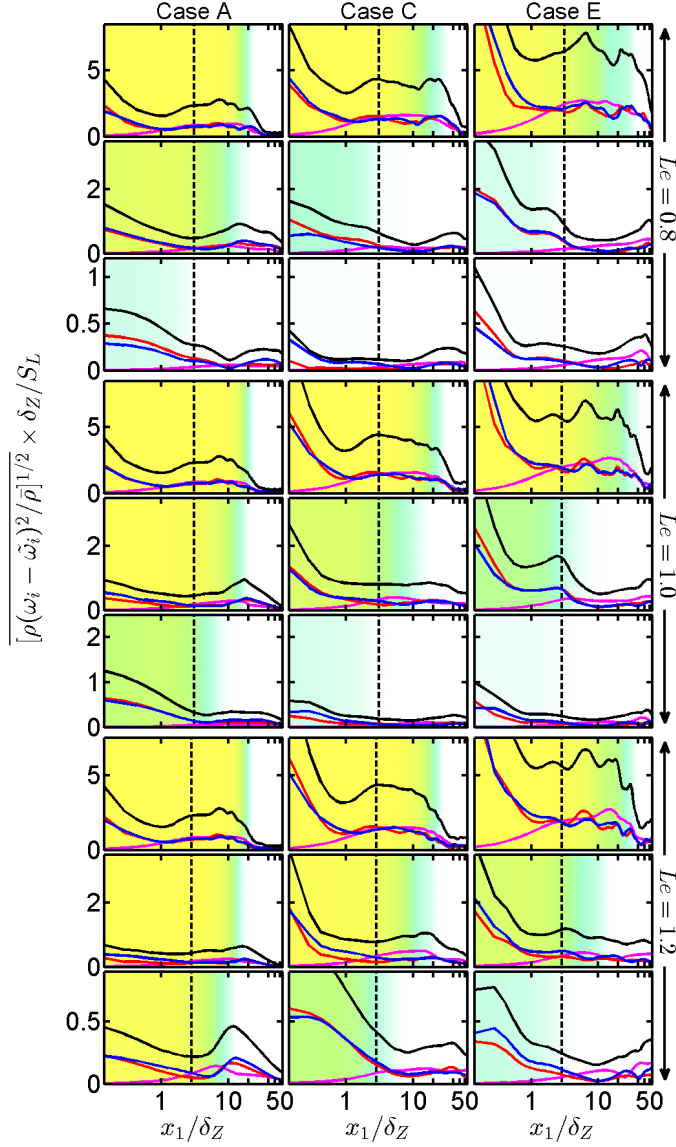


Fig. 5.8 Variations of $[\rho(\omega_i - \tilde{\omega}_i)^2 / \bar{\rho}]^{1/2} \times \delta_Z / S_L$ (—), $[\rho(\omega_1 - \tilde{\omega}_1)^2 / \bar{\rho}]^{1/2} \times \delta_Z / S_L$ (—), $[\rho(\omega_2 - \tilde{\omega}_2)^2 / \bar{\rho}]^{1/2} \times \delta_Z / S_L$ (—) and $[\rho(\omega_3 - \tilde{\omega}_3)^2 / \bar{\rho}]^{1/2} \times \delta_Z / S_L$ (—) with x_1 / δ_Z (log scale) for cases A, C and E (1st -3rd column) at $t = 2\delta_Z / S_L, 6\delta_Z / S_L$ and $10\delta_Z / S_L$ (1st -3rd row).

5.3.3 Statistical behaviour of vorticity transport

It is necessary to analyse the statistical behaviour of the terms of Eq. 2.34 (or see Eq. 5.1 below) to explain the near-wall behaviour of $(\overline{\omega_i \omega_i})^{1/2}$ and $[\rho(\omega_i - \tilde{\omega}_i)^2 / \bar{\rho}]^{1/2}$,

and the observed anisotropy of their components.

$$\frac{\partial \omega_i}{\partial t} + u_k \frac{\partial \omega_i}{\partial x_k} = \underbrace{\omega_k \frac{\partial u_i}{\partial x_k}}_{t_{1i}} - \underbrace{\epsilon_{ijk} \frac{1}{\rho^2} \frac{\partial \rho}{\partial x_j} \frac{\partial \tau_{kl}}{\partial x_l}}_{t_{21i}} + \underbrace{\frac{\epsilon_{ijk}}{\rho} \frac{\partial^2 \tau_{kl}}{\partial x_j \partial x_l}}_{t_{22i}} - \underbrace{\omega_i \frac{\partial u_k}{\partial x_k}}_{t_{3i}} + \underbrace{\frac{\epsilon_{ijk}}{\rho^2} \frac{\partial \rho}{\partial x_j} \frac{\partial p}{\partial x_k}}_{t_{4i}} \quad (5.1)$$

t_{1i} vortex-stretching term

t_{21i} density variation term

t_{22i} viscous stress term

t_{22i} vorticity destruction by dilatation term

t_{4i} baroclinic effects term

The variations of $\overline{(t_{1t}t_{1t})^{1/2}}$, $\overline{(t_{21t}t_{21t})^{1/2}}$, $\overline{(t_{22t}t_{22t})^{1/2}}$, $\overline{(t_{3t}t_{3t})^{1/2}}$ and $\overline{(t_{4t}t_{4t})^{1/2}}$ with x_1/δ_Z are shown Fig. 5.9 for cases A, C and E, where $\overline{(t_{qt}t_{qt})^{1/2}} = \overline{[(\delta_{ij} - n_i n_j) t_{qi} t_{qj}]^{1/2}}$ with $q = 1, 21, 22, 3, 4$ and \vec{n} is the normal vector pointing outward on the wall (i.e. positive x_1 – direction for this configuration). The corresponding variations $\overline{(t_{1n}t_{1n})^{1/2}}$, $\overline{(t_{21n}t_{21n})^{1/2}}$, $\overline{(t_{22n}t_{22n})^{1/2}}$, $\overline{(t_{3n}t_{3n})^{1/2}}$ and $\overline{(t_{4n}t_{4n})^{1/2}}$ with x_1/δ_Z are shown Fig. 5.10 where $\overline{(t_{qn}t_{qn})^{1/2}} = \overline{[(n_i n_j) t_{qi} t_{qj}]^{1/2}}$ with $q = 1, 21, 22, 3, 4$. It is important to note that three time instants $t_1 = 2\delta_Z/S_L$, $t_2 = 6\delta_Z/S_L$ and $t_3 = 10\delta_Z/S_L$ are shown in Figs. 5.9 and 5.10. The flame quenching has started at these time instants for all cases, but they are at different stages of flame quenching. The cases with higher u'/S_L propagates faster and starts to interact with the wall at an earlier time instant. Similarly, the cases with smaller values of Le propagate faster towards the wall and thus the effects of flame quenching set in at an earlier time instant in these cases. Thus, the effects of flame quenching will be initiated at a much earlier time in case E than the quenching initiation in case A.

Figures 5.9 and 5.10 indicate that the magnitudes of all the terms increase with a decreasing (increasing) value of Le (u'/S_L). The contributions of the vortex-stretching and the combined molecular diffusion and dissipation (i.e. $\overline{(t_{1n}t_{1n})^{1/2}}$ or $\overline{(t_{1t}t_{1t})^{1/2}}$ and $\overline{(t_{22n}t_{22n})^{1/2}}$ or $\overline{(t_{22t}t_{22t})^{1/2}}$) are of substantial importance in the vorticity transport for all cases when the flame is away from the wall. However, the magnitudes of $\overline{(t_{1n}t_{1n})^{1/2}}$, $\overline{(t_{1t}t_{1t})^{1/2}}$ and $\overline{(t_{22n}t_{22n})^{1/2}}$ decrease as the wall is approached by the flame (see black solid lines associated with different instants in Figs. 5.9 and 5.10 or red dashed lines in Fig. 5.10). For all time instants are shown here, the magnitude of $\overline{(t_{22t}t_{22t})^{1/2}}$ increases significantly in the near-wall region (see red dashed lines Fig. 5.9). The strong vorticity diffusion at the wall and high values of vorticity gradient magnitude, along with the gradient of dilatation rate, are responsible for the rise of the magnitude of the term

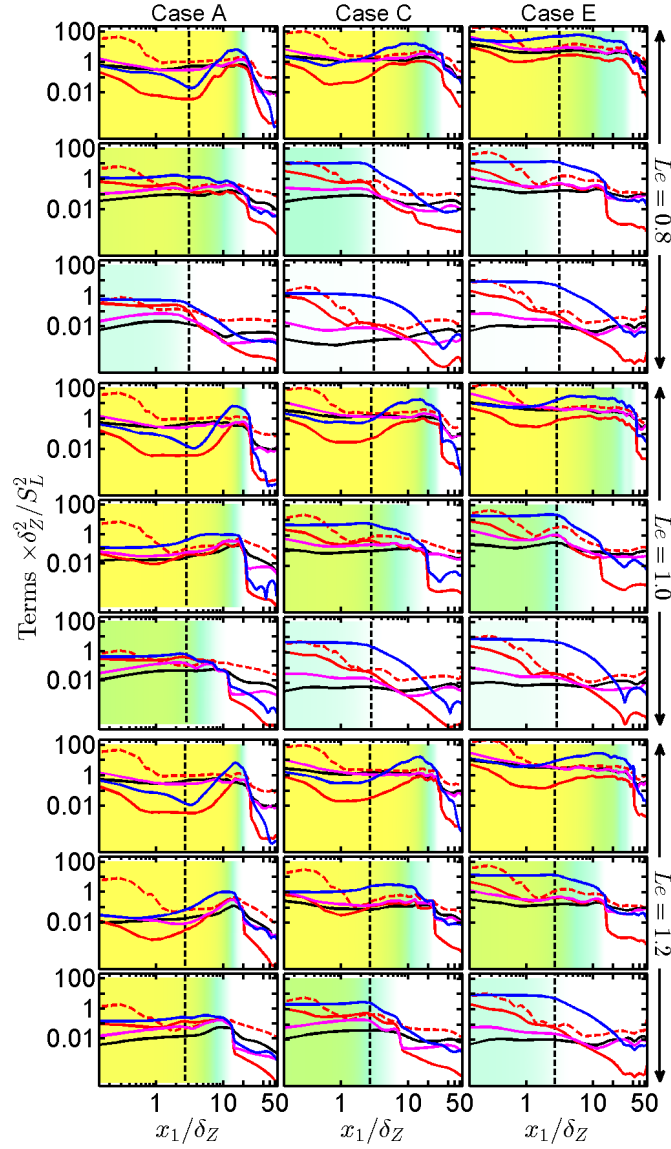


Fig. 5.9 Variations of $\overline{(t_{1t}t_{1t})^{1/2}} \times \delta_Z^2/S_L^2$ (—), $\overline{(t_{21t}t_{21t})^{1/2}} \times \delta_Z^2/S_L^2$ (—), $\overline{(t_{22t}t_{22t})^{1/2}} \times \delta_Z^2/S_L^2$ (---), $\overline{(t_{3t}t_{3t})^{1/2}} \times \delta_Z^2/S_L^2$ (—) and $\overline{(t_{4t}t_{4t})^{1/2}} \times \delta_Z^2/S_L^2$ (—) with x_1/δ_Z (log scale) for cases A, C and E (1st -3rd column) at $t = 2\delta_Z/S_L$, $6\delta_Z/S_L$ and $10\delta_Z/S_L$ (1st -3rd row).

$\vec{t}_{22} = (\mu/\rho)\nabla^2\vec{\omega} + (\mu/3\rho)\nabla \times \nabla(\nabla \cdot \vec{u})$ in transverse directions in the near-wall region. At large u'/S_L (case E), the magnitude of baroclinic torque term \vec{t}_4 becomes comparable to the combined molecular diffusion and dissipation term (i.e. \vec{t}_{22}) in the near-wall region, see red dashed and solid blue lines. This effect becomes increasingly pronounced with decreasing Le .

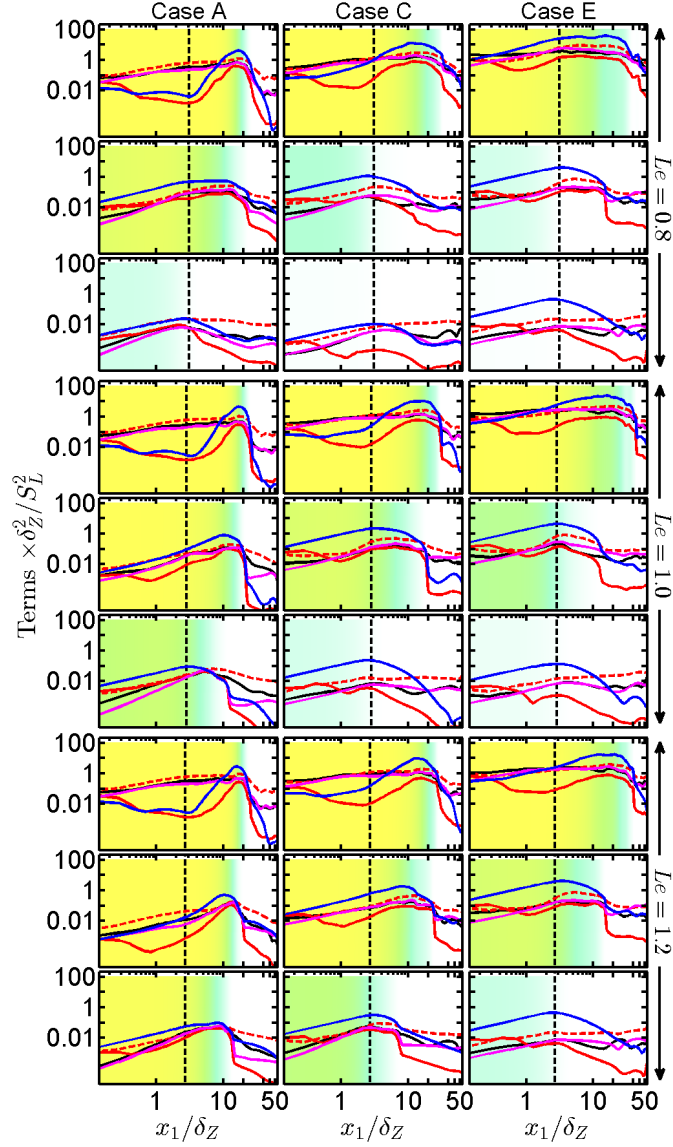


Fig. 5.10 Variations of $\overline{(t_{1n}t_{1n})^{1/2}} \times \delta_Z^2/S_L^2$ (—), $\overline{(t_{21n}t_{21n})^{1/2}} \times \delta_Z^2/S_L^2$ (—), $\overline{(t_{22n}t_{22n})^{1/2}} \times \delta_Z^2/S_L^2$ (---), $\overline{(t_{3n}t_{3n})^{1/2}} \times \delta_Z^2/S_L^2$ (—) and $\overline{(t_{4n}t_{4n})^{1/2}} \times \delta_Z^2/S_L^2$ (—) with x_1/δ_Z (log scale) for cases A, C and E (1st -3rd column) at $t = 2\delta_Z/S_L$, $6\delta_Z/S_L$ and $10\delta_Z/S_L$ (1st -3rd row).

A comparison between Figs. 5.9 and 5.10 reveals that $\overline{(t_{4t}t_{4t})^{1/2}}$ remains greater than $\overline{(t_{4n}t_{4n})^{1/2}}$ in the flame-brush region before flame quenching for cases C and E but this effect is relatively less pronounced for case A. Figure 5.10 shows that $\overline{(t_{4n}t_{4n})^{1/2}}$ becomes one of the dominant terms as the flame starts to interact with the wall. For low Mach number $Le = 1.0$ flames c can be equated to non-dimensional temperature $T = (\hat{T} - T_0)/(T_{ad} - T_0)$ when the flame is away from the wall and thus

$\nabla\rho = \nabla[\rho_0(1 + \tau T)]$ can be equated to $\nabla\rho = -\tau\rho^2\nabla c/\rho_0 = \tau\rho^2|\nabla c|\vec{N}/\rho_0$ (where $\vec{N} = -\nabla c/|\nabla c|$ is the local flame normal vector [191]), which implies $\nabla\rho$ and ∇c are parallel to each other when the flame is away from the wall. As the flame normal vector \vec{N} and the unit normal vector \vec{n} outward on the wall are mostly aligned with each other in the case of HOQ of statistically planar flames (not shown here), $\overline{(t_{4n}t_{4n})}^{1/2}$ is negligible when the flame is away from the wall in the $Le = 1.0$ case. However, $c \neq T$ in the near-wall region even for $Le = 1.0$ and this non-equality holds both away from and near to the wall for flames with $Le \neq 1.0$. When a flame is close to the wall, the misalignment between $\nabla\rho$ and ∇c (or ∇T and ∇c) in the near-wall region leads to a rise in $\overline{(t_{4n}t_{4n})}^{1/2}$. The misalignment of $\nabla\rho$ and ∇c leads to a non-negligible magnitude of $\overline{(t_{4n}t_{4n})}^{1/2}$ within a flame even when the flame is away from wall for $Le \neq 1.0$, with the magnitude of $\overline{(t_{4n}t_{4n})}^{1/2}$ rising in the near-wall region due to the increased misalignment between $\nabla\rho$ and ∇c . Figures 5.9 and 5.10 suggest that the baroclinic terms are principally responsible for the anisotropy between the vorticity components. It is important to note that flame quenching gives rise to high-temperature gradient close to the wall, which in turn leads to a considerable density gradient in the near wall region, and thus the baroclinic torque contribution assumes significant values at the wall. The baroclinic torque contribution $\overline{(t_{4t}t_{4t})}^{1/2}$ to the evolution of the vorticity field near the wall is weakest in case A. It is shown in Fig. 5.3 that the flame quenching initiates at an earlier time instant for higher values of u'/S_L . Thus, at a given instant, case A is associated with an earlier stage of quenching in comparison to cases C and E, because the weakly turbulent case A propagates at a slower rate towards the wall than cases C and E. This effect is manifested in the near-wall behaviour of the baroclinic torque $\overline{(t_{4t}t_{4t})}^{1/2}$ in Fig 5.9 which shows that the magnitude of $\overline{(t_{4t}t_{4t})}^{1/2}$ close to the wall is smaller in case A than in cases C and E due to relatively smaller extent of flame-wall interaction in this case in comparison to the other cases.

The dilatation contributions $\overline{(t_{3n}t_{3n})}^{1/2}$ and $\overline{(t_{3t}t_{3t})}^{1/2}$ (see violet lines in Figs. 5.9 and 5.10) exhibit significant magnitudes within the flame-brush but they become negligible on burned gas sides, because the density is almost constant during the quenching event (or exactly constant when the flame is far from the wall). However, the terms $\overline{(t_{3n}t_{3n})}^{1/2}$ and $\overline{(t_{3t}t_{3t})}^{1/2}$ are significant in the burned gas in the near-wall region even after the quenching is initiated. There is a considerable amount of density variation in the near-wall region due to sharp change in temperature even after the flame is quenched, which gives rise to significant values of dilatation rate $\nabla \cdot \vec{u}$ and the dilatation contributions $\overline{(t_{3n}t_{3n})}^{1/2}$ and $\overline{(t_{3t}t_{3t})}^{1/2}$. However, $\overline{(t_{3n}t_{3n})}^{1/2}$ and $\overline{(t_{3t}t_{3t})}^{1/2}$ eventually decay with the decay in vorticity magnitude.

The contributions $\overline{(t_{21n}t_{21n})^{1/2}}$ and $\overline{(t_{21t}t_{21t})^{1/2}}$ are significant within the flame-brush (where the density variation is significant) before flame quenching, and their magnitudes increase near the wall due to non-zero $\nabla\rho$ and high values of $\partial\tau_{ki}/\partial x_i$ induced by the wall.

5.3.4 Statistical behaviour of the enstrophy transport

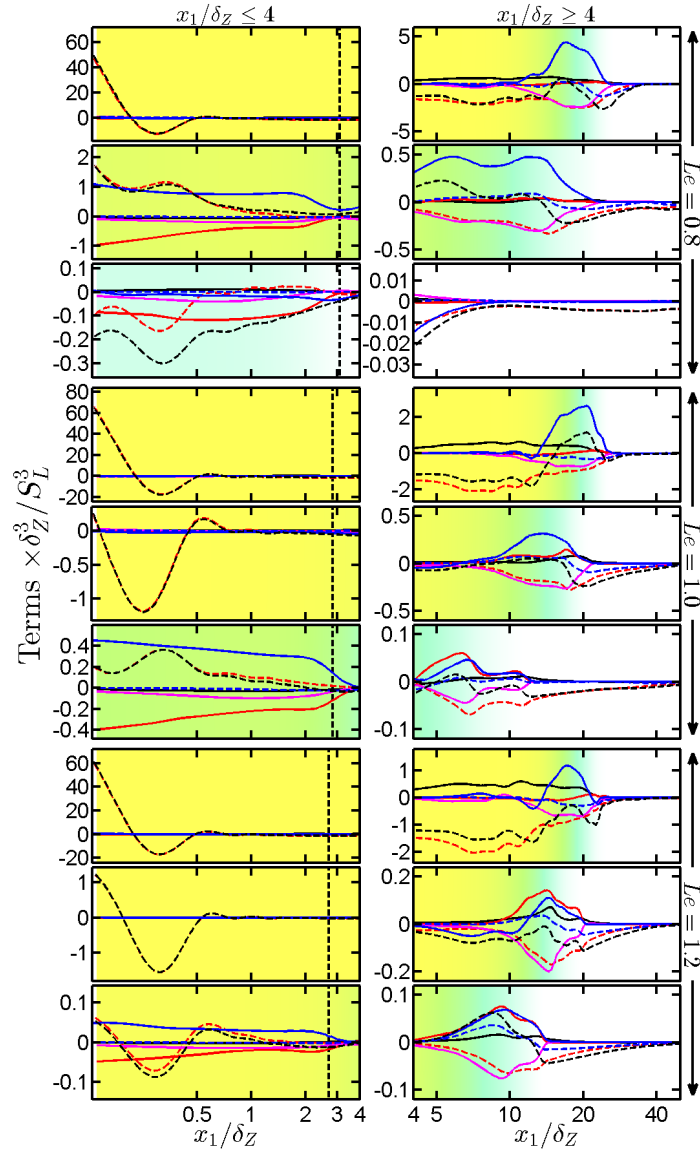


Fig. 5.11 Variations of $T_I \times \delta_Z^3 / S_L^3$ (—), $T_{II} \times \delta_Z^3 / S_L^3$ (—), $T_{III} \times \delta_Z^3 / S_L^3$ (---), $T_{IV} \times \delta_Z^3 / S_L^3$ (—), $T_V \times \delta_Z^3 / S_L^3$ (—), $T_{VI} \times \delta_Z^3 / S_L^3$ (---) and $\bar{D}\Omega/\bar{D}t \times \delta_Z^3 / S_L^3$ (---) with x_1/δ_Z (log scale) for case A at $t = 2\delta_Z/S_L, 6\delta_Z/S_L$ and $10\delta_Z/S_L$ (1st–3rd row).

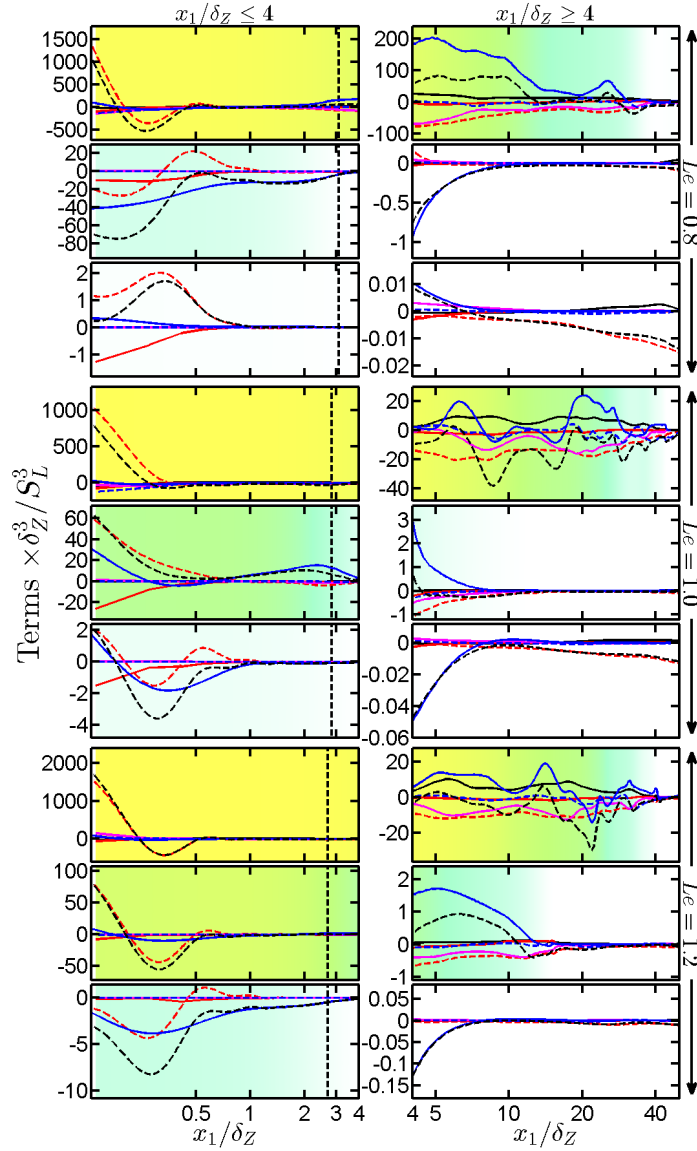


Fig. 5.12 Variations of $T_I \times \delta_Z^3/S_L^3$ (—), $T_{II} \times \delta_Z^3/S_L^3$ (—), $T_{III} \times \delta_Z^3/S_L^3$ (---), $T_{IV} \times \delta_Z^3/S_L^3$ (—), $T_V \times \delta_Z^3/S_L^3$ (—), $T_{VI} \times \delta_Z^3/S_L^3$ (---) and $\bar{D}\Omega/\bar{D}t \times \delta_Z^3/S_L^3$ (---) with x_1/δ_Z (log scale) for case E at $t = 2\delta_Z/S_L, 6\delta_Z/S_L$ and $10\delta_Z/S_L$ (1st–3rd row).

The Reynolds-averaged enstrophy transport equation can be seen in Eq. 2.36 (or see Eq. 5.2 below).

$$\frac{\partial \bar{\Omega}}{\partial t} + \overline{u_k \frac{\partial \Omega}{\partial x_k}} = \underbrace{\overline{\omega_i \omega_k \frac{\partial u_i}{\partial x_k}}}_{T_I} - \underbrace{\overline{\epsilon_{ijk} \omega_i \frac{1}{\rho^2} \frac{\partial \rho}{\partial x_j} \frac{\partial \tau_{kl}}{\partial x_l}}}_{T_{II}} + \underbrace{\overline{\frac{\epsilon_{ijk} \omega_i}{\rho} \frac{\partial^2 \tau_{kl}}{\partial x_j \partial x_l}}}_{T_{III}} - \underbrace{\overline{2\Omega \frac{\partial u_k}{\partial x_k}}}_{T_{IV}} + \underbrace{\overline{\frac{\epsilon_{ijk} \omega_i}{\rho^2} \frac{\partial \rho}{\partial x_j} \frac{\partial p}{\partial x_k}}}_{T_V} \quad (5.2)$$

T_I	vortex-stretching term
T_{II}	misalignment between gradients of density and viscous stresses
T_{III}	molecular diffusion and dissipation of mean enstrophy Ω due to viscous action
T_{IV}	dissipation of enstrophy due to dilatation
T_V	baroclinic torque term

The variations of T_I , T_{II} , T_{III} , T_{IV} and T_V with x_1/δ_Z are reported in Fig. 5.11 and 5.12 for cases A and E respectively (a monotonic qualitative trend is observed from case A to case E). Figure 5.11 and 5.12 show that the magnitudes of these terms increase significantly with decreasing (increasing) Le (u'/S_L). The vortex-stretching term T_I remains positive throughout the flame-brush for all cases away from the wall, but negative values of T_I have been found in the near-wall region. The vortex-stretching term T_I can be expressed as: $T_I = \overline{2\Omega(e_\alpha \cos^2 2\theta_\alpha + e_\beta \cos^2 2\theta_\beta + e_\gamma \cos^2 2\theta_\gamma)}$ [29, 44], where e_α , e_β and e_γ are the most extensive (i.e. positive), intermediate, and the most compressive (i.e. negative) principal strain rates, and θ_α , θ_β and θ_γ are the angles between $\vec{\omega}$ and the eigenvectors associated with the eigenvalues e_α , e_β and e_γ respectively. A negative contribution of T_I suggests a weak (strong) alignment of $\vec{\omega}$ with e_α (e_γ) in the near-wall region. The extent of $\vec{\omega}$ alignment with the principal strain rate e_i can be quantified from the values of $\Psi_i = |\cos\theta_i|$ (where $i = \alpha, \beta, \gamma$) and Ψ_i is equal to 1.0 (0.0) for collinear (perpendicular) alignment between $\vec{\omega}$ and the eigenvector corresponding to e_i . Accordingly, a collinear alignment of $\vec{\omega}$ with e_α (e_γ) leads to a positive (negative) value of $T_I = \overline{2\Omega(e_\alpha \cos^2 2\theta_\alpha + e_\beta \cos^2 2\theta_\beta + e_\gamma \cos^2 2\theta_\gamma)}$ [29, 44]. The variations of $\overline{\Psi_\alpha}$, $\overline{\Psi_\beta}$ and $\overline{\Psi_\gamma}$ with x_1/δ_Z for cases A, C and E are reported in Fig 5.13, which demonstrates that $\overline{\Psi_\beta}$ has a magnitude which is either greater than or comparable to $\overline{\Psi_\alpha}$ and $\overline{\Psi_\gamma}$. Thus, it suggests a predominant alignment of $\vec{\omega}$ with the eigenvector associated with intermediate strain rate e_β , and this is consistent with previous findings [6, 13, 91, 92, 99, 103, 131, 134, 147, 172, 173, 195, 197, 214], which demonstrated that the vorticity vector aligns with the intermediate principal strain rate e_β in in turbulent non-reacting and reacting flows regardless of the regime of combustion, heat release parameter and Lewis number. Furthermore, Figure 5.13 shows that the alignment of $\vec{\omega}$ with e_α (i.e. in other words the magnitude of $\overline{\Psi_\alpha}$) decreases in the regions where the effects of heat release are weak, which is also consistent with previous observations [13, 91, 99]. The extent of alignment of $\vec{\omega}$ with e_γ also decreases on the unburned gas side of the flame brush. It can be seen from Fig. 5.13 that both $\overline{\Psi_\beta}$ and $\overline{\Psi_\gamma}$ assume greater magnitudes than $\overline{\Psi_\alpha}$ as the flame approaches the wall. This leads to negative values of T_I in the near-wall region.

Figures 5.11 and 5.12 show that the magnitude of viscous torque term T_{II} remains small in comparison to the other terms when the flame is away from the wall, but it becomes a dominant sink in the near-wall region when the flame approaches the wall.

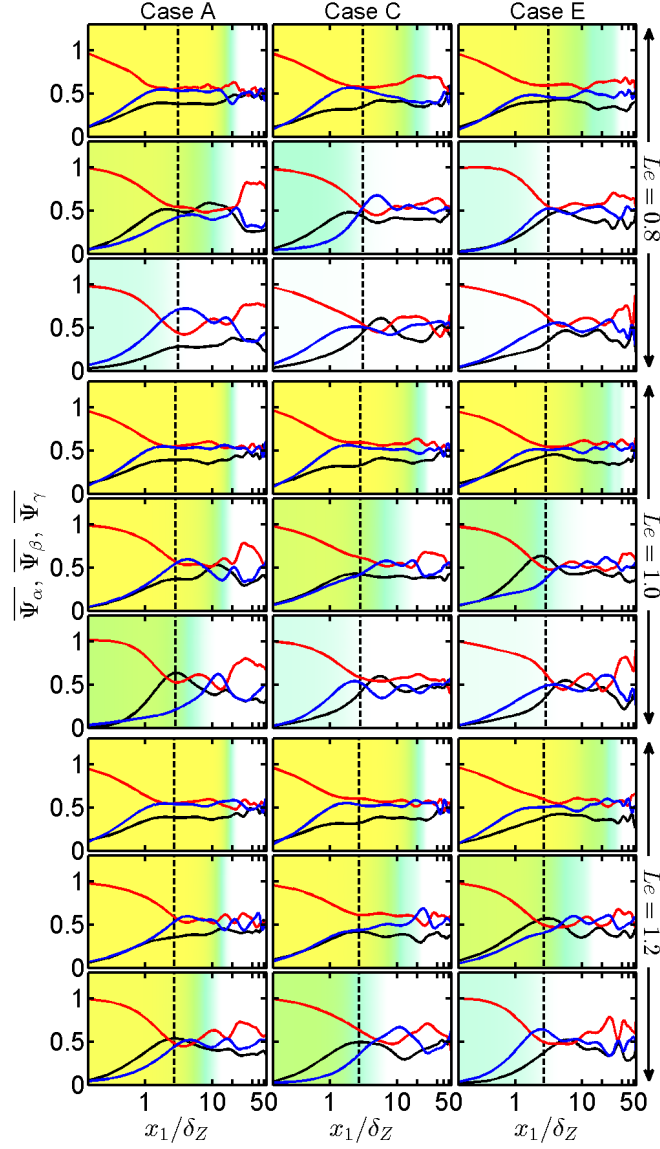


Fig. 5.13 Variations of $\overline{\Psi}_\alpha = |\cos\theta_\alpha|$ (—), $\overline{\Psi}_\beta = |\cos\theta_\beta|$ (—) and $\overline{\Psi}_\gamma = |\cos\theta_\gamma|$ (—) with x_1/δ_Z (log scale) for cases A, C and E (1st -3rd column) at $t = 2\delta_Z/S_L, 6\delta_Z/S_L$ and $10\delta_Z/S_L$ (1st -3rd row).

The term T_{III} remains negative away from the wall for all cases but it becomes positive for $x_1/\delta_Z < (Pe_{\min})_L$. Substituting $\tau_{kl} = \mu(\partial u_k/\partial x_l + \partial u_l/\partial x_k) - 2(\mu/3)\delta_{kl}(\partial u_m/\partial x_m)$ in $T_{III} = \overline{\epsilon_{ijk}\omega_i/\rho(\partial^2\tau_{kl}/\partial x_j\partial x_l)}$ leads to: $T_{III} = (\mu/\rho)\nabla^2\overline{\Omega} + (\mu/3\rho)\vec{\omega} \cdot [\nabla \times \nabla(\nabla \cdot \vec{u})] + f(\mu) - D_v$ where $f(\mu)$ represents the contributions from

viscosity gradients and $-D_v = -\overline{(\mu/\rho)(\partial\omega_i/\partial x_l)(\partial\omega_i/\partial x_l)}$ is the molecular dissipation of enstrophy. The variations of $\overline{(\mu/\rho)\nabla^2\Omega}$, $\overline{(\mu/3\rho)\vec{\omega} \cdot [\nabla \times \nabla(\nabla \cdot \vec{u})]}$ and $(-D_v)$ with x_1/δ_Z are reported in Figs 5.14 and 5.15 for cases A and E respectively (a monotonic qualitative trend is observed from case A to case E). The term $f(\mu)$ is identically zero for the cases considered here (i.e. $mu = \text{constant}$) and thus is not shown in Figs 5.14 and 5.15. It can be seen from Figs 5.14 and 5.15 that the magnitude of $\overline{(\mu/3\rho)\vec{\omega} \cdot [\nabla \times \nabla(\nabla \cdot \vec{u})]}$ remains negligible in comparison to that of $\overline{(\mu/\rho)\nabla^2\Omega}$ and $(-D_v)$ away from the wall, and the term T_{III} is negative principally due to $(-D_v)$. On the contrary, in the near-wall region, the contribution of $\overline{(\mu/\rho)\nabla^2\Omega}$ overwhelms the sink contribution of $(-D_v)$, and yields a positive value of T_{III} .

The dilatation term T_{IV} is negative and plays an important role only within the flame-brush away from the wall. The baroclinic torque term T_V remains positive but vanishes outside the flame brush when the flame is away from the wall. Moreover, this term can exhibit negative values of T_V in the near-wall region during flame quenching (note that flame quenching for case E starts at $t < 2\delta_Z/S_L$). At the last stage of flame-wall interaction, e.g. at $t = 10\delta_Z/S_L$ in case E, see Fig 5.12, both the baroclinic torque term T_{IV} and the molecular diffusion and dissipation term T_{III} play significant roles in the near-wall region, see the left column in Fig. 5.12, for all Lewis number cases considered here.

Equation 2.36 can be rewritten as:

$$\bar{D}\bar{\Omega}/\bar{D}t = T_I + T_{II} + T_{III} + T_{IV} + T_V - \overline{u'_k \partial\Omega'/\partial x_k} \quad (5.3)$$

where $\bar{D}()/\bar{D}t = \partial()/\partial t + \bar{u}_k \partial()/\partial x_k$ is the material derivative associated with the mean flow. Although $T_{VI} = -\overline{u'_k \partial\Omega'/\partial x_k}$ (see blue dashed lines in Figs 5.11 and 5.12) exhibits local positive (negative) values in cases A and B (cases C - E), $\bar{D}\bar{\Omega}/\bar{D}t$ remains predominantly negative (see black dashed lines), but is positive in the near-wall region (i.e. $x_1/\delta_Z < (Pe_{\min})_L$) at early times for small values of u'/S_L (e.g. case A). A predominantly negative value of $\bar{D}\bar{\Omega}/\bar{D}t$ for the major part of the flame-brush is consistent with the decay of $\overline{(\omega_i\omega_i)^{1/2}} \times \delta_{th}/S_L$ from unburned to burned gas side of the flame brush (see Fig. 5.7). As the quenching progresses $\bar{D}\bar{\Omega}/\bar{D}t$ shows more likelihood of exhibiting negative values close to the wall, which acts to reduce $\overline{(\omega_i\omega_i)^{1/2}}$ in the near-wall region.

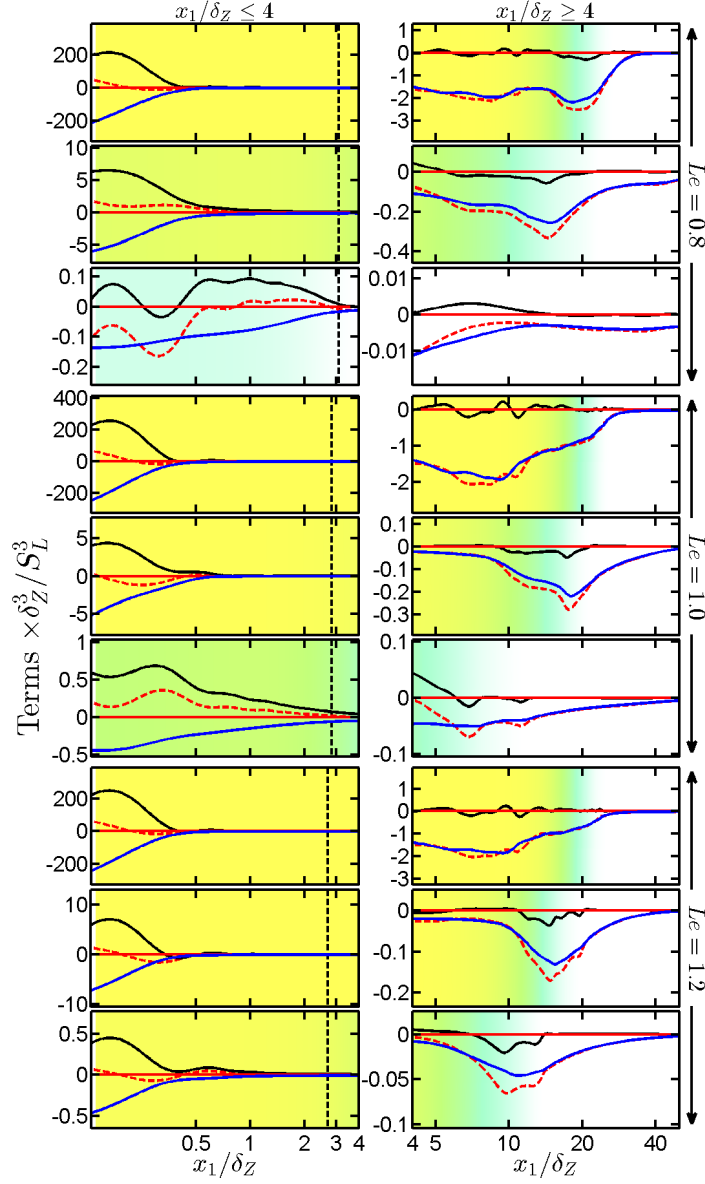


Fig. 5.14 Variations of $T_{III} \times \delta_Z^3 / S_L^3$ (— — —), $\overline{(\mu/\rho)\Delta^2\Omega} \times \delta_Z^3 / S_L^3$ (—), $\overline{(\mu/3\rho)\vec{\omega} \cdot [\nabla \times \nabla(\nabla \cdot \vec{u})]} \times \delta_Z^3 / S_L^3$ (—) and $(-D_\nu) \times \delta_L^3 / S_L^3$ (—) with x_1/δ_Z (log scale) for case A at $t = 2\delta_Z/S_L, 6\delta_Z/S_L$ and $10\delta_Z/S_L$ (1st -3rd row).

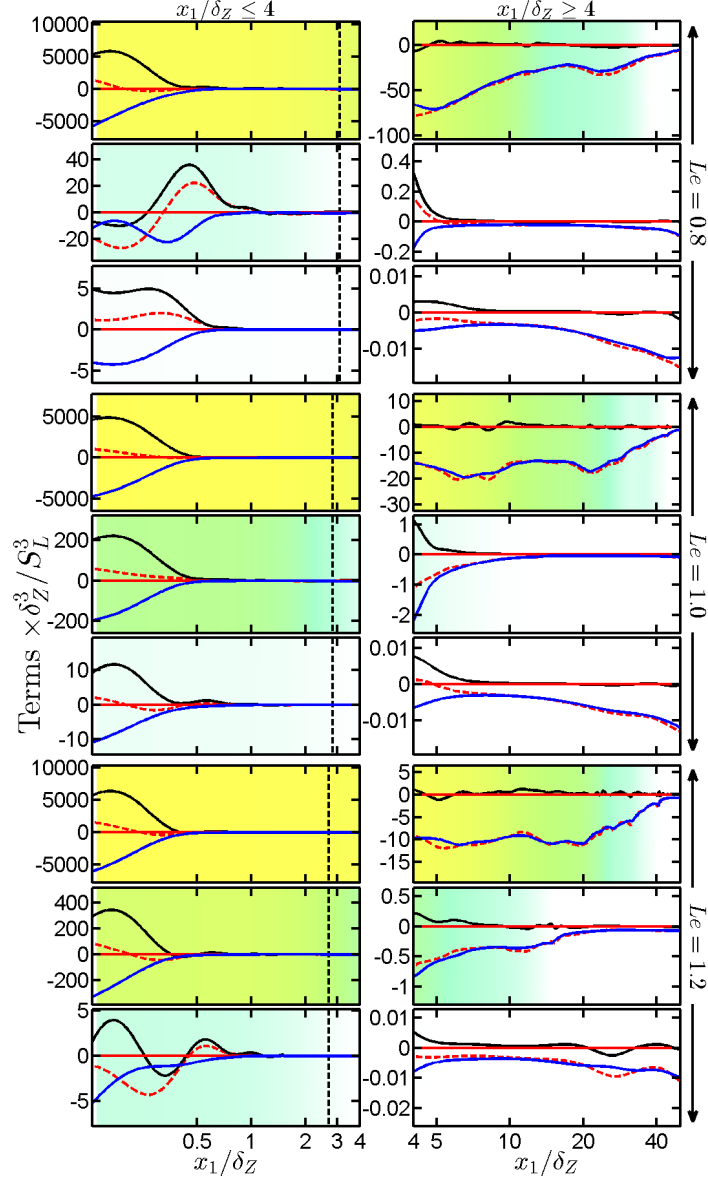


Fig. 5.15 Variations of $T_{III} \times \delta_Z^3/S_L^3$ (—), $(\mu/\rho)\Delta^2\Omega \times \delta_Z^3/S_L^3$ (—), $(\mu/3\rho)\vec{\omega} \cdot [\nabla \times \nabla(\nabla \cdot \vec{u})] \times \delta_Z^3/S_L^3$ (—) and $(-D_\nu) \times \delta_L^3/S_L^3$ (—) with x_1/δ_Z (log scale) for case E at $t = 2\delta_Z/S_L, 6\delta_Z/S_L$ and $10\delta_Z/S_L$ (1st–3rd row).

5.3.5 Summary of the key results

In all cases, the vorticity magnitude $\sqrt{\omega_i \omega_i}$ drops from the unburned side (which is in contact with the wall) to the burned gas side of the flame-brush and the highest magnitude of $\sqrt{\omega_i \omega_i}$ is obtained at the wall. Furthermore, both $\sqrt{\omega_i \omega_i}$ and the magnitudes of the terms of the vorticity transport equation increase with decreasing (increasing) Le (u'/S_L). The presence of the flame and wall induce a significant amount of anisotropy between vorticity components, and the baroclinic torque has been shown to be principally responsible for this anisotropic behaviour. The vortex-stretching and viscous dissipation terms have been found to be the significant contributors to the enstrophy transport for all cases when the flame is away from the wall. As the flame approaches the wall, the baroclinic torque begins to play increasingly important roles in the enstrophy transport. Furthermore, combined molecular diffusion and dissipation contribution remains negative away from the wall but becomes positive near the wall due to the molecular diffusion of enstrophy.

5.4 Flow topology distribution

The distribution of flow topologies within the flame and their evolution with flame quenching have been analysed in this section. The main objectives are:

- To demonstrate the influence of the wall on flow topology distribution and statistical behaviours of P , Q and R (refer to Eq. 2.38 - 2.40) during head-on quenching.
- To provide the physical explanations for the observed behaviours of P , Q and R , and the flow topology distribution.
- To indicate the implications on these behaviours on vortex-stretching, flame normal straining and wall heat flux during head-on quenching of turbulent premixed flames.

5.4.1 Distributions of P , Q and R

Equations 2.38 - 2.40 show the 1th - 3rd invariants (P , Q and R) of velocity gradient tensor, the terms $Q_S = 0.5(P^2 - S_{ij}S_{ij})$ and $Q_W = 0.5(W_{ij}W_{ij})$ are the second invariants of the strain rate (i.e. symmetric part of $\partial u_i/\partial x_j$) and rotation rate (i.e. anti-symmetric part of $\partial u_i/\partial x_j$) tensors.

The instantaneous distributions of $P^* = P \times (\delta_Z/S_L)$, $Q^* = Q \times (\delta_Z/S_L)^2$ and $R^* = R \times (\delta_Z/S_L)^3$ at different stages of quenching are shown for cases A, C and E in Figs. 5.16-5.18 respectively. A comparison between Figs. 5.5 and 5.16 reveals that high negative values of P^* are obtained within the flame (i.e. $0 < c < 1$) and P^* assumes vanishingly small values outside the flame in both unburned gases and fully burned products in the $Le = 1.0$ cases when the flame is away from the wall (i.e. before the quenching is initiated, and thus this effect is prominent in case A because the flame started to quench by the time $t = 2\delta_Z/S_L$ in cases C and E). The inhomogeneity in the burned gas temperature is observed in non-unity Lewis number cases, and this behaviour is particularly prevalent in the $Le = 0.8$ cases because of high rates of localised burning and relatively weak thermal diffusion rate. Thus, the effects of dilatation rate $\nabla \cdot \vec{u} = -P$ in the $Le = 0.8$ cases persist also in the burned gas beyond the flame, whereas these effects are weak in the $Le = 1.2$ cases. Moreover, it can be seen from Figs. 5.5 and 5.16 that comparatively high (small) magnitude of P^* is obtained for the locations where the c -isosurfaces are concavely (convexly) curved towards the reactants. Focussing (defocussing) of heat at the concavely (convexly)

curved zones gives rise to high positive (either small positive or negative) dilatation rate $(\partial u_i/\partial x_i) \times \delta_Z/S_L = -P^*$. Thus negative values of P^* with high magnitude are obtained in the regions which are concavely curved towards the reactants, whereas either small negative or positive values of P^* are observed for the locations which are convex towards the reactants. Furthermore, it can be seen from Fig. 5.16 that the likelihood of obtaining the high magnitude of P^* drops significantly with time as quenching progress which leads to weakening of the effects of thermal expansion.

A comparison between Figs. 5.5 and Fig. 5.17 shows that high magnitudes of Q^* are obtained only on the unburned gas side of the flame. For all cases, the magnitude of Q^* drops significantly across the flame within the burned gases. As P remains small outside the flame, the positive value of Q^* on the unburned gas side of the flame indicates the vorticity-dominated (i.e. $W_{ij}W_{ij} > S_{ij}S_{ij}$) regions, whereas negative Q^* indicates dominance of strain rate magnitude over vorticity magnitude (i.e. $W_{ij}W_{ij} < S_{ij}S_{ij}$). The value of Q^* changes from positive (i.e. vorticity dominated region) to negative (i.e. strain rate dominated region) in a short span of space and the extent of this intermittent behaviour increases with increasing turbulence intensity u'/S_L . It can further be seen by comparing Figs. 5.5 and 5.17 that high positive values of Q^* are obtained within the flame (i.e. $0 < c < 1$) where the c -isosurfaces are concavely curved towards the reactants. It has already been discussed that high magnitudes of negative P^* at the concavely curved regions (see Fig. 5.16), which leads to high values of P^2 giving rise to high positive values of $Q^* = 0.5(-S_{ij}S_{ij} + P^2 + W_{ij}W_{ij}) \times (\delta_Z/S_L)^2$. Figure 5.17 indicates that the magnitude of Q^* increases with increasing (decreasing) u'/S_L (Le), whereas $|Q^*|$ decreases as time progresses with the advancement of flame quenching for all cases.

The expression for the third invariant R in eq. 2.40 can be recast in terms of the sum of the terms which play roles in dissipation rate generation $(-S_{ij}S_{jk}S_{ki}/3)$ and enstrophy production $(PQ_W - \omega_i S_{ij} \omega_j/4)$:

$$\begin{aligned} R &= \frac{1}{3}(-P^3 + 3PQ - S_{ij}S_{jk}S_{ki}) - \frac{1}{4}\omega_i S_{ij} \omega_j \\ &= \underbrace{\frac{1}{3}(-P^3 + 3PQ_S - S_{ij}S_{jk}S_{ki})}_{R_S} + PQ_W - \frac{1}{4}\omega_i S_{ij} \omega_j \end{aligned} \quad (5.4)$$

where R_S is the third invariant of the strain rate $0.5(\partial u_i/\partial x_j + \partial u_j/\partial x_i)$ tensor. Equation 5.4 suggests that $R^* = R \times (\delta_Z/S_L)^3$ may assume high positive or negative values where there is an imbalance of the terms contributing to dissipation rate generation and production of enstrophy. This imbalance is pronounced on both the

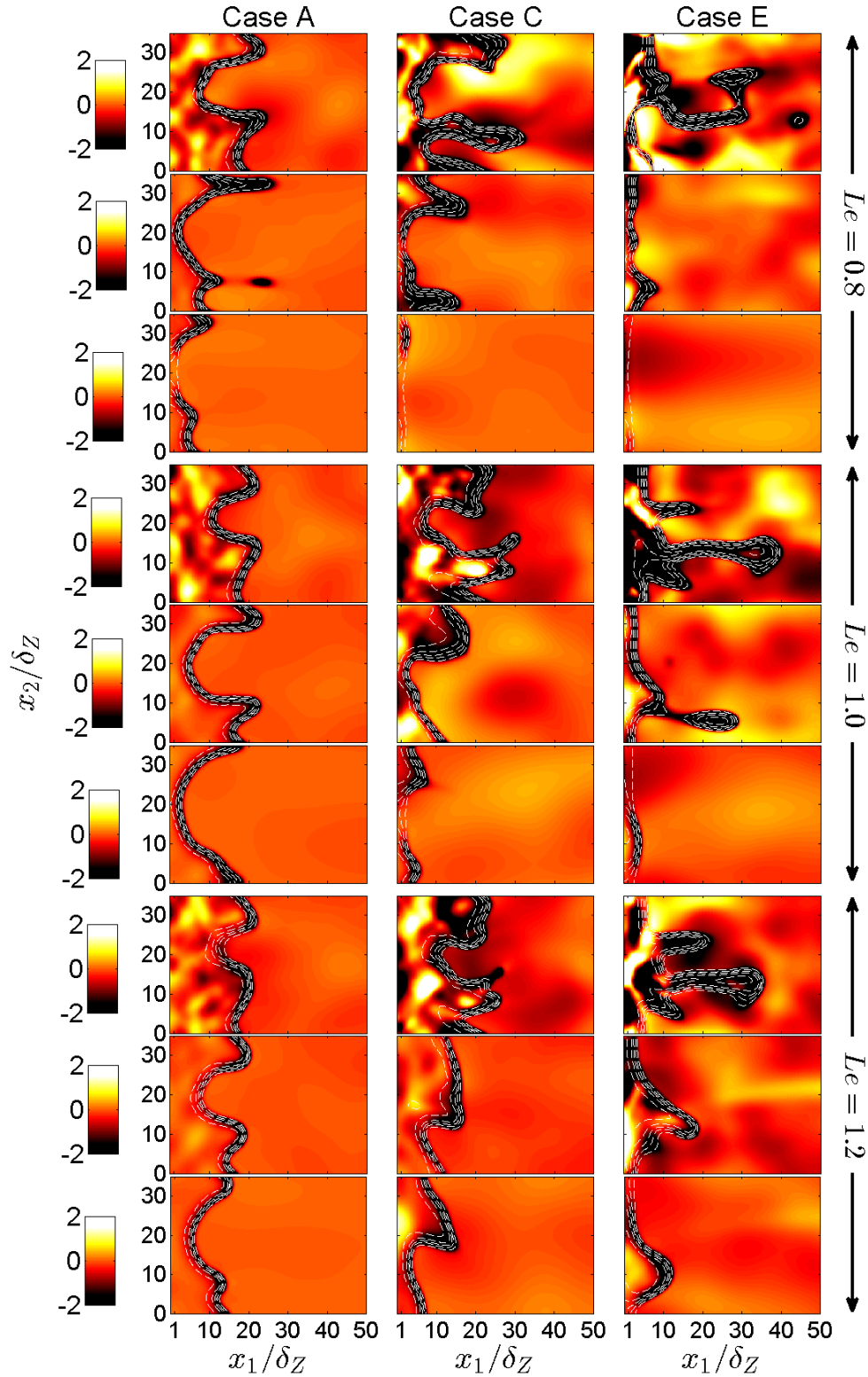


Fig. 5.16 Instantaneous $P^* = P \times \delta_Z/S_L$ fields for cases A, C and E (1st-3rd column) at $t = 2\delta_Z/S_L$, $4\delta_Z/S_L$ and $6\delta_Z/S_L$ (1st-3rd row), white line presents c field from 0.1 to 0.9 with interval of 0.2 from left to right.

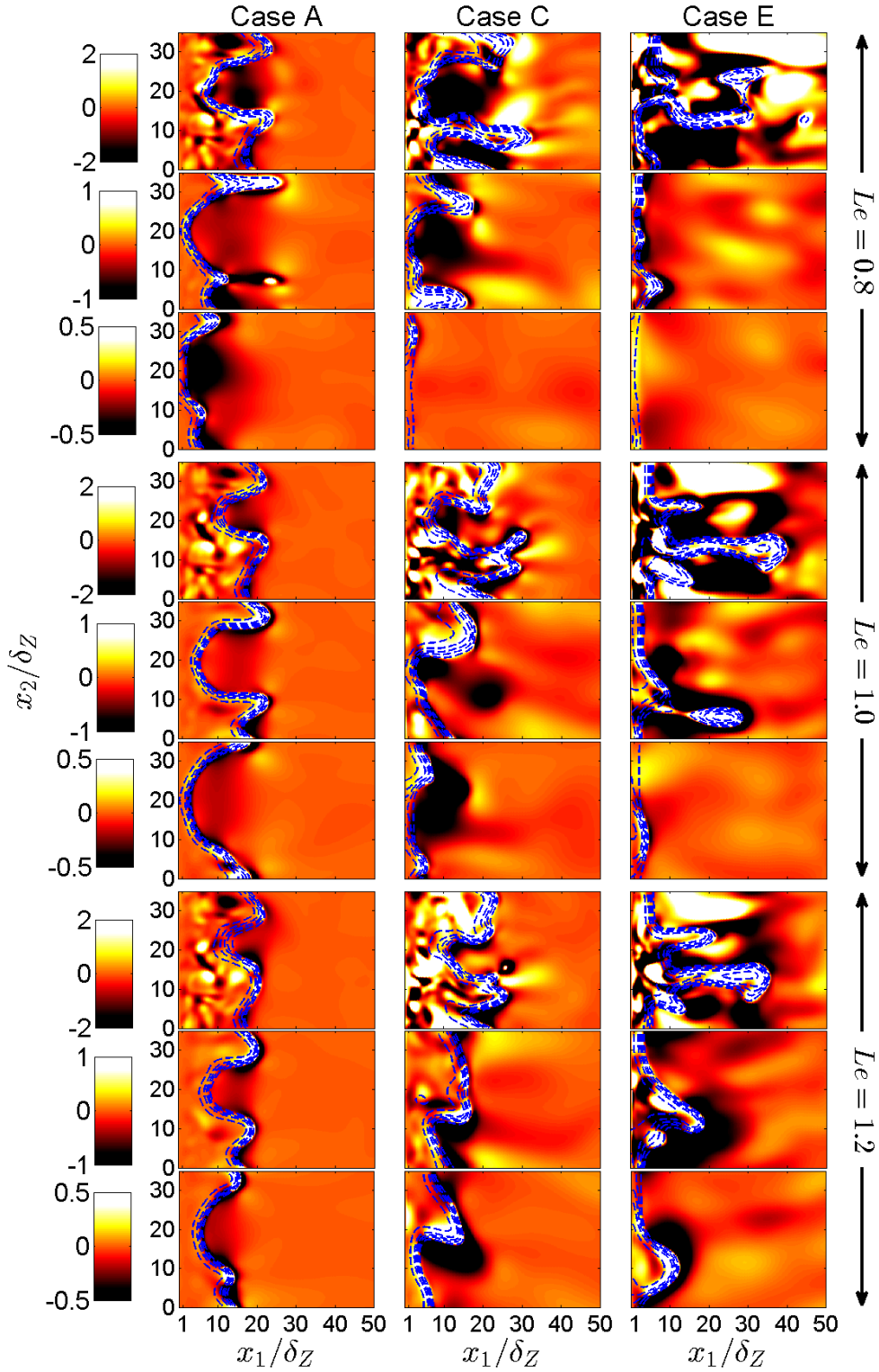


Fig. 5.17 Instantaneous $Q^* = Q \times (\delta_Z/S_L)^2$ fields for cases A, C and E (1st-3rd column) at $t = 2\delta_Z/S_L$, $4\delta_Z/S_L$ and $6\delta_Z/S_L$ (1st-3rd row), blue line presents c field from 0.1 to 0.9 with interval of 0.2 from left to right.

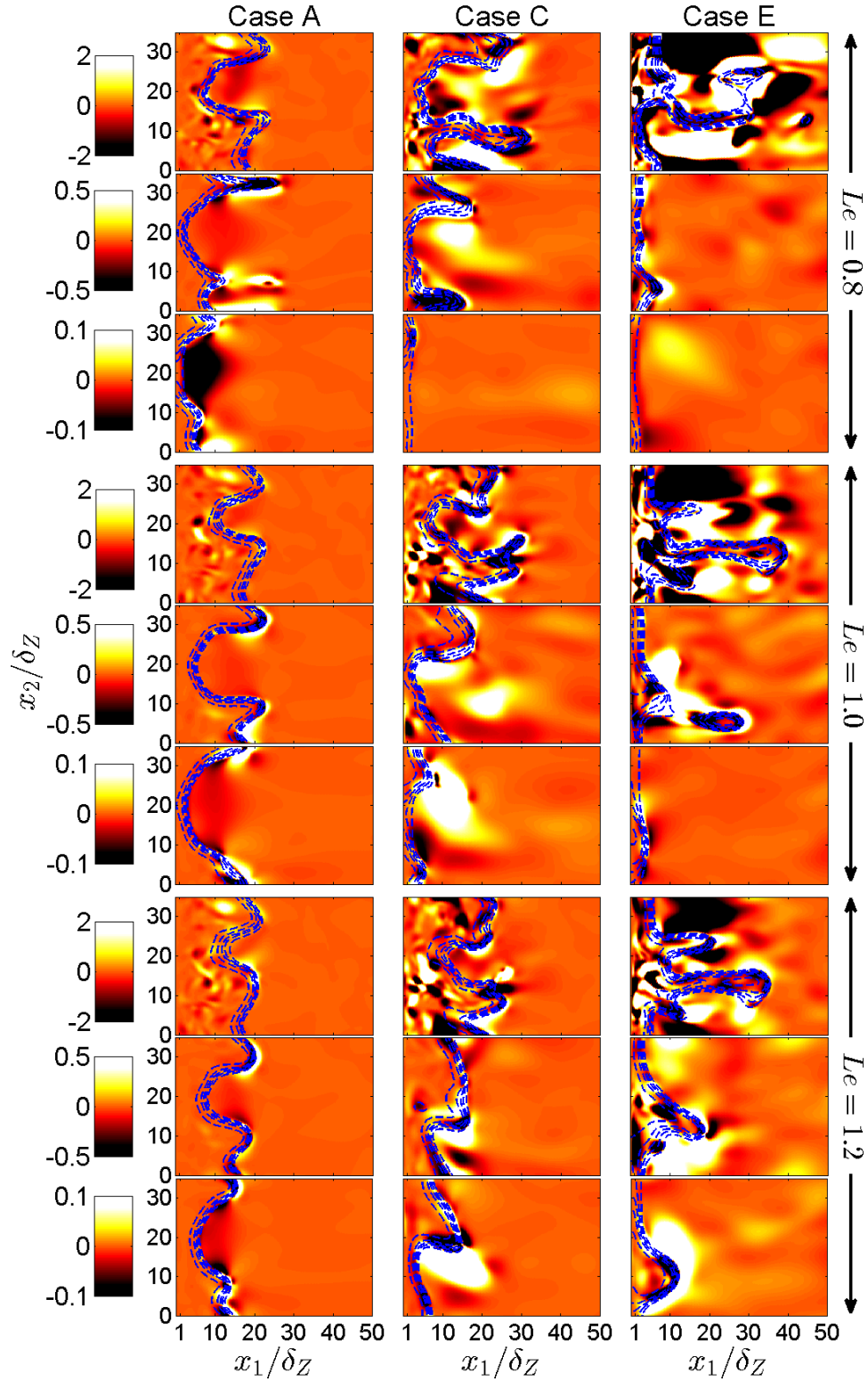


Fig. 5.18 Instantaneous $R^* = R \times (\delta_Z/S_L)^3$ fields for cases A, C and E (1st-3rd column) at $t = 2\delta_Z/S_L$, $4\delta_Z/S_L$ and $6\delta_Z/S_L$ (1st-3rd row), blue line presents c field from 0.1 to 0.9 with interval of 0.2 from left to right.

unburned gas side and within the flame, and both positive and negative values of R^* are observed. This magnitude of R^* drops sharply across the flame for the $Le = 1.0$ and 1.2 cases (see Figs. 5.5 and 5.18). A comparison between Figs. 5.5 and 5.18 reveals that R^* assumes significant magnitude not only in the unburned gas and within the flame but also in the burned gas due to appreciable presence of dilatation rate $\nabla \cdot \vec{u} = -P$ in the burned gas (see P dependence of R in eq. 5.4) in the $Le = 0.8$ cases. The likelihood of obtaining high magnitudes of R^* increases with increasing (decreasing) u'/S_L (Le) and $|R^*|$ decreases as quenching progresses with time.

The variations of normalised mean value of the first invariant $\langle P^* \rangle$ (where $\langle q \rangle = 1/(L_2 L_3) \int_0^{L_3} \int_0^{L_2} q dx_2 dx_3$ for a general quantity q) with wall normal distance are shown in Fig. 5.19 for cases A, C and E at different time instants. It can be seen from Fig. 5.19 that $\langle P^* \rangle$ remains predominantly negative values because of overwhelmingly positive values of dilatation rate in premixed turbulent flames (see a high likelihood of obtaining a negative value of P^* in Fig. 5.16). However, the magnitude of the negative mean value of P^* decreases with time as the quenching progresses. The effects of heat release weaken as quenching progress which reduces the extent of positive dilatation rate. It is worth noting turbulence severely decays in the burned gas, and $\partial u_i / \partial x_i$ becomes negative close to the wall due to the direction of flow reversal at the late stages of flame quenching which leads to a positive value of $\langle P^* \rangle$ at later times.

The variation of $\langle Q^* \rangle = \langle Q \rangle \times (\delta_Z / S_L)^2$, and its components, $\{\langle Q_S \rangle, \langle Q_W \rangle\} \times (\delta_Z / S_L)^2$, with normalised wall normal distance x_1 / δ_Z for cases A, C and E are shown in Fig. 5.20 for different time instants. Equation 2.39 suggests that $\nabla \cdot \vec{u} = -P$ and $\sqrt{S_{ij} S_{ij}}$ affect $Q_S = (P^2 - S_{ij} S_{ij})/2$, whereas the component $Q_W = W_{ij} W_{ij}/2$ depends on enstrophy Ω (i.e. $W_{ij} W_{ij}/2 = \omega_i \omega_i/4 = \Omega/2$ where ω_i is the i^{th} component of vorticity). The contribution of $\langle Q_W \rangle$ is deterministically positive and it is evident from Fig. 5.20 that $\langle Q_W \rangle$ assumes high values of at the wall but also increases within the flame due to flame generated vorticity due to baroclinic torque.

The sign of $\langle Q_S \rangle = \langle P^2 - S_{ij} S_{ij} \rangle/2$ depends on the relative magnitudes of $\langle P^2 \rangle$ and $\langle S_{ij} S_{ij} \rangle$. It can be seen from Fig. 5.20 that $\langle Q_S \rangle$ predominantly assumes negative values and assumes locally small positive values away from the wall within the flame where $\langle P^2 \rangle/2$ dominates over $\langle -S_{ij} S_{ij} \rangle/2$. The effects of dilatation rate $\nabla \cdot \vec{u} = -P$ remains weak close to the wall and thus $\langle -S_{ij} S_{ij} \rangle/2$ dominates over $\langle P^2 \rangle/2$ to give rise to a negative value of $\langle Q_S \rangle$. The magnitude of $\langle S_{ij} S_{ij} \rangle/2$ decreases within the flame whereas $\langle P^2 \rangle/2$ increases in reaction zone, so $\langle P^2 \rangle/2$ is likely to overcome $\langle -S_{ij} S_{ij} \rangle/2$ in this region and yield a positive value of $\langle Q_S \rangle$. The quantity $\langle Q_S \rangle$ can be expressed as: $\langle Q_S \rangle = \langle Q_{S1} \rangle + \langle Q_{S2} \rangle = \langle P^2/3 \rangle - \langle E/4\nu \rangle$ with $E = (\tau_{ij} \partial u_i / \partial x_j) / \rho$

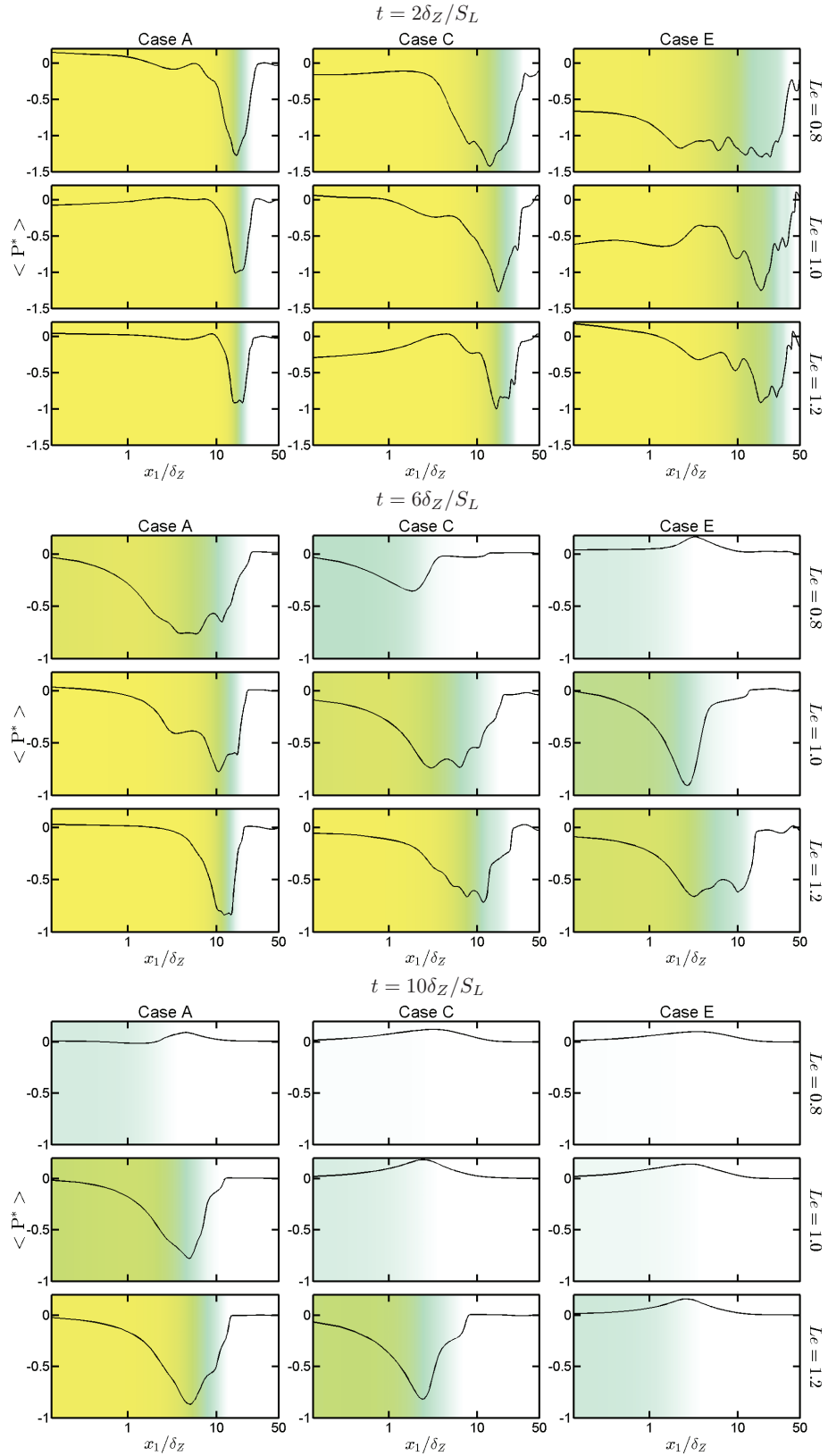


Fig. 5.19 Variations of $\langle P^* \rangle = \langle P \rangle \times \delta_Z / S_L$ with x_1 / δ_Z for $t = 2\delta_Z / S_L$, $6\delta_Z / S_L$, $10\delta_Z / S_L$. See Fig. 5.7 for background colour, also apply to Fig. 5.20 - 5.22, 5.27 and 5.28.

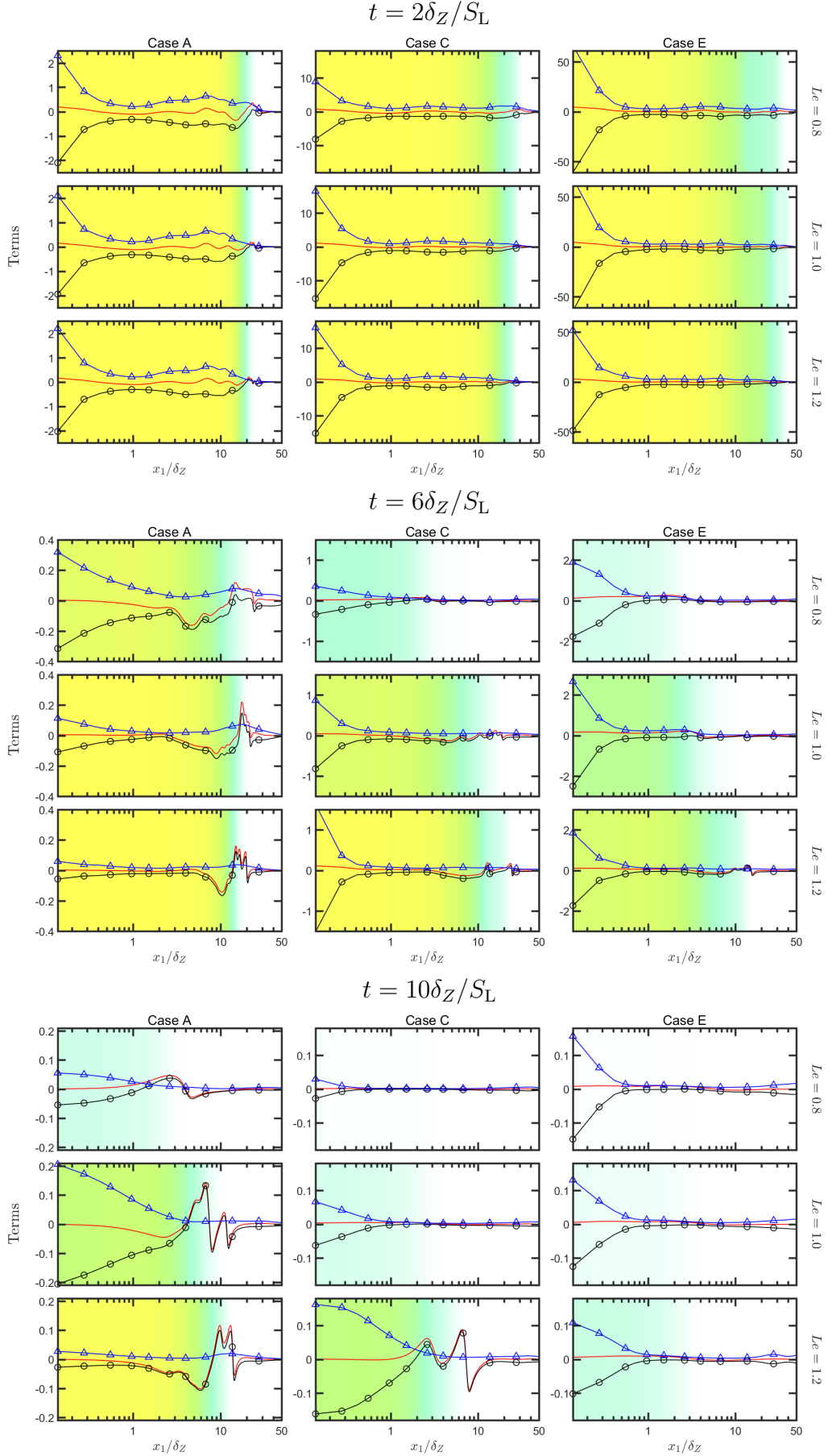


Fig. 5.20 Variations of normalised terms $\{\langle Q \rangle(\text{---}), \langle Q_S \rangle(\text{---} \circ \text{---}), \langle Q_W \rangle(\text{---} \triangle \text{---})\} \times (\delta_Z/S_L)^2$ with x_1/δ_Z for $t = 2\delta_Z/S_L, 6\delta_Z/S_L, 10\delta_Z/S_L$.

and ν being the dissipation rate of instantaneous kinetic energy (i.e. $u_i u_i/2$) and kinematic viscosity respectively. Thus, $\langle Q_S \rangle > 0$ ($\langle Q_S \rangle < 0$) corresponds to dilatation (dissipation) dominated regions. Wacks *et al.* [205] demonstrated that one obtains $Q_{S1}/|Q_{S2}| \sim \tau^2 K a^{-2}$, using $Q_{s1} = P^2/3 \sim \{\tau S_L/\delta_{th}\}^2$ (Refs. [43, 49, 205]) and $|Q_{S2}| = |-E/4\nu| \sim 1/\tau_\eta^2$ with τ_η being the Kolmogorov time scale. For all cases considered here $Ka \gg 1$ and thus $|\langle Q_{S2} \rangle|$ dominates over $\langle Q_{S1} \rangle$ to yield predominantly negative value of $\langle Q_S \rangle$.

In all cases $\langle Q_S \rangle$ and $\langle Q_W \rangle$ mostly balance each other, and as a result, the magnitude of $\langle Q \rangle$ remains negligible in comparison to those of $\langle Q_S \rangle$ and $\langle Q_W \rangle$. The magnitudes of $\langle Q_S \rangle$ and $\langle Q_W \rangle$ are greater for higher values of u'/S_L at a given value Le . On the other hand, both $\langle Q_S \rangle$ and $\langle Q_W \rangle$ assume higher values for the cases with smaller values of Le at a given value of u'/S_L . The magnitudes of $\langle Q \rangle$, $\langle Q_S \rangle$ and $\langle Q_W \rangle$ decay with time as quenching progresses.

The variations of $\langle R^* \rangle = \langle R \rangle \times (\delta_Z/S_L)^3$, and its components, $\{\langle R_S \rangle, \langle PQ_W \rangle, -\langle \omega_i S_{ij} \omega_j/4 \rangle\} \times (\delta_Z/S_L)^3$, with normalised wall normal distance x_1/δ_Z for cases A, C and E are shown in Fig. 5.21 for different time instants. It can be seen from eq. 5.4 that $R_S = (-P^3 + 3PQ_S - S_{ij}S_{jk}S_{ki})/3$ contains a contribution to the strain rate transport (i.e. $-S_{ij}S_{jk}S_{ki}$), whereas $(PQ_W - \omega_i S_{ij} \omega_j/4)$ is related to the enstrophy transport [59, 58, 205]. It is possible to approximate $R_S \approx -S_{ij}S_{jk}S_{ki}/3 > 0$ and $PQ_W - \omega_i S_{ij} \omega_j/4 \approx -\omega_i S_{ij} \omega_j/4 < 0$ away from the flame front, where $P \approx 0$, hence, R^* may assume high positive or negative values where there is an imbalance of $(-S_{ij}S_{jk}S_{ki}/3)$ and $(-\omega_i S_{ij} \omega_j/4)$ away from the flame [59, 58, 205]. The contributions of $\langle PQ_W - (\omega_i S_{ij} \omega_j)/4 \rangle$ and $\langle R_S \rangle$ appear to balance across the flame brush in all cases (see Fig. 5.21).

Finally, Fig. 5.22 shows the variation of the normalised values of the components $\langle R_S \rangle \times (\delta_Z/S_L)^3$: $\{-\langle P^3/3 \rangle, \langle PQ_S \rangle, \langle -S_{ij}S_{jk}S_{ki}/3 \rangle\} \times (\delta_Z/S_L)^3$ with normalised wall normal distance x_1/δ_Z for cases A, C and E for different time instants. In all cases $\langle -P^3/3 \rangle$ assumes predominantly positive values within the flame due to the overwhelming probability of obtaining negative values of P when the flame remains away from the wall. However, the magnitude of $\langle -P^3/3 \rangle$ decreases significantly as the quenching progresses. The predominantly negative values of P and Q_S (see Figs. 5.20 and 5.22) give rise to predominantly positive values of $\langle PQ_S \rangle$. However, it has been mentioned earlier that Q_S can assume positive within the flame where $P^2/2$ overcomes $-S_{ij}S_{ij}/2$, which acts to promote negative values of $\langle PQ_S \rangle$. The magnitude of $\langle PQ_S \rangle$ decreases as time progresses due to decays of the magnitudes of P and Q_S . The behaviour of the contribution of $\langle -S_{ij}S_{jk}S_{ki}/3 \rangle$ shows dependence on turbulence intensity u'/S_L and

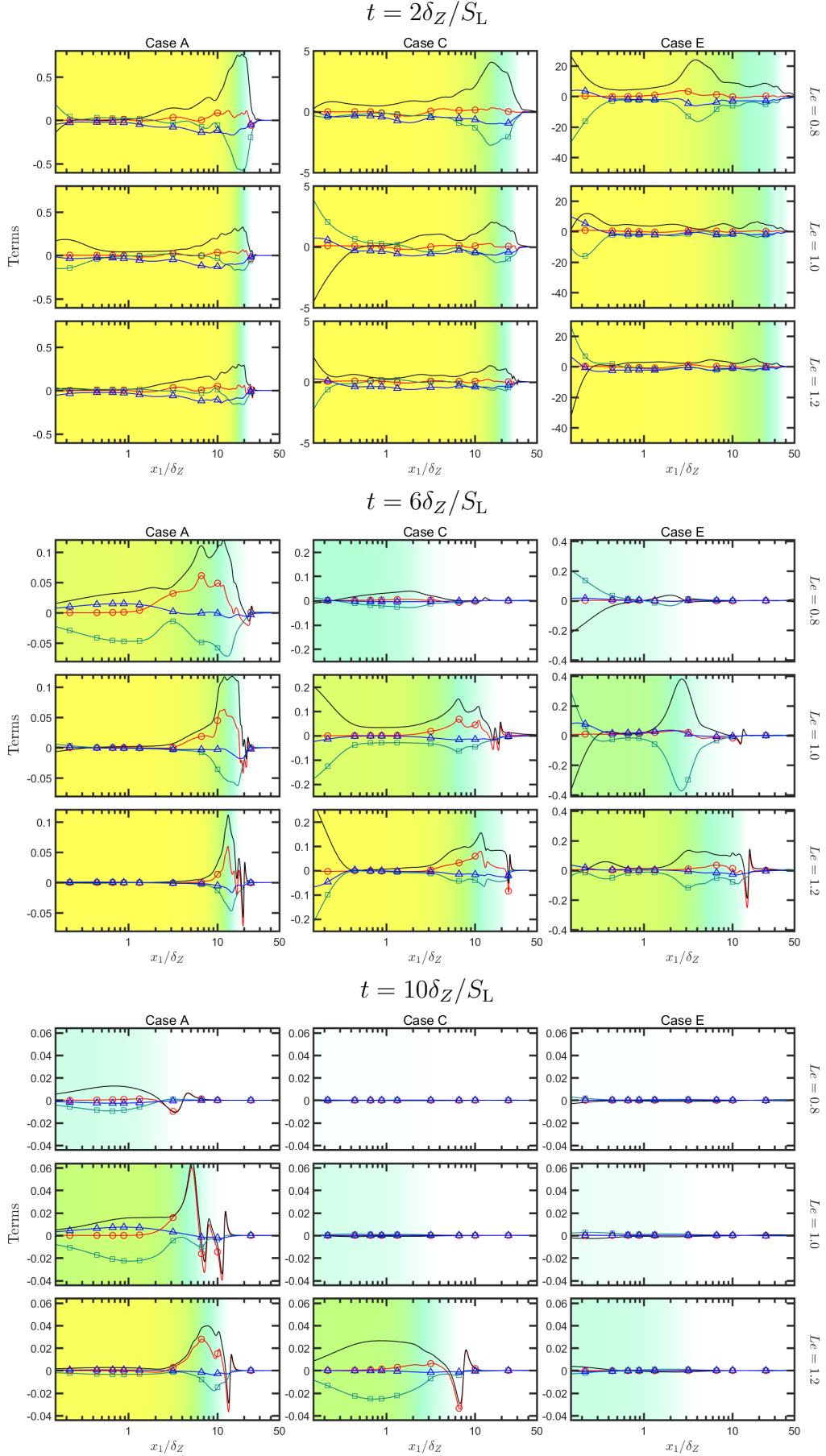


Fig. 5.21 Variations of normalised vorticity magnitude $\{ \langle R \rangle$ (— \circ —), $\langle R_S \rangle$ (—), $\langle PQ_W \rangle$ (— \square —), $\langle -\omega_i S_{ij} \omega_j / 4 \rangle$ (— \triangle —) $\times (\delta_Z/S_L)^2$ with x_1/δ_Z for $t = 2\delta_Z/S_L$, $6\delta_Z/S_L$, $10\delta_Z/S_L$.

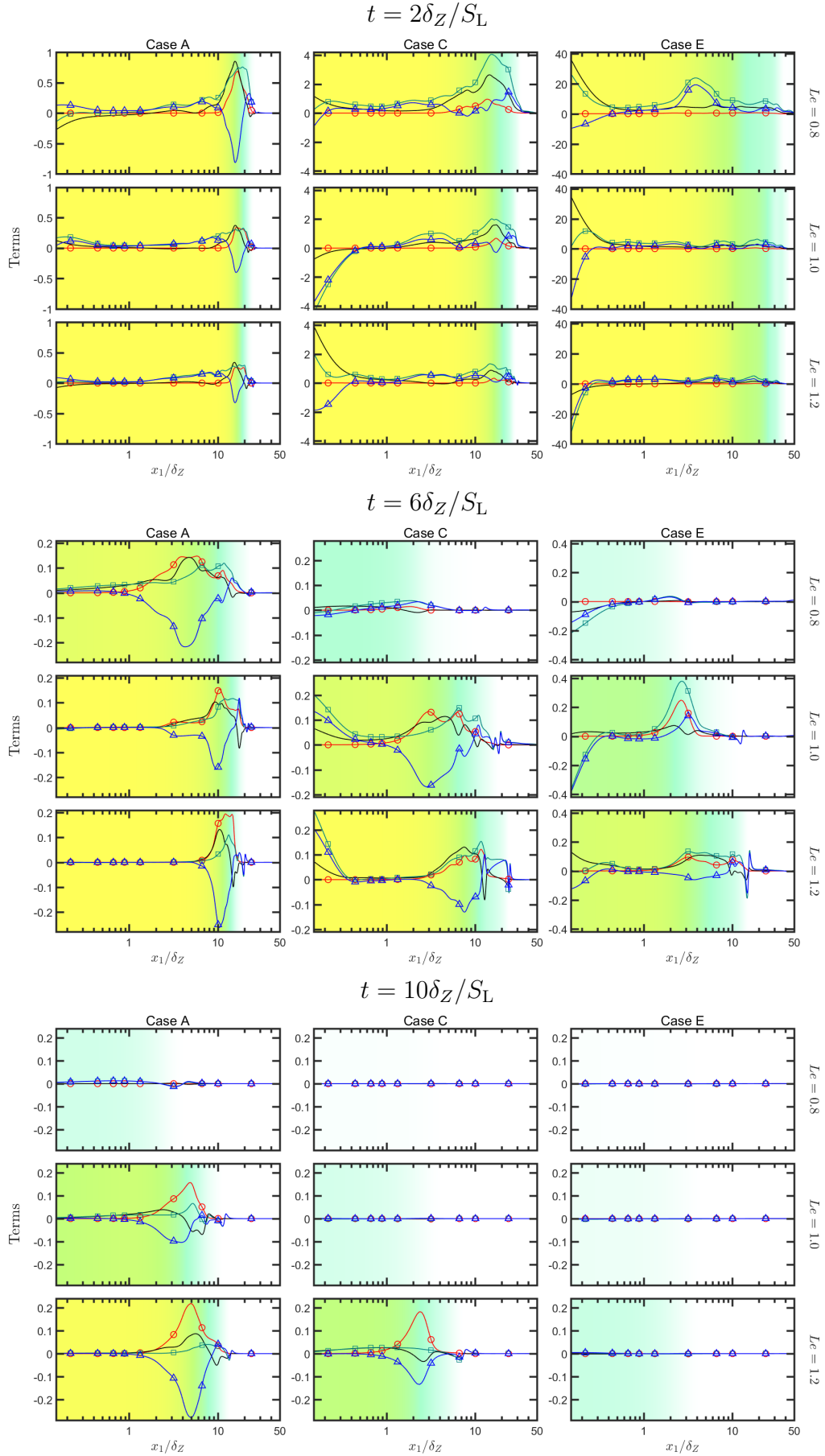


Fig. 5.22 Variations of normalised vorticity magnitude $\{\langle R_S \rangle$ (—□—), $\langle -P^3/3 \rangle$ (—○—), $\langle PQ_S \rangle$ (—), $\langle -S_{ij}S_{jk}S_{ki}/3 \rangle$ (—△—) $\times (\delta_Z/S_L)^3$ with x_1/δ_Z for $t = 2\delta_Z/S_L$, $6\delta_Z/S_L$, $10\delta_Z/S_L$.

global Lewis number Le at early times (e.g. $t = 2\delta_Z/S_L$). For example, $\langle -S_{ij}S_{jk}S_{ki}/3 \rangle$ shows large negative values within the flame brush for case A, whereas positive values of $\langle -S_{ij}S_{jk}S_{ki}/3 \rangle$ within the flame brush have been found for cases C and E. The magnitude of positive contribution of $\langle -S_{ij}S_{jk}S_{ki}/3 \rangle$ within the flame brush decreases with increasing Le . A negative contribution of $\langle -S_{ij}S_{jk}S_{ki}/3 \rangle$ does not necessarily indicate that the strain rate destruction instead of its generation. The combination of the terms $\langle -S_{ij}S_{jk}S_{ki}/3 - \omega_i\omega_jS_{ij}/4 - S_{ij}(\partial^2 p/\partial x_i\partial x_j) \rangle$ represents the inviscid production of total strain rate. Thus, the behaviour of $\langle -\omega_i\omega_jS_{ij}/4 - S_{ij}(\partial^2 p/\partial x_i\partial x_j) \rangle$ in addition to the distribution of $\langle -S_{ij}S_{jk}S_{ki}/3 \rangle$ determines the overall strain rate production statistics.

The contours of joint pdf between Q^* and R^* for case E with $Le = 1.0$ are exemplarily shown in Fig. 5.23 for $c = 0.1, 0.3, 0.5, 0.7$ and 0.9 at $t = 2\delta_Z/S_L$ and $6\delta_Z/S_L$. The other cases are not shown because the qualitative behaviour of this joint pdf does not change with the variations of u'/S_L and Le . A dominant negative correlation between Q^* and R^* has been observed within the flame front when the flame remains away from the wall. However, this negative correlation between Q^* and R^* weakens as time progresses and the flame approaches the wall. At $t = 6\delta_Z/S_L$ the joint pdf between Q^* and R^* exhibits weak negative correlation towards the unburned gas side, and these quantities do not show any appreciable correlation as c increases towards the burned gas side.

5.4.2 Flow topology distribution

Figure 5.24 shows the variations of the volume fractions VF of individual flow topologies $S1 - S8$ conditional on c across the flame front (over the range $0.01 \leq c \leq 0.99$) for cases A, C and E for $Le = 0.8, 1.0$ and 1.2 at different time instants. It is worth noting that the range of c obtained at a given instant of time changes as the quenching progresses (see Fig. 5.5 and also a temporal evolution of the probability density function of c) and the probability of obtaining $c \approx 1.0$ increases as the time elapses. A similar presentation of volume fraction of individual flow topologies was used by Cifuentes and his co-workers [59, 58]. It can be seen from Fig. 5.24 that VF of all topologies remain significant within the flame except for $S5$ and $S6$ when the flames are away from the wall, which is consistent with previous analyses. [59, 58] Strong thermal expansion within the flame leads to strongly negative values of P (i.e. high positive values of dilatation rate $\nabla \cdot \vec{u}$), which implies that the occurrence of $P > 0$ topologies (i.e. $S5$ and $S6$) is greatly disadvantaged. Figure 5.16 shows sporadic existences of $P > 0$ in the burned gas region for non-unity Lewis number flames and also for unity Lewis

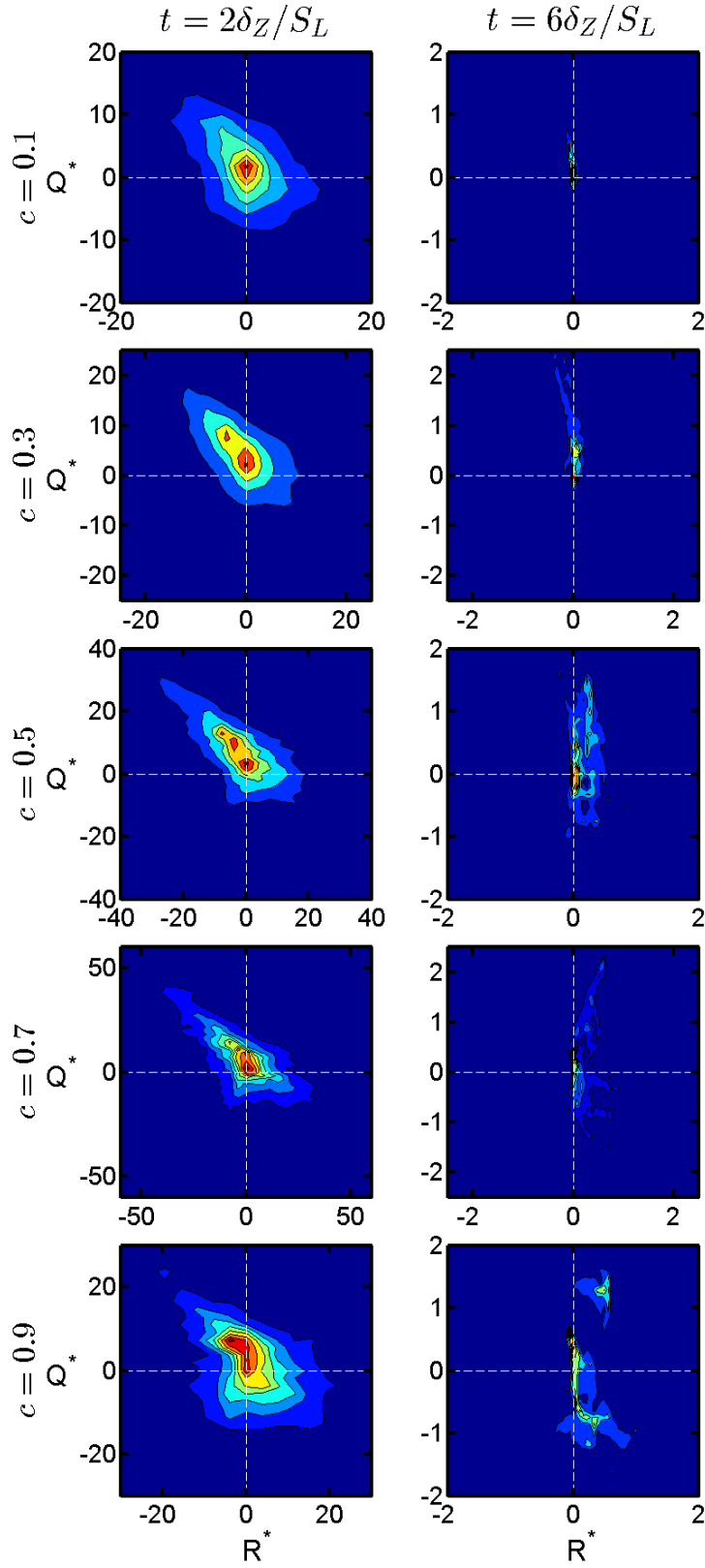


Fig. 5.23 Joint PDFs of $Q^* = Q \times (\delta_Z/S_L)^2$ and $R^* = R \times (\delta_Z/S_L)^3$ on c -isosurfaces $c = 0.1, 0.3, 0.5, 0.7, 0.9$ for $t = 2\delta_Z/S_L$ and $6\delta_Z/S_L$ with case E and $Le = 1.0$.

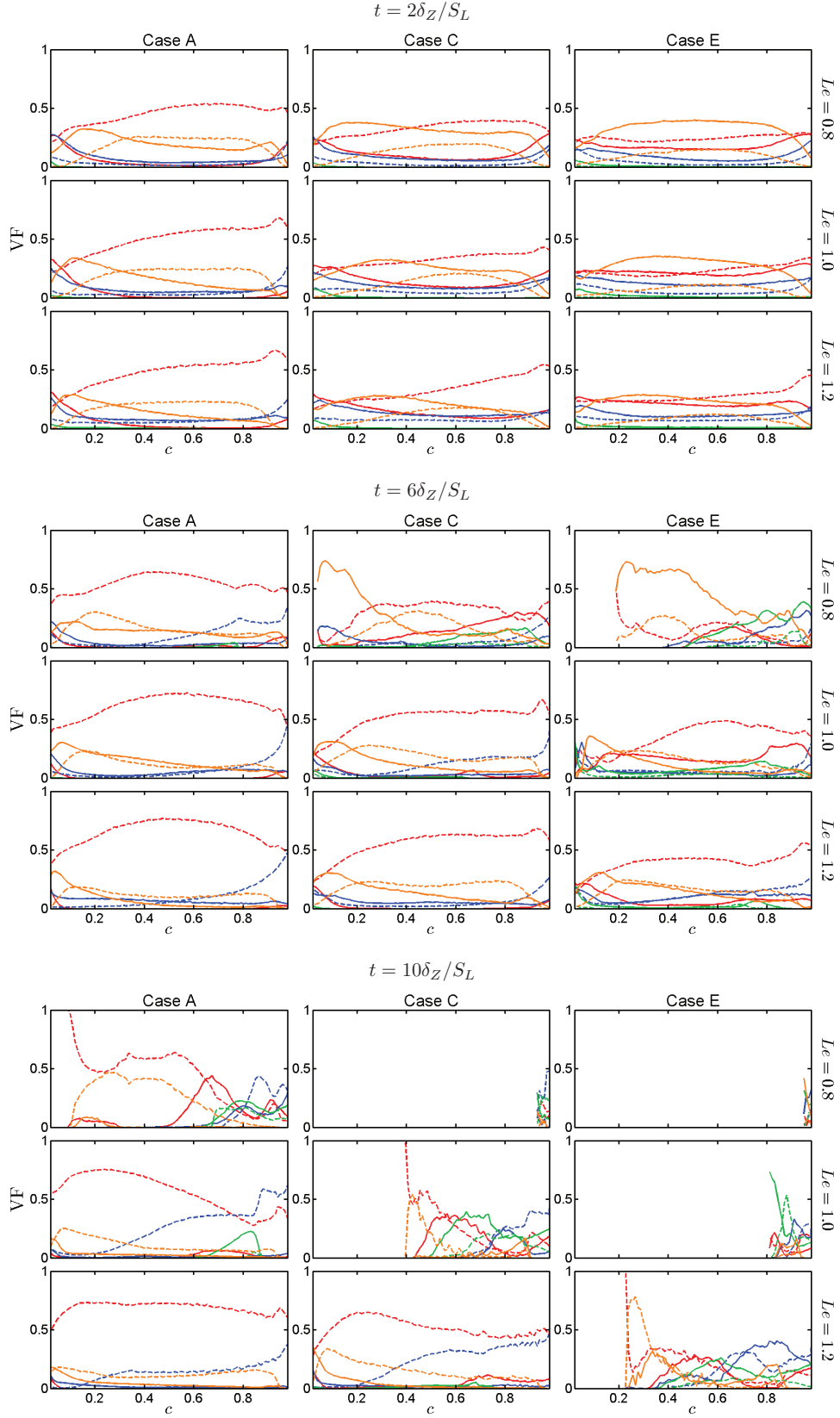


Fig. 5.24 Variations of volume fractions VF for topologies: Focal topologies S1 (—), S4 (—), S5 (—), S7 (—), nodal topologies S2 (---), S3 (---), S6 (---), S8 (---) with c for $t = 2\delta_Z/S_L$, $6\delta_Z/S_L$, $10\delta_Z/S_L$ for cases A, C and E with $Le = 0.8, 1.0$ and 1.2 .

number flames once the quenching is initiated. These positive P locations ultimately give rise to finite probabilities of finding $S5$ and $S6$ topologies towards the burned gas side, but VF of $S5$ remains much higher than that of $S6$ in the burned gas region ($\tilde{c} \rightarrow 1.0$). However, the volume fractions of $S5$ and $S6$ topologies increase significantly as flame quenching progresses with time. The mean flow reverses its direction from towards the wall to away from the wall, and this behaviour leads to $P > 0$ at the final stages of quenching. The topologies $S7$ and $S8$ are typical of positive values of dilatation rate $\nabla \cdot \vec{u}$ (i.e. negative values of P), and it can be seen from Fig. 5.24 that the volume fraction of $S7$ topology remains a significant contributor within the flame front, and the probability of obtaining $S7$ topology increases with decreasing (increasing) Le (u'/S_L) when the flame is away from the wall. The extent of flame wrinkling increases with decreasing (increasing) Le (u'/S_L) when the flame is away from the wall (see Table 5.1), which enhances the likelihood of obtaining curvatures which are concave to the reactants where the effects of focussing of heat are strong. This increases the probability of finding negative values of P with high magnitude (i.e. high positive values of dilatation rate $\nabla \cdot \vec{u}$), which in turn results in a greater volume fraction of $S7$ within the flame front. The volume fractions of $S7$ and $S8$ decrease towards the burned gas side of the flame with the weakening of the effects of dilatation rate. The volume fractions of $S3$ and $S4$ topologies increase towards the burned gas side for all cases even when the flame quenches. Especially the relative contribution of $S3$ volume fraction increases as the quenching progresses with time. The volume fraction of $S2$ topology assumes a high value within the flame throughout the duration of head-on quenching. The volume fraction of $S1$ topology assumes significant values towards the burned gas side, and its volume fraction decreases in the unburned gas. As the topologies $S1, S2, S3$ and $S4$ are present irrespective of the value of P , the probability of finding these topologies remain significant in all cases at all stages of flame quenching.

The distributions of volume fractions of focal ($S1, S2, S4, S5, S7$) and nodal ($S2, S3, S6, S8$) topologies conditional on c for cases A, C and E are shown in Fig. 5.25 for $Le = 0.8, 1.0$ and 1.2 . In general, the volume fraction of focal topologies decreases from the unburned to the burned gas side of the flame which is consistent with the decay of enstrophy across the flame brush in these cases. This behaviour is also consistent with previous findings by Cifuentes and his co-workers. [59, 58] The decrease (increase) in volume fraction of focal (nodal) topologies across the flame brush is relatively less prominent in high values of u'/S_L . The likelihood of obtaining nodal and focal topologies are almost equally probable at the unburned gas as the quenching progresses

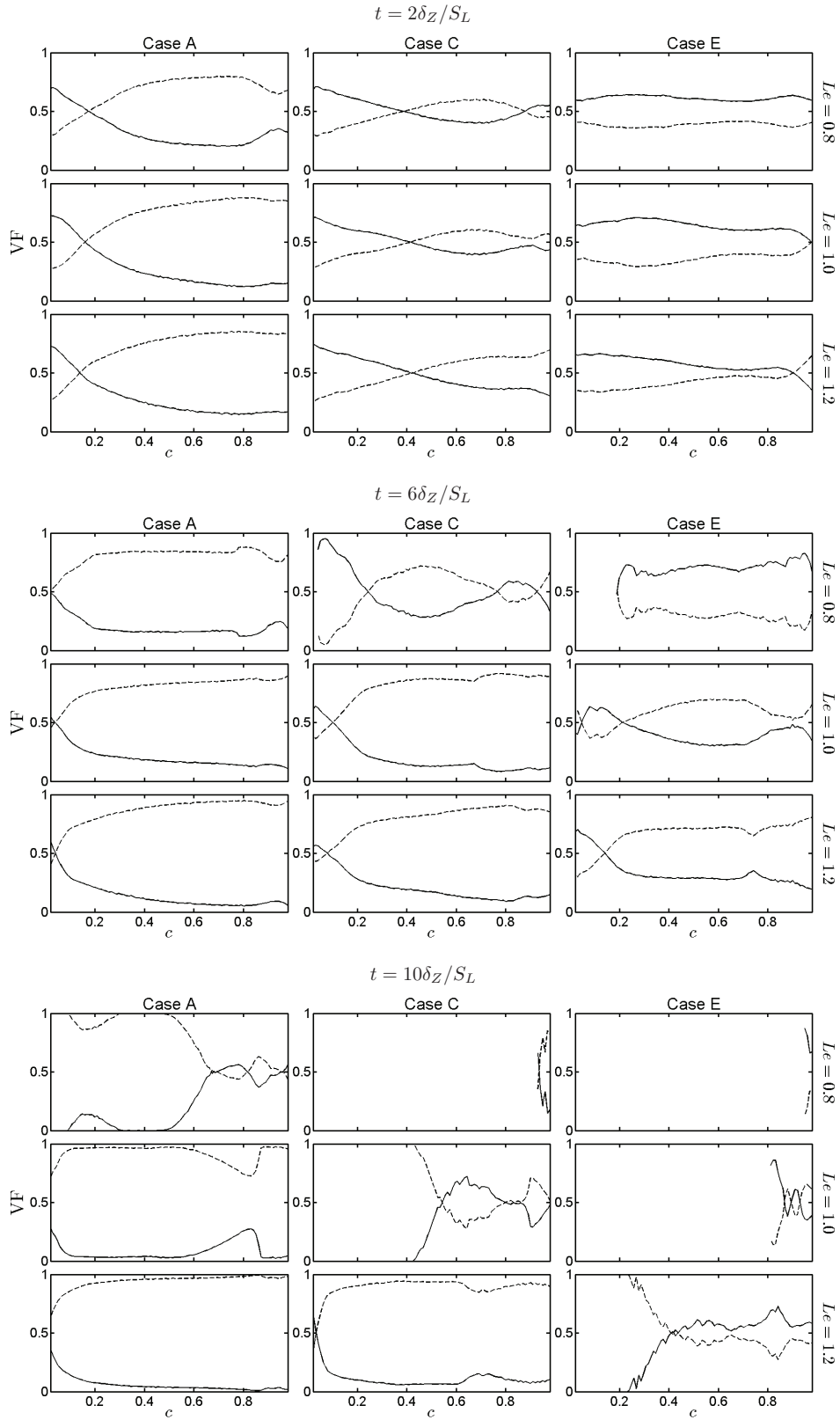


Fig. 5.25 Variations of volume fractions VF for focal (—) and nodal (---) topologies with c for $t = 2\delta_Z/S_L, 6\delta_Z/S_L, 10\delta_Z/S_L$ for cases A, C and E with $Le = 0.8, 1.0$ and 1.2.

which implies that the volume fractions of nodal and focal topologies remain comparable at the wall where the unburned gas is confined at the final stage of quenching. Both global Lewis number Le and turbulence intensity u'/S_L have noticeable effects on the distributions of nodal and focal topologies. The focal topologies remain dominant in case of E with $Le = 0.8$ when the flame is away from the wall and also during flame quenching, but the case E with $Le = 1.0$ and 1.2 shows a monotonic decay (increase) of volume fractions of focal (nodal) topologies with increasing c . In summary, an increase (decrease) in u'/S_L (Le) promotes focal topologies when the flame is away from the wall, but the probability of obtaining nodal (focal) topologies increases (decreases) as quenching progresses.

The interaction of flow topologies and flame topology is of fundamental importance in flame-turbulence interaction. According to Dopazo *et al.* [75] the flame topology can be described in terms of its mean and Gauss curvatures, κ_m and κ_g , respectively, where $\kappa_m = (\kappa_1 + \kappa_2)/2 = 1/2 \nabla \cdot (-\nabla c/|\nabla c|)$ and $\kappa_g = \kappa_1 \kappa_2$, in which κ_1 and κ_2 are the principal curvatures. It is worth noting that the region $\kappa_g > \kappa_m^2$ in the $\kappa_m - \kappa_g$ plane, indicates complex curvatures and thus is non-physical. According to the present convention, positive (i.e. $\kappa_m > 0$) curvature is associated with the wrinkles which are convex to the reactants, whereas negative (i.e. $\kappa_m < 0$) curvature represents wrinkles which are concave to the reactants. The combination of $\kappa_m > 0$ ($\kappa_m < 0$) and $\kappa_g > 0$ indicates cup convex (cup concave) flame topology, whereas the combination of $\kappa_m > 0$ ($\kappa_m < 0$) and $\kappa_g < 0$ represents saddle convex (saddle concave) flame topology. The combination of $\kappa_m > 0$ ($\kappa_m < 0$) and $\kappa_g = 0$ represents tile convex (tile concave) flame topology. Figure 5.26 shows a Joint PDF between the mean and Gaussian curvatures for cases A, C and E at $t = 2\delta_Z/S_L$ and $6\delta_Z/S_L$ for $Le = 1.0$ where the plots are coloured to highlight the highest concentrations of data points. The other cases are not explicitly shown because of their qualitative similarity to the scatter shown in Fig. 5.26. It can be from Fig. 5.26 that the distribution of $S1$ and $S2$ topologies are almost symmetrical about $\kappa_m = 0$, whereas $S7$ and $S8$ topologies appear to slightly favour $\kappa_m < 0$ and $\kappa_g > 0$ and $S5$ and $S6$ appear to slightly favour $\kappa_m, \kappa_g > 0$ when the flame is away from the wall (e.g. $t = 2\delta_Z/S_L$). The topologies $S7$ and $S8$ topologies are associated with for high positive dilatation rates (i.e. negative values of P) which are likely to be observed in the zones which are concavely curved towards the reactants (i.e. $\kappa_m < 0$) due to focussing of heat. By contrast, $S5$ and $S6$ topologies are associated with for negative dilatation rates (i.e. positive values of P) which are likely to be observed in the zones which are convexly curved towards the reactants (i.e. $\kappa_m > 0$) due to defocussing of heat. Thus, the topologies $S7$ and $S8$ ($S5$ and $S6$) show a preference to

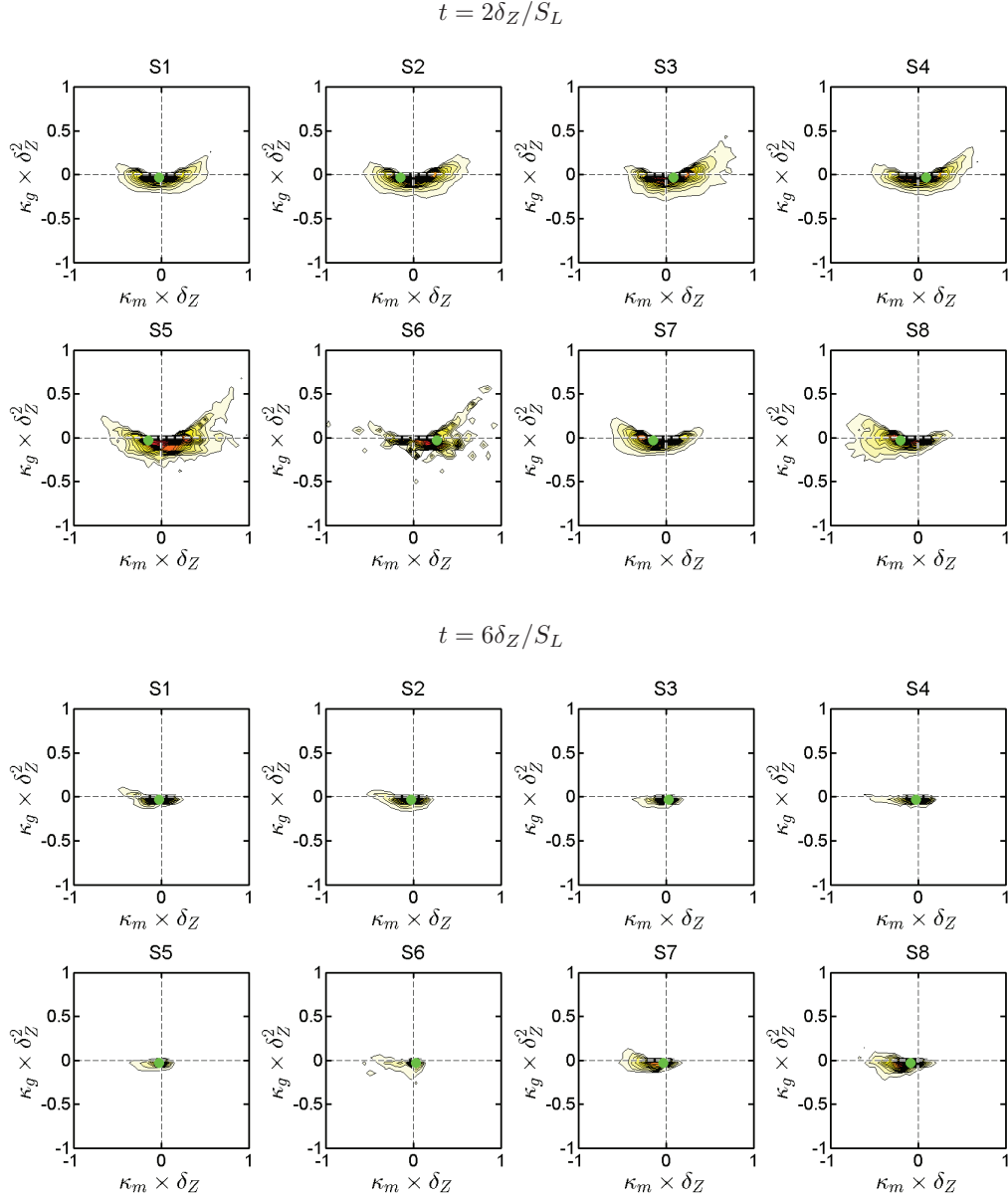


Fig. 5.26 Joint PDF between mean and Gaussian curvatures (i.e. $\kappa_m \times \delta_Z$ and $\kappa_g \times \delta_Z^2$) for S1-8 at $t = 2\delta_Z/S_L$ and $6\delta_Z/S_L$ for cases E with $Le = 1.0$.

$\kappa_m < 0$ ($\kappa_m > 0$) and $\kappa_g > 0$. As the flame quenching progresses with time, the scatter in $\kappa_m - \kappa_g$ plane remains concentrated around the origin (see $t = 6\delta_Z/S_L$) with the but even then $S7$, and $S8$ topologies continue to show a preference towards $\kappa_m < 0$ and $\kappa_g > 0$.

It is worth noting that each of the flow topologies is associated with different types of generic flow structures. Thus, it is worth understanding the alignments of ∇c and vorticity $\vec{\omega}$ with local principal strain rates for individual topologies so that the contributions of these topologies to the scalar dissipation rate (SDR), $N_c = D\nabla c \cdot \nabla c$ (where D is the thermal diffusivity), and enstrophy $\Omega = \vec{\omega} \cdot \vec{\omega}/2$ transports in turbulent premixed flames can be understood. The transport equations of N_c and Ω are given as [195, 121, 43, 45, 39, 29]:

$$\begin{aligned} \rho \frac{DN_c}{Dt} = & \frac{\partial}{\partial x_j} \left(\rho D \frac{\partial N_c}{\partial x_j} \right) - 2D \frac{Dc}{Dt} \frac{\partial c}{\partial x_k} \frac{\partial \rho}{\partial x_k} - 2\rho D \underbrace{\frac{\partial c}{\partial x_i} \frac{\partial u_i}{\partial x_j} \frac{\partial c}{\partial x_j}}_{\Lambda} \\ & + 2D \frac{\partial \dot{\omega}}{\partial x_k} \frac{\partial c}{\partial x_k} - 2\rho D^2 \frac{\partial^2 c}{\partial x_k \partial x_i} \frac{\partial^2 c}{\partial x_k \partial x_i} + f(D) \end{aligned} \quad (5.5a)$$

$$\begin{aligned} \frac{D\Omega}{Dt} = & \underbrace{\omega_i \omega_k \frac{\partial u_i}{\partial x_k}}_V - \epsilon_{ijk} \omega_i \frac{1}{\rho^2} \frac{\partial \rho}{\partial x_j} \frac{\partial \tau_{kl}}{\partial x_l} + \frac{\epsilon_{ijk} \omega_i}{\rho} \frac{\partial^2 \tau_{kl}}{\partial x_j \partial x_l} \\ & - 2 \frac{\partial u_k}{\partial x_k} \Omega + \epsilon_{ijk} \frac{\omega_i}{\rho^2} \frac{\partial \rho}{\partial x_j} \frac{\partial p}{\partial x_k} \end{aligned} \quad (5.5b)$$

where ρ , p , $\dot{\omega}$, τ_{ij} and $f(D)$ are the density, pressure, chemical source term and viscous stress tensor component and the contributions due to diffusivity gradients, respectively. The terms $-2\rho D\Lambda$ and V are responsible for the generation/destruction of scalar gradients by flame normal straining, and vortex-stretching terms respectively [29, 39, 43, 45, 195]. The terms Λ and V depend on the alignment of ∇c and $\vec{\omega}$ with the most extensive, intermediate and the most compressive strain rates (i.e. e_α , e_β and e_γ) in the following manner: $\Lambda = (\partial c/\partial x_i)(\partial u_i/\partial x_j)(\partial c/\partial x_j) = (e_\alpha \cos^2 2\alpha + e_\beta \cos^2 2\beta + e_\gamma \cos^2 2\gamma) \nabla c \cdot \nabla c$ and $V = 2(e_\alpha \cos^2 2\alpha' + e_\beta \cos^2 2\beta' + e_\gamma \cos^2 2\gamma') \Omega$ where α , β , γ (α' , β' , γ') are the angles between ∇c ($\vec{\omega}$) and the eigendirections associated with e_α , e_β and e_γ respectively. The above expression indicates that a collinear alignment between ∇c ($\vec{\omega}$) and the most extensive principal strain rate e_α (i.e. most positive principal strain rate) leads to $\cos^2 2\alpha = 1$ ($\cos^2 2\alpha' = 1$), which promotes a positive value of Λ (V). By contrast, a collinear alignment between ∇c ($\vec{\omega}$) and the most compressive

principal strain rate e_γ (i.e. most negative principal strain rate) leads to $\cos^2 2\gamma = 1$ ($\cos^2 2\gamma' = 1$), which in turn gives rise to negative values of Λ (V).

Figure 5.27 shows the contributions of $\langle \Lambda^* \rangle = \langle \Lambda \rangle \times (\delta_Z^3 / S_L)$ for individual flow topologies $S1 - S8$ for cases A, C and E for $Le = 0.8, 1.0$ and 1.2 at different time instants. In all cases, the total contribution of $\langle \Lambda^* \rangle$ remains positive throughout the flame brush when the flame remains away from the wall. However, $\langle \Lambda^* \rangle$ assumes negative values in cases C and E at the late stages of flame quenching. The expression $\Lambda = (e_\alpha \cos^2 2\alpha + e_\beta \cos^2 2\beta + e_\gamma \cos^2 2\gamma) \nabla c \cdot \nabla c$ indicates that a positive (negative) value of this quantity is indicative of preferential alignment of ∇c with the eigenvector associated with the most extensive (compressive) principal strain rate e_α (e_γ). It has been demonstrated elsewhere [43, 39, 47, 112] that ∇c aligns with the most extensive principal strain rate when the strain rate induced by flame normal acceleration overcomes turbulence straining, and conversely preferential alignment of ∇c with e_γ , similar to the case in passive scalar mixing, is obtained when turbulence straining overwhelms the strain rate induced by flame normal acceleration. The strain rate due to flame normal acceleration can be scaled using $\tau S_L / \delta_{th}$, whereas turbulence straining scales as u' / l . [43, 39, 47, 112] For the cases considered here $\tau S_L / \delta_{th}$ remains of the same order but greater than u' / l , and, as a result, straining due to flame normal acceleration dominates over turbulent straining to result in a preferential alignment with the most extensive principal strain rate (and thereby positive values of $\langle \Lambda^* \rangle$) when the flame is away from the wall. The effects of flame normal acceleration weaken after flame quenching and thus ∇c tends to align with the most compressive principal strain rate and in turn, gives rise to negative values of $\langle \Lambda^* \rangle$. The effects of turbulent straining are stronger in cases C and E than in case A due to higher u' / S_L , and also due to the fact that the quenching is more advanced stage in case C (case E) than in case A (case C) at a given instant of time. Thus, at final stages of flame quenching $\langle \Lambda^* \rangle$ shows negative values in cases C and E (see $t = 10\delta_Z / S_L$). It can be seen from Fig. 5.27 that $\langle \Lambda^* \rangle$ conditional on $S2, S7$ and $S8$ topologies exhibit positive values, and these topologies offer dominant contributions to $\langle \Lambda^* \rangle$ for all cases when the flame is away from the wall. The $S2$ topology makes the highest contribution to the value of $\langle \Lambda^* \rangle$ for all cases. During flame quenching $\langle \Lambda^* \rangle$ decays significantly when the topologies $S3$ and $S8$ contribute significantly while the contribution of $S2$ topology determines the behaviour of $\langle \Lambda^* \rangle$. The topologies $S7$ and $S8$ are obtained where positive dilatation rate (i.e. thermal expansion) effects are dominant and thus in these locations the strain rate due to thermal expansion dominates over turbulent straining to give rise to a strong alignment between ∇c with e_α which is reflected in the positive contributions of

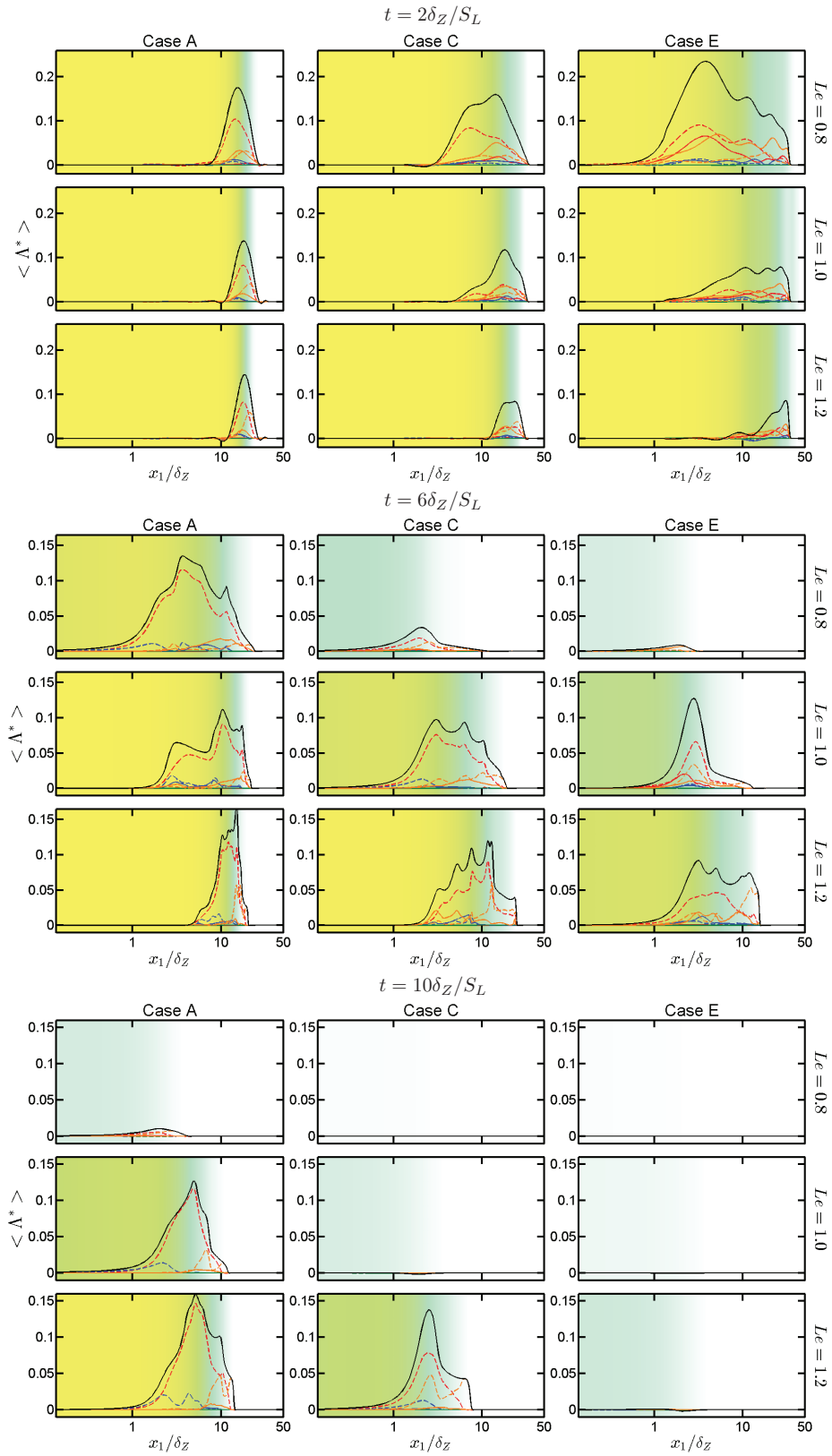


Fig. 5.27 Variations of $\langle \Lambda^* \rangle = \langle \Lambda \rangle \times \delta_Z^3/S_L$ (—) with x_1/δ_Z for $t = 2\delta_Z/S_L$, $6\delta_Z/S_L$, $10\delta_Z/S_L$ for cases A, C and E with $Le = 0.8, 1.0$ and 1.2 (Focal topologies S1 (—), S4 (—), S5 (—), S7 (—), nodal topologies S2 (---), S3 (---), S6 (---), S8 (---)).

$\langle \Lambda^* \rangle$. The $S1$ topology also makes a dominant positive $\langle \Lambda^* \rangle$ contribution in case E at early times (e.g. $t = 2\delta_Z/S_L$). The topologies $S3$ and $S4$ also exhibit positive values of $\langle \Lambda^* \rangle$ but the magnitudes of these contributions remain smaller than the conditional mean values for $S2$, $S7$ and $S8$ topologies for all cases for $Le = 0.8$ and 1.0 . The value of $\langle \Lambda^* \rangle$ conditional on $S3$ and $S4$ topologies exhibit weak negative values for $Le = 1.2$ at early times (e.g. $t = 2\delta_Z/S_L$) in the highest u'/S_L case (i.e. case E), whereas these topologies show positive values for $Le = 0.8$ and 1.0 cases at $t = 2\delta_Z/S_L$ and later times for all cases irrespective of the Lewis number. The effects of thermal expansion are the weakest in the $Le = 1.2$ case among all the Lewis number cases considered here. As a result, turbulent straining overcomes the strain rate induced by flame normal acceleration for the highest u'/S_L case (i.e. case E) with $Le = 1.2$, which leads to preferential alignment ∇c with e_γ , and thereby negative values of $\langle \Lambda^* \rangle$ are obtained for $S3$ and $S4$ topologies. By contrast, the strain rate induced by flame normal acceleration dominates over turbulent straining for $Le = 0.8$ and 1.0 even in case E, and thus positive values of $\langle \Lambda^* \rangle$ are obtained. As time progress the effects of turbulent straining weaken with the decay of u' , and as a result, the strain rate due to flame normal acceleration dominates over turbulent strain rate even for case E with $Le = 1.2$ at later times.

The contributions of $\langle V^* \rangle = \langle V \rangle \times (\delta_Z/S_L)^3$ for individual flow topologies $S1 - S8$ for cases A, C and E in Fig. 5.28 for $Le = 0.8, 1.0$ and 1.2 at different time instants. It can be seen that $\langle V^* \rangle$ remains predominantly positive away from the wall, but this quantity assumes negative values close to the wall. The negative value of $\langle V^* \rangle$ at the near-wall region becomes increasingly prominent as the time progresses. It has been demonstrated in section 5.2 that the alignment of $\vec{\omega}$ with the most compressive principal strain rate e_γ strengthens in the near-wall region, whereas $\vec{\omega}$ preferentially aligns with the intermediate and most extensive principal strain rates (i.e. e_β and e_α) away from the wall. Accordingly, $\langle V^* \rangle$ shows positive values away from the wall and negative values in the vicinity of it. It can be seen from Fig. 5.28 that the topology $S7$, which is a focal topology associated with stretching (see Fig. 2.2), shows positive value of $\langle V^* \rangle$ even at the wall for all cases at $t = 2\delta_Z/S_L$ and $6\delta_Z/S_L$, which is indicative of predominant $\vec{\omega}$ alignment with the intermediate and most extensive principal strain rates for this flow topology. The contribution of $\langle V^* \rangle$ arising from $S8$ topology induces positive values of $\langle V^* \rangle$ even at the vicinity of the wall for case E with $Le = 0.8$ at early times (e.g. $t = 2\delta_Z/S_L$). The $S4$ topology, which is also a focal topology associated with stretching becomes the leading order contributor to $\langle V^* \rangle$ away from the wall at early times (e.g. $t = 2\delta_Z/S_L$) but the contribution of $\langle V^* \rangle$ arising from $S4$ decreases in

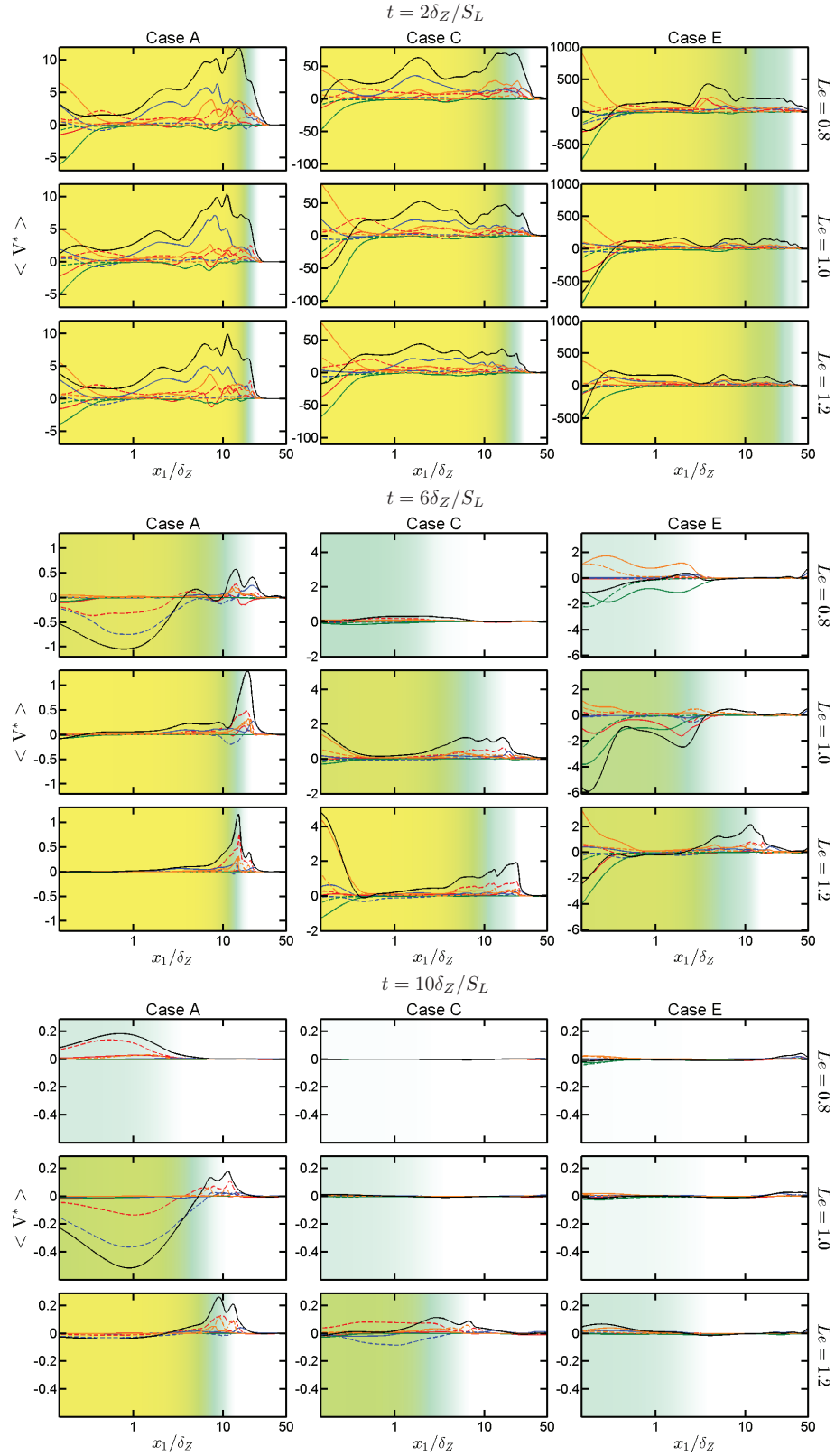


Fig. 5.28 Variations of $\langle V^* \rangle = \langle V \rangle \times (\delta_Z/S_L)^3$ (—) with x_1/δ_Z for $t = 2\delta_Z/S_L$, $6\delta_Z/S_L$, $10\delta_Z/S_L$ for cases A, C and E with $Le = 0.8, 1.0$ and 1.2 (Focal topologies S1 (—), S4 (—), S5 (—), S7 (—), nodal topologies S2 (---), S3 (---), S6 (---), S8 (---)).

magnitude close to the wall but still remains positive. The negative value of $\langle V^* \rangle$ at the wall arises due to $S1, S5$ and $S6$ topologies. The contributions of nodal topologies $S2$ and $S3$ lead to predominantly negative values of $\langle V^* \rangle$ for case A with $Le = 0.8$ ($Le = 1.0$) at $t = 2\delta_Z/S_L$ ($6\delta_Z/S_L$), whereas $\langle V^* \rangle$ conditional on $S2$ exhibits positive values at the final stage of quenching (e.g. $t = 10\delta_Z/S_L$) for case A with $Le = 0.8$ and also for case C with $Le = 1.2$. The observations made from Fig. 5.28 indicates that the focal topologies associated with stretching tend to promote a positive value of $\langle V^* \rangle$, whereas the negative values of $\langle V^* \rangle$ especially at the wall originate principally due to nodal topologies. A comparison between Figs. 5.24 and 5.28 indicates the distributions of focal and nodal topologies determine the nature of $\langle V^* \rangle$ variation in all cases considered here.

5.4.3 Influence of flow topology on the wall heat flux

Figure 5.29a shows the temporal evolutions of maximum, mean and minimum values of Φ for the turbulent cases. It can be observed from Fig. 5.29 that an increase in u' leads to an increase in maximum wall heat flux Φ_{\max} . A comparison between different Le cases indicates that the maximum heat flux in the turbulent $Le = 0.8$ case is greater than the turbulent $Le \leq 1$ cases. Figure 5.16 shows the existence of thermal inhomogeneity in the burned gas for the non-unity Lewis number flames even before the initiation of flame quenching. Super-adiabatic temperatures ($T > 1$) are observed for non-unity Le cases when the flame is away from the wall. The high (low) values of temperature are associated with the region where the flame curvatures which are convex (concave) towards the reactants for turbulent $Le = 0.8$ cases. An opposite behaviour is observed for the turbulent $Le = 1.2$ cases. Simultaneous strong focusing of reactants and weak defocussing of heat in the turbulent $Le = 0.8$ cases lead to high magnitudes of reaction rate and burned gas temperature in these regions. Just the opposite mechanism gives rise to high-temperature values in the regions where the flame front is concavely curved towards the reactants for the turbulent $Le = 1.2$ cases. Figure 5.16 shows that the flame elements which are convex towards the reactants are likely to reach near the wall at an earlier time. As high-temperature zones are associated with the zones which are convex towards the reactants for the $Le = 0.8$ cases, the maximum value of Φ is obtained at an earlier time for smaller values of Le . The flame quenching starts in the turbulent $Le = 0.8$ cases when the super-adiabatic regions reach close to the wall. In these cases, the high rate of chemical reaction enables the convexly curved regions to reach closer to the wall than the corresponding laminar flame-quenching distance, which along with the super-adiabatic temperature

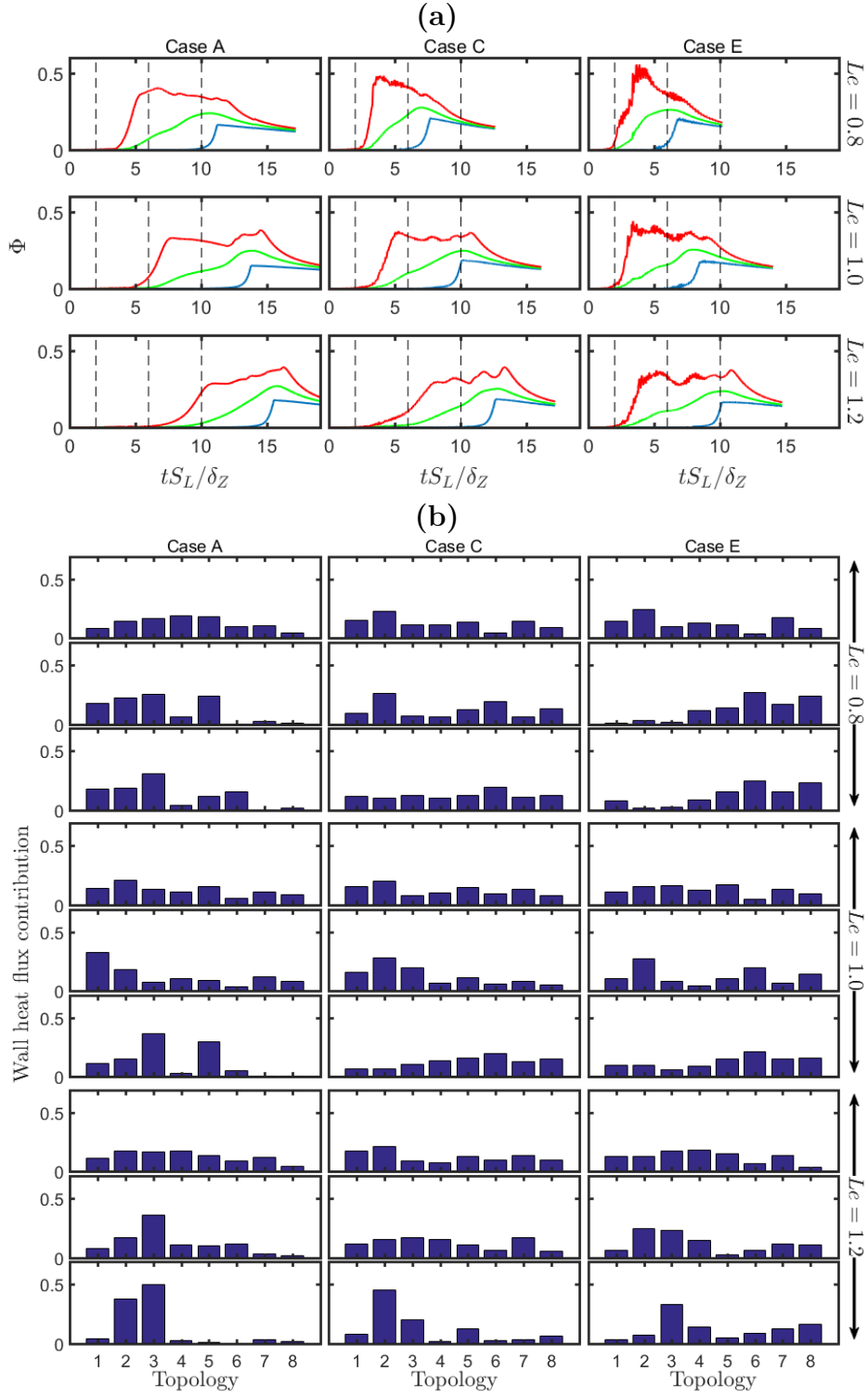


Fig. 5.29 (a) Temporal evolution of maximum (—), mean (—) and minimum (—) values of wall heat flux Φ for Case A, C and E with $Le = 0.8, 1.0$ and 1.2 . Vertical lines indicate time instants for $t = 2\delta_Z/S_L$, $6\delta_Z/S_L$ and $10\delta_Z/S_L$ (left to right) (b) Wall heat flux contributions from topology S1 – S8 for $Le = 0.8, 1.0$ and 1.2 at different time instant $t = 2\delta_Z/S_L$, $6\delta_Z/S_L$ and $10\delta_Z/S_L$ (top to bottom) with Case A, B and C.

gives rise to higher values of maximum wall heat flux in these cases in comparison to the corresponding turbulent $Le = 1.0$ cases. The super-adiabatic values of temperature in the $Le = 1.2$ cases are associated with the curvatures which are concave towards the reactants and therefore quenching starts before these zones get a chance to interact with the wall. As a result of this, the maximum wall heat flux for the turbulent $Le = 1.2$ cases remains comparable to the corresponding value for laminar premixed flame-wall interaction.

The normalised wall heat flux can be expressed as $\Phi = \sum \Phi_{Si}$ where $i = 1 - 8$ with Φ_{Si} being normalised wall heat flux contribution for each individual topology. The fractional contributions of each flow topology towards total wall heat flux magnitude (i.e. Φ_{Si}/Φ) are also shown in Fig. 5.29b for cases A, C and E for different time instants. For cases A-C the wall heat flux remains small for $t \leq 2\delta_Z/S_L$ as the flame remains sufficiently away from the wall to influence Φ (see Fig. 5.29a). Under this condition, Φ_{Si}/Φ remains comparable for all flow topologies. However, the flame starts to quench by $t = 2\delta_Z/S_L$ in case E with $Le = 0.8$, which is reflected in the temporal increase in wall heat flux in Fig. 5.29a. A comparison between Figs. 5.29a and 5.29b reveals that S2 and S3 topologies remain the significant contributors to the overall wall heat flux during high wall heat flux period during flame quenching (e.g. compare Figs. 5.29a and 5.29b at $t = 6\delta_Z/S_L$ for cases A-E with $Le = 1.0$ and 1.2 and cases A-C with $Le = 0.8$). However, the topologies S6 and S8 become the leading order contributors at the final stage of flame quenching when the wall heat flux starts to decrease with time (compare Figs. 16a and 16b at $t = 10\delta_Z/S_L$ for cases A-E with $Le = 0.8$ and 1.0). In general, the nodal topologies have been found to contribute heavily to the wall heat flux when the flame interacts with the wall during head-on quenching irrespective of the value of global Lewis number.

5.4.4 Summary of the key results

The flow topology distribution and statistical behaviours of the invariants of velocity gradient tensor P , Q and R have been analysed for head-on quenching of statistically planar turbulent premixed flames by isothermal inert walls using three-dimensional DNS data for different values of Lewis numbers at different turbulence intensities u'/S_L and integral length scale to flame thickness ratios l/δ_{th} . The flow topologies have been characterised by the first, second and third invariants (i.e. P , Q and R) of the velocity gradient $\partial u_i/\partial x_j$ tensor. The first invariant is the negative of dilatation rate (i.e. $(\partial u_i/\partial x_i) = -P$) and thus assumes significant negative values within the flame (i.e. $0 < c < 1$), but it assumes vanishingly small values outside the flame in

both unburned gases and fully burned products in the $Le = 1.0$ cases when the flame remains away from the wall. The positive dilatation rate effects (i.e. effects of negative P) remain significant not only within the flame, but also in the burned gas due to considerable amount of thermal inhomogeneity resulting from imbalance of species and heat diffusion rates in the case of non-unity Lewis number flames even when they are away from the wall. The strengthening of burning leads to an increase in the magnitude of negative contribution of P within the flame with decreasing Le . The effects of positive dilatation rate weaken close to the wall due to flame quenching. The magnitude of the second invariant Q drops significantly across the flame within the burned gases and it changes from positive (i.e. vorticity dominated region) to negative (i.e. strain rate dominated region) in a short span of space depending on local values of $S_{ij}S_{ij}$ and $W_{ij}W_{ij}$. Furthermore, the extent of this intermittent behaviour increases with increasing turbulence intensity. Moreover, the likelihood of obtaining high magnitudes of the third invariant R increases with increasing (decreasing) u'/S_L (Le) and $|R|$ decreases as quenching progresses with time. A dominant negative correlation between Q and R is obtained when the flame is away from the wall but this negative correlation weakens as time progresses and the flame approaches the wall. The distributions of volume fractions of focal ($S1, S4, S5, S7$) and nodal ($S2, S3, S6, S8$) topologies have been investigated in detail. This paper provides information on the evolution of dominant flow topologies with the progress of head-on quenching. Furthermore, this analysis also provides information about the evolution of dominant flow topology contributions to the scalar-turbulence interaction, vortex-stretching terms and wall heat flux during head-on quenching. The volume fraction of focal topologies decreases from the unburned to the burned gas side of the flame brush which is consistent with the decay of enstrophy across the flame brush in these cases. The decrease (increase) in volume fraction of focal (nodal) topologies across the flame brush is less prominent for high values of u'/S_L . It has been found that the flow topologies $S7$ - $S8$, which are present only for positive values of dilatation rate (i.e. negative values of $-P$), occupy a significant fraction of the flame front when the flame remains away from the wall but the probability of their occurrence drops with progress of head-on quenching and the topologies $S1$ - $S4$ (and mainly $S2$), which are obtained for all possible values of dilatation rate, play dominant roles during flame quenching. The contributions of individual topologies to scalar-turbulence interaction and vortex-stretching terms in the scalar dissipation rate and enstrophy transport equations, respectively have been analysed. It has been found that the mean scalar-turbulence interaction term $\langle \Lambda \rangle$ remains mostly positive due to predominant alignment of scalar gradient with the

most extensive principal strain rate. The $S2$, $S7$ and $S8$ topologies have been found to be leading order contributors to $\langle \Lambda \rangle$, but the contributions of $S7$ and $S8$ topologies weaken close to the wall as these topologies are specific to positive dilatation rate which weakens at the wall due to flame quenching. It has been found that the focal topologies $S4$ and $S7$ associated with stretching promote a positive mean value of the vortex-stretching term $\langle V \rangle$, whereas the negative values of $\langle V \rangle$ especially at the wall originate principally due to nodal topologies $S2$ and $S3$. Furthermore $S2$ and $S3$ topologies have been found to be the major contributors to the wall heat flux during flame quenching when high magnitudes of wall heat flux are obtained. However, $S6$ and $S8$ topologies become the leading contributors to wall heat flux during final stages of flame quenching. The flow topology contributions to wall heat flux remain qualitatively similar for the values Le considered here. It can be seen from Fig. 2.2 that each of these topologies is associated with canonical flow configurations and thus the distributions of the topologies and their contributions to wall heat flux, and the scalar-turbulence interaction and vortex-stretching terms in the scalar dissipation rate and enstrophy transport equations, respectively could be used to design simplified experimental and computational configurations. In addition to these simplified analyses, further investigation on flow topology distribution for higher turbulent Reynolds number flows will be necessary for gaining further physical insights.

5.5 Statistical analysis and modelling of the turbulent kinetic energy transport

Here, the turbulent kinetic energy transport and its modelling in the near-wall region have been analysed. The main objectives of this section are:

- To analyse the statistical behaviour of turbulent kinetic energy \tilde{k} and the unclosed terms of its transport equation in the near-wall region for head-on quenching of turbulent premixed flames.
- To discuss the modelling implications of the unclosed terms of the turbulent kinetic energy \tilde{k} transport equation in the near-wall region based on *a-priori* analysis of DNS data.

5.5.1 Distributions of turbulent kinetic energy \tilde{k} and its dissipation rate $\tilde{\varepsilon}$

The variations of \tilde{k} and $\tilde{\varepsilon}$ in the wall normal direction for cases A, C and E are shown in Fig. 5.30 for different time instants. The magnitude of \tilde{k} is found to increase with increasing u'/S_L , as expected. A comparison between Figs 5.30 and 5.31 reveals that both \tilde{k} and $\tilde{\varepsilon}$ decay across the flame brush. Moreover, turbulent kinetic energy decays significantly in the near-wall region (i.e. $x_1/\delta_Z < Pe_{\min}$) due to strong viscous action. The variation of $\tilde{\varepsilon}$ with x_1/δ_Z in Fig. 5.30 shows that the high values of $\tilde{\varepsilon}$ are obtained in the near-wall region (i.e. $x_1/\delta_Z < Pe_{\min}$). The magnitudes of turbulent kinetic energy and its dissipation rate decrease by a large margin, as the flame quenching progresses. Furthermore, it can be seen from Fig. 5.30 that the magnitudes of \tilde{k} and $\tilde{\varepsilon}$ increase with decreasing global Lewis number Le . It is useful to analyse the statistical behaviours of the unclosed terms of the turbulent kinetic energy transport equation (see Eq. 2.46) to explain the variation of \tilde{k} in the near-wall region.

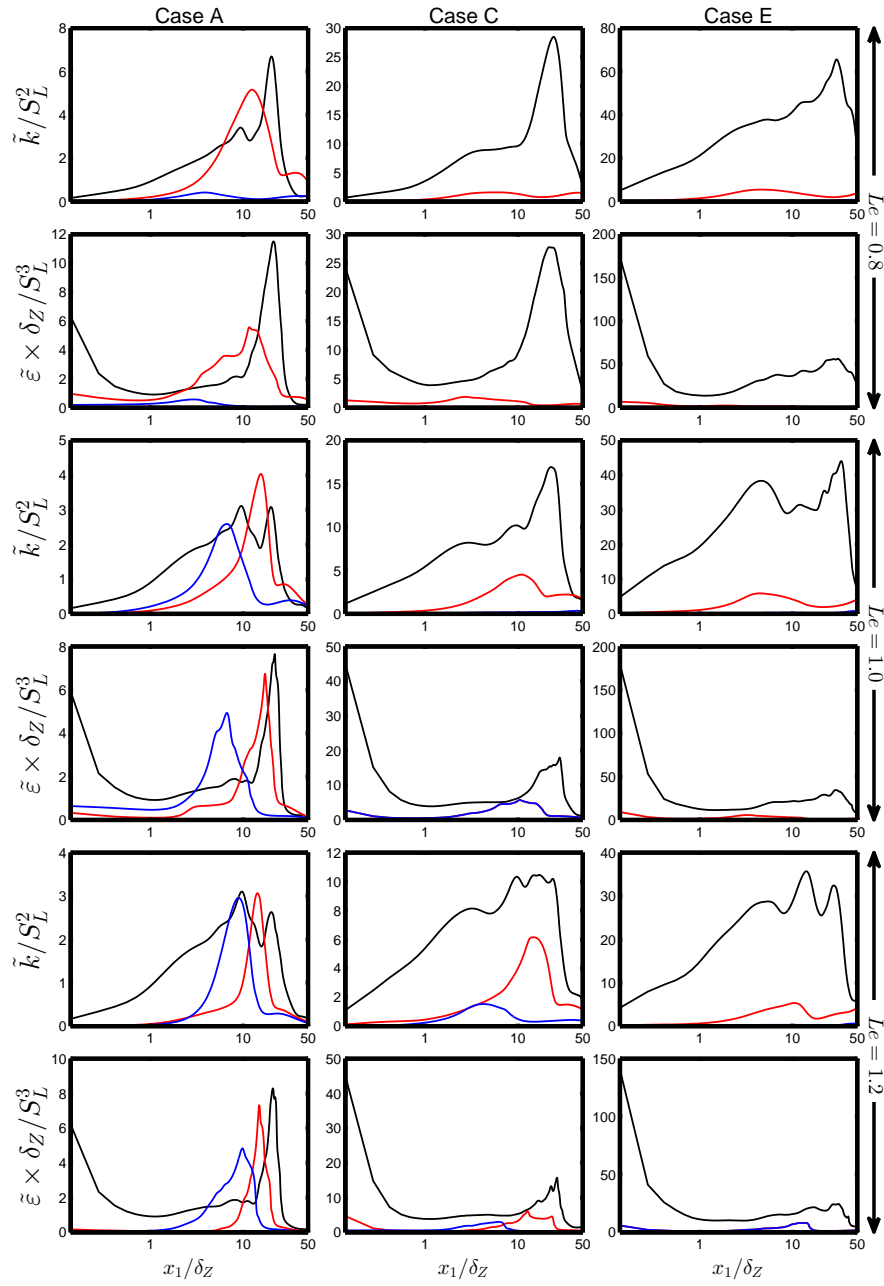


Fig. 5.30 Variations of \tilde{k}/S_L^2 and $\tilde{\varepsilon} \times \delta_Z/S_L^3$ for cases A, C and E (1st-3rd column) at $t = 2\delta_Z/S_L$ (—), $6\delta_Z/S_L$ (—) and $10\delta_Z/S_L$ (—).

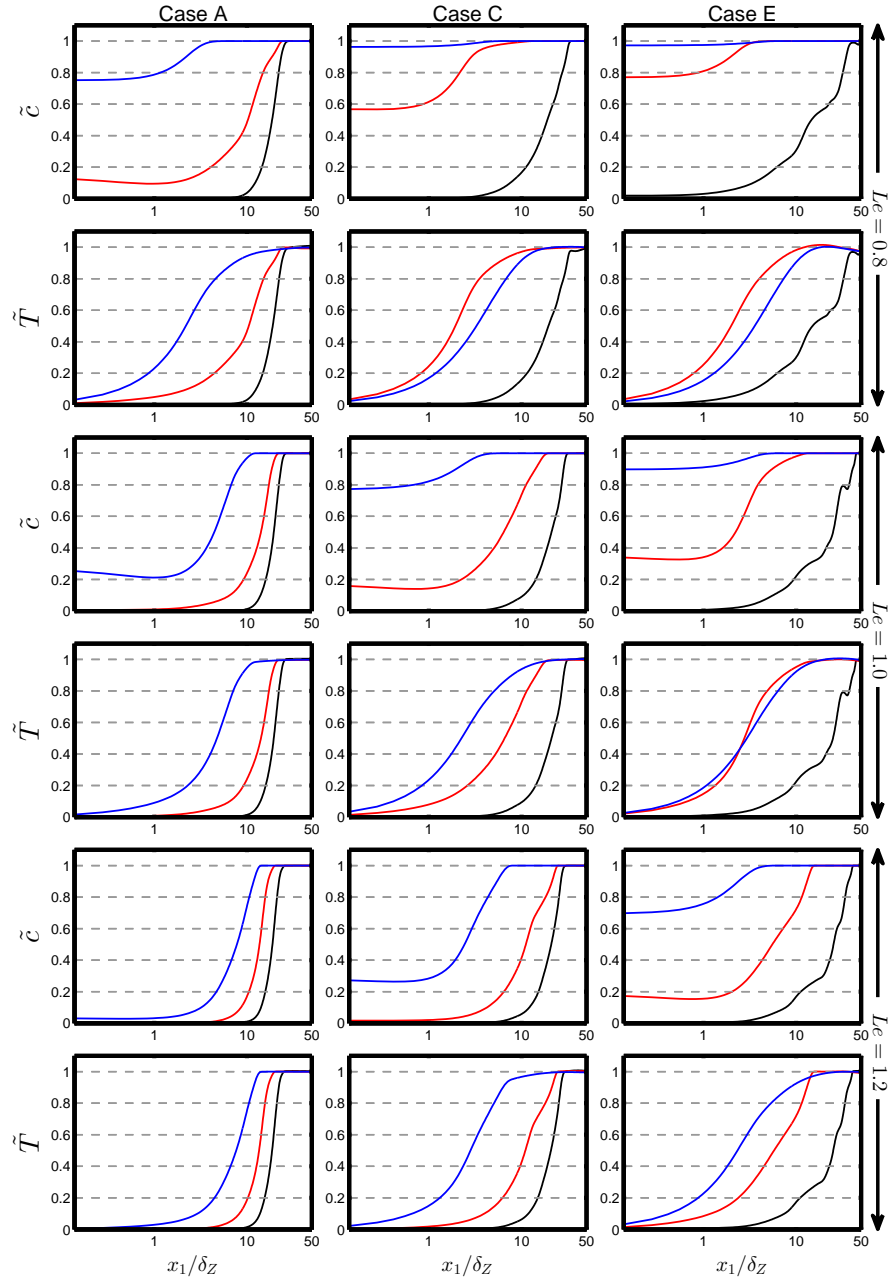


Fig. 5.31 Variations of \tilde{c} and \tilde{T} for cases A, C and E (1st-3rd column) at $t = 2\delta_Z/S_L$ (—), $6\delta_Z/S_L$ (—) and $10\delta_Z/S_L$ (—).

5.5.2 Statistical behaviour of the turbulent kinetic energy transport

The transport equation of turbulent kinetic energy can be seen in Eq. 2.46 (or see Eq. 5.6 below).

$$\frac{\partial \bar{\rho} \tilde{k}}{\partial t} + \frac{\partial \bar{\rho} \tilde{u}_j \tilde{k}}{\partial x_j} = \underbrace{-\overline{\rho u_i'' u_j''} \frac{\partial \tilde{u}_i}{\partial x_j}}_{T_{K1}} \underbrace{- \tilde{u}_i'' \frac{\partial \tilde{p}}{\partial x_i}}_{T_{K2}} + \underbrace{\overline{p' \frac{\partial u_k''}{\partial x_k}}}_{T_{K3}} + \underbrace{\overline{u_i'' \frac{\partial \tau_{ij}}{\partial x_j}}}_{T_{K4}} \underbrace{- \frac{\partial (\overline{p' u_i''})}{\partial x_i}}_{T_{K5}} \underbrace{- \frac{\partial (\frac{1}{2} \overline{\rho u_i'' u_k'' u_k''})}{\partial x_i}}_{T_{K6}} \quad (5.6)$$

T_{K1} production/destruction of \tilde{k} by the mean velocity gradient

T_{K2} the mean pressure gradient term

T_{K3} pressure dilatation term

T_{K4} molecular diffusion and viscous dissipation effects term

T_{K5} transport of \tilde{k} by pressure fluctuations

T_{K6} transport of \tilde{k} by turbulent velocity fluctuations

The variations of the terms $T_{K1} - T_{K6}$ in the wall normal direction are shown in Fig. 5.32. The mean velocity gradient term $T_{K1} = -\overline{\rho u_1'' u_1''} \partial \tilde{u}_1 / \partial x_1$ acts as a sink (i.e. negative term) for all cases because both $\overline{\rho u_1'' u_1''}$ and $\partial \tilde{u}_1 / \partial x_1$ remain positive throughout the flame brush. The magnitude T_{K1} becomes negligible in the near-wall region (i.e. $x_1 / \delta_Z < (Pe_{\min})_L$). The magnitude of the Reynolds stress $\overline{\rho u_1'' u_1''}$ decays close to the wall due to viscous actions which lead to the decay of the magnitude of T_{K1} . The quantity $\partial \tilde{u}_1 / \partial x_1$ represents the resolved dilatation rate in the context of RANS of statistically planar flames, and its magnitude increases with decreasing Le due to stronger thermal expansion effects for smaller values of global Lewis number as a result of enhanced burning rate [40, 60, 151, 174, 1, 126, 163, 95, 170, 192, 30, 42, 93, 33]. Thus, the magnitude of the sink contribution of T_{K1} increases with decreasing Le . The viscous dissipation term T_{K4} remains the dominant sink in all locations, even at the near-wall region. The large magnitude of the dissipation rate of turbulent kinetic energy $\tilde{\epsilon}$ in the near-wall region (i.e. see Fig. 5.30) is responsible for the high magnitude of T_{K4} (see Eq. 2.48). The mean pressure gradient term T_{K2} acts as a leading order source within the flame brush away from the wall where the pressure gradient depends mainly on the density variation within the flame. The flame normal acceleration tends to induce a negative mean pressure gradient (i.e. $\partial \tilde{p} / \partial x_1 < 0$) across the flame brush. A high rate of heat release in flames with small values of

Le gives rise to strengthening of flame normal acceleration effects with decreasing global Lewis number. This leads to an increase in the magnitude of the negative mean pressure gradient $\partial\bar{p}/\partial x_1$ with decreasing Le . The term $\overline{u_1''}$ can be expressed as: $\overline{u_1''} \sim (\rho_0^{-1} - \rho_\infty^{-1})\overline{\rho u_1'' c''}/\bar{\rho}$ [145, 41, 40] (where ρ_∞ is the burned gas density), and thus the behaviour of the turbulent scalar flux $\overline{\rho u_1'' c''}$ affects the behaviour of T_{K2} . Furthermore, the turbulent scalar flux $\overline{\rho u_1'' c''}$ exhibits predominantly counter-gradient transport (i.e. $\overline{\rho u_1'' c''} > 0$ where $\partial\tilde{c}/\partial x_1 > 0$ in all cases considered here, which along with predominantly negative values of $\partial\bar{p}/\partial x_1$ gives rise to the positive contribution of the mean pressure gradient term T_{K2} . The magnitude of T_{K2} decreases significantly as the flame approaches the wall due to reduced magnitude of $\partial\bar{p}/\partial x_1$ as a result of flame quenching and diminishing magnitude of $\overline{u_1''}$ due to damping of turbulence in the near-wall region.

The pressure dilatation term T_{K3} and the pressure transport term T_{K5} exhibit both positive and negative values. The magnitudes of T_{K3} and T_{K5} remain comparable for all cases irrespective of the value of Le . The negative values of the pressure dilatation term T_{K3} are consistent with the previous DNS based findings [40], but are in contrast to the models proposed by Zhang and Rutland [215] and Nishiki *et al.* [145], which only predict positive values of T_{K3} proportional to $\tau^2 S_L^3 \rho_0 / \delta_{th}$. Thus improved models for the pressure dilatation term T_{K3} will be necessary. The effects of dilatation rate and pressure fluctuations due to heat release in the near-wall region weaken with the progress of flame quenching and consequently the magnitudes of T_{K3} and T_{K5} in the near-wall region (i.e. $x_1/\delta_Z < (Pe_{min})_L$) decrease with time. As the effects of dilatation rate and heat release induced pressure fluctuation strengthen with decreasing Le , the magnitudes of T_{K3} and T_{K5} also increase with decreasing global Lewis number. The magnitude of the turbulent transport term T_{K6} has been found to be smaller than the other terms in Eq. 2.46. It is evident from Fig. 5.32 that the sink contribution of T_{K4} remains the leading order contributor to \tilde{k} transport in the near-wall region and its magnitude overwhelms the positive contributions of other source terms, and thus, \tilde{k} decays significantly in the near-wall region.

5.5.3 Modelling of the mean velocity gradient term T_{K1}

The closure of T_{K1} depends on the modelling of the Reynolds stress $(-\overline{\rho u_i'' u_j''})$, which is usually modelled using the Boussinesq's hypothesis as [79, 162, 105, 210]:

$$\frac{\overline{\rho u_i'' u_j''}}{\bar{\rho}} = -\nu_t \left(\frac{\partial \tilde{u}_i}{\partial x_j} + \frac{\partial \tilde{u}_j}{\partial x_i} \right) + \frac{2}{3} \delta_{ij} \left(\nu_t \frac{\partial \tilde{u}_k}{\partial x_k} + \tilde{k} \right) \quad (5.7)$$

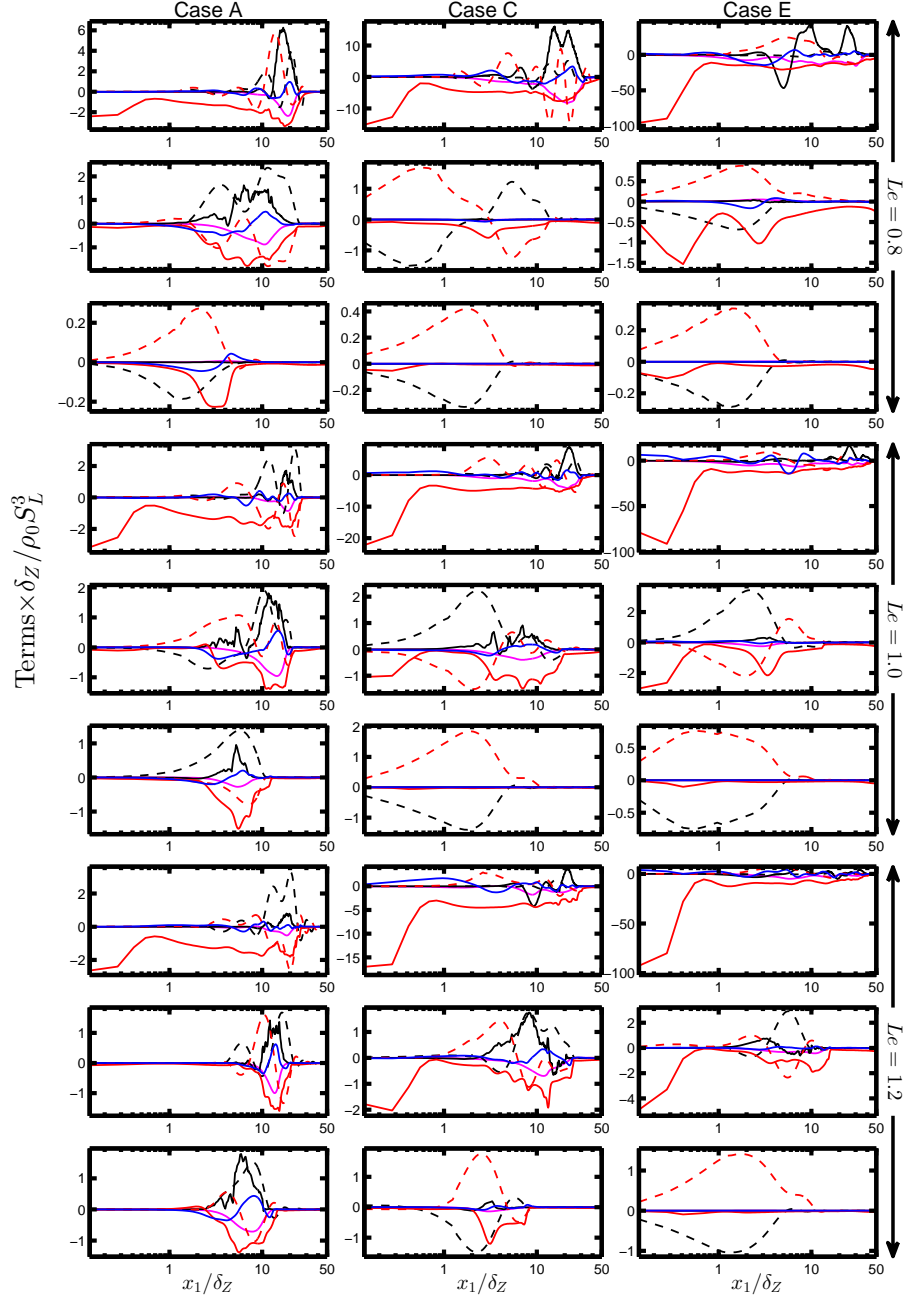


Fig. 5.32 Variations of term T_{K1} (—), T_{K2} (—), T_{K3} (— — —), T_{K4} (—), T_{K5} (— — —) and T_{K6} (—) with x_1/δ_Z for cases A, C and E (1st-3rd column) at $t = 2\delta_Z/S_L$, $6\delta_Z/S_L$ and $10\delta_Z/S_L$ (1st-3rd row). All terms are non-dimensionalised by $\rho_0 S_L^3/\delta_Z$.

where the eddy kinematic viscosity is given by $\nu_t = C_\mu \tilde{k}^2 / \tilde{\varepsilon}$ where $C_\mu = 0.09$ is the model constant. According to Eq. 5.7 the Reynolds stress $\overline{\rho u_1'' u_1''}$ in the direction of mean flame propagation is given by:

$$\frac{\overline{\rho u_1'' u_1''}}{\bar{\rho}} = -\frac{4}{3} \nu_t \frac{\partial \tilde{u}_1}{\partial x_1} + \frac{2}{3} \tilde{k} \quad (5.8)$$

The variations of $\widetilde{u_1'' u_1''} / S_L^2$ in the wall normal direction for cases A, C and E are shown in Fig. 5.33 along with the predictions of Eq. 5.8. It can be seen from Fig. 5.33 that Eq. 5.8 tends to underpredict the magnitude of $\widetilde{u_1'' u_1''} / S_L^2$ when the flame is away from the wall, but at later stages of flame-wall interaction Eq. 5.8 significantly overpredicts $\widetilde{u_1'' u_1''} / S_L^2$. At a given instant of time the flames with higher u' / S_L and smaller values of Le exhibit greater extent of flame-wall interaction, and thus the overprediction of $\widetilde{u_1'' u_1''} / S_L^2$ by Eq. 5.8 close to the wall is more prominent for case E and for $Le = 0.8$ than the cases with smaller u' / S_L (e.g. case A) and higher Le (e.g. $Le = 1.2$). By the same token, the underprediction of $\widetilde{u_1'' u_1''} / S_L^2$ by Eq. 5.8 away from the wall is more prominent for case A and for $Le = 1.2$ than the cases with higher u' / S_L (e.g. case E) and smaller Le (e.g. $Le = 0.8$).

According to Bray-Moss-Libby (BML) analysis [19], which assumes a bi-modal probability density function (PDF) of c , which assumes impulses at $c = 0$ and $c = 1.0$ leads to an alternative expression of $\overline{\rho u_i'' u_j''}$:

$$\frac{\overline{\rho u_i'' u_j''}}{\bar{\rho}} = (1 - \tilde{c}) \overline{(u_i' u_j')_R} + \tilde{c} \overline{(u_i' u_j')_P} + \frac{(\overline{\rho u_i'' c''})(\overline{\rho u_j'' c''})}{\bar{\rho}^2 \tilde{c} (1 - \tilde{c})} + O(1/Da) \quad (5.9a)$$

which leads to:

$$\frac{\overline{\rho u_1'' u_1''}}{\bar{\rho}} = (1 - \tilde{c}) \overline{(u_1'^2)_R} + \tilde{c} \overline{(u_1'^2)_P} + \frac{(\overline{\rho u_1'' c''})^2}{\bar{\rho}^2 \tilde{c} (1 - \tilde{c})} + O(1/Da) \quad (5.9b)$$

where $\overline{(u_1'^2)_R}$ and $\overline{(u_1'^2)_P}$ the conditionally averaged mean-squared velocity fluctuations in the x_1 -direction. The contribution $(1 - \tilde{c}) \overline{(u_1'^2)_R} + \tilde{c} \overline{(u_1'^2)_P}$ accounts for the influence of background fluid turbulence and $(\overline{\rho u_1'' c''})^2 / [\bar{\rho}^2 \tilde{c} (1 - \tilde{c})]$ is the contribution arising from flame normal acceleration. The last term on right hand side of Eqs. 5.9a and 5.9b originates from the interior of the flame and this contribution remains negligible for high Damköhler number (i.e. $Da \gg 1$) flames. Chakraborty *et al.* [40] modelled the

contribution of $(1 - \tilde{c})(\overline{u_1'^2})_R + \tilde{c}(\overline{u_1'^2})_P$ by Boussinesq's hypothesis as:

$$(1 - \tilde{c})(\overline{u_1'^2})_R + \tilde{c}(\overline{u_1'^2})_P = -\frac{4}{3} \frac{C_\mu}{\sigma_{Le}} \frac{\rho_0 \tilde{k}^2}{\bar{\rho} \tilde{\varepsilon}} \frac{\partial \tilde{u}_1}{\partial x_1} + \frac{2}{3} \tilde{k} \quad (5.10)$$

where ρ_0 is the unburned gas density and $\bar{\rho} \tilde{\varepsilon} / \rho_0$ the density-weighted dissipation rate which is used here to account for changes in the viscosity with temperature and $\sigma_{Le} = Le^{-1}$ is a turbulent Prandtl number which will be used to account for Lewis number effects. Furthermore, for a presumed bi-modal distribution of reaction progress variable with impulses at $c = 0$ and 1 yields $\overline{\rho c'' c''} = \bar{\rho} \tilde{c}(1 - \tilde{c}) + O(1/Da)$. This enabled Chakraborty *et al.* [40] to propose an alternative model:

$$\frac{\overline{\rho u_1'' u_1''}}{\bar{\rho}} = -\frac{4}{3} \frac{C_\mu}{\sigma_{Le}} \frac{\rho_0 \tilde{k}^2}{\bar{\rho} \tilde{\varepsilon}} \frac{\partial \tilde{u}_1}{\partial x_1} + \frac{2}{3} \tilde{k} + \frac{\overline{\rho u_1'' c''} \overline{\rho u_1'' c''}}{\bar{\rho} \overline{\rho c'' c''}} \quad (5.11)$$

The predictions of Eq. 5.11 are also shown in Fig. 5.33, which shows a better level of agreement with DNS data than the model given by Eq. 5.8 when the flame is away from the wall. However, the performance of the models given by Eqs. 5.8 and 5.11 remain mostly comparable in the near-wall region. Similar to Eq. 5.8 the model given by Eq. 5.11 also overpredicts $\widetilde{u_1'' u_1''}$ close to the wall during flame-wall interaction. This over-prediction originates due to simultaneous dampening of $\widetilde{u_1'' u_1''}$ and strengthening the magnitude of $\partial \tilde{u}_1 / \partial x_1$ close to the wall. This deficiency is addressed here by an adjustment to Eq. 5.11 in the following manner:

$$\frac{\overline{\rho u_1'' u_1''}}{\bar{\rho}} = Q_1 \left[-\frac{4}{3} \frac{C_\mu}{\sigma_{Le}} \frac{\rho_0 \tilde{k}^2}{\bar{\rho} \tilde{\varepsilon}} \frac{\partial \tilde{u}_1}{\partial x_1} + \frac{2}{3} \tilde{k} + \frac{\overline{\rho u_1'' c''} \overline{\rho u_1'' c''}}{\bar{\rho} \overline{\rho c'' c''}} \right] \quad (5.12)$$

where $Q_1 = 0.5[\text{erf}(x_1/\delta_Z - \Pi) + 1]$ is a damping function and the parameterised minimum Peclet number Π for turbulent flames is:

$$\Pi = (Pe_{\min})_L [\text{erf}(8 - 6.0Le) + 1] / 2 \quad (5.13)$$

with $(Pe_{\min})_L$ being the minimum Peclet number based on laminar head on quenching calculation. This parameterisation accounts for $\Pi < (Pe_{\min})_L$ ($\Pi \approx (Pe_{\min})_L$) for turbulent $Le < 1.0$ ($Le \geq 1.0$) cases, as observed in Fig. 5.3. The Q_1 asymptotically approaches unity away from the wall (i.e. $x_1/\delta_Z > (Pe_{\min})_L$) and thus Eq. 5.12 becomes identical to Eq. 5.11. The predictions of Eq. 5.12 in Fig. 5.33 reveals that this model does not overpredict $\widetilde{u_1'' u_1''}$ in the near-wall region and its performance is comparable to

Eq. 5.11 away from the wall. Thus, Eq. 5.12 performs better than the other alternative models. It is worth noting that the turbulent scalar flux $\overline{\rho u_1'' c''}$ in Eqs. 5.11 and 5.12 is also unclosed and needs modelling. The closure of $\overline{\rho u_1'' c''}$ for head-on quenching of turbulent premixed flames will be addressed later in this thesis.

5.5.4 Modelling of the mean pressure gradient term T_{K2}

The modelling of the mean pressure gradient term T_{K2} translates to the modelling of $\overline{u_i''}$. The quantity can be expressed as [145]:

$$\overline{u_i''} = \int_0^1 u_1'' P(c) dc = \int_0^1 \rho u_1'' \frac{P(c)}{\rho} dc \quad (5.14)$$

where $P(c)$ is the PDF of reaction progress variable. For unity Lewis number flames, the gas density can be expressed as [145]:

$$\frac{1}{\rho} = \frac{(1 + \tau c)}{\rho_0} = \frac{c}{\rho_\infty} + \frac{1 - c}{\rho_0} \quad (5.15)$$

Substituting Eq. 5.15 in Eq. 5.14 leads to the following expression proposed by Nishiki *et al.* [145]:

$$T_{K2} = -\frac{\tau}{\rho_0} \overline{\rho u_1'' c''} \frac{\partial \bar{p}}{\partial x_1} \quad (5.16)$$

Chakraborty *et al.* [40] modified the model given by Eq. 5.16 for non-unity Lewis number flames in the following manner:

$$T_{K2} = -\frac{\tau}{\rho_0} \left[f \overline{\rho u_1'' c''} + (1 - f) \overline{\rho u_1'' T''} \right] \frac{\partial \bar{p}}{\partial x_1} \quad \text{where } f = 0.5 \quad (5.17)$$

Figure 5.34 shows the comparison between the predictions of Eqs. 5.16 and 5.17 along with T_{K2} extracted from DNS for cases A, C and E at different time instants. The mean pressure gradient term T_{K2} starts from zero at the wall and its magnitude gradually increases toward the coming flame. Both Eqs. 5.16 and 5.17 predict T_{K2} in a satisfactory manner. However, non-negligible values of turbulent scalar flux $\overline{\rho u_1'' c''}$ leads to over-prediction of T_{K2} in the near-wall region by Eqs. 5.16 and 5.17. Therefore, the turbulent scalar flux $\overline{\rho u_1'' c''}$ contribution is required to be damped in the near-wall

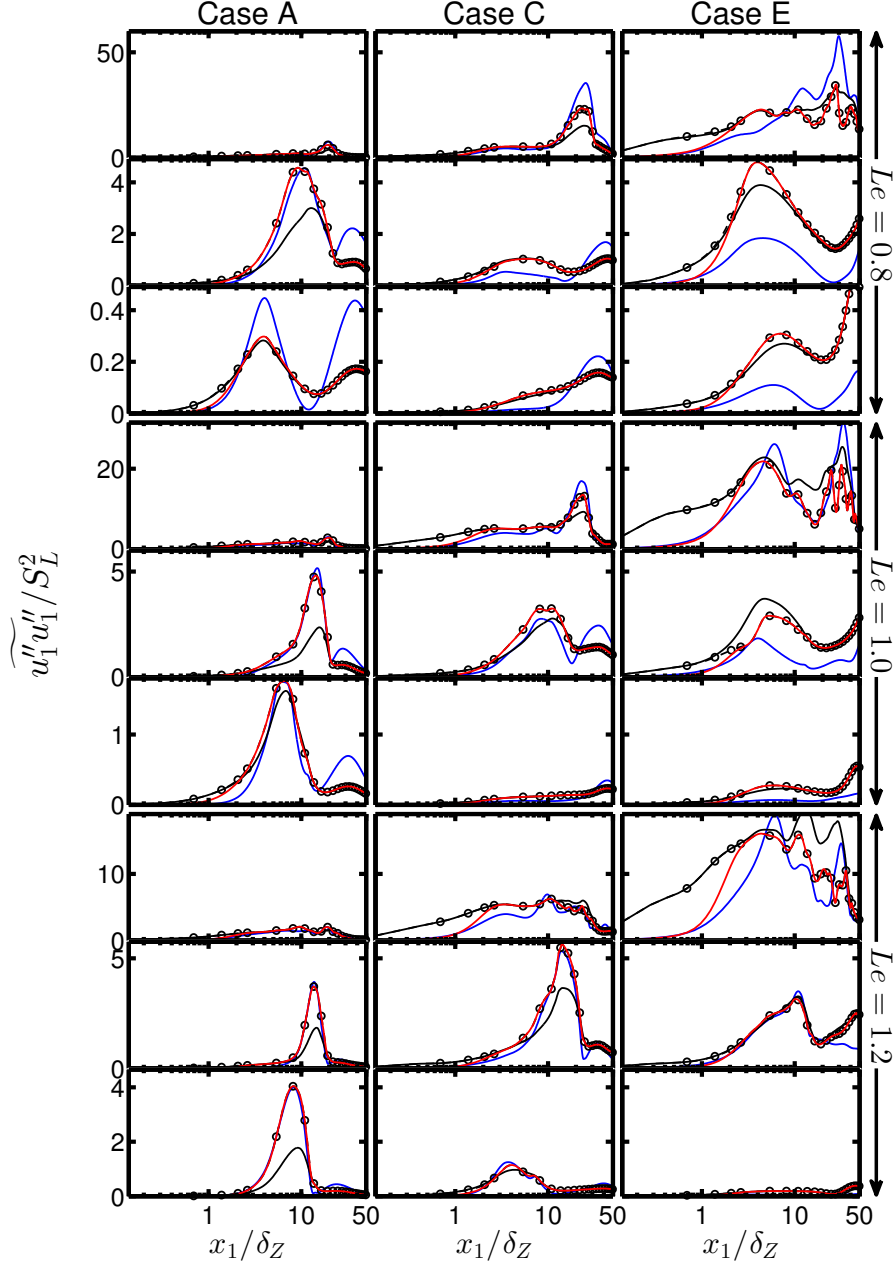


Fig. 5.33 Variations of $\widetilde{u_1''u_1''}/S_L^2$ from DNS data (—○—) and according to the predictions of Eq. 5.8 (—), Eq. 5.11 (—○—) and Eq. 5.12 (—) with x_1/δ_Z for cases A, C and E (1st-3rd column) at $t = 2\delta_Z/S_L$, $6\delta_Z/S_L$ and $10\delta_Z/S_L$ (1st-3rd row).

region. Thus, Eq. 5.17 is modified here in the following manner:

$$T_{K2} = -\frac{\tau}{\rho_0} \left[f_w \overline{\rho u_1'' c''} + (1-f) \overline{\rho u_1'' T''} \right] \frac{\partial \bar{p}}{\partial x_1} \quad \text{where } f_w = 0.5 \exp \left[-2 \left(\tilde{c} - \tilde{T} \right) \right] \quad (5.18)$$

Equation 5.18 approaches Eq. 5.17 away from the wall where $\tilde{c} \approx \tilde{T}$. This can be substantiated from Fig. 5.34 which shows that Eq. 5.18 predicts T_{K2} satisfactorily for both close to and away from the wall. Moreover, the performance of Eq. 5.18 remains comparable to Eqs. 5.16 and 5.17 away from the wall.

5.5.5 Modelling of the pressure dilatation term T_{K3}

Figure 5.35 presents the variations of the pressure dilatation term T_{K3} with x_1/δ_Z . It can be seen that the contribution of T_{K3} changes sign across the flame brush but predominantly assumes positive values when the flame is away from the wall. However, negative contribution of T_{K3} can be found in the near-wall region as flame approaches the wall in all cases. According to Zhang and Rutland [215] the pressure dilatation term T_{K3} can be expressed in the following manner:

$$T_{K3} = \overline{p' \frac{\partial u_i''}{\partial x_i}} = \frac{1}{V} \int_V p' \frac{\partial u_i''}{\partial x_i} dV = \frac{1}{V} \int_S \int p' \frac{u_i''}{\partial x_i} d\xi dS \quad (5.19)$$

where dS and dV denote the elemental surface and volume elements, ξ is the local flame normal direction, and $\Sigma = |\nabla c|$ is the generalised Flame Surface Density (FSD) [12]. The pressure dilatation rate term T_{K3} is given by: $T_{K3} = \langle I \rangle_s \Sigma$ where I is given by:

$$I = \int_\delta (p - \bar{p}) \left(\frac{du_n}{d\xi} - \frac{\partial \tilde{u}_i}{\partial x_i} \right) d\xi \quad (5.20)$$

where u_n is the velocity component in the flame normal direction. A one-dimensional analysis of fluid flow in the flame normal direction yields the following relation:

$$p = p_R - \rho_0 u_R (u_n - u_R) \quad (5.21)$$

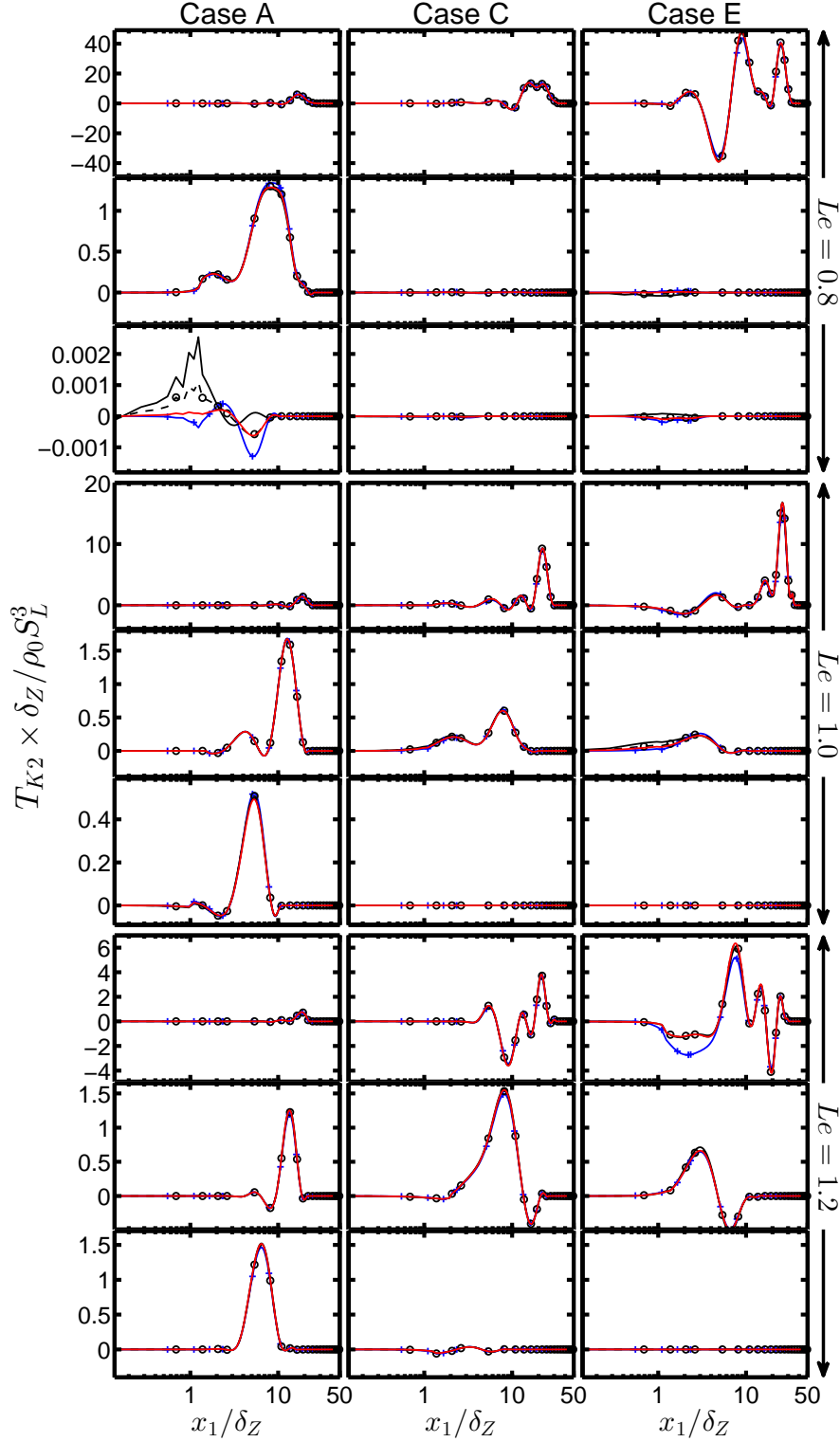


Fig. 5.34 Variations of $T_{K2} \times \delta_Z / \rho_0 S_L^3$ from DNS (— + —) and according to the predictions of Eq. 5.16 (—), Eq. 5.17 (— o —) and Eq. 5.18 (—) with x_1 / δ_Z for cases A, C and E (1st-3rd column) at $t = 2\delta_Z / S_L$, $6\delta_Z / S_L$ and $10\delta_Z / S_L$ (1st-3rd row).

the subscript R is used to denote the values in the unburned reactants. Equation 5.21 yields:

$$\langle I \rangle_s = \langle (p_R - \bar{p})\Delta u \rangle_s - 0.5 \langle \rho_0 u_R (\Delta u)^2 \rangle_s - \langle (p - \bar{p})(\partial \tilde{u}_i / \partial x_i) \delta \rangle_s \quad (5.22)$$

where δ is a length scale characterising the flame thickness. The pressure drop $(p_R - \bar{p})$ remains positive for positive values of Δu , which leads to a positive contribution of $\langle (p_R - \bar{p})\Delta u \rangle_s$ throughout the flame brush. The second term on the right-hand side of Eq. 5.22 is a negative term. For the unity Lewis number flames the following scalings can be used [215]:

$$\langle (p_R - \bar{p})\Delta u \rangle_s \sim \tau^2 \rho_0 S_L^3; \langle \rho_0 u_R (\Delta u)^2 \rangle_s \sim \tau^2 \rho_0 S_L^3 \quad (5.23)$$

where $(p_R - \bar{p})$ is scaled with respect to the pressure drop across the laminar flame (i.e. $\tau^2 \rho_0 S_L^3$) and the quantities Δu and $\rho_0 u_R$ are scaled using $\Delta u \sim \tau S_L$ and $\rho_0 u_R \sim \rho_0 S_L$ for the unity Lewis number flames. The last term on the right-hand side of Eq. 5.22 scales in the following manner for the unity Lewis number flames:

$$\langle (p - \bar{p})(\partial \tilde{u}_i / \partial x_i) \delta \rangle_s \sim \tau \rho_0 S_L^3 \left(\frac{U_{\text{mean}}}{u'} \right) Da^{-1} \quad (5.24)$$

Here, $(p - \bar{p})$ and $(\partial \tilde{u}_i / \partial x_i)$ are scaled as $\tau \rho_0 S_L^2$ and U_{mean}/l respectively with U_{mean} being the characteristic mean velocity scale. Thus, the last term on the right hand side of Eq. 5.22 remains negligible in comparison to the other terms for high Damköhler number Da flames. However, this contribution may not be negligible for low Da flames.

Zhang and Rutland [215] utilised the scalings given by Eq. 5.23 to model the pressure dilatation term T_{K3} (stated as PDZ model) in the following manner:

$$T_{K3} = \frac{1}{2} C_Z \rho_0 S_L^3 \tau^2 \bar{\omega} \quad (5.25)$$

where C_Z is a model parameter with a value equal to 1.35. Nishiki *et al.* [145] proposed an alternative model (stated as PDN model) as:

$$T_{K3} = C_N S_L^2 \tau^2 \bar{\omega} \quad (5.26)$$

where C_N is equal to 0.35 and $\bar{\omega}$ is the mean reaction rate of reaction progress variable. It is worth noting that Eqs. 5.25 and 5.26 only predict the positive values of T_{K3} whereas negative values of T_{K3} can be observed from Fig. 5.35. Furthermore, Eqs. 5.25 and 5.26 were proposed for unity Lewis number flames. Chakraborty *et al.* [40] proposed a model which take into the consideration of Lewis number effects and the possibility of negative value of T_{K3} , which is expressed as (i.e. PDC model):

$$T_{K3} = \bar{\omega} \left[\frac{(1 + \tau)\tilde{c}}{(1 + \tau\tilde{c})} - \frac{1}{2} \right] [f(Le)\tau S_L]^2 - C_c D_0 \frac{\bar{\omega}}{S_L} \frac{\partial \tilde{u}_k}{\partial x_k} [f(Le)\tau S_L] \quad (5.27)$$

where $f(Le) = \exp[Le^{-n} - 1]$ with $n = 0.5$ and $C_c = 0.1$ is a model constant. In the derivation of Eq. 5.27 the quantities $\langle (p_R - \bar{p})\Delta u \rangle_s \Sigma$ and $\langle \rho_0 u_R (\Delta u)^2 \rangle_s \Sigma$ are scaled as:

$$\langle (p_R - \bar{p})\Delta u \rangle_s \Sigma \sim \bar{\omega} \frac{(1 + \tau)\tilde{c}}{(1 + \tau\tilde{c})} [f(Le)\tau S_L]^2; \quad \langle \rho_0 u_R (\Delta u)^2 \rangle_s \Sigma \sim \bar{\omega} [f(Le)\tau S_L]^2 \quad (5.28)$$

where $(p_R - \bar{p})$ is scaled as: $(p_R - \bar{p}) \sim \bar{\omega}(1 + \tau)\tilde{c}/(1 + \tau\tilde{c})\rho_0 u_R \Delta u$ according to Domingo and Bray [74], whereas Δu and $\rho_0 u_R$ are estimated as: $\Delta u \sim f(Le)\tau S_L$ and $\rho_0 u_R \sim \bar{\omega}/\Sigma$ respectively where $f(Le)$ is a function of Lewis number which accounts for strengthening of flame normal acceleration with decreasing Lewis number. The term $\langle (p - \bar{p})(\partial \tilde{u}_i / \partial x_i) \delta \rangle_s \Sigma$ in the PDC model is approximated as:

$$\langle (p - \bar{p})(\partial \tilde{u}_i / \partial x_i) \delta \rangle_s \Sigma = C_{T3} D_0 \frac{\bar{\omega}}{S_L} \frac{\partial \tilde{u}_k}{\partial x_k} [f(Le)\tau S_L] \quad (5.29)$$

Both PDZ and PDN models assume a situation where $p_R > \bar{p}$ which associates the pressure drop across the flame brush only due to flame normal acceleration, and it predicts positive values of T_{K3} . However, it has been demonstrated by Chakraborty *et al.* [40] that the negative values of T_{K3} is obtained at the flame front location which states $p_R < \bar{p}$. These effects are neglected by the PDZ and PDN models. Both the PDZ and PDN models do not adequately capture the qualitative behaviour of T_{K3} for all cases considered here and predict the wrong sign close to the wall. The absence of $\bar{\omega}$ in the near-wall region due to flame quenching severely damps the predictions of the PDN and PDC models, whereas T_{K3} assumes non-negligible magnitude close to the wall. Since, the PDC model provides the best performance among all these models, in terms of qualitative and quantitative agreements with DNS data away from the wall,

this model has been considered here for the modification in the near-wall region:

$$T_{K3} = \rho_0 S_L \Sigma \left[\frac{(1 + \tau)\tilde{c}}{1 + \tau\tilde{c}} - \frac{1}{2} \exp(1.2\tilde{c}_w) \right] [f(Le)\tau S_L]^2 - C_4 D_0 \rho_0 \Sigma \frac{\partial \tilde{u}_k}{\partial x_k} [f(Le)\tau S_L] \quad (5.30)$$

The quantity $[(1 + \tau)\tilde{c}/(1 + \tau\tilde{c}) - 1/2]$ in the PDC model plays an important role in the prediction of negative values of T_3 . In the near-wall region, the contribution of $\langle \rho_0 u_R (\Delta u)^2 \rangle_s$ is expected to be greater than the contribution arising from flame normal acceleration because no-slip condition at the wall sets up a stronger $\langle \rho_0 u_R (\Delta u)^2 \rangle_s$ than in a freely propagating flame away from the wall. This aspect is accounted for by the factor $\exp(1.2\tilde{c}_w)$ where \tilde{c}_w is the value of \tilde{c} at the wall and $\exp(1.2\tilde{c}_w)$ becomes identically equal to 1.0 when the flame is away from the wall when $\tilde{c}_w = 0$. Furthermore, $\bar{\omega}$ in the PDC model has been replaced by $\rho_0 S_L \Sigma$, because $\bar{\omega}$ vanishes for $x_1/\delta_Z < Pe_{\min}$ due to flame quenching, but Σ assumes non-zero values even at the wall. It can be seen from Fig. 5.35 that the model given by Eq. 5.30 satisfactorily predicts T_3 both close to and away from the wall.

5.5.6 Modelling of the molecular diffusion and dissipation contribution T_{K4}

The variations of T_{K4} , $\nabla \cdot (\mu \nabla \tilde{k})$, $(-\bar{\rho}\tilde{\epsilon})$ and T_V in the wall normal direction are shown in Fig. 5.36 for cases A, C and E. Figure 5.36 shows that $(-\bar{\rho}\tilde{\epsilon})$ remains the major contributor to T_{K4} and the magnitude of T_V remain smaller than $(-\bar{\rho}\tilde{\epsilon})$ for all cases considered here. The magnitude of T_V remain insignificant in comparison to the magnitudes of $\nabla \cdot (\mu \nabla \tilde{k})$ and $(-\bar{\rho}\tilde{\epsilon})$ in the near-wall region. Moreover, the magnitude of $\nabla \cdot (\mu \nabla \tilde{k})$ remains insignificant in comparison to $(-\bar{\rho}\tilde{\epsilon})$ away from the wall but these contributions become comparable in the near-wall region. The term T_V acts as a sink term, which is consistent with the earlier findings [215, 145, 40]. The magnitudes of T_{K4} , $\nabla \cdot (\mu \nabla \tilde{k})$, $(-\bar{\rho}\tilde{\epsilon})$ and T_V diminish with time subsequent to flame quenching.

Nishiki *et al.* [145] estimated the order of magnitude of T_V as:

$$T_V = u_i'' \frac{\partial}{\partial x_k} \left(\mu \frac{\partial u_k''}{\partial x_i} \right) - \frac{2}{3} u_i'' \frac{\partial}{\partial x_i} \left(\mu \frac{\partial u_k''}{\partial x_k} \right) \sim O(-\rho_0 \tau S_L^2 \sqrt{\tilde{k}} \Sigma) \quad (5.31a)$$

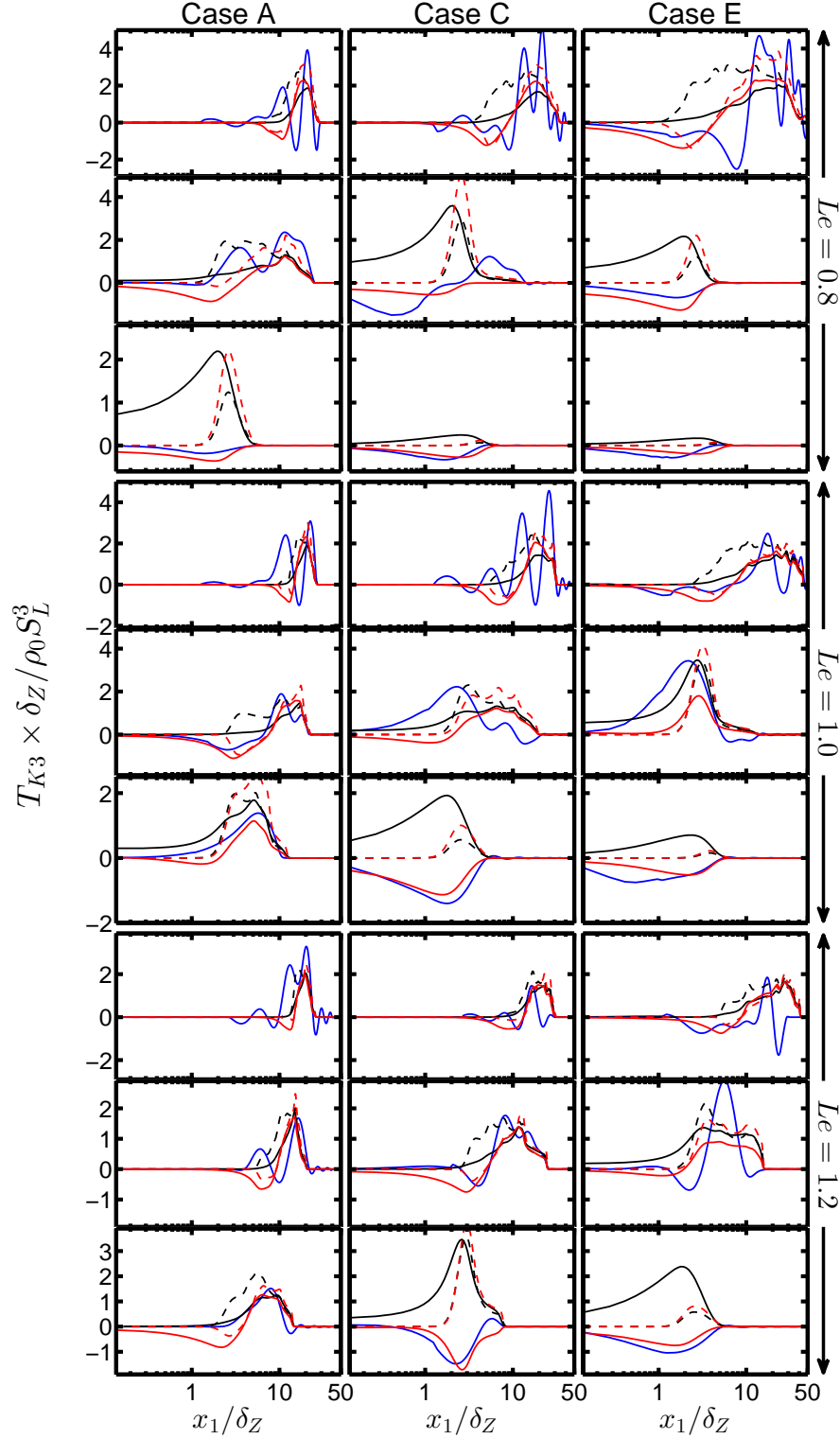


Fig. 5.35 Variations of $T_{K3} \times \delta_Z / \rho_0 S_L^3$ from DNS (—) and according to the predictions of PDZ (—), PDN (---), PDC (---) and Eq. 5.30 (—) with x_1 / δ_Z for cases A, C and E (1st-3rd column) at $t = 2\delta_Z/S_L, 6\delta_Z/S_L$ and $10\delta_Z/S_L$ (1st-3rd row).

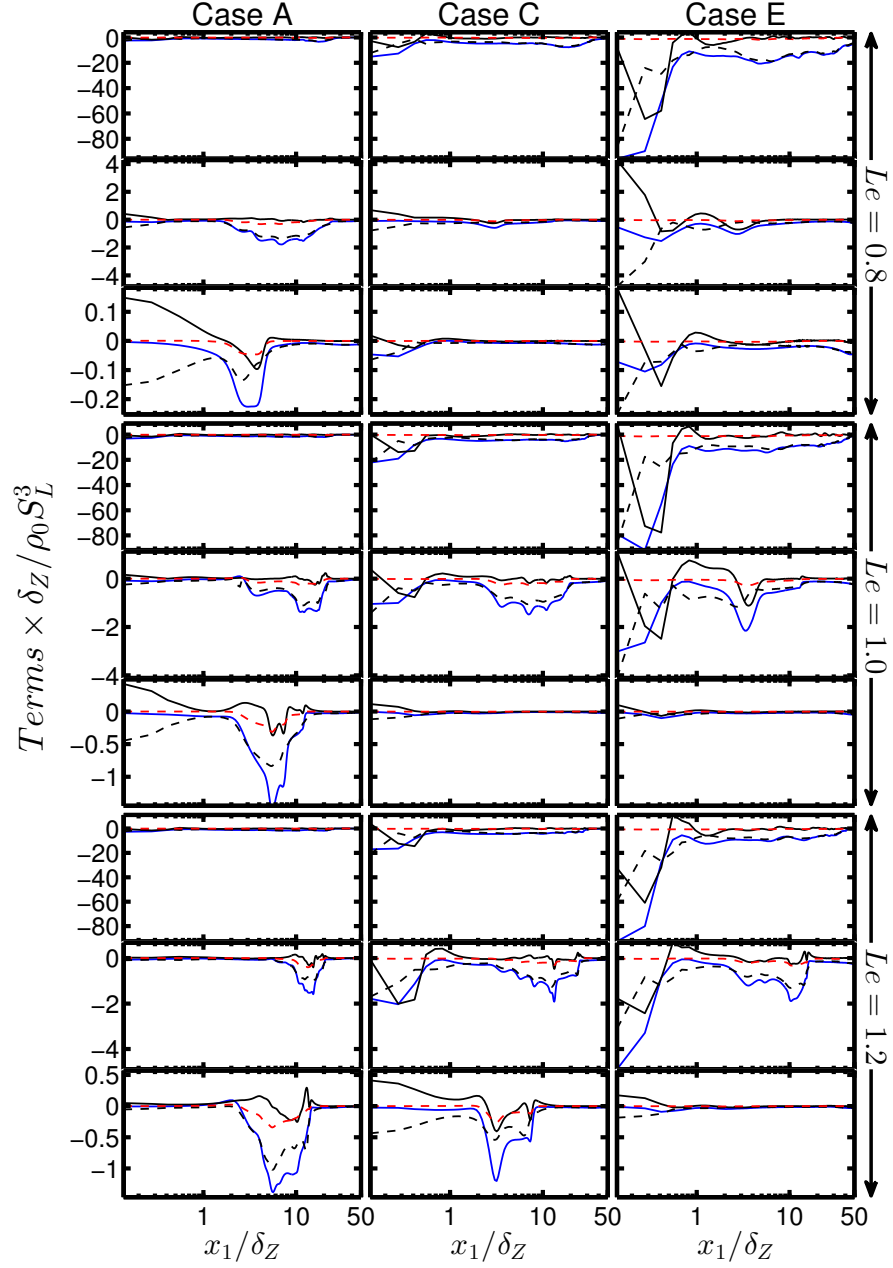


Fig. 5.36 Variations of $T_{K4} \times \delta_Z / \rho_0 S_L^3$ (—), $\nabla \cdot (\mu \cdot \nabla \tilde{k}) \times \delta_Z / \rho_0 S_L^3$ (—), $(-\bar{\rho} \tilde{\varepsilon}) \times \delta_Z / \rho_0 S_L^3$ (---) and $T_V \times \delta_Z / \rho_0 S_L^3$ (---) with x_1 / δ_Z for cases A, C and E (1st-3rd column) at $t = 2\delta_Z / S_L$, $6\delta_Z / S_L$ and $10\delta_Z / S_L$ (1st-3rd row).

where u_i'' , μ and $\partial u_k''/\partial x_k$ are scaled using $\sqrt{\tilde{k}}$, $\rho_0 S_L \delta_{th}$ and $\tau S_L \Sigma \sim \tau S_L / \delta_{th}$ respectively. This yields the following model for T_V according to Nishiki *et al.* [145]:

$$T_V = -C_{add} \rho_0 \tau S_L^2 \sqrt{\tilde{k}} \Sigma \quad (5.31b)$$

where C_{add} is a model constant which is taken to be 0.25. In Eq. 5.31b the spatial derivative of $\partial u_k''/\partial x_k$ is scaled with respect to δ_{th} . This scaling may not be valid only in the thin reaction zones regime as the effects of dilatation rate is not likely to be confined in a thin region. As a result of better mixing in the thin reaction zones regime it can be assumed that the spatial derivative of $\partial u_k''/\partial x_k$ is scaled with respect to the flame brush thickness which can be scaled using the integral length scale (i.e. $1/|\nabla \tilde{c}| \sim l \sim \tilde{k}^{1.5}/\tilde{\varepsilon}$), which leads to an alternative order of magnitude estimate for T_V :

$$T_V \sim O(-\tilde{\varepsilon} \mu_0 \Delta u_s / \tilde{k} \delta_{th}) \quad (5.31c)$$

where μ_0 is the dynamic viscosity in the reactants and $\partial u_k''/\partial x_k$ is scaled as: $\partial u_k''/\partial x_k \sim \Delta u_s / \delta_{th}$ where Δu_s represents an appropriate slip velocity which is taken to be $\Delta u_s = \tau S_L / Le^r$ (where $r > 0$) as the effects of dilatation rate strengthen with decreasing Lewis number. This suggests that the order of magnitude estimate presented in Eq. 5.31c can be rewritten as:

$$T_V = -O(\rho_0 \tau S_L^2 \sqrt{\tilde{k}} \Sigma Le^{-r} Re_t^{-0.5} Da^{-0.5}) \quad (5.31d)$$

Chakraborty *et al.* [40] utilised Eq. 5.31d to propose an alternative model:

$$T_V = -C_{VM} \frac{\tilde{\varepsilon}}{\tilde{k}} \mu_0 \tau S_L \frac{\tilde{c}^p (1 - \tilde{c})^q}{Le^r \delta_{th}} \quad (5.31e)$$

where $C_{VM} = 0.32$ is a model constant, and $p = 3.33 - 2.45Le$, $q = 0.64 + 0.78Le$ and $r = 3.0$ are the model parameters. The predictions of the models given by Eqs. 5.31b and 5.31e are compared to T_V obtained from DNS data in Fig. 5.37. The model given by Eq. 5.31b overpredicts the magnitude of T_V away from the wall for cases with high u'/S_L (e.g. case E). By contrast, Eq. 5.31e satisfactorily predicts the magnitude of T_V in cases A-C but significantly underpredicts the magnitude of T_V in case E when the flame is away from the wall. However, Eq. 5.31e severely overpredicts the magnitude

of T_V close to the wall. The combination of large magnitude of $\tilde{\varepsilon}$ and small value of \tilde{k} reduces the local turbulent Reynolds number $Re_t = \rho_0 \tilde{k}^2 / \tilde{\varepsilon} \mu_0$ in the near-wall region. Moreover chemical activity weakens due to flame quenching close to the wall, which is expected to be reflected in the drop of local Damköhler number $Da \propto \tilde{k} S_L / \tilde{\varepsilon} \delta_{th}$ in the near-wall region. A comparison between Eqs. 5.31a and 5.31c reveals that the prediction of Eq. 5.31e is likely to yield greater magnitudes of T_V than Eq. 5.31b. Here the models given by Eqs. 5.31a and 5.31b have been combined to propose the following expression according to the suggestion by Chakraborty *et al.* [41]:

$$T_V = E_3 \left\{ -f(Ka_L) C_{add} \tau \tilde{k}^{1/2} S_L \bar{\omega} - E_1 [1 - f(Ka_L)] C_{VM} \frac{\tilde{\varepsilon}}{\tilde{k}} \mu_0 \tau S_L \frac{\tilde{c}^p (1 - \tilde{c})^q}{Le_r \delta_L} \right\} \quad (5.32)$$

where $f(Ka_L) = \exp(-1.92 \times 0.5^{E_2} \times [Ka_L / (1 + Ka_L)]^{1.83})$, $E_1 = 0.5\{erf[x_1/\delta_Z - 0.5\exp(\tilde{c}_w - \tilde{T}_w)\Pi] + 1\}$, $E_2 = 1 - 0.5[erf(x_1/\delta_Z - 10) + 1]$ and $E_3 = \exp[-Le(\tilde{c} - \tilde{T})]$ with $Ka_L = (\tilde{\varepsilon} \delta_{th})^{0.5} S_L^{-1.5}$ being the local Karlovitz number. The function $f(Ka_L)$ increases increasing local Karlovitz number Ka_L which ensures the contribution of Eq. 5.31b (Eq. 5.31e) weakens (strengthens) with increasing Ka_L and *vice versa*. The parameter E_1 damps the large magnitude of $(\tilde{\varepsilon}/\tilde{k})$ close to the wall, whereas E_3 damps the overall magnitude of the model expression close to the wall. It can be seen from Fig. 5.37 that Eq. 5.32 predicts T_V more satisfactorily than Eqs. 5.31b and 5.31e. However, Eq. 5.32 does not adequately predict T_V at all locations, but the magnitude of T_V remains small in comparison to the leading order contributions of $(-\bar{\rho}\tilde{\varepsilon})$ so the modelling inaccuracies of T_V are unlikely to play an important role in modelling \tilde{k} transport.

5.5.7 Modelling of the pressure transport term T_{K5}

The pressure transport term T_{K5} is often stated as:

$$T_{K5} = -\frac{\overline{\partial(p'u_i'')}}{\partial x_i} = -\overline{u_i'' \frac{\partial p'}{\partial x_i}} = -\overline{p' \frac{\partial u_i''}{\partial x_i}} = -\overline{u_i'' \frac{\partial p'}{\partial x_i}} - T_{K3} \quad (5.33)$$

where the term $-\overline{u_i'' \partial p' / \partial x_i}$ is called the fluctuating pressure gradient term. In order to model T_{K5} , it will be easier to model the fluctuating pressure gradient term $-\overline{u_i'' \partial p' / \partial x_i}$, since T_{K3} as been discussed in the previous section. Launder *et al.* [123] proposed a

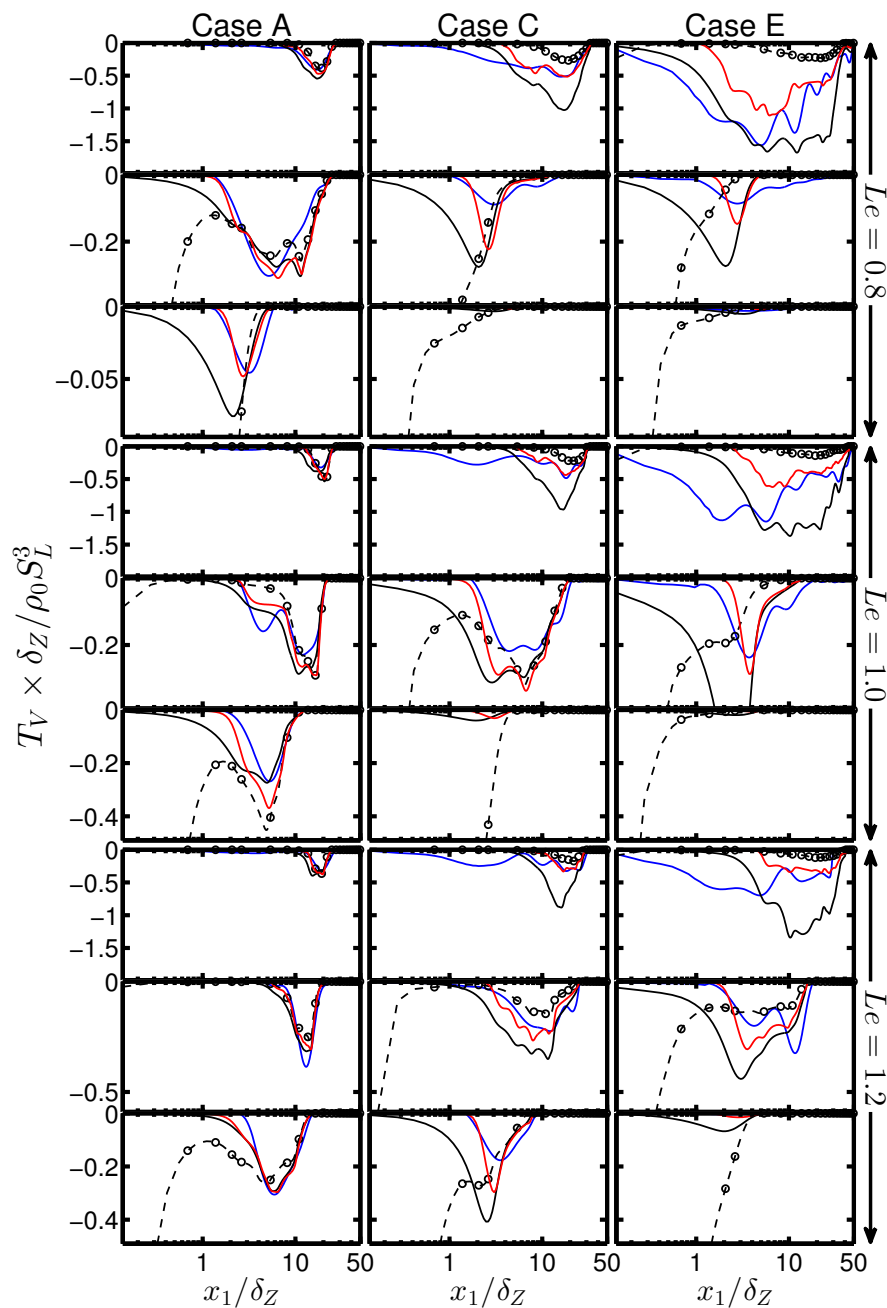


Fig. 5.37 Variations of $T_V \times \delta_Z / \rho_0 S_L^3$ from DNS data (—), Eq. 5.31b (—), Eq. 5.31e (— o —) and Eq. 5.32 (—) with x_1 / δ_Z for cases A, C and E (1st-3rd column) at $t = 2\delta_Z / S_L$, $6\delta_Z / S_L$ and $10\delta_Z / S_L$ (1st-3rd row).

model (denoted as the PTL model) for $-\overline{u''_i \partial p' / \partial x_i}$ which is given as:

$$-\overline{u''_i \frac{\partial p'}{\partial x_i}} = C_L \overline{\rho u''_i u''_j} \frac{\partial \tilde{u}_i}{\partial x_j} - C_{L2} \bar{\rho} \tilde{\varepsilon} \quad (5.34)$$

where $C_L = 1.5$ and $C_{L2} = 0.2$ are the model constants. According to Strahle [181] the term $-\overline{u''_i \partial p' / \partial x_i}$ can be modelled as (denoted as the PTS model):

$$-\overline{u''_i \frac{\partial p'}{\partial x_i}} = \frac{1}{2} C_{st} \overline{\rho u''_i u''_j} \frac{\partial \tilde{u}_i}{\partial x_j} \quad (5.35)$$

where C_{st} is the order of unity. The model proposed by Zhang and Rutland [215] (PTZR) is given by:

$$-\overline{u''_i \frac{\partial p'}{\partial x_i}} = \frac{1}{2} \rho_0 S_L^3 \Sigma \tau^3 \frac{(\tilde{c}(1 - \tilde{c}))}{(1 + \tau)} \quad (5.36)$$

Domingo and Bray [74] provided a model for the quantity $-\overline{u''_i \partial p / \partial x_i} = T_2 - \overline{u''_i \partial p' / \partial x_i}$ in the following manner for strict flamelet combustion (i.e. $Da \gg 1$):

$$\begin{aligned} -\overline{u''_i \frac{\partial p}{\partial x_i}} &= -\frac{\overline{\rho u''_i c''}}{\bar{\rho}(1 + \tau \tilde{c})} \left[-\frac{\partial \bar{p}_R}{\partial x_i} + (1 + \tau) \frac{\partial \bar{p}_P}{\partial x_i} \right] - \frac{(1 - \tilde{c})}{(1 + \tau \tilde{c})} \overline{u'_{R,i} \frac{\partial p'_R}{\partial x_i}} \\ &\quad - \frac{(1 + \tilde{c})}{(1 + \tau \tilde{c})} \overline{u'_{P,i} \frac{\partial p'_P}{\partial x_i}} + \frac{1}{2} \rho_0 \tau S_L^2 \Sigma < \vec{N} \cdot \vec{M}_i > \frac{\overline{\rho u''_i c''}}{\bar{\rho}(1 - \tilde{c})} \\ &\quad + 0.35 \rho_0 \tau^2 S_L^3 \Sigma < \vec{N} \cdot \vec{M}_i > < \vec{N} \cdot \vec{M}_i > \end{aligned} \quad (5.37)$$

where the subscripts R and P refer to conditional values in reactants and products respectively, $\vec{N} = -\nabla c / |\nabla c|$ is the local flame normal vector and \vec{M}_i is the component of unit vector describing the mean flame propagation. The value of $< \vec{N} \cdot \vec{M}_i >$ varies between -0.5 to -0.3 in the present cases which is consistent with earlier findings [74]. The conditional values in reactants and products are evaluated using samples corresponding to $0 \leq c \leq 0.1$ and $0.9 \leq c \leq 1.0$ respectively, following previous analyses [40, 74]. The prediction of (Eq. 5.37– T_{K2}) is referred to as the PTDB model in Fig. 5.38. Chakraborty *et al.* [40] extended the PTDB model for $Da < 1$ combustion (denoted as

the PTNKC model) as:

$$\begin{aligned}
-\overline{u_i'' \frac{\partial p'}{\partial x_i}} &= -g \frac{\overline{\rho u_i'' c''}}{\bar{\rho}(1 + \tau \tilde{c})} \left[-\frac{\partial \bar{p}_R}{\partial x_i} + (1 + \tau \frac{\partial \bar{p}_P}{\partial x_i}) \right] - g \frac{(1 - \tilde{c})}{(1 + \tau \tilde{c})} \overline{u_{R,i}' \frac{\partial p'_R}{\partial x_i}} \\
&\quad - g \frac{(1 + \tilde{c})}{(1 + \tau \tilde{c})} \overline{u_{P,i}' \frac{\partial p'_P}{\partial x_i}} + g \frac{1}{2} \rho_0 \tau S_L^2 \Sigma < \vec{N} \cdot \vec{M}_i > \frac{\overline{\rho u_i'' c''}}{\bar{\rho}(1 - \tilde{c})} \\
&\quad + 0.35 g \rho_0 \tau^2 S_L^3 \Sigma < \vec{N} \cdot \vec{M}_i > < \vec{N} \cdot \vec{M}_i > \\
&\quad + (1 - g) C_{1N} \overline{\rho u_i'' u_j''} \frac{\partial \tilde{u}_i}{\partial x_j} - (1 - g) C_{2N} \bar{\rho} \tilde{\varepsilon} + \frac{g \tau}{\rho_0} \left[f \overline{\rho u_i'' c''} + (1 - f) \overline{\rho u_i'' T''} \right] \frac{\partial \bar{p}}{\partial x_i}
\end{aligned} \tag{5.38}$$

where $g = \tilde{c}''^2 / \tilde{c}(1 - \tilde{c})$ is the segregation factor and $C_{1N} = 1.05$, $C_{2N} = 0.14$ and $f = 0.5$ are the model parameters. The PTDB model is valid for the reactive region in the corrugated flamelets regime whereas the model PTL was suggested for the non-reacting flows. A linear bridging model based on segregation factor $g = \tilde{c}''^2 / \tilde{c}(1 - \tilde{c})$ is used in the PTNKC model.

Figure 5.38 presents the variations of $-\overline{u_i'' \partial p' / \partial x_i}$ with x_1 / δ_Z for cases A, C and E. Figure 5.38 shows the PTNKC model has an advantage over the other alternative models in terms of the prediction of $-\overline{u_i'' \partial p' / \partial x_i}$ from DNS data when the flame is far away from the wall. The PTL and PTS models do not sufficiently capture the qualitative and quantitative behaviours of $-\overline{u_i'' \partial p' / \partial x_i}$, whereas the PTZR and PTDB models to some extent capture the qualitative behaviour of $-\overline{u_i'' \partial p' / \partial x_i}$. It is worth noting that the agreement between the PTZR model and DNS data improves as the flame approaches the wall. The contribution of $(-\bar{\rho} \tilde{\varepsilon})$ in the PTL and PTNKC models is responsible for large negative values in the near-wall region, whereas DNS data shows negligible values of $-\overline{u_i'' \partial p' / \partial x_i}$ close to the wall. Here, the PTKNC and PZR models

have been combined here to propose a new model as:

$$\begin{aligned}
-\overline{u_i'' \frac{\partial p'}{\partial x_i}} &= -g^* \frac{\overline{\rho u_i'' c''}}{\bar{\rho}(1+\tau\tilde{c})} \left[-\frac{\partial \bar{p}_R}{\partial x_i} + (1+\tau) \frac{\partial \bar{p}_P}{\partial x_i} \right] - g^* \frac{(1-\tilde{c})}{(1+\tau\tilde{c})} \overline{u'_{R,i} \frac{\partial p'_R}{\partial x_i}} \\
&\quad - g^* \frac{(1+\tilde{c})}{(1+\tau\tilde{c})} \overline{u'_{P,i} \frac{\partial p'_P}{\partial x_i}} + g^* \frac{1}{2} \rho_0 \tau S_L^2 \Sigma < \vec{N} \cdot \vec{M}_i > \frac{\overline{\rho u_i'' c''}}{\bar{\rho}(1-\tilde{c})} \\
&\quad + 0.35 g^* \rho_0 \tau^2 S_L^3 \Sigma < \vec{N} \cdot \vec{M}_i > < \vec{N} \cdot \vec{M}_i > \\
&\quad + \left[(1-g) C_{1N} \overline{\rho u_i'' u_j''} \frac{\partial \tilde{u}_i}{\partial x_j} - (1-g) C_{2N} \bar{\rho} \tilde{\varepsilon} \right] f_{err} + \left[0.1 \rho_0 S_L^3 \Sigma \tau^3 \frac{\tilde{c}(1-\tilde{c})}{(1+\tau)} \right] (1-f_{err}) \\
&\quad + \frac{g\tau}{\rho_0} \left[f \overline{\rho u_i'' c''} + (1-f) \overline{\rho u_i'' T''} \right] \frac{\partial \bar{p}}{\partial x_i}
\end{aligned} \tag{5.39}$$

where g^* and f_{err} are given as:

$$g^* = \exp(\tilde{c}_w - \tilde{T}_w) \left[\frac{\tilde{c}''^2}{\tilde{c}(1-\tilde{c})} \right]^{0.5 \left[\text{erf} \left(\frac{x_1}{\delta_Z} - 10 \right) + 1 \right]}; \quad f_{err} = 0.5 [\text{erf}(x_1/\delta_Z - \Pi) + 1] \tag{5.40}$$

The PTKNC model underpredicts the magnitude of $-\overline{u_i'' \partial p / \partial x_i}$ in the near-wall region due to the negligible value of the segregation factor g in that zone [141, 18]. The $\exp(\tilde{c}_w - \tilde{T}_w)$ dependence of g^* increases the magnitude of the prediction of the PTDB model as $(\tilde{c}_w - \tilde{T}_w)$ increases as the flame quenching progresses (because \tilde{c}_w remains zero away from the wall but it approaches unity as the flame quenching progresses, whereas $T_w = 0$ at the isothermal wall). The satisfactory performance of the PTZR model in the near-wall region is utilised to add the contribution of $[0.1 \rho_0 S_L^3 \Sigma \tau^3 \tilde{c}(1-\tilde{c})/(1+\tau)](1-f_{err})$ in the model expression given by Eq. 5.40 to provide an accurate prediction in the region given by $x_1/\delta_Z < Pe_{\min}$. It can be seen in Fig. 5.38 that Eq. 5.40 provides the better qualitative and quantitative agreements with DNS data than the other alternative model expressions.

5.5.8 Modelling of the turbulent transport term T_{K6}

The closure of the turbulent transport term T_{K6} translates to the modelling of $\overline{\rho u_i'' k} = \overline{\rho u_i'' u_j'' u_j''}/2$, which in turn boils down to the closure of $\overline{\rho u_1'' k} = \overline{\rho u_1'' u_j'' u_j''}/2$ for statistically

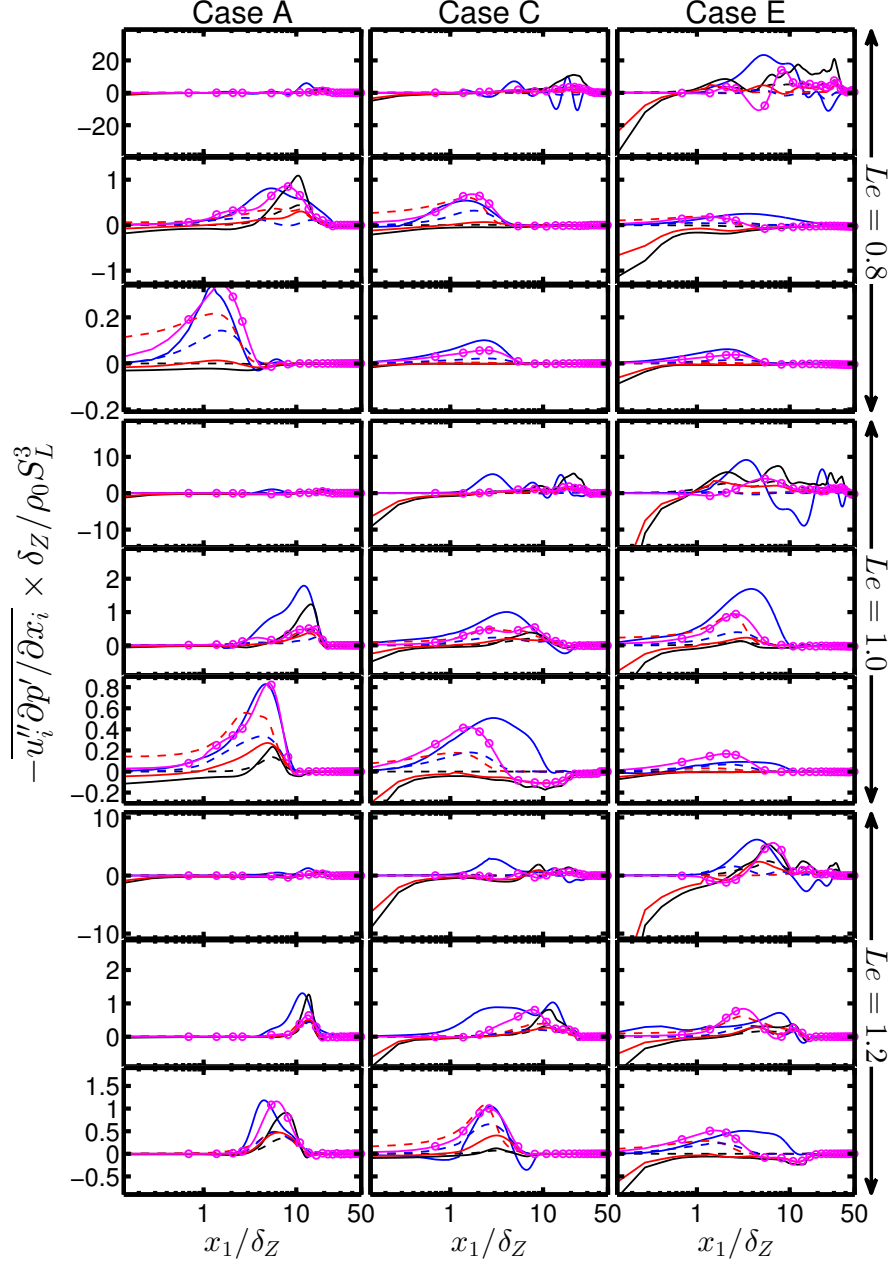


Fig. 5.38 Variations of $-\overline{u''_i \partial p' / \partial x_i} \times \delta_Z / \rho_0 S_L^3$ from DNS data (—), PTL (—), PTS (— —), PTZR (— —), PTDB (— —), PTNKC (— —) and Eq. 5.39 (— ○ —) with x_1 / δ_Z with x_1 / δ_Z for cases A, C and E (1st-3rd column) at $t = 2\delta_Z / S_L$, $6\delta_Z / S_L$ and $10\delta_Z / S_L$ (1st-3rd row).

planar flames. According to Bray-Moss-Libby (BML) analysis [19] one gets:

$$\begin{aligned} \overline{\rho u_1'' k} &= \frac{\overline{\rho u_1'' u_j'' u_j''}}{2} = \bar{\rho} \{ (1 - \tilde{c}) \overline{u'_{1R} k_R} + \tilde{c} \overline{u'_{1P} k_P} + \tilde{c} (1 - \tilde{c}) (\bar{u}_{1P} - \bar{u}_{1R}) (\bar{k}_P - \bar{k}_R) \\ &\quad + \frac{1}{2} \tilde{c} (1 - \tilde{c}) (\bar{u}_{1P} - \bar{u}_{1R})^3 (1 - 2\tilde{c}) \} \end{aligned} \quad (5.41a)$$

where $\bar{k}_R = \overline{u'_{1R} u'_{1R}}/2$ and $\bar{k}_P = \overline{u'_{1P} u'_{1P}}/2$ are the conditional values of the turbulent kinetic energy in reactants and products respectively. The contribution $\bar{\rho} \{ (1 - \tilde{c}) \overline{u'_{1R} k_R} + \tilde{c} \overline{u'_{1P} k_P} \}$ represents the non-reacting contribution to the unclosed turbulent flux of turbulent kinetic energy. In the case of non-reacting turbulent flows $\overline{\rho u_1'' k}$ is usually modelled using a gradient hypothesis in the following manner [79, 210]:

$$\overline{\rho u_1'' k} = -\bar{\rho} C_{T1} \frac{\tilde{k}^2}{\tilde{\varepsilon}} \frac{\partial \tilde{k}}{\partial x_1} \quad (5.41b)$$

The same approach can be applied for the closure of the non-reacting contribution $\bar{\rho} \{ (1 - \tilde{c}) \overline{u'_{1R} k_R} + \tilde{c} \overline{u'_{1P} k_P} \}$ as [41, 40]:

$$\bar{\rho} \{ (1 - \tilde{c}) \overline{u'_{1R} k_R} + \tilde{c} \overline{u'_{1P} k_P} \} = -\bar{\rho} C_{T2} \frac{\tilde{k}^2}{\tilde{\varepsilon}} \frac{\partial \tilde{k}}{\partial x_1} \quad (5.41c)$$

According to BML analysis [19] the slip velocity $(\bar{u}_{1P} - \bar{u}_{1R})$ in Eq. 5.41a can be expressed as:

$$(\bar{u}_{1P} - \bar{u}_{1R}) = \frac{\overline{\rho u_1'' c''}}{\rho c''^2} \quad (5.41d)$$

Chakraborty *et al.* [41, 40] modelled the difference in the mean turbulent kinetic energy between products and reactants as:

$$(\bar{k}_P - \bar{k}_R) = -C_{T3} \frac{1}{\Sigma} M_i \frac{\partial \tilde{k}}{\partial x_i} \quad (5.41e)$$

where $M_i = -(\partial \tilde{c} / \partial x_i) / |\nabla \tilde{c}|$ is the resolved flame normal vector component in the i^{th} direction. Combining Eqs. 5.41a, 5.41c, 5.41d, 5.41e yields [41, 40]:

$$\overline{\rho u_1'' k} = -\bar{\rho} C_{T2} \frac{\tilde{k}^2}{\tilde{\varepsilon}} \frac{\partial \tilde{k}}{\partial x_1} - C_{T3} \overline{\rho u_1'' c''} \frac{1}{\Sigma} M_i \frac{\partial \tilde{k}}{\partial x_i} + \frac{1}{2(\rho c''^2)^2} (\overline{\rho u_1'' c''})^3 (1 - 2\tilde{c}) \quad (5.41f)$$

It is worth noting that the BML analysis assumes a bi-modal probability density function (pdf) of c with impulses at $c = 0$ and $c = 1$ but it has been demonstrated elsewhere [119, 120] and in the next chapter that the pdf of c does not remain bi-modal in the near-wall region. Chakraborty *et al.* [40] modified Eq. 5.41f for the conditions where pdf of c shows a departure from bi-modal distribution in the following manner:

$$\overline{\rho u_1'' k} = -\bar{\rho} C_{T2} \frac{\tilde{k}^2}{\tilde{\varepsilon}} \frac{\partial \tilde{k}}{\partial x_1} - C_{T3} \overline{\rho u_1'' c''} \frac{1}{\Sigma} M_i \frac{\partial \tilde{k}}{\partial x_i} + \frac{1}{2(\overline{\rho c''^2})^2} (\overline{\rho u_1'' c''})^3 (1 - 2\tilde{c}g^s) \quad (5.41g)$$

where $g = \tilde{c}^2 / (\tilde{c}(1 - \tilde{c}))$ is the segregation factor which assumes a value of unity for bi-modal distribution with impulses at $c = 0$ and $c = 1$ and it becomes increasingly smaller than unity for increasing deviation of the pdf of c from a bi-modal distribution. Chakraborty *et al.* [40] suggested $C_{T2} = 0.22$, $C_{T3} = 1.0$ and $s = 2$ for the model parameters.

The predictions of $-\mu_t(\partial \tilde{k} / \partial x_1)$ (where $\mu_t = 0.09\bar{\rho}(\tilde{k}^2 / \tilde{\varepsilon})$), Eqs. 5.41f and 5.41g are compared to $\overline{\rho u_i'' k}$ extracted from DNS data in Fig. 5.39. In non-reacting turbulent flows $\overline{\rho u_1'' u_j'' u_j''} / 2$ is often modelled as $\overline{\rho u_1'' u_j'' u_j''} / 2 = -(\mu_t / \delta_k)(\partial \tilde{k} / \partial x_1)$ using a gradient hypothesis [79, 105, 210]. It has been found that both $\overline{\rho u_1'' u_j'' u_j''} / 2$ and $-\mu_t(\partial \tilde{k} / \partial x_1)$ assume the same sign in the near-wall region (i.e. $0 < x_1 / \delta_Z < (Pe_{\min})_L$) in all cases. However, $\overline{\rho u_1'' u_j'' u_j''} / 2$ and $-\mu_t(\partial \tilde{k} / \partial x_1)$ assume opposite signs at some locations within the flame brush when the flame is away from the wall, and this behaviour is more prevalent in the $Le = 0.8$ case than in the $Le \geq 1.0$ cases because the strong flame normal acceleration in a low Lewis number flame is more likely to overwhelm the effects of turbulent velocity fluctuations to give rise to counter-gradient transport [41, 40]. The effects of flame normal acceleration weaken due to flame quenching, and thus the gradient transport dominates in the near-wall region.

Equations 5.41f and 5.41g are more successful in capturing the qualitative behaviour of $\overline{\rho u_1'' k}$ extracted from DNS data than the gradient hypothesis model (i.e. Eq. 5.41b) when the flame is away from the wall and quantitative agreement with DNS data is marginally better for Eq. 5.41g than in Eq. 5.41f. However, in the near-wall region, Eqs. 5.41f and 5.41g start to over-predict by large margin, and at the advanced stage of quenching, no models predict the correct sign and magnitude of turbulent flux of kinetic energy $\overline{\rho u_1'' k}$. In order to capture the near-wall behaviour of $\overline{\rho u_1'' k}$ Eq. 5.41g has been modified here in the following manner:

$$\overline{\rho u_1'' k} = \alpha_4 \left[-\bar{\rho} C_{T2} \frac{\tilde{k}^2}{\tilde{\varepsilon}} \frac{\partial \tilde{k}}{\partial x_1} - C_{T3} \overline{\rho u_1'' c''} \frac{1}{\Sigma} M_i \frac{\partial \tilde{k}}{\partial x_i} + \frac{1}{2(\overline{\rho c''^2})^2} (\overline{\rho u_1'' c''})^3 (1 - 2\tilde{c}g^s) \right] \quad (5.42)$$

where $C_{T3W} = [(-2)^{\alpha_2} \exp(\tilde{c}_w)]^{\alpha_1}$ with $a_1 = 1 - 0.5[\operatorname{erf}(x_1/\delta_Z - \Pi) + 1]$ and $a_2 = 0.5[\operatorname{erf}(\tilde{c}_w - 0.55Le) + 1]$ and $a_4 = 0.5[\operatorname{erf}(x_1/\delta_Z - \exp(-\tilde{c}_w)\Pi) + 1]$. The modification of C_{T3W} allows for dampening of turbulent kinetic energy close to the wall. The model parameter a_2 makes sure that the modification of C_{T3} becomes active only at an advanced stage of quenching and a_1 restricts the region of modification close to the wall. The model parameter a_4 ensures the magnitude of $\overline{\rho u_1'' k}$ is adequately captured. The predictions of Eq. 5.42 are shown in Fig. 5.39 which reveals that the predictions of Eq. 5.42 are in better agreement with $\overline{\rho u_1'' k}$ from DNS than the other model expressions. However, the level of agreement between DNS data and the prediction of Eq. 5.42 is relatively better for $Le = 1.0$ and 1.2 cases than the $Le = 0.8$ cases. It can be seen from Fig. 5.39 that Eq. 5.42 does not adequately capture the qualitative/quantitative behaviour of $\overline{\rho u_1'' k}$ at some instants of time (e.g. at $t = 10\delta_Z/S_L$ for case A and at $t = 2\delta_Z/S_L$ and $6\delta_Z/S_L$ for case E). It has been shown in Fig. 5.32 that T_{K6} remains small in comparison to the leading order contributors to turbulent kinetic energy \tilde{k} transport so the modelling inaccuracies of $\overline{\rho u_1'' k}$ may not have a significant role in modelling \tilde{k} transport.

5.5.9 Summary of the key results

The statistical behaviour and modelling of the transport of turbulent kinetic energy in the case of head-on quenching of turbulent premixed flames by an isothermal inert wall have been investigated. The turbulent kinetic energy decays significantly in the vicinity of the wall, whereas its dissipation rate increases close to the wall. It has been found that the mean pressure gradient term T_{K2} remains the leading order source for all cases whereas the viscous contribution T_{K4} acts as a leading order sink. The contributions arising from mean velocity gradient and turbulent transport (i.e. T_{K1} and T_{K5}) remain negligible in comparison to the magnitude of the viscous contribution T_{K4} for all cases considered here. The magnitudes and the strengths of mean pressure gradient and pressure dilatation terms (i.e. T_{K2} and T_{K3}) decrease with increasing Lewis number due to the weakening of burning rate and flame normal acceleration. The pressure dilatation and pressure transport terms (i.e. T_{K2} and T_{K3}) have been found to play significant roles in the turbulent kinetic energy transport, and the behaviours of T_{K3} , T_{K4} , T_{K5} and T_{K6} have been found to be significantly affected by the presence of the wall. Furthermore, the turbulent flux of kinetic energy has been found to exhibit counter-gradient behaviour, and the extent of counter-gradient transport weakens with increasing Lewis number Le . The existing models for T_{K3} , T_{K4} , T_{K5} and T_{K6} have been assessed in comparison to the corresponding terms extracted from explicitly Reynolds

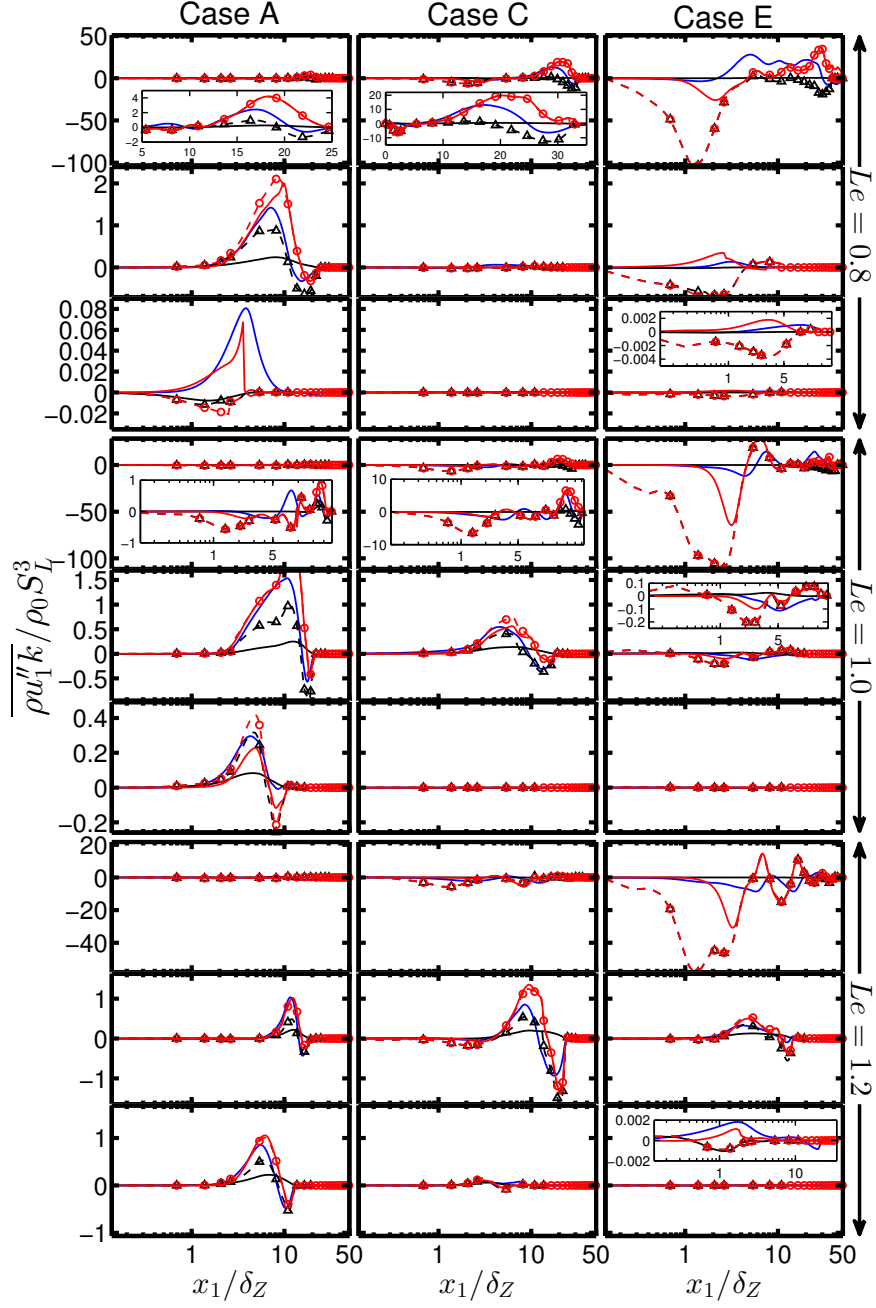


Fig. 5.39 Variations of $\overline{\rho u_1'' k} / \rho_0 S_L^3$ from DNS data (—), $(-\mu_t \partial \tilde{k} / \partial x_1) / \rho_0 S_L^3$ (—), Eq. 5.41f (— \triangle —), Eq. 5.41g (— \circ —) and Eq. 5.42 (—) with x_1 / δ_Z for cases A, C and E (1st-3rd column) at $t = 2\delta_Z / S_L$, $6\delta_Z / S_L$ and $10\delta_Z / S_L$ (1st-3rd row).

averaged DNS data and it has been found that the existing models for T_{K3} , T_{K4} , T_{K5} and T_{K6} need modification in order to provide satisfactory prediction in the vicinity of the wall. Modifications to the existing model expressions which yield satisfactory performance away from the wall have been suggested so that they predict the behaviour of DNS data both away from and close to the wall.

5.6 Statistical analysis and modelling of the scalar variance transport

The main investigation of the current section is statistical analysis and modelling of the progress variable variance $\widetilde{c''^2}$ transport (see below).

$$\frac{\partial \bar{\rho} \widetilde{c''^2}}{\partial t} + \frac{\partial \bar{\rho} \widetilde{u_j c''^2}}{\partial x_j} = \underbrace{\frac{\partial}{\partial x_j} \left[\rho D \frac{\partial \widetilde{c''^2}}{\partial x_j} \right]}_{D_{1v}} - \underbrace{\frac{\partial \bar{\rho} u'' c''^2}{\partial x_j}}_{T_{1v}} - \underbrace{2 \bar{u_j''} c'' \frac{\partial \widetilde{c}}{\partial x_j}}_{T_{2v}} + \underbrace{2(\bar{\omega} \widetilde{c} - \bar{\omega} \widetilde{c})}_{T_{3v}} - \underbrace{2 \bar{\rho} \widetilde{\varepsilon_c}}_{D_{2v}} \quad (5.43)$$

D_{1v} turbulent transport term

T_{1v} generation/destruction by the mean scalar gradient

T_{2v} pressure dilatation term

T_{3v} reaction rate contribution term

D_{2v} molecular dissipation term

It yields to the primary objectives of current section to:

- To identify the near-wall effects on the statistical behaviour of the unclosed terms of the scalar variance $\widetilde{c''^2}$ transport equation.
- To propose modifications to the existing models of the unclosed terms of the $\widetilde{c''^2}$ transport equation in order to account for the near-wall behaviour.

5.6.1 Statistical Behaviour of the Variance $\widetilde{c''^2}$ Transport

The variations of T_{1v} , T_{2v} , T_{3v} and $(-D_{2v})$ with normalised wall normal distance x_1/δ_Z are shown in Fig. 5.40 for all the cases considered here. The following observations can be made from the variations of T_{1v} , T_{2v} , T_{3v} and $(-D_{2v})$ with x_1/δ_Z for all cases considered here:

- For all cases, the reaction rate term T_{3v} and the molecular dissipation term $(-D_{2v})$ remain leading order source and sink terms respectively in the $\widetilde{c''^2}$ transport equation when the flame is away from the wall. The magnitudes of both the terms decrease with time as flame starts to quench. The terms T_{3v} and $(-D_{2v})$ remain of the same order of magnitude away from the wall but T_{3v} vanishes in the region given by $x_1/\delta_Z < Pe_{\min}$ due to flame quenching, whereas $(-D_{2v})$ continues to act as a dominant sink term even when T_{3v} disappears. However, $(-D_{2v})$ eventually vanishes when the flame is completely quenched.

- The mean scalar gradients term T_{1v} shows negative values close to the wall but assumes positive values away from the wall during early stages of flame quenching. However, T_{1v} assumes positive values in the near-wall region and negative values away from the wall as a result of the reversal of flow direction (after quenching the flow is directed towards the wall in contrast to the flow away from the wall before quenching) at later stages of flame quenching.
- One obtains the following scaling estimates of T_{1v} , T_{2v} , T_{3v} and $(-D_{2v})$ according to the scaling arguments of Swaminathan and Bray [185]:

$$\begin{aligned} T_{1v} &\sim O\left(\frac{\rho_0 S_L}{\delta_{th}}; \frac{1}{\sqrt{Re_t Da}}\right); & T_{2v} &\sim O\left(\frac{\rho_0 S_L}{\delta_{th}}; \frac{1}{\sqrt{Re_t Da}}\right); \\ T_{3v} &\sim O\left(\frac{\rho_0 S_L}{\delta_{th}}; 1\right); & D_{2v} &\sim O\left(\frac{\rho_0 S_L}{\delta_{th}}; 1\right) \end{aligned} \quad (5.44)$$

where the gas density is scaled using the unburned gas density ρ_0 , the turbulent velocity fluctuations associated with scalar fluctuations are scaled using the unstrained laminar burning velocity S_L , the mean gradients are scaled using the turbulence integral length scale l and the length scale associated with gradient of fluctuating quantities is scaled using the flame thickness δ_{th} . In Eq. 5.44, $\dot{\omega}$ is scaled as $\dot{\omega} \sim \rho_0 S_L / \delta_{th}$. It can be seen from Fig. 5.40 that the magnitudes of the turbulent transport and mean scalar gradient terms T_{1v} and T_{2v} remain smaller than those of T_{3v} and $(-D_{2v})$ especially when the flame is away from the wall before flame, which is consistent with the scaling estimates presented in Eq. 5.44. Furthermore, it can be seen from Fig. 5.40 that the magnitudes of T_{3v} and $(-D_{2v})$ increase with decreasing Le , which is consistent with previous findings by Chakraborty and Swaminathan [50].

5.6.2 Modelling of Turbulent Transport of Scalar Variances

According to BML [19] for high Damköhler number and unity Lewis number flames the joint pdf between velocity vector \vec{u} and reaction progress variable c can be expressed as:

$$P(\vec{u}, c) = \alpha_c P_R(\vec{u}, 0) + \beta_c P_P(\vec{u}, 1) + \gamma_c f(\vec{u}, c) [H(c) - H(c - 1)] \quad (5.45)$$

where α_c , β_c and γ_c are the weights associated with the pdf contributions, $P_R(\vec{u}, 0)$ and $P_P(\vec{u}, 1)$ are the conditional velocity pdfs in reactants and products respectively,

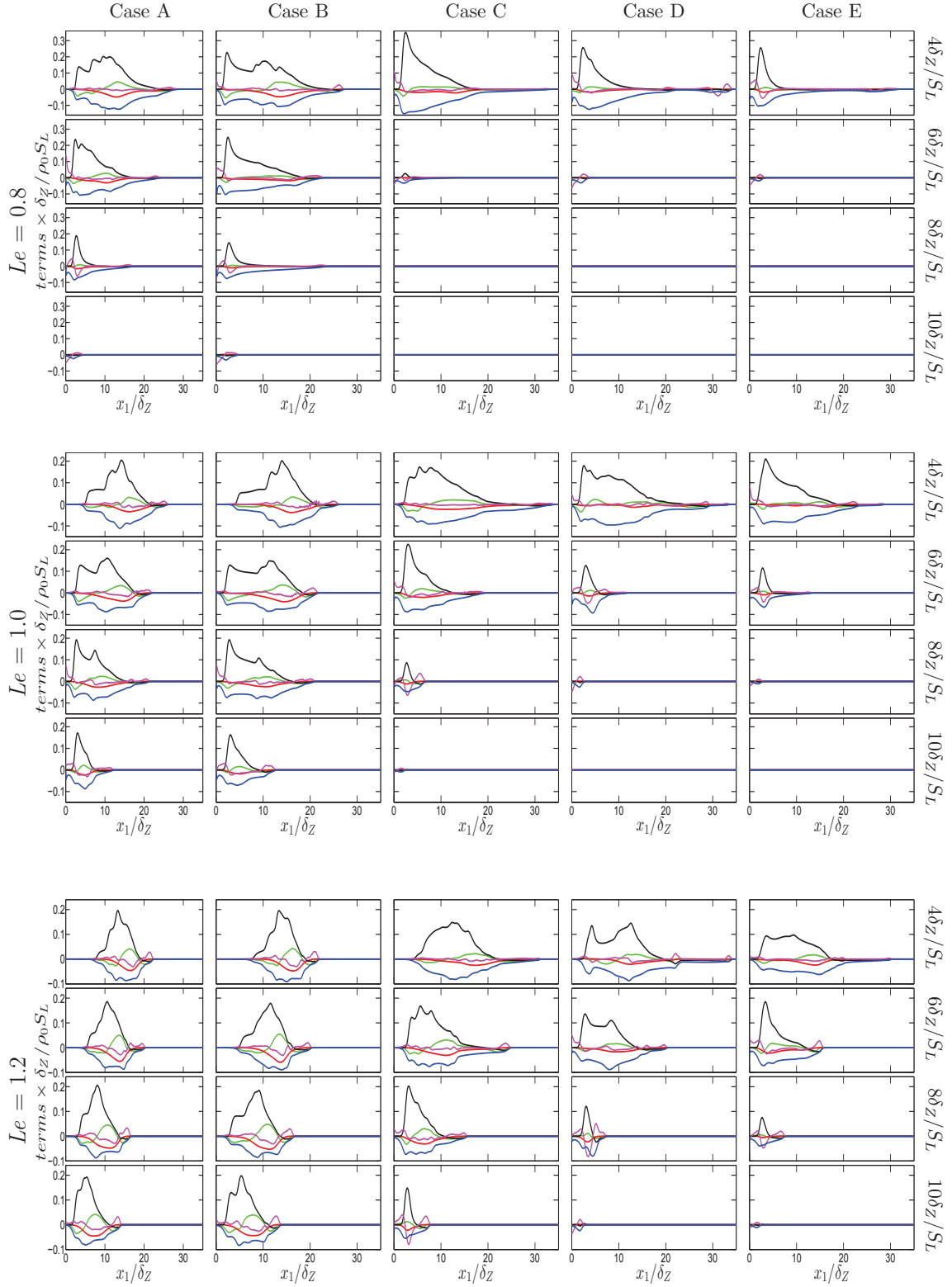


Fig. 5.40 Variations of T_{1v} (—), T_{2v} (—), T_{3v} (—), D_{1v} (—), $(-D_{2v})$ (—) with x_1/δ_Z at $t = 4\delta_Z/S_L$, $6\delta_Z/S_L$, $8\delta_Z/S_L$, $10\delta_Z/S_L$ for turbulent cases A - E with $Le = 0.8$, 1.0 and 1.2 .

$f(\vec{u}, c)$ originates from the interior of the flame. For high Damköhler number flames the third contribution can be ignored and in the case of unity Lewis number flames one gets: $\alpha_c = (1 - \tilde{c})/(1 + \tau\tilde{c})$ and $\beta_c = (1 + \tau)\tilde{c}/(1 + \tau\tilde{c})$ [19]. Based on Eq. 5.45 one gets the following expressions for high Damköhler number (i.e. $Da \gg 1$ flames [19]:

$$\begin{aligned}
\bar{\rho}\tilde{u}_i &= \int_{-\infty}^{\infty} \int_0^1 \rho u_i P(\vec{u}, c) dc du_i = (1 - \tilde{c})\overline{(u_i)_R} + \tilde{c}\overline{(u_i)_P} + O(\gamma_c) \\
\overline{\rho u_i'' c''} &= \int_{-\infty}^{\infty} \int_0^1 \rho (u_i - \tilde{u}_i)(c - \tilde{c}) P(\vec{u}, c) dc du_i \\
&= \bar{\rho}\tilde{c}(1 - \tilde{c})[\overline{(u_i)_P} - \overline{(u_i)_R}] + O(\gamma_c) \\
\overline{\rho u_i'' c''^2} &= \int_{-\infty}^{\infty} \int_0^1 \rho (u_i - \tilde{u}_i)(c - \tilde{c})^2 P(\vec{u}, c) dc du_i \\
&= \bar{\rho}\tilde{c}(1 - \tilde{c})(1 - 2\tilde{c})[\overline{(u_i)_P} - \overline{(u_i)_R}] + O(\gamma_c) = \overline{\rho u_i'' c''}(1 - 2\tilde{c}) + O(\gamma_c)
\end{aligned} \tag{5.46}$$

where $\overline{(u_i)_R}$ and $\overline{(u_i)_P}$ are the i^{th} components of mean velocity conditional on reactants and products respectively. The last terms on the right hand side of Eq 5.46 can be ignored for $Da \gg 1$. Chakraborty and Swaminathan [50] demonstrated that $\overline{\rho u_i'' c''}(1 - 2\tilde{c})$ does not adequately predict $\overline{\rho u_i'' c''^2}$ obtained from DNS data for low Damköhler number (i.e. $Da < 1$) combustion and proposed an alternative model as:

$$\overline{\rho u_i'' c''^2} = \overline{\rho u_i'' c''} \left(1 - 2\tilde{c} \left[\frac{\widetilde{c''^2}}{\tilde{c}(1 - \tilde{c})} \right]^m \right) \frac{2\widetilde{c''^2}}{\widetilde{c''^2} + \tilde{c}(1 - \tilde{c})} \tag{5.47}$$

where $m = 0.3$ is a model parameter. It is worth to noting that $O(\gamma_c)$ contribution for low Damköhler number (i.e. $Da < 1$) combustion is represented by $2\widetilde{c''^2}/[\widetilde{c''^2} + \tilde{c} \cdot (1 - \tilde{c})]$ in Eq. 5.47. The term $[\widetilde{c''^2}/\tilde{c}(1 - \tilde{c})]^m$ accounts for transition of $\overline{\rho u_i'' c''^2}/\overline{\rho u_i'' c''}$ from positive to negative value at the proper \tilde{c} location. Moreover, $g = \widetilde{c''^2}/\tilde{c}(1 - \tilde{c})$ becomes unity for high Damköhler number (i.e. $Da \gg 1$) combustion (because $\widetilde{c''^2} \approx \tilde{c}(1 - \tilde{c})$) and thus, Eq. 5.47 becomes identical to Eq. 5.46.

For statistically planar flames $\overline{\rho u_i'' c''^2}$ remains the only non-zero component of $\overline{\rho u_i'' c''^2}$. Figure 5.41 the variations of $\overline{\rho u_i'' c''^2}$ with normalised wall normal distance x_1/δ_Z as obtained from DNS data along with the predictions of Eq. 5.47 for all cases considered here. Equation 5.47 mostly provides satisfactory performance away from the wall but this model under-predicts the magnitude of the negative contribution

of $\overline{\rho u_1'' c''^2}$ in the near-wall region when the flame starts to interact with the wall (see Fig. 5.41). Based on this observation Eq. 5.47 has been modified in the following manner:

$$\overline{\rho u_1'' c''^2} = \overline{\rho u_1'' c''} \left(A_w^3 - 2\tilde{c} \left[\frac{\tilde{c}''^2}{\tilde{c}(1 - \tilde{c})} \right]^m \right) \frac{2\tilde{c}''^2}{\tilde{c}''^2 + \tilde{c}(1 - \tilde{c})} \quad (5.48)$$

where $A_w = -\exp[Le(\tilde{c} - \tilde{T})] + 2$ is the model parameter, which remains active close to the wall where $\tilde{c} \neq \tilde{T}$, but the magnitude of A_w increases with increasing wall normal distance and asymptotically approach 1.0 away from the wall where $\tilde{c} \approx \tilde{T}$. It can be seen from Fig. 5.41 that the model given by Eq. 5.47 starts to underpredict the magnitude of $\overline{\rho u_1'' c''^2}$ at an early stage of flame quenching (e.g. $t = 8\delta_Z/S_L$ for $Le = 1.0$ and $t = 6\delta_Z/S_L$ for $Le = 0.8$). Furthermore, Eq. 5.47 starts to predict wrong sign of $\overline{\rho u_1'' c''^2}$ at later stages of flame quenching in $Le = 0.8$ cases (e.g. $t = 6\delta_Z/S_L$ for $Le = 0.8$). The sign of $\overline{\rho u_1'' c''^2}$ is incorrectly predicted when $\overline{\rho u_1'' c''^2}/[\overline{\rho u_1'' c''}(1 - 2g^m\tilde{c})]$ becomes negative. In order to avoid this discrepancy $(A_w^3 - 2g^m\tilde{c})$ is introduced in Eq. 5.48, which assumes a negative value in the near-wall region where $(1 - 2g^m\tilde{c})$ remains positive. The term A_w remains active in the near-wall region where \tilde{c} and \tilde{T} are different from each other as a result of flame quenching. The non-zero value of $(\tilde{c} - \tilde{T})$ arises due to different boundary conditions used for the reaction progress variable and non-dimensional temperature at the isothermal inert wall (i.e. Dirichlet boundary condition for non-dimensional temperature and Neumann boundary condition for reaction progress variable). The $(\tilde{c} - \tilde{T})$ dependence of A_w ensures that the effects of enthalpy loss due to wall heat transfer are reflected on both the qualitative and quantitative variations of $\overline{\rho u_1'' c''^2}$ depending on the distance of the flame from the wall. The quantities, \tilde{c} and \tilde{T} approach each other away from the wall (i.e. $x_1/\delta_Z \gg Pe_{\min}$), but $\tilde{c} \neq \tilde{T}$ and $\tilde{c} > \tilde{T}$ in the near-wall region during flame quenching. A model parameter similar to A_w was previously used in the context of FSD based closure for flame-wall interaction [21]. The quantities, \tilde{c} and \tilde{T} approach each other away from the wall (i.e. $x_1/\delta_Z \gg Pe_{\min}$), which leads to $A_w = 1.0$ and thus Eq. 5.48 reduces to Eq. 5.47 away from the wall. The wall normal distance at which \tilde{c} and \tilde{T} approach each other, and the discrepancy between the prediction of Eq. 5.47 and DNS data depend on Le (e.g. the discrepancy is greater in extent in the $Le = 0.8$ case than in the $Le = 1.0$ and 1.2 cases) and thus A_w is taken to be Lewis number dependent. It can be seen from Fig. 5.41 that the under-prediction of $\overline{\rho u_1'' c''^2}$ by Eq. 5.47 in the near-wall region can be eliminated by the modification proposed in Eq. 5.48.

It is worth noting that the success of the model given by Eqs. 5.46, 5.47 and 5.48 depend on appropriate modelling of turbulent scalar flux $\overline{\rho u_i'' c''}$. Furthermore, the

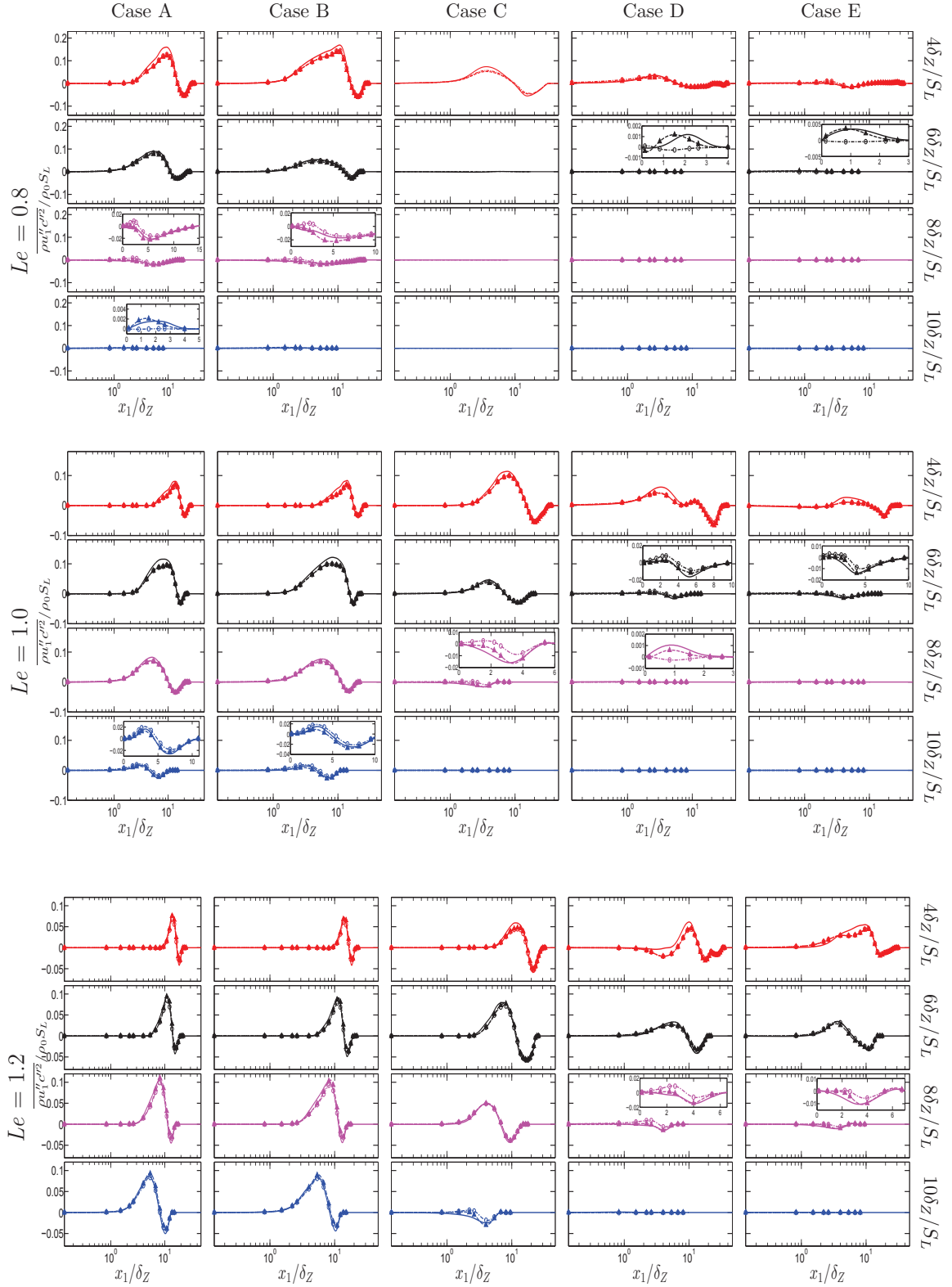


Fig. 5.41 Variations of $\overline{\rho u_1'' c''^2}$ extracted from DNS data (solid line) along with the predictions of Eqs. 5.47 (dotted line) and 5.48 (broken line) with x_1 / δ_Z at $t = 4\delta_Z / S_L$, $6\delta_Z / S_L$, $8\delta_Z / S_L$, $10\delta_Z / S_L$ for turbulent cases A - E with $Le = 0.8, 1.0$ and 1.2 .

modelling of $\overline{\rho u_i'' c''}$ plays a pivotal role in the evaluation of T_{2v} . The near-wall modelling of turbulent scalar flux $\overline{\rho u_i'' c''}$ will be addressed in the following section.

5.6.3 Algebraic Closure of Turbulent Scalar Flux $\overline{\rho u_i'' c''}$

Using Eq. 5.46 one obtains [34, 136, 38]:

$$\frac{\partial \tilde{u}_i}{\partial x_i} \sim \left\{ \overline{(u_i)_P} - \overline{(u_i)_R} \right\} \frac{\partial \tilde{c}}{\partial x_i} \quad (5.49)$$

The slip velocity $\left\{ \overline{(u_i)_P} - \overline{(u_i)_R} \right\}$ can be expressed as [34]:

$$\left\{ \overline{(u_i)_P} - \overline{(u_i)_R} \right\} = -[\Delta u_{\text{turb}} + \Delta u_{\text{hr}}] M_i \quad (5.50)$$

where $M_i = -(\partial \tilde{c} / \partial x_i) / |\nabla \tilde{c}|$ is the i^{th} component of the flame normal vector based on Favre averaged reaction progress variable, Δu_{turb} is the contribution to the slip velocity arising from turbulence and Δu_{hr} is the contribution to the slip velocity arising from heat release. Using Eqs. 5.49 and 5.50 one obtains:

$$\frac{\partial \tilde{u}_i}{\partial x_i} \sim \{ \Delta u_{\text{turb}} + \Delta u_{\text{hr}} \} |\nabla \tilde{c}| \quad (5.51)$$

$$\left[\frac{\partial \tilde{u}_i}{\partial x_i} - \Delta u_{\text{turb}} |\nabla \tilde{c}| \right] \sim \Delta u_{\text{hr}} |\nabla \tilde{c}| \quad (5.52)$$

Using $\Delta u_{\text{turb}} = -\alpha_2 \sqrt{2\tilde{k}/3}$ (where α_2 is a model parameter and $\tilde{k} = \overline{\rho u_j'' u_j''} / 2\bar{\rho}$ is the turbulent kinetic energy) [34] one obtains:

$$\left[\frac{\partial \tilde{u}_i}{\partial x_i} + \alpha_2 \sqrt{2\tilde{k}/3} |\nabla \tilde{c}| \right] \sim \Delta u_{\text{hr}} |\nabla \tilde{c}| \quad (5.53)$$

The quantity $|\nabla \tilde{c}|$ can be scaled as $|\nabla \tilde{c}| \sim 1/\delta_b$ where δ_b is the flame brush thickness. Accordingly, the velocity jump due to heat release over a distance equal to the flame thickness based on reaction progress variable gradient for a corresponding laminar flame (i.e. $\delta_L \sim 1/|\nabla c|_L$) can be estimated as:

$$V_{hr} = \Delta u_{\text{hr}} |\nabla \tilde{c}| \frac{\delta_{\text{th}}}{\tilde{c}(1 - \tilde{c})Le} = \left[\frac{\partial \tilde{u}_i}{\partial x_i} + \alpha_2 \sqrt{2\tilde{k}/3} |\nabla \tilde{c}| \right] \frac{\delta_{\text{th}}}{\tilde{c}(1 - \tilde{c})Le} \quad (5.54)$$

where $|\nabla c|_L$ is estimated as $|\nabla c|_L \sim \tilde{c}(1 - \tilde{c})Le/\delta_{th}$, in which δ_{th}/Le provides an estimate for the laminar flame thickness based on the reaction progress variable gradient. According to Veynante *et al.* [202] $\{(\overline{u_i})_P - (\overline{u_i})_R\}$ can be expressed as: $\{(\overline{u_i})_P - (\overline{u_i})_R\} = -\left\{-\alpha_1\sqrt{2\tilde{k}/3} + V_{hr}\right\}M_i$ which upon using in Eq. 5.46 yields [34, 38]:

$$\overline{\rho u_i'' c''} = \bar{\rho} \left\{ -\alpha_1 \sqrt{2\tilde{k}/3} + \left[\frac{\partial \tilde{u}_j}{\partial x_j} + \alpha_2 \sqrt{2\tilde{k}/3} |\nabla \tilde{c}| \right] \frac{\delta_{th}}{\tilde{c}(1 - \tilde{c})Le} \right\} \tilde{c}(1 - \tilde{c}) \frac{1}{|\nabla \tilde{c}|} \frac{\partial \tilde{c}}{\partial x_i} \quad (5.55)$$

where $\alpha_1 = 0.75 + 0.6\text{erfc}[(Re_L + 1)^{3/2}/60]$ and $\alpha_2 = 2 + \text{erf}[(Re_L + 1)/30]$ [38].

For statistically planar flames $\overline{\rho u_1'' c''}$ remains the only non-zero component of $\overline{\rho u_i'' c''}$. Figure 5.42 shows the variations of $\overline{\rho u_1'' c''}$ with normalised wall normal distance x_1/δ_Z as obtained from DNS data along with the predictions of Eq. 5.55 for all cases considered here. It can be seen that $\overline{\rho u_1'' c''}$ is positive throughout the flame brush and gradually reduces zero at the wall. The positive value of $\overline{\rho u_1'' c''}$ is indicative of counter-gradient transport as $\partial \tilde{c}/\partial x_1$ remains positive in the positive x_1 -direction. It can be seen from Fig. 5.42 that Eq. 5.55 satisfactorily predicts the qualitative behaviour of $\overline{\rho u_1'' c''}$ when the flame is away from the wall but this model significantly over-predicts $\overline{\rho u_1'' c''}$ once the flame approaches the wall and Eq. 5.55 predicts non-zero values of $\overline{\rho u_1'' c''}$ at the wall. This starts to happen at an earlier time for higher values of $u'/S_L \sim Re_t^{1/4} Ka^{1/2} \sim Re_t^{1/2} Da^{-1/2}$ because the flame starts to interact with the wall at an earlier time instant due to greater extent of flame wrinkling. In order to eliminate the inadequacies of Eq. 5.42 in the near-wall region the following modification has been suggested:

$$\overline{\rho u_i'' c''} = \bar{\rho} A_1 \left\{ -\alpha_1 \sqrt{2\tilde{k}/3} + \left[\frac{\partial \tilde{u}_j}{\partial x_j} + \alpha_2 \sqrt{2\tilde{k}/3} |\nabla \tilde{c}| \right] \frac{\delta_{th}}{\tilde{c}(1 - \tilde{c})Le} \right\} \tilde{c}(1 - \tilde{c}) \frac{1}{|\nabla \tilde{c}|} \frac{\partial \tilde{c}}{\partial x_i} \quad (5.56)$$

where $A_1 = \text{erf}\{0.05\exp[2Le(\tilde{c} - \tilde{T})]x_1/\delta_Z\}$ is the model parameter. Figure 5.42 shows that Eq. 5.55 over-predicts the magnitude of $\overline{\rho u_1'' c''}$ in the near-wall region. The presence of wall leads to a decay in turbulent velocity fluctuation which gives rise to a reduction in the magnitude of scalar flux $\overline{\rho u_1'' c''}$. However, this behaviour is not sufficiently captured by Eq. 5.55 and it overpredicts the magnitude of $\overline{\rho u_1'' c''}$. For this reason Eq. 5.55 is revised to propose a new model (i.e. Eq. 5.56) where the parameter A_1 accounts for the reduction of scalar flux magnitude due to the presence of wall. The model parameter

A_1 is responsible for eliminating the overprediction of $\overline{\rho u_1'' c''}$ in the near-wall region. The functional dependence of A_1 on $Le(\tilde{c} - \tilde{T})$ and x_1/δ_Z ensures that this parameter remains active close to the wall where $\tilde{c} \neq \tilde{T}$. The turbulent scalar flux components $\overline{\rho u_1'' c''}$ vanish at the wall (i.e. $x_1 = 0$) because the velocity component fluctuations u_i'' vanish at the wall due to no-slip condition. The model parameter A_1 contains an error function which depends on x_1/δ_Z which ensures that both $\overline{\rho u_1'' c''} = 0$ and $A_1 = 0$ at $x_1/\delta_Z = 0$. Furthermore, the error function in A_1 ensures that it increases from 0 at $x_1 = 0$ with increasing x_1/δ_Z and asymptotically approaches 1.0 away from the wall (i.e. $x_1/\delta_Z \gg (Pe_{\min})_L$) where Eq. 5.56 reduces to Eq. 5.55. The wall normal distance over which \tilde{c} and \tilde{T} are significantly different from each other depends on Lewis number and this is reflected in Le dependence of A_1 . It can be seen from Fig. 5.42 that Eq. 5.56 significantly reduces the over-prediction of $\overline{\rho u_1'' c''}$ in comparison to Eq. 5.55 and satisfactorily captures the qualitative behaviour of turbulent scalar flux $\overline{\rho u_1'' c''}$ in the near-wall region for all cases considered here.

5.6.4 Modelling of Reaction Rate Term T_{3v}

According to Bray *et al.* [19], the reaction rate contribution T_{3v} can be expressed as:

$$T_{3v} = 2\bar{\omega}(c_m - \tilde{c}) \quad (5.57)$$

where c_m is given by: $c_m = \int_0^1 [\dot{\omega} c f_b(c)]_L dc / \int_0^1 [\dot{\omega} f_b(c)]_L dc$ with $f_b(c)$ being the burning mode pdf. This parameter c_m has been found to be equal to 0.87, 0.85 and 0.83 for $Le = 0.8, 1.0$ and 1.2 respectively. Bray [17] proposed the following closure for the mean reaction rate of reaction progress variable $\bar{\omega}$ in terms of scalar dissipation rate $\tilde{\epsilon}_c$ for $Da \gg 1$ flames based on a presumed bi-modal pdf of c with impulses at $c = 0$ and $c = 1.0$: $\bar{\omega} = 2\bar{\rho}\tilde{\epsilon}_c/(2c_m - 1)$. It was shown by Chakraborty and Cant [36] and Chakraborty and Swaminathan [51] based on scaling arguments and DNS data that the mean reaction rate model also remains valid for $Da < 1$ as long as the flamelet assumption remains valid. Thus, the reaction rate term T_{3v} can be expressed as:

$$T_{3v} = \frac{\bar{\rho}\tilde{\epsilon}_c(c_m - 1\tilde{c})}{2c_m - 1} \quad (5.58)$$

Figure 5.43 shows the variations of T_{3v} with normalised wall normal distance x_1/δ_Z as obtained from DNS data along with the predictions of Eq. 5.57 for all cases considered here. It can be seen from Fig. 5.43 that Eq. 5.57 satisfactorily predicts T_{3v} when the flame is away from wall but once the quenching starts, Eq. 5.57 predicts non-zero

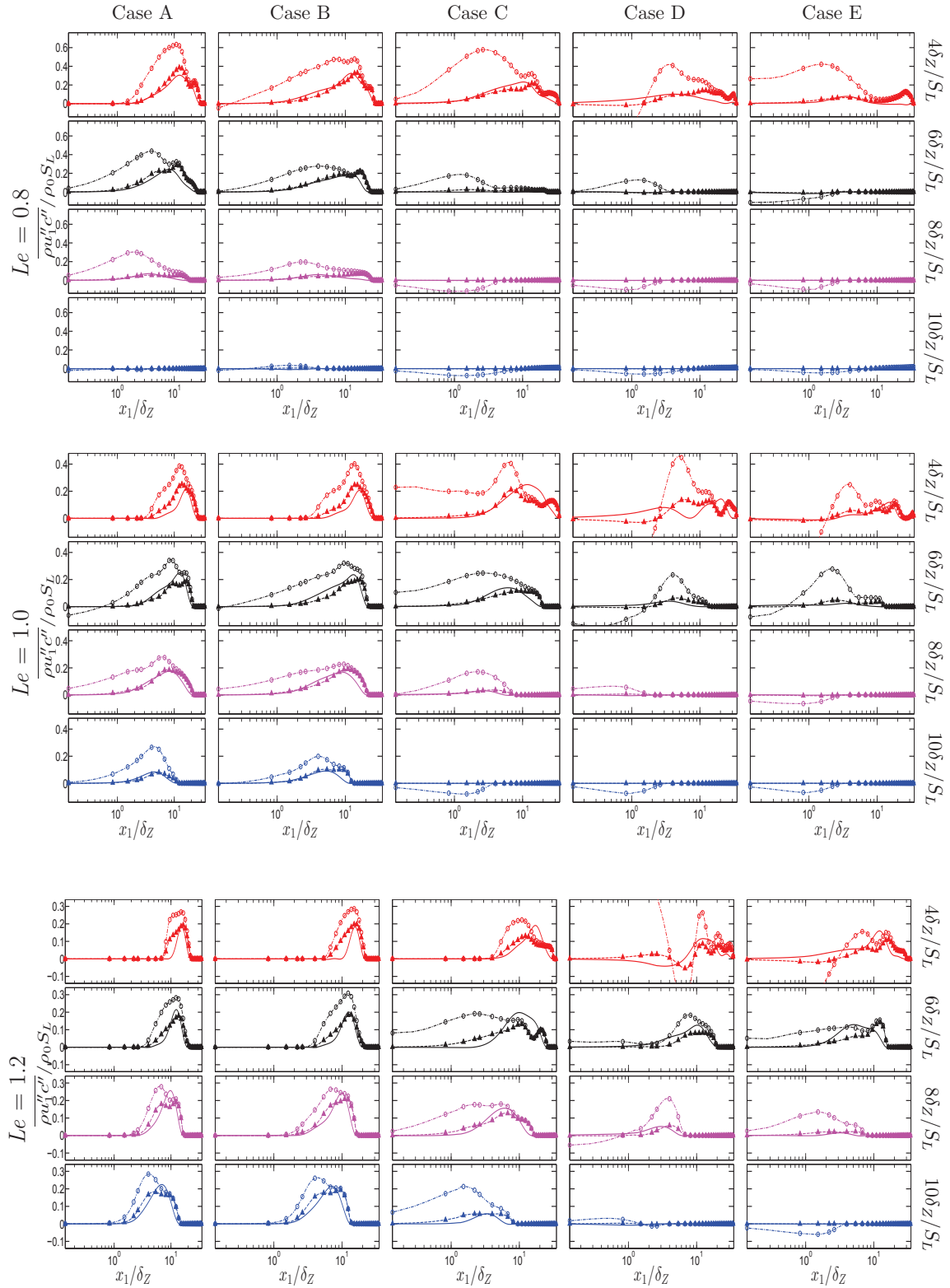


Fig. 5.42 Variations of $\overline{\rho u_1'' c''}$ extracted from DNS data (solid line) along with the predictions of Eqs. 5.55 (dotted circle line) and 5.56 (broken triangle line) with x_1 / δ_Z at $t = 4\delta_Z / S_L, 6\delta_Z / S_L, 8\delta_Z / S_L, 10\delta_Z / S_L$ for turbulent cases A - E with $Le = 0.8, 1.0$ and 1.2 .

values at the wall and in the near-wall region, where T_{3v} either vanishes or assumes negligible values. This behaviour originates due to non-zero value of $2\bar{\rho}\tilde{\varepsilon}_c/(2c_m - 1)$ in the near-wall region where $\tilde{\omega}$ vanishes due to flame quenching. With the accurate prediction of the mean reaction rate $\bar{\omega}$, Eq. 6.2 in the next chapter extended the expression given by Eq. 5.57 to predict $\tilde{\omega}$ accurately in the near-wall region.

5.6.5 Summary of the key results

The reaction progress variable variance \tilde{c}''^2 transport and its modelling in the context of RANS have been analysed for head-on quenching of turbulent premixed flame. The statistical behaviours of the unclosed terms in the transport equation of \tilde{c}''^2 have been analysed in detail, and their relative magnitudes have been explained based on scaling arguments. It has been found that the reaction rate contribution T_{3v} and the molecular dissipation term $(-D_{2v})$ are the leading order source and sink terms, respectively, in the \tilde{c}''^2 transport equation. However, the reaction rate contribution T_{3v} vanishes in the near-wall region due to flame quenching, whereas $(-D_{2v})$ continues to act as a dominant sink. The mean scalar gradient term T_{2v} acts as the sink term for all cases considered here, since the turbulent scalar flux $\overline{\rho u_1'' c''}$ shows counter-gradient transport in these cases. The turbulent flux of scalar variance $\overline{\rho u_1'' c''^2}$ assumes positive values in the near-wall region but becomes negative away from the wall at early stages of flame quenching, but an opposite behaviour is observed at the final stage of quenching. The performances of previously proposed models for turbulent fluxes $\overline{\rho u_i'' c''^2}$ and $\overline{\rho u_i'' c''}$, reaction rate contribution T_{3v} and scalar dissipation rate $\tilde{\varepsilon}_c$ have been assessed with respect to the corresponding quantities extracted from DNS data. It has been found that the aforementioned models do not adequately predict the near-wall behaviour of the unclosed terms of the variance \tilde{c}''^2 transport equation. The existing models for the unclosed terms of the variance \tilde{c}''^2 transport equation have been modified to account for the near-wall behaviour in such a manner that the modified models asymptotically approach the existing model expressions away from the wall. The functional forms of the modelling parameters have been proposed in such a manner that they follow the asymptotic behaviour in terms of the normalized wall normal distance x_1/δ_Z .

5.6.6 Chapter closing remarks

Chapter 5 has provided the physical insights of flame-wall interaction by investigating the three dimensional DNS of head-on quenching turbulent premixed flame. It has been found that the turbulent flames quench earlier than the corresponding laminar

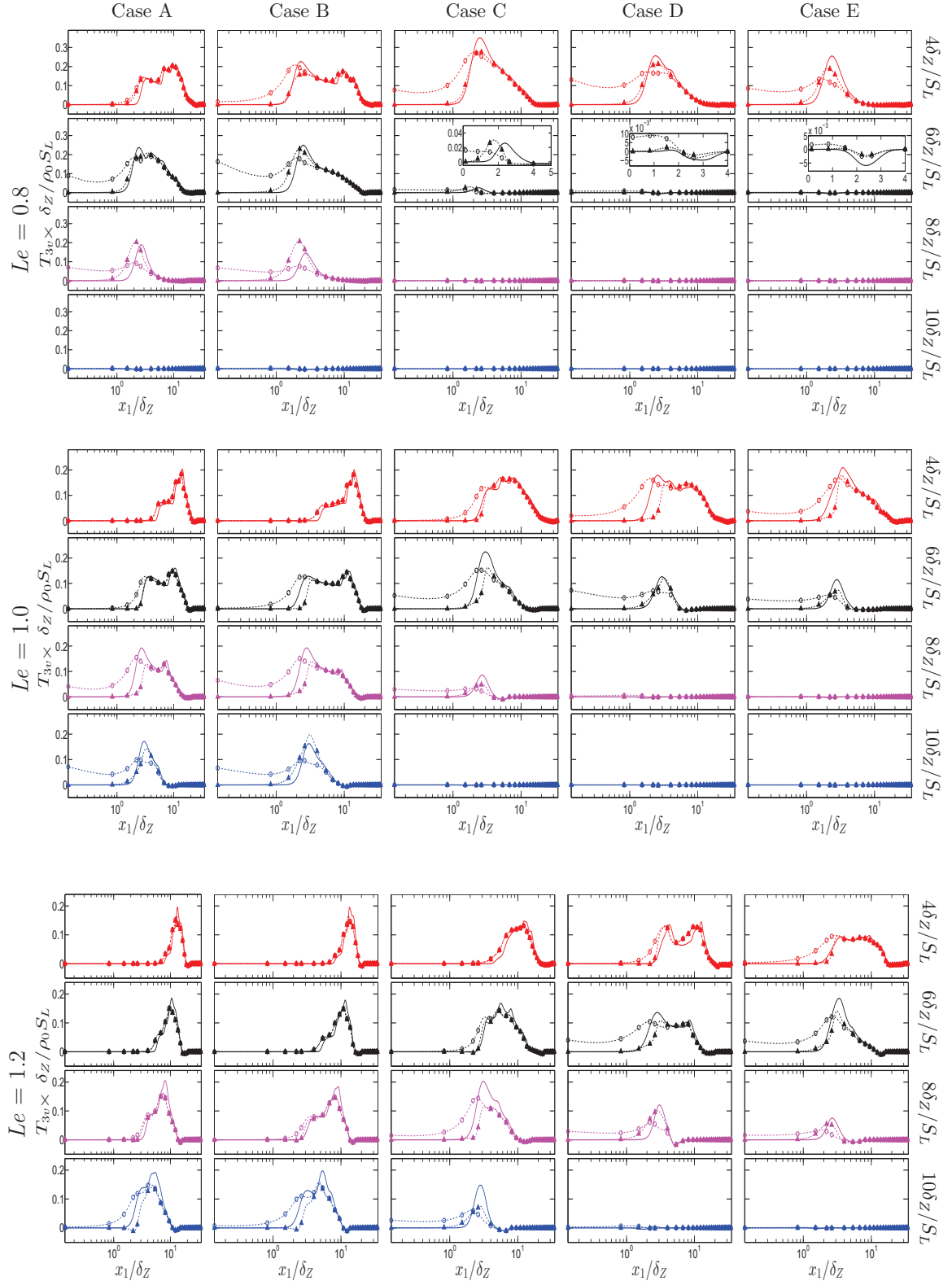


Fig. 5.43 Variations of T_{3v} extracted from DNS data (solid line) along with the predictions of Eqs. 5.58 (dotted circle line) and 6.2 (broken triangle line) with x_1/δ_Z at $t = 4\delta_Z/S_L, 6\delta_Z/S_L, 8\delta_Z/S_L, 10\delta_Z/S_L$ for turbulent cases A - E with $Le = 0.8, 1.0$ and 1.2 .

flames because of a greater extent of flame wrinkling, and this effect strengthens with increasing value of turbulent intensity and for decreasing values of global Lewis number. It reveals how the small piece of *mother nature fabric* shapes the combustion, and where *star-crossed lovers'* story starts. Moreover, an analysis has been conducted on the statistical behaviour of vorticity and enstrophy transport, flow topology, and following by the turbulent kinetic energy and scalar variance transport. Furthermore, the modelling for the turbulent kinetic energy and scalar variance transport terms have been provided. The cold wall has a huge impact on the coming flame, the existing models do not adequately capture the near wall behaviour. Additionally, the new models have been proposed. The following chapter will seek to provide the analysis and modelling of the reaction rate and scalar flux.

Chapter 6

Results & Discussion 2: The Combustion Modelling

The focus of this chapter is on the statistical analysis and modelling of mean reaction rate and the scalar flux in the case of the head-on quenching of turbulent premixed flames. It begins with the scalar dissipation rate transport based closure, followed by the flame surface density based closure and ends with the turbulent scalar flux transport.

6.1 Statistical analysis and modelling of the scalar dissipation rate transport

The main objectives of this section are:

- To analyse of the influences of global Lewis number on the closures of mean reaction rate and SDR in the context of head on quenching of turbulent premixed flames and indicate the associated modelling implications
- To identify the near-wall effects on the unclosed terms of the SDR transport equation
- To model the near-wall effects on the unclosed terms of the SDR transport equation

6.1.1 Modelling of mean reaction rate closure and its Lewis number dependence

The variations of the normalised values of $\bar{\omega}$ and $2\bar{\rho}\tilde{\epsilon}_c/(2c_m - 1)$ (where $c_m \approx 0.87, 0.85$ and 0.83 for $Le = 0.8, 1.0$ and 1.2 respectively for the present thermo-chemistry) with the normalised wall normal distance x_1/δ_Z for different time instants are shown in Figs. 6.1, 6.2 and 6.3 for $Le = 0.8, 1.0$ and 1.2 respectively in order to assess the validity of Eq. 2.50 in the near wall region. A comparison between Figs. 5.3 and 6.1- 6.3 reveals that $\bar{\omega}$ vanishes in the region given by $x_1/\delta_Z < Pe_{\min}$ for all cases. Figures 6.1- 6.3 further show that $2\bar{\rho}\tilde{\epsilon}_c/(2c_m - 1)$ satisfactorily predicts $\bar{\omega}$ for $x_1/\delta_Z > Pe_{\min}$ before flame quenching. However, in the turbulent $Le \leq 1.0$ ($Le = 1.2$) cases $2\bar{\rho}\tilde{\epsilon}_c/(2c_m - 1)$ differs significantly from $\bar{\omega}$ at $t > 4\delta_Z/S_L$ ($t > 6\delta_Z/S_L$) when the flame begins to interact with the wall and quenching starts to take place (see Fig. 5.3). As a result of this, Eq. 2.50 fails to predict the negligible value of $\bar{\omega}$ at the wall ($x_1/\delta_Z = 0$) where $2\bar{\rho}\tilde{\epsilon}_c/(2c_m - 1)$ assumes a non-zero value and it underestimates the value of $\bar{\omega}$ in the region given by $0 < x_1/\delta_Z < Pe_{\min}$ during the flame quenching.

It is worth noting that Eq. 2.50 was originally derived based on a presumed bi-modal probability density function (pdf) of c with impulse functions at $c = 0$ and $c = 1.0$. Figure 6.4 shows the pdf of c in the region corresponding to $0 \leq x_1/\delta_Z \leq (Pe_{\min})_L$ at different time instants, which reveals that the probability of finding $c = 0$ is high in the region corresponding to $0 \leq x_1/\delta_Z \leq (Pe_{\min})_L$ at early times when the flame is away from the wall. The pdfs of c show the probability of finding $0 < c < 1$ as the flame approaches the wall but the pdf of c eventually shows high probability of finding $c \approx 1.0$ with the progress of flame quenching. The high probability of finding $c \approx 1.0$ in the region given by $0 \leq x_1/\delta_Z \leq (Pe_{\min})_L$ is obtained at earlier time instants for the cases with higher value of $u'/S_L \sim Re_t^{1/4} Ka^{1/2} \sim Re_t^{1/2} Da^{1/2}$ and/or smaller values of Le , because of quicker initiation of flame quenching for these cases (see Fig. 5.3). Thus, the pdfs of c tend towards a mono-modal distribution with a peak at $c = 1.0$ for high u'/S_L and/or small Le cases by $t = 10\delta_Z/S_L$ (e.g. cases D-E for all values of Le and $Le = 0.8$ and $Le = 1.0$ and 1.0 flames in case C). Although pdfs of c do not approach a mono-modal distribution by $t = 10\delta_Z/S_L$ for the cases with small u'/S_L and/or high Le , the peak of pdf is attained at a c value close to unity but not at $c = 1.0$ (e.g cases A and B for $Le = 1.0$ and 1.2 , and case C with $Le = 1.2$). Irrespective of whether the pdf of c shows a mono-modal distribution with a peak at $c = 1.0$, Fig. 6.4 demonstrates that the pdfs of c do not exhibit a bi-modal distribution with impulses at $c = 0$ and $c = 1.0$ at any stage in the region given by $0 \leq x_1/\delta_Z \leq (Pe_{\min})_L$. Thus, the underlying assumption behind Eq. 2.50 does not remain valid in the region given by:

$0 \leq x_1/\delta_Z \leq (Pe_{\min})_L$ and as a result where $2\bar{\rho}\tilde{\varepsilon}_c/(2c_m - 1)$ fails to accurately predict the mean reaction rate $\bar{\omega}$ in this region. This can further be supported by Fig. 6.5 which shows the temporal evolutions of \tilde{c}''^2 and $\tilde{c}(1 - \tilde{c})$ in the direction normal to the wall. The variance of reaction progress variable \tilde{c}''^2 can be expressed as [19]:

$$\tilde{c}''^2 = \tilde{c}(1 - \tilde{c}) + O(1/Da) \quad (6.1)$$

For $Da \gg 1$ flames \tilde{c}''^2 becomes equal to $\tilde{c}(1 - \tilde{c})$ [19] as a result of a pure bi-modal pdf of c with impulse functions at $c = 0$ and $c = 1.0$. It can be seen from Fig. 6.5 that \tilde{c}''^2 remains smaller than $\tilde{c}(1 - \tilde{c})$ even when the flame is away from the wall in all turbulent cases due to small values of Damköhler number (i.e. $Da < 1.0$; see Table 4.1) but during flame quenching \tilde{c}''^2 drops significantly and eventually vanishes in the regions close to the wall, where $\tilde{c}(1 - \tilde{c})$ assumes non-zero values (i.e. $\tilde{c}(1 - \tilde{c}) \neq 0$). A comparison between Figs. 6.1- 6.3 and 6.5 indicates that Eq. 2.50 ceases to predict $\bar{\omega}$ accurately when $\tilde{c}''^2 \ll \tilde{c}(1 - \tilde{c})$ (i.e. $\tilde{c}''^2 < 0.07\tilde{c}(1 - \tilde{c})$ for the cases considered here). Thus, it is necessary to modify the model given by Eq. 2.50 in order to predict $\bar{\omega}$ during the quenching of premixed turbulent flames.

It can be seen from Figs. 6.1 - 6.3 that $\bar{\omega} = \rho_0 S_L \Sigma_{\text{gen}}$ (where $\Sigma_{\text{gen}} = |\overline{\nabla c}|$ is the generalised FSD [12]) overestimates $\bar{\omega}$ in the near wall region during quenching process, which is consistent with previous findings [157, 20]. For unity Lewis number flames $\rho_0 S_L \Sigma_{\text{gen}}$ accurately predicts $\bar{\omega}$ away from the wall but $\rho_0 S_L \Sigma_{\text{gen}}$ underpredicts (overpredicts) $\bar{\omega}$ for the $Le = 0.8$ ($Le = 1.2$) cases when the flame is away from the wall. By contrast, $2\bar{\rho}\tilde{\varepsilon}_c/(2c_m - 1)$ predicts $\bar{\omega}$ satisfactorily for all cases irrespective of Le when the flame away from the wall (i.e. before the initiation of flame quenching), which is consistent with previous findings by Chakraborty and Cant [33]. Here, the aforementioned observed behaviours of both the SDR and FSD based closures in the near wall region have been utilised to propose the following modification to Eq. 2.50 by considering the effects of Le :

$$\bar{\omega} = \frac{2\bar{\rho}\tilde{\varepsilon}_c}{2c_m - 1} A_1 \exp[Le(\tilde{c} - \tilde{T})] + A_2 A_3 \frac{\rho_0 S_L}{Le^B} \sqrt{\frac{\tilde{\varepsilon}_c}{D}} \exp\left[0.5 \left(\frac{x_1}{\delta_Z} - \Pi\right)^2\right] \quad (6.2)$$

where Π is stated in Eq. 5.13. The parameters A_1, A_2, A_3 and B in Eq. 6.2 are given by:

$$A_1 = 0.5\{\text{erf}[3.0(x_1/\delta_Z - \Pi)] + 1\} \quad (6.3)$$

$$A_2 = 0.5[\text{erf}(x_1/\delta_Z - \psi\Pi) + 1] \quad (6.4)$$

$$A_3 = 2.31\text{erf}[2.6(\tilde{c} - \tilde{T})] \quad (6.5)$$

$$B = -6(Le - 1) \quad (6.6)$$

$$\psi = \max[5(\tilde{c}_w - \tilde{T}_w), 1]^{0.3} \quad (6.7)$$

where \tilde{Q}_w is the Favre mean value at the wall for a general quantity Q at a given instant of time. In Eq. 6.2, the generalised FSD is estimated using a scaling argument as $\Sigma_{\text{gen}} \sim \sqrt{\tilde{\varepsilon}_c/\tilde{D}}$ and $(\tilde{c}_w - \tilde{T}_w)$ dependence of A_2 ensures that the prediction of Eq. 6.2 captures the correct spatial distribution of mean reaction rate $\bar{\omega}$ at different stages of flame quenching depending on the values of \tilde{c}_w and \tilde{T}_w (see the values of \tilde{c}_w change with time as quenching progresses from Fig. 5.5). For the $Le = 1.0$ cases, \tilde{c} and \tilde{T} are identical to each other away from the wall which leads to $A_1 \exp[Le(\tilde{c} - \tilde{T})] = 0$ and $A_2 A_3 = 0$, and thus Eq. 6.2 reduces to Eq. 2.50. For $Le \neq 1.0$ cases \tilde{c} and \tilde{T} are not equal to each other even when the flame is away from wall, and the involvement of Le on the first term on the right hand side of Eq. 6.2 accounts for this effect. The involvement of $1/Le^B$ in the second term on right hand side of Eq. 6.2 compensates the underprediction (overprediction) of $\bar{\omega}$ by $\rho_0 S_L \Sigma_{\text{gen}}$ for turbulent $Le < 1$ ($Le > 1$) cases. Figures 6.1 - 6.3 show that Eq. 6.2 predicts the mean reaction rate $\bar{\omega}$ accurately within the quenching zone $0 \leq x_1/\delta_Z \leq (Pe_{\min})_L$. The satisfactory performance of Eq. 6.2 indicates that $\bar{\omega}$ in turbulent premixed flame-wall interaction can be modelled if the SDR $\tilde{\varepsilon}_c$ is accurately predicted.

6.1.2 Statistical behaviour of the SDR transport

It is instructive to understand the statistical behaviour of the unclosed terms in the SDR $\tilde{\varepsilon}_c$ in the near wall region (See Eq. 2.56). The variations of normalised values of $T_1, T_2, T_3, T_4, (-D_2)$ and $f(D)$ with normalised wall normal wall distance x_1/δ_Z at different time instants for cases A-E are shown in Figs. 6.6 - 6.8 for $Le = 0.8, 1.0$ and 1.2 respectively. Swaminathan and Bray [185] proposed the following scaling estimates for the unclosed terms of SDR $\tilde{\varepsilon}_c$ transport equation where the velocity fluctuations and length scales associated with scalar fluctuations are scaled with respect to S_L and δ_Z respectively, whereas the gradients of Favre/Reynolds averaged quantities are scaled

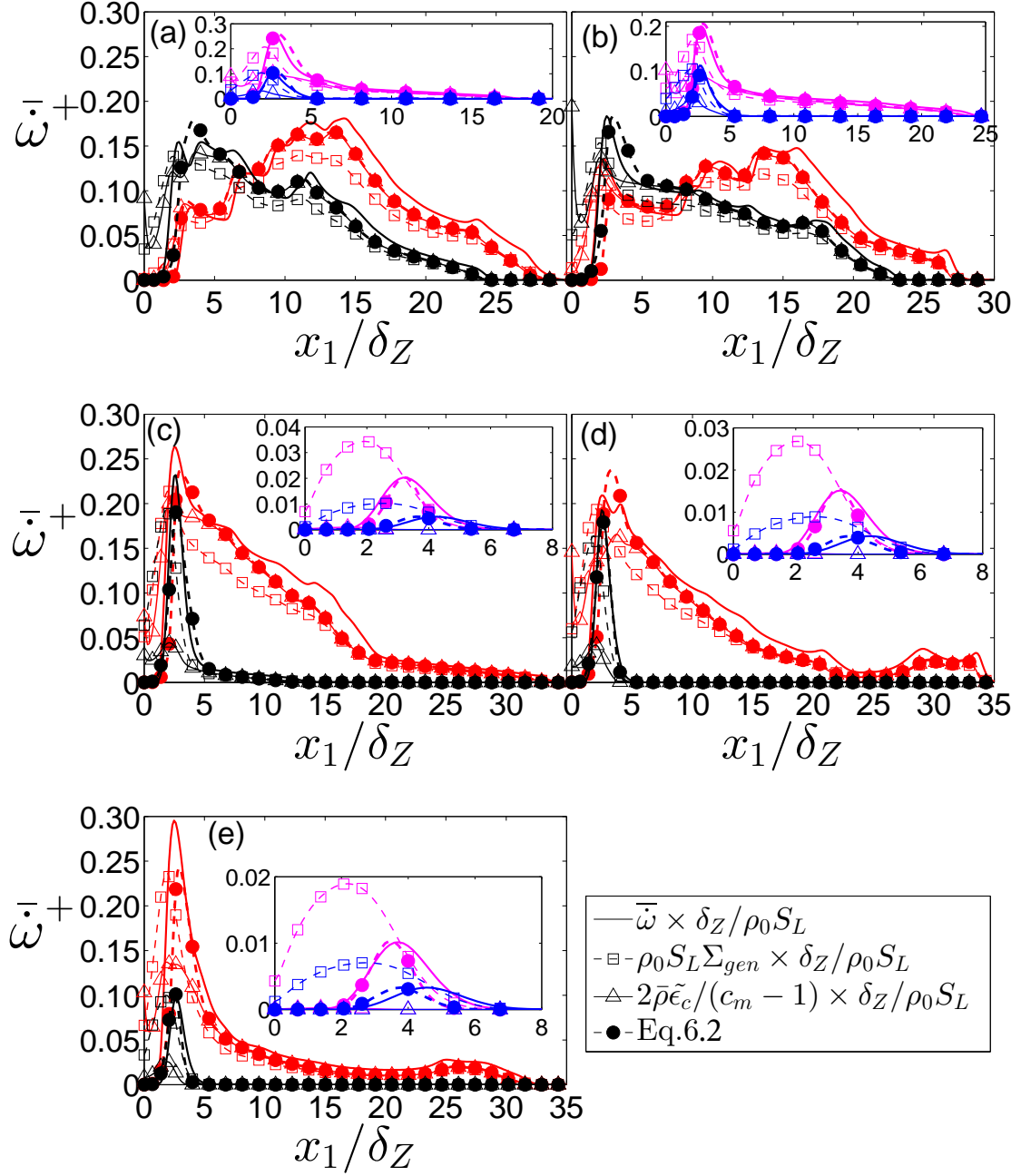


Fig. 6.1 Variations of $\bar{\omega}^+ = \bar{\omega} \times \delta_Z / \rho_0 S_L$, $\rho_0 S_L \Sigma_{gen} \times \delta_Z / \rho_0 S_L$, $2\bar{\rho}\tilde{\epsilon}_c / (c_m - 1) \times \delta_Z / \rho_0 S_L$ and the prediction of Eq. 6.2 with x_1/δ_Z at different time instants for turbulent cases (a-e) A-E with $Le = 0.8$. Please refer to the table in Fig. 5.4 for the colour scheme.

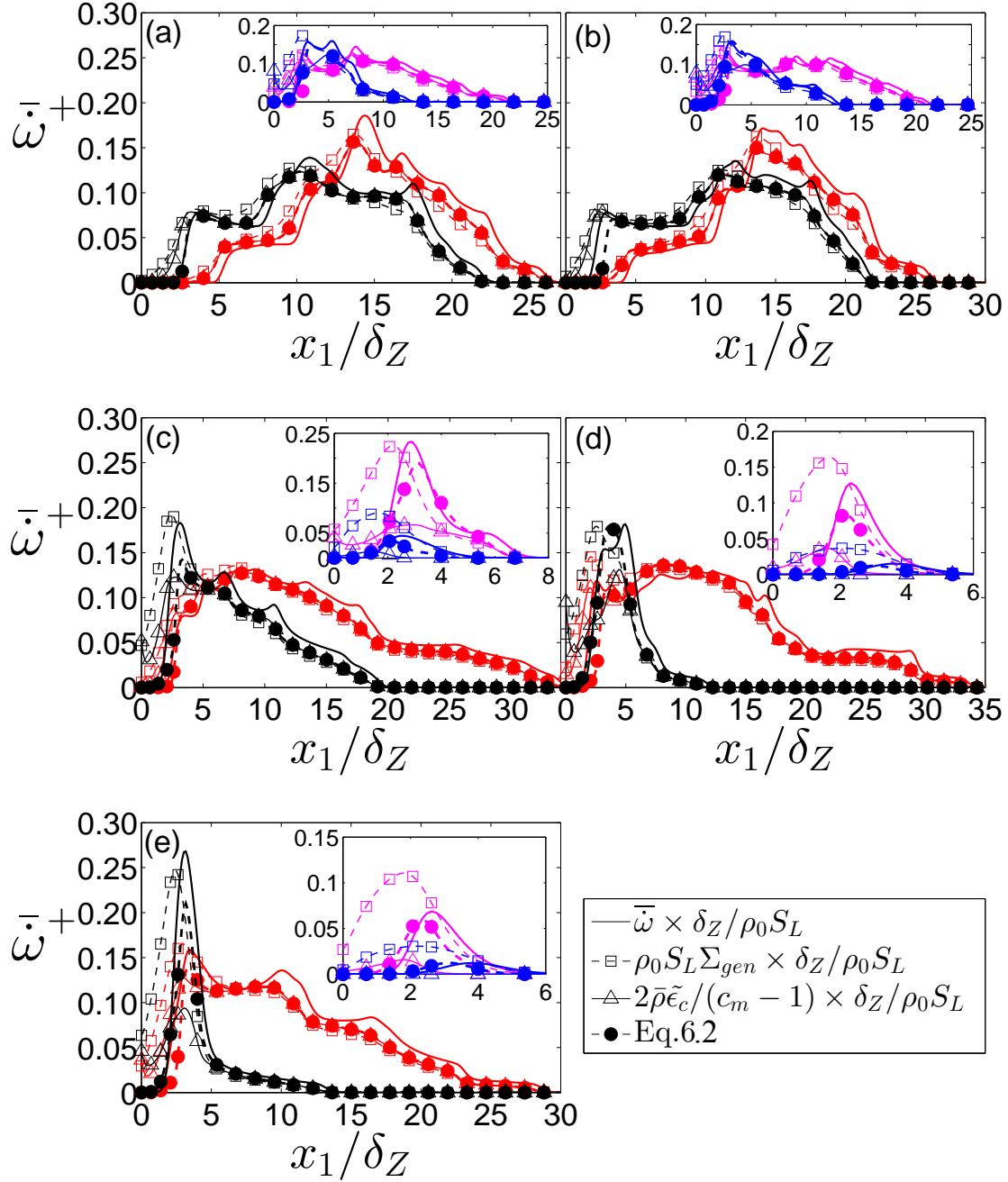


Fig. 6.2 Variations of $\bar{w}^+ = \bar{w} \times \delta_Z / \rho_0 S_L$, $\rho_0 S_L \Sigma_{gen} \times \delta_Z / \rho_0 S_L$, $2\bar{\rho}\tilde{\epsilon}_c / (c_m - 1) \times \delta_Z / \rho_0 S_L$ and the prediction of Eq. 6.2 with x_1/δ_Z at different time instants for turbulent cases (a-e) A-E with $Le = 1.0$. Please refer to the table in Fig. 5.4 for the colour scheme.

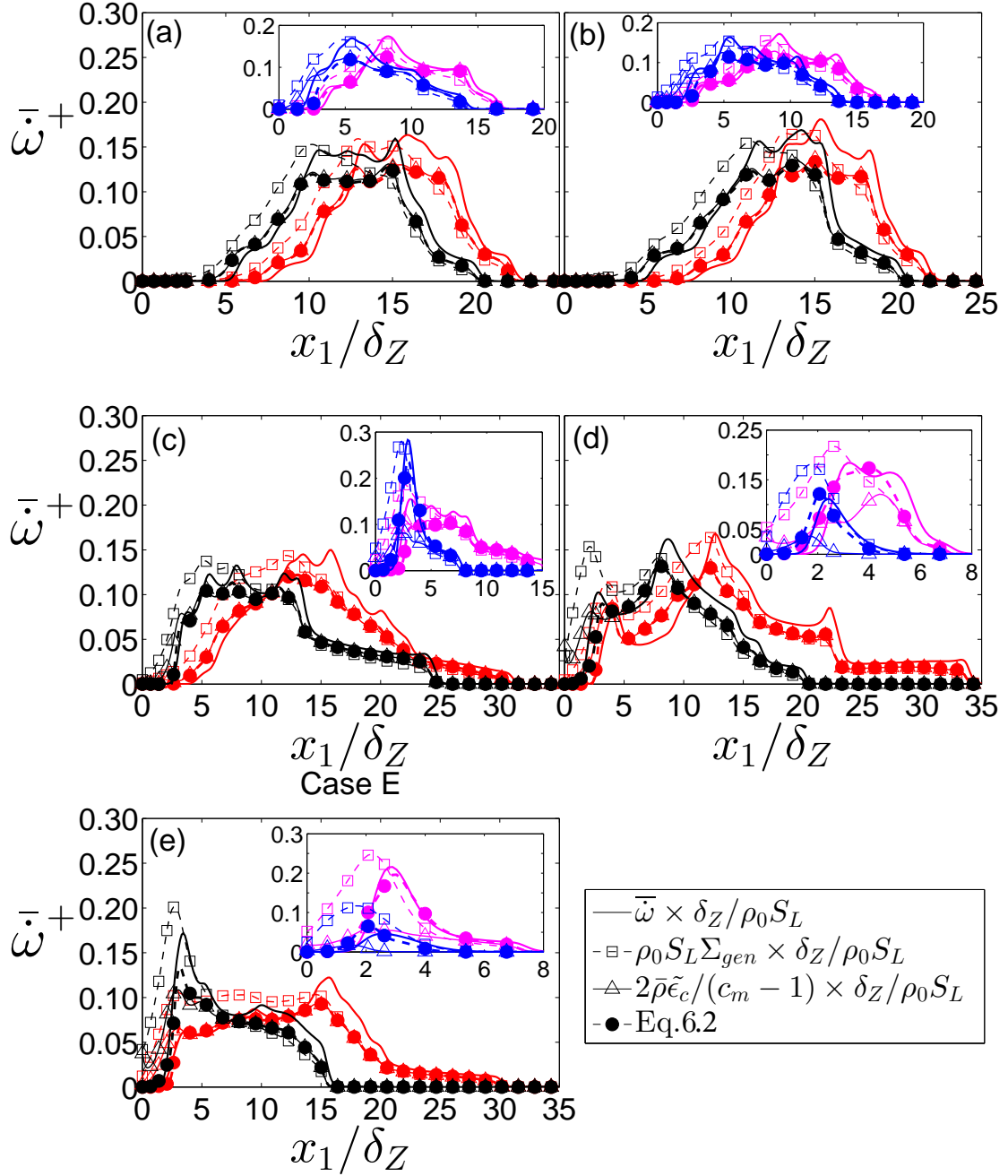


Fig. 6.3 Variations of $\bar{\omega}^+ = \bar{\omega} \times \delta_Z / \rho_0 S_L$, $\rho_0 S_L \Sigma_{gen} \times \delta_Z / \rho_0 S_L$, $2\bar{\rho}\tilde{\epsilon}_c / (c_m - 1) \times \delta_Z / \rho_0 S_L$ and the prediction of Eq. 6.2 with x_1/δ_Z at different time instants for turbulent cases (a-e) A-E with $Le = 1.2$. Please refer to the table in Fig. 5.4 for the colour scheme.

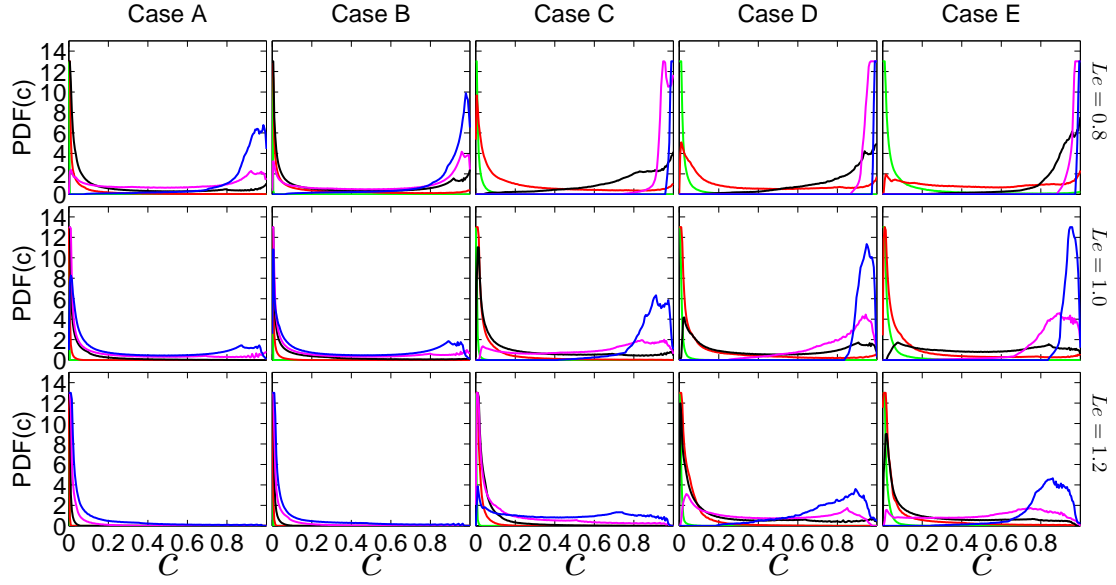


Fig. 6.4 Pdfs of c for $0 \leq x_1/\delta_Z \leq (Pe_{\min})_L$ at different time instants for turbulent cases A - E and $Le = 0.8, 1.0$ and 1.2 . Please refer to the table in Fig. 5.4 for the colour scheme.

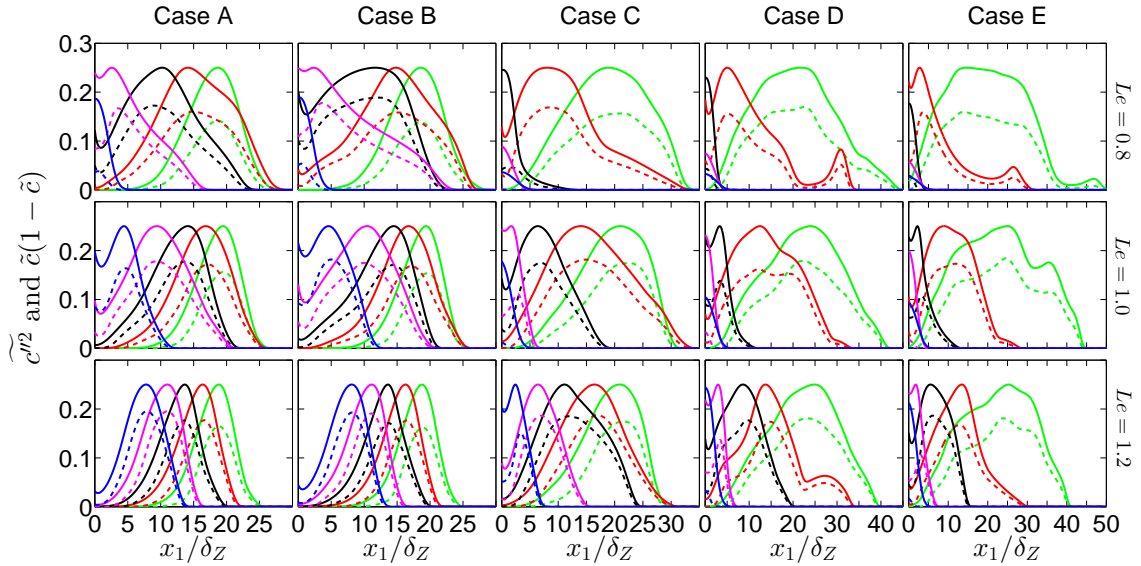


Fig. 6.5 Variations of $\tilde{c}(1 - \tilde{c})$ (solid line) and \tilde{c}''^2 (dash line) at different time instants for turbulent cases A - E and $Le = 0.8, 1.0$ and 1.2 . Please refer to the table in Fig. 5.4 for the colour scheme.

with respect to the integral length scale l :

$$\begin{aligned}
T_{11} &\sim (\rho_0 S_L^2 / \delta_Z^2) Da^{-1}; & T_{12} &\sim (\rho_0 S_L^2 / \delta_Z^2) Da^{-1} Re_t^{-1} \\
T_2 &\sim \rho_0 S_L^2 / \delta_Z^2 \\
T_{31} &\sim (\rho_0 S_L^2 / \delta_Z^2) Re_t^{-1/2}; & T_{32} &\sim (\rho_0 S_L^2 / \delta_Z^2); & T_{33} &\sim (\rho_0 S_L^2 / \delta_Z^2) Da^{-1} U_{\text{ref}} / u' \\
T_4 &\sim \rho_0 S_L^2 / \delta_Z^2 \\
-D_2 &\sim \rho_0 S_L^2 / \delta_Z^2 \\
f(D) &\sim \rho_0 S_L^2 / \delta_Z^2
\end{aligned} \tag{6.8}$$

Mantel and Borghi [137] proposed the following alternative scaling estimates of T_1 , T_3 and T_4 , where the velocity fluctuations and length scales associated with scalar fluctuations are scaled with respect to rms turbulent velocity u' and Taylor micro-scale $\lambda \sim l Re_t^{-1/2}$ respectively, whereas the gradients of Favre/Reynolds averaged quantities are scaled with respect to the integral length scale l [189]:

$$T_{11} \sim (\rho_0 u'^2 / l^2); \quad T_{12} \sim (\rho_0 u'^2 / l^2) Re_t^{-1} \tag{6.9}$$

$$T_{31} \sim (\rho_0 u'^2 / l^2); \quad T_{32} \sim (\rho_0 u'^2 / l^2) Re_t^{-1}; \quad T_{33} \sim (\rho_0 u'^2 / l^2) \tag{6.10}$$

It is possible to obtain an alternative scaling estimate for $(-D_2)$ if the length scale associated with the second derivative of the fluctuations of progress variable, and it is scaled with respect to the Kolmogorov length scale η [39]:

$$(-D_2) \sim (\rho_0 u'^2 / l^2) Re_t \tag{6.11}$$

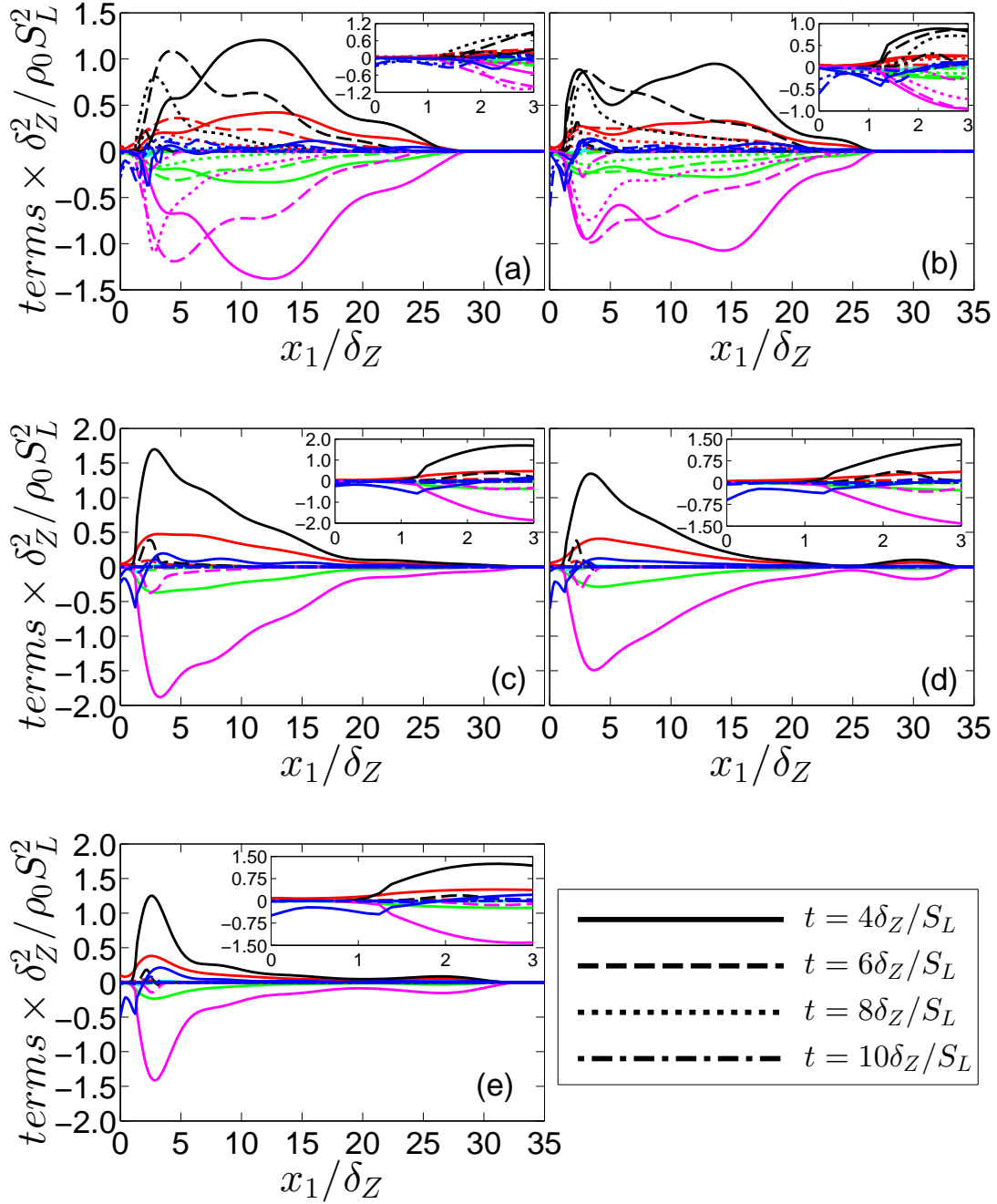


Fig. 6.6 Variations of T_1 , T_2 , T_3 , T_4 , $(-D_2)$, $f(D)$ with x_1 / δ_Z at $t = 4\delta_Z / S_L, 6\delta_Z / S_L, 8\delta_Z / S_L, 10\delta_Z / S_L$ for turbulent cases (a-e) A - E with $Le = 0.8$.

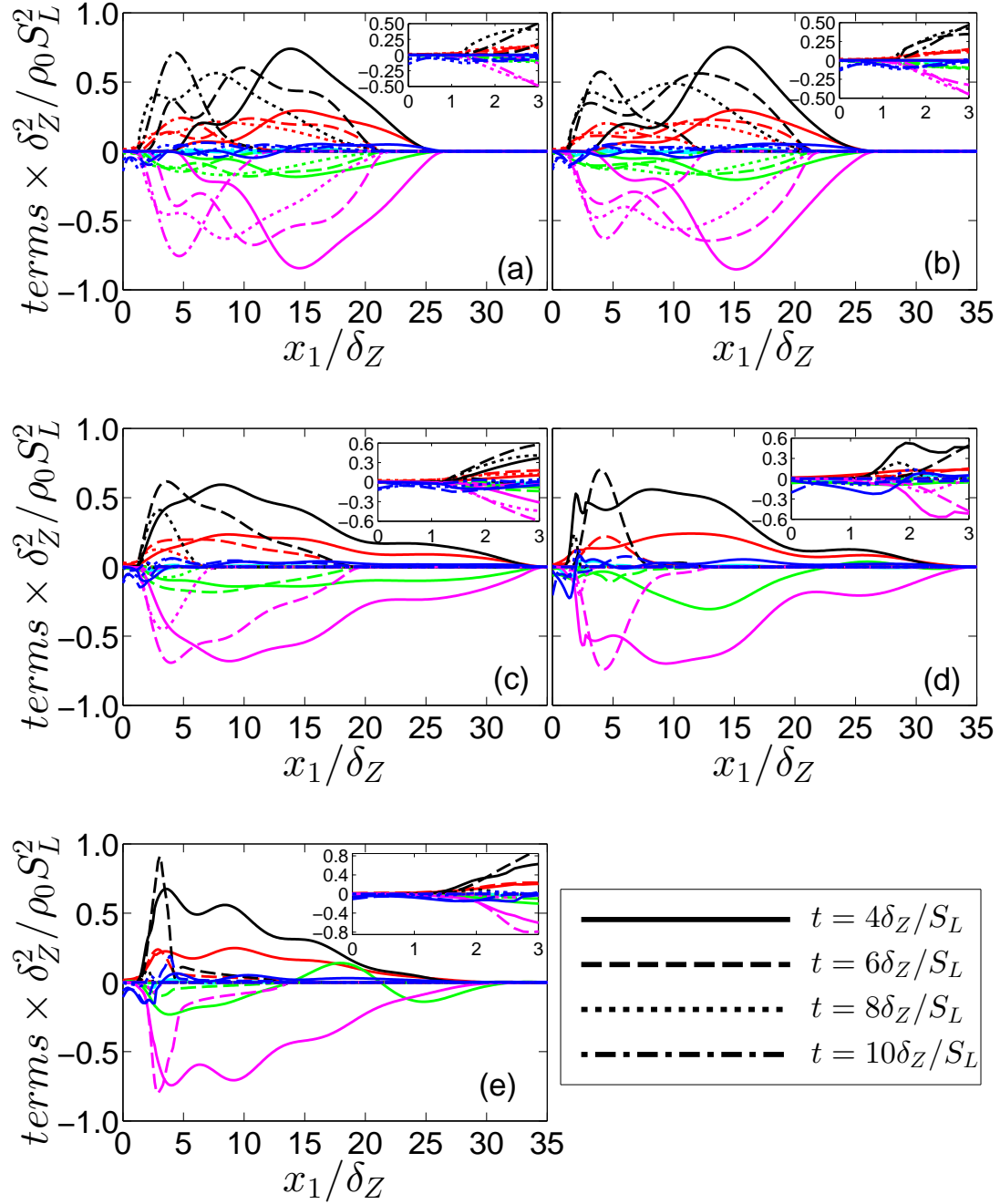


Fig. 6.7 Variations of T_1 ; T_2 ; T_3 ; T_4 ; $(-D_2)$; $f(D)$ with x_1/δ_Z at $t = 4\delta_Z/S_L, 6\delta_Z/S_L, 8\delta_Z/S_L, 10\delta_Z/S_L$ for turbulent cases (a-e) A - E with $Le = 1.0$.

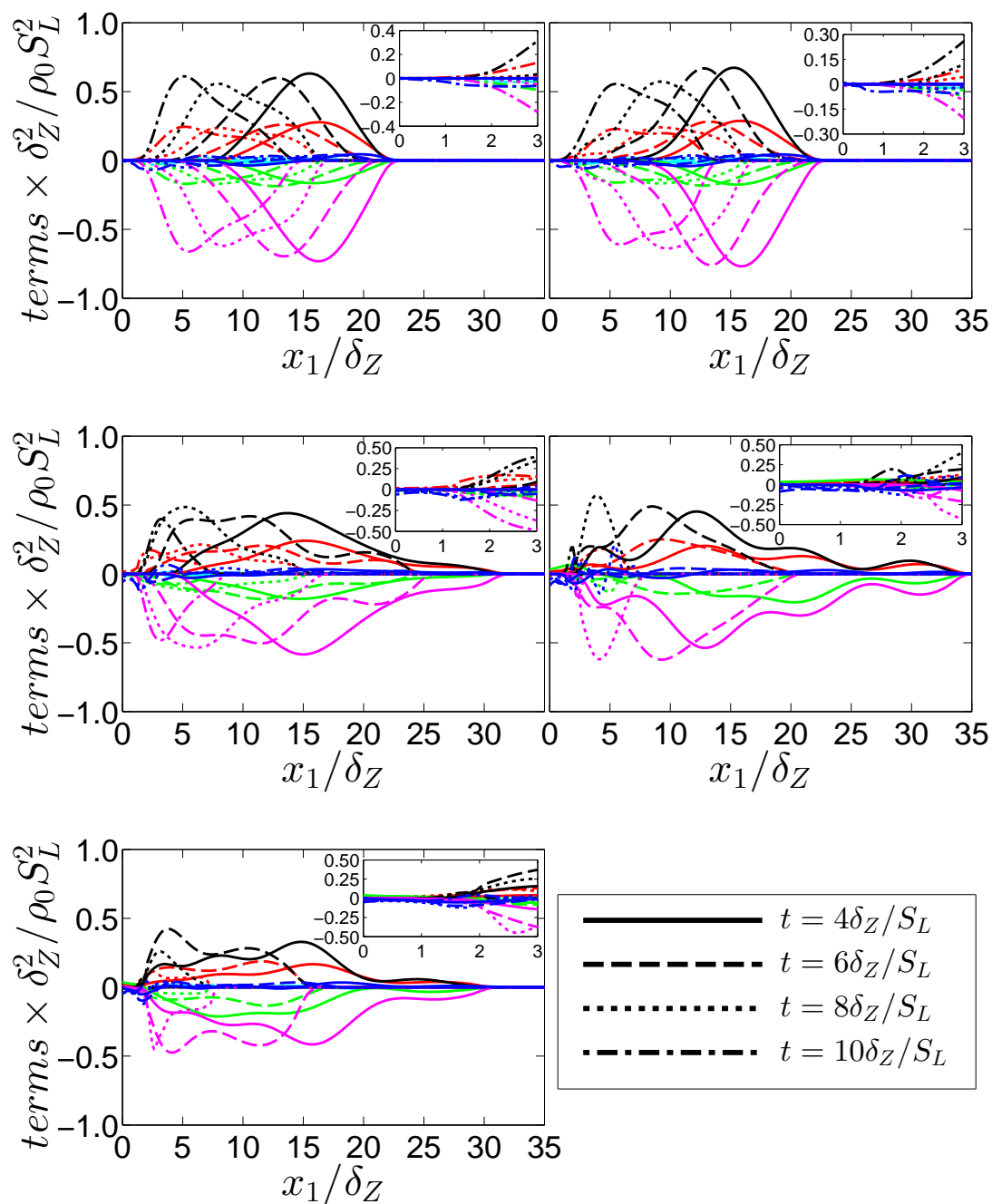


Fig. 6.8 Variations of T_1 , T_2 , T_3 , T_4 , $(-D_2)$, $f(D)$ with x_1/δ_Z at $t = 4\delta_Z/S_L, 6\delta_Z/S_L, 8\delta_Z/S_L, 10\delta_Z/S_L$ for turbulent cases (a-e) A - E with $Le = 1.2$.

It is worth noting that T_2 , T_4 and $f(D)$ were not included in the scaling analysis by Mantel and Borghi [137], and thus, the scaling estimates of T_2 , T_4 and $f(D)$ are not provided in Eqs. 6.9 and 6.11.

Equations 6.8 - 6.11 suggest that T_2 , T_3 , T_4 , $(-D_2)$ and $f(D)$ are expected to be leading order contributors to the SDR $\tilde{\varepsilon}_c$ transport irrespective of the value of Da and Re_t , which can be substantiated from the behaviours of T_2 , T_3 , T_4 , $(-D_2)$ and $f(D)$ away from the wall for all cases considered here. It can be seen from Figs. 6.6 - 6.8 that T_2 , T_3 , T_4 , $(-D_2)$ indeed scale with $\rho_0 S_L^2 / \delta_Z^2$ away from the wall but their magnitudes decrease once the quenching starts. However, the terms of the SDR transport equation assume higher magnitudes for high values of $u'/S_L \sim Re_t^{1/4} Ka^{1/4} \sim Re_t^{1/2} Da^{-1/2}$. Figures 6.6 - 6.8 show that the contribution of the turbulent transport term T_1 remains negligible in comparison to the other terms in the $\tilde{\varepsilon}_c$ transport equation for all Lewis number and turbulent cases at all times. The chemical reaction rate term T_4 acts as the most dominant source away from the wall but its magnitude drops significantly in the near wall region (i.e. $x_1/\delta_Z < Pe_{\min}$) due to the negligible value of $\bar{\omega}$ as a result of flame quenching. The density variation term T_2 acts as a leading order source away from the wall and this term assumes non-zero values in the near wall region because of significant variations of density due to temperature gradient close to the wall even though the chemical reaction ceases to take place. The magnitudes of T_2 and T_4 increase from cases A to E, because the scalar gradient assumes high magnitudes for high values of $u'/S_L \sim Re_t^{1/4} Ka^{1/4} \sim Re_t^{1/2} Da^{-1/2}$. The effects of chemical reaction and heat release are strong for flames with small values of Le , and thus, the magnitudes of T_2 and T_4 away from the wall increase with decreasing Le .

The scalar-turbulence interaction term T_3 acts as a sink for all cases with $Le \leq 0.8$ and for cases A-C with $Le = 1.0$ and 1.2 . However, the scalar-turbulence interaction term T_3 locally assumes positive values in case D and E for the turbulent $Le = 1.0$ and 1.2 flames, but this term assumes negative values as time progresses before vanishing altogether following flame quenching. The term T_3 can be expressed in the following manner [47, 43, 187, 135]:

$$T_3 \approx -2(e_\alpha \cos^2 \alpha + e_\beta \cos^2 \beta + e_\gamma \cos^2 \gamma) \rho \varepsilon_c \quad (6.12)$$

where e_α , e_β and e_γ are the most extensive, intermediate and most compressive principal strain rates respectively and α , β and γ are the angles of ∇c with the eigenvectors associated with e_α , e_β and e_γ respectively. This suggests that a predominant alignment of ∇c with e_α (i.e. high probability of obtaining $|\cos \alpha| \approx 1$) gives rise to a negative contribution of T_3 , whereas a preferential alignment of ∇c with e_γ gives rise to a positive

contribution of T_3 . It has been demonstrated elsewhere [47, 43, 187, 135] that ∇c preferentially aligns with e_α when the strain rate induced by flame normal acceleration a_{chem} dominates over turbulent straining a_{turb} , whereas ∇c preferentially aligns with e_γ when a_{turb} is stronger than a_{chem} . Moreover, a_{chem} weakens in comparison to a_{turb} for increasing (decreasing) Ka (Da). Furthermore, the effects of the strain rate induced by flame normal acceleration a_{chem} strengthen with decreasing Le due to strong heat release for the flames with small values of global Lewis number [47]. In the turbulent $Le = 0.8$ cases considered here, a_{chem} dominates over a_{turb} to give rise to a preferential ∇c alignment with e_α , leading to negative values of T_3 . Thus, a_{turb} is likely to dominate over a_{chem} in some locations in the high u'/S_L cases such as in case E with $Le = 1.0$ and 1.2, which gives rise to local positive values of T_3 . The effects of turbulence are weak in cases A-C due to comparatively small values of Re_t and thus ∇c preferentially aligns with e_α , leading to predominantly negative values of T_3 . However, due to the turbulence decaying both with time and in the vicinity of the wall, ∇c predominantly aligns with e_α . This leads to negative values of T_3 close to the wall, and the likelihood of obtaining negative values of T_3 increases as time progresses even for the cases where positive values of T_3 were obtained at a previous time instant (see Figs. 6.6 - 6.8). The aforementioned behaviour can be substantiated from Fig. 6.9 where the variation of scalar gradient alignment markers $\overline{\Psi}_\alpha$, $\overline{\Psi}_\beta$ and $\overline{\Psi}_\gamma$ with x_1/δ_Z for cases A-E are shown, where $\overline{\Psi}_\alpha$, $\overline{\Psi}_\beta$ and $\overline{\Psi}_\gamma$ are defined as:

$$\Psi_\alpha = |\cos\alpha|, \Psi_\beta = |\cos\beta|, \Psi_\gamma = |\cos\gamma| \quad \text{when} \quad 0.01 \leq c \leq 0.99 \quad (6.13)$$

$$\text{Otherwise} \quad \Psi_\alpha = \Psi_\beta = \Psi_\gamma = 0$$

A high magnitude of $\overline{\Psi}_\alpha$ ($\overline{\Psi}_\gamma$) implies that a predominant collinear alignment between ∇c and e_α (e_γ). It can be seen from 6.9 that $\overline{\Psi}_\alpha$ assumes higher values than $\overline{\Psi}_\beta$ and $\overline{\Psi}_\gamma$ at all locations in cases A and B at all times, which justifies the negative values of T_3 in these cases at locations at all times. In case C, $\overline{\Psi}_\alpha$ assumes higher values than $\overline{\Psi}_\beta$ and $\overline{\Psi}_\gamma$ for in all locations when the flame is away from the wall (i.e. $\overline{\Psi}_\gamma$). However, during the final stage of flame extinction (e.g. $t = 10\delta_Z/S_L$) $\overline{\Psi}_\gamma$ assumes higher values than $\overline{\Psi}_\alpha$ and $\overline{\Psi}_\beta$ but a comparison between Figs. 6.6, 6.7, 6.8 and 6.9 reveals that the probability of finding almost fully burned mixture is predominant in the near wall region (i.e. $x_1/\delta_Z < Pe_{\text{min}}$) at that time which leads to weak heat release effects and thus justifies a greater extent of ∇c alignment with e_γ than with e_α . The

magnitude of ∇c is small in almost fully burned mixture and as a result T_3 assumes negligible magnitude in the near wall region (i.e. $x_1/\delta_Z < Pe_{\min}$) at $t = 10\delta_Z/S_L$ in case C. A similar behaviour has been observed for cases D and E but $\bar{\Psi}_\gamma$ starts to assume higher values than $\bar{\Psi}_\alpha$ and $\bar{\Psi}_\beta$ in the near wall region (i.e. $x_1/\delta_Z < Pe_{\min}$) from an earlier time (e.g. $t = 6\delta_Z/S_L$) than in case C. However, in high Ka flames (e.g. case E) $\bar{\Psi}_\gamma$ can also locally assume higher values than $\bar{\Psi}_\alpha$ and $\bar{\Psi}_\beta$ even when the flame is away from the wall (i.e. $x_1/\delta_Z > Pe_{\min}$) due to predominant ∇c alignment with e_γ as a result of the domination of a_{turb} over a_{chem} (see $15 \leq x_1/\delta_Z \leq 20$ in case E at $t = 4\delta_Z/S_L$). However, turbulence decays with time and also close to the wall, which leads to predominant alignment of ∇c with e_α , leading to negative values of T_3 close to the wall even for the cases where positive values of T_3 were obtained away from the wall. Although $\bar{\Psi}_\gamma$ assumes higher values than $\bar{\Psi}_\alpha$ and $\bar{\Psi}_\beta$ in the near wall region during flame quenching in case E, the scalar-turbulence interaction term T_3 assumes negligible values in the region given by $x_1/\delta_Z < Pe_{\min}$ due to the availability of the small values of ∇c in almost fully burned mixture (see Figs. 6.6, 6.7, 6.8 and 6.9).

The molecular dissipation term ($-D_2$) is the dominant sink term for all cases, and its magnitude remains comparable to that of T_4 away from the wall. The diffusivity gradient term $f(D)$ shows both positive and negative values but the negative contribution remains dominant close to the wall. The magnitude of $f(D)$ remains smaller than T_2 , T_3 , T_4 and ($-D_2$) when the flame is away from the wall, but it becomes a leading order sink in the near wall region. The magnitudes of ($-D_2$) and $f(D)$ also increase with decreasing Le due to high magnitudes of the scalar and diffusivity gradients, and high progress variable diffusivity in flames with small values of Le .

A comparison of the magnitudes of T_2 , T_3 , T_4 , ($-D_2$) and $f(D)$ in Figs. 6.6- 6.8 reveals that the terms T_3 , T_4 , ($-D_2$) and $f(D)$ in the near wall region assume negligible values in comparison to T_2 , which acts to generate $\tilde{\varepsilon}_c$ in the near wall region even when $\bar{\omega}$ vanishes. Figures 6.6- 6.8 further indicate that the net contribution of T_2 , T_3 , T_4 , ($-D_2$) and $f(D)$ remain in rough equilibrium except in the near wall region. This can be confirmed from the variations of $(T_2 + T_3 + T_4 + f(D))$ and ($-D_2$) with the normalised wall normal distance x_1/δ_Z which are shown in Figs. 6.10 - 6.12 for $Le = 0.8, 1.0$ and 1.2 respectively. Figures 6.10 - 6.12 reveal that the terms $(T_2 + T_3 + T_4 + f(D))$ and ($-D_2$) assume values with same order of magnitude away from the wall which is consistent with the scaling estimates given by Eqs. 6.4 and 6.5. However, the magnitude of $(T_2 + T_3 + T_4 + f(D))$ remains much greater than ($-D_2$) in the near-wall region, which suggests that the equilibrium of the generation and destruction rates of the SDR (i.e.

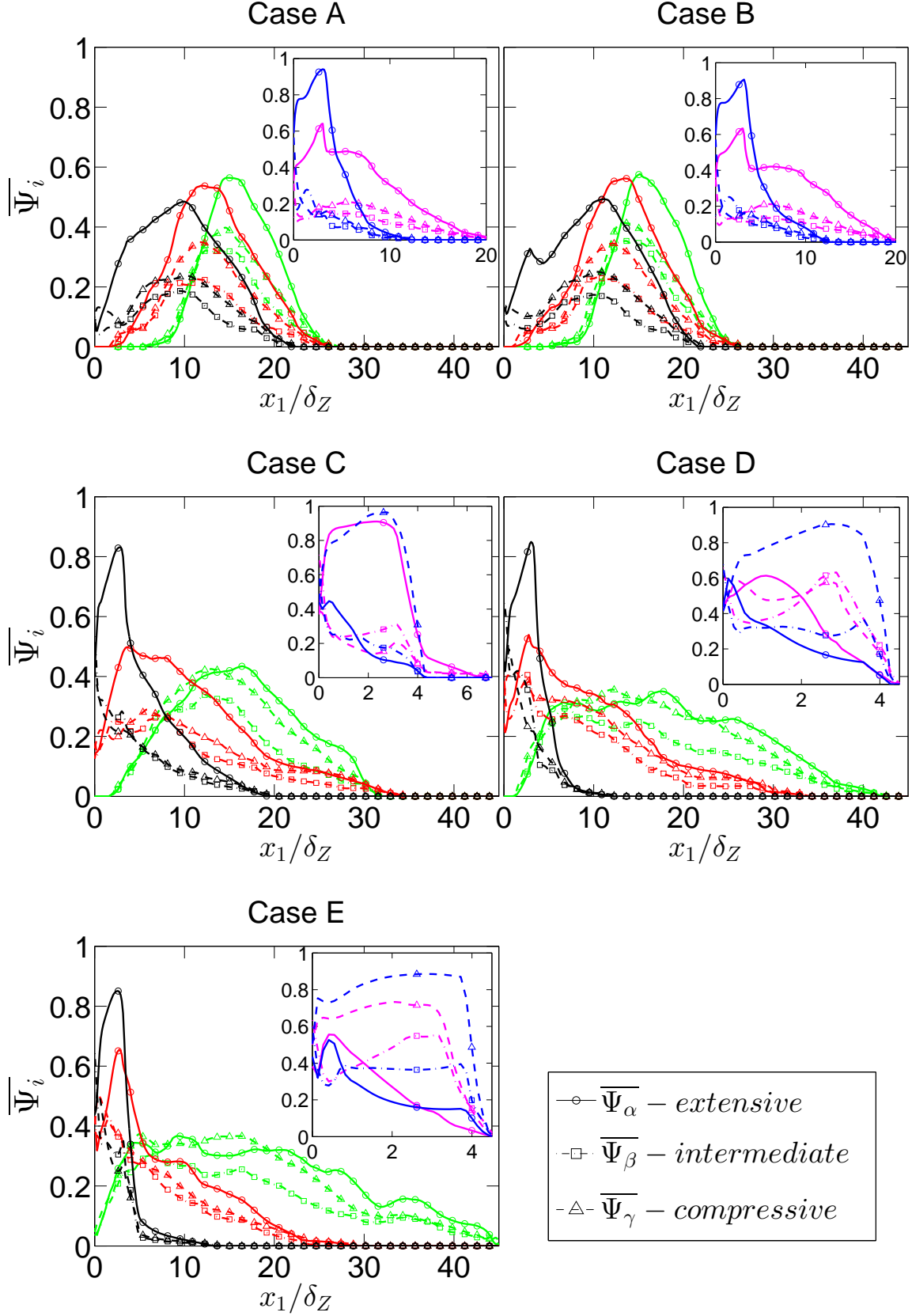


Fig. 6.9 Variations of scalar gradient alignment markers $\overline{\Psi}_\alpha$, $\overline{\Psi}_\beta$ and $\overline{\Psi}_\gamma$ with x_1/δ_Z at $t = 4\delta_Z/S_L$, $6\delta_Z/S_L$, $8\delta_Z/S_L$, $10\delta_Z/S_L$ and $12\delta_Z/S_L$ for turbulent cases A-E for $Le = 1.0$. The x-axis is shown in log scale for the inset. Please refer to the table in Fig. 5.4 for the colour scheme.

equilibrium of the terms $(T_2 + T_3 + T_4 + f(D))$ and $(-D_2)$ cannot be assumed in the near wall region.

6.1.3 Algebraic closure of SDR

Kolla *et al.* [114] proposed an algebraic model for $\tilde{\varepsilon}_c$ in the following manner assuming an equilibrium of the terms T_2 , T_3 , T_4 , $(-D_2)$ and $f(D)$ for $Da \gg 1$ flames with unity Lewis number:

$$\tilde{\varepsilon}_c = \frac{1}{\beta'} \left(2K_c^* \frac{S_L}{\delta_{th}} + C_3 \frac{\tilde{\varepsilon}}{\tilde{k}} - \tau C_4 \frac{S_L}{\delta_{th}} \right) \tilde{c}(1 - \tilde{c}) \quad (6.14)$$

where K_c^* is a thermo-chemical parameter, which is defined as [114]:

$$K_c^* = \frac{\delta_{th} \int_0^1 [\rho(D \nabla c \cdot \nabla c) \nabla \cdot \vec{u} f(c)]_L dc}{S_L \int_0^1 [\rho(D \nabla c \cdot \nabla c) f(c)]_L dc} \quad (6.15)$$

The parameter K_c^* is equal to 0.74τ , 0.78τ and 0.80τ for $Le = 0.8$, 1.0 and 1.2 respectively. In Eq. 6.14, $\beta' = 6.7$, $C_3 = 1.5\sqrt{Ka_L}/(1 + \sqrt{Ka_L})$ and $C_4 = 1.1/(1 + Ka_L)^{0.4}$ are the model parameters where $Ka_L = (\delta_{th}\tilde{\varepsilon}/S_L^3)^{1/2}$ is the local Karlovitz number and $\tilde{\varepsilon}$ is the dissipation rate of turbulent kinetic energy \tilde{k} . The terms $2K_c^*(S_L/\delta_{th})$, $(C_3\tilde{\varepsilon}/\tilde{k} - \tau C_4 S_L/\delta_{th})$ and $\tilde{c}(1 - \tilde{c})/\beta'$ originate due to the models for T_2 , T_3 , and $(T_4 - D_2 + f(D))$ respectively and interested readers are referred to Ref. [114] for further information on the derivation of Eq. 6.14. It has been demonstrated by Chakraborty and Swaminathan [50] that the model given by Eq. 6.14 predicts $\tilde{\varepsilon}_c$ satisfactorily for the turbulent $Le \approx 1.0$ flames even for $Da < 1$ flamelet combustion. However, Eq. 6.14 significantly underpredicts $\tilde{\varepsilon}_c$ for flames with $Le \ll 1$. Thus, Chakraborty and Swaminathan [50] modified Eq. 6.14 in the following manner in order to account for the non-unity Lewis number effects using the models proposed for T_2 , T_3 , and $(T_4 - D_2 + f(D))$ in Ref. [49]:

$$\tilde{\varepsilon}_c = \frac{1}{\beta'} \left(2 \frac{K_c^*}{Le^{0.88}} \frac{S_L}{\delta_{th}} + C_3 \frac{\tilde{\varepsilon}}{\tilde{k}} - \tau \frac{C_4(1 - \tilde{c})^\phi}{Le^{2.57}} \frac{S_L}{\delta_{th}} \right) \tilde{c}(1 - \tilde{c}) \quad (6.16)$$

where $\beta' = 6.7$, $\phi = 0.2 + 1.5(1 - Le)$, $C_3 = 2\sqrt{Ka_L}/(1 + \sqrt{Ka_L})$ and $C_4 = 1.2/(1 + Ka_L)^{0.4}$ are the model parameters. In Eq. 6.16, the Lewis number dependence in $2(Ka_c^*/Le^{1.88})(S_L/\delta_{th})$, and $-\tau [C_4(1 - \tilde{c})^\phi/Le^{2.57}] (S_L/\delta_{th})$ account for the high magnitudes of positive contribution of T_2 and negative contribution of T_3 for small values of Le .

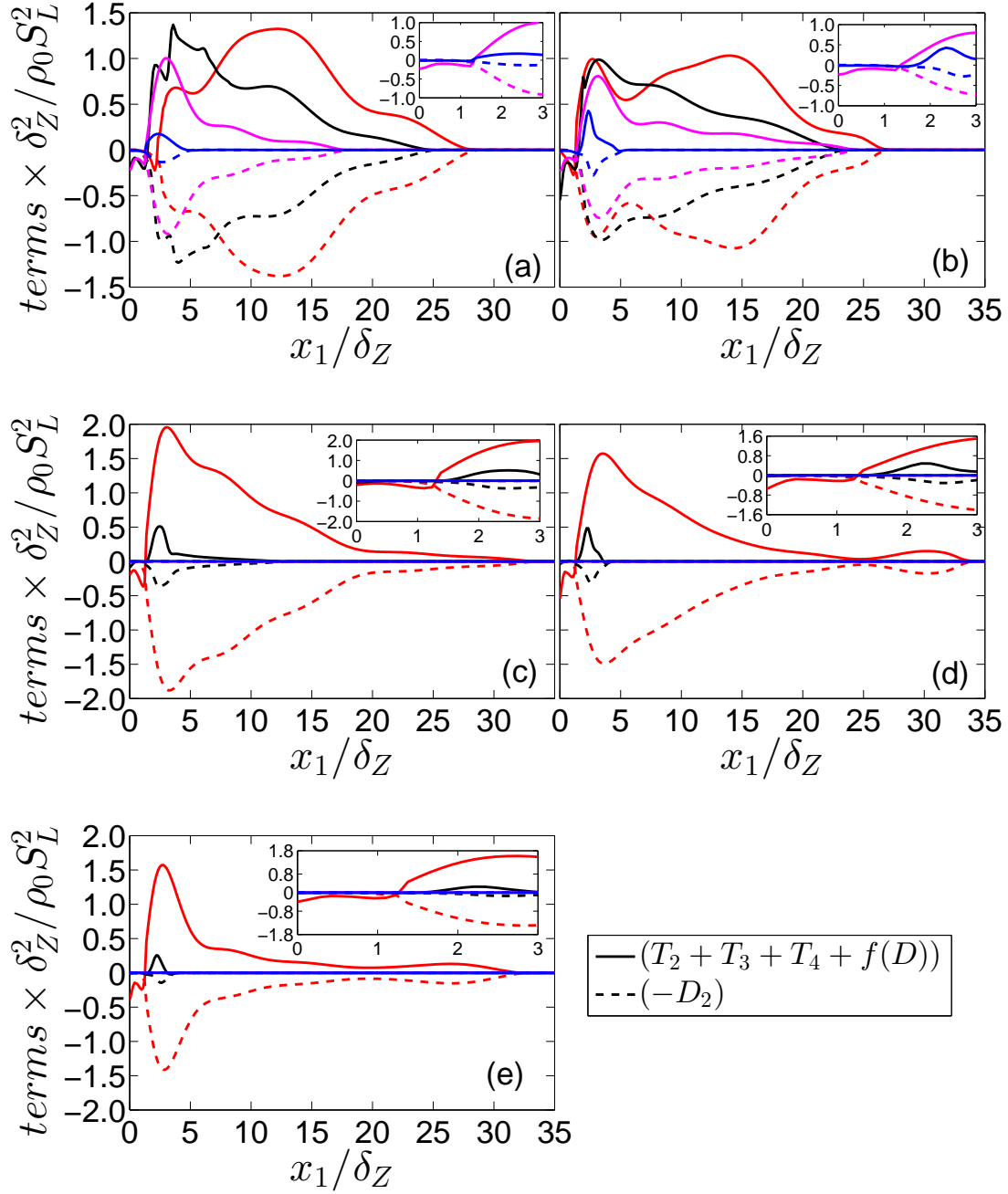


Fig. 6.10 Variations of $(T_2 + T_3 + T_4 + f(D))$ and $(-D_2)$ with x_1/δ_Z at $t = 4\delta_Z/S_L, 6\delta_Z/S_L, 8\delta_Z/S_L, 10\delta_Z/S_L$ for turbulent cases (a-e) A - E with $Le = 0.8$. Please refer to the table in Fig. 5.4 for the colour scheme.

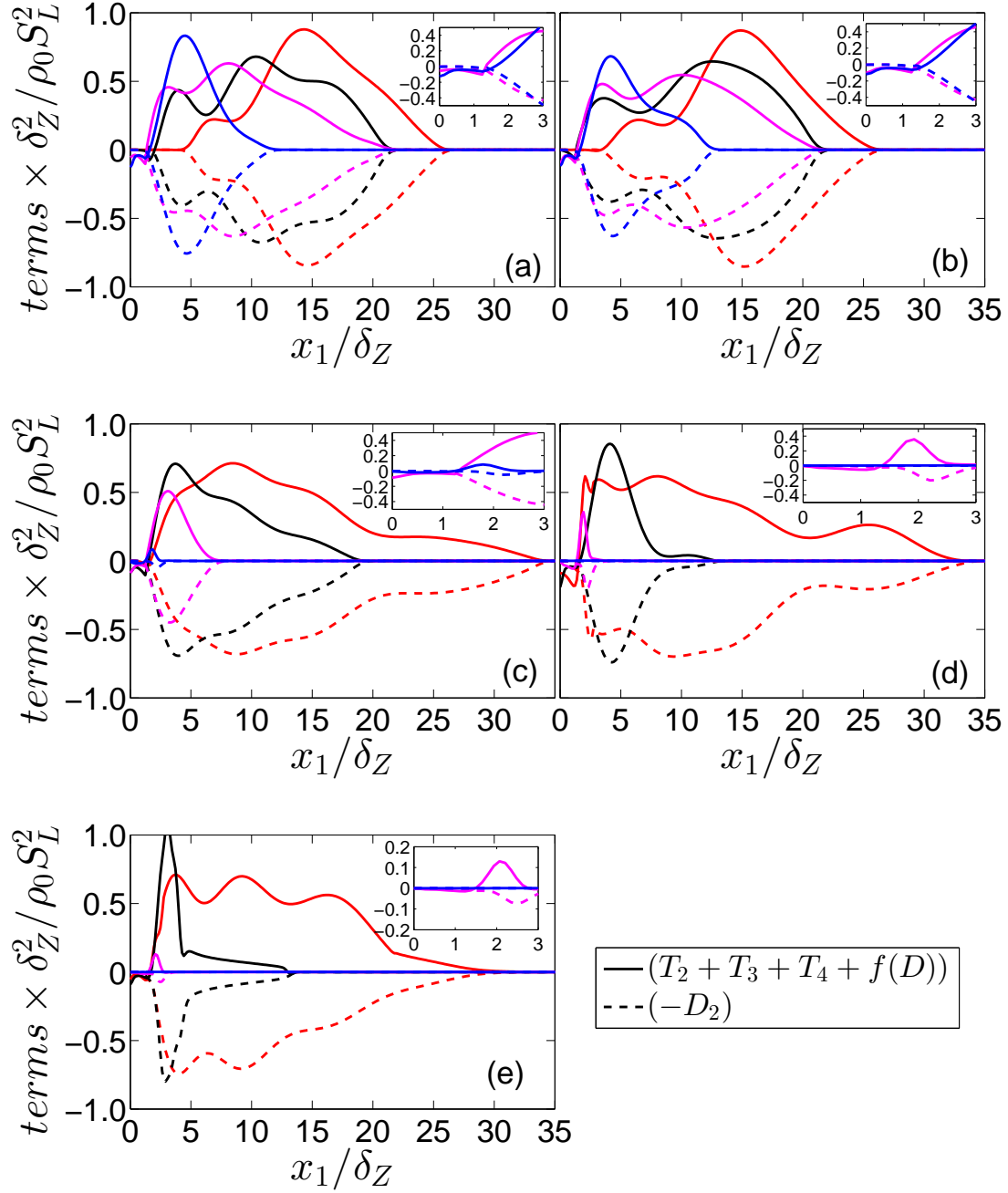


Fig. 6.11 Variations of $(T_2 + T_3 + T_4 + f(D))$ and $(-D_2)$ with x_1/δ_Z at $t = 4\delta_Z/S_L, 6\delta_Z/S_L, 8\delta_Z/S_L, 10\delta_Z/S_L$ for turbulent cases (a-e) A - E with $Le = 1.0$. Please refer to the table in Fig. 5.4 for the colour scheme.

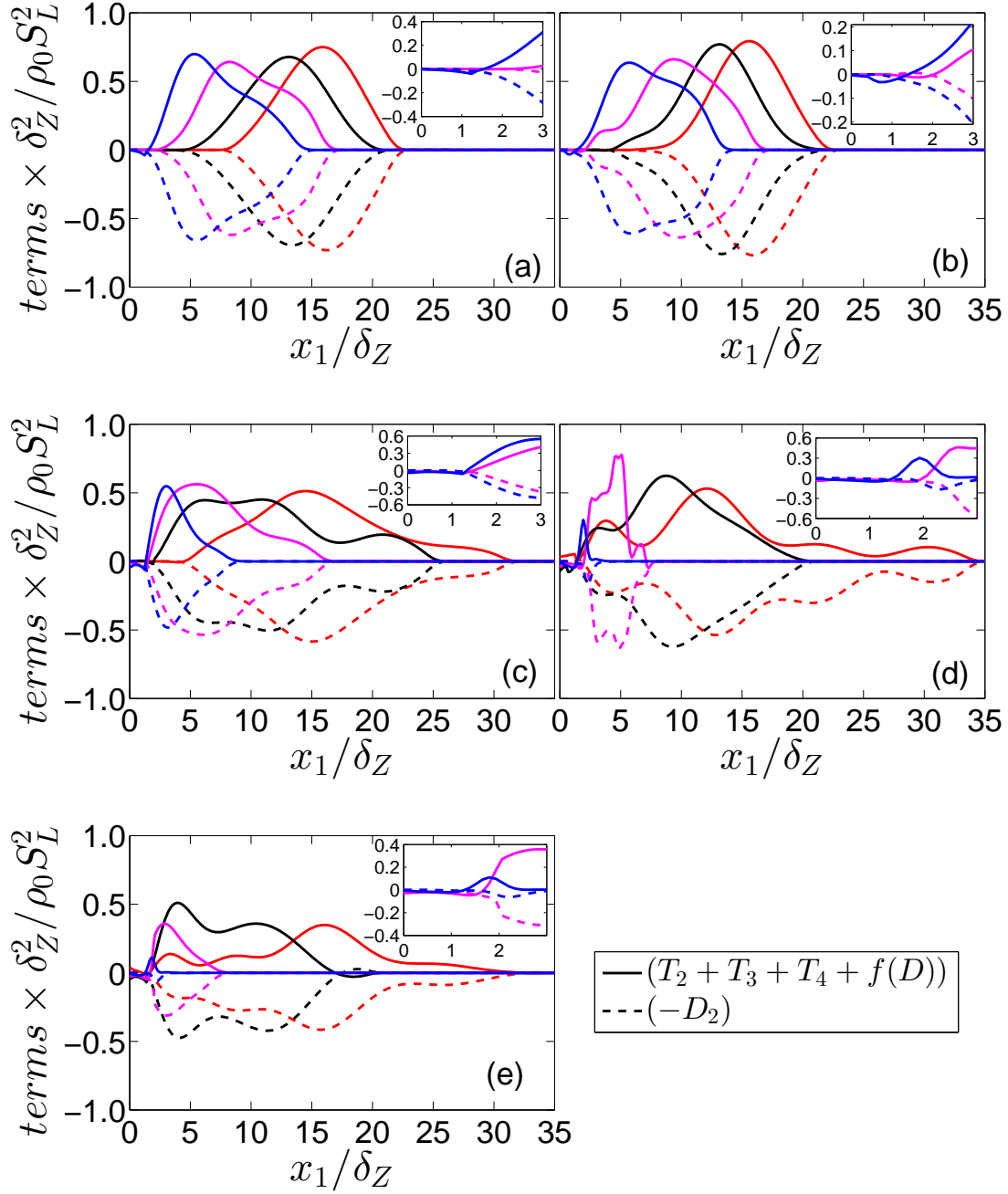


Fig. 6.12 Variations of $(T_2 + T_3 + T_4 + f(D))$ and $(-D_2)$ with x_1/δ_Z at $t = 4\delta_Z/S_L, 6\delta_Z/S_L, 8\delta_Z/S_L, 10\delta_Z/S_L$ for turbulent cases (a-e) A - E with $Le = 1.2$. Please refer to the table in Fig. 5.4 for the colour scheme.

The variations of $\tilde{\varepsilon}_c$ with the normalised wall normal distance x_1/δ_Z are shown in Figs. 6.13 - 6.15 for $Le = 0.8, 1.0$ and 1.2 respectively. Figures 6.13 - 6.15 show that Eq. 6.16 predicts $\tilde{\varepsilon}_c$ satisfactorily when the flame is away from the wall where the terms $T_2, T_3, T_4, (-D_2)$ and $f(D)$ remain in approximate equilibrium (see Figs. 6.10-6.12). However, Eq. 6.16 significantly overpredicts $\tilde{\varepsilon}_c$ in the near wall region (i.e. $0 < x_1/\delta_Z < Pe_{\min}$) where the unclosed source and sink terms of the SDR transport equation are not in equilibrium (see Figs. 6.10- 6.12), and $\tilde{\varepsilon}/\tilde{k}$ assumes large magnitudes near the wall. Equation 6.16 is modified here in the following manner in order to account for the near wall behaviour:

$$\tilde{\varepsilon}_c = \frac{A_\epsilon e^{-1.2Le(\tilde{c}_w - \tilde{T}_w)^3}}{\beta'} \left(2 \frac{K_c^*}{Le^{0.88}} \frac{S_L}{\delta_{th}} + C_3 \frac{\tilde{\varepsilon}}{\tilde{k}} - \tau \frac{C_4(1 - \tilde{c})^\phi}{Le^{2.57}} \frac{S_L}{\delta_{th}} \right) \tilde{c}(1 - \tilde{c}) \quad (6.17)$$

where the model parameters are $A_\epsilon = 0.5[\text{erf}(x_1/\delta_Z - \Pi) + 1]$ and $\exp[-1.2Le(\tilde{c}_w - \tilde{T}_w)^3]$ only remain active close to the wall to account for the flame-wall interaction and they asymptotically approach 1.0 away from the wall. Figures 6.13 - 6.15 show that Eq. 6.17 is able to predict $\tilde{\varepsilon}_c$ accurately for both near to and away from the wall. Thus, Eq. 6i in conjunction with Eq. 6.17 can be used for the mean reaction rate $\bar{\omega}$ closure in the premixed flame wall interaction for a range of different values of global Lewis number.

6.1.4 Modelling of turbulent transport term T_1

It can be seen from Eqs. 6.8 that the magnitude of T_{12} is expected to negligible in comparison to that of T_{11} for high values of Re_t . Hence, T_1 in practical high Re_t turbulent flows can be approximated as:

$$T_1 \approx -\frac{\partial(\overline{\rho u_j'' \varepsilon_c})}{\partial x_j} \quad (6.18)$$

In order to model turbulent transport T_1 , it is essential to model the turbulent flux $\overline{\rho u_j'' \varepsilon_c}$, which is often modelled for passive scalar mixing using a gradient flux model for $\overline{\rho u_j'' \varepsilon_c}$:

$$\overline{\rho u_j'' \varepsilon_c} = -\frac{\mu_t}{\sigma_\varepsilon} \frac{\partial \tilde{\varepsilon}_c}{\partial x_j} \quad (6.19)$$

where $\mu_t = \bar{\rho} C_\mu \tilde{k}^2 / \tilde{\varepsilon}$ is the eddy viscosity, $C_\mu = 0.09$ model constant and σ_ε is the turbulent Schmidt number. However, it is well known that turbulent fluxes of the

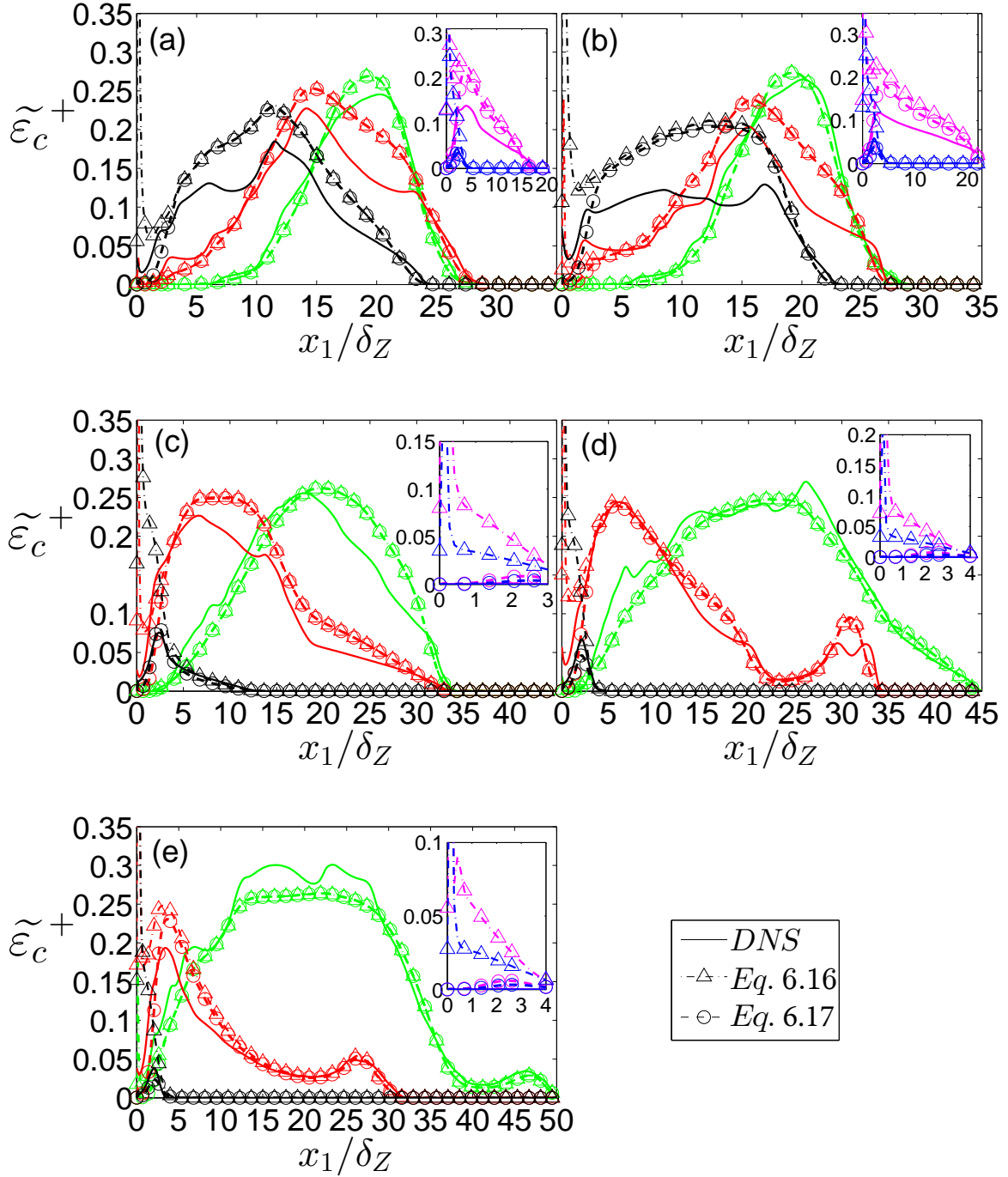


Fig. 6.13 Variations of $\tilde{\varepsilon}_c^+ = \tilde{\varepsilon}_c \times \delta_Z/S_L$ obtained from DNS and the prediction of Eq. 6.16 and 6.17 with x_1/δ_Z at $t = 4\delta_Z/S_L, 6\delta_Z/S_L, 8\delta_Z/S_L, 10\delta_Z/S_L$ for turbulent cases (a-e) A - E with $Le = 0.8$. Please refer to the table in Fig. 5.4 for the colour scheme.

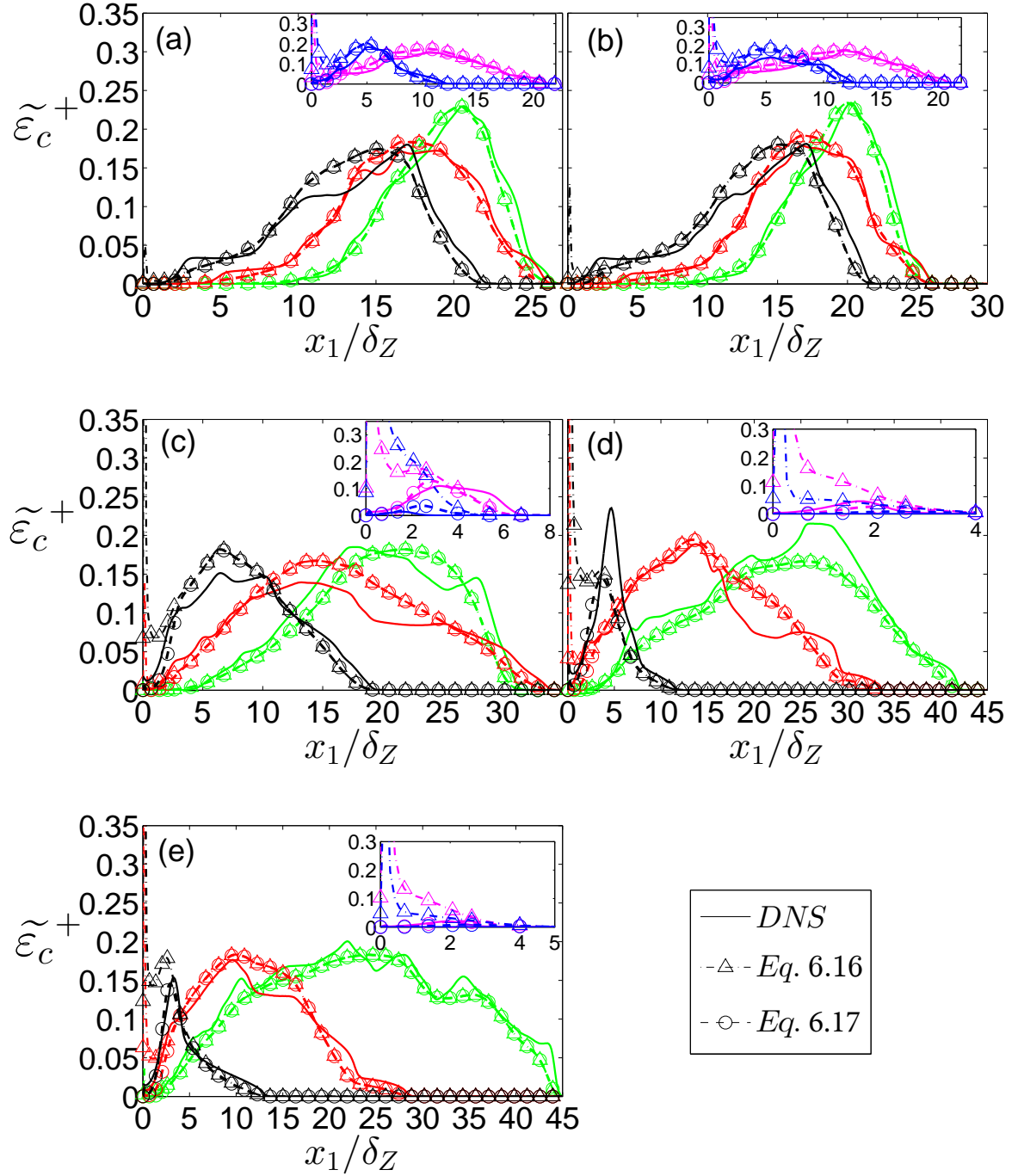


Fig. 6.14 Variations of $\tilde{\varepsilon}_c^+ = \tilde{\varepsilon}_c \times \delta_Z/S_L$ obtained from DNS and the prediction of Eq. 6.16 and 6.17 with x_1/δ_Z at $t = 4\delta_Z/S_L, 6\delta_Z/S_L, 8\delta_Z/S_L, 10\delta_Z/S_L$ for turbulent cases (a-e) A - E with $Le = 1.0$. Please refer to the table in Fig. 5.4 for the colour scheme.

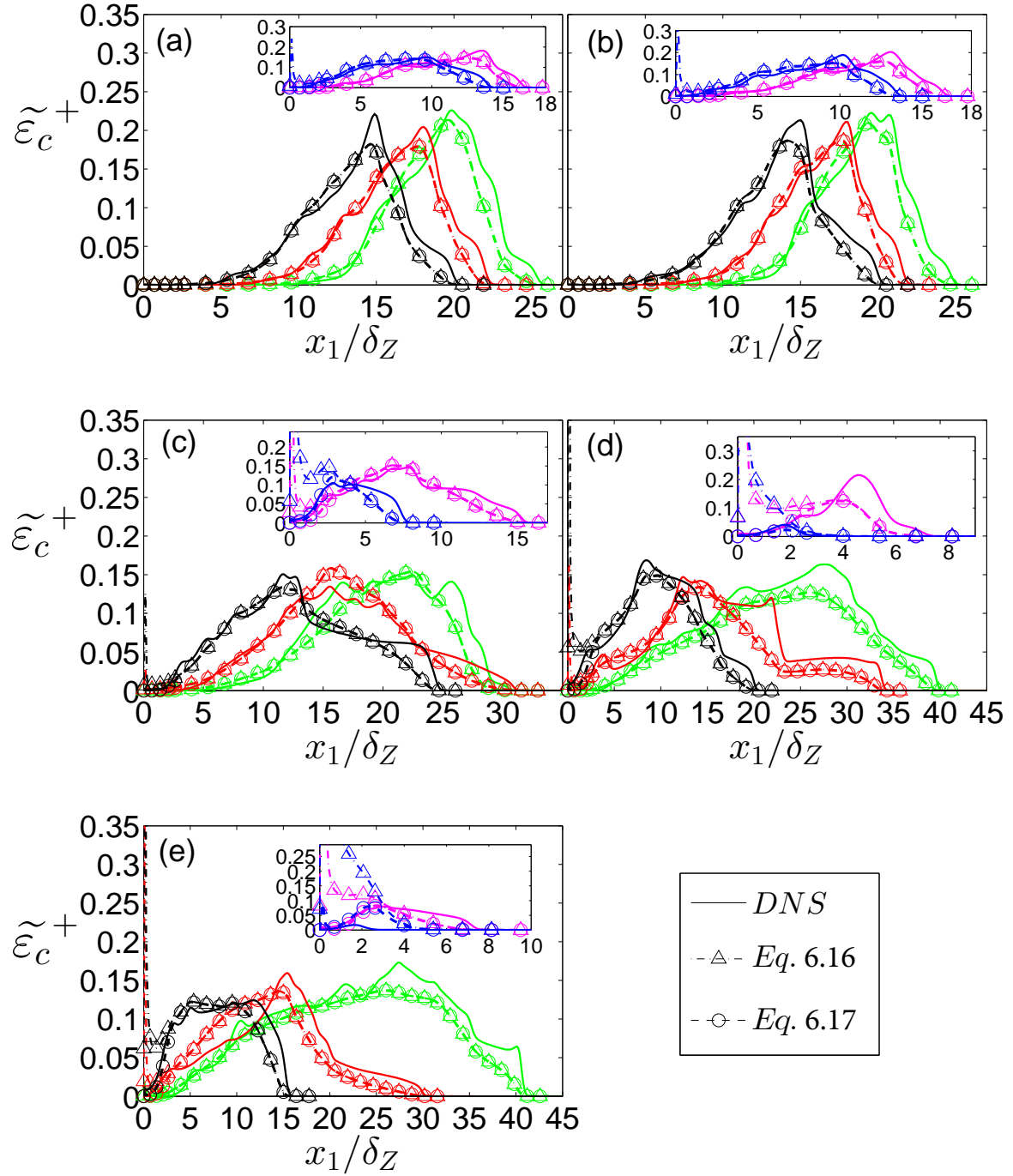


Fig. 6.15 Variations of $\tilde{\varepsilon}_c^+ = \tilde{\varepsilon}_c \times \delta_Z/S_L$ obtained from DNS and the prediction of Eq. 6.16 and 6.17 with x_1/δ_Z at $t = 4\delta_Z/S_L, 6\delta_Z/S_L, 8\delta_Z/S_L, 10\delta_Z/S_L$ for turbulent cases (a-e) A - E with $Le = 1.2$. Please refer to the table in Fig. 5.4 for the colour scheme.

quantities related to turbulent scalar gradient exhibit counter-gradient (gradient) when turbulent scalar flux $\overline{\rho u_i'' c''}$ shows counter-gradient (gradient) type behaviour [33, 49, 202]. One obtains counter-gradient transport when the velocity jump due to flame normal acceleration dominates over turbulent velocity fluctuations and *vice versa* [33, 49, 202].

Chakraborty and Swaminathan [49] proposed a model (referred to as the T1CS model here) for $\overline{\rho u_j'' \varepsilon_c}$ in terms of $\overline{\rho u_i'' c''}$, which is capable of predicting both gradient and counter-gradient type transport:

$$\overline{\rho u_j'' \varepsilon_c} = \lambda_c (\Phi - \tilde{c}) \frac{\overline{\rho u_i'' c''}}{[\widetilde{c''^2} + \tilde{c}(1 - \tilde{c})]} \tilde{\varepsilon}_c \quad (6.20)$$

where the model parameters are given by: $\lambda_c = 2$ and $\Phi = 0.5$ [49]. Figure 6.16 shows that the T1CS model under-predicts the turbulent flux $\overline{\rho u_1'' \varepsilon_c}$ in a region where $x_1/\delta_Z \leq (Pe_{\min})_L$. As the flame propagates towards the quenching zone, the SDR flux $\overline{\rho u_1'' \varepsilon_c}$ exhibits mainly gradient type transport. The T1CS model assumes the transition of $\overline{\rho u_j'' \varepsilon_c}/\overline{\rho u_i'' c''}$ from a negative to a positive value at $\tilde{c} \approx 0.5$ by using the factor $(\Phi - \tilde{c})$. This transition is no longer valid in the near wall region because of predominantly gradient transport and also due to the absence of the effects of flame normal acceleration as a result of flame quenching. The T1CS model has been revised here in the following manner:

$$\overline{\rho u_j'' \varepsilon_c} = \lambda_c^* (\Phi^* - \tilde{c}) \frac{\overline{\rho u_i'' c''}}{[\widetilde{c''^2} + \tilde{c}(1 - \tilde{c})]} \tilde{\varepsilon}_c \quad (6.21)$$

where $\lambda_c^* = 2A_1$, $\Phi^* = 0.5^{1-\tilde{c}_w}$, $A_1 = 1.95^{\text{erf}\{[(Pe_{\min})_L - x_1/\delta_Z] + 1\}}$. The model parameter A_1 remains active only in the near wall region, and it increases the multiplier of $(\Phi^* - \tilde{c})\overline{\rho u_i'' c''}\tilde{\varepsilon}_c/[\widetilde{c''^2} + \tilde{c}(1 - \tilde{c})]$ and avoids the near wall underprediction of $\overline{\rho u_1'' \varepsilon_c}$ by the T1CS model. The parameter Φ^* has been modified in such a manner that it increases threshold of the transition of $\overline{\rho u_1'' \varepsilon_c}/\overline{\rho u_i'' c''}$ from negative to positive value according to the value of Favre averaged reaction progress variable at the wall $\tilde{c}_w = \tilde{c}$ ($x_1 = 0$). Furthermore, the model parameters λ_c^* and Φ^* have been parameterised in such a manner that Eq. 6.21 approaches Eq. 6.20 away from the wall (i.e. $x_1/\delta_Z \gg (Pe_{\min})_L$). It can be seen from Fig. 6.16 that the revised model captures both qualitative and quantitative behaviours of $\overline{\rho u_1'' \varepsilon_c}$ both away from and close to the wall.

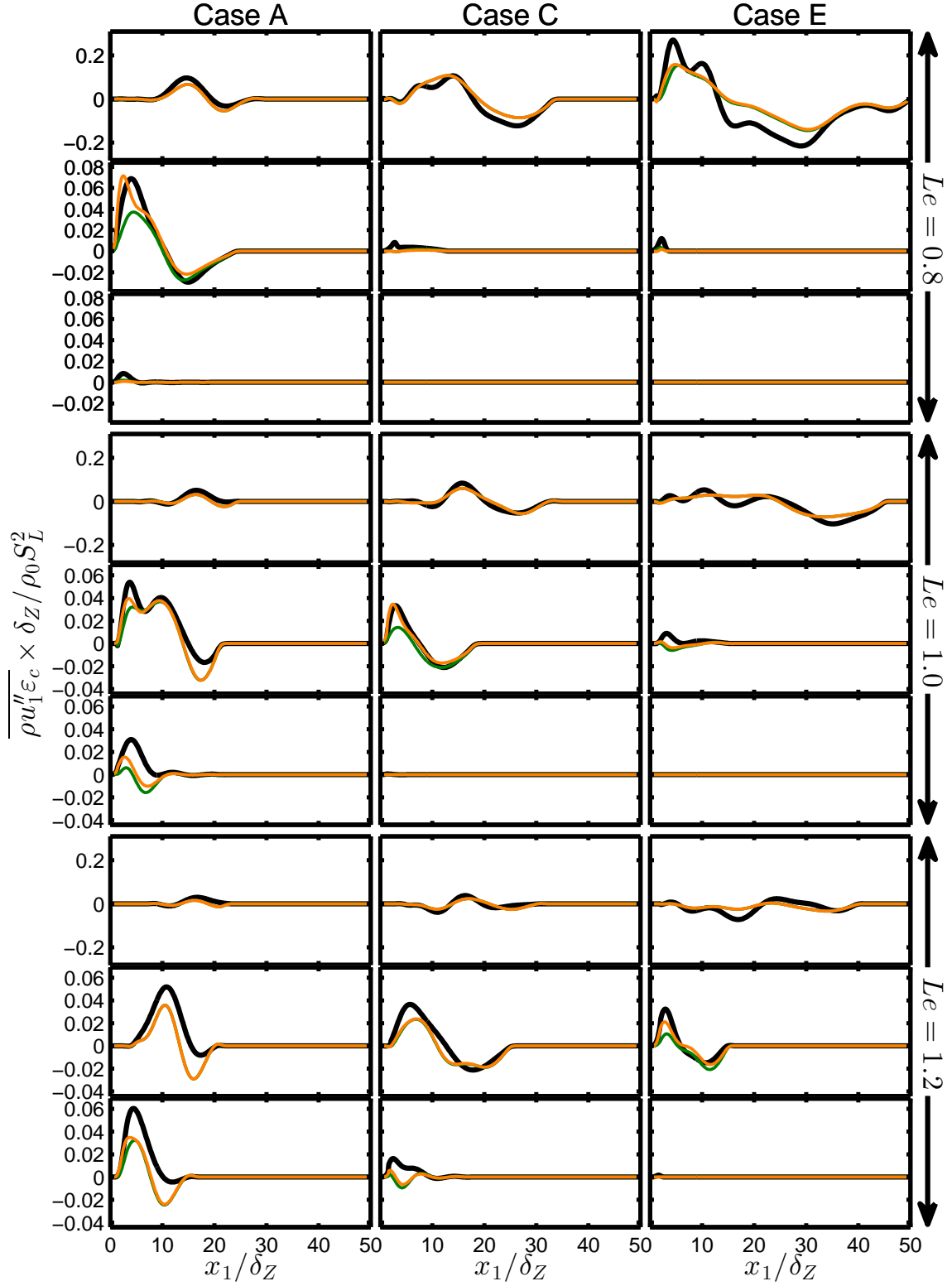


Fig. 6.16 Variations of $\overline{\rho u_1'' \varepsilon_c} \times \delta_Z / \rho_0 S_L^2$ (—) with x_1 / δ_Z along with the predictions by the T1CS model (—) and Eq. 6.21 (—) at for cases A, C and E (1st - 3rd column) at $t = 2\delta_Z/S_L$, $6\delta_Z/S_L$ and $10\delta_Z/S_L$ (1st - 3rd row).

6.1.5 Modelling of density variation term T_2

The fluid density ρ in low Mach number combustion is given by [19]:

$$\rho = \frac{\rho_0}{(1 + \tau T)} \quad (6.22)$$

The non-dimensional temperature T can be equated to the reaction progress variable c (e.g. $T = c$) for globally adiabatic unity Lewis number flames in absence of the wall. Thus, under the aforementioned condition ρ and $\bar{\rho}$ can be expressed in term of c and \tilde{c} as:

$$\rho = \frac{\rho_0}{(1 + \tau c)} \quad \text{and} \quad \bar{\rho} = \frac{\rho_0}{(1 + \tau \tilde{c})} \quad (6.23)$$

Using Eq. 6.23, T_2 can be expressed in the following manner [46, 49, 36, 185]:

$$T_2 = \overline{2\rho N_c \frac{\partial u_j}{\partial x_j}} - \overline{2\rho D \nabla \tilde{c} \cdot \nabla \tilde{c} \frac{\partial \tilde{u}_j}{\partial x_j}} \quad (6.24)$$

According to above equation, an alternative expression for T_2 can be obtained in the following manner:

$$T_2 = \underbrace{\overline{2\rho \varepsilon_c \frac{\partial u_j}{\partial x_j}}}_{T_{21}} + \underbrace{\overline{4\rho D \frac{\partial c''}{\partial x_j} \frac{\partial u_k}{\partial x_k} \frac{\partial \tilde{c}}{\partial x_j}}}_{T_{22}} + \underbrace{\overline{2\nabla \tilde{c} \cdot \nabla \tilde{c} \rho D \frac{\partial u_j''}{\partial x_j}}}_{T_{23}} \quad (6.25)$$

According to the scaling argument by Swaminathan and Bray [185], the terms T_{21} , T_{22} and T_{23} can be scaled in the following manner:

$$T_{21} \sim O\left(\frac{\rho_0 S_L^2}{\delta_Z^2}\right); \quad T_{22} \sim O\left(\frac{\rho_0 S_L^2}{\delta_Z^2} \times \frac{1}{\sqrt{Re_t Da}}\right); \quad T_{23} \sim O\left(\frac{\rho_0 S_L^2}{\delta_Z^2} \times \frac{1}{Re_t Da}\right) \quad (6.26)$$

where the velocity fluctuation, gradients of fluctuation and its mean quantities are scaled using S_L , δ_Z and l respectively. Equation 6.26 suggests that T_{22} and T_{23} becomes negligible in comparison to T_{21} for high values of Re_t . Consequently, T_2 can be taken to scale with $\rho_0 S_L^2 / \delta_Z^2$ [185]. For unity Lewis number flame, the dilatation rate $\nabla \cdot \vec{u}$ is scaled as $\nabla \cdot \vec{u} \sim \tau S_L / \delta_{th}$ [185, 47, 48, 46], and SDR scales with $\tilde{\varepsilon}_c \sim S_L / \delta_{th}$. The aforementioned scaling arguments have been taken into account in the model proposed

by Chakraborty *et al.* [46] for T_2 which takes the following form for unity Lewis number:

$$T_2 = 2C_{T_2}\tau \frac{S_L}{\delta_{th}} \bar{\rho} \tilde{\varepsilon}_c \quad (6.27)$$

where $C_{T_2} = B_{T_2}/(1 + Ka_L)^{0.5}$ is the model parameter with $B_{T_2} = 2.0$ and $Ka_L \approx (S_L)^{-3/2}(\tilde{\varepsilon}\delta_{th})^{1/2}$ is the local Karlovitz number. The Karlovitz number Ka_L dependence of C_{T_2} accounts for weakening of T_2 magnitude for large values of Ka_L due to diminished heat release effects as the broken reaction zones regime is approached [153]. Chakraborty and Swaminathan [49] shows that Eq. 6.27 is inadequate to capture T_2 behaviour in nonunity Lewis number flames, since the c and T field differ from each other as well as $\widetilde{T''^2}$ and $\widetilde{c''^2}$. For non-unity Le the dilatation rate in flamelets can be scaled as [49]:

$$\nabla \cdot \vec{u} \sim \tau \frac{1}{Le^m} \frac{S_L}{\delta_Z} \quad (6.28)$$

where the model parameter m is a positive number of order unity. Equation 6.28 shows the strength of the dilatation rate increases with decreasing Le . The refined model for non-unity Lewis number is proposed in the following manner (T2CS):

$$T_2 = 2 \frac{\tau}{Le^m} \frac{\delta_Z}{\delta_{th}} \sqrt{\frac{\widetilde{T''^2}}{\widetilde{c''^2}}} \frac{B_{T_2}}{(1 + Ka_L)^{1/2}} \frac{S_L}{\delta_{th}} \bar{\rho} \tilde{\varepsilon}_c \quad (6.29)$$

where the quantity $(\delta_Z/\delta_{th}) \cdot \left(\sqrt{\widetilde{T''^2}}/\sqrt{\widetilde{c''^2}} \right) \cdot \tilde{\varepsilon}_c$ accounts for $\overline{D(\nabla T \cdot \nabla c)}$ in non-unity Le flames and $\delta_Z Le^m \approx \delta_{th} Le^n$. It is worth noting that the Eq. 6.29 reverts to Eq. 6.27 for $Le = 1.0$. The variations of T_2 with normalised wall normal distance x_1/δ_Z at different time instants are shown in Fig. 6.17 for all cases considered here. Figure 6.17 shows that T_2 acts as a source term and assumes higher magnitudes before quenching than after it because most of the density variation occurs due to the chemical heat release. The magnitude of T_2 also diminishes as reaction rate sharply reduces close to wall, but non-zero value of T_2 has been observed during quenching because of the density variation driven by the temperature change across the thermal boundary layer on the isothermal wall. It can be seen from Fig. 6.17 that the T2CS model satisfactorily predicts T_2 extracted from DNS data before flame quenching (i.e. when the flame is away from the wall). However, the T2CS model gives rise to significant over-prediction of T_2 when flame-wall interaction takes place. Here, the T2CS model has been modified

in the following manner to account for flame-wall interaction:

$$T_2 = 2 \frac{\tau}{Le^m} \frac{\delta_Z}{\delta_{th}} \sqrt{\frac{\widetilde{T''^2}}{c''^2}} \frac{A_2 B_{T_2}}{(1 + Ka_L)^{A_3}} \frac{S_L}{\delta_{th}} \bar{\rho} \tilde{\epsilon}_c \quad (6.30)$$

In Eq. 6.30, $A_2 = \exp[-2(\tilde{c} - \tilde{T})]$ and $A_3 = 0.5\text{erf}[(Pe_{\min})_L - x_1/\delta_Z] + 1$ account for the effects of the wall. For unity Lewis number flames $(\tilde{c} - \tilde{T})$ vanishes away from the wall but $(\tilde{c} - \tilde{T})$ assumes non-zero values only in the near wall region. This type of $(\tilde{c} - \tilde{T})$ dependence was used by Bruneaux *et al.* [21] in the context of FSD modelling and the same approach has been adopted here. The exponent A_3 rises in the near wall region, which acts to mimic the reduction of T_2 magnitude as a result of weakening of heat release effects arising from flame quenching. It is worth noting that A_2 and A_3 approach 1.0 and 0.5 respectively away from the wall and Eq. 6.30 becomes identical to the T2CS model (i.e. Eq. 6.29) for $x_1/\delta_Z \gg (Pe_{\min})_L$. It can be seen from Fig. 6.17 that Eq. 6.29 reduces the over-prediction of T_2 , and its predictions are in better agreement with DNS data than the T2CS model in the near wall region when the flame interacts with the wall. Furthermore, the prediction of Eq. 6.30 becomes identical to the T2CS model away from the wall before the flame quenching is initiated.

6.1.6 Modelling of the turbulent scalar interaction term T_3

The variations of T_{31} , T_{32} and T_{33} with x_1/δ_Z at different time instants for cases A-E are shown in Fig. 6.18. It can be seen that T_{31} and T_{33} assume predominantly negative values when the flame is away from the wall. The contribution of T_{32} remains dominant contribution to T_3 . However, as flame interacts with the wall, the magnitude of T_{32} drops significantly. At quenching stage, the magnitudes of T_{31} and T_{33} gradually become comparable to that of T_{32} in the near wall region. The local Damköhler number $Da_L = \tilde{k}S_L/\tilde{\epsilon}\delta_{th}$ drops close to the wall due to the combination of the decay of turbulent kinetic energy \tilde{k} , and a sharp increase of dissipation of turbulent kinetic energy in the near wall region. This drop in Da_L leads to an enhancement in magnitudes of T_{31} and T_{33} according to Eq. 6.8. At the final stage of quenching, T_{33} assumes positive values because of predominantly negative values of $\partial\tilde{u}_1/\partial x_1$ as a result of the reversal of the direction of the flow (after quenching flow is directed towards the wall in contrast to the flow away from the wall before quenching). The statistical behaviour of T_3 can

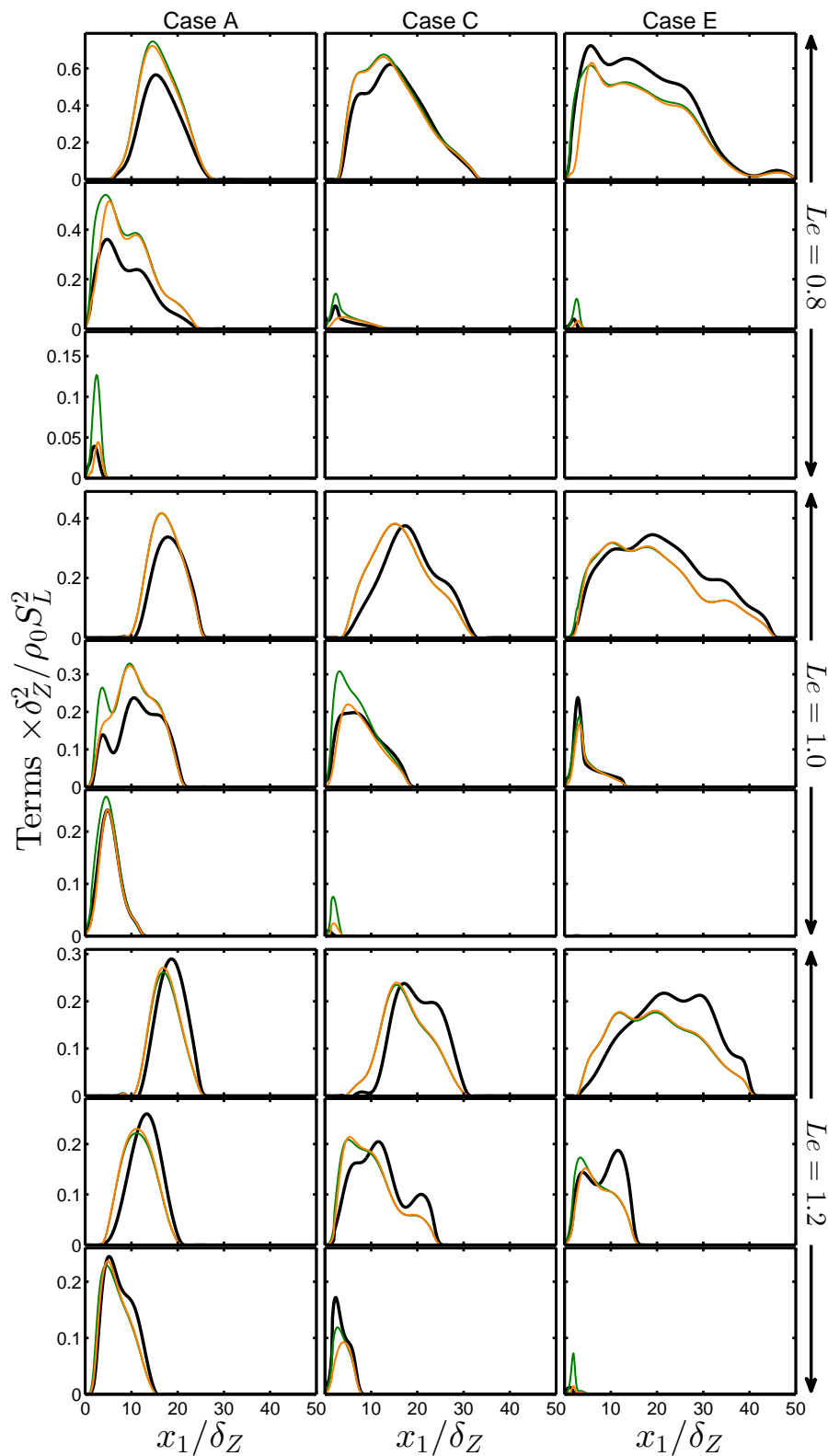


Fig. 6.17 Variations of $T_2 \times \delta_Z^2 / \rho_0 S_L^2$ (—) with x_1 / δ_Z along with the predictions by the TICS model (—) and Eq. 6.30 (—) at for cases A, C and E (1st - 3rd column) at $t = 2\delta_Z/S_L$, $6\delta_Z/S_L$ and $10\delta_Z/S_L$ (1st - 3rd row).

also be explained by using the scalar-turbulence interaction contribution Λ :

$$\begin{aligned}\Lambda &= -2\rho D \overline{\frac{\partial c}{\partial x_i} \frac{\partial u_i}{\partial x_j} \frac{\partial c}{\partial x_j}} = -2\rho(e_\alpha \cos^2 \theta_\alpha + e_\beta \cos^2 \theta_\beta + e_\gamma \cos^2 \theta_\gamma) \overline{N_c} \\ &= T_{31} + T_{32} + T_{33} - 2\rho D \overline{\frac{\partial \tilde{c}}{\partial x_i} \frac{\partial \tilde{u}_i}{\partial x_j} \frac{\partial \tilde{c}}{\partial x_j}}\end{aligned}\quad (6.31)$$

where e_α , e_β and e_γ are the most extensive, intermediate and most compressive principal strain rates and θ_α , θ_β and θ_γ are the angles between ∇c and the eigenvectors associated with e_α , e_β and e_γ respectively. According to Swaminathan and Bray [185], following scaling relation can be obtained:

$$-2\rho D \overline{\frac{\partial \tilde{c}}{\partial x_i} \frac{\partial \tilde{u}_i}{\partial x_j} \frac{\partial \tilde{c}}{\partial x_j}} \sim O(\rho_0 S_L^2 / \delta_{th}^2 \times Re_t^{-3/2} Da^{-3/2} \times U_{ref} / S_L) \quad (6.32)$$

It can be deduced from Eq. 6.32 that the quantity $-2\rho D (\partial \tilde{c} / \partial x_i) (\partial \tilde{u}_i / \partial x_j) (\partial \tilde{c} / \partial x_j)$ remains negligible in comparison to the contributions from T_{31} , T_{32} and T_{33} . It can be seen from Eq. 6.31 that a preferential alignment of ∇c with e_α (e_γ) leads to a negative (positive) contributions of Λ and T_3 . Several previous analyses [187, 47, 48, 33] indicated that ∇c aligns preferentially with the most extensive principal strain rate e_α when the strain rate a_{chem} induced by flame normal acceleration dominates over the effects of turbulent straining a_{turb} . By contrast, a preferential alignment of ∇c with e_γ occurs when turbulent straining a_{turb} overwhelms the influences of strain rate a_{chem} arising from flame normal acceleration. Scaling a_{chem} and a_{turb} by $\tau S_L / \delta_{th}$ and u' / l (alternatively u' / γ) respectively yields $(a_{chem} / a_{turb}) \sim \tau Da$ (alternatively $(a_{chem} / a_{turb}) \sim \tau Da / Re_t^{1/2} \sim \tau / Ka$) [187, 47, 48, 33], which suggests that a_{chem} is likely overwhelm a_{turb} for large values of Da and/or τ . For the cases considered here, a_{chem} dominates over a_{turb} in spite of $Da < 1$ due to large value of τ . Thus, ∇c predominantly aligns with e_α for all cases, which predominantly gives rise to negative values of T_3 except at the final stage of flame quenching when T_3 assumes positive values close to the wall due to positive values of T_{33} due to flow direction reversal. From the aforementioned discussion it is clear that the models of T_3 components need to account for ∇c alignment characteristics with local principal strain rates.

For the present analysis four existing models of T_{31} have been considered for model comparison, which are listed as:

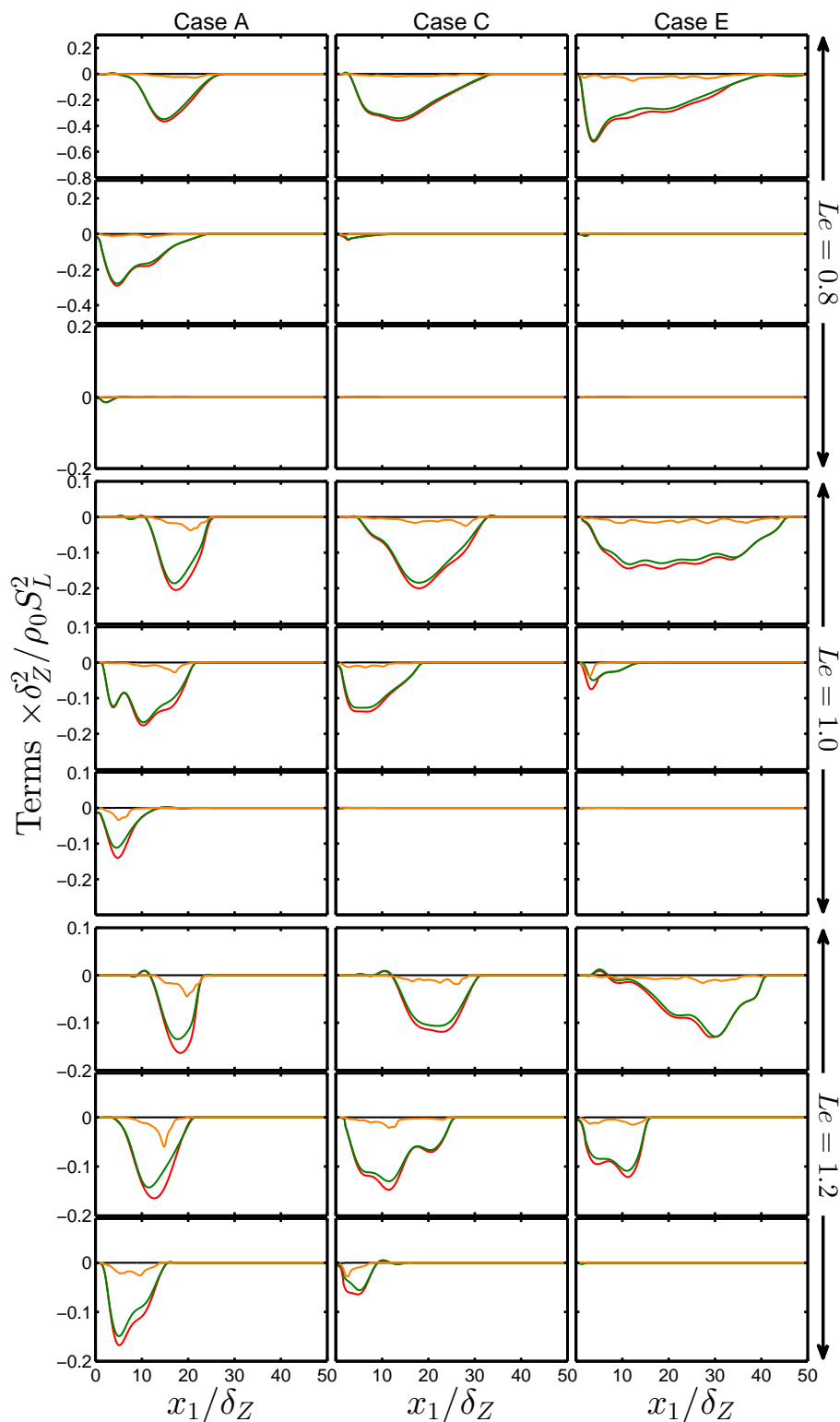


Fig. 6.18 Variations of $T_3 \times \delta_Z^2 / \rho_0 S_L^2$ (—) with x_1 / δ_Z along with T_{31} (—), T_{32} (—) and T_{33} (—) at for cases A, C and E (1st - 3rd column) at $t = 2\delta_Z / S_L$, $6\delta_Z / S_L$ and $10\delta_Z / S_L$ (1st - 3rd row).

T31MB [137]

$$T_{31} = -C_{1\text{MB}}\bar{\rho}\left(\frac{\tilde{\varepsilon}}{\tilde{k}}\right)\widetilde{u_j''c''}\left(\frac{\partial\tilde{c}}{\partial x_j}\right) \quad \text{where} \quad C_{1\text{MB}} = 1.0 \quad (6.33)$$

T31M1 [144]

$$T_{31} = -C_{\text{PM}}\bar{\rho}\left(\frac{\tilde{\varepsilon}_c}{\widetilde{c''^2}}\right)\widetilde{u_j''c''}\left(\frac{\partial\tilde{c}}{\partial x_j}\right) \quad \text{where} \quad C_{\text{PM}} = 1.0 \quad (6.34)$$

T31M2 [144]

$$T_{31} = -\tau S_L \bar{\rho} \tilde{\varepsilon}_c < \vec{n}_f \cdot \vec{x}_j > \left(\frac{\partial\tilde{c}}{\partial x_j} \right) \quad \text{where} \quad (6.35)$$

where $\vec{n}_f = \nabla c / |\nabla c|$ is a local flamelet normal vector;

T31CS [52]

$$T_{31} = -[C_1 + C_2 Da_L^*]\bar{\rho}\left(\frac{\tilde{\varepsilon}}{\tilde{k}}\right)\widetilde{u_j''c''}\left(\frac{\partial\tilde{c}}{\partial x_j}\right) - C_c \tau S_L \bar{\rho} \tilde{\varepsilon}_c < \vec{n}_f \cdot \vec{x}_j > \left(\frac{\partial\tilde{c}}{\partial x_j} \right) \tilde{c}^{1.5} \quad (6.36)$$

where Da_L^* is local density-weighted Damköhler number, $C_1 = 0.5$ and $C_2 = 1.3Ka_L^2/(1+Ka_L)^2$ are the model parameters, and the model parameter C_c is expressed as:

$$C_c = \left[1.2 + 0.6\text{erfc}\left(\frac{Re_L}{5}\right) \right] \left[\frac{1}{1 + \exp[-10(Ka_L - 1)]} \right] \quad (6.37)$$

It was demonstrated by Chakraborty and Swaminathan [52] that the T31CS model captures both the qualitative and quantitative behaviours of T_{31} for a range of values of Da , Ka and Re_t in the absence of the wall. The variations of T_{31} with normalised wall normal distance x_1/δ_Z are shown in Fig. 6.19 along with the predictions of the T31MB, T31M1, T31M2, T31CS models for different time instants for all cases considered here. All these models underpredict the magnitude of T_{31} and the extent of this underprediction is particularly severe for the T31MB and T3M1 models. The agreement of the T3M2 and T3CS model predictions with DNS data remains better than the other models when the flame is away from wall (i.e. $t \leq 4\delta_Z/S_L$) and also when the quenching starts. Nonetheless, the T31M2 and T31CS models do not adequately predict T_{31} extracted from DNS data in the near wall region. The T31CS model starts to underpredict the DNS data once the quenching is initiated. In order to address this

deficiency, the following modification to the T31CS model has been proposed here:

$$T_{31} = -A_4[C_1 + C_2 Da_L^*] \bar{\rho} \left(\frac{\tilde{\varepsilon}}{\tilde{k}} \right) \widetilde{u_j'' c''} \left(\frac{\partial \tilde{c}}{\partial x_j} \right) - C_c \tau S_L \bar{\rho} \tilde{\varepsilon}_c < \vec{n}_f \cdot \vec{x}_j > \left(\frac{\partial \tilde{c}}{\partial x_j} \right) \tilde{c}^{1.5 A_5} \quad (6.38)$$

where $A_4 = 0.5\{\text{erf}[x_1/(\delta_Z - 0.5(Pe_{\min})_L] + 1\}$ and $A_5 = \exp[-8Le(\tilde{c} - \tilde{T})]$ are the model parameters, which account for the wall effects. The model parameter A_4 acts to reduce the over-prediction of T_{31} magnitude once the flame starts to interact with the wall (see $t \geq 6\delta_Z/S_L$ in Fig. 6.19). The model parameter A_5 becomes active in the near wall region where $\tilde{c} \neq \tilde{T}$, and is responsible for damping the magnitude of T_{31} close to the near wall region. The term $-C_c \tau S_L \bar{\rho} \tilde{\varepsilon}_c < \vec{n}_f \cdot \vec{x}_j > (\partial \tilde{c} / \partial x_j) \tilde{c}^{1.5}$ is necessary to accurately predict T_{31} away from wall. However it has strong dependence on $\tilde{c}^{1.5}$, and \tilde{c} changes rapidly in the near wall region due to the interaction of the flame with the wall. The involvement of A_5 in Eq. 6.38 reduces this $\tilde{c}^{1.5}$ dependence close to the wall. It can be seen from Fig. 6.19 that the model given by Eq. 6.38 provides better performance than the other available models and thus is recommended for T_{31} modelling.

Mantel and Borghi [137] proposed the following model for T_{32} (T32MB):

$$T_{32} = A_e \left(\frac{\tilde{\varepsilon}}{\tilde{k}} \right) \tilde{\varepsilon}_c \quad (6.39)$$

where $A_e = 0.9$ is a model parameter. Mura *et al.* [144] proposed the following models for T_{32} based on *a priori* analysis of DNS data for high Da flames:

$$T_{32} = \bar{\rho} \left[A_{M1} \left(\frac{\tilde{\varepsilon}}{\tilde{k}} \right) - 2C_A \tau Da_L \tilde{\varepsilon}_c \right] \tilde{\varepsilon}_c \quad (6.40)$$

$$T_{32} = \bar{\rho} \left[A_{M1} \left(\frac{\tilde{\varepsilon}}{\tilde{k}} \right) - 2C_B \ln(\tau + 1) Da_L \tilde{\varepsilon}_c \right] \tilde{\varepsilon}_c \quad (6.41)$$

where $A_{M1} = 1.0$, $C_A = 0.6$ and $C_B = 1.6$ are the model constants. Equations 6.40 and 6.41 will henceforth be referred to as the T32M1 and T32M2 models in this paper. Chakraborty and Swaminathan [49] proposed a model for T_{32} , which includes non-unity Lewis number effects (T32CS):

$$T_{32} = \bar{\rho} \left[C_3^* - C_4^* \tau \frac{(1 - \tilde{c})^{\Phi(Le)}}{Le^P} \cdot Da_L^* \right] \left(\frac{\tilde{\varepsilon}}{\tilde{k}} \right) \tilde{\varepsilon}_c \quad (6.42)$$

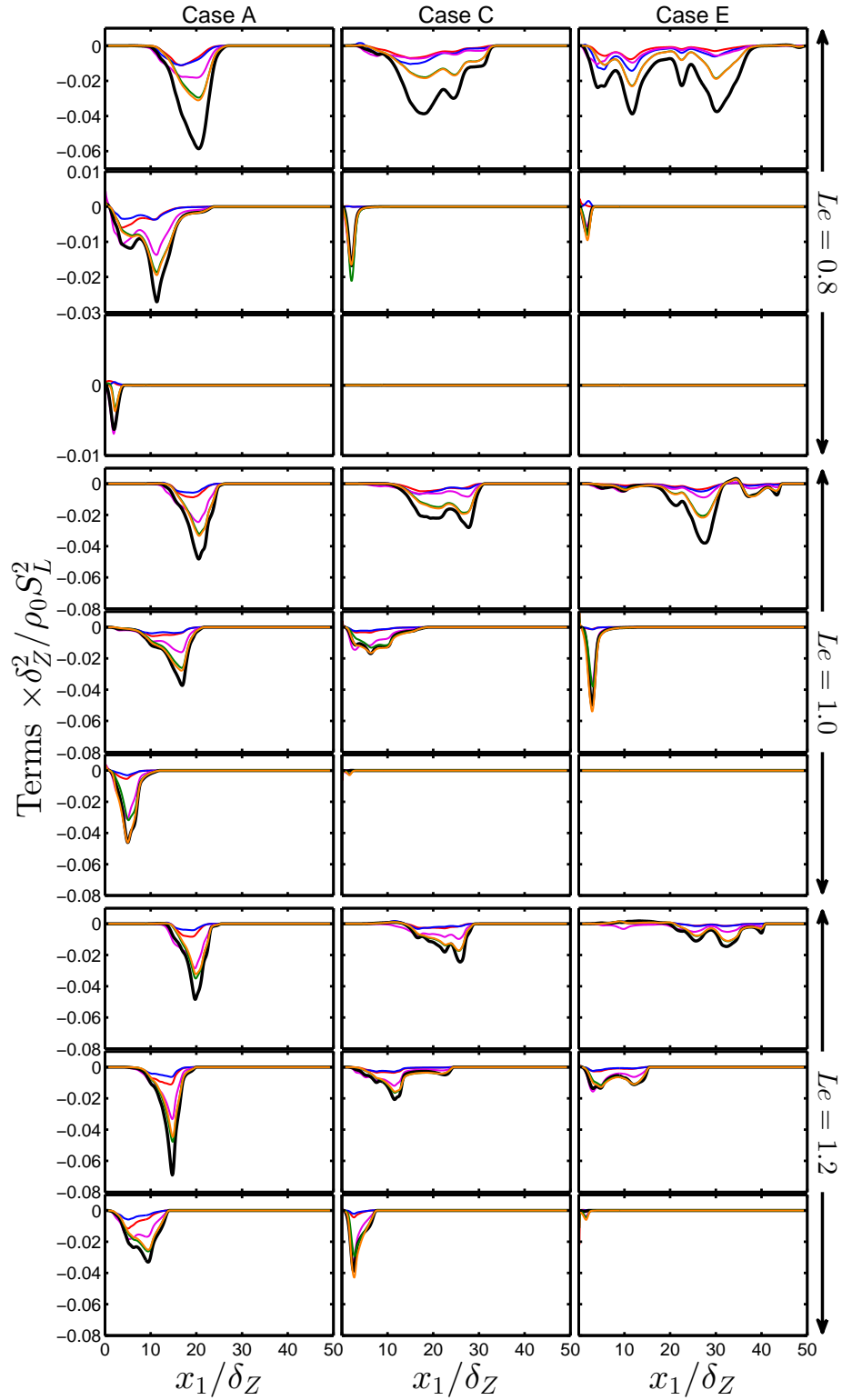


Fig. 6.19 Variations of $T_{31} \times \delta_Z^2 / \rho_0 S_L^2$ (—) with x_1 / δ_Z along with T31MB (—), T31CS (—), T31M1 (—), T31M2 (—) and Eq. 6.38 (—) at for cases A, C and E (1st - 3rd column) at $t = 2\delta_Z / S_L$, $6\delta_Z / S_L$ and $10\delta_Z / S_L$ (1st - 3rd row).

where $C_3^* = 2.0$, $C_4^* = 1.2(1 + Ka_L)^{-0.4}$, $\Phi(Le) = 0.2 + 1.5(1 - Le)$ and $P = 2.57$ are the model parameters. The term $\bar{\rho}C_3^*(\tilde{\varepsilon}/\tilde{k})\tilde{\varepsilon}_c$ accounts for scalar gradient generation due to preferential alignment between ∇c and e_γ (see Eq. 6.31). By contrast, $-\bar{\rho}C_4^*\tau\frac{(1-\tilde{c})^{\Phi(Le)}}{Le^P}Da_L^*(\tilde{\varepsilon}/\tilde{k})\tilde{\varepsilon}_c = -\rho_0C_4^*\tau\frac{(1-\tilde{c})^{\Phi(Le)}}{Le^P}Da_L^*(S_L/\delta_{th})\tilde{\varepsilon}_c$ accounts for the destruction of scalar gradient as a result of preferential alignment between ∇c and e_α (see Eq. 6.31), and the local Karlovitz number Ka_L dependence of C_4^* accounts for weakening of ∇c alignment with e_α with increasing Karlovitz number due to diminishing influence of flame normal acceleration for high Karlovitz number combustion. The involvement of Le^{-P} in the second term on the right hand side of Eq. 6.42 allows for strengthening of flame normal acceleration with decreasing Le [33, 49]. The involvement of $(1-\tilde{c})^{\Phi(Le)}$ ensures that the qualitative behaviour of T_{32} variation with \tilde{c} is adequately captured [49, 52].

The predictions of the T32MB, T32M1, T32M2 and T32CS models are compared to T_{32} extracted from DNS data in Fig. 6.20. It can be seen from the variations of T_{32} with normalised wall normal distance x_1/δ_Z in Fig. 6.20 that the T32MB model fails to predict the negative values of T_{32} for all cases. The performances of the T32M1 and T32M2 models remain comparable but their predictions remain an order of magnitude smaller than the corresponding quantity extracted from DNS data. The agreement between the T32CS model prediction with DNS data is better than the other models before quenching is initiated (i.e. when the flame remains away from the wall by the wall) in spite of over-predictions of the magnitude of the negative values of T_{32} for the flames considered here. However, the quantity $\tilde{\varepsilon}/\tilde{k}$ assumes large values close to the wall (due to augmentation of $\tilde{\varepsilon}$ and decay of \tilde{k} in the vicinity of the wall), which leads to severe over-prediction of T_{32} by all the models in the near wall region. In order to capture the near wall behaviour of T_{32} the T32CS model has been modified in the following manner:

$$T_{32} = A_6\bar{\rho}\left[C_3^* - C_{4w}^*\tau\frac{(1-\tilde{c})^{\Phi(Le)}}{Le^P}Da_L^*\right]\left(\frac{\tilde{\varepsilon}}{\tilde{k}}\right)\tilde{\varepsilon}_c \quad (6.43)$$

Here, the modified parameters are $A_6 = 0.5\{\text{erf}[2(x_1/\delta_Z) - (Pe_{\min})_L] + 1\}\exp[-6Le(\tilde{c} - \tilde{T})]$, $C_{4w}^* = 1.2(1 + Ka_L)^{-A_7}$ and $A_7 = 0.4^{1-\tilde{c}_w}$.

Mantel and Borghi [137] proposed the following model for T_{33} :

$$T_{33} = -C_{P2}\bar{\rho}\tilde{\varepsilon}_c\left(\frac{\widetilde{u_j''u_k''}}{\tilde{k}}\right)\frac{\partial\tilde{u}_j}{\partial x_k} \quad \text{where} \quad C_{P2} = 1.0 \quad (6.44)$$

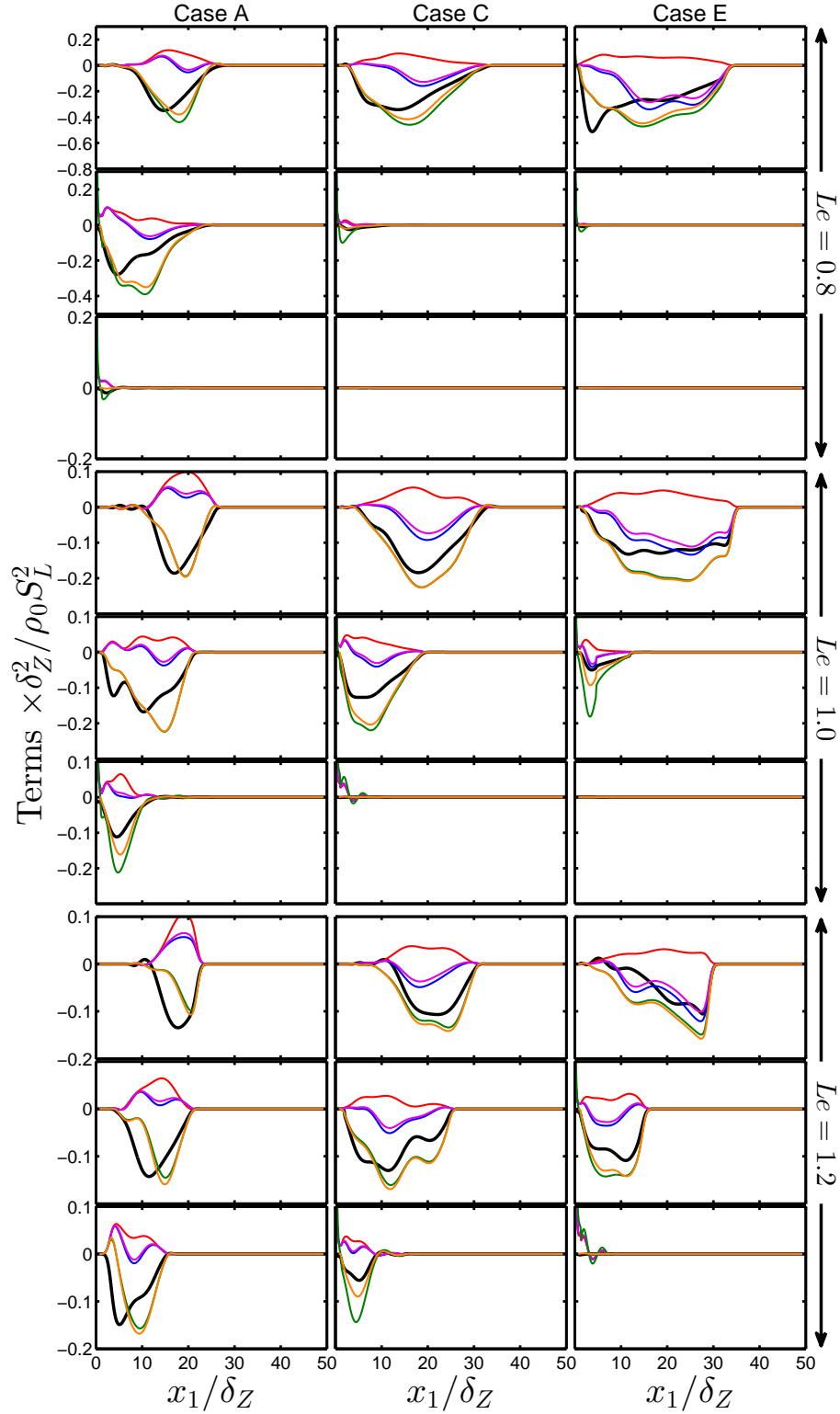


Fig. 6.20 Variations of $T_{32} \times \delta_Z^2 / \rho_0 S_L^2$ (—) with x_1 / δ_Z along with T32MB (—), T32M1 (—), T32M2 (—), T31CS (—), and Eq. 6.43 (—) at for cases A, C and E (1st - 3rd column) at $t = 2\delta_Z / S_L$, $6\delta_Z / S_L$ and $10\delta_Z / S_L$ (1st - 3rd row).

Chakraborty and Swaminathan [31] proposed an alternative model for T_{33} :

$$T_{33} = -C_5 \bar{\rho} \tilde{\varepsilon}_c \left[\psi_i \psi_j + \frac{1}{3} \delta_{ij} (1 - \psi_k \psi_k) \right] \frac{\partial \tilde{u}_i}{\partial x_j} \quad (6.45)$$

where $C_5 = 1 + 2Ka_L^{-0.23}$, $\psi_i = (-\partial\phi/\partial x_i) \cdot \sqrt{\rho_0 D_0 / (\bar{\rho} \tilde{\varepsilon}_c)}$ and $\phi = \tau \tilde{c}(1 - \tilde{c}) / (1 + \tau \tilde{c})$ are the model parameters. Mura *et al.* [144] proposed the following models for T_{33} :

$$T_{33} = -\frac{2}{3} \bar{\rho} \tilde{\varepsilon}_c \frac{\partial \tilde{u}_i}{\partial x_j} \quad (6.46)$$

$$T_{33} = -2 \bar{\rho} \tilde{\varepsilon}_c^2 \frac{\overline{\rho u_i'' c''} \cdot \overline{\rho u_j'' c''}}{\tilde{\varepsilon} (\overline{\rho c''^2})^2} \frac{\partial \tilde{u}_i}{\partial x_j} \quad (6.47)$$

$$T_{33} = -2 \bar{\rho} \tilde{\varepsilon}_c^2 (\tau S_L)^2 \frac{\langle \vec{n}_f \cdot \vec{x}_i \rangle \langle \vec{n}_f \cdot \vec{x}_j \rangle}{\tilde{\varepsilon}} \frac{\partial \tilde{u}_i}{\partial x_j} \quad (6.48)$$

The models given by Eqs. 6.46 - 6.48 will henceforth be referred to as the T33M1, T33M2 and T33M3 respectively.

The predictions of the T33MB, T33CS, T33M1, T33M2, and T33M3 models are compared with DNS data in Fig. 6.21. It can be seen from Fig. 6.21 that the T33MB model over-predicts the magnitude of the negative contribution of T_{33} for cases A and B when the flame is away from the wall. However, it performs satisfactorily away from the wall in cases C-E before flame quenching. However, the model T33MB under-predicts the magnitude of T_{33} in the near wall region once the flame quenching is initiated. It can be seen from Fig. 6.21 that the T33M1 model satisfactorily predicts T_{33} for cases A and B when the flame is away from wall as well as at the quenching stage. The models T33M2 and T33M3 over-predict the magnitude of the negative value of T_{33} when the flame is away from the wall (e.g. $t \leq 4\delta_Z/S_L$), nonetheless, the T33M2 model under-predicts whereas the T33M3 model significantly over-predicts the magnitude of T_{33} during the final stage of quenching.

It is worth noting that the T33M1 model is consistent with the scaling arguments given by Eqs. 6.8 and 6.9. By contrast, the T33M2 model is consistent with the scaling given by Eq. 6.9 (i.e. $T_{33} \sim O(\rho_0 u'^2/l^2)$), but the scaling arguments by Swaminathan and Bray [185] indicates that: $T_{33M3} \sim O(\rho_0 S_L^2/\delta_Z^2 \times U_{\text{ref}}/u' \times Da/Re_t)$. Moreover, the T33M3 model scales as $\rho_0 S_L^2/\delta_Z^2 \times U_{\text{ref}}/u' \times Da/Re_t$ and $\rho_0 u'^2/l^2 \times Da/Re_t$ according to the scaling arguments by Swaminathan and Bray [185] and Mantel and Borghi [137]

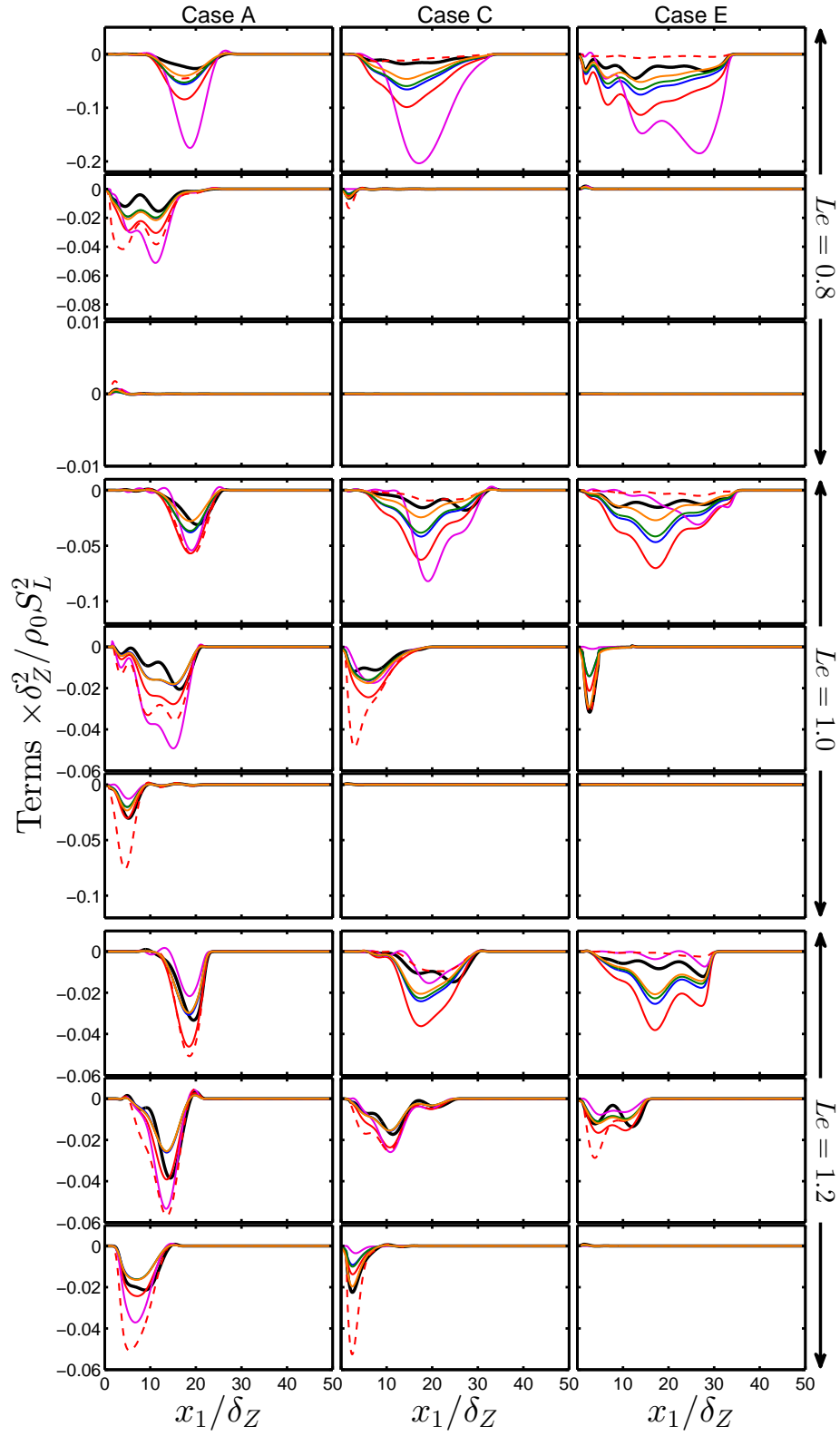


Fig. 6.21 Variations of $T_{33} \times \delta_Z^2 / \rho_0 S_L^2$ (—) with x_1 / δ_Z along with T33MB (—), T33M1 (—), T33M2 (—), T33M3 (---), T33CS (—), and Eq. 6.49 (—) at for cases A, C and E (1st - 3rd column) at $t = 2\delta_Z / S_L$, $6\delta_Z / S_L$ and $10\delta_Z / S_L$ (1st - 3rd row).

respectively, which are different from the scalings of T_{33} given by Eqs. 6.8 and 6.9. The model expression T33M3 can be scaled as $T_{33M3}/T_{33} \sim O(Da^2/Re_t) \sim O(Ka^{-1})$ according to Swaminathan and Bray [185] and thus the T33M3 model underpredicts the magnitude of T_{33} away from the wall for the thin reaction zones regime flames (i.e. $Ka > 1$) considered here.

It can be seen from Fig. 6.21 that the performance of the T33CS model remains comparable to that of T33M1 for high turbulent Reynolds number cases (i.e. cases C-E) when the flame is away from the wall. However, the T33CS model offers more accurate prediction than the T3M1 model for cases A and B before the flame interacts with the wall. However, the T33CS model under-predicts the magnitude of T_{33} at the final stage of quenching. This inadequacy is addressed here by the following modification:

$$T_{33} = -C_5^* \bar{\rho} \tilde{\epsilon}_c \left[\psi_i \psi_j + \frac{1}{3} \delta_{ij} (1 - \psi_k \psi_k) \right] \frac{\partial \tilde{u}_i}{\partial x_j} \quad (6.49)$$

where $C_5^* = A_8 + 2\exp(Le(\tilde{c} - \tilde{T}))Ka_L^{-0.23}$ and $A_8 = \text{erf}(1 - x_1/\delta_Z) + 2$ are the model parameters. The parameter A_8 and the involvement of $\exp(\tilde{c} - \tilde{T})$ in C_5^* increase the magnitude of the model prediction in the near wall region where the magnitude of T_{33} is under-predicted by the T33CS model. The model parameter A_8 asymptotically approaches unity and C_5^* approaches C_5 away from the wall where $\tilde{c} = \tilde{T}$. It can be seen from Fig. 6.21 that the new model given by Eq. 6.48 predicts the quantitative behaviour of T_{33} more satisfactorily than the other available models both away from and near to the wall.

6.1.7 Modelling of the Combined Reaction Rate, Dissipation and Diffusivity Gradient Terms ($T_4 - D_2 + f(D)$)

The transport equation of $N_c = D\nabla c \cdot \nabla c$ can be rearranged into following manner [46, 87]:

$$\begin{aligned} \rho \frac{\partial N_c}{\partial t} + \rho u_j \frac{\partial N_c}{\partial x_j} = & -2\rho D \frac{\partial c}{\partial x_j} \frac{\partial c}{\partial x_i} \frac{\partial u_i}{\partial x_j} + 2\rho S_d \frac{\partial n_i}{\partial x_i} N_c - 2D \frac{\partial(\rho S_d n_i |\nabla c|)}{\partial x_i} |\nabla c| \\ & + 2S_d n_i \frac{\partial \rho}{\partial x_i} N_c + \rho |\nabla c|^2 \left(\frac{\partial D}{\partial t} + u_j \frac{\partial D}{\partial x_j} \right) \end{aligned} \quad (6.50)$$

where $S_d = [\dot{\omega} + \nabla \cdot (\rho D \nabla c)]/\rho |\nabla c|$ is the local flame displacement speed [46] and $\vec{n} = -\nabla c/|\nabla c|$ is the local flame normal vector. Consequently, the combined contribution

of the terms D_1 , T_4 , $(-D_2)$ and $f(D)$ can be written as [46, 52]:

$$\begin{aligned}
 D_1 + T_4 - D_2 + f(D) \approx & -2\overline{D\nabla \cdot (\rho S_d \vec{n} |\nabla c|) |\nabla c|} + 2\widetilde{D\nabla \cdot (\rho S_d |\nabla c| \vec{m}) |\nabla c|} \\
 & + 2\rho\overline{D(S_r + S_n)\nabla \cdot \vec{n} |\nabla c|^2} - 2\widetilde{D\rho(S_r + S_n)\nabla \cdot \vec{m} |\nabla c|} \\
 & - 2\rho\overline{D^2(\nabla \cdot \vec{n})^2 |\nabla c|^2} + 2\widetilde{D\rho D(\nabla \cdot \vec{n}) |\nabla c| \nabla \cdot \vec{m} |\nabla c|}
 \end{aligned} \tag{6.51}$$

where $\vec{m} = -\nabla \tilde{c}/|\nabla c|$ is the resolved flame normal, $S_r = \dot{\omega}/(\rho|\nabla c|)$ and $S_n = \vec{N} \cdot \nabla(\rho D \vec{N} \cdot \nabla c)/(\rho|\nabla c|)$ are the reaction and normal diffusion components of the displacement speed respectively [154, 80]. It can be seen with Eq. 6.51 that the net contribution of $D_1 + T_4 - D_2 + f(D)$ specifies the effect due to flame normal propagation and flame curvature. Followed by previous analyses [137, 46, 52], it might be more convenient to model the net contribution of $D_1 + T_4 - D_2 + f(D)$ rather than its individual components. Mantel and Borghi [137] proposed the following model for $D_1 + T_4 - D_2$:

$$D_1 + T_4 - D_2 = -\frac{2}{3}\beta_1 \bar{\rho} \frac{\tilde{\epsilon}_c^2}{\tilde{c}(1 - \tilde{c})} \left[\frac{3}{2} - C_\epsilon \frac{S_L}{\tilde{k}} \right] \tag{6.52}$$

where $\beta_1 = 4.2$ and $C_\epsilon = 0.1$ are the model parameters. Since, D_1 is a close term, it is more convenient to model only $T_4 - D_2 + f(D)$. Chakraborty *et al.* [46] proposed the following model for $T_4 - D_2$:

$$T_4 - D_2 = -\beta_2 \bar{\rho} \frac{\tilde{\epsilon}_c^2}{\tilde{c}(1 - \tilde{c})} \tag{6.53}$$

where $\beta_2 = 6.7$ is a model parameter. It is worth noting that $f(D)$ was ignored by Mantel and Borghi [137] and Chakraborty *et al.* [46] and thus the models given by Eqs. 6.52 and 6.53 will not be discussed further in this paper. Recently Gao *et al.* [87] extended the model given by Eq. 6.53 in the following manner (i.e. T4D2CS model):

$$T_4 - D_2 + f(D) = -\beta_v \bar{\rho} \frac{\tilde{\epsilon}_c^2}{\tilde{c}(1 - \tilde{c})} \tag{6.54}$$

where $\beta_v = 6.7$ is a model parameter. The predictions of the T4D2CS model are compared with DNS data in Fig. 6.22, which shows the variation of $T_4 - D_2 + f(D)$ with normalised wall normal distance x_1/δ_Z at different time instants. The net contribution

of $T_4 - D_2 + f(D)$ remains negative when the flame is away from the wall (i.e. $x_1/\delta_Z \gg (Pe_{\min})_L$). However, a weakly positive contribution of $T_4 - D_2 + f(D)$ is observed in the region given by $(Pe_{\min})_L \leq x_1/\delta_Z \leq 2(Pe_{\min})_L$. The magnitude of negative contribution of $T_4 - D_2 + f(D)$ increases significantly in the region given by $x_1/\delta_Z \leq (Pe_{\min})_L$ during flame quenching. This increase in the sink contribution of $T_4 - D_2 + f(D)$ arises due to significant $f(D)$ contribution in the near wall region. It can be seen from Fig. 10 that the T4D2F model is able to capture $T_4 - D_2 + f(D)$ obtained from the DNS data satisfactorily when the flame is away from the wall (i.e. $x_1/\delta_Z \geq (Pe_{\min})_L$). However, the T4D2F model does not adequately capture the qualitative and quantitative behaviours of $T_4 - D_2 + f(D)$ in the near wall region. Here the T4D2F model has been modified in the following manner in order to improve the near wall predictions:

$$T_4 - D_2 + f(D) = -\beta_V \bar{\rho} \frac{\tilde{\varepsilon}_c^2}{\tilde{c}(1 - \tilde{c})} [A_9(\tilde{c} - A_{10})]^\Phi \quad (6.55)$$

The corresponding model parameters are given as:

$$A_9 = 5.25 \left\{ \operatorname{erf} \left[2 \left(\frac{x_1}{\delta_Z} - 0.7(Pe_{\min})_L \right) \right] - 0.81 \right\} \quad (6.56)$$

$$A_{10} = 0.6 \left\{ \operatorname{erf} \left[-2 \left(\frac{x_1}{\delta_Z} + 0.7(Pe_{\min})_L \right) \right] + 0.9 \right\} \quad (6.57)$$

$$\Phi = 0.5 \left\{ 1 - \operatorname{erf} \left[\frac{x_1}{\delta_Z} - 1.9(Pe_{\min})_L \right] \right\} \quad (6.58)$$

The model parameter A_9 has been introduced in order to capture the augmentation of negative contribution of $T_4 - D_2 + f(D)$ in the near wall region, whereas A_{10} is responsible for changing the sign of the model prediction and Φ makes sure this change in sign becomes active at $x_1/\delta_Z \approx 1.9(Pe_{\min})_L$. However, Φ vanishes away from the wall (i.e. $x_1/\delta_Z \gg (Pe_{\min})_L$) and thus, Eq. 6.55 becomes identical to the T4D2CS model (i.e. Eq. 6.54), which can be substantiated from Fig. 6.22 where the predictions of Eq. 6.55 are also shown. It can be seen from Fig. 6.22 that the model given by Eq. 6.55 adequately predicts the augmentation of the magnitude of negative contribution of $T_4 - D_2 + f(D)$ in the near wall region and also captures slightly positive value of $T_4 - D_2 + f(D)$ in the region given by $(Pe_{\min})_L \leq x_1/\delta_Z \leq 2(Pe_{\min})_L$. Thus, Eq. 6.55 can be used for modelling $T_4 - D_2 + f(D)$ both close to and away from the wall.

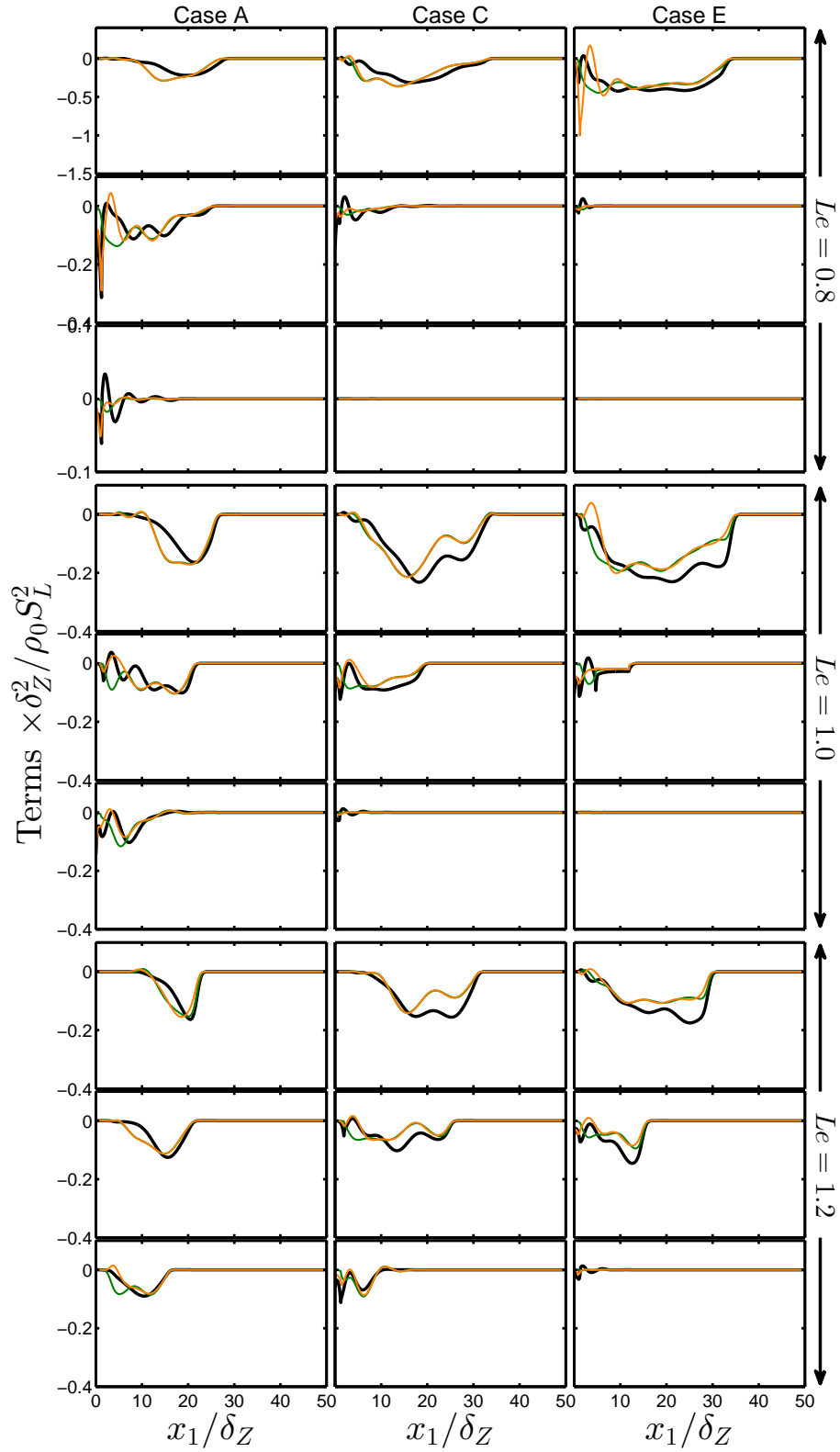


Fig. 6.22 Variations of $[T_4 - D_2 + f(D)] \times \delta_Z^2 / \rho_0 S_L^2$ (—) with x_1 / δ_Z along with T4D2CS (—), and Eq. 6.55 (—) at for cases A, C and E (1st - 3rd column) at $t = 2\delta_Z / S_L$, $6\delta_Z / S_L$ and $10\delta_Z / S_L$ (1st - 3rd row).

6.1.8 Summary of the key results

The SDR $\tilde{\varepsilon}_c$ transport and its modelling in the context of RANS have been analysed for head-on quenching of turbulent premixed flame by an inert isothermal wall based on three-dimensional simple chemistry DNS data. It has been found that an increase in u'/S_L leads to an increase in the magnitudes of the unclosed terms of the SDR transport equation. For all cases the terms arising from density variation, scalar-turbulence interaction, reaction rate gradient, molecular diffusivity gradient and molecular dissipation (i.e. T_2 , T_3 , T_4 , $f(D)$ and $(-D_2)$) remain the leading order contributors to the SDR $\tilde{\varepsilon}_c$ transport away from the wall and the turbulent transport and molecular diffusion terms remain negligible in comparison to the aforementioned leading order terms. The performances of previously proposed models for T_1 , T_2 , T_{31} , T_{32} , T_{33} and $(T_4 - D_2 + f(D))$ have been assessed with respect to the corresponding quantities extracted from DNS data. It has been found that the aforementioned models do not adequately predict the near wall behaviour of the unclosed terms of the SDR transport equation. The models, which exhibit the most promising performance away from the wall, have been modified to account for the near wall behaviour in such a manner that they asymptotically approach the existing model expressions away from the wall. Although the functional form of the modelling parameters have been proposed so that they follow the asymptotic behaviour in terms of Da_L , Ka_L and x_1/δ_Z , it is likely that they will need to be modified when datasets with a larger range of Re_t with detailed chemistry will be explored. It is worth noting that several previous DNS analyses on flame-wall interaction used a simple chemical mechanism [156, 20, 21, 3, 2], and the same approach has been followed here. Moreover, all existing SDR transport closures have been proposed based on simple chemistry DNS data [39, 185, 47, 48, 144, 114, 49]. Since statistical behaviours of $|\nabla c|$ have been adequately captured by single-step chemistry (see [46, 52] for scalar gradient statistics based on both simple and detailed chemistry DNS data), it can be expected that the findings will at least be qualitatively valid in the context of detailed chemistry and transport. Moreover, Lewis number may have some influences on the modelling of SDR transport, but the qualitative nature of the present findings is unlikely to be modified.

6.2 Statistical analysis and modelling of flame surface density transport

The main objectives of this section are:

- To identify the near wall effects on the unclosed terms of the FSD transport equation
- To model the near wall effects on the unclosed terms of the FSD transport equation

6.2.1 Closure for the mean reaction rate $\bar{\omega}$

Figure 6.23 shows that before the onset of HOQ, $\rho_0 S_L \Sigma_{\text{gen}}$ predicts $\bar{\omega}$ satisfactorily for $Le = 1.0$ but underpredicts (overpredicts) $\bar{\omega}$ for $Le = 0.8$ ($Le = 1.0$). This is consistent with previous finding [36], which suggested that $\overline{(\rho_0 S_d)_s}$ is not approximated well by $\rho_0 S_L$ in non-unity Lewis number flames. Moreover, $\rho_0 S_L \Sigma_{\text{gen}}$ overpredicts $\bar{\omega}$ when the flame approaches the wall for all Le cases, because high magnitudes of ∇c occur in the near-wall region, whereas the temperature is not sufficient to support the chemical reaction. As a result, $\rho_0 S_L \Sigma_{\text{gen}} = \rho_0 S_L |\nabla c|$ overpredicts $\bar{\omega}$ in the near-wall region during flame quenching, which is consistent with previous findings [2, 20]. Alshaalan and Rutland [2] proposed the near-wall modification as:

$$\Sigma_{\text{gen}} = |\nabla c| (1 + c_y \tilde{A}_w) \exp \left[-\beta \left(\frac{\tau \tilde{A}}{(1 + \tau \tilde{T})(1 + \tau \tilde{c})} \right)^{c_x} \right] \quad (6.59)$$

where $c_x = 0.25$ and $c_y = 48$ are the model parameters, $\tilde{A} = (\tilde{c} - \tilde{T})$ is a non-adiabaticity parameter. This modification leads to a significant underprediction of $\bar{\omega}$ when the flame is away from the wall (see Fig. 6.23), whereas $\bar{\omega}$ is overpredicted close to the wall.

Bruneaux *et al.* [20] proposed a modification to the conventional $\bar{\omega}$ closure by a multiplier $Q_m = \exp[-2\beta(\tilde{c} - \tilde{T})]$ in the model expression ($\bar{\omega} = Q_m \rho_0 S_L \Sigma_{\text{gen}}$) where Q_m is unity when the flame is away from the wall but decreases in the near-wall region. However, the prediction of $Q_m \rho_0 S_L \Sigma_{\text{gen}}$ differs significantly from $\bar{\omega}$ when the flame begins to interact with the wall especially for non-unity Lewis number flames. Chakraborty and Cant demonstrated [36] that away from the wall, $\overline{(\rho S_d)_s}$ can be approximated by $\rho_0 S_L / Le$. Using this, a revised closure has been proposed as $\bar{\omega} = A_1 (\rho_0 S_L / Le) \Sigma_{\text{gen}}$, where $A_1 = 0.5[\text{erf}(x_1/\delta_Z - 0.7\Pi) + 1]$ is a wall correction that damps the magnitude of $(\rho_0 S_L / Le) \Sigma_{\text{gen}}$ in the near-wall region $x_1/\delta_Z \ll Pe_{\text{min}}$

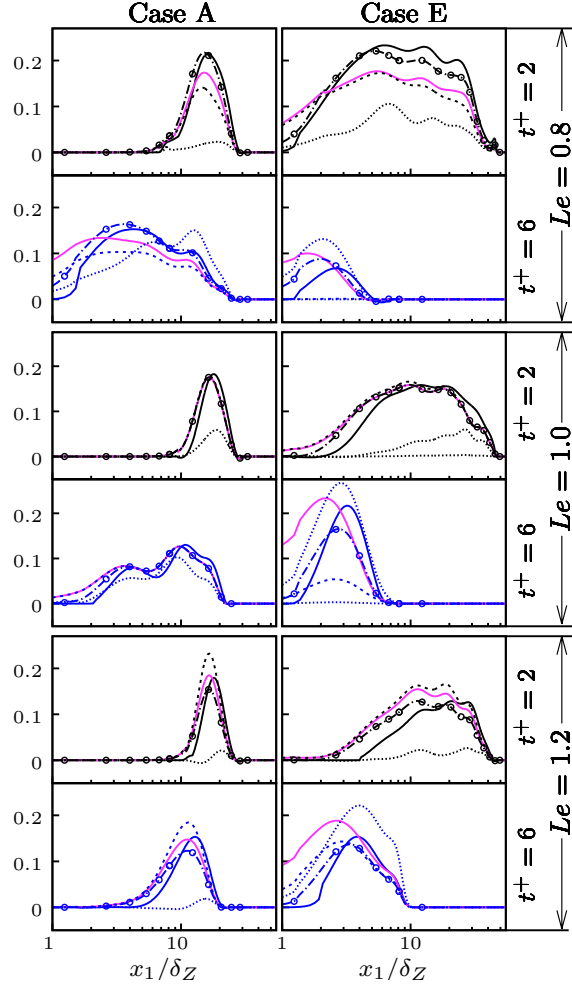


Fig. 6.23 Variations of the normalised mean reaction rate $\bar{\omega} \times \delta_Z / S_L$ (solid line), along with the predictions of $\rho_0 S_L \Sigma_{\text{gen}} \times \delta_Z / \rho_0 S_L$ (—), $Q_m \rho_0 S_L \Sigma_{\text{gen}} \times \delta_Z / \rho_0 S_L$ (dashed line), Al-shaalan and Rutland [2] model (dotted line), and $A_1 (\rho_0 S_L / Le) \Sigma_{\text{gen}} \times \delta_Z / \rho_0 S_L$ (dashed circle line) at different $t^+ = t S_L / \delta_Z = 2$ (—); 6 (—). The same colour key applies for Figs.

but asymptotically approaches unity for $x_1/\delta_Z \gg Pe_{\min}$. Figure 6.23 shows that $A_1(\rho_0 S_L/Le)\Sigma_{\text{gen}}$ predicts $\bar{\omega}$ satisfactorily both away from the wall and close to it. The expression $A_1(\rho_0 S_L/Le)\Sigma_{\text{gen}}$ can therefore be used to predict $\bar{\omega}$ if Σ_{gen} is modelled accurately, the closure of the transport equation terms for Σ_{gen} will be discussed next. The Reynolds-averaged flame surface density transport equation can be seen in Eq. 2.55(or see Eq. 6.60 below).

$$\begin{aligned} \frac{\partial \Sigma_{\text{gen}}}{\partial t} + \frac{\partial \tilde{u}_j \Sigma_{\text{gen}}}{\partial x_j} = & \underbrace{\frac{\partial [\overline{(u_i)_s} - \tilde{u}_i] \Sigma_{\text{gen}}}{\partial x_i}}_{T_{F1}} + \underbrace{\left((\delta_{ij} - N_i N_j) \frac{\partial u_i}{\partial x_j} \right)_s \Sigma_{\text{gen}}}_{T_{F2}} \\ & + \underbrace{\frac{\partial}{\partial x_i} [(S_d N_i)_s \Sigma_{\text{gen}}]}_{T_{F3}} + \underbrace{\left(S_d \frac{\partial N_i}{\partial x_i} \right)_s \Sigma_{\text{gen}}}_{T_{F4}} \end{aligned} \quad (6.60)$$

T_{F1} turbulent transport term

T_{F2} tangential strain rate term

T_{F3} propagation term

T_{F4} curvature term

6.2.2 Modelling of the turbulent transport term T_{F1}

The behaviour of T_{F1} , which depends on the turbulent flux $[\overline{(u_i)_s} - \tilde{u}_i] \Sigma_{\text{gen}}$, is shown in Fig. 6.24 for cases A and E at different times for $Le = 0.8$, $Le = 1.0$ and $Le = 1.2$. An increased u'/S_L leads to an increase in magnitude of $[\overline{(u_i)_s} - \tilde{u}_i] \Sigma_{\text{gen}}$, whereas the magnitude of the FSD flux increases with decreases Le . Figure 6.24 indicates that $[\overline{(u_i)_s} - \tilde{u}_i] \Sigma_{\text{gen}}$ is significantly affected by the wall and that $[\overline{(u_i)_s} - \tilde{u}_i] \Sigma_{\text{gen}}$ only exhibits positive values close to the wall before vanishing altogether following gradient hypothesis model:

$$[\overline{(u_i)_s} - \tilde{u}_i] \Sigma_{\text{gen}} = -\frac{\nu_t}{\sigma_\Sigma} \frac{\partial \Sigma_{\text{gen}}}{\partial x_i} \quad (6.61)$$

Here, $\nu_t = \min(0.09\tilde{k}^2/\tilde{\epsilon}, 0.20(x(1 - e^{-x^+/26}))\tilde{k}^{1/2})$ and σ_Σ are the eddy viscosity and turbulent Schmidt number respectively, with τ_w , $x^+ = \rho x(\tau_w/\bar{\rho})^{1/2}/\mu$ being the wall shear stress, the non-dimensional wall distance respectively.

For $\sigma_\Sigma = 1.0$, Eq. 6.61 does not predict the qualitative behaviour of $[\overline{(u_i)_s} - \tilde{u}_i] \Sigma_{\text{gen}}$ both far from the wall and close to it for the cases considered here, and predicts an opposite sign to that of $[\overline{(u_i)_s} - \tilde{u}_i] \Sigma_{\text{gen}}$ obtained from DNS data (see Eq. 6.61). This discrepancy originates from the predominantly counter-gradient behaviour of

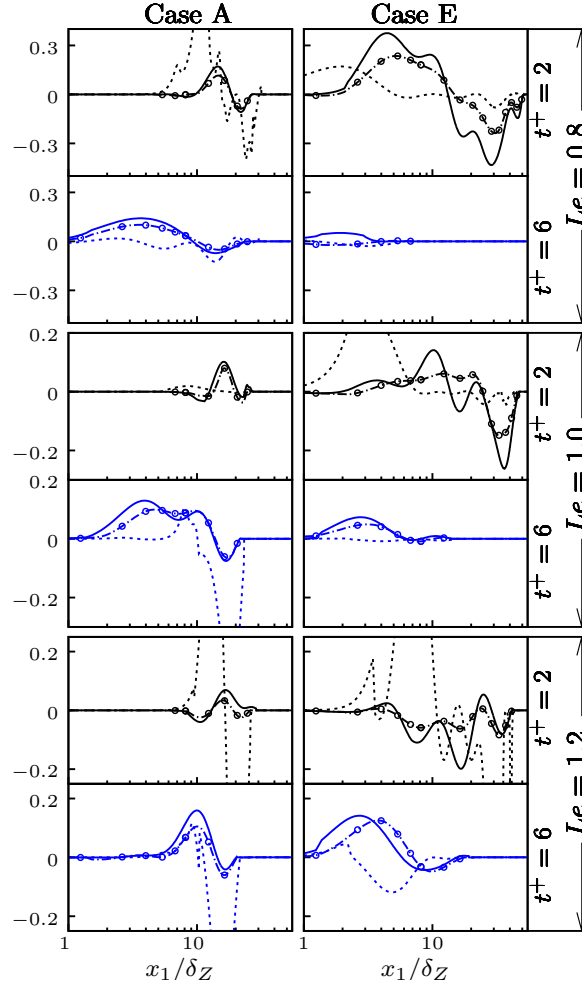


Fig. 6.24 Variations of the normalised turbulent flux $[(\overline{u_i})_s - \tilde{u}_i]\Sigma_{\text{gen}} \times \delta_Z/S_L$ (solid line) and the prediction of Eq. 6.62 (dashed line), and Eq. 6.62 with near-wall modification (dashed circle line) at different $t^+ = tS_L/\delta_Z$.

$[(\overline{u_i})_s - \tilde{u}_i]\Sigma_{\text{gen}}$ in the cases considered here. Chakraborty and Cant [36] proposed a model that also accounts for both gradient and counter gradient transport:

$$[(\overline{u_i})_s - \tilde{u}_i]\Sigma_{\text{gen}} = \frac{(A_2 - A_3\tilde{c})\overline{\rho u_i'' c''}\Sigma_{\text{gen}}}{\overline{\rho c''^2} + \tilde{\rho}\tilde{c}(1 - \tilde{c})} \quad (6.62)$$

Equation 6.62 with the model parameters $A_2 = 1.0$ and $A_3 = 2.0$ shows a satisfactory behaviour away from the wall but it underpredicts the magnitude of $[(\overline{u_i})_s - \tilde{u}_i]\Sigma_{\text{gen}}$ close to the wall. To improve the predictions of Eq. 6.62, the following expressions are suggested: $A_2 = 1.06 - 0.06\text{erf}(x_1/\delta_Z - 2.0\Pi)$ and $A_3 = 0.93 + 1.07\text{erf}(x_1/\delta_Z - 2.0\Pi)$ so that A_2 and A_3 approach 1.0 and 2.0, respectively, away from the wall ($x_1/\delta_Z > 2.0\Pi$), whereas they increase and decrease respectively close to the wall ($x_1/\delta_Z < 2.0\Pi$).

Figure 6.24 shows that Eq. 6.62 with near-wall modification satisfactorily predicts the behaviour of $[(\overline{u_i})_s - \tilde{u}_i]\Sigma_{\text{gen}}$ both far from the wall and close to it.

6.2.3 Modelling of the tangential strain rate term T_{F2}

The variation of T_{F2} with x_1/δ_Z is shown in Fig 6.25 for the cases A and E at different times for $Le = 0.8$, $Le = 1.0$ and $Le = 1.2$. The term T_{F2} assumes positive values but its magnitude decreases with time when the flame starts to interact with the wall and eventually. Bruneaux *et al.* [20] used the model $T_{F2} = \alpha_m(\tilde{\epsilon}/\tilde{k})\Gamma(u'/S_L, l/\delta_Z)\Sigma_{\text{gen}}$ where $\alpha_m \approx 2.0$ is a model parameter and $\Gamma(u'/S_L, l/\delta_Z)$ is an efficiency function [139]. The predictions of the Bruneaux *et al.* [20] ($T_{F2} = \alpha_m(\tilde{\epsilon}/\tilde{k})\Gamma(u'/S_L, l/\delta_Z)\Sigma_{\text{gen}}$) are shown in Fig 6.25 this model does not capture the qualitative behaviour of T_{F2} for the cases considered here and overpredicts the magnitude of T_{F2} . This warrants for a new modelling methodology for T_{F2} . This term T_{F2} can be decomposed [108, 36] into T_D , the contribution due to dilatation $\partial u_i/\partial x_i$, and T_N , the contribution of the normal strain rate $N_i N_j \partial u_i/\partial x_j$:

$$T_{F2} = \underbrace{(\overline{\partial u_i/\partial x_i})_s \Sigma_{\text{gen}}}_{T_D} - \underbrace{(\overline{N_i N_j \partial u_i/\partial x_j})_s \Sigma_{\text{gen}}}_{T_N} \quad (6.63)$$

The dilatation rate term T_D can be decomposed into the resolved T_{D1} (i.e. it can be obtained without model in RANS) and unresolved T_{D2} parts (i.e. it requires model): $T_D = T_{D1} + T_{D2}$. The resolved part is defined [108] as: $T_{D1} = (\partial \tilde{u}_i/\partial x_i)|\nabla \bar{c}|$, which needs evaluation of \bar{c} from \tilde{c} . Here, $\bar{c} = (1 + \tau g^a Le^{-b})\tilde{c}/(1 + \tau g^a Le^{-b}\tilde{c})$ is considered following previous analyses [108, 36], where $a = \tilde{c}''^2/[\tilde{c}(1 - \tilde{c})]$ is the segregation factor, and Le^{-b} accounts for the strengthening of heat release effects with decreasing Le . Figure 6.26 shows that the approximation $\bar{c} = (1 + \tau g^a Le^{-b})\tilde{c}/(1 + \tau g^a Le^{-b}\tilde{c})$ enables a satisfactory prediction of T_{D1} both away from the wall and close to it.

For the unresolved dilatation term $T_{D2} = (\overline{\partial u_i/\partial x_i})|\nabla \bar{c}| - (\partial \tilde{u}_i/\partial x_i)|\nabla \bar{c}|$, Katragadda *et al.* [108] suggested the following model:

$$T_{D2} = \left(\tau S_L/\delta_{\text{th}} Le^{1.845}\right) \left[A_4 \cdot (1 - \tilde{c})^\xi (\Sigma_{\text{gen}} - |\nabla \bar{c}|)\right] \quad (6.64)$$

The parameters are $A_4 = 1.8/(1 + Ka_L)^{0.35}$ and $\xi = 1.5 - 1.8Le$ with $Ka_L = \tilde{\epsilon}\delta_{\text{th}}/S_L^{1.5}$ being the local Karlovitz number. The Karlovitz number dependence of A_4 ensures weakening of dilatation effects for high values of Ka_L [108, 36]. Figure 6.26 shows that Eq. 6.64 provides a satisfactory prediction of T_{D2} but the near-wall behaviour has been found to be inadequate. Here A_4 and ξ have been modified to account for the near-

wall behaviour as: $A_4 = 0.9\exp[1.2(\tilde{c}_w - \tilde{T}_w)][\text{erf}(Le x_1/\delta_Z) + 1]/(1 + Ka_L)^{0.35}$ and $\xi = 1.5\exp[0.2(\tilde{c}_w - \tilde{T}_w)] - 1.8Le$. Note that $(\tilde{c}_w - \tilde{T}_w)$ not only accounts for non-adiabaticity induced by the wall but also acts as a quenching sensor (i.e. $(\tilde{c}_w - \tilde{T}_w)$ remains zero when the flame is away from the wall but it rises once the flame quenching is initiated). Thus, the involvement of $(\tilde{c}_w - \tilde{T}_w)$ in A_4 and ξ modifies the prediction of Eq. 6.64 in the near-wall region only when the flame starts to quench. The modified parameters A_4 and ξ approach the earlier expressions [108] away from the wall. Equation 6.64 with the modified A_4 and ξ provides a satisfactory prediction of T_{D2} both away from the wall and near to it (see Fig. 6.26).

The normal strain rate term T_N can also be split into resolved (T_{N1}) and unresolved (T_{N2}) parts:

$$-T_N = -\underbrace{\overline{(N_i N_j)_s}(\partial \tilde{u}_i / \partial x_j) \Sigma_{\text{gen}}}_{T_{N1}} - \underbrace{\overline{(N_i N_j \partial u_i'' / \partial x_j)_s} \Sigma_{\text{gen}}}_{T_{N2}} \quad (6.65)$$

The resolved component T_{N1} can be closed if $\overline{(N_i N_j)_s} = \overline{(N_i)_s (N_j)_s} + (\delta_{ij}/3)[1 - \overline{(N_k)_s (N_k)_s}]$ [25]. Katragadda *et al.* [108] suggested the following model for $(-T_{N2})$:

$$-T_{N2} = \left(\epsilon / \tilde{k} \right) [C_1 - \tau C_2 f(Le) Da_L] \Sigma_{\text{gen}} \quad (6.66)$$

here, C_1 and C_2 are model parameters, $Da_L = \tilde{k} S_L / (\tilde{\epsilon} \delta_{\text{th}})$ is the local Damk ohler number, and $f(Le) = \exp(Le^{-0.945} - 1)$ is a function, accounting for increased flame normal acceleration with decreasing Le [108]. The term $C_1 \epsilon / \tilde{k} \Sigma_{\text{gen}}$ is responsible for FSD generation due to alignment of ∇c with the most extensive principal strain rate induced by flame normal acceleration ($\sim \tau f(Le) S_L / \delta_{\text{th}}$) [108]. Based on the present analysis, $C_1 = \text{erf}(0.1x_1/\delta_Z)$ and $C_2 = A_5(1 - \overline{(N_k)_s (N_k)_s}) / (1 + Ka_L)^{0.35}$ have been proposed guided by the analysis of Katragadda *et al.* [108] where A_5 is given by:

$$A_5 = 0.471 \text{erf}(0.5x_1/\delta_Z) \exp\left(2.0(\tilde{c}_w - \tilde{T}_w)\right) \times \left[\frac{0.3}{\text{erf}(Re_L + 0.01)^{0.5\exp(-\tilde{c}_w)}} \right]^{A_6} \quad (6.67)$$

In this expression $A_6 = 0.5(\text{erf}(-x_1/\delta_Z + \Pi^3) + 1)$ and $Re_L = (\rho_0 \tilde{k}^2 / \mu_0 \tilde{\epsilon})$ is the local turbulent Reynolds number, μ_0 is the unburned gas viscosity. The error function $\text{erf}(0.5x_1/\delta_Z)$ in Eq. 6.67 allows for the gradual increase of $(-T_{N2})$ from the wall. The combined effects from error function and exponential function in $\text{erf}(0.5x_1/\delta_Z) \exp(2.0(\tilde{c}_w - \tilde{T}_w))$ are needed to capture the correct magnitude in the near-wall region ($x_1/\delta_Z < \Pi$) at all times. The expression $[0.3/\text{erf}(Re_L + 0.01)^{0.5\exp(-\tilde{c}_w)}]^{A_6}$ is

responsible for the correct prediction of $(-T_{N2})$ away from the wall. The involvement of $(\tilde{c}_w - \tilde{T}_w)$ and \tilde{c}_w ensures that the near-wall modification takes effect only when the flame quenching takes effect. The Karlovitz number dependence of C_2 ensures the weakening of flame normal acceleration effects for high values of Ka_L [108].

Figure 6.25 shows the prediction of T_{F2} when T_{D1} , T_{N1} , T_{D2} and T_{N2} are modelled with $\bar{c} = (1 + \tau g^a Le^{-b})\tilde{c}/(1 + \tau g^a Le^{-b}\tilde{c})$, $\overline{(N_i N_j)_s} = \overline{(N_i)_s (N_j)_s} + (\delta_{ij}/3)[1 - \overline{(N_k)_s N_{ks}}]$, Eqs. 6.64 and 6.66 respectively. This model captures qualitative and quantitative behaviour of T_2 both away from the wall and near to it, except in case E for $Le = 0.8$ where a slight overprediction is observed. However, this model is more successful in capturing both qualitative and quantitative behaviour of T_2 than the Bruneaux *et al.* [20] model both away from and close to the wall.

6.2.4 Modelling of propagation and curvature terms $T_{F3} + T_{F4}$

Several previous analysis [36] modelled propagation and curvature terms together. The variation of $(T_{F3} + T_{F4})$ with x_1/δ_Z is presented in Fig. 6.27 for case A and E at different times for $Le = 0.8, 1.0$ and 1.2 . The combined term $(T_{F3} + T_{F4})$ shows positive (negative) values towards the unburned (burned) gas side of the flame brush. Bruneaux *et al.* [20] proposed separate models for T_{F3} and T_{F4} ($T_{F3} = -\partial\{S_L M_i \Sigma_{gen}(1 - (1 - Q_m))/\gamma_\omega\}/\partial x_i$) and $T_{F4} = -S_L \Sigma_{gen}^2 / \bar{c}(1 - \bar{c})$ with $\gamma_\omega = 0.3$, $Q_m = \exp[-2\beta(\tilde{c} - \tilde{T})]$ and the resolved flame normal vector $\vec{M} = -\nabla\tilde{c}/|\nabla\tilde{c}|$. Figure 6.27 shows that the Bruneaux *et al.* [20] model does not capture the qualitative behaviour of $(T_{F3} + T_{F4})$ obtained from DNS data.

Chakraborty and Cant [36] proposed the following model for $(T_3 + T_4)$ with the model parameters $\beta_0 = 8.0$ and $c_{cp} = 0.35$:

$$T_{F3} + T_{F4} = -\frac{\partial}{\partial x_i} \left[\frac{\rho_0 S_L}{\bar{\rho}} \overline{(N_i)_s} \Sigma_{gen} \right] + \frac{\rho_0 S_L}{\bar{\rho}} \frac{\partial \overline{(N_i)_s}}{\partial x_i} \Sigma_{gen} - \beta_0 \left[1 - \overline{(N_k)_s (N_k)_s} \right] \frac{(\bar{c} - c_{cp}) S_L \Sigma_{gen}^2}{\bar{c}(1 - \bar{c})} \quad (6.68)$$

Equation 6.68 provides a satisfactory prediction away from the wall but overpredicts the magnitude of $(T_{F3} + T_{F4})$ close to the wall. This deficiency is avoided when S_L in Eq. 6.68 is replaced by a modified flame speed $S'_L = S_L \exp[-8.0(\tilde{c} - \tilde{T})]$ and Fig. 6.27 shows that Eq. 6.68 with S'_L satisfactorily predicts $(T_{F3} + T_{F4})$ both away from the wall and close to it. The improvement of $(\tilde{c} - \tilde{T})$ in the modified flame speed S'_L accounts for the reduction in flame propagation rate during flame quenching.

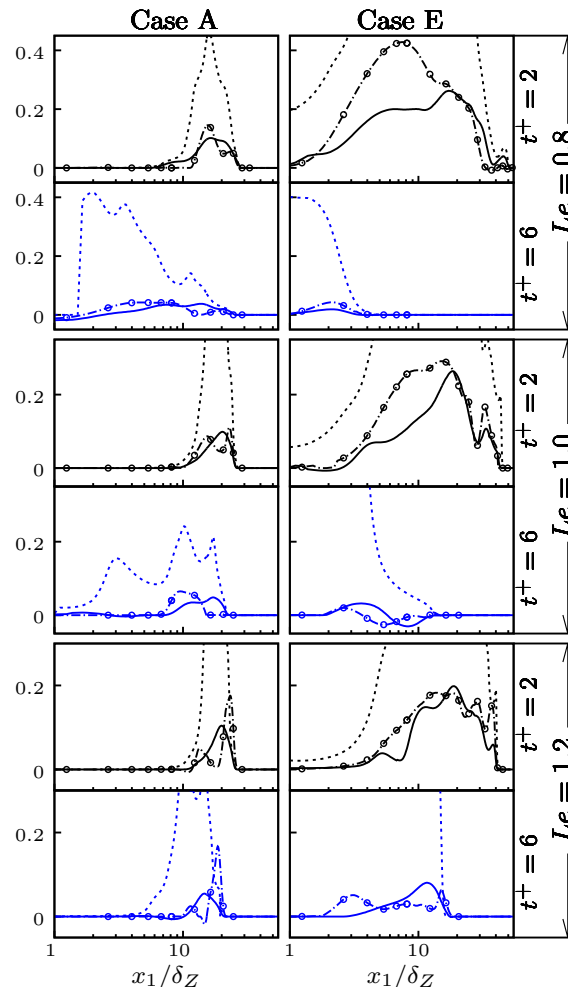


Fig. 6.25 Variations of the strain rate term $T_{F2} \times \delta_Z^2 S_L$ (solid line) along with the predictions of the Bruneaux *et al.* [20] model (dashed line) and the combined outcome of the models of T_{D1} , T_{N1} , T_{N2} with wall modifications (dashed circle line) at different $t^+ = t_{S_L}/\delta_Z$.

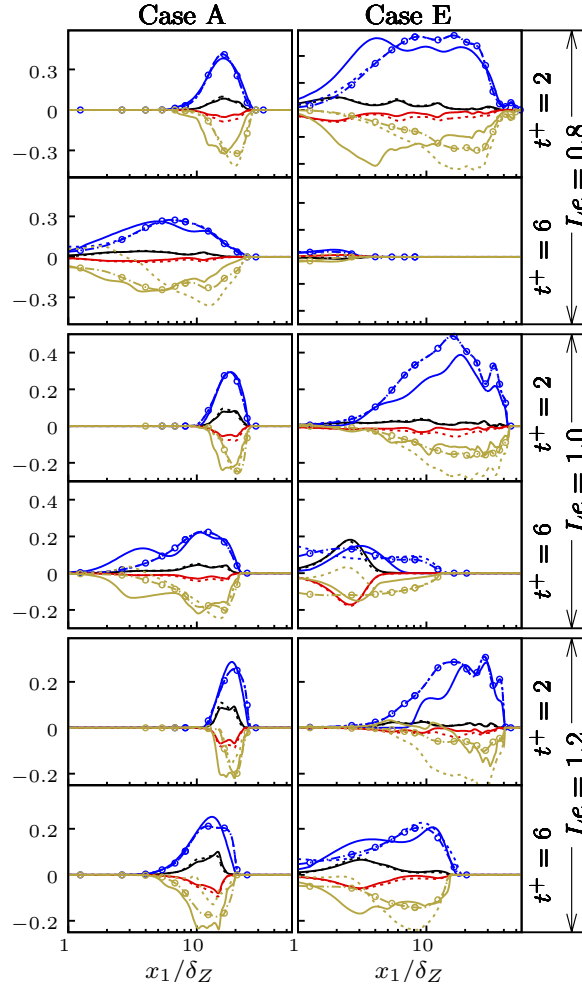


Fig. 6.26 Variations of $(T_{D1}$ (—), T_{D2} (—), $-T_{N1}$ (—), $-T_{N2}$ (—)) $\times \delta_Z^2 / S_L$ obtained from DNS (solid line) and the model predictions according to $\bar{c} = (1 + \tau g^a Le^{-b}) \tilde{c} / (1 + \tau g^a Le^{-b} \tilde{c})$, $(N_i N_j)_s = (N_i)_s (N_j)_s + (\delta_{ij} / 3) [1 - (N_k)_s (N_k)_s]$, Eqs. 6.64 and respectively, with (dashed circle line) and without (dashed line) wall modifications at different $t^+ = t S_L / \delta_Z$.

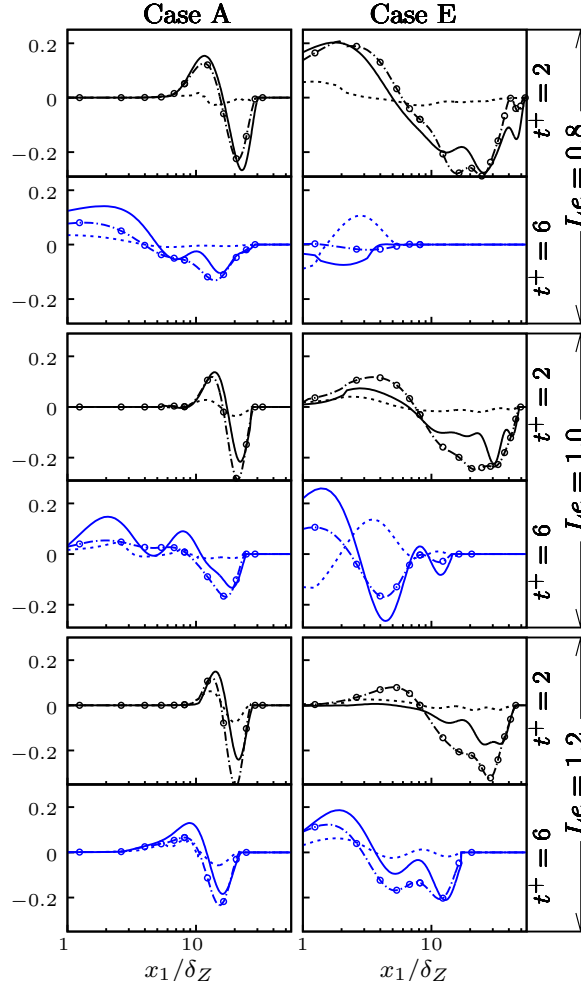


Fig. 6.27 Variations of the normalised curvature and propagation term $(T_{F3} + T_{F4}) \times \delta_Z^2 / S_L$ obtained from DNS data (solid line) and the predictions of the Bruneaux *et al.* [20] model (dashed line) and Eq. 6.68 with near-wall modification (dashed circle line) at different $t^+ = tS_L / \delta_Z$.

6.2.5 Summary of the key results

The near wall behaviour of the FSD based reaction rate closure and the unclosed terms of the FSD transport equation in the case of the head-on quenching have been analysed here. A comparison between $\rho_0 S_L \Sigma_{\text{gen}}$ and $\bar{\omega}$ from DNS data reveals that the original model overestimates the value of the mean reaction rate in near wall region. A modified FSD based closure for $\bar{\omega}$ in terms of Σ_{gen} has been proposed here which has been shown to capture the near wall behaviour of $\bar{\omega}$ satisfactorily for all cases considered here. The existing models for the unclosed terms T_{F1} , T_{F2} and $(T_{F3} + T_{F4})$ of the FSD transport equations have also been modified, which are based on *a-priori* analysis using explicitly Reynolds averaged DNS data, so that they can satisfactorily predict the corresponding terms extracted from DNS data for both away from and near to the wall.

6.3 Statistical analysis and modelling of turbulent scalar flux transport

The main objectives of the current section are:

- To demonstrate the near wall behaviour of the unclosed terms of the transport equation of the turbulent scalar flux of reaction progress variable
- To propose models for the near wall behaviour of the terms of the turbulent scalar flux transport equation

6.3.1 Statistical behaviours of the terms in turbulent scalar flux transport equation

The Reynolds-averaged turbulent scalar flux transport equation can be seen in Eq. 2.57a (or see Eq. 6.69 below).

$$\begin{aligned}
 \frac{\partial \overline{\rho u_i'' c''}}{\partial t} + \frac{\partial \overline{\rho \tilde{u}_j u_i'' c''}}{\partial x_j} = & \underbrace{-\frac{\partial \overline{\rho u_i'' u_j'' c''}}{\partial x_j}}_{T_{1c}} - \underbrace{\overline{\rho u_i'' u_j''} \frac{\partial \tilde{c}}{\partial x_j}}_{T_{2c}} - \underbrace{\overline{\rho u_j'' c''} \frac{\partial \tilde{u}_i}{\partial x_j}}_{T_{3c}} - \underbrace{\overline{c''} \frac{\partial \tilde{P}}{\partial x_i}}_{T_{4c}} \\
 & \underbrace{-\overline{c''} \frac{\partial \tilde{P}'}{\partial x_i}}_{T_{5c}} + \underbrace{\left[\overline{u_i''} \frac{\partial}{\partial x_k} \left(\rho D \frac{\partial c}{\partial x_k} \right) \right]}_{T_{6c}} + \underbrace{\left[c_i'' \frac{\partial \tau_{ik}}{\partial x_k} \right]}_{T_{7c}} + \underbrace{\overline{u_i'' \dot{\omega}}}_{T_{8c}}
 \end{aligned} \tag{6.69}$$

- T_{1c} turbulent transport term
 T_{2c} mean scalar gradients term
 T_{3c} velocity gradients term
 T_{4c} mean pressure gradient term
 T_{5c} fluctuating pressure gradient term
 T_{6c} mass diffusion term
 T_{7c} viscous stress term
 T_{8c} reaction rate term

The variations of $T_{1c} - T_{8c}$ for the $\overline{\rho u_1'' c''}$ transport equation with normalised wall normal distance x_1/δ_Z for cases A, C and E are shown in Fig. 6.28 for different time instants. The positive contributions in Fig. 6.28 act to promote a counter-gradient transport, whereas negative contributions tend to induce a gradient transport. It

can be seen from Fig. 6.28 that the reaction contribution T_{8c} assumes predominantly positive values, whereas both T_{6c} and T_{7c} exhibit negative values at all times. The pressure gradient terms T_{4c} and T_{5c} play important roles in the transport of $\overline{\rho u_1'' c''}$ for all cases when the flame is away from the wall. The mean pressure gradient term T_{4c} assumes a positive value for the major part of the flame brush although local negative values of T_{4c} are also obtained within the flame brush when the flame is away from the wall. The fluctuating pressure gradient term T_{5c} also exhibits both positive and negative values within the flame brush. The contributions of T_{2c} and T_{3c} remain negative, whereas the turbulent transport term T_{1c} exhibits both positive and negative values. The relative magnitudes of T_{1c} , T_{2c} and T_{3c} in comparison to the pressure gradient terms T_{4c} and T_{5c} decrease with increasing Re_t (i.e. from case A to case E). The magnitudes of T_{1c} - T_{8c} decrease considerably as the quenching progresses and they eventually vanish altogether. The terms T_{1c} - T_{8c} can be scaled in the following manner:

$$\begin{aligned}
 T_{1c} &\sim (\rho_0 S_L^2 / \delta_{th}) (\overline{\rho u_1'' c''} / \rho_0 S_L)^2 Da^{-0.5} Re_t^{-0.5}; \\
 T_{2c} &\sim (\rho_0 S_L^2 / \delta_{th}) Da^{-1.5} Re_t^{-0.5}; \\
 T_{3c} &\sim (\rho_0 S_L^2 / \delta_{th}) (\overline{\rho u_1'' c''} / \rho_0 S_L)^2 (U_{ref} / S_L) Da^{-0.5} Re_t^{-0.5} \\
 T_{4c} &\sim (\rho_0 S_L^2 / \delta_{th}) Da^{-1.5} Re_t^{0.5} \\
 T_{5c} &\sim (\rho_0 S_L^2 / \delta_{th}) (\overline{\rho u_1'' c''} / \rho_0 S_L)^2 \\
 T_{6c} &\sim (\rho_0 S_L^2 / \delta_{th}) (\overline{\rho u_1'' c''} / \rho_0 S_L) \\
 T_{7c} &\sim (\rho_0 S_L^2 / \delta_{th}) (\overline{\rho u_1'' c''} / \rho_0 S_L) \\
 T_{8c} &\sim (\rho_0 S_L^2 / \delta_{th}) (\overline{\rho u_1'' c''} / \rho_0 S_L)
 \end{aligned} \tag{6.70}$$

Here the gradients of the mean quantities are scaled using l and the quantities $\overline{\rho u_1'' u_1'' c''}$ and $\overline{\rho u_1'' u_1''}$ are scaled with respect to $(\rho u_1'' c'')^2 / \rho_0$ and $\rho_0 u^2$ respectively. The mean pressure gradient can be taken to scale as $\partial \bar{p} / \partial x_1 \sim \partial (\overline{\rho u_1'' u_1''}) / \partial x_1$ for flows with u' either greater than or comparable to \tilde{u}_1 , as in the cases considered here. In terms

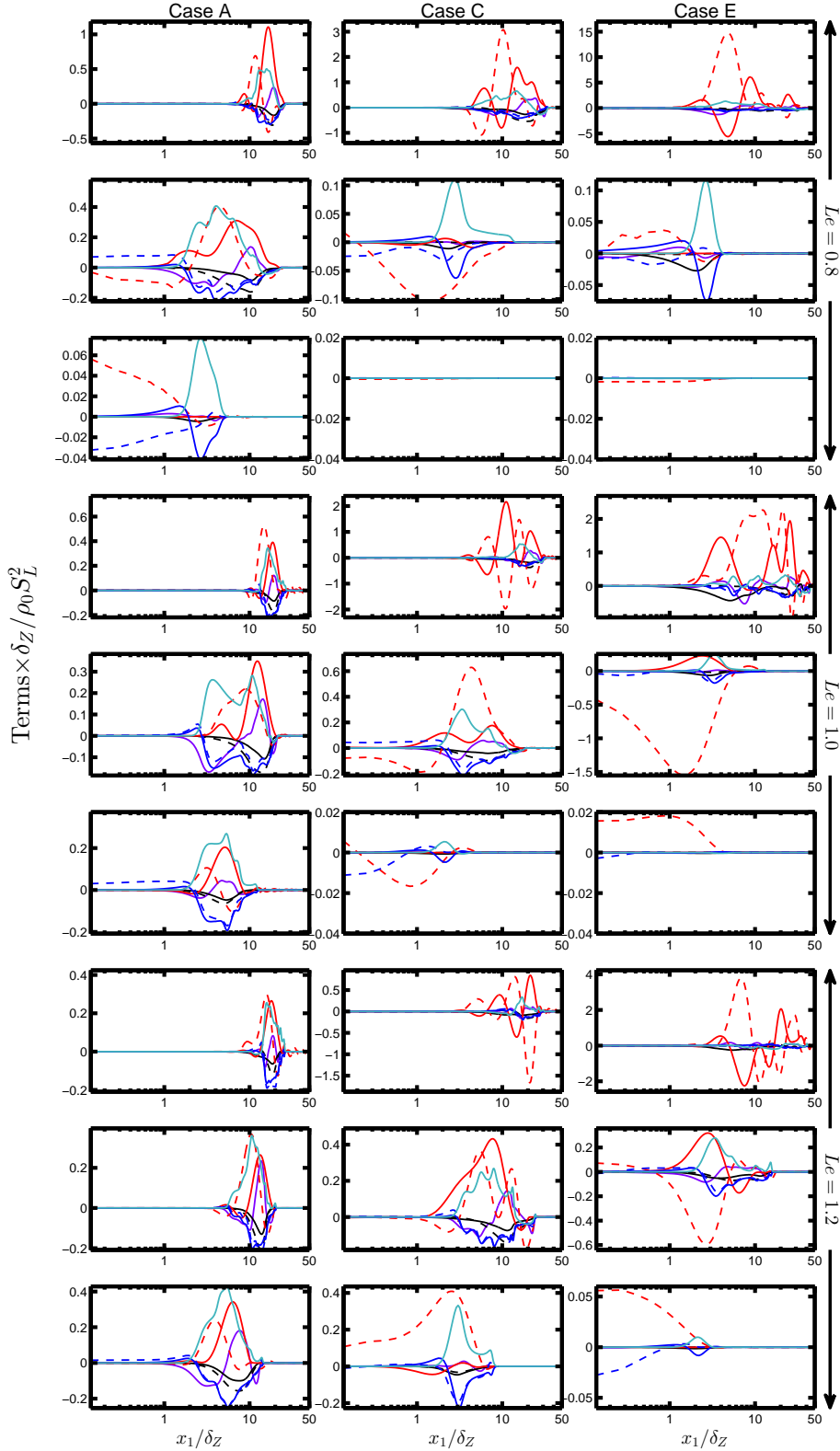


Fig. 6.28 Variation of terms T_{1c} (—), T_{2c} (—), T_{3c} (— — —), T_{4c} (—), T_{5c} (— — —), T_{6c} (—), T_{7c} (— — —) and T_{8c} (—) with x_1/δ_Z at $t = 2\delta_Z/S_L$, $6\delta_Z/S_L$, and $10\delta_Z/S_L$ for turbulent cases A - E with $Le = 0.8$, 1.0 and 1.2 . All terms are non-dimensionalised by $\rho_0 S_L^2/\delta_Z$.

T_{5c} - T_{8c} the scalings of the key quantities may be taken as $\partial p'/\partial x_1 \sim (\rho u_1'' c'')^2/\rho \delta_{th}$, $u_1'' \sim \rho u_1'' c''/\rho_0$ and $\partial \tau_{ik}/\partial x_k \sim (\rho u_1'' c'') S_L/\delta_{th}$. The molecular diffusion rate and reaction rate in T_{7c} and T_{8c} have been scaled with respect to $\rho_0 S_L/\delta_{th}$ (i.e. $\dot{\omega} \sim \rho_0 S_L/\delta_{th}$ and $\nabla \cdot (\rho D \nabla c) \sim \rho_0 S_L/\delta_{th}$). The scaling estimates given by Eq. 6.70 indicate that the terms T_{2c} , T_{4c} - T_{8c} are expected to be the leading order contributors for $Da < 1$, whereas the contributions of T_{1c} and T_{3c} are expected to become progressively less important with increasing Re_t . The terms T_{2c} and T_{3c} are closed in the context of second-moment closure, and thus the modelling of T_{1c} and T_{4c} to T_{8c} will be discussed next.

6.3.2 Modelling of the turbulent transport term T_{1c}

The turbulent transport term is given by: $T_{1c} = \partial(\overline{\rho u_j'' u_i'' c''})/\partial x_j$, and therefore modelling of this term depends on $\overline{\rho u_j'' u_i'' c''}$. The model (referred to as the TDH model) by Daly and Harlow [66] is one of the widely used models for $\overline{\rho u_j'' u_i'' c''}$ closure for passive scalars:

$$\overline{\rho u_i'' u_j'' c''} = -C_{CS} \frac{\tilde{k}}{\tilde{\varepsilon}} \overline{\rho u_j'' u_k''} \frac{\partial(\overline{\rho u_i'' c''}/\bar{\rho})}{\partial x_k} \quad (6.71)$$

where $C_{CS} \approx 0.22$ is the model constant. The predictions of the TDH model are compared to $\overline{\rho u_i'' u_j'' c''}$ extracted from DNS data in Fig. 7. The TDH model fails to capture the quantitative and qualitative behaviour of the DNS data, for cases A-C. However, for high values of $u'/S_L \sim Re_t^{1/4} Ka^{1/2} \sim Re_t^{1/2} Da^{-1/2}$ (e.g. cases D and E) the TDH model exhibits slightly improved agreement with DNS data at $t \leq 6\delta_Z/S_L$ but this model fails to predict the near-wall behaviour of $\overline{\rho u_i'' u_j'' c''}$ at $t \geq 8\delta_Z/S_L$. The TDH model is proposed for non-reacting flow based on gradient hypothesis, and it does not take into account for the effect of chemical reaction. According to the BML analysis (i.e. subject to the assumption of bi-modal probability density function of c (i.e. $P(c)$) with impulses at $c = 0$ and $c = 1$) the Favre-average velocity component takes the following form: $\tilde{u}_j = \overline{(u_j)}_P \tilde{c} + (1 - \tilde{c}) \overline{(u_j)}_R + O(1/Da)$, which once used in $\overline{\rho u_i'' u_j'' c''} = \int_{-\infty}^{\infty} \int_{-\infty}^{\infty} \int_0^1 \rho(u_i - \tilde{u}_i)(u_j - \tilde{u}_j) P(u_i; u_j c) du_i du_j dc$ yield [38]:

$$\begin{aligned} \overline{\rho u_1'' u_1'' c''} &\approx \bar{\rho} [\overline{(u_1)}_P - \overline{(u_1)}_R]^2 \tilde{c}(1 - \tilde{c})(1 - 2\tilde{c}) - \bar{\rho} \overline{(u_1' u_1')}_R \tilde{c}(1 - \tilde{c}) \\ &\quad + \bar{\rho} \overline{(u_1' u_1')}_P \tilde{c}(1 - \tilde{c}) + O(1/Da) \end{aligned} \quad (6.72)$$

The first term on the right hand side represents the reacting contribution to $\overline{\rho u_1'' u_1'' c''}$, whereas the combined action of second and third terms represent the effects of turbulence on $\overline{\rho u_1'' u_1'' c''}$. The last term $O(1/Da)$ originates from the interior of the flame and this contribution becomes negligible for $Da \gg 1$. It has been demonstrated elsewhere in earlier section that the probability density function of c cannot be approximated by a bi-modal distribution in the near-wall region. The departure from a bi-modal distribution is often quantified in terms of a segregation factor $g = \overline{\rho c''^2} / \bar{\rho} \tilde{c}(1 - \tilde{c})$. Chakraborty and Cant [34, 38] utilised the TDH model for the turbulent contribution part in Eq. 6.72 and utilised the segregation factor to propose a model (referred to as the CC model here) based on a-priori DNS analyses for the flames without any influence of walls in the following manner:

$$\begin{aligned} \overline{\rho u_1'' u_1'' c''} = & -C_{CS} \frac{\tilde{k}}{\tilde{\varepsilon}} \overline{\rho u_1'' u_1''} \frac{(\overline{\rho u_1'' c''} / \bar{\rho})}{\partial x_1} \\ & + \bar{\rho} \left[\frac{\overline{\rho u_1'' c''}}{\bar{\rho} \tilde{c}(1 - \tilde{c})} + \alpha_3 \sqrt{\overline{\rho u_1'' u_1''} / \bar{\rho}} \right]^2 \tilde{c}(1 - \tilde{c})(1 - 2\sqrt{g}\tilde{c}) \end{aligned} \quad (6.73)$$

where $\left[\frac{\overline{\rho u_1'' c''}}{\bar{\rho} \tilde{c}(1 - \tilde{c})} + \alpha_3 \sqrt{\overline{\rho u_1'' u_1''} / \bar{\rho}} \right]$ represents $[(u_j)_P - (u_j)_R]$ in Eq. 6.73 where $\alpha_3 = 0.2 + 0.3\text{erf}(Re_L/20)$ is a model parameter. The predictions of the CC model (Eq. 6.73) are also shown in Fig. 6.29, which indicates that the CC model is more successful in capturing the behaviour of $\overline{\rho u_1'' u_1'' c''}$ than the TDH model when the flame is away from the wall, where the CC model reasonably captures both the quantitative and qualitative behaviours of $\overline{\rho u_1'' u_1'' c''}$. However, during flame quenching \tilde{c} approaches 1.0 and as a result the second term on right hand side of Eq. 6.73 disappears and thus the CC model prediction approaches to that of the TDH model in the near-wall region. Thus, the CC model does not adequately capture the near-wall behaviour of $\overline{\rho u_1'' u_1'' c''}$. Here the CC model has been modified in the following manner:

$$\begin{aligned} \overline{\rho u_1'' u_1'' c''} = & -C_{CS} \frac{\tilde{k}}{\tilde{\varepsilon}} \overline{\rho u_1'' u_1''} \frac{(\overline{\rho u_1'' c''} / \bar{\rho})}{\partial x_1} \\ & + \bar{\rho} \tilde{c}(1 - \tilde{c})(1 - 2g^{0.5(1-\tilde{c}_w)\tilde{c}}) \left[A_w \left(\frac{\overline{\rho u_1'' c''}}{\bar{\rho} \tilde{c}(1 - \tilde{c})} + \alpha_{3w} \sqrt{\frac{\overline{\rho u_1'' u_1''}}{\bar{\rho}}} \right) \right] \end{aligned} \quad (6.74)$$

where

$$\begin{aligned}
 \alpha_{3w} &= 0.2[3(1 - \tilde{c}_w)]^{\eta_1} + 0.3\text{erf}(Re_L/20) \\
 \eta_1 &= 0.5\text{erf}[-0.5(x_1/\delta_Z - 5(Pe_{\min})_L)] \\
 A_w &= \exp\left[-\frac{\tilde{c}_w - \tilde{T}_w}{Le}\eta_2\right] \\
 \eta_2 &= 0.5\text{erf}[-0.5(x_1/\delta_Z - 5(Pe_{\min})_L)]
 \end{aligned} \tag{6.75}$$

The model parameter α_{3w} is modified form of α_3 in the CC model, and this modification accounts for the dampening of turbulence close to the wall. The magnitude of $\overline{\rho u_1'' u_1'' c''}$ drops during flame quenching, especially in near wall region, and the presence of flame close to the wall is sensed by A_w due to an increase in the value of $\tilde{c}_w - \tilde{T}_w$ during flame quenching, and this damps the contribution arising from velocity jump across the flame brush due to thermal expansion. The extent of velocity jump across the flame brush is dependent on Le , and thus the damping factor A_w is dependent on Le . Both the TDH and CC models do not adequately predict the negative values of $\overline{\rho u_1'' u_1'' c''}$ close to the wall but this behaviour cannot be captured by $(1 - 2\sqrt{g}\tilde{c})$ because $\overline{\rho c''^2}/\bar{\rho}$ (and thus g) drops drastically during flame quenching. However, the modification $g^{0.5(1-\tilde{c}_w)}$ allows the term $(1 - 2g^{0.5(1-\tilde{c}_w)}\tilde{c})$ to assume negative values during flame quenching when \tilde{c}_w approaches unity (i.e. $\tilde{c}_w \rightarrow 1.0$). It can be seen from Fig. 6.29 that the model given by Eq. 6.75 (referred to as the new model) predicts both qualitative and quantitative behaviours of $\overline{\rho u_1'' u_1'' c''}$ satisfactorily for both far from and near to the wall for all cases considered here.

It is worth noting that the modifications of model parameters given by Eq. 6.75 are empirical in nature but they are proposed in such a manner that the modified model given by Eq. 6.75 asymptotically approaches previously proposed model for unbounded flows (see Eq. 6.72) away from the wall. The involvements of exponential function and Re_L in the empirical functions are similar to the van Driest's damping function [79]. Furthermore, the empirical parameters given by Eq. 6.75 are taken to be functions of $(Pe_{\min})_L$, \tilde{c}_w and $(\tilde{c}_w - \tilde{T}_w)$. The involvement of $(Pe_{\min})_L$ implicitly includes reacting boundary layer information into the model, whereas the $(\tilde{c}_w - \tilde{T}_w)$ dependence of the model parameter ensures that the effects of enthalpy loss due to wall heat transfer are reflected on the qualitative and quantitative variations of $\overline{\rho u_1'' u_1'' c''}$ depending on the distance of the flame from the wall. As the value of \tilde{c}_w changes with time (it remains

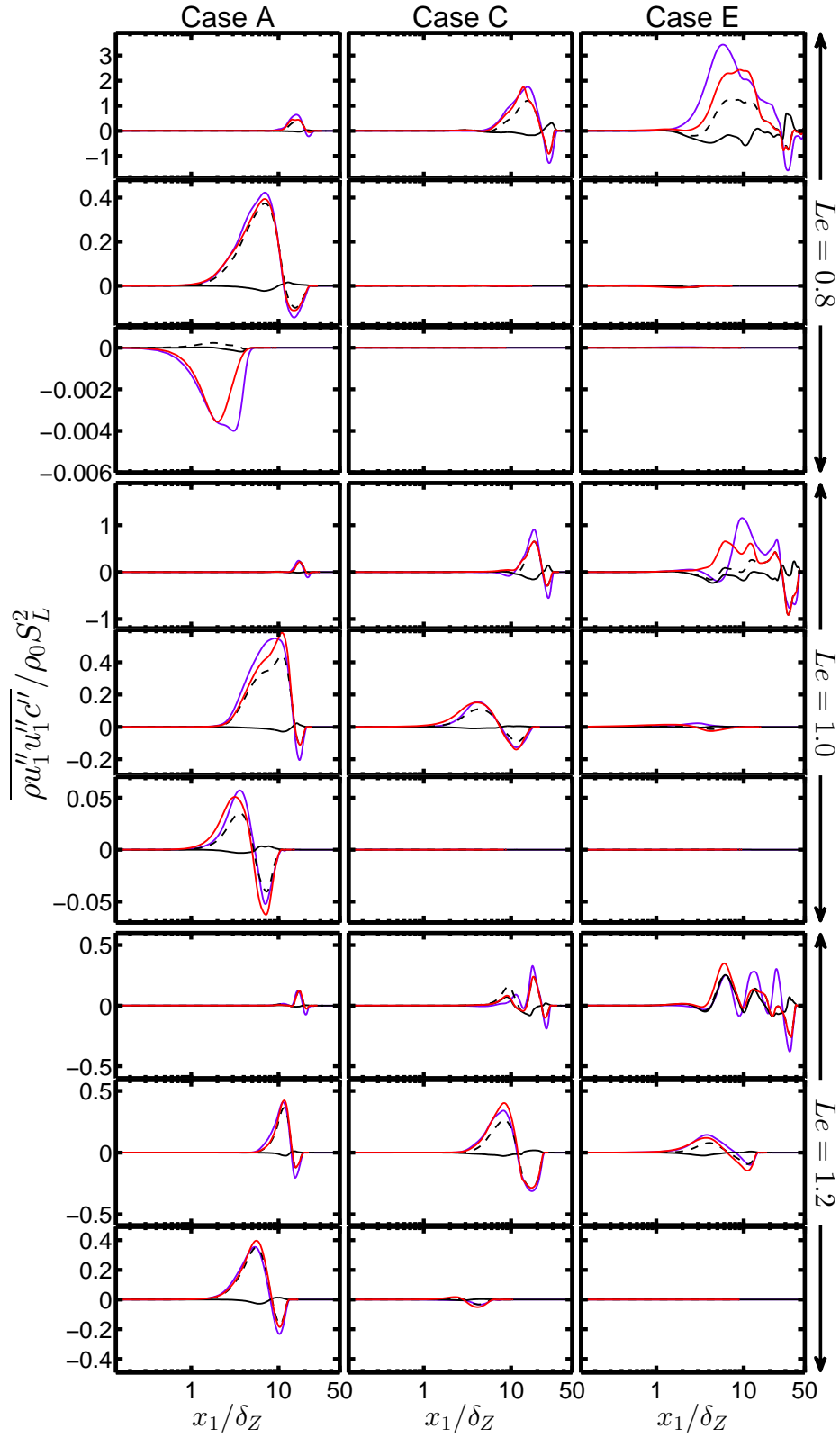


Fig. 6.29 Variation of terms $\overline{\rho u_1'' u_1'' c''} / \rho_0 S_L^2$ from DNS data (—), TDH (—), CC (— —) and New model (—) with x_1 / δ_Z at $t = 2\delta_Z/S_L$, $6\delta_Z/S_L$, and $10\delta_Z/S_L$ (1st - 3rd row) for turbulent cases A, C, and E (1st - 3rd column) with $Le = 0.8, 1.0$ and 1.2 .

0 when the flame is away from the wall but it increases from 0 and approaches 1.0 with the advancement of quenching so the dependence of \tilde{c}_w in the model parameters acts as the sensor of flame position from the wall. Similar modelling approaches were previously adopted by Bruneaux *et al.* [20] and Alshaalan *et al.* [3] in the context of Flame Surface Density (FSD) closures for wall-bound turbulent premixed flames.

6.3.3 Modelling of the turbulent transport term ($T_{4c} + T_{5c}$)

Both the mean and fluctuating pressure terms are often modelled in a combined manner due to their similar origin [34, 38, 79]. There are several available models for the closure of $(T_{4c} + T_{5c})$. Three of these models take the following form by combining conventional closures of slow and rapid terms [79]:

$$T_{4c} + T_{5c} = -C_{1c} \frac{\tilde{\varepsilon}}{\bar{k}} \overline{\rho u_i'' c''} + C_{2c} \overline{\rho u_k'' c''} \frac{\partial \tilde{u}_i}{\partial x_k} + C_{3c} \overline{\rho u_k'' c''} \frac{\partial \tilde{u}_k}{\partial x_i} + C_{4c} \overline{\rho u_i'' u_k''} \frac{\partial \tilde{c}}{\partial x_k} \quad (6.76)$$

where the slow part is represented by $-C_{1c}(\tilde{\varepsilon}/\bar{k})$ and the rapid part is given by: $C_{2c} \overline{\rho u_k'' c''} \partial(\tilde{u}_i/\partial x_k) + C_{3c} \overline{\rho u_k'' c''} (\partial \tilde{u}_k/\partial x_i) + C_{4c} \overline{\rho u_i'' u_k''} (\partial \tilde{c}/\partial x_k)$ with C_{1c} , C_{2c} , C_{3c} and C_{4c} being the model parameters. Launder [124] suggested that $C_{1c} = 3.0$, $C_{2c} = 0$, $C_{3c} = 0$ and $C_{4c} = 0.4$, and this model will henceforth be referred to the PL model. Craft *et al.* [64] adopted a similar model (referred to as the PC model) with $C_{1c} = 3.0$, $C_{2c} = 0.5$, $C_{3c} = 0$ and $C_{4c} = 0.4$. Durbin [79] suggested an alternative model (PD model) where $C_{1c} = 2.5$, $C_{2c} = 0$, $C_{3c} = 0$ and $C_{4c} = 0.45$. In addition, Jones [106] and Bradley *et al.* [16] proposed alternative models for $T_{4c} + T_{5c}$ in the following manner:

$$T_{4c} + T_{5c} = -\bar{c''} \frac{\partial \bar{P}}{\partial x_i} - C_{\Phi 1} \frac{\tilde{\varepsilon}}{\bar{k}} \overline{\rho u_i'' c''} + C_{\Phi 2} \overline{\rho u_k'' c''} \frac{\tilde{u}_i}{\partial x_k} \quad (6.77)$$

Jones [106] considered $C_{\Phi 1} = 3.0$ and $C_{\Phi 2} = 0.5$ for this (PJ model) model. By contrast, Bradley *et al.* [16] chose $C_{\Phi 1} = 3.0$ and $C_{\Phi 2} = 0$ for their model (PB model). Another alternative model (PLV model) was proposed by Lindstedt and Vaos [127]:

$$T_{4c} + T_{5c} = -\bar{c''} \frac{\partial \bar{P}}{\partial x_i} + \overline{\rho u_i'' c''} G_{il} + C_{As} \bar{c''} \frac{\partial \bar{P}}{\partial x_i} \quad (6.78)$$

where $C_{As} = 1/3$ and G_{il} is the generalized Langevin coefficient which is a function of Reynolds stress $\overline{\rho u_i'' u_i''}$ and the mean velocity gradient $\partial \tilde{u}_i/\partial x_j$ [127]. Domingo and Bray [58] proposed a model expression (PDB model) for the strict flamelet burning of

premixed turbulent flames:

$$T_{4c} + T_{5c} = \frac{\tilde{c}(1 - \tilde{c})}{(1 + \tau\tilde{c})} \left[-\frac{\partial \bar{P}_R}{\partial x_i} + (1 + \tau) \frac{\partial \bar{P}_P}{\partial x_i} \right] - 0.5 \overline{(\vec{N} \cdot \vec{M}_i)} \tau \rho_0 S_L^2 (0.7 - \tilde{c}) \Sigma_{\text{gen}} \quad (6.79)$$

where \bar{P}_R and \bar{P}_P represent the conditional mean pressure in reactants and products respectively, $\Sigma_{\text{gen}} = |\nabla c|$ represents the generalized flame surface density [12], $\vec{N} = -\nabla c / |\nabla c|$ is the local flame normal vector and \vec{M}_i is the unit vector in the x_1 -direction. Nishiki *et al.* [146] proposed the following model (PN model) based on *a-priori* DNS analysis:

$$T_{4c} + T_{5c} = -C_D \frac{\bar{\rho}}{\rho_0} \cdot (1 - \tilde{c}) \tau \frac{\partial \bar{P}}{\partial x_i} - C_{E1} \frac{\tilde{\varepsilon}}{\bar{k}} \overline{\rho u_i'' c''} + C_{E2} \tau \dot{S}_L \bar{\omega} (1 - \tilde{c})^{1.7} \quad (6.80)$$

where $C_D = 0.8$, $C_{E1} = 0.38$ and $C_{E2} = 0.66$ model constants. In the context of BML analysis $\overline{c''}$ can be expressed as $\overline{c''} = (\bar{\rho}/\rho_0) \tilde{c}(1 - \tilde{c}) \tau$ when the pdf of c can be assumed to follow a bi-modal distribution with impulses at $c = 0$ and $c = 1.0$ [19]. Thus, the first term on the right hand side of Eq. 6.80 accounts for the contribution of $T_{4c} = -\overline{c''} \partial \bar{P} / \partial x_i$.

The predictions of all these model are compared to $(T_{4c} + T_{5c})$ extracted from DNS data for cases A, C and E in Fig. 6.30 for different time instants. It is clear from Fig. 6.30 that each of the PL, PC and PD models exhibit negative values for all cases, and fail to capture both the qualitative and quantitative behaviours of $(T_{4c} + T_{5c})$ extracted from DNS data. These models (i.e. PL, PC and PD models) were originally proposed for incompressible non-reacting flows [124, 64, 78] where the contribution of $-\overline{c''} \partial \bar{P} / \partial x_i$ was ignored. However, it can be seen from Fig. 6.28 that T_4 plays a key role in turbulent scalar flux transport in turbulent premixed flames so it is not surprising that the PL, PC and PD models do not adequately capture the behaviour of $(T_{4c} + T_{5c})$. The PJ model predicts positive values of $(T_{4c} + T_{5c})$ but overpredicts the magnitude obtained from DNS data in case A. The quantitative agreement between the PJ model and DNS data in case C is better than case A. However, the prediction of the PJ model does not adequately capture the behaviour of $(T_{4c} + T_{5c})$ for high values of $u'/S_L \sim Re_t^{1/4} Ka^{1/2} \sim Re_t^{1/2} Da^{-1/2}$ (e.g. case E) and at some time instants (e.g. $t \geq 6\delta_Z/S_L$) this model also does not even predict the correct qualitative behaviour. The PB model satisfactorily captures the qualitative behaviour of $(T_{4c} + T_{5c})$ with some underprediction for case A until $t \leq 8\delta_Z/S_L$. However, the PB model locally overpredicts $(T_{4c} + T_{5c})$ at the later times (see $t \geq 10\delta_Z/S_L$). The PB model shows some

qualitative agreement with DNS data in cases C and E at early times when the flame is away from the wall (e.g. $t = 4\delta_Z/S_L$), whereas both the qualitative and quantitative agreement remain poor at later times when the flame quenching is in progress.

The PLV model captures the qualitative behaviour of DNS in case A, but it overpredicts the magnitude of $(T_{4c} + T_{5c})$ for all time steps. For cases with high $u'/S_L \sim Re_t^{1/4} Ka^{1/2} \sim Re_t^{1/2} Da^{-1/2}$ (e.g. cases C and E) the PLV model overpredicts the DNS data for $t \leq 6\delta_Z/S_L$ when the flame is away from the wall. As the flame approaches the wall the PLV models fails to capture both quantitative and qualitative DNS behaviour. Whilst the PDB model captures the qualitative behaviour but overpredicts the magnitude of $(T_{4c} + T_{5c})$ for case A when the flame is away from the wall (e.g. $t = 4\delta_Z/S_L$), as the flame starts to approach the wall the PDB model predicts negative values whereas $(T_{4c} + T_{5c})$ remains positive. The predictions of the PDB model do not perform satisfactorily for high $u'/S_L \sim Re_t^{1/4} Ka^{1/2} \sim Re_t^{1/2} Da^{-1/2}$ cases (e.g. cases C and E) and the predictions show large extent of noise. This noise originates due to limited sample size in the evaluation of conditional mean pressures \bar{P}_R and \bar{P}_P . This spiky behaviour was also reported in the original paper by Domingo and Bray [74] and previous analyses [33, 38] which dealt with this model. The PDB model was originally proposed for the strict flamelet regime (i.e. $Ka < 1$ and $Da > 1$) where the pdf of c can be approximated by a bi-modal distribution with impulses at $c = 0$ and 1.0 but such an assumption is not valid for the flames (where $Ka > 1$ and $Da < 1$) considered here. Furthermore, it has been shown earlier section that the pdf of c does not show bi-modality at any stage of head-on quenching so it is not surprising that the PDB model does not adequately capture the behaviour of $(T_{4c} + T_{5c})$ during flame quenching.

Finally, the PN model captures both the qualitative and quantitative behaviours of $(T_{4c} + T_{5c})$ better than the other alternative models. However, for high values of $u'/S_L \sim Re_t^{1/4} Ka^{1/2} \sim Re_t^{1/2} Da^{-1/2}$ the PN model overpredicts the behaviour of $(T_{4c} + T_{5c})$. The agreement with the PN model prediction and $(T_{4c} + T_{5c})$ from DNS data deteriorates at later times during flame quenching for all cases.

The models (e.g. PL, PC, PD models) which neglected the leading contribution of $T_{4c} = -\bar{c}''\partial\bar{P}/\partial x_i$ are not successful in capturing the DNS data. However, the PJ, PB and PN models, which account for $T_{4c} = -\bar{c}''\partial\bar{P}/\partial x_i$ are more successful in capturing the behaviour of $(T_{4c} + T_{5c})$ than the PL, PC, PD models which ignore this contribution. However, some near-wall corrections are needed to account for the behaviour of $(T_{4c} + T_{5c})$ during flame quenching. Here the following near-wall

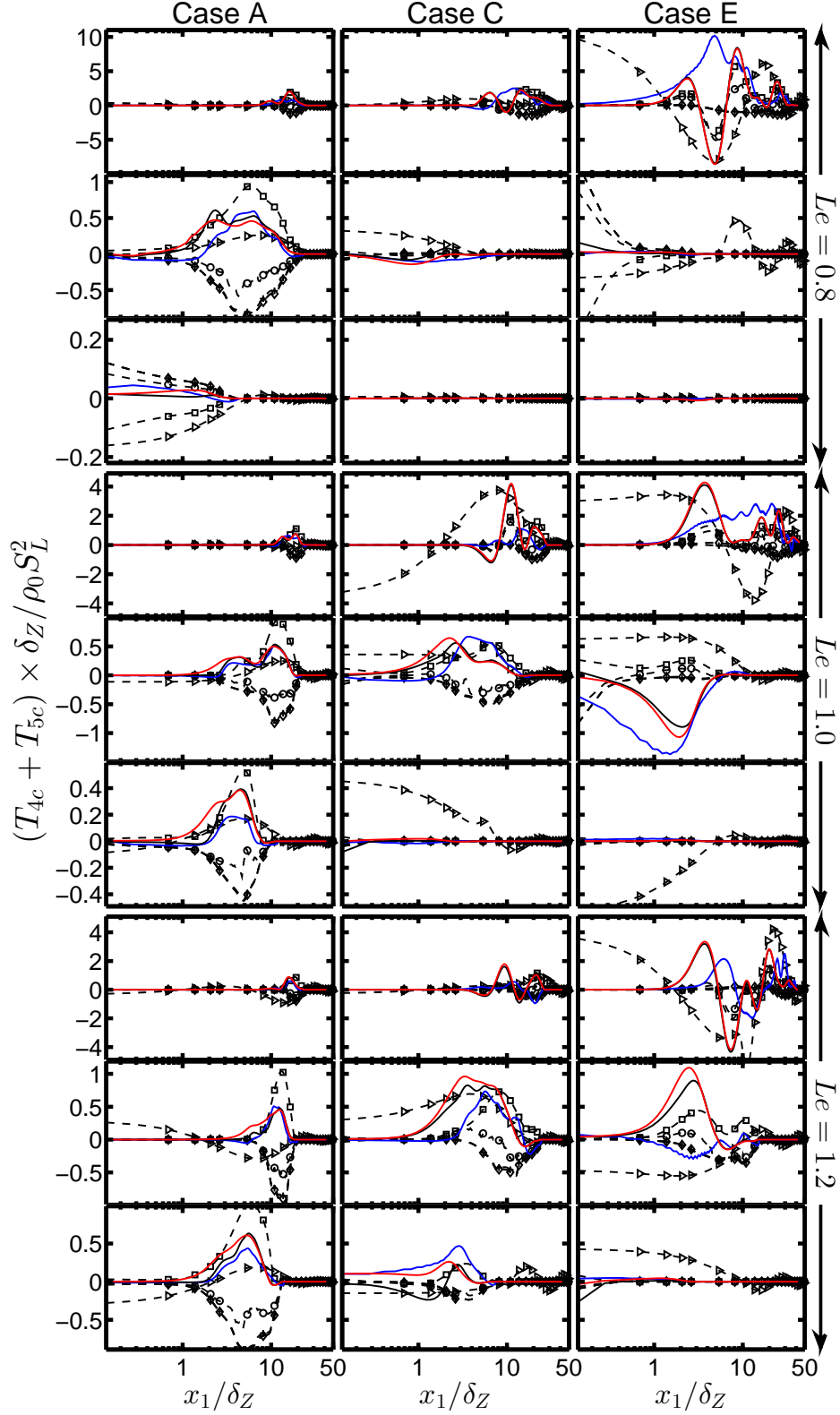


Fig. 6.30 Variation of terms $(T_{4c} + T_{5c}) \times \delta_Z / \rho_0 S_L^2$ from DNS data (—), PN (—), PC (— + —), PD (— ◇ —), PJO (— □ —), PLV (— ○ —), PDB (— △ —), modified PN model (—) with x_1/δ_Z at $t = 2\delta_Z/S_L$, $6\delta_Z/S_L$, and $10\delta_Z/S_L$ (1st - 3rd row) for turbulent cases A, C, and E (1st - 3rd column) with $Le = 0.8$, 1.0 and 1.2.

modification has been suggested for the PN model:

$$T_{4c} + T_{5c} = -C_D \frac{\bar{\rho}}{\rho_0} \cdot \tilde{c}(1 - \tilde{c})\tau \frac{\partial \bar{P}}{\partial x_i} - C_{E1}^* \frac{\tilde{\varepsilon}}{\tilde{k}} \overline{\rho u_i'' c''} + C_{E2}^* \tau S_L [\rho_0 S_L \Sigma_{\text{gen}}] (1 - \tilde{c})^{1.7} \quad (6.81)$$

where $C_{E1}^* = 0.38\eta_2 5^{1-0.5[\text{erf}(x_1/\delta_Z - \Phi)+1]}$, $C_{E2}^* = 0.66\eta_2^{1-0.5[\text{erf}(5(\tilde{c}_w - 0.5))+1]}$ and $\eta_2 = 0.5[\text{erf}(x_1/\delta_Z - 0.5(Pe_{\min})_L) + 1]$ are the model parameters and $\Phi = 0.5(Pe_{\min})_L(\text{erf}(8Le - 6) + 1)$ is the parameterisation of minimum Peclet number for turbulent flames. The involvement of error functions in the model parameters C_{E1}^* and C_{E2}^* ensure that they approach asymptotically to $C_{E1} = 0.38$ and $C_{E2} = 0.66$ away from the wall in the absence of flame quenching. The involvement of $\Sigma_{\text{gen}} = |\nabla \tilde{c}|$ in the third term on right hand side of Eq. 6.81 allows for a non-zero prediction at the wall which is identically zero in the PN model because $\bar{\omega}$ vanishes at the wall due to flame quenching. The involvement of $(Pe_{\min})_L$ and Φ in C_{E1}^* and η_2 implicitly includes reacting boundary layer information into the revised model, whereas \tilde{c}_w dependence of C_{E2}^* senses the flame quenching and modifies the value accordingly. It can be seen from Fig. 6.30 that the modified PN model (Eq. 6.81) captures the near-wall behaviour of $(T_{4c} + T_{5c})$ during flame quenching better than any other available models.

6.3.4 Modelling of the molecular dissipation terms $(T_{6c} + T_{7c})$

The terms T_{6c} and T_{7c} tend to reduce the magnitude of the scalar flux (i.e. behaves as a sink), and are usually modelled together. The most common model for $(T_{6c} + T_{7c})$ is the one which was proposed in the context of BML analysis [19] (i.e. referred to as the DBML model in this analysis):

$$T_{6c} + T_{7c} = -K_1 \overline{\rho u_i'' c''} \frac{\bar{\omega}}{[\tilde{\rho}\tilde{c}(1 - \tilde{c})]} \quad (6.82)$$

where $K_1 \approx 0.85$ is the model parameter. An alternative model was proposed by Nishiki *et al.* [146] (DN model) in the following manner:

$$T_{6c} + T_{7c} = -C_F \tau S_L \bar{\omega} \quad (6.83)$$

where $C_F \approx 0.4$ is the model parameter. However, Eq. 6.83 is only valid for counter-gradient transport and thus Chakraborty and Cant [38] suggested a combination of DBML and DL model, which was shown previously to model $(T_{6c} + T_{7c})$ satisfactorily

even for low Damköhler number combustion without the influence of walls. The expression proposed by Chakraborty and Cant [38] (DC model) is given by:

$$T_{6c} + T_{7c} = -0.5C_F\tau S_L\bar{\omega} - 0.5K_1\overline{\rho u_i''c''} \times \frac{\bar{\omega}}{[\bar{\rho}\tilde{c}(1-\tilde{c})]} \quad (6.84)$$

The predictions of the DBML, DN and DC models are compared to $(T_{6c} + T_{7c})$ extracted from DNS data in Fig. 6.31. It can be seen from Fig. 6.31 that the DBML model captures the correct qualitative behaviour of $(T_{6c} + T_{7c})$ but it underestimates the negative contribution of $(T_{6c} + T_{7c})$ in cases C-E. For cases A and B, the DBML model underpredicts both negative (away from the wall) and positive (when the flame is close to the wall) contribution of $(T_{6c} + T_{7c})$. The DN model provides a satisfactory qualitative prediction of $(T_{6c} + T_{7c})$ for all cases but this model overpredicts (underpredicts) the magnitude of negative (positive) contribution of $(T_{6c} + T_{7c})$ for $t \geq 6\delta_Z/S_L$ in cases A and B. In other cases the DN model exhibits overprediction of the magnitude of the negative contribution of $(T_{6c} + T_{7c})$. The agreement between the DC model prediction and DNS data remains better than the DBML and DN models. However, the DC model still underpredicts (overpredicts) the magnitude of positive (negative) contribution of $(T_{6c} + T_{7c})$ for all cases considered here but this is much smaller in extent in comparison to the DN model. It can further be seen from Fig. 9 that all the available models (i.e. DBML, DN and DC models) cannot predict the non-zero contributions of $(T_{6c} + T_{7c})$ in the near-wall region (and at the wall) because T_7 exhibits non-zero values even when the flame is quenched (i.e. $\bar{\omega} = 0$). To avoid this problem, the following modification to the DN model is proposed here (referred to here as the new model):

$$T_{6c} + T_{7c} = -0.5C_F\tau S_L(\rho_0 S_L \Sigma_{\text{gen}} Q^p) - 0.5K_1\overline{\rho u_i''c''} \times \frac{\bar{\omega}}{[\bar{\rho}\tilde{c}(1-\tilde{c})]} \quad (6.85)$$

where $Q = \text{erf}[2(\tilde{c}_w - 0.5)]$ and $p = 0.5[\text{erf}(x_1/\delta_Z - 0.7(Pe_{\min})_L) + 1]$. The involvement of $\Sigma_{\text{gen}} = |\nabla c|$ allows for a non-zero prediction at the wall which was not possible by the other alternative models. At the beginning of quenching, a positive value of $(T_{6c} + T_{7c})$ is obtained at the wall but it becomes negative at later stages. The model parameter Q accounts for the change of sign of $(T_{6c} + T_{7c})$ depending of the value of Favre averaged progress variable at the wall \tilde{c}_w , whereas p ensures that Q^p modifies the magnitude of Eq. 6.85 to predict $(T_{6c} + T_{7c})$ extracted from DNS data. Here, $(Pe_{\min})_L$ dependence of p implicitly accounts for the reacting boundary layer information and the error functions ensure that Eq. 6.85 approaches Eq. 6.84 for $x_1/\delta_Z \gg (Pe_{\min})_L$. It

is evident from Fig. 6.31 that the model given by Eq. 6.85 satisfactorily captures both qualitative and quantitative behaviours of $(T_{6c} + T_{7c})$ both away from and close to the wall.

6.3.5 Modelling of the reaction rate velocity correlation term

T_{8c}

The model proposed for the reaction rate velocity correlation term $T_{8c} = \overline{u_i'' \dot{\omega}}$ in the context of BML analysis (referred to as the RB model here) takes the form [19]:

$$T_{8c} = -C_R(\psi_m - \tilde{c})\bar{\omega} \frac{\overline{\rho u_i'' c''}}{\rho c''^2} \quad (6.86)$$

where the model parameters are given by $C_R \approx 1$ and $\psi_m \approx 0.5$. *A-priori* DNS analysis by Chakraborty and Cant [38] showed that the RB model captures the qualitative behaviour of T_{8c} even for low Damköhler number (i.e. $Da < 1$) combustion but revealed some turbulent Reynolds number dependence of ψ_m and the following parameterisation was proposed for ψ_m :

$$\psi_m = 0.57 + 0.6\text{erfc}[(Re_L + 1)/10] \quad (6.87)$$

Equation 6.86 with ψ_m parameterisation given by Eq. 6.87 will henceforth be referred to as the RB-M model. The predictions of the RB and RB-M models are compared to T_{8c} extracted from DNS data in Fig. 6.32 for cases A,C and E for different time instants. Figure 6.32 shows that the RB model captures quantitative and qualitative behaviours of T_{8c} for cases A before the initiation of flame quenching in this case (i.e. $t \leq 6\delta_Z/S_L$). However, this model overpredicts the magnitude of positive and negative values of T_{8c} close to the wall and away from the wall respectively for case A at $t > 6\delta_Z/S_L$. For cases B-E, the RB model overpredicts of both negative (away from wall region) and positive (near wall region) values of T_{8c} . As the flame propagates towards the wall and the flame starts to quench, the RB model fails to predict the reaction rate velocity correlation term T_{8c} , as shown in Fig. 6.32. By contrast, the RB-M model captures both quantitative and qualitative behaviour of reaction rate-velocity correlation term T_{8c} more satisfactorily than the RB model in spite of slight underprediction of T_{8c} for cases with high values of $u'/S_L \sim Re_t^{1/4} Ka^{1/2} \sim Re_t^{1/2} Da^{-1/2}$ (e.g. cases D and E). The prediction of T_{8c} can further be improved by modifying the RB-M model in the

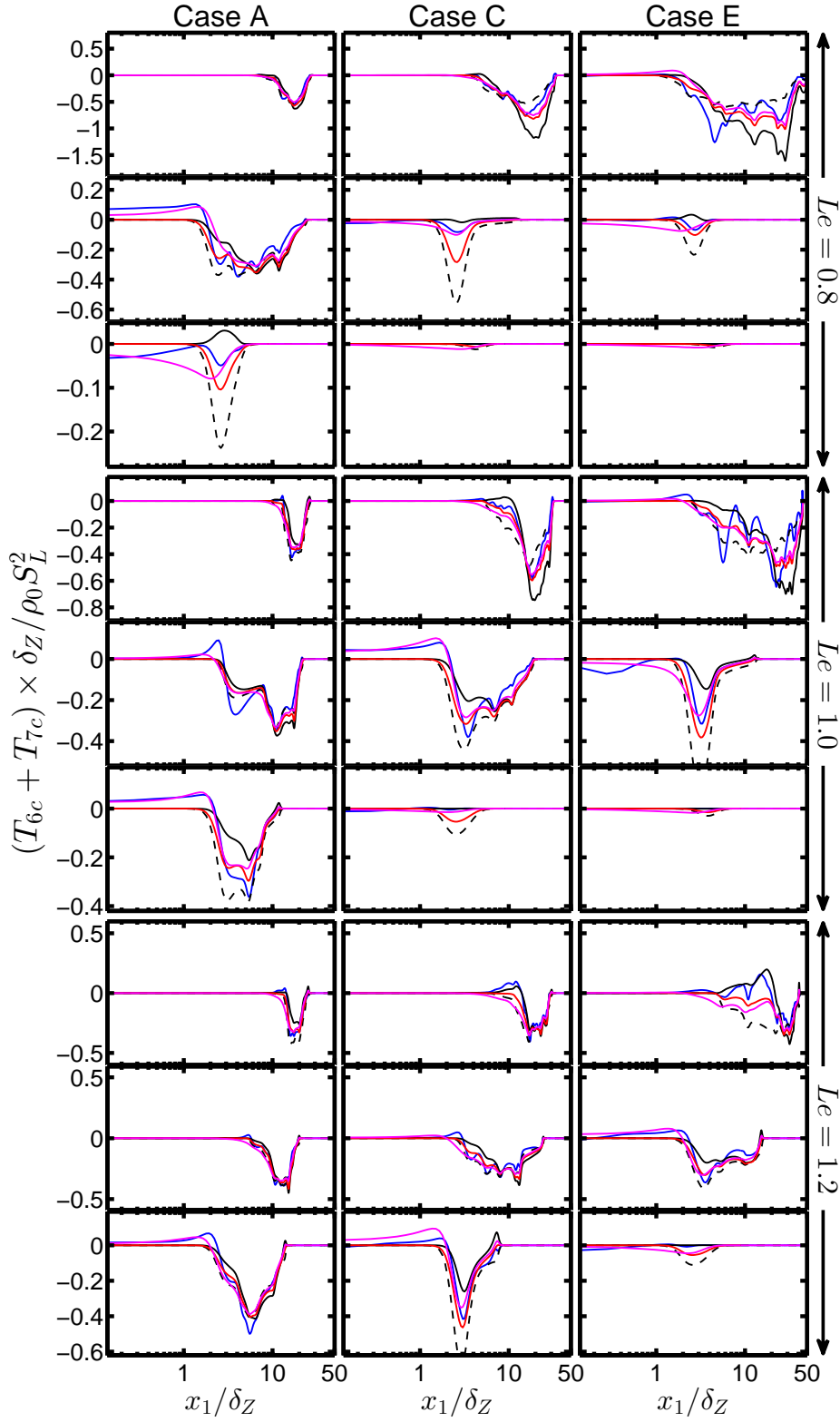


Fig. 6.31 Variation of terms $(T_{6c} + T_{7c}) \times \delta_Z / \rho_0 S_L^2$ from DNS data (—), DBML (—), DN (— —), CC (—) and New model (—) with x_1/δ_Z at $t = 2\delta_Z/S_L$, $6\delta_Z/S_L$, and $10\delta_Z/S_L$ (1st - 3rd row) for turbulent cases A, C, and E (1st - 3rd column) with $Le = 0.8, 1.0$ and 1.2 .

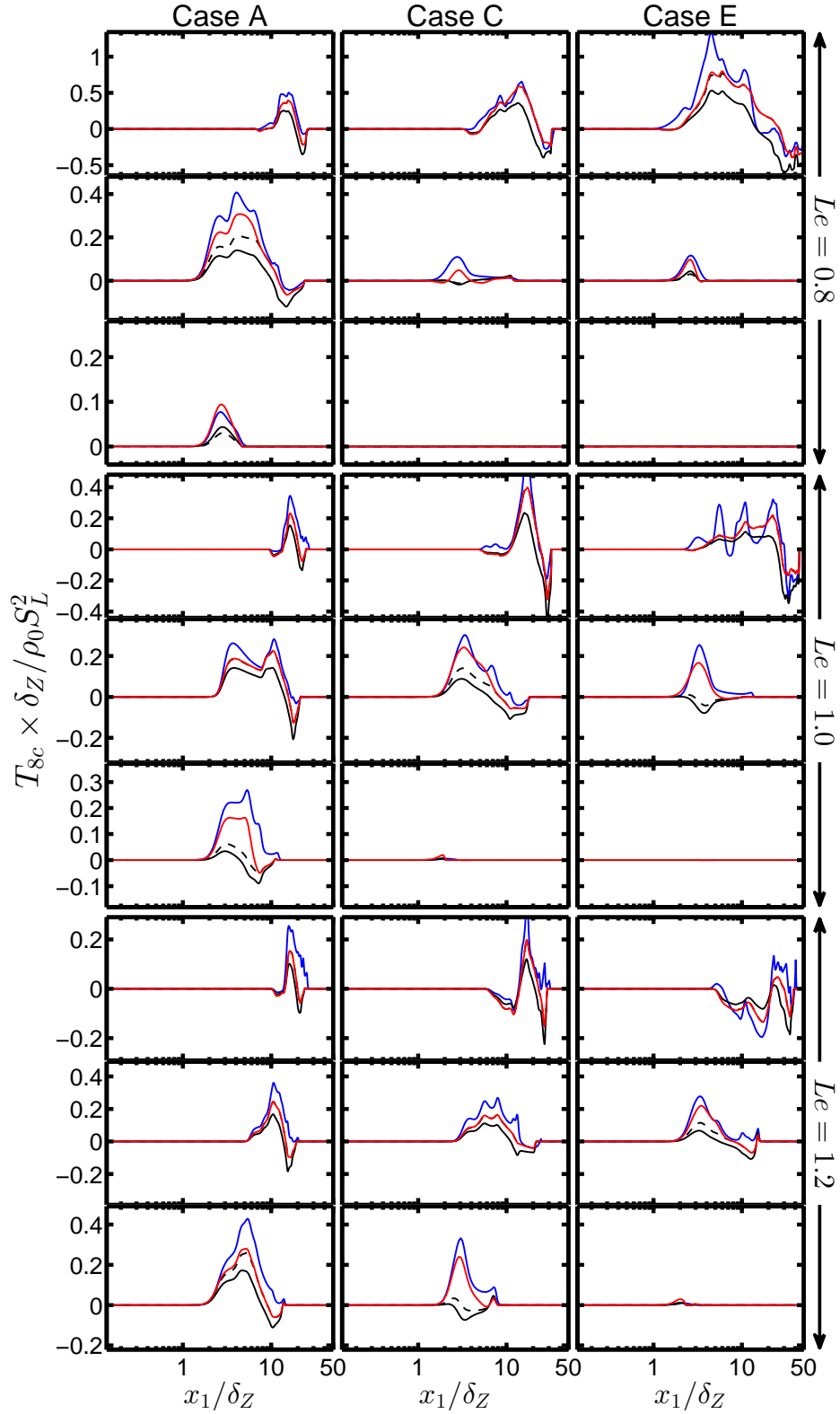


Fig. 6.32 Variation of terms $T_{8c} \times \delta_Z / \rho_0 S_L^2$ from DNS data (—), RB (—), RBM (---) and New model (—) with x_1 / δ_Z at $t = 2\delta_Z / S_L$, $6\delta_Z / S_L$, and $10\delta_Z / S_L$ (1st - 3rd row) for turbulent cases A, C, and E (1st - 3rd column) with $Le = 0.8$, 1.0 and 1.2.

following manner (i.e. new model):

$$T_{8c} = C_R(\psi_m \exp[2(\tilde{c}_w - \tilde{T}_w)\xi] - \tilde{c})\bar{\omega} \frac{\overline{\rho u_i'' c''}}{\rho c''^2} \quad (6.88)$$

where $x_i = 1 - 0.5[\text{erf}(x_1/\delta_Z - (Pe_{\min})_L) + 1]$. The factor $(\psi_m \exp[2(\tilde{c}_w - \tilde{T}_w)\xi] - \tilde{c})$ approaches $\psi_m - \tilde{c}$ for $x_1/\delta_Z \gg (Pe_{\min})_L$. A comparison between the predictions of the RB-M and the new models indicates that $(\psi_m \exp[2(\tilde{c}_w - \tilde{T}_w)\xi] - \tilde{c})$ in Eq. 6.88 modifies the RB-M model close to the wall depending on the value of $(\tilde{c}_w - \tilde{T}_w)$ to yield better agreement with model prediction with T_{8c} extracted from DNS data than the other available models especially in the vicinity of the wall.

6.3.6 Summary of the key results

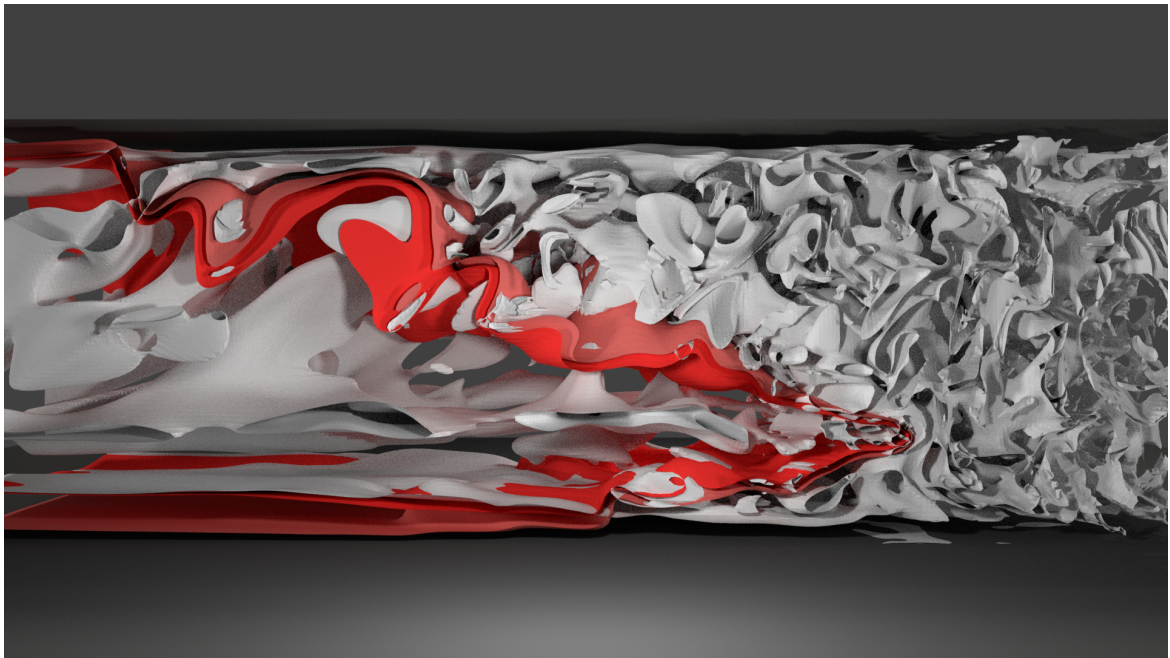
The modelling of turbulent scalar flux $\overline{\rho u_i'' c''}$ transport has been analysed for head-on quenching of statistically planar turbulent premixed flames by an isothermal inert wall using three-dimensional DNS data. The statistical behaviour of the unclosed terms of the transport equation of $\overline{\rho u_i'' c''}$, especially in the near-wall region, has been analysed in detail. The magnitudes of the turbulent transport and mean velocity gradient terms remain small in comparison to the contributions of the other terms when the flame is away from the wall, but the magnitudes of all the terms diminish during flame-wall interaction and become comparable at the final stage of quenching before vanishing altogether. The modelling of the unclosed terms has been addressed in detail, and it has been found that existing models for the turbulent transport, pressure gradient, molecular dissipation and velocity-reaction rate terms do not adequately capture the behaviour of these terms close to the wall. The models for the turbulent transport, pressure gradient, molecular dissipation and velocity-reaction rate terms have been modified in terms of blending functions, similar to the van Driest's correction for mixing length used for damping eddy viscosity close to the wall [79], in such a manner that the models satisfactorily capture the behaviour obtained from DNS data both close to the wall and far from it. However, further validation based on three-dimensional DNS and experimental data with detailed thermochemistry will be necessary for more comprehensive validation of the models discussed here. Furthermore, the models proposed here have to be implemented in actual RANS simulations for configurations with well-documented experimental data for the purpose of *a-posteriori* assessment.

6.4 Chapter closing remark

This chapter provided the analysis and modelling of SDR, FSD and turbulent scalar flux transports. A full package of wall-modified models has been completed for RANS based on *a-priori* analysis on HOQ. Questions arise, what happens for the oblique quenching and what happens for more detailed chemistry flames? The following chapter will show a glimpse of this horizon.

Chapter 7

Results & Discussion 3: Oblique Quenching and Detailed Chemistry Simulations



Turbulent flame-wall interaction in a channel ¹

¹Red shows the flame front. Grey indicates the vorticity magnitude of the flow. Metal surfaces on top and bottom indicate the upper wall and lower wall respectively.

In the previous two chapters, the statistical analysis and modelling of the head-on quenching of turbulent premixed flames based on a single-step Arrhenius type irreversible chemical mechanism have been carried out. This chapter will focus on the comparison between the oblique quenching with the head-on quenching of turbulent premixed flames. Moreover, the HOQ statistics obtained from the simple chemistry calculations have been compared to the results obtained from the detailed chemistry based DNS for the same set of simulation parameters. Firstly, the wall heat flux and flame quenching distance statistics for the oblique flame-wall interaction in the case of turbulent V-flames have been compared to the corresponding values obtained for the HOQ configuration. Then, a multi-step chemical mechanism for methane-air combustion is used for the purpose of the comparison between the HOQ statistics from the detailed DNS with the corresponding results extracted from a simple chemistry simulation.

7.1 Oblique quenching by isothermal inert walls

7.1.1 Heat flux and quenching distance

The schematic diagram of the configuration used for the oblique quenching of turbulent premixed flames can be found in chapter 4. The instantaneous distribution of vorticity magnitude (i.e. $\sqrt{\omega_i \omega_i}$ with ω_i being the i^{th} component of vorticity) is shown in Fig. 7.1a which shows the magnitude of $\sqrt{\omega_i \omega_i}$ decreases significantly across the flame. The instantaneous distributions of non-dimensional temperature (i.e. $T = (\hat{T} - T_0)/(T_{\text{ad}} - T_0)$) on the $x_1 - x_2$ side plane and fuel mass fraction Y_F on the bottom wall surface are also shown in Fig. 7.1a. The flame quenches due to heat loss through the wall which leads to diffusion of remaining fuel from the near-wall region to the gaseous mixture at the interior of the domain and thus the magnitude of fuel mass fraction Y_F drops in the region where the flame interacts with the wall. For the present analysis, the reaction progress variable c is defined in terms of the fuel mass fraction Y_F as $c = (Y_{F0} - Y_F)/(Y_{F0} - Y_{F\infty})$ where the subscripts 0 and ∞ denote the values in the unburned gas and fully burned products, respectively. The contours of T and c are shown for the $x_1 - x_2$ mid-plane in Fig. 7.1b. A careful comparison between c and T reveals that $c = T$ where the flame is away from the wall. However, inequality between the reaction progress variable and non-dimensional temperature (i.e. $c \neq T$) is obtained in the vicinity of the wall. The difference in boundary condition (i.e. Dirichlet

boundary condition for temperature and Neumann boundary condition for species mass fractions) leads to inequality between c and T .

The temporal evolutions of non-dimensional wall heat flux magnitude $\Phi = |q_w|/[\rho_0 C_P S_L (T_{ad} - T_0)]$ and Peclet number $Pe = X/\delta_Z$ for top and bottom walls for the V-flame case are shown in Fig. 7.2, where X is the wall normal distance of the nearest $T = 0.9$ isosurface [156] and $q_w = -\lambda(\partial\hat{T}/\partial n)_w$ is the wall heat flux with C_P , λ and n being the specific heat at constant pressure, thermal conductivity and wall normal direction respectively. The corresponding temporal variations of Φ and Peclet number Pe for HOQ of a statistically planar flame with initial values of u'/S_L and l/δ_{th} equal to the inlet values for the turbulent V-flame case are also shown in Fig. 7.2. The Peclet number drops for HOQ with time as the flame advances towards the wall. The mean value of Φ increases as the mean Peclet number Pe decreases with time. The maximum value of normalised wall heat flux Φ_{max} in the case of HOQ is obtained at a time when the minimum Peclet number Pe_{min} is attained. The values of Φ_{max} and Pe_{min} for laminar HOQ are given by 0.39 and 2.53 respectively. These values are consistent with previous experimental [98, 100] and computational [156] findings. The magnitude of $|q_w|$ can be scaled as: $|q_w| \sim \lambda(T_{ad} - T_0)/X$, which leads to $\Phi \sim 1/Pe$ and accordingly one obtains the following relation: $\Phi_{max} \sim 1/Pe_{min}$. For turbulent HOQ one obtains $\Phi_{max} = 0.42$ and $Pe_{min} = 2.16$ which suggest that the maximum heat flux and the minimum Peclet number values in turbulent HOQ remain almost equal to the corresponding values for laminar HOQ. By contrast, Pe_{min} for the turbulent V-flame case is found to be 1.71 whereas Φ_{max} assumes a value of 0.63. According to the scaling $\Phi_{max} \sim 1/Pe_{min}$, a smaller value of Pe_{min} in the turbulent V-flame case than in the HOQ of statistically planar leads to a higher value of normalised wall heat flux Φ_{max} in the turbulent V-flame case. It can be seen from Fig. 7.2 that Pe values are higher for the top wall than for the bottom wall because the flame holder is placed closer to the bottom wall so that the flame-wall interaction takes place more readily for the bottom wall. For the turbulent HOQ case, the maximum value of Peclet number increases initially with time due to flame wrinkles which are concavely curved towards the reactants. As the flame advances towards the wall the maximum, mean and minimum values of Peclet number decrease until flame quenching. The decreases of the maximum, mean and minimum values of Peclet number are associated with the increases in minimum, mean and maximum values of Φ with time. After flame quenching the isotherms move away from the wall in the HOQ configuration. By contrast, the Peclet number Pe does not change much following flame quenching in the V-flame configuration. In the case of oblique flame quenching, the fluid velocity remains small in the near-wall region, and

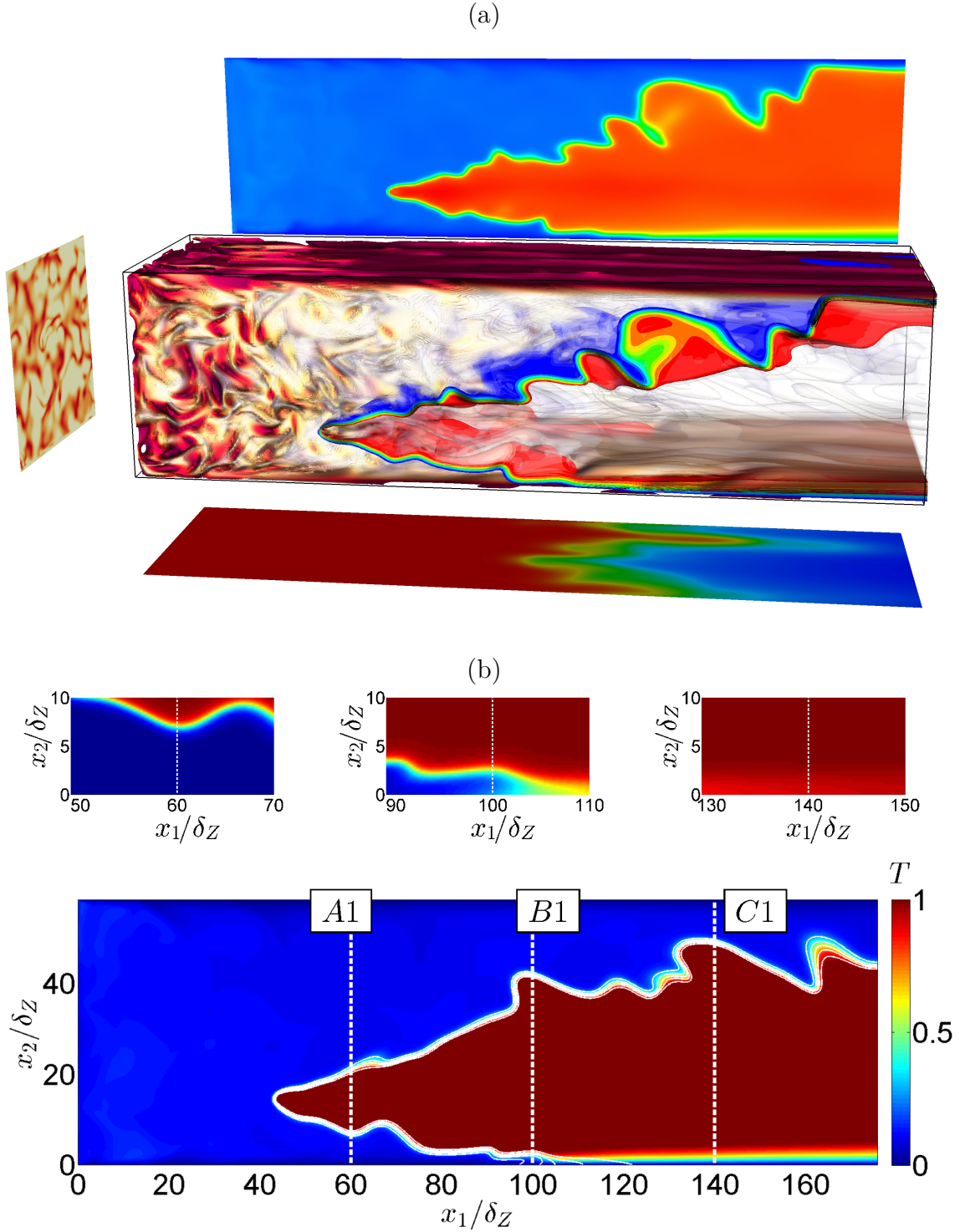


Fig. 7.1 (a) The instantaneous distribution of vorticity magnitude (background: red-high and white-low) and non-dimensional temperature (isosurface and side view, red-high and blue-low) and fuel mass fraction (lower wall view, red-high and blue-low) for the V-flame case. (b) Distributions of T and c (shown by white lines from 0 to 1 with 0.2 interval) at $t = 2t_{ft}$ for $x_1 - x_2$ mid-plane. Distributions of c around locations A1, B1 and C1 are shown in the inset. The locations A1, B1 and C1 in Fig. 7.1b correspond to $x_1 = 60\delta_Z$, $100\delta_Z$ and $140\delta_Z$ respectively.

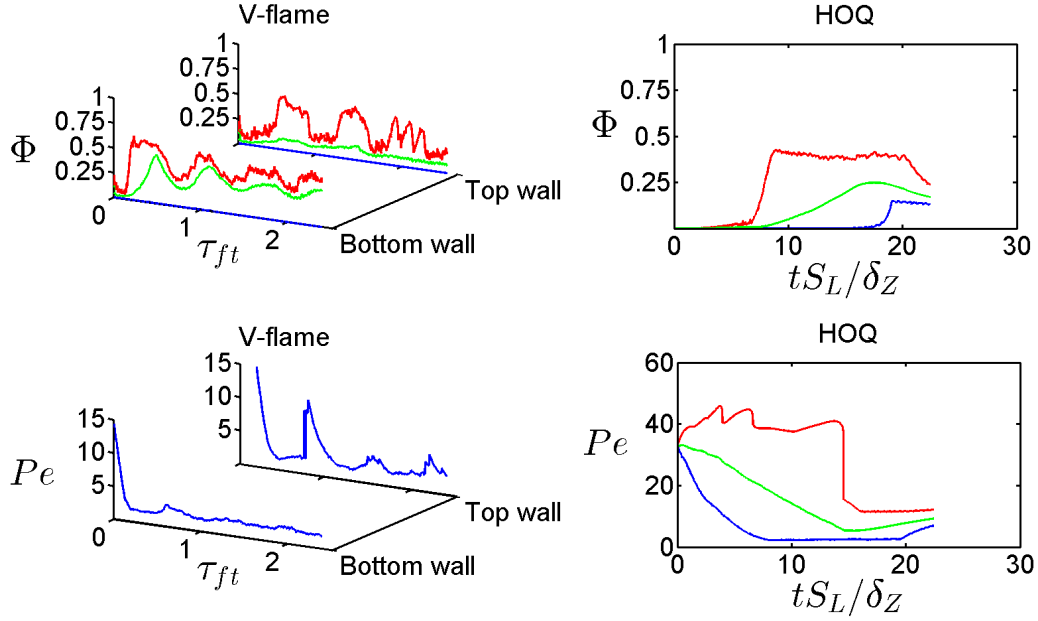


Fig. 7.2 Variations of Φ and Pe (maximum (—); mean (—); minimum (—)) with flow-through time $t_{ft} = L_1/U_{\text{mean}}$.

thus the flame can reach closer to the wall before quenching than in the corresponding HOQ case. It can be seen from Fig. 7.2 that the maximum normalised heat flux Φ_{max} for both top and bottom walls remain comparable, but Φ_{max} for the bottom wall attains higher value than the value obtained for the top wall. The smaller values of the minimum Peclet number for the bottom wall are reflected in the higher value of Φ_{max} than in the case of the top wall. Moreover, the mean heat flux is greater for the bottom wall than that of the top wall because the flame remains closer to the bottom wall. It can further be seen from Fig. 7.2 that the extent of the fluctuation of Φ_{max} for the top wall is greater than the bottom wall. The wall heat flux rises sharply when the turbulent fluid motion brings the flame elements close to the wall and similarly heat flux drops when either the flame quenches, or the flame moves away from the wall under the influence of turbulence. Since the bottom wall remains closer to the flame, it interacts more readily than the top wall, which leads to less rapid changes in the Φ_{max} for the bottom wall.

7.1.2 Flow topology analysis

In order to understand the flow contribution to the wall heat flux, the distributions of the volume fractions VF of the flow topologies conditional on reaction progress variable c at locations A1, B1 and C1 are shown in Fig. 7.3 for $t = 2.39t_{ft}$ but the qualitative

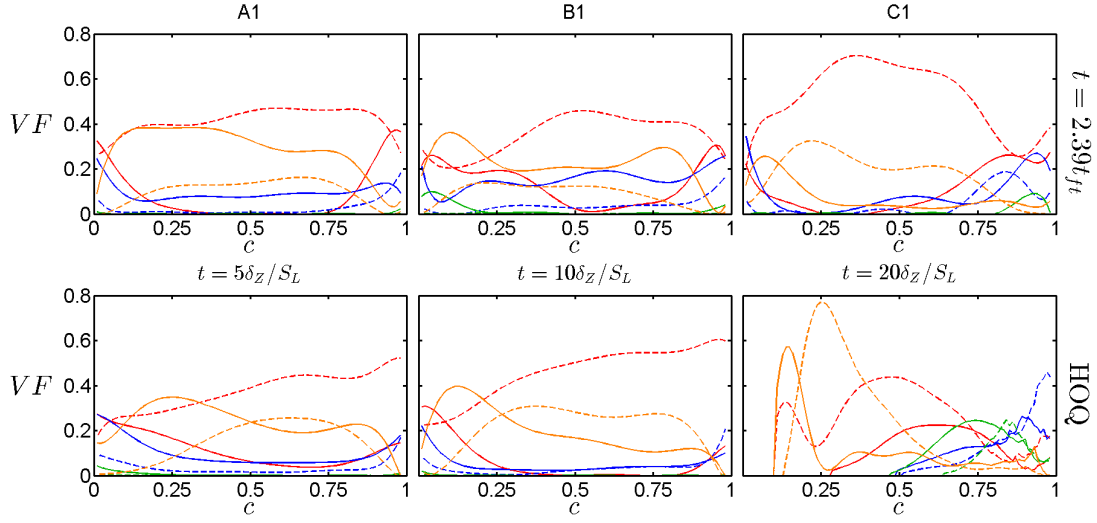


Fig. 7.3 Variations of volume fraction VF for topologies conditional on c . Top figures: locations A1, B1 and C1 in the V-flame case at $t = 2.39t_{ft}$; Bottom figures: for the HOQ case at three time instants. Focal topologies S1 (—), S4 (—), S5 (—), S7 (—), nodal topologies S2 (---), S3 (---), S6 (---), S8 (---).

nature of the distribution remains unchanged since $t = 1.0t_{ft}$. It is worth noting that the flame does not interact with the wall at location A1 where the volume fractions of S2 and S7 topologies are the leading contributors within the flame front. This is consistent with the topology variation in the corresponding turbulent HOQ case. The topologies which are typical of negative dilatation rate (i.e. S5 and S6) are rare at location A1, but the volume fraction of S5 topology assumes non-negligible value at locations B1 and C1. A similar increase of VF of S5 and S6 topologies can be observed at later times in the turbulent HOQ case during the advanced stage of quenching (i.e. $t = 20\delta_Z/S_L$). A comparison between locations A1, B1 and C1 reveals that the flame-wall interaction and flow development in the downstream of the flame holder significantly affect the distribution of flow topologies. The relative contribution of the S7 topology decreases from A1 to C1, whereas the relative contribution of S8 topology increases in the downstream and it becomes a dominant contributor at location C1. A qualitatively similar transition in behaviour can also be observed in the turbulent HOQ case, as the quenching progresses with time. The S2 topology remains a dominant contributor and the contributions of S1, S3 and S4 remain significant at all locations (times) for the V-flame case (HOQ case).

The percentages of wall heat flux magnitude contribution by individual flow topologies for the V-flame and HOQ cases are shown in Fig. 7.4 at different time instants.

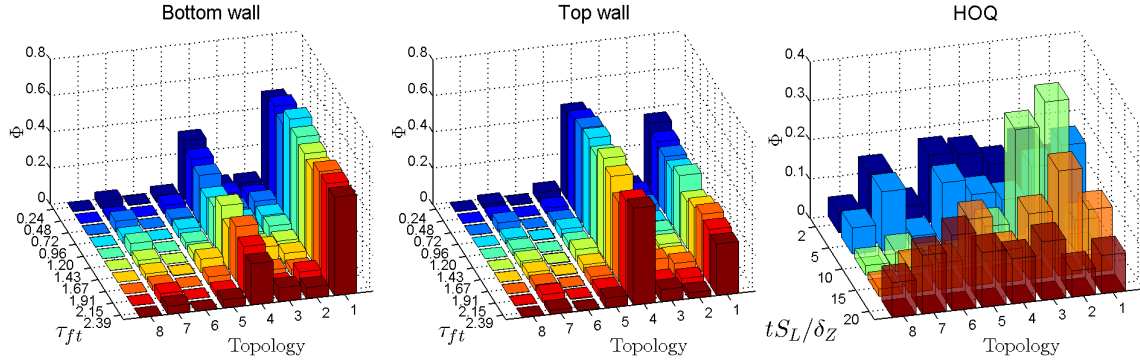


Fig. 7.4 Percentages of wall heat flux magnitude contributions arising from individual flow topologies S1-S8 in the V-flame case from $0.24t_{ft}$ to $2.39t_{ft}$ (1st - 2nd column) and HOQ case from $t = 2\delta_Z/S_L$ to $20\delta_Z/S_L$ (3rd column).

Figure 7.3 shows that the S1 and S4 topologies contribute significantly to heat flux for both walls in the V-flame case. However, the S1 topology is the leading contributor for the bottom wall, whereas the S4 topology is the leading contributor for the top wall in the V-flame case. It can be seen from Fig. 7.3 that VF values for the S1 and S4 topologies increase in the unburned and burned gas regions ($c = 0$ and $c = 1$). As either unburned or burned gases are predominantly found on the wall, the topologies S1 and S4 contribute significantly to the wall heat flux. Moreover, the shear rate introduced by the walls generate vorticity in the near-wall region and thus the focal topologies S1 and S4 contribute to wall heat flux in the V-flame case. A comparison between Figs. 7.2 and 7.4 for the HOQ case reveals that all topologies except S5 and S6 have comparable wall heat flux contributions when the flame begins to interact with the wall. The nodal topologies S2 and S3 become the major contributors to the wall heat flux when Φ_{max} attains its peak value. The contributions of all flow topologies to the wall heat flux become comparable when the maximum, mean and minimum values of Φ approach each other but the contributions of the S1, S3-S8 topologies remain greater than the S2 topology.

7.1.3 Summary of the key results for the oblique quenching

The statistics of wall heat flux, flame quenching distance in the case of oblique quenching of a turbulent V-flame flame by isothermal inert walls has been analysed in terms of the distributions of flow topologies and their contributions using DNS data. It has been found that the maximum (minimum) wall heat flux (Peclet number) in the case of oblique flame quenching assumes greater (smaller) value than in the corresponding

turbulent HOQ case. Although the volume fractions of S2 and S7 topologies assume high values within the flame front, the focal topologies S1 and S4 have been found to contribute to wall heat flux in the case oblique flame quenching. By contrast, nodal topologies S2 and S3 remain major contributors to the wall heat flux when it attains large magnitude in the HOQ case, but all topologies contribute comparably to the wall heat flux at later stages of flame quenching.

7.2 Turbulent premixed methane-air flames using a detailed chemistry mechanism

7.2.1 Quenching characteristics

The instantaneous three-dimensional distributions of c based on Y_{CH_4} and non-dimensional temperature T at different time instants for the detailed chemistry case (i.e. case A) are shown in Fig. 7.5a. For the purpose of qualitative comparison, the instantaneous distributions of c and T at different time instants for simple chemistry are shown in Fig. 7.5b. It is evident from Fig. 7.5a that c and T distributions remain different from each other and the extent of this inequality becomes more prominent as the flame approaches the wall in case A. The extent of this inequality between c and T remains small when the flame is away from the wall in case B, but this inequality remains significant for case A even when the flame is not in the vicinity of the wall. The light species with sub-unity Lewis number (i.e. $Le < 1$) such as H and H_2 are present within the methane-air flame in the detailed chemistry case, and thus these light species induce local influences of differential diffusion of heat and mass even in a flame which is globally thermo-diffusively neutral in nature. Furthermore, the consumption layer of methane is not coincident with the heat release layer in the stoichiometric methane-air flame, which also contributes to the local inequality between c and T .

The inequality between c and T is also reflected in the behaviour of their Favre-averaged counterparts, which can be seen from the temporal evolutions of \tilde{c} and \tilde{T} for both cases A and B in Fig. 7.6. In accordance with the observations made from Fig. 7.5, it can be seen that the inequality between \tilde{c} and \tilde{T} becomes dominant in the vicinity of the wall. The value of \tilde{c} at the wall increases from 0 as the flame interacts with it, whereas \tilde{T} remains zero at the wall. A similar qualitative behaviour has also been observed for c and T distributions for laminar premixed flames. This can be substantiated from Fig. 7.7, where the distributions of c , T and normalised heat release rate $\Omega_T = \dot{\omega}_T \times \delta_{\text{th}} / [\rho_0 S_L C_{p0} T_0]$ (where $\dot{\omega}_T = -\sum_{i=1}^{16} \dot{\omega}_i h_{fi}^0$ is the dimensional heat release term with $\dot{\omega}_i$, C_{p0} and h_{fi}^0 being the reaction rate, mixture specific heat at constant pressure in the unburned gas and enthalpy of formation of species i , respectively) in the wall normal direction are shown at different time instants for both simple and detailed chemistry cases. The time instants are shown in Fig. 7.7 are different for detailed and simple chemistry cases because δ_{th} values for these cases are not the same due to the difference in thermo-chemistry. It can be seen from Fig. 7.7 that Ω_T drops significantly once the flame reaches the wall and it vanishes

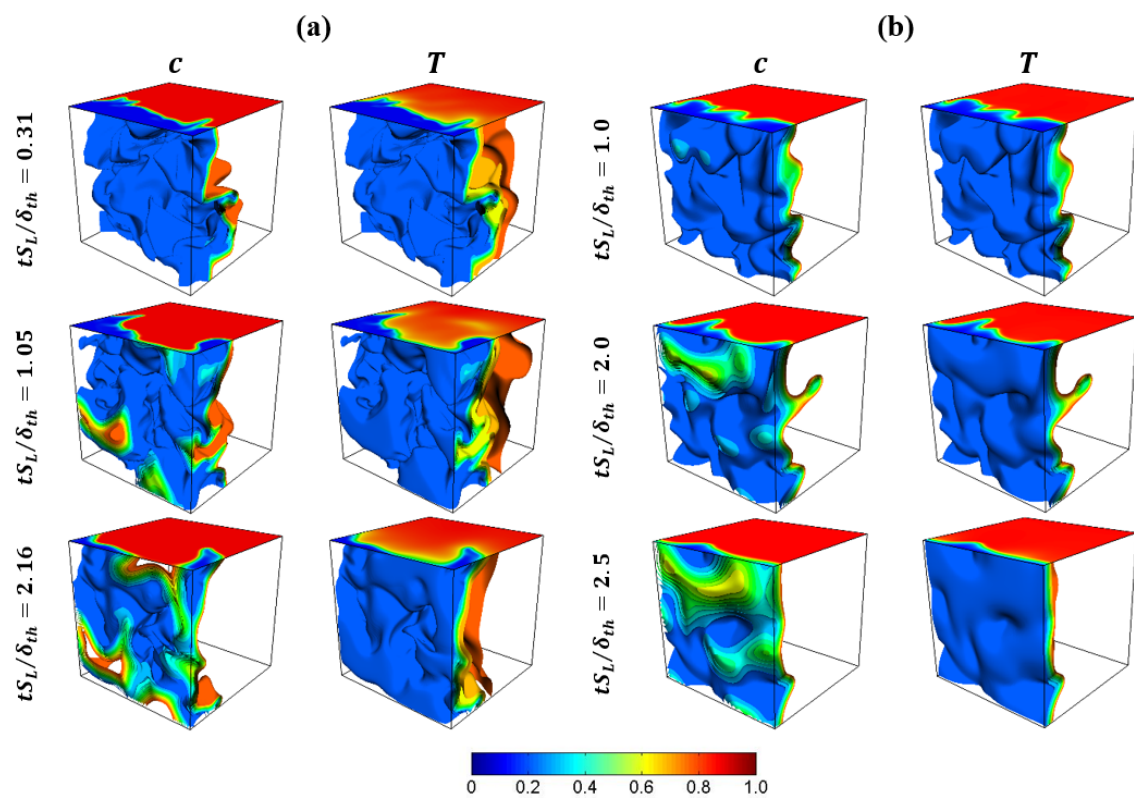


Fig. 7.5 Distributions of c based on Y_{CH_4} and non-dimensional temperature T at different time instants for (a) detailed chemistry case A, (b) simple chemistry case B. The time instants are different between cases A and B because of the difference in δ_{th} values.

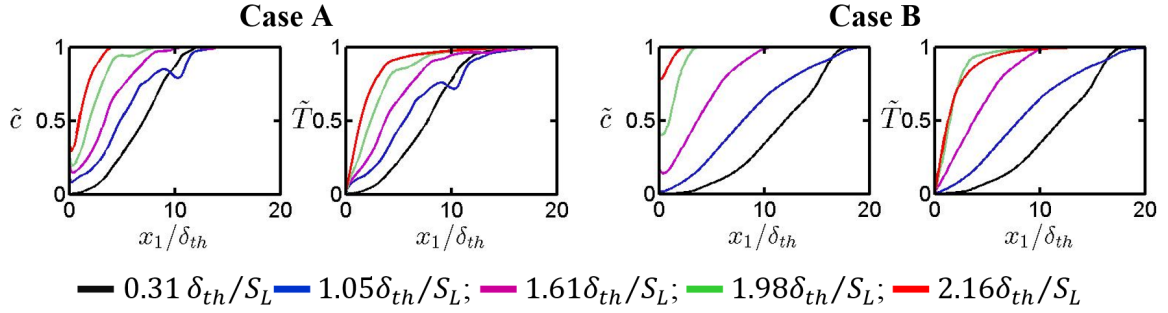


Fig. 7.6 Variation of c and T with x_1/δ_{th} at different time instants for case A and case B (right).

completely once the distance between the flame and the wall becomes smaller than a threshold distance in the simple chemistry case B. The reaction rate of progress variable $\dot{\omega}$ vanishes once temperature drops in the vicinity of the wall, which leads to the total disappearance of heat release rate at the near-wall region in the simple chemistry case because the heat release is directly proportional to the reaction rate $\dot{\omega}$ of reaction progress variable in the context of single-step chemical mechanism. Although the normalised heat release rate Ω_T drops significantly in the vicinity of the wall, Ω_T does not vanish at the wall during early stages of FWI in the detailed chemistry case even though the normalised reaction rate of reaction progress variable (given by $\Omega_c = \dot{\omega} \times \delta_{th}/\rho_0 S_L = \{-\dot{\omega}_{CH_4}/(Y_{R0} - Y_{R\infty})\} \times \delta_{th}/\rho_0 S_L$ for case A) remains zero at the wall at all times. However, Ω_T eventually vanishes with the progress of flame quenching even in the detailed chemistry case. It is instructive to look at the species distributions in the detailed chemistry case B in order to explain this behaviour.

The temporal evolutions of the distributions of the mass fractions of CH_4 , O_2 , CO_2 , H_2O , CO , OH , HO_2 and H_2O_2 in the wall normal distance for head-on quenching of laminar stoichiometric methane-air premixed flame are shown in Fig. 7.8. It can be seen from Fig. 7.8 that the mass fractions of CH_4 and O_2 both at and in the vicinity of the wall decrease with time as the flame quenches due to heat loss through the wall. This drop in CH_4 mass fraction is reflected in an increase in c with the progress of flame quenching. By contrast, the mass fractions of CO_2 and H_2O both at and in the vicinity of the wall increase with time as the flame quenching advances. This is qualitatively consistent with the observation made from simple chemistry case in Fig. 7.7 which indicates that the likelihood of finding products in the vicinity of the wall increases with time during head-on quenching. The mass fractions of CO , OH and H (not shown here for conciseness) remain zero in the unburned gas, but they assume peak values within the flame before decreasing weakly towards the burned gas side. However, the

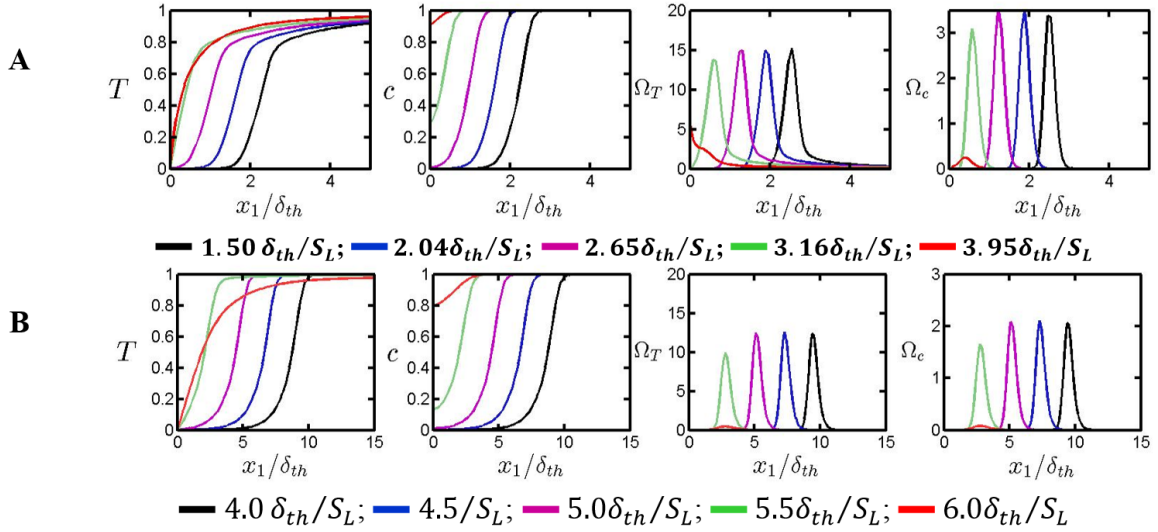


Fig. 7.7 Variation of c , T , Ω_T and $\Omega_c = \dot{\omega} \times \delta_{th}/\rho_0 S_L$ with x_1/δ_{th} at different time instants for laminar head-on quenching for both detailed (A) and simple (B) chemistry cases.

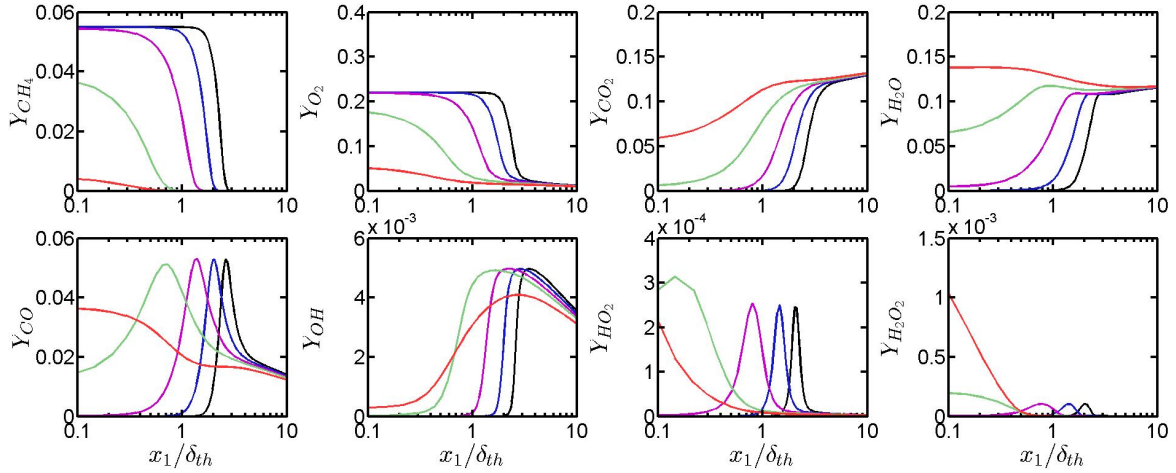


Fig. 7.8 Variation of mass fractions of CH_4 , O_2 , CO_2 , H_2O , CO , OH , HO_2 and H_2O_2 in the wall normal distance for head-on quenching of a laminar stoichiometric planar premixed flame at $t = 1.50 \delta_{th}/S_L$ (—); $2.04 \delta_{th}/S_L$ (—); $2.65 \delta_{th}/S_L$ (—); $3.16 \delta_{th}/S_L$ (—); $3.95 \delta_{th}/S_L$ (—).

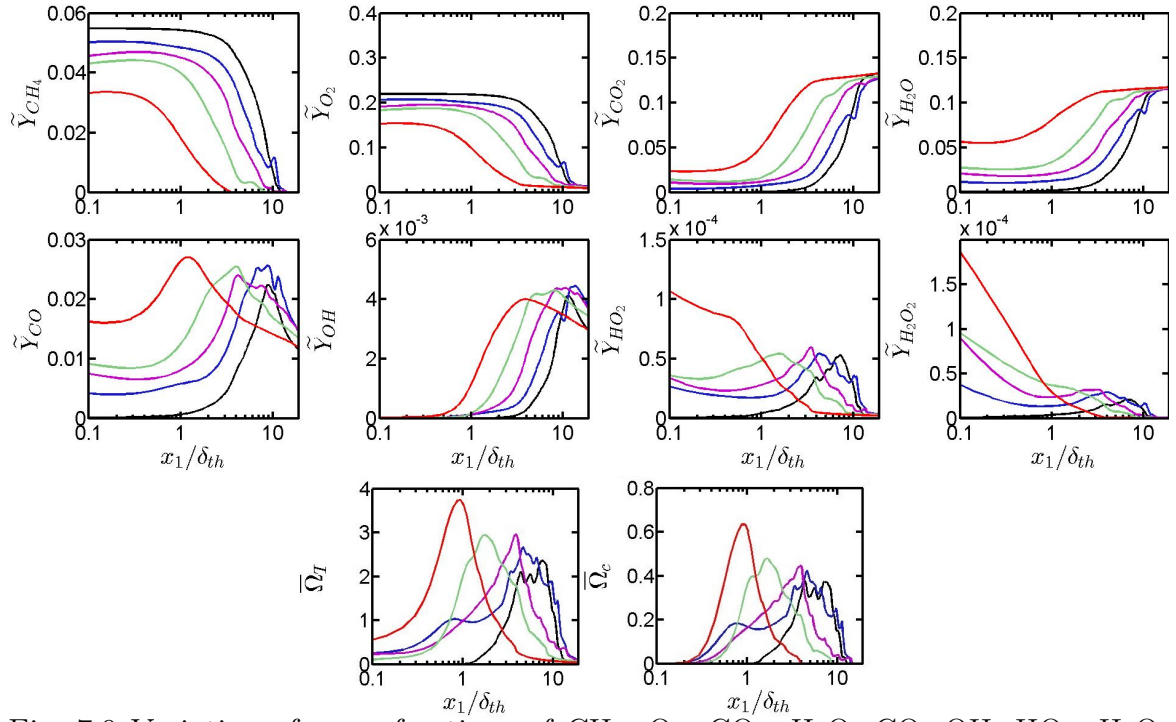


Fig. 7.9 Variation of mass fractions of CH_4 , O_2 , CO_2 , H_2O , CO , OH , HO_2 , H_2O_2 and $\bar{\Omega}_T$ and $\bar{\Omega}_c$ in the wall normal distance for head-on quenching of a turbulent stoichiometric planar premixed flame (case A) at $t = 0.31\delta_{th}/S_L$ (—); $1.05\delta_{th}/S_L$ (—); $1.61\delta_{th}/S_L$ (—); $1.98\delta_{th}/S_L$ (—); $2.16\delta_{th}/S_L$ (—).

near-wall behaviour of these species is markedly different. The mass fractions of CO at the wall increases with time during FWI, but the concentration of CO at the wall eventually decreases with time once the flame quenching is an advanced stage. The mass fractions of OH and H remain small at the wall, and their values increase in the wall normal direction. It is worth noting that OH is responsible for CO oxidation according to $\text{CO} + \text{OH} \rightarrow \text{CO}_2 + \text{H}$ and this step also gives rise to H which is crucial for chain propagation reactions (e.g. $\text{H} + \text{O}_2 \rightarrow \text{OH} + \text{O}$; $\text{O} + \text{H}_2\text{O} \rightarrow \text{OH} + \text{OH}$). The absence of OH and low temperature in the near-wall region at the advanced stage of flame quenching give rise to accumulation (depletion) of CO (H) in this region because CO is not oxidised and H is not produced. The diffusion of CO away from the wall to the interior of the domain eventually leads to a decrease in the CO mass fraction at the wall. It can be seen from Fig. 7.8 that HO_2 and H_2O_2 exhibit a significant increase in concentration at the wall during advanced stages of flame quenching. It is worth noting that the reaction steps $\text{O}_2 + \text{H} + \text{M} \rightarrow \text{HO}_2 + \text{M}$ and $2\text{HO}_2 \rightarrow \text{H}_2\text{O}_2 + \text{O}_2$ can take place at a low temperature due to low activation energy, and these reaction steps are responsible for the considerable rise of HO_2 and H_2O_2 at the wall. A similar observation was previously reported by Dabireau *et al.* [65] for premixed FWI of H_2 - O_2 mixtures based on two-dimensional simulations. The formation of H_2O_2 gives rise to heat release rate at the wall during early stages of FWI. The temporal evolutions of Favre-averaged mass fractions of CH_4 , O_2 , CO_2 , H_2O , CO , OH , HO_2 and H_2O_2 , and the Reynolds-averaged heat release rate $\bar{\Omega}_T$ for turbulent case A are shown in Fig. 7.9. A comparison between Figs. 7.8 and 7.9 reveals that the species and heat release distributions in the wall normal distance for the turbulent flame remain qualitatively similar to the corresponding distributions in the case of laminar head-on quenching.

The temporal evolutions of the maximum, minimum and mean values of Pe and Φ for cases A and B are shown in Fig. 7.10a along with the corresponding variation obtained for head on quenching of a laminar one-dimensional flame. The temporal variations of T and reaction rate $\dot{\omega}$ of reaction progress variable for laminar flame simulations are also shown in Fig. 7.10b. It can be seen from Fig. 7.10a that the flame normal distance of $T = 0.9$ isosurface (or in other words Pe) in the laminar flame decreases with time as the flame approaches the cold wall, this leads to an increase in wall heat flux Φ with time for both simple and detailed chemistry cases. The Peclet number in laminar flame attains the minimum value when the flame quenches (i.e. $T = 0.9$ isosurface is the closest to the wall), which provides the measure of laminar quenching distance. The wall heat flux assumes the peak value in laminar head-on quenching when the minimum value of Peclet number is obtained. Subsequent to flame

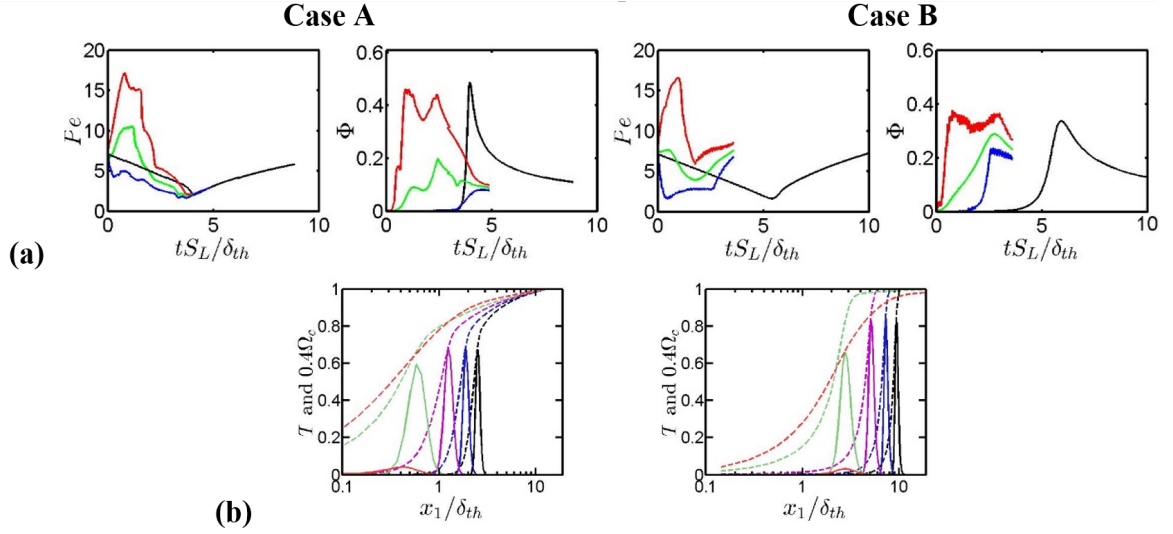


Fig. 7.10 (a) Temporal evolution of maximum, mean and minimum values of wall Peclet number Pe (based on $T = 0.9$ isosurface) and non-dimensional wall heat flux Φ along with the corresponding variation obtained for head on quenching of a laminar one-dimensional flame (maximum —; mean —; minimum —; laminar —). (b) Variations of T (broken line) and $\Omega_c \times 0.4$ (solid line) for laminar flame simulation at $t = 1.50\delta_{th}/S_L$ (—); $2.04\delta_{th}/S_L$ (—); $2.65\delta_{th}/S_L$ (—); $3.16\delta_{th}/S_L$ (—); $3.95\delta_{th}/S_L$ (—) for case A (left) and case B (right).

quenching, the isotherms move away from the cold wall leading to a continuous increase (decrease) in Pe (Φ) with time. Based on laminar flame calculation the minimum value of Peclet number is found to be $Pe_{min} = 1.6$, whereas the maximum normalised heat flux is found to be $(\Phi_{max})_L = 0.34$ for the simple chemistry case. By contrast, detailed chemistry case yields $(\Phi_{max})_L = 0.48$ and $(Pe_{min})_L = 2.2$. It is possible to scale Φ as: $\Phi \sim \delta_Z/X \sim 1/Pe$ and thus a higher value of $(\Phi_{max})_L$ is expected to be associated with a smaller value of $(Pe_{min})_L$. Nevertheless, the values of $(\Phi_{max})_L$ and $(Pe_{min})_L$ for simple and detailed chemistry cases are close to each other, and these values are consistent with the previous experimental [98, 100] and computational [156] findings at least in the order of magnitude sense.

It is worth noting that in a freely propagating laminar premixed flame the maximum reaction rate $\dot{\omega}$ of reaction progress variable takes place close to $T \approx 0.85$ in the context of simple chemistry case (see Fig. 7.10b). Here the wall Peclet number is evaluated based on wall normal distance of $T = 0.9$ isosurface following Poinot *et al.* [156]. However, the maximum value of $\dot{\omega}$ occurs at a smaller value of T (i.e. $T \approx 0.7$) in the detailed chemistry case than in the corresponding simple chemistry case (see Fig. 7.10b). Thus, an alternative evaluation of the minimum Peclet number based on

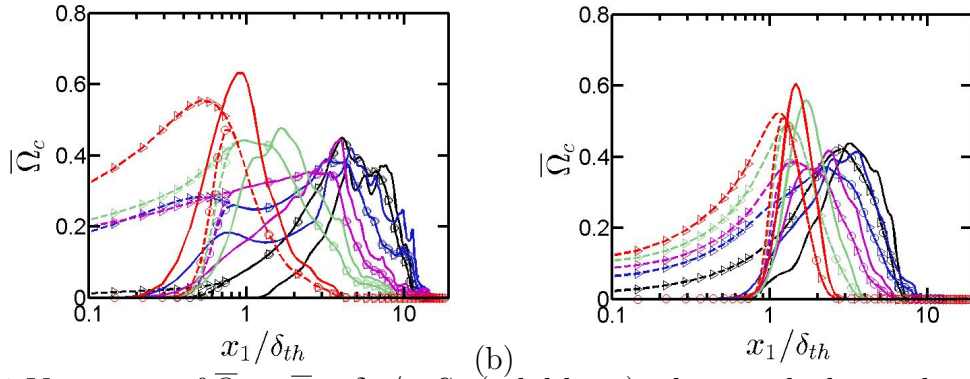


Fig. 7.11 Variations of $\bar{\Omega}_c = \bar{\omega} \times \delta_{th}/\rho_0 S_L$ (solid lines), along with the predictions of $\rho_0 S_L \Sigma_{gen} \times \delta_{th}/\rho_0 S_L$ (\triangle) and $A_1 \rho_0 S_L \Sigma_{gen} \times \delta_{th}/\rho_0 S_L$ (\circ) with x_1/δ_{th} for (a - b) cases A and B at $t = 0.31\delta_{th}/S_L$ (—); $1.05\delta_{th}/S_L$ (—); $1.61\delta_{th}/S_L$ (—); $1.98\delta_{th}/S_L$ (—); $2.16\delta_{th}/S_L$ (—).

the wall normal distance of the isosurface of T for which the maximum value of $\dot{\omega}$ occurs will bring the magnitude of $(Pe_{min})_L$ down for the detailed chemistry case (i.e. $(Pe_{min})_L$ based on wall-normal distance of $T \approx 0.7$ turns out to be 1.5) and it will be comparable to $(Pe_{min})_L$ in the simple chemistry case. In the detailed chemistry case the thermal conductivity and specific heat increase towards the burned gas side due to their temperature dependences conductivity, whereas these dependencies were not accounted for in the simple chemistry case. This gives rise to the difference in $(\Phi_{max})_L$ values between the detailed chemistry and simple chemistry cases. Figure 7.10a shows that the temporal variations of Pe and Φ in turbulent flames remain qualitatively similar to the corresponding variations in the laminar premixed flame. However, Φ_{max} in the turbulent cases is found to be comparable to the corresponding laminar flame case for the parameter considered here. Turbulence leads to a broadening of the flame brush due to a greater extent of wrinkling, which initiates flame element quenching earlier than the corresponding laminar flame. However, it can be seen from Fig. 7.10 that the minimum value of wall Peclet number Pe_{min} in turbulent flames remains comparable to the corresponding value in the case of laminar premixed flame-wall interaction for both simple and detailed chemistry cases.

7.2.2 Modelling of the mean reaction rate closure

The temporal evolutions of mean reaction rate $\bar{\omega}$ of reaction progress variable (i.e. $\bar{\omega} = -\bar{\omega}_{CH_4}/(Y_{R0} - Y_{R\infty})$) in the wall normal direction are shown in Fig. 7.11 for cases A and B. The mean reaction rate $\bar{\omega}$ in turbulent premixed flames is often modelled with the help of generalised FSD $\Sigma_{gen} = \overline{(\rho S_d)_s} \Sigma_{gen}$ [12]. In the context of RANS

modelling $\overline{(\rho S_d)}_s$ is often modelled as $\overline{(\rho S_d)}_s \approx \rho_0 S_L$ [12]. The temporal evolutions of $\rho_0 S_L \Sigma_{\text{gen}}$ in the wall normal direction are also shown in Fig. 7.11. It can be seen from Fig. 7.11 that $\rho_0 S_L \Sigma_{\text{gen}}$ overpredicts $\bar{\omega}$ in the near wall region. It is worthwhile to note that $\bar{\omega}$ vanishes completely for $x_1/\delta_{\text{th}} < (Pe_{\text{min}})_L$ but $\rho_0 S_L \Sigma_{\text{gen}}$ continues to predict non-zero values in this region for both simple and detailed chemistry cases. The model expression based on a-priori DNS analysis from Chapter 6 takes the form of $\bar{\omega} = A_1(\rho_0 S_L / Le) \Sigma_{\text{gen}}$ and $A_1 = 0.5[\text{erf}(x_1/\delta_Z - 0.7\Pi) + 1]$, where $\Pi = (Pe_{\text{min}})_L \delta_{\text{th}}/\delta_Z$ and $\Pi = (Pe_{\text{min}})_L$ is evaluated based on the wall normal distance of $T = 0.7$ ($T = 0.9$) isosurface for case A (case B) following the previous discussion on the equivalence of minimum Peclet number. It can be seen from Fig. 7.11 that $A_1 \rho_0 S_L \Sigma_{\text{gen}}$ satisfactorily captures the variation of $\bar{\omega}$ for both simple and detailed chemistry cases both away from and close to the wall. Thus, the reaction rate closure proposed previously based on a-priori analysis of simple chemistry DNS data for FWI remains valid also for detailed chemistry simulations of head-on quenching.

7.2.3 Summary of the key results for the detailed chemistry simulation

The head-on quenching of statistically turbulent planar flames by an isothermal inert walls has been analysed in this study based on three-dimensional compressible DNS simulations for a representative single-step simple chemistry and a multi-step detailed chemical mechanism of methane-air mixture. A chemical mechanism involving 16 species and 25 reactions for methane-air combustion is used for the purpose of detailed chemistry simulation of head-on quenching of a stoichiometric methane-air flame. The distributions of reaction progress variable c and non-dimensional temperature T remain identical to each other away from the wall for simple chemistry simulations but this equality does not hold during head-on quenching. The inequality between c defined based on CH_4 mass fraction and non-dimensional temperature T holds both away from and close to the wall for detailed chemistry simulations. However, the extent of this inequality becomes particularly prominent in the near-wall region. The value of reaction progress variable c and its Favre averaged counterpart \tilde{c} increase at the wall during FWI. In the simple chemistry case the heat release rate vanishes once the flame reaches a threshold distance away from the wall but non-zero heat release rate can be obtained at the wall during early stages of FWI in the detailed chemistry case. Detailed chemistry simulations also revealed that the reaction steps $\text{O}_2 + \text{H} + \text{M} \rightarrow \text{HO}_2 + \text{M}$ and $2\text{HO}_2 \rightarrow \text{H}_2\text{O}_2 + \text{O}_2$ can take place at low temperatures

which lead to a considerable accumulation of HO_2 and H_2O_2 at the wall during advanced stages of flame quenching. The formation of H_2O_2 is responsible for heat release at the wall during early stages of FWI. The temporal evolutions of wall heat flux and wall Peclet number (i.e. normalized wall-normal distance of $T = 0.9$ isosurface) for both simple and detailed chemistry laminar and turbulent cases have been found to be qualitatively similar. However, small differences have been found between the numerical values of the maximum normalised wall heat flux magnitude $(\Phi_{\max})_{\text{L}}$ and the minimum Peclet number $(Pe_{\min})_{\text{L}}$ based on simple and detailed chemistry laminar head-on quenching calculations. It has been found that the maximum reaction rate of progress variable takes place around $T = 0.9$ for a freely propagating laminar premixed flame under the assumption of simple chemistry but this occurs at around $T = 0.7$ for detailed chemistry. The minimum Peclet number defined based on wall-normal distance of $T = 0.7$ isosurface in the detailed chemistry case is found to be in good agreement with $(Pe_{\min})_{\text{L}}$ obtained for simple chemistry. The temperature dependence of thermal conductivity and specific heat in the detailed chemistry case leads to higher value of $(\Phi_{\max})_{\text{L}}$ than the corresponding value for the laminar simple chemistry case. It has been found that the conventional FSD closure $\bar{\omega} = \rho_0 S_{\text{L}} \Sigma_{\text{gen}}$ overpredicts the mean reaction rate of reaction progress variable $\bar{\omega}$ in the near-wall region for both simple and detailed chemistry simulations. A recently proposed FSD based reaction rate closure based on a-priori DNS analysis of simple chemistry DNS data has been found to perform satisfactorily also for the detailed chemistry case. Thus, the models, which have been proposed based on *a-priori* analysis of simple chemistry DNS of head-on quenching of turbulent premixed flames, have the potential to be valid even in the presence of detailed chemistry and transport. However, further investigation in this regard will be necessary, which will form the basis of future analyses.

Chapter 8

Conclusions & Future work

8.1 Conclusions

In this thesis, three-dimensional Direct Numerical Simulation (DNS) of turbulent premixed flame-wall interaction has been carried out. The head on quenching of statistically planar turbulent premixed flames based on a single-step Arrhenius-type irreversible chemical reaction by an isothermal inert wall has been analysed for different values of global Lewis number Le (0.8, 1.0 and 1.2) and turbulent Reynolds number Re_t . The statistics of head on quenching have been analysed in terms of the wall Peclet number Pe and the normalised wall heat flux Φ . It has been found that the turbulent flames quench earlier than the corresponding laminar flames because of greater extent of flame wrinkling, and this effect strengthens with increasing values of turbulence intensity $u'/S_L \sim Re_t^{1/4} Ka^{1/2} \sim Re_t^{1/2} Da^{-1/2}$, and for decreasing values of global Lewis number Le . The magnitude of the maximum wall heat flux Φ_{\max} increases with increasing u'/S_L . The maximum wall heat flux for the turbulent $Le = 0.8$ cases is found to be considerably greater than the corresponding laminar value. However, the maximum heat flux for the turbulent $Le = 1.0$ and 1.2 cases remain comparable to the corresponding values obtained for the laminar premixed flame-wall interaction. By contrast, the minimum Peclet number for the turbulent $Le = 0.8$ cases with high u'/S_L has been found to be smaller than the corresponding laminar flame value, whereas the minimum Peclet numbers for the turbulent $Le = 1.0$ and 1.2 cases remain comparable to the corresponding values obtained for the laminar premixed flame-wall interaction. It has been found that the maximum (minimum) value of Φ (Pe) for the turbulent $Le = 0.8$ cases are greater (smaller) than the corresponding laminar value, whereas both Pe and Φ in turbulent cases remain comparable to the corresponding laminar

values for $Le = 1.0$ and 1.2 . Detailed physical explanations are provided for the observed Le dependencies of Pe and Φ in Chapter 5.

The statistical behaviour of vorticity and enstrophy transport in HOQ of statistically planar turbulent premixed flames by an isothermal inert wall has been analysed. In all cases, the vorticity magnitude shows its maximum value at the wall, and the vorticity magnitude drops significantly from the unburned to the burned gas side of the flame-brush. Moreover, the vorticity magnitude shows an increasing trend with decreasing Le and increasing turbulence intensity. A significant amount of anisotropy has been observed between the vorticity components within the flame-brush, and this anisotropy increases as the wall are approached. The baroclinic torque term has been found to be principally responsible for this anisotropic behaviour. The vortex-stretching and viscous dissipation terms remain the leading order contributors to the vorticity and enstrophy transport for all cases when the flame is away from the wall, but as flame approach the wall, the baroclinic torque begins to play an increasingly important role. The combined molecular diffusion and dissipation contribution to the enstrophy transport remains negative away from the wall, but it changes its sign near the wall due to the torque arising from dilatation rate gradient.

The distribution of flow topologies within the flame and their evolution with flame quenching have been analysed using the HOQ database. It has been found that dilatation rate plays a key role in determining the flow topology distribution within the flame and this dilatation rate field is significantly affected by the flame quenching in the vicinity of the wall. The influence of the wall on dilatation rate field, in turn, influences the statistical behaviour of all three invariants of the velocity gradient tensor and the distribution of flow topologies. The effects of heat release and thermal expansion strengthen with decreasing Lewis number which leads to an increase in the probability of obtaining topologies which are specific to high positive values of dilatation rate. As the dilatation rate effects weaken with flame quenching, the probability of finding the topologies, which are obtained only for positive values of dilatation rate decreases close to the wall. The interrelation between the flow and flame topologies has been analysed in terms of Gaussian flame curvature and mean of principal flame curvatures. The contributions of individual flow topologies on the mean behaviour of wall heat flux, and the scalar-turbulence interaction and vortex-stretching terms in the scalar dissipation rate and enstrophy transport equations, respectively have been analysed in detail and dominant flow topologies which dictate the mean behaviours of these quantities have been identified. The nodal flow topologies have been found to be the

significant contributors to the wall heat flux during head-on quenching of turbulent premixed flames irrespective of the value of global Lewis number.

This thesis investigates the statistical behaviour of the turbulent kinetic energy transport for moderate values of turbulent Reynolds number Re_t in turbulent premixed flames by using HOQ database. The magnitudes of turbulent kinetic energy and the terms of its transport equation have been found to increase with a reduction in global Lewis number. The magnitudes of all the terms except the viscous dissipation rate drops sharply near the wall whereas the magnitude of viscous dissipation rate exhibits a sharp increase in the near-wall region. The statistical behaviours of the terms arising from turbulent transport, pressure fluctuation transport, mean pressure gradient, pressure dilatation and viscous dissipation have been analysed by explicit Reynolds averaging of DNS data. It has been found that the viscous dissipation term acts as a major sink for all cases and all locations. The mean pressure gradient acts as the leading order source for all cases. However, the magnitudes of the mean pressure gradient, pressure dilatation and transport terms diminish with increasing Lewis number. Moreover, the turbulent flux of kinetic energy has been found to exhibit counter-gradient transport, and its extent diminishes with increasing Lewis number as a result of the weakening of flame normal acceleration. Existing models for the unclosed terms have been modified for accurate prediction of the corresponding terms extracted from DNS data especially in the near-wall region.

The statistical behaviour of the transport of reaction progress variable variance $\widetilde{c''^2}$ has been analysed by using the HOQ database. It has been found that reaction rate contribution to the variance $\widetilde{c''^2}$ transport acts as a leading order source, whereas the molecular dissipation term remains as the leading order sink for all cases considered here. However, all of the terms of the variance $\widetilde{c''^2}$ transport equation decay significantly in the near-wall region once the quenching starts. The existing models for the turbulent transport, reaction, and dissipation contributions to the variance $\widetilde{c''^2}$ transport do not adequately capture the near-wall behaviour. The wall effects on the unclosed terms of the variance $\widetilde{c''^2}$ transport equation have been analysed using explicitly Reynolds averaged DNS data, and the existing closures of the unclosed terms have been modified to account for the near-wall effects. *A-priori* DNS analysis suggests that the proposed modifications to the existing closures for the unclosed terms of the variance $\widetilde{c''^2}$ transport equation provide satisfactory predictions both away from and near to the wall.

The existing closure of mean reaction rate $\bar{\omega}$ using the SDR in the near wall region has been assessed based on *a-priori* analysis of DNS data and modifications to the existing closures of mean reaction rate and SDR have been suggested to account for

the wall effects in such a manner that the modified closures perform well both near to and away from the wall. The statistical behaviour and modelling of SDR transport wall have been analysed in the context of RANS simulations. It has been found that the density variation, scalar-turbulence interaction, reaction rate gradient, molecular diffusivity gradient and molecular dissipation terms (i.e. T_2 , T_3 , T_4 , $f(D)$ and $(-D_2)$ respectively) act as leading order contributors to the SDR $\tilde{\epsilon}_c$ transport away from the wall and the turbulent transport and molecular diffusion terms remain negligible in comparison to the other terms. The leading order contributors to the SDR transport have been found to be in a rough equilibrium away from the wall before the quenching is initiated but this equilibrium is not maintained once the flame quenching is initiated. The predictions of the existing models for the unclosed terms of the SDR transport equation have been assessed with respect to the corresponding quantities extracted from DNS data. No existing models have been found to predict the near wall behaviour of the unclosed terms of the SDR transport equation. The models, which exhibit the most satisfactory performance away from the wall, have been modified to account for near wall behaviour in such a manner that the modified models asymptotically approach the existing model expressions away from the wall.

The near-wall behaviour of the generalised FSD transport in the context of RANS simulations has been analysed. It has been found that the statistical behaviour of the FSD based reaction rate closure and the terms of the FSD transport equation are significantly affected by the presence of the wall and by the global Lewis number. The near-wall predictions of the standard FSD based mean reaction rate closure and existing sub-models for the unclosed terms of the FSD transport equation have been found to be inadequate based on *a-priori* DNS assessment, and modifications to these models have been suggested so that the predictions of modified models for reaction rate closure and FSD transport remain satisfactory, both close to the wall and away from it over a wide range of global Lewis number.

The statistical behaviour and the modelling of turbulent scalar flux transport have been analysed. The magnitudes of the turbulent transport and mean velocity gradient terms in the turbulent scalar flux transport equation remain small in comparison to the pressure gradient, molecular dissipation and reaction-velocity fluctuation correlation terms in the turbulent scalar flux transport equation when the flame is away from the wall, but the magnitudes of all these terms diminish and assume comparable values during flame quenching before vanishing altogether. It has been found that the existing models for the turbulent transport, pressure gradient, molecular dissipation and reaction-velocity fluctuation correlation terms in the turbulent scalar flux transport

equation do not adequately address the respective behaviours extracted from DNS data in the near-wall region during flame quenching. Existing models for transport equation based closures of turbulent scalar flux have been modified in such a manner that these models provide satisfactory prediction both near to and away from the wall.

The 3D compressible DNS simulations of turbulent V-flame with walls in a channel have been carried out in this thesis. The wall heat flux and flame quenching distance statistics for oblique flame-wall interaction in the case of turbulent V-flames have been compared to the corresponding values obtained for the HOQ configuration. The statistics of wall heat flux, flame quenching distance in the case of oblique quenching of a turbulent V-flame flame by isothermal inert walls have been analysed in terms of the distributions of flow topologies and their contributions using DNS data. It has been found that the maximum (minimum) wall heat flux (Peclet number) in the case of oblique flame quenching assumes greater (smaller) value than in the corresponding turbulent HOQ case. Although the volume fractions of $S2$ and $S7$ topologies assume high values within the flame front, the focal topologies $S1$ and $S4$ have been found to contribute to wall heat flux in the case oblique flame quenching.

A three-dimensional compressible DNS analysis has been carried out for head-on quenching of a statistically planar methane flame by an isothermal inert wall. A multi-step chemical mechanism for methane-air combustion is used for the purpose of detailed chemistry DNS. For head-on quenching of stoichiometric methane-air flames, the mass fractions of major reactant species such as methane and oxygen tend to vanish at the wall during flame quenching, whereas the mass fractions of major products (e.g. H_2O) approach an asymptotic value corresponding to the fully burned state. However, it is found that the near-wall behaviour of intermediate species is markedly different in comparison to the distribution away from the wall. For example, the absence of OH at the wall gives rise to accumulation of carbon monoxide during advanced stages of flame quenching because CO cannot be oxidised anymore. Furthermore, it has been found that low-temperature reactions give rise to accumulation of HO_2 and H_2O_2 at the wall during advanced stages of flame quenching. Moreover, the formation of H_2O_2 results in a non-zero heat release rate at the wall during early stages of flame-wall interaction. By contrast, heat release rate vanishes once the flame reaches a threshold distance from the wall in the comparable simple chemistry simulation. In order to carry out an in-depth comparison between both approaches, a corresponding simulation has been carried out for the same turbulence parameters for a representative single-step Arrhenius type irreversible chemical mechanism. The distributions of reaction progress variable c and non-dimensional temperature T are found to be identical to each other

away from the wall for the simple chemistry simulation, but this equality does not hold during head-on quenching. The inequality between c defined based on CH_4 mass fraction and non-dimensional temperature T holds both away from and close to the wall for the detailed chemistry simulation, but this becomes particularly prominent in the near-wall region. The temporal evolutions of wall heat flux and wall Peclet number for both simple and detailed chemistry laminar and turbulent cases have been found to be qualitatively similar. However, small differences have been observed in the numerical values of the maximum normalised wall heat flux magnitude $(\Phi_{\max})_{\text{L}}$ and the minimum Peclet number $(Pe_{\min})_{\text{L}}$ obtained from simple and detailed chemistry based laminar HOQ calculations. The usual FSD based reaction rate closure has been found to overpredict the mean reaction rate of reaction progress variable in the near-wall region for both simple and detailed chemistry simulations. Despite the observed differences, it has been found that a recently proposed FSD based reaction rate closure based on *a-priori* DNS analysis of simple chemistry data performs satisfactorily also for the detailed chemistry case both away from and close to the wall without any adjustment to the model parameters.

8.2 Future follow up

The present study addressed some major issues relevant to the modelling of the flame-wall interaction for turbulent premixed flames based on an *a-priori* DNS analysis. Although the newly developed closures and models have been found to yield promising results, there are scopes for further improvement which are listed below:

- The proposed FSD based reaction rate closure based on *a-priori* DNS analysis of simple chemistry data performs satisfactorily for the detailed chemistry case both away from and close to the wall. However, further *a-posteriori* assessments of the proposed models in the current study need to be carried out.
- In the current DNS analysis, cases with moderate values of turbulent Reynolds numbers have been considered. It is extremely expensive to achieve high turbulent Reynolds numbers by using DNS. However, further assessment for the algebraic and transport equation based closures will be needed in the near-wall region for higher values of Re_{t} .
- The current study focuses on a premixed turbulent combustion and provides valuable physical insights of the effects of turbulence, Lewis number, chemical

mechanism and walls configurations. However, the effects of equivalence ratio or non-premixed modelling of turbulent flame-wall interaction have not yet been conducted.

References

- [1] Abdel-Gayed, R., Bradley, D., Hamid, M., and Lawes, M. (1985). Lewis number effects on turbulent burning velocity. In *Symposium (International) on Combustion*, volume 20, pages 505–512. Elsevier.
- [2] Alshaalan, T. and Rutland, C. J. (2002). Wall heat flux in turbulent premixed reacting flow. *Combustion Science and Technology*, 174(1):135–165.
- [3] Alshaalan, T. M. and , C. J. (1998). Turbulence, scalar transport, and reaction rates in flame-wall interaction. In *Symposium (International) on Combustion*, volume 27, pages 793–799. Elsevier.
- [4] Aly, S. and Hermance, C. (1981). A two-dimensional theory of laminar flame quenching. *Combustion and Flame*, 40:173–185
- [5] Angelberger, C., Poinso, T., and Delhay, B. (1997). Improving near-wall combustion and wall heat transfer modeling in SI engine computations. Technical report.
- [6] Ashurst, W. T., Kerstein, A., Kerr, R., and Gibson, C. (1987). Alignment of vorticity and scalar gradient with strain rate in simulated Navier–Stokes turbulence. *The Physics of fluids*, 30(8):2343–2353.
- [7] Batchelor, G. and Townsend, A. (1948). Decay of turbulence in the final period. In *Proceedings of the Royal Society of London A: Mathematical, Physical and Engineering Sciences*, volume 194, pages 527–543. The Royal Society.
- [8] Baum, M., Poinso, T., and Thévenin, D. (1995). Accurate boundary conditions for multicomponent reactive flows. *Journal of computational physics*, 116(2):247–261.
- [9] Berna, F., Goldberg, P., Horwitz, L. K., Brink, J., Holt, S., Bamford, M., and Chazan, M. (2012). Microstratigraphic evidence of in situ fire in the acheulean strata of wonderwerk cave, northern cape province, south africa. *Proceedings of the National Academy of Sciences*, 109(20):1215–1220.
- [10] Bilger, R. (2004). Some aspects of scalar dissipation. *Flow, turbulence and combustion*, 72(2-4):93–114.
- [11] Blackburn, H. M., Mansour, N. N., and Cantwell, B. J. (1996). Topology of fine-scale motions in turbulent channel flow. *Journal of Fluid Mechanics*, 310:269–292.

- [12] Boger, M., Veynante, D., Boughanem, H., and Trouvé, A. (1998). Direct numerical simulation analysis of flame surface density concept for large eddy simulation of turbulent premixed combustion. In *Symposium (International) on Combustion*, volume 27, pages 917–925. Elsevier.
- [13] Boratav, O., Elghobashi, S., and Zhong, R. (1996). On the alignment of the α -strain and vorticity in turbulent nonpremixed flames. *Physics of Fluids*, 8(8):2251–2253.
- [14] Boratav, O., Elghobashi, S., and Zhong, R. (1998). On the alignment of strain, vorticity and scalar gradient in turbulent, buoyant, nonpremixed flames. *Physics of Fluids*, 10(9):2260–2267.
- [15] Borghi, R. (1990). Turbulent premixed combustion: Further discussions on the scales of fluctuations. *Combustion and Flame*, 80(3):304–312.
- [16] Bradley, D., Gaskell, P., and Gu, X. (1994). Application of a reynolds stress, stretched flamelet, mathematical model to computations of turbulent burning velocities and comparison with experiments. *Combustion and flame*, 96(3):221–248.
- [17] Bray, K. (1980). Turbulent flows with premixed reactants. In *Turbulent reacting flows*, pages 115–183. Springer.
- [18] Bray, K., Libby, P. A., Masuya, G., and Moss, J. (1981). Turbulence production in premixed turbulent flames.
- [19] Bray, K., Libby, P. A., and Moss, J. (1985). Unified modeling approach for premixed turbulent combustion—part i: General formulation. *Combustion and flame*, 61(1):87–102.
- [20] Bruneaux, G., Akselvoll, K., Poinso, T., and Ferziger, J. (1996). Flame-wall interaction simulation in a turbulent channel flow. *Combustion and flame*, 107(1):27–44.
- [21] Bruneaux, G., Poinso, T., and Ferziger, J. (1997). Premixed flame–wall interaction in a turbulent channel flow: budget for the flame surface density evolution equation and modelling. *Journal of Fluid Mechanics*, 349:191–219.
- [22] Candel, S. M. and Poinso, T. J. (1990). Flame stretch and the balance equation for the flame area. *Combustion Science and Technology*, 70(1-3):1–15.
- [23] Cant, R. and Bray, K. (1989). Strained laminar flamelet calculations of premixed turbulent combustion in a closed vessel. In *Symposium (International) on Combustion*, volume 22, pages 791–799. Elsevier.
- [24] Cant, R. and Mastorakos, E. (2008). *An introduction to turbulent reacting flows*. Imperial College Press.
- [25] Cant, R., Pope, S., and Bray, K. (1991). Modelling of flamelet surface-to-volume ratio in turbulent premixed combustion. In *Symposium (International) on Combustion*, volume 23, pages 809–815. Elsevier.

- [26] Cant, S. (2012a). *Initial conditions for direct numerical simulation of turbulence*. University of Cambridge, Department of Engineering.
- [27] Cant, S. (2012b). *SENGA2 user guide*. University of Cambridge, Department of Engineering.
- [28] Chacin, J. M. and Cantwell, B. J. (2000). Dynamics of a low reynolds number turbulent boundary layer. *Journal of Fluid Mechanics*, 404:87–115.
- [29] Chakraborty, N. (2014). Statistics of vorticity alignment with local strain rates in turbulent premixed flames. *European Journal of Mechanics-B/Fluids*, 46:201–220.
- [30] Chakraborty, N. and Cant, R. (2005). Influence of lewis number on curvature effects in turbulent premixed flame propagation in the thin reaction zones regime. *Physics of Fluids (1994-present)*, 17(10):105105.
- [31] Chakraborty, N. and Cant, R. (2007). A priori analysis of the curvature and propagation terms of the flame surface density transport equation for large eddy simulation. *Physics of Fluids (1994-present)*, 19(10):105101.
- [32] Chakraborty, N. and Cant, R. (2009a). Direct numerical simulation analysis of the flame surface density transport equation in the context of large eddy simulation. *Proceedings of the combustion institute*, 32(1):1445–1453.
- [33] Chakraborty, N. and Cant, R. (2009b). Effects of lewis number on scalar transport in turbulent premixed flames. *Physics of Fluids (1994-present)*, 21(3):035110.
- [34] Chakraborty, N. and Cant, R. (2009c). Effects of Lewis number on turbulent scalar transport and its modelling in turbulent premixed flames. *Combustion and Flame*, 156(7):1427–1444.
- [35] Chakraborty, N. and Cant, R. (2009d). Physical insight and modelling for lewis number effects on turbulent heat and mass transport in turbulent premixed flames. *Numerical Heat Transfer, Part A: Applications*, 55(8):762–779.
- [36] Chakraborty, N. and Cant, R. (2011). Effects of lewis number on flame surface density transport in turbulent premixed combustion. *Combustion and Flame*, 158(9):1768–1787.
- [37] Chakraborty, N. and Cant, R. (2013). Turbulent reynolds number dependence of flame surface density transport in the context of reynolds averaged Navier–Stokes simulations. *Proceedings of the Combustion Institute*, 34(1):1347–1356.
- [38] Chakraborty, N. and Cant, R. (2015). Effects of turbulent reynolds number on the modelling of turbulent scalar flux in premixed flames. *Numerical Heat Transfer, Part A: Applications*, 67(11):1187–1207.
- [39] Chakraborty, N., Champion, M., Mura, A., and Swaminathan, N. (2011a). Scalar dissipation rate approach.
- [40] Chakraborty, N., Katragadda, M., and Cant, R. (2011b). Effects of lewis number on turbulent kinetic energy transport in premixed flames. *Physics of Fluids (1994-present)*, 23(7):075109.

- [41] Chakraborty, N., Katragadda, M., and Cant, R. S. (2011c). Statistics and modelling of turbulent kinetic energy transport in different regimes of premixed combustion. *Flow, turbulence and combustion*, 87(2-3):205–235.
- [42] Chakraborty, N. and Klein, M. (2008). Influence of lewis number on the surface density function transport in the thin reaction zone regime for turbulent premixed flames. *Physics of Fluids (1994-present)*, 20(6):065102.
- [43] Chakraborty, N., Klein, M., and Swaminathan, N. (2009). Effects of lewis number on the reactive scalar gradient alignment with local strain rate in turbulent premixed flames. *Proceedings of the Combustion Institute*, 32(1):1409–1417.
- [44] Chakraborty, N., Konstantinou, I., and Lipatnikov, A. (2016a). Effects of lewis number on vorticity and enstrophy transport in turbulent premixed flames. *Physics of Fluids*, 28(1):015109.
- [45] Chakraborty, N., Konstantinou, I., and Lipatnikov, A. (2016b). Effects of lewis number on vorticity and enstrophy transport in turbulent premixed flames. *Physics of Fluids (1994-present)*, 28(1):015109.
- [46] Chakraborty, N., Rogerson, J., and Swaminathan, N. (2008). A priori assessment of closures for scalar dissipation rate transport in turbulent premixed flames using direct numerical simulation. *Physics of Fluids*, 20(4):045106.
- [47] Chakraborty, N. and Swaminathan, N. (2007a). Influence of the damkohler number on turbulence-scalar interaction in premixed flames. i. physical insight. *Physics of Fluids*, 19:045103.
- [48] Chakraborty, N. and Swaminathan, N. (2007b). Influence of the damköhler number on turbulence-scalar interaction in premixed flames. ii. model development. *Physics of Fluids*, 19(4):045104.
- [49] Chakraborty, N. and Swaminathan, N. (2010). Effects of lewis number on scalar dissipation transport and its modeling in turbulent premixed combustion. *Combustion Science and Technology*, 182(9):1201–1240.
- [50] Chakraborty, N. and Swaminathan, N. (2011a). Effects of lewis number on scalar variance transport in premixed flames. *Flow, turbulence and combustion*, 87(2-3):261–292.
- [51] Chakraborty, N. and Swaminathan, N. (2011b). Effects of lewis number on scalar variance transport in premixed flames. *Flow, turbulence and combustion*, 87(2-3):261–292.
- [52] Chakraborty, N. and Swaminathan, N. (2013). Reynolds number effects on scalar dissipation rate transport and its modeling in turbulent premixed combustion. *Combustion Science and Technology*, 185(4):676–709.
- [53] Chen, J. H., Cantwell, B. J., and Mansour, N. N. (1989). The topology and vorticity dynamics of a three-dimensional plane compressible wake. In *Proc. Tenth Australasian Fluid Mechanics Conference*, pages 5–1.

- [54] Chen, J. H., Choudhary, A., De Supinski, B., DeVries, M., Hawkes, E., Klasky, S., Liao, W., Ma, K., Mellor-Crummey, J., Podhorszki, N., et al. (2009). Terascale direct numerical simulations of turbulent combustion using s3d. *Computational Science & Discovery*, 2(1):015001.
- [55] Cheng, R. and Shepherd, I. (1991). The influence of burner geometry on premixed turbulent flame propagation. *Combustion and Flame*, 85(1-2):7–26.
- [56] Chong, M., Soria, J., Perry, A., Chacin, J., Cantwell, B., and Na, Y. (1998). Turbulence structures of wall-bounded shear flows found using DNS data. *Journal of Fluid Mechanics*, 357:225–247.
- [57] Chong, M. S., Perry, A. E., and Cantwell, B. J. (1990). A general classification of three-dimensional flow fields. *Physics of Fluids A: Fluid Dynamics (1989-1993)*, 2(5):765–777.
- [58] Cifuentes, L. (2015). *Local flow topologies and scalar structures in turbulent combustion*. Ph.D. thesis, University of Zaragoza.
- [59] Cifuentes, L., Dopazo, C., Martin, J., and Jimenez, C. (2014). Local flow topologies and scalar structures in a turbulent premixed flame. *Physics of Fluids (1994-present)*, 26(6):065108.
- [60] Clavin, P. and Williams, F. (1982). Effects of molecular diffusion and of thermal expansion on the structure and dynamics of premixed flames in turbulent flows of large scale and low intensity. *Journal of fluid mechanics*, 116:251–282.
- [61] Commission, E. (2005). Eur 21612 - strengths, weaknesses, opportunities and threats in energy research.
- [62] Conant, J. B. (1950). *The Overthrow of the Phlogiston theory: the Chemical Revolution of 1775-1789*, volume 2. Harvard University Press.
- [63] Cooper, J. C. (1990). *Chinese alchemy: the Taoist quest for immortality*. Sterling Pub Co Inc.
- [64] Craft, T., Graham, L., and Launder, B. E. (1993). Impinging jet studies for turbulence model assessment—ii. an examination of the performance of four turbulence models. *International Journal of Heat and Mass Transfer*, 36(10):2685–2697.
- [65] Dabireau, F., Cuenot, B., Vermorel, O., and Poinso, T. (2003). Interaction of flames of $\text{H}_2 + \text{O}_2$ with inert walls. *Combustion and flame*, 135(1):123–133.
- [66] Daly, B. J. and Harlow, F. H. (1970). Transport equations in turbulence. *The Physics of Fluids*, 13(11):2634–2649.
- [67] Davidson, P. (2015). *Turbulence: an introduction for scientists and engineers*. Oxford University Press, USA.
- [68] Davies, R. (2004). *George Stephenson: the Remarkable Life of the Founder of the Railways*. The History Press.

- [69] Davy, H. (1817). Some new experiments and observations on the combustion of gaseous mixtures, with an account of a method of preserving a continued light in mixtures of inflammable gases and air without flame. *Philosophical Transactions of the Royal Society of London*, 107:77–85.
- [70] De Lataillade, A., Dabireau, F., Cuenot, B., and Poinso, T. (2002). Flame/wall interaction and maximum wall heat fluxes in diffusion burners. *Proceedings of the Combustion Institute*, 29(1):775–779.
- [71] Demesoukas, S., Caillol, C., Higelin, P., and Boiarciuc, A. (2013). Zero-Dimensional Spark Ignition Combustion Modeling-A Comparison of Different Approaches. Technical report, SAE Technical Paper.
- [72] Demesoukas, S., Caillol, C., Higelin, P., Boiarciuc, A., and Floch, A. (2015). Near wall combustion modeling in spark ignition engines. Part A: Flame-wall interaction. *Energy Conversion and Management*, 106:1426–1438.
- [73] Dinkelacker, F., Manickam, B., and Muppala, S. (2011). Modelling and simulation of lean premixed turbulent methane/hydrogen/air flames with an effective lewis number approach. *Combustion and Flame*, 158(9):1742–1749.
- [74] Domingo, P. and Bray, K. (2000). Laminar flamelet expressions for pressure fluctuation terms in second moment models of premixed turbulent combustion. *Combustion and flame*, 121(4):555–574.
- [75] Dopazo, C., Martín, J., and Hierro, J. (2007). Local geometry of isoscalar surfaces. *Physical Review E*, 76(5):056316.
- [76] Duclos, J., Bruneaux, G., and Baritaud, T. (1996). 3D modelling of combustion and pollutants in a 4-valve SI engine; effect of fuel and residuals distribution and spark location. Technical report.
- [77] Dunstan, T. D., Swaminathan, N., Bray, K. N., and Cant, R. S. (2011). Geometrical properties and turbulent flame speed measurements in stationary premixed V-flames using direct numerical simulation. *Flow, turbulence and combustion*, 87(2-3):237–259 1386–6184.
- [78] Durbin, P. (1993). A reynolds stress model for near-wall turbulence. *Journal of Fluid Mechanics*, 249:465–498.
- [79] Durbin, P. A. and Reif, B. P. (2011). *Statistical theory and modeling for turbulent flows*. John Wiley & Sons.
- [80] Echehki, T. and Chen, J. H. (1999). Analysis of the contribution of curvature to premixed flame propagation. *Combustion and Flame*, 118(1):308–311.
- [81] Eddy, M. D., Mauskopf, S. H., and Newman, W. R. (2014). An Introduction to Chemical Knowledge in the Early Modern World. *Osiris*, 29(1):1–15.
- [82] EIA, U. E. I. A. (2016). Analysis of the impacts of the clean power plan.

- [83] Ellison, L. R. and Moser, M. D. (2004). Combustion instability analysis and the effects of drop size on acoustic driving rocket flow. URL: <http://reap.uah.edu/publications/Ellison.pdf> [cited 15 December 2005].
- [84] Elsinga, G. and Marusic, I. (2010). Universal aspects of small-scale motions in turbulence. *Journal of Fluid Mechanics*, 662:514–539.
- [85] Ferguson, C. R. and Keck, J. C. (1977). On laminar flame quenching and its application to spark ignition engines. *Combustion and Flame*, 28:197–205.
- [86] Frenken, K. (2000). A complexity approach to innovation networks. The case of the aircraft industry (1909–1997). *Research Policy*, 29(2):257–272.
- [87] Gao, Y., Chakraborty, N., and Swaminathan, N. (2015). Dynamic closure of scalar dissipation rate for large eddy simulations of turbulent premixed combustion: A direct numerical simulations analysis. *Flow, Turbulence and Combustion*, 95(4):775–802.
- [88] Gouldin, F., Bray, K., and Chen, J.-Y. (1989). Chemical closure model for fractal flamelets. *Combustion and flame*, 77(3):241–259.
- [89] Grout, R., Gruber, A., Yoo, C. S., and Chen, J. (2011). Direct numerical simulation of flame stabilization downstream of a transverse fuel jet in cross-flow. *Proceedings of the Combustion Institute*, 33(1):1629–1637.
- [90] Gruber, A., Sankaran, R., Hawkes, E., and Chen, J. (2010). Turbulent flame–wall interaction: a direct numerical simulation study. *Journal of Fluid Mechanics*, 658:5–32.
- [91] Hamlington, P. E., Poludnenko, A. Y., and Oran, E. S. (2011). Interactions between turbulence and flames in premixed reacting flows. *Physics of Fluids*, 23(12):125111.
- [92] Hamlington, P. E., Schumacher, J., and Dahm, W. J. (2008). Local and nonlocal strain rate fields and vorticity alignment in turbulent flows. *Physical Review E*, 77(2):026303.
- [93] Han, I. and Huh, K. Y. (2008). Roles of displacement speed on evolution of flame surface density for different turbulent intensities and lewis numbers in turbulent premixed combustion. *Combustion and Flame*, 152(1):194–205.
- [94] Hawkes, E. and Cant, R. (2001). Implications of a flame surface density approach to large eddy simulation of premixed turbulent combustion. *Combustion and Flame*, 126(3):1617–1629.
- [95] Haworth, D. and Poinso, T. (1992). Numerical simulations of lewis number effects in turbulent premixed flames. *Journal of Fluid Mechanics*, 244:405–436.
- [96] Heywood, J. B. (1988). *Internal combustion engine fundamentals*, volume 930. McGraw-hill New York.
- [97] Huai, Y., Sadiki, A., Pfadler, S., Löffler, M., Beyrau, F., Leipertz, A., and Dinkelacker, F. (2006). *Experimental assessment of scalar flux models for large eddy simulations of non-reacting flows*. Begel House Inc.

- [98] Huang, W., Vosen, S., and Greif, R. (1988). Heat transfer during laminar flame quenching: effect of fuels. In *Symposium (International) on Combustion*, volume 21, pages 1853–1860. Elsevier.
- [99] Jaberri, F., Livescu, D., and Madnia, C. (2000). Characteristics of chemically reacting compressible homogeneous turbulence. *Physics of Fluids*, 12(5):1189–1209.
- [100] Jarosiński, J. (1983). Flame quenching by a cold wall. *Combustion and Flame*, 50:167–175.
- [101] Jarosinski, J. (1986). A survey of recent studies on flame extinction. *Progress in energy and combustion science*, 12(2):81–116.
- [102] Jenkins, K. W. and Cant, R. S. (1999). Direct numerical simulation of turbulent flame kernels. In *Recent Advances in DNS and LES*, pages 191–202. Springer.
- [103] Jiménez, J. (1992). Kinematic alignment effects in turbulent flows. *Physics of Fluids A: Fluid Dynamics*, 4(4):652–654.
- [104] Jones, W. and Launder, B. (1972). The prediction of laminarization with a two-equation model of turbulence. *International journal of heat and mass transfer*, 15(2):301–314.
- [105] Jones, W. and Launder, B. (1973). The calculation of low-reynolds-number phenomena with a two-equation model of turbulence. *International Journal of Heat and Mass Transfer*, 16(6):1119–1130.
- [106] Jones, W. P. (1994). *Turbulence modelling and numerical solution methods for variable density and combustng flows*. Academic Press, p. a. libby and f. a. williams, ed. edition.
- [107] Karman, T. v. (1941). The buckling of thin cylindrical shells under axial compression. *Journal of the Aeronautical Sciences*, 8(8):303–312.
- [108] Katragadda, M., Malkeson, S. P., and Chakraborty, N. (2011). Modelling of the tangential strain rate term of the flame surface density transport equation in the context of reynolds averaged Navier–Stokes simulation. *Proceedings of the Combustion Institute*, 33(1):1429–1437.
- [109] Kee, R., Rupley, F., Miller, J., Coltrin, M., Grcar, J., Meeks, E., Moffat, H., Lutz, A., Dixon-Lewis, G., and Smooke, M. (2000). Chemkin collection. *Reaction Design, release*, 3.
- [110] Kee, R. J., Rupley, F. M., Meeks, E., and Miller, J. A. (1996). Chemkin-iii: A fortran chemical kinetics package for the analysis of gas-phase chemical and plasma kinetics. *Sandia national laboratories report SAND96-8216*.
- [111] Kim, J. and Moin, P. (1989). Transport of passive scalars in a turbulent channel flow. In *Turbulent Shear Flows 6*, pages 85–96. Springer.
- [112] Kim, S. H. and Pitsch, H. (2007). Scalar gradient and small-scale structure in turbulent premixed combustion. *Physics of Fluids (1994-present)*, 19(11):115104.

- [113] Klimenko, A. Y. and Bilger, R. W. (1999). Conditional moment closure for turbulent combustion. *Progress in Energy and Combustion Science*, 25(6):595–687.
- [114] Kolla, H., Rogerson, J., Chakraborty, N., and Swaminathan, N. (2009). Scalar dissipation rate modeling and its validation. *Combustion Science and Technology*, 181(3):518–535.
- [115] Kolmogorov, A. N. (1941). The local structure of turbulence in incompressible viscous fluid for very large reynolds numbers. In *Dokl. Akad. Nauk SSSR*, volume 30, pages 301–305. JSTOR.
- [116] Kuhn, T. S. (2012). *The structure of scientific revolutions*. University of Chicago press.
- [117] Kuo, K. K. (1986). *Principles of Combustion*. Wiley New York et al.
- [118] Labuda, S., Karrer, M., Sotton, J., and Bellenoue, M. (2011). Experimental study of single-wall flame quenching at high pressures. *Combustion Science and Technology*, 183(5):409–426.
- [119] Lai, J. and Chakraborty, N. (2016a). Effects of lewis number on head on quenching of turbulent premixed flames: A direct numerical simulation analysis. *Flow, Turbulence and Combustion*, 96(2):279–308.
- [120] Lai, J. and Chakraborty, N. (2016b). Statistical behavior of scalar dissipation rate in head-on quenching of turbulent premixed flames: A direct numerical simulation analysis. *Combustion Science and Technology*, 188(2):250–276.
- [121] Lai, J., Chakraborty, N., and Lipatnikov, A. (2016). Statistical behaviour of vorticity and enstrophy transport in head-on quenching of turbulent premixed flames. *European Journal of Mechanics-B/Fluids*.
- [122] Launder, B. (1976). *Heat and mass transport*, pages 231–287. Springer.
- [123] Launder, B., Reece, G. J., and Rodi, W. (1975). Progress in the development of a reynolds-stress turbulence closure. *Journal of fluid mechanics*, 68(03):537–566.
- [124] Launder, B. E. (1989). Second-moment closure: present... and future? *International Journal of Heat and Fluid Flow*, 10(4):282–300.
- [125] Launder, B. E. and Spalding, D. (1974). The numerical computation of turbulent flows. *Computer methods in applied mechanics and engineering*, 3(2):269–289.
- [126] Libby, P. A., Liñán, A., and Williams, F. A. (1983). Strained premixed laminar flames with nonunity lewis numbers. *Combustion Science and Technology*, 34(1-6):257–293.
- [127] Lindstedt, R. and Váos, E. (1999). Modeling of premixed turbulent flames with second moment methods. *Combustion and Flame*, 116(4):461–485.
- [128] Lipatnikov, A. and Chomiak, J. (2002). Turbulent flame speed and thickness: phenomenology, evaluation, and application in multi-dimensional simulations. *Progress in energy and combustion science*, 28(1):1–74.

- [129] Lipatnikov, A., Nishiki, S., and Hasegawa, T. (2014). A direct numerical simulation study of vorticity transformation in weakly turbulent premixed flames. *Physics of Fluids*, 26(10):105104.
- [130] Louch, D. and Bray, K. (2001). Vorticity in unsteady premixed flames: vortex pair-premixed flame interactions under imposed body forces and various degrees of heat release and laminar flame thickness. *Combustion and flame*, 125(4):1279–1309.
- [131] Lüthi, B., Tsinober, A., and Kinzelbach, W. (2005). Lagrangian measurement of vorticity dynamics in turbulent flow. *Journal of Fluid mechanics*, 528:87–118.
- [132] Ma, T., Stein, O., Chakraborty, N., and Kempf, A. (2014). A posteriori testing of the flame surface density transport equation for les. *Combustion Theory and Modelling*, 18(1):32–64.
- [133] Maekawa, H., Hiyama, T., and Matsuo, Y. (1999). Study of the geometry of flow patterns in compressible isotropic turbulence. *JSME International Journal Series B*, 42(3):336–343.
- [134] Majda, A. J. (1991). Vorticity, turbulence, and acoustics in fluid flow. *Siam Review*, 33(3):349–388.
- [135] Malkeson, S. P. and Chakraborty, N. (2011). Alignment statistics of active and passive scalar gradients in turbulent stratified flames. *Physical Review E*, 83(4):046308.
- [136] Malkeson, S. P. and Chakraborty, N. (2012). A Priori DNS Modeling of the Turbulent Scalar Fluxes for Low Damköhler Number Stratified Flames. *Combustion Science and Technology*, 184(10-11):1680–1707.
- [137] Mantel, T. and Borghi, R. (1994). A new model of premixed wrinkled flame propagation based on a scalar dissipation equation. *Combustion and Flame*, 96(4):443–457.
- [138] Marble, F. and Broadwell, J. (1977). The coherent flame model of non-premixed turbulent combustion. *Project Squid TRW-9-PU, Project Squid Headquarters, Chaffee Hall, Purdue University*.
- [139] Meneveau, C. and Poinso, T. (1991). Stretching and quenching of flamelets in premixed turbulent combustion. *Combustion and Flame*, 86(4):311–332.
- [140] Mizomoto, M., Asaka, S., Ikai, S., and Law, C. (1984). Effects of preferential diffusion on the burning intensity of curved flames. In *Symposium (International) on Combustion*, volume 20, pages 1933–1940.
- [141] Moreau, P. and Boutier, A. (1977). Laser velocimeter measurements in a turbulent flame. In *Symposium (International) on Combustion*, volume 16, pages 1747–1756. Elsevier.
- [142] Müller-Baden, E. (1905). *Bibliothek allgemeinen und praktischen Wissens für Militär-Anwärter - Zum Studium und Selbstunterricht in den ahuptsächlichen Wissenszweigen und Sprachen*. Bong.

- [143] Mura, A. and Borghi, R. (2003). Towards an extended scalar dissipation equation for turbulent premixed combustion. *Combustion and flame*, 133(1):193–196.
- [144] Mura, A., Robin, V., Champion, M., and Hasegawa, T. (2009). Small scale features of velocity and scalar fields in turbulent premixed flames. *Flow, turbulence and combustion*, 82(3):339–358.
- [145] Nishiki, S., Hasegawa, T., Borghi, R., and Himeno, R. (2002). Modeling of flame-generated turbulence based on direct numerical simulation databases. *Proceedings of the Combustion Institute*, 29(2):2017–2022.
- [146] Nishiki, S., Hasegawa, T., Borghi, R., and Himeno, R. (2006). Modelling of turbulent scalar flux in turbulent premixed flames based on DNS databases. *Combustion Theory and Modelling*, 10(1):39–55.
- [147] Nomura, K. and Elghobashi, S. (1993). The structure of inhomogeneous turbulence in variable density nonpremixed flames. *Theoretical and Computational Fluid Dynamics*, 5(4):153–175.
- [148] OECD/IEA (2014). Key world energy statistics 2014. *International Energy Agency*.
- [149] Olivelle, P. (1998). *The Early Upanishads: annotated text and translation*. Oxford University Press.
- [150] Ooi, A., Martín, J., Soria, J., and Chong, M. (1999). A study of the evolution and characteristics of the invariants of the velocity-gradient tensor in isotropic turbulence. *Journal of Fluid Mechanics*, 381:141–174.
- [151] Pelce, P. and Clavin, P. (1982). Influence of hydrodynamics and diffusion upon the stability limits of laminar premixed flames. *Journal of Fluid Mechanics*, 124:219–237.
- [152] Perry, A. E. and Chong, M. S. (1987). A description of eddying motions and flow patterns using critical-point concepts. *Annual Review of Fluid Mechanics*, 19(1):125–155.
- [153] Peters, N. (2000). *Turbulent combustion*. Cambridge university press.
- [154] Peters, N., Terhoeven, P., Chen, J. H., and Echehki, T. (1998). Statistics of flame displacement speeds from computations of 2-d unsteady methane-air flames. In *Symposium (International) on Combustion*, volume 27, pages 833–839. Elsevier.
- [155] Poinso, T., Echehki, T., and Mungal, M. (1992). A study of the laminar flame tip and implications for premixed turbulent combustion. *Combustion Science and Technology*, 81(1-3):45–73.
- [156] Poinso, T., Haworth, D., and Bruneaux, G. (1993). Direct simulation and modeling of flame-wall interaction for premixed turbulent combustion. *Combustion and Flame*, 95(1):118–132.
- [157] Poinso, T. and Veynante, D. (2005). Theoretical and numerical combustion.
- [158] Poinso, T., Veynante, D., and Candel, S. (1991). Quenching processes and premixed turbulent combustion diagrams. *Journal of Fluid Mechanics*, 228:561–606.

- [159] Poinso, T. J. and Lelef, S. (1992). Boundary conditions for direct simulations of compressible viscous flows. *Journal of computational physics*, 101(1):104–129.
- [160] Pope, S. (1988). The evolution of surfaces in turbulence. *International journal of engineering science*, 26(5):445–469.
- [161] Pope, S. B. (1985). PDF methods for turbulent reactive flows. *Progress in Energy and Combustion Science*, 11(2):119–192 0360–1285.
- [162] Pope, S. B. (2001). *Turbulent flows*. Cambridge University Press.
- [163] Renou, B., Boukhalfa, A., Puechberty, D., and Trinité, M. (1998). Effects of stretch on the local structure of preely propagating premixed low-turbulent flames with various lewis numbers. In *Symposium (International) on Combustion*, volume 27, pages 841–847. Elsevier.
- [164] Reynolds, O. (1883). An experimental investigation of the circumstances which determine whether the motion of water shall be direct or sinuous, and of the law of resistance in parallel channels. *Proceedings of the royal society of London*, 35(224-226):84–99.
- [165] Richard, S., Colin, O., Vermorel, O., Benkenida, A., Angelberger, C., and Veynante, D. (2007). Towards large eddy simulation of combustion in spark ignition engines. *Proceedings of the Combustion Institute*, 31(2):3059–3066 1540–7489.
- [166] Richardson, L. F. (2007). *Weather prediction by numerical process*. Cambridge University Press.
- [167] Rogallo, R. S. (1981). *Numerical experiments in homogeneous turbulence*. NASA Technical Memorandum B1315.
- [168] Rudy, D. H. and Strikwerda, J. C. (1980). A nonreflecting outflow boundary condition for subsonic Navier-Stokes calculations. *Journal of Computational Physics*, 36(1):55–70
- [169] Rutland, C. and Cant, R. (1994). Studying turbulence using numerical simulation databases v. In *Proceedings of the 1994 Summer Program, Center for Turbulence Research, Stanford University*, pages 75–94.
- [170] Rutland, C. and Trouvé, A. (1993). Direct simulations of premixed turbulent flames with nonunity lewis numbers. *Combustion and Flame*, 94(1):41–57.
- [171] Semenov, N. N. (1935). Chemical kinetics and chain reactions. *Journal of Chemical Education*, 12(6):298.
- [172] She, Z.-S., Jackson, E., and Orszag, S. A. (1991). Structure and dynamics of homogeneous turbulence: models and simulations. In *Proceedings of the Royal Society of London A: Mathematical, Physical and Engineering Sciences*, volume 434, pages 101–124. The Royal Society.
- [173] Siggia, E. D. (1981). Numerical study of small-scale intermittency in three-dimensional turbulence. *Journal of Fluid Mechanics*, 107:375–406.

- [174] Sivashinsky, G. I. (1983). Instabilities, pattern formation, and turbulence in flames. *Annual Review of Fluid Mechanics*, 15(1):179–199.
- [175] Smooke, M. D. and Giovangigli, V. (1991). *Premixed and nonpremixed test problem results*, pages 29–47. Springer.
- [176] Sondergaard, R., Chen, J., Soria, J., and Cantwell, B. (1991). Local topology of small scale motions in turbulent shear flows. In *8th Symposium on Turbulent Shear Flows*, volume 1, pages 16–1.
- [177] Soria, J., Sondergaard, R., Cantwell, B., Chong, M., and Perry, A. (1994). A study of the fine-scale motions of incompressible time-developing mixing layers. *Physics of Fluids (1994-present)*, 6(2):871–884.
- [178] Spalding, D. (1971). Mixing and chemical reaction in steady confined turbulent flames. In *Symposium (International) on Combustion*, volume 13, pages 649–657. Elsevier.
- [179] Spalding, D. (1996). Multi-fluid models of turbulent combustion. In *CTAC95 Biennial Conference, Melbourne, Australia, World Scientific Publishing Co*, pages 59–81. World Scientific.
- [180] Spalding, D. B. (2013). *Combustion and mass transfer: a textbook with multiple-choice exercises for engineering students*. Elsevier, Oxford; New York; Pergamon Press.
- [181] Strahle, W. (1983). Velocity-pressure gradient correlation in reactive turbulent flows. *Combustion Science and Technology*, 32(5-6):289–305.
- [182] Stumpf, D. K. (2000). *Titan II: A History of a Cold War Missile Program*. University of Arkansas Press.
- [183] Suman, S. and Girimaji, S. S. (2010). Velocity gradient invariants and local flow-field topology in compressible turbulence. *Journal of Turbulence*, (11):N2.
- [184] Sutherland, J. C. and Kennedy, C. A. (2003). Improved boundary conditions for viscous, reacting, compressible flows. *Journal of computational physics*, 191(2):502–524 0021–9991.
- [185] Swaminathan, N. and Bray, K. (2005). Effect of dilatation on scalar dissipation in turbulent premixed flames. *Combustion and flame*, 143(4):549–565.
- [186] Swaminathan, N. and Bray, K. N. C. (2011). *Turbulent premixed flames*. Cambridge University Press.
- [187] Swaminathan, N. and Grout, R. (2006). Interaction of turbulence and scalar fields in premixed flames. *Physics of Fluids*, 18(4):045102.
- [188] Tanahashi, M., Fujimura, M., and Miyauchi, T. (2000). Coherent fine-scale eddies in turbulent premixed flames. *Proceedings of the Combustion Institute*, 28(1):529–535.
- [189] Tennekes, H. and Lumley, J. L. (1972). *A first course in turbulence*. MIT press.

- [190] Thurston, R. H. (1887). *A History of the Growth of the Steam-Engine*. Number 24. Kegan Paul.
- [191] Treurniet, T., Nieuwstadt, F., and Boersma, B. (2006). Direct numerical simulation of homogeneous turbulence in combination with premixed combustion at low mach number modelled by the g -equation. *Journal of Fluid Mechanics*, 565:25–62.
- [192] Trouvé, A. and Poinso, T. (1994). The evolution equation for the flame surface density in turbulent premixed combustion. *Journal of Fluid Mechanics*, 278:1–31.
- [193] Truffin, K., Leveugle, B., Bruneaux, G., Angelo, Y., and Reveillon, J. (2012). Modeling the effect of flame-wall interaction on the wall heat flux. *ICHMT DIGITAL LIBRARY ONLINE*.
- [194] Tsien, H.-S. (1939). Two-dimensional subsonic flow of compressible fluids. *Journal of the Aeronautical Sciences*, 6(10):399–407.
- [195] Tsinober, A. (2000). *Vortex stretching versus production of strain/dissipation*. Cambridge University Press, New York, NY, USA.
- [196] Tsinober, A., Kit, E., and Dracos, T. (1992). Experimental investigation of the field of velocity gradients in turbulent flows. *Journal of Fluid Mechanics*, 242:169–192.
- [197] Tsinober, A., Shtilman, L., and Vaisburd, H. (1997). A study of properties of vortex stretching and enstrophy generation in numerical and laboratory turbulence. *Fluid Dynamics Research*, 21(6):477–494.
- [198] Tullis, S. and Cant, R. (2002). Scalar transport modeling in large eddy simulation of turbulent premixed flames. *Proceedings of the Combustion Institute*, 29(2):2097–2104 1540–7489.
- [199] Turner, S. (1972). *An introduction to combustion, concepts and applications*. McGraw-Hill, New York City.
- [200] Vervisch, L., Bidaux, E., Bray, K., and Kollmann, W. (1995a). Surface density function in premixed turbulent combustion modeling, similarities between probability density function and flame surface approaches. *Physics of Fluids (1994-present)*, 7(10):2496–2503 1070–6631.
- [201] Vervisch, L., Bidaux, E., Bray, K., and Kollmann, W. (1995b). Surface density function in premixed turbulent combustion modeling, similarities between probability density function and flame surface approaches. *Physics of Fluids*, 7(10):2496–2503.
- [202] Veynante, D., Trouvé, A., Bray, K., and Mantel, T. (1997). Gradient and counter-gradient scalar transport in turbulent premixed flames. *Journal of Fluid Mechanics*, 332:263–293.
- [203] Von Kármán, T. and Millán, G. (1953). Thermal theory of a laminar flame front near a cold wall. In *Symposium (International) on Combustion*, volume 4, pages 173–177. Elsevier.

- [204] Vosen, S., Greif, R., and Westbrook, C. (1985). Unsteady heat transfer during laminar flame quenching. In *Symposium (International) on Combustion*, volume 20, pages 75–83. Elsevier.
- [205] Wacks, D. and Chakraborty, N. (2016). Flow topology and alignments of scalar gradients and vorticity in turbulent spray flames: A direct numerical simulation analysis. *Fuel*, 184:922–947.
- [206] Wacks, D. H., Chakraborty, N., Klein, M., Arias, P. G., and Im, H. G. (2016). Flow topologies in different regimes of premixed turbulent combustion: A direct numerical simulation analysis. *Physical Review Fluids*, 1:083401.
- [207] Wang, L. and Lu, X.-Y. (2012). Flow topology in compressible turbulent boundary layer. *Journal of Fluid Mechanics*, 703:255–278.
- [208] Westbrook, C. K., Adamczyk, A. A., and Lavoie, G. A. (1981). A numerical study of laminar flame wall quenching. *Combustion and Flame*, 40:81–99.
- [209] Wiessner, P. W. (2014). Embers of society: Firelight talk among the ju/’hoansi bushmen. *Proceedings of the National Academy of Sciences*, 111(39):14027–14035.
- [210] Wilcox, D. (1998). Turbulence Modelling for CFD DCW Industries Inc. *La Canada, CA, USA*.
- [211] Wines, M. (2009). Qian xuesen, father of china’s space program, dies at 98. *New York Times*, 11(3).
- [212] Wray, A. (1990). Minimal storage time advancement schemes for spectral methods. *NASA Ames Research Center, California, Report No. MS*, 202.
- [213] Yoo, C. S., Wang, Y., Trouvé, A., and Im, H. G. (2005). Characteristic boundary conditions for direct simulations of turbulent counterflow flames. *Combustion Theory and Modelling*, 9(4):617–646.
- [214] Zeff, B. W., Lanterman, D. D., McAllister, R., Roy, R., Kostelich, E. J., and Lathrop, D. P. (2003). Measuring intense rotation and dissipation in turbulent flows. *Nature*, 421(6919):146–149.
- [215] Zhang, S. and Rutland, C. J. (1995). Premixed flame effects on turbulence and pressure-related terms. *Combustion and Flame*, 102(4):447–461.

Appendix A

List of Publications

Journal articles

The results from this thesis have been published as the following journal articles and book chapter.

1. **Lai, J.**, Chakraborty, N. “Effects of Lewis number on head on quenching of turbulent premixed flames: a Direct Numerical Simulation analysis”, *Flow Turbulence and Combustion*, 96(2):279–308, 2016.
2. **Lai, J.**, Chakraborty, N. “Statistical behavior of scalar dissipation rate in head-on quenching of turbulent premixed flames: a Direct Numerical Simulation analysis”, *Combustion Science and Technology*, 188(2):250–276, 2016.
3. **Lai, J.**, Chakraborty, N. “A priori Direct Numerical Simulation modeling of scalar dissipation rate transport in head-on quenching of turbulent premixed flames”, *Combustion Science and Technology*, 188(9):1440–1471, 2016.
4. Sellmann, J., **Lai, J.**, Kempf, A.M., Chakraborty, N. “Flame surface density based modelling of head-on quenching of turbulent premixed flames”, *Proceedings of the Combustion Institute*, 2016.
5. **Lai, J.**, Chakraborty, N. “Modeling of progress variable variance transport in head-on quenching of turbulent premixed flames: A Direct Numerical Simulation analysis”, *Combustion Science and Technology*, 188(11-12):1925–1950, 2016.
6. **Lai, J.**, Lipatnikov, A., Chakraborty, N. “Statistical behaviour of vorticity and enstrophy transport in head-on quenching of turbulent premixed flames”, *European Journal of Mechanics / B Fluids*, 2016.

7. **Lai, J.**, Moody, A., Chakraborty, N. “Turbulent kinetic energy transport in head-on quenching of turbulent premixed flames in the context of Reynolds Averaged Navier–Stokes Simulations”, *Fuel*, 199:456–477, 2017.
8. **Lai, J.**, Klein, M., Chakraborty, N. “Assessment of Algebraic Flame Surface Density Closures in the Context of Large Eddy Simulations of Head-On Quenching of Turbulent Premixed Flames”, *Combustion Science and Technology*, 189(11), 2017.
9. **Lai, J.**, Alwazzan, D., Chakraborty, N. “Turbulent scalar flux transport in head-on quenching of turbulent premixed flames: a direct numerical simulations approach to assess models for Reynolds averaged Navier Stokes simulations”, *Journal of Turbulence*, 18(11):1–34, 2017.
10. Chakraborty, N., **Lai, J.** “Direct Numerical Simulations of Premixed Turbulent Combustion: Relevance and Applications to Engineering Computational Analyses”, *In book: Modeling and Simulation of Turbulent Combustion*, pp.135-180, 2018

Conference proceedings

A number of the works have been presented at the following conferences and symposiums.

1. Lai, J., Chakraborty, N. “Effects of Lewis number on head-on quenching of turbulent premixed flame: A Direct Numerical Simulation analysis”, SPEIC-14–Towards Sustainable Combustion. 2014, Lisboa, Portugal.
2. Lai J, Chakraborty N. “Direct Numerical Simulation analysis of turbulent kinetic energy transport in head on quenching of turbulent premixed flames”, 7th European Combustion Meeting. 2015, Budapest, Hungary.
3. Lai J, Chakraborty N. “Statistical behaviour of scalar dissipation rate for head-on quenching of turbulent premixed flames: A Direct Numerical Simulation analysis”, 9th Mediterranean Combustion Symposium. 2015, Rhodes, Greece.
4. Sellmann J, Lai J, Kempf AM, Chakraborty N. “Statistical behaviour of Flame Surface Density transport in head on quenching of turbulent premixed flames: A Direct Numerical Simulation Analysis”. Clean Air 2015. 2015, Lisboa, Portugal.

-
5. Lai J, Chakraborty N. “Modelling of progress variable variance transport in head on quenching of turbulent premixed flames: A Direct Numerical Simulation analysis”. International Colloquium on the Dynamics of Explosions and Reactive Systems. 2015, Leeds, UK.
 6. Sellmann J, Lai J, Kempf AM, Chakraborty N. “Flame Surface Density based modelling of head-on quenching of turbulent premixed flames”. 36th International Combustion Symposium. 2016, Seoul, Korea.
 7. Lai, J., Klein, M., Chakraborty, N. “A priori Direct Numerical Simulation assessment of algebraic flame surface density models for turbulent flame-wall interaction in the context of Large Eddy Simulation”. 11th International ERCOFTAC Symposium on Engineering Turbulence modelling and Measurements. 2016, Sicily, Italy.
 8. Lai J, Chakraborty N. “Heat flux and flow topologies in head-on quenching of statistically planar turbulent premixed flames by isothermal inert walls”. European Combustion Meeting. 2017, Dubrovnik, Croatia.
 9. Lai J, Chakraborty N, Klein M. “Direct Numerical Simulation of head-on quenching of statistically planar methane-air flames using a detailed chemical mechanism”. 10th Mediterranean Combustion Symposium. 2017, Napoli, Italy.
 10. Lai J, Chakraborty N. “Heat flux and flow topology statistics in oblique quenching of turbulent premixed flames by isothermal inert walls”. 26th International Colloquium on Dynamics of Explosions and Reactive Systems. 2017, Boston, USA.

